Universität Bielefeld
Fakultät für Physik

Habilitationsschrift

Strong coupling methods for lattice QCD

Dr. rer. nat. Wolfgang Unger

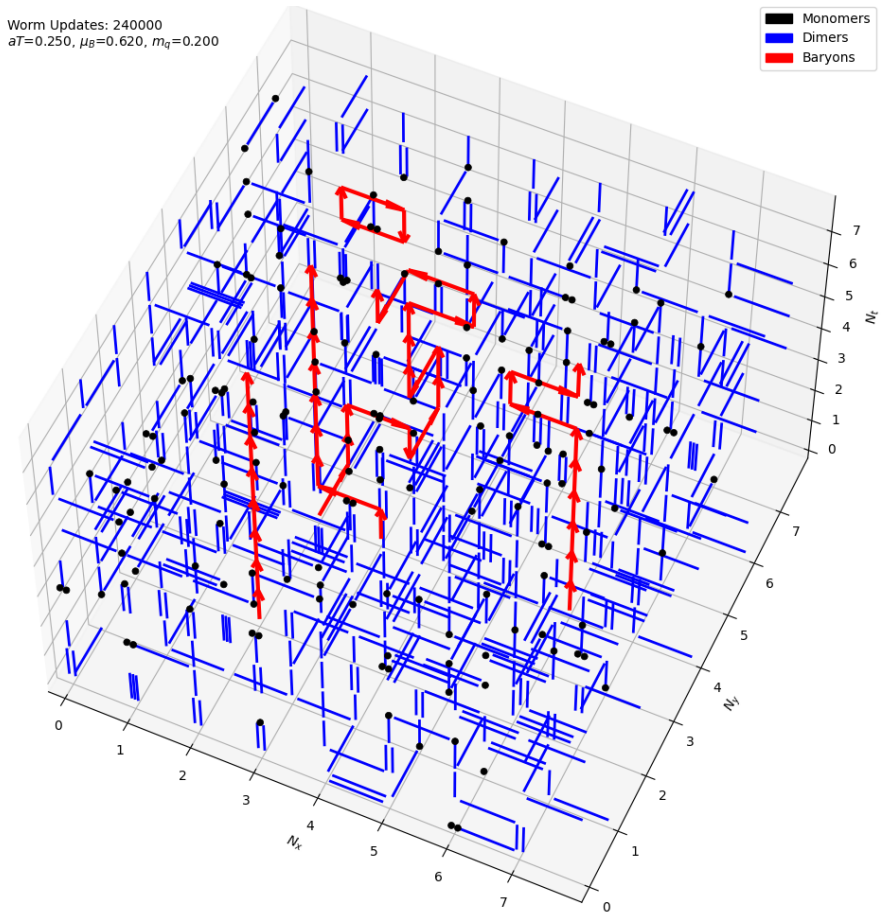

April 2021

Physics is mathematical not because we know so much about the physical world, but because we know so little: it is only its mathematical properties that we can discover.

Bertrand Russell

Abstract

Strong coupling methods for lattice QCD

Wolfgang Unger

Lattice QCD at finite baryon density suffers from the numerical finite density sign problem. Strong coupling methods, expanding in the inverse gauge coupling, give rise to alternative representations of the partition function that can make the sign problem milder. This Habilitation discusses the strong coupling methods developed by the author and colleagues to study lattice QCD at vanishing and non-vanishing baryon density. The main results summarized and covered in the attached papers are (1) chiral symmetry breaking and its restoration at zero temperature for a large number of flavors, (2) the QCD phase diagram, in particular the location of the chiral/nuclear critical endpoint, (3) bulk thermodynamics and (4) Hamiltonian formulation and Quantum Monte Carlo simulations. Most of the results were obtained via a dual formulation for lattice QCD derived from a strong coupling expansion. All results are limited to the strong coupling regime, i.e. valid on coarse lattices, where the sign problem is under control.

Gitter QCD bei endlicher Baryondichte leidet am numerischen Vorzeichenproblem. Starkkopplungsmethoden, die auf der Entwicklung der inversen Eichkopplung basieren, könne alternative Darstellungen der Zustandsfunktion ergeben, die das Vorzeichnproblem milder machen. Diese Habilitation befasst sich mit den Starkkopplungsmethoden, die vom Autor in Zusammenarbeit mit Kollegen entwickelt wurden, und fasst Resultate bei verschwindender und nicht-verschwindender Baryondichte zusammen. Die wichtigsten Resultate, die in den angehängten Publikationen veröffentlicht sind, beinhalten (1) chirale Symmetriebrechung und Restoration in Abhängigkeit von der Zahl der Flavors, (2) das QCD Phasendiagram, insbesondere die Verortung des chiralen/nuklearen kritischen Endpunkts, (3) Bulk-Thermodynamik (4) Hamiltonsche Formulierung und Quantum Monte Carlo Simulationen. Die meisten Resultate wurden mittels der dualen Darstellung der Gitter-QCD erhalten, die durch die Starkkopplungsentwicklung hergeleitet ist. Alle Resultate sind auf das Regime starker Kopplung beschränkt, also auf groben Gittern, wo das Vorzeichenproblem unter Kontrolle ist.

Preface

Quantum Chromodynamics (QCD) is the fundamental theory of the strong interactions, which confine the quarks and gluons into baryons (*e.g.* protons and neutrons) and mesons. At high temperatures similar to those in the early universe, a new state of QCD matter - the quark gluon plasma - exists. This plasma has been observed in heavy ion collision experiments at RHIC and LHC. However, it is an open question what features the phase diagram has at non-zero baryon densities, and in particular whether there exists a chiral critical endpoint.

Since QCD is non-perturbative in this regime - asymptotic freedom that allows for perturbative methods sets in at much higher energies - lattice gauge theory is the method of choice: The phenomena such as quark confinement and spontaneous chiral symmetry breaking, as well as the phase structure at non-zero temperatures and densities can be investigated only via computer simulations from first principles. The usual simulations are based on the fermion determinant. However, due to the "sign problem", no direct simulations at non-zero baryon density can be performed. Hence, also the question about the existence of the critical point can not be addressed directly.

The main objective of this Habilitation is to study QCD thermodynamics and to get insight into the full QCD phase diagram in the μ_B-T-plane, based on a dual representation of lattice QCD with staggered fermions in terms of color singlets. This is obtained by integrating out all gauge degrees of freedom in a systematic "strong coupling expansions".

The strong coupling regime is the converse of the continuum limit, where weak coupling expansions can be carried out systematically via Feynman diagrams. In the early days of lattice QCD, where supercomputers were not yet available, strong coupling and mean-field methods were developed for pure gauge theory [1]. The inclusion of dynamical fermions is much more challenging. In the limit of infinite coupling, the pure gauge sector can be neglected such that the gauge links entering in the Dirac operator factorize and can be integrated out analytically. The resulting partition function has a very mild sign problem, thus the full phase diagram can be obtained.

Now, it is important to go beyond the strong coupling limit to make qualitative statements about the phase structure away from the strong coupling limit. For this purpose, more complicated gauge integrals have to be computed which enter the gauge corrections of higher order, which are addressed in this Habilitation. Also new strategies to simulate lattice QCD in a Hamiltonian formulation via quantum Monte Carlo algorithms is summarized.

So far, this kind of simulation has been applied to so-called staggered fermions including the first order gauge corrections, but as a matter of principle the same formalism can be applied to Wilson fermions as well, and quantum Monte Carlo simulations could be performed. Both discretizations (staggered and Wilson) are very different in the limit of strong coupling, in particular concerning the realization of spin. Future research aims to compare both discretizations order by order in the strong coupling expansion such that the physical content can be isolated from the lattice artifacts.

The Habilitation has two parts: the first part is organized in five chapters, the first chapter serves as introduction to the lattice methods utilized. The second, third and fourth chapter summarize my research on lattice QCD in the strong coupling regime: the second chapter pertains the phase diagram in the strong coupling limit, whereas the third chapter summarizes the progress on the gauge corrections to the strong coupling limit. The fourth chapter summarizes the research on the Hamiltonian approach to lattice QCD which naturally arises in the continuous Euclidean time limit. The fifth chapter provides an outlook for further investigations. The second part of the Habilitation consists of the reprints of 7 peer-reviewed publications and 11 Proceedings that expand on the material.

I am grateful for the support by Philippe de Forcrand and Owe Philipsen in the last years, both had a strong influence by forming my interest in the strong coupling methods to tackle the finite density sign problem. I am indebted to Edwin Laermann, who was my PhD advisor and continued to be my mentor until his sudden death. I also thank my colleagues Christian Schmidt, Olaf Kaczmarek and Frithjof Karsch for their support within the lattice group in Bielefeld. I also thank my former PhD students Giuseppe Gagliardi, Marc Klegrewe and my former Postdoc Jangho Kim with whom I carried out the research program summarized here.

Numerical simulations have been carried out on the BRUTUS cluster at ETH Zürich, at the Goethe Center for Scientific Computing in Frankfurt, and at the Paderborn Center for Parallel Computing (PC^2). This work is supported by the Deutsche Forschungsgemeinschaft (DFG) through the Emmy Noether Program under Grant No. UN 370/1 and through the CRC-TR 211 "Strong-interaction matter under extreme conditions," Project No. 315477589 TRR 211.

My very deepest thanks goes to my family: my wife Sabine who supported me greatly in my scientific career, and my son Jonathan, who always cheers me up.

Wolfgang Unger, Bielefeld, April 2021

Contents

Abstract iii

Preface iv

1 Introduction: Lattice QCD in the strong coupling regime 1
- 1.1 The QCD phase diagram . . . 1
- 1.2 Lattice QCD at finite temperature and baryon density . . . 3
  - 1.2.1 Setup: Staggered fermions and Wilson gauge action . . . 4
  - 1.2.2 Temperature and chemical potential on the lattice . . . 5
  - 1.2.3 Finite density sign problem . . . 6
  - 1.2.4 Lattice gauge theory in the strong coupling regime . . . 9
- 1.3 The dual representation of lattice QCD . . . 10
  - 1.3.1 Basic idea . . . 11
  - 1.3.2 Link integration . . . 12
  - 1.3.3 Grassmann integration . . . 13
  - 1.3.4 Dual partition function . . . 13
- 1.4 Monte Carlo methods for the dual representation . . . 15
  - 1.4.1 Worm algorithm . . . 16
  - 1.4.2 Remarks on the software development . . . 17

2 The phase diagram in the strong coupling limit 19
- 2.1 Many-flavored QCD and conformality . . . 19
- 2.2 Combinatorial identities . . . 21
- 2.3 Anisotropic lattices . . . 22
- 2.4 Thermodynamic observables and phase diagram . . . 25
- 2.5 Equation of state and nuclear potential at strong coupling . . . 28

3 Phase Diagram in the strong coupling regime, $\beta > 0$ 33
- 3.1 Reweighting approach . . . 33
- 3.2 Direct sampling based on plaquette occupation numbers . . . 37
- 3.3 Tensor network representation . . . 40

4 Hamiltonian formulation of strong coupling lattice QCD 45
- 4.1 The Euclidean continuous time limit . . . 45
- 4.2 The Quantum Hamiltonian . . . 48
- 4.3 Grand-canonical and canonical phase diagram . . . 50
- 4.4 Meson pole masses . . . 56

5 Summary and Outlook **59**
5.1 Summary . . . 59
5.2 Future research . . . 61

References **63**
Articles reviewed in Chapter 2 . . . 63
Articles reviewed in Chapter 3 . . . 64
Articles reviewed in Chapter 4 . . . 65
Further References . . . 65

A Reprint of articles reviewed in Chapter 2 **77**
A.1 Conformality in many-flavour lattice QCD at strongcoupling [A1] . . . 77
A.2 Combinatorics of Lattice QCD at Strong Coupling [A2] . . . 94
A.3 Thermodynamics of strongly-coupled lattice QCD in the chiral limit [A3] 102
A.4 Strong-coupling lattice QCD on anisotropic lattice [A4] . . . 110
A.5 Thermodynamics at strong coupling on anisotropic lattices [A5] . . . 121
A.6 Quark Mass Dependence of the QCD Critical End Point in the Strong Coupling Limit [A6] . . . 129

B Reprint of articles reviewed in Chapter 3 **137**
B.1 The Phase Diagram of Lattice QCD in the Strong Coupling Limit and Away from It [B1] . . . 137
B.2 Lattice QCD Phase Diagram In and Away from the Strong Coupling Limit [B2] . . . 148
B.3 QCD phase diagram from the lattice at strong coupling [B3] . . . 156
B.4 Dual Formulation and Phase Diagram of Lattice QCD in the Strong Coupling Regime [B4] . . . 166
B.5 On the β- and quark mass dependence of the nuclear transition in the strong coupling regime [B5] . . . 182
B.6 Gauge Corrections to Strong Coupling Lattice QCD on Anisotropic Lattices [B6] . . . 190
B.7 Towards a Dual Representation of Lattice QCD [B7] . . . 198
B.8 New dual representation for staggered lattice QCD [B8] . . . 206

C Reprint of articles reviewed in Chapter 4 **227**
C.1 Continuous Time Monte Carlo for Lattice QCD in the Strong Coupling Limit [C1] . . . 227
C.2 Strong coupling lattice QCD in the continuous time limit [C2] . . . 235
C.3 New algorithms and new results for strong coupling LQCD [C3] . . . 271
C.4 Temporal Correlators in the Continuous Time Formulation of Strong Coupling Lattice QCD [C4] . . . 279

Chapter 1

Introduction: Lattice QCD in the strong coupling regime

1.1 The QCD phase diagram

QCD at finite temperature and baryon density applies to various phenomena, such as the early universe, heavy ion collisions and neutron stars. Most of the work described below is motivated by the QCD phase diagram. I will shortly outline the historic developments that led to present-day knowledge on the phase diagram.

The first considerations that there should be a limiting temperature at which bound states of hadronic matter cease to exist predate the formulation of QCD: in the 1960s Hagedorn introduced a temperature T_H above which hadronic matter is no longer stable, as an exponential growth in the density of states occurs [2] . After QCD was established as the fundamental theory for strong interactions [3] and asymptotic freedom was proven [4,5], it was conjectured that there should be a phase transition from confined hadronic matter to a new state of matter of quasi-free quarks [6,7], termed the quark-gluon plasma (QGP).

A criterion for the formation of a QGP was formulated by Matsui and Satz [8]: the J/Ψ, which is the lightest $\bar{c}c$ bound state, will likely dissolve above the transition temperature to form open charm mesons after hadronization. The formation of the quark-gluon plasma in heavy ion collisions has been under investigation at various experiments: first at the Super Proton Synchrotron (SPS) at CERN, at the Relativistic Heavy Ion Colllider (RHIC) at the Brookhaven National Laboratory and the Large Hadron Collider, CERN. Future heavy ion experiments will be carried out at J-PARC (Ibaraki, Japan) and at NICA (Dubna, Russia) and FAIR (Darmstadt, Germany), which are both currently

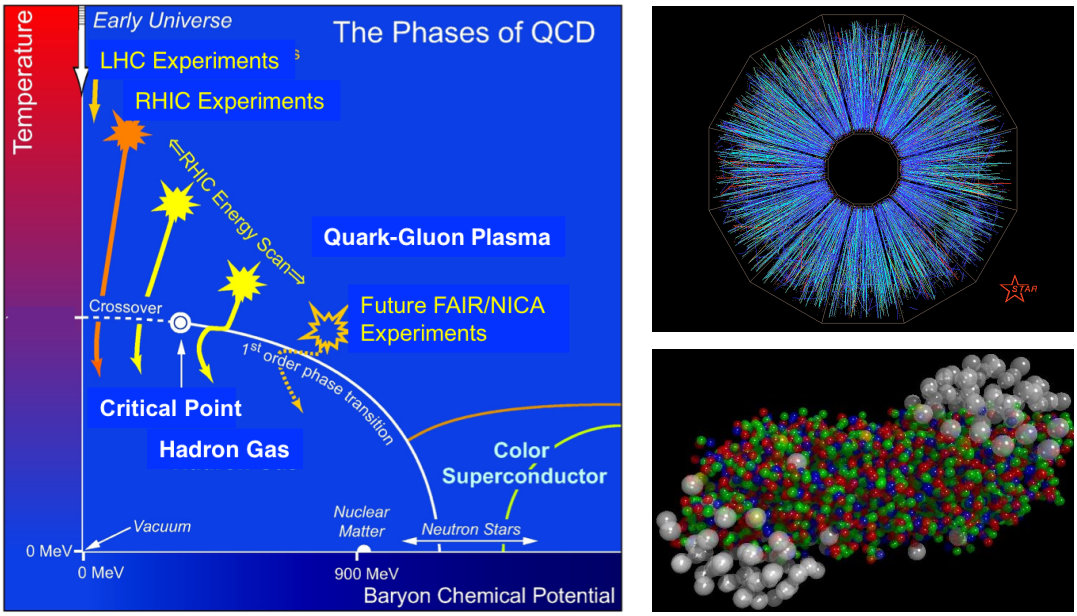

FIGURE 1.1: Left: The conjecture QCD phase diagram. *Right top:* Au+Au collision in the STAR detector at the Relativistic Heavy Ion Collider. *Right bottom:* Illustration of a heavy ion collision, from the CERN press release at Feb. 10, 2000.

under construction. They will aim for lower temperatures and higher densities to search for a possible critical end-point.

The first announcement of the QGP ("a new state of matter") was in 2000 from SPS [9] in Pb-Pb collisions, followed by the discovery of the QGP at the STAR collaboration at RHIC in 2005 [10] in Au-Au collisions (see Fig. 1.1, top right). Also the ALICE collaboration at LHC created the QGP in Pb-Pb collisions and found that it behaves as a perfect fluid [11]. An estimate of the transition temperature could be obtained from the chemical freezeout, estimated to happen at $T_{\mathrm{c.f}} = 156(2)$ MeV [12].

An estimate of the deconfinement temperature at vanishing baryon density was provided by the MIT bag model, which considers hadrons as bags [13] with a constant energy density B, the bag constant. By equating the pressure of the exterior (physical QCD vacuum) with the pressure of the interior region, one obtains roughly $T_{\mathrm{dec}} = 144$ MeV for $N_f = 2$, with a large uncertainty due to the poor estimate of B. In the same year, Kenneth Wilson invented the lattice discretization of QCD (LQCD) to show that it is a confining theory [14], with the linear confinement evident in the quark potential parameterized by the string tension. However, only Monte Carlo simulations could give evidence that QCD is indeed confining also beyond the strong coupling regime. Monte Carlo simulations at finite temperature [15] saw many theoretical refinements and algorithmic improvements, and profited from an exponential increase in computing power from a few 100 Megaflop to about 100 Petaflop nowadays. For physical quark masses,

lattice results provided strong evidence that the deconfinment and chiral transition coincide and are a crossover rather than a true phase transition. The last decade saw a lot of progress towards the continuum limit for physical quark masses, and nowadays the two major collaborations, HotQCD and the BMW [16,17], agree on the chiral transition temperature $T_c = 154(9)$ MeV.

The situation at non-zero baryon density is much less clear, both experimentally and from the lattice. We know that there is a first order transition from the hadron gas to nuclear matter at a value close to the baryon mass, $\mu_B \sim m_B$, and that this transition is of a liquid-gas type with a nuclear critical end-point at around $T_c^{\mathrm{Nucl}} \sim 18$ MeV, $\mu_{B,c}^{\mathrm{Nucl}} \sim 900$ MeV [18]. More exotic phases of QCD matter are conjectured at large chemical potential, which may be relevant for the physics of neutron stars: the quaryonic phase [19] and at even higher densities a color superconducting phase [20]. The fluctuations at the vicinity of a possible chiral critical endpoint [21] could provide a signal that is sought for at heavy ion collision experiments (in particular with the energy beam scans at RHIC).

Lattice QCD could provide the curvature of the phase boundary, i.e. the prefactor of the term $(\mu_B/T_c)^2$, which has been determined [22,23,24] to $\kappa_2 = 0.016(6)$. However, direct Monte Carlo simulations at finite chemical potential are hindered by the finite density sign problem (see Sec.1.2.3). The phase transition for larger values of the chemical potential is still out of reach, in particular it is still not known whether there exists a chiral critical end-point and a first order transition extending to low temperatures.

The work discussed in the subsequent chapters unravels the structure of the phase diagram on the lattice in a regime where the sign problem is under control and the chiral and nuclear transition can be studied from first principles, with the caveat that these results are only valid for coarse lattices. The strong coupling methods developed in the attached publications have the potential to make the connection to the continuum.

1.2 Lattice QCD at finite temperature and baryon density

Many important phenomena such as the hadron spectrum, chiral symmetry breaking, or the topological features of the QCD vacuum are within the non-perturbative regime of QCD. This is still the case at temperatures around and at the chiral and deconfinement phase transition of about 155 MeV and above up to several GeV, as the gauge coupling is still too large to apply perturbative methods based on asymptotic freedom.

Hence it is necessary to use non-perturbative tools to study QCD thermodynamics such as the QCD phase diagram and the equation of state. The only non-perturbative

gauge invariant regulator is the lattice: fermions and gluons are distributed on a 3+1 dimensional hypercubic lattice according to the Dirac operator and the gauge action.

Due to the correspondence of the path integral in Euclidean time with the partition sum in statistical mechanics

$$Z = \int DU\, D\bar{\psi}\, D\psi\, e^{-S_g - S_f} \qquad \longleftrightarrow \qquad Z = \mathrm{Tr}\left(e^{-\beta\hat{\mathcal{H}}}\right), \tag{1.1}$$

Monte Carlo simulations are applicable to study lattice QCD.

1.2.1 Setup: Staggered fermions and Wilson gauge action

All lattice simulations pursued in the publications and discussed in the subsequent chapters are based on staggered fermions, and for those publications that are concerned with the incorporation of the gauge action, the Wilson gauge action has been used. This lattice discretization is unimproved, which is necessary to derive the dual representation (see Sec. 1.3).

Since staggered fermions are a particular solution to the fermion doubling problem [25], by diagonalizing the Dirac matrices γ_μ and by introducing a 2^d hypercubic sublattice on which spin is encoded in so-called staggered phases η_μ [26]. In four dimensions we have 4 taste partners per flavor, and the 16 degrees of freedom in a 4-dimensional hypercubic cell corresponds to 4×4 degrees of freedom in the spin$\otimes$taste basis. We do not apply rooting, such that one flavor at strong coupling corresponds to 4 flavors in the continuum. We always consider mass-degenerated flavors. The partition function for staggered fermions is:

$$\begin{aligned}
\mathcal{Z} &= \int [\mathcal{D}\bar{\chi}\chi]\, e^{-2\hat{m}_q \bar{\chi}_x \chi_x} \left[\prod_\ell \int_{\mathrm{SU}(N)} DU_\ell\right] e^{-S_g[U] - D_f[\bar{\chi},\chi,U]}, \\
S_g[U] &= -\frac{\beta}{2N} \sum_{x,\mu<\nu} \mathrm{Tr}\; U_{x,\mu} U_{x+\mu,\nu} U^\dagger_{x+\nu,\mu} U^\dagger_{x,\nu} + h.c., \\
D_f[\bar{\chi},\chi,U] &= \sum_{x,\mu} \eta_\mu(x) \left(e^{+\mu_q \delta_{\mu,0}} \bar{\chi}_x U_{x,\mu} \chi_{x+\mu} - e^{-\mu_q \delta_{\mu,0}} \bar{\chi}_{x+\mu} U^\dagger_{x,\mu} \chi_x\right).
\end{aligned} \tag{1.2}$$

The gauge links $U_\mu(x)$ are SU(N) elements, DU is the Haar measure and S_g, D_f are respectively the plaquette gauge action and the massless staggered Dirac operator.

Staggered fermions have the advantage that chiral symmetry is not completely broken by lattice artifacts as for Wilson fermions. In the chiral limit the lattice action is

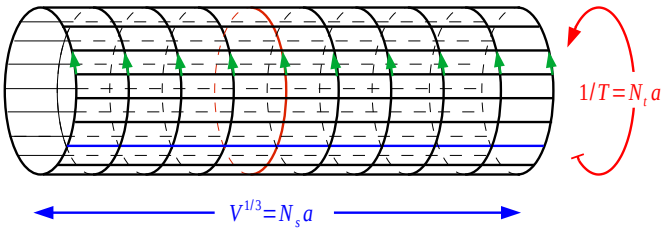

FIGURE 1.2: The lattice discretization at finite temperature.

invariant under the symmetry group $U_B(1) \times U_{55}(1)$:

$$\chi(x) \mapsto e^{i\theta_B + i\epsilon(x)\theta_{55}}\chi(x), \qquad \epsilon(x) = (-1)^{\sum_\mu x_\mu} \tag{1.3}$$

which is due to the even-odd decomposition of the bipartite lattice for staggered fermions, i.e. even and odd sites can be transformed independently. The symmetry $e^{i\theta_B} \in U_B(1)$ corresponds to baryon conservation and $e^{i\theta_{55}} \in U(1)_{55}$ is a subgroup of the full $SU(4)_L \times SU(4)_R$ chiral symmetry for unrooted staggered fermions. In the spin-taste basis this corresponds to the channel $\gamma_5 \otimes \xi_5$. At finite quark mass $U(1)_{55}$ is explicitly broken.

1.2.2 Temperature and chemical potential on the lattice

The partition function of QCD at finite temperature and density is studied via the partition function

$$\begin{aligned} Z(V,T,\mu_q) &= \mathrm{Tr}_V[e^{-(\hat{\mathcal{H}}-\mu_q\hat{N})/T}] = \int DAD\psi D\bar{\psi}e^{-S_E}, \\ S_E = (V,T,\mu_q) &= \int_0^{1/T} dx_0 \int_V d^3x \mathcal{L}_E(A,\psi,\bar{\psi},\mu_q) \end{aligned} \tag{1.4}$$

Finite temperature and density requires specific conditions in Euclidean time: fermions are subject to anti-periodic boundary conditions in the temporal direction to incorporate Fermi statistics, the temperature T is given by the inverse temporal extent and fermions that loop around in the temporal direction couple to the quark chemical potential μ_q. On the lattice, where $T = (N_t a(\beta))^{-1}$ and $V = (aN_\sigma)^3$ (see Fig. 1.2), the temporal gauge links pick up the chemical potential [27] (but also see [28] for alternative assignments):

$$U_0(n) \mapsto e^{a\mu_q}U_0(n), \qquad U_0(n)^\dagger \mapsto e^{-a\mu_q}U_0^\dagger(n). \tag{1.5}$$

For details on thermodynamics on the lattice see the review [29]. In the strong coupling regime, where we usually fix β, the temperature cannot be varied with the lattice spacing.

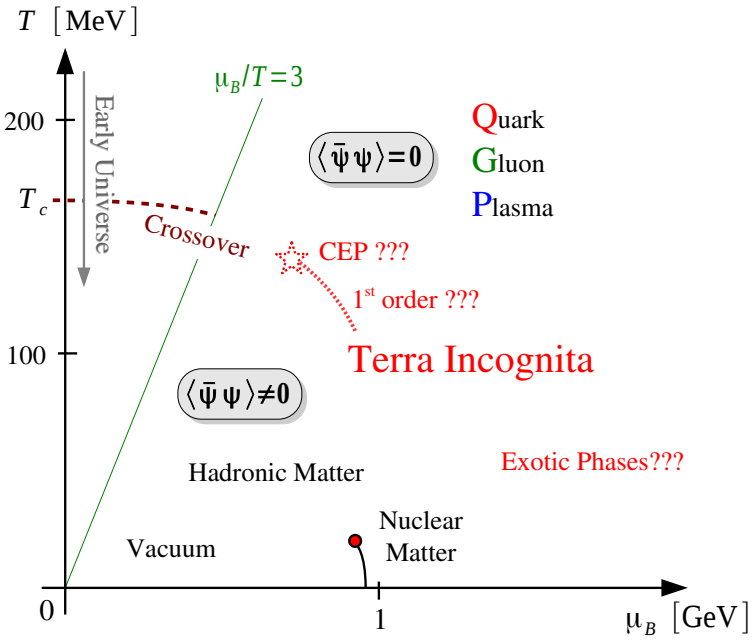

FIGURE 1.3: Limitations on our knowledge about the phase diagram due to the sign problem.

Instead, we consider anisotropic lattices and vary the ratio $\xi = \frac{a}{a_t}$ indirectly via the bare anisotropy γ. This is discussed in detail in Sec. 2.3.

1.2.3 Finite density sign problem

The finite density sign problem is a long-standing problem, and many approaches have been attempted. Due to this challenge in numerical simulations, only little is known about the QCD phase diagram from first principles, see Fig. 1.3. I will shortly review the numerical sign problem in lattice QCD and the main approaches to circumvent it.

The standard approach of lattice QCD is based on the fermion determinant $\det D$: the Gaussian integral over the Grassmann-valued fermions is integrated out. This approach allows to evaluate observables via hybrid Monte Carlo (HMC) [30], which consists of molecular dynamics followed by a Metropolis accept/reject step. Monte Carlo simulations at finite baryon density are however hindered by the finite density sign problem: a non-zero chemical potential renders the fermion determinant complex and prohibits a probability interpretation of the corresponding weight in the partition function. To see this, consider the Dirac operator which fulfills γ_5-Hermiticity at zero-chemical potential, but it becomes broken at non-zero μ due to the imbalance given in Eq. (1.5):

$$\gamma_5 D(\mu)\gamma_5 = D(-\mu)^\dagger \qquad \rightarrow \qquad \det D(\mu) = \det{}^* D(-\mu), \tag{1.6}$$

which renders the fermion determinant complex. Without addressing the sign problem, it is exponentially difficult to study finite density QCD. To see this, consider a partition function with complex weights $w(C)$ on a given configuration C:

$$Z = \sum_{\{C\}} w(C), \qquad Z_{||} = \sum_{\{C\}} |w(C)|, \qquad w(C) = |w(C)|e^{i\phi(C)} \tag{1.7}$$

with $Z_{||}$ the so-called phase-quenched partition function which neglects the complex phase. A measure for the severity of the numerical sign problem is then given by the difference of the free energy density Δf between the full theory and the quenched theory:

$$\langle \sigma \rangle \equiv \left\langle e^{i\phi} \right\rangle_{||} = e^{-\frac{V}{T}\Delta f}, \qquad \Delta f = f - f_{||}, \qquad \langle \mathcal{O} \rangle = \frac{\langle \mathcal{O}\sigma \rangle_{||}}{\langle \sigma \rangle_{||}}. \tag{1.8}$$

The sign problem is a particular signal-to-noise problem: the observable $\langle \mathcal{O} \rangle$ will be drowned in the noise as $\langle \sigma \rangle \to 0$ as the thermodynamic limit $V \to \infty$ is approached.

Sign problems occur in many field theories and condensed matter systems. A general solution to the sign problem for any theory cannot be found [31], but since the sign problem is representation dependent, for a particular system such as lattice QCD a solution to the sign problem may be found, or at least Δf can be made mild enough to study finite density QCD for sufficiently large volumes.

Many strategies are available to circumvent the sign problem for small values of the chemical potential. The established indirect methods are: (1) The Taylor expansion method [32], which computes Taylor coefficients c_{2n} in a series in $(\mu_B/T)^{2n}$; (2) Simulations at imaginary chemical potential [33, 34] which do not suffer from the sign problem and can be analytically continued towards real chemical potential [35]. (3) The reweighting method [36] which computes observables reweighted to non-zero density and has led to a first estimate of the position of the critical endpoint on a coarse lattice [37]. In general, however, reweighting may suffer from the lack of overlap between the sampled $\mu_B = 0$ ensemble and the target ensemble at $\mu_B > 0$.

There are also direct methods that allow to simulate lattice QCD or related models directly at non-zero chemical potential and are not limited to small μ_B/T. They can be roughly classified in three categories: (a) complexified lattice QCD, (b) world-line methods (which include the strong coupling methods), and (c) alternatives to Monte Carlo:

(a) Complexification methods such as the complex Langevin approach or the Lefschetz thimble approach are based on the idea to enlarge the configuration space to

complex values. The complex Langevin approach is based on a stochastic quantization [38, 39] and explores the full complexified parameter space. Since the revival of this idea [40] and after its application to lattice QCD [41], there have been plenty of results and refinements [42]. However, the method suffers from a possible convergence to the wrong limit [43], and the situation in QCD is still not settled, in particular in the confined phase. As it stands, complex Langevin results require crosschecks from alternative methods. A second rather recent approach is the Lefschetz thimble method [44] which is a high-dimensional analogue of the saddle point method, obtained by deforming the contour of integration into a homologically equivalent complex manifolds on which the sign is constant. This method has only been applied to low-dimensional QCD-like models [45, 46] but Monte Carlo sampling remains challenging as soon as more than one thimble contributes [47], which is already the case in 1-dimensional QCD.

(b) World-line methods include dual representations (discussed in detail in the next section) and other effective theories based on rewriting the partition function in a different basis. Examples of the latter are the meron cluster [48] and fermion bag approach [49]; the 3-dim. effective theory [50, 51], which is a joint strong coupling and hopping parameter expansion that is expressed in terms of Polyakov loops after integrating out the spatial gauge links; decoupling the gauge links using Hubbard-Stratonovich transformations [52]; or "Induced QCD" based on an alternative discretization of Yang Mills Theory [53, 54].

(c) An example of numerical simulations without Monte Carlo is the Wang-Landau method [55] or as its refinement the density of states method [56], which sample histograms from which thermodynamic observables can be determined.

All these approaches have their shortcomings, and a method that allows to simulate lattice QCD at finite density fully has not yet been established. There are other QCD-like theories that are sign-problem free such as 2-color "QCD" [57] or QCD with a finite isospin chemical potential $\mu_I = \mu_d - \mu_u$ [58, 59], which actually corresponds to the phase-quenched situation: $\det[D(\mu_u)]\det[D(\mu_d)] = |\det[D(\mu_u)]\det[D(\mu_d)]|$. It should be noted that since the sign problem only occurs in numerical simulations, any analytic treatment has no sign problem. This is particularly the case within the 3-dim. effective theory in terms of an SU(3) spin model, which can be studied via linked cluster expansion and Padé approximants to capture phase transitions [60].

Most of the work discussed in the subsequent chapters utilze the dual representation which will be introduced in the next section. Dual representations can be combined with the approaches discussed above, e.g. one can consider reweighting (see Sec. 3.1),

Taylor expansion, imaginary chemical potential and the Wang-Landau method based on the dual variables, all these methods discussed in Sec. 4.3. This allows to extend strong coupling lattice QCD in various directions and/or provides additional crosschecks with the aforementioned methods.

1.2.4 Lattice gauge theory in the strong coupling regime

Strong coupling expansions (SCE) may give rise to dual representations as discussed in Sec. 1.3 to solve the finite density sign problem.

The strong coupling expansion of pure Yang-Mills theory has a long history [61,62,63] and has been carried out in a character expansion, with $\chi_r(U) = \sum_\alpha D^r_{\alpha\alpha}(U)$ the character of an irreducible representation r. The characters are constant on a conjugacy class, e.g. for SU(3):

$$U = \mathrm{diag}(e^{i\theta_1}, e^{i\theta_2}, e^{-i(\theta_1+\theta_2)}), \qquad \chi_3(\theta_1,\theta_2) = e^{i\theta_1} + e^{i\theta_2} + e^{-i(\theta_1+\theta_2)}, \tag{1.9}$$

with χ_3 the character of the fundamental representation and higher dimensional irreps obtained from product representations. Identities typically used to integrate out the gauge links are based on the invariance of the Haar measure, $DU = DU^{-1}$ and $D(UV) = D(VU)$ for all V, and the orthogonality/completeness relations for characters:

$$\int DU\, \chi_r(U)\chi_s^*(U) = \delta_{rs}, \quad \sum_r d_r \chi_r(UV^{-1}) = \delta(U,V),$$
$$\int DU \chi_r(UV_1)\chi_s(U^{-1}V_2) = d_r^{-1}\delta_{rs}\chi_r(V_1V_2). \tag{1.10}$$

Any class function f can be expanded in characters, with f_r its "Fourier"-coefficients:

$$f(U) = \sum_r \chi_r(U) f_r, \qquad f_r = \int DU\, \chi_r^*(U) f(U).$$

An important example of a class functions is the Boltzmann weight, expanded in $\beta = \frac{2N_c}{g^2}$:

$$e^{\beta\chi_f(U)} = \sum_r \tilde{\beta}_r \chi_r(U), \qquad \tilde{\beta}_r = \int dU \chi_r^*(U) e^{\beta\chi(U)},$$
$$e^{\beta S} = \prod_p e^{\beta\chi(U_p)} = \prod_p \left[1 + \beta\chi(U_p) + \frac{\beta^2}{2}\chi^2(U_p) + \ldots\right] \tag{1.11}$$

with $\tilde{\beta}_r$ the character coefficients and $0 \le \beta_r \equiv \frac{\tilde{\beta}_r}{d_r\tilde{\beta}_0} \le 1$ the normalized character coefficients. The fundamental normalized character coefficient is $u(\beta) \equiv \beta_f$. Every term

in Eq. (1.11) can be integrated over $U_\ell \equiv U_\mu(x)$, which generates a series expansion of the partition function Z and observables derived from Z. In a character expansion, each plaquette appears at most once, which decouples geometric counting from group-theoretic factors. The strong coupling expansion has finite radius of convergence, even in a finite volume. Consequences are exponential clustering and the area law of the Wilson loop. It should be stressed that these limitations pertain to analytic SCE, but not necessarily for Monte Carlo simulations based on an all-order expansion. [64]

The strong coupling regime of lattice gauge theories may have different properties than the weak coupling regime. Consider for example the pure gauge theories (no fermions) with gauge groups $\mathbb{Z}_2$, U(1), U(2), U(3), SU(2), SU(3) at zero temperature, which is extensively discussed in [1]. Pure gauge theory in two dimensions is trivial, as link integration can be interchanged with plaquette integration,

$$Z = \int \prod_\ell DU_\ell \, e^{\sum_p \beta\chi(U_p)} = \int \prod_p DU_p \, e^{\sum_p \beta\chi(U_p)} = \left(\int DU \, e^{\sum_p \beta\chi(U)} \right)^N ,$$
$$\langle \chi_r(U_C) \rangle = Z^{-1} \int \prod_p DU_p \, \chi_r(U_{p_1} U_{p_1'} \dots U_{p_2} \dots) e^{\beta S} = d_r \beta_r^A = d_r e^{A \ln \beta_r}, \qquad (1.12)$$

and confinement prevails for all values of the gauge coupling: the Wilson loop of contour C and area A in representation r fulfills the area law. In three dimensions, $\mathbb{Z}_2$ gauge theory is identical to the Ising model and has a transition at $\beta = 0.76$ [65], whereas for all other gauge groups there is no transition and it remains confining. In four dimensions, whether there is a transition depends on the gauge group: $\mathbb{Z}_2$ has a 1^{st} order transition at $\beta = 0.44$, U(1) has a 1^{st} order transition to the Coulomb phase at $\beta = 0.99$, U(2) and U(3) have a first order transition, and SU(2), SU(3) have most likely no transition but are always confining, with a crossover near $\beta = 2.2$ for SU(2), $\beta = 5.6$ for SU(3). In higher dimensions, for all gauge groups the transition is of 1^{st} order.

Character expansions with matter fields have been established for Wilson fermions with heavy quarks [66,67,50,51]. In contrast, a dual representation based on the strong coupling expansion with staggered fermions is valid for any quark mass, but cannot be formulated yet via a character expansion (but see Sec. 5.2 for an outlook).

1.3 The dual representation of lattice QCD

I will shortly review dual representations in general and will then specify to the dualization of strong coupling lattice QCD with staggered fermions. Generalizations of this formulation derived in my work are addressed in the subsequent Chap. 2,3,4.

1.3.1 Basic idea

The idea of dual representations is old, and in the last decade, many different sign problems in spin models and lattice field theories have been solved in this way. Some of the hallmarks in the context of spin models are the O(N) and CP($N-1$) models [64,68,69], and in the context of lattice field theories are the charged scalar ϕ^4 theory [70], the Abelian gauge-Higgs model [71,72], the SU(2) principle chiral model [73] and scalar QCD [74].

The characteristic feature of dual representations is that the original degrees of freedom are integrated out by introducing discrete variables that encode nearest neighbour interaction, e.g. so-called bond variables. These are based on a high temperature or strong coupling expansion [75,76] or similar Taylor expansions, and can be expressed in terms of oriented fluxes and/or unoriented occupation numbers (usually called monomers and dimers). A dual representation is then oftentimes called a world-line representation, or a dimerization, or is a combination of both. An important feature is that the original symmetries of the system are translated into constraints such as flux conservation or restrictions on the allowed occupation numbers.

Typically these constraints are central in Monte Carlo simulations such as in the worm algorithm, or generalizations thereof, see Sec. 1.4.1. Dual representations are in general not unique: a model can have several dual representations which may have different residual sign problems. In some cases, a dual representations can introduce a sign problem that did not exist in the original formulation. An important example is the lattice Schwinger model at finite mass. Its dual representation is only sign problem-free in the massless case [77,78].

The strong coupling methods to be discussed date back to the early 1980s and were first studied via mean-field theory in a $1/d$ expansion [79,80,81]. After an exact mapping of strong coupling LQCD to a dimer system was found [82] (MDP for monomer-dimer-polymer), it was also studied via Monte Carlo [82,83,84,85]. The mean-field theory was further refined (in the strong coupling limit [86,87] and beyond strong coupling [88,89]) and also the Monte Carlo simulations have been improved drastically [90,91] due to the applicability of the worm algorithm, see Sec. 1.4.1.

I will further review the basic steps that lead to the partition function of the dual representation of lattice QCD in the strong coupling limit, which was already derived in [82]. In contrast to the standard formulation, the order of integration is interchanged: First, the gauge links are integrated out, thereafter the Grassmann valued fermion fields.

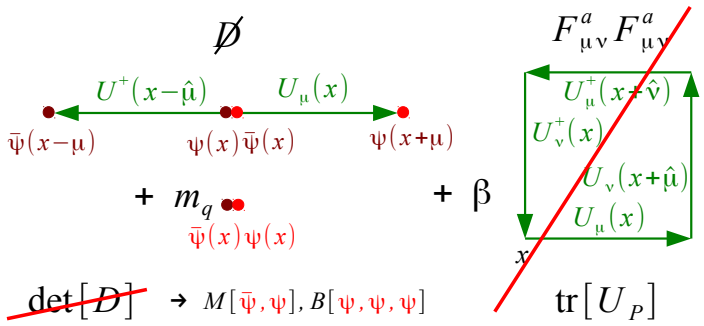

FIGURE 1.4: The strong coupling limit $\beta = 0$ only contains the Dirac operator, not the Wilson gauge action. Instead of the fermion determinant, the partition function is expressed in terms of hadronic degrees of freedom.

1.3.2 Link integration

Here I discuss the - by now classical - dual representation of staggered strong coupling lattice QCD first derived in [82] which also serves as a starting point for all further developments presented in the subsequent chapters. The formulation presented here is valid for gauge groups U(N_c) or SU(N_c) to see the general structure with respect to the number of colors.

In the strong coupling limit $g \to \infty$, the lattice gauge coupling $\beta = \frac{2N_c}{g^2} = 0$, hence the Wilson plaquette action is absent as illustrated in Fig. 1.4. As a result of this limit, link integration factorizes:

$$Z = \int \prod_x \left(d\chi_x d\bar{\chi}_x e^{2am_q \bar{\chi}_x \chi_x} \prod_\nu \left(dU_\nu(x) e^{\eta_\nu(x)(\bar{\chi}_x U_\nu(x) \chi_{x+\hat{\nu}} - \bar{\chi}_{x+\hat{\nu}} U^\dagger_\nu(x) \chi_x)} \right) \right) \tag{1.13}$$

and the gauge links $U \equiv U_\nu(x)$ can be integrated out systematically to yield invariants in the fermion fields $\mathcal{M}_{ij} = \eta_\nu(x)\bar{\chi}^j_{x+\hat{\nu}}\chi_{i,x}$:

$$\mathcal{J}_0(\mathcal{M},\mathcal{M}^\dagger) = \int_G dU e^{\mathrm{tr}[U\mathcal{M}^\dagger + \mathcal{M}U^\dagger]} = \sum_{k=0}^{N_c} \left\{ \frac{(N_c-k)!}{N_c!k!} \left((\eta_\nu(x))^2 \bar{\chi}_x \chi_x \bar{\chi}_{x+\hat{\mu}} \chi_{x+\hat{\mu}} \right)^k \right\}$$
$$+ \frac{\kappa}{N_c!} \left\{ (\rho_\nu(x)\bar{\chi}_x\chi_{x+\hat{\nu}})^{N_c} + (-\rho_\nu(x)\bar{\chi}_{x+\hat{\nu}}\chi_x)^{N_c} \right\},$$
$$\text{with} \quad \kappa = \begin{cases} 0 & \mathrm{U}(N_c) \\ 1 & \mathrm{SU}(N_c) \end{cases} \quad \text{and} \quad \rho_\nu(x) = \eta_\nu(x) = \begin{cases} e^{\pm a_t \mu} & \nu = 0 \\ 1 & \text{else} \end{cases}. \tag{1.14}$$

The invariant integration required for the first equation was derived in [92] by employing the cofactor (as $U^{-1} = U^\dagger$). Gauge integrals required for the gauge corrections to the strong coupling limit will be discussed in Sec. 3.1.

1.3.3 Grassmann integration

It remains to integrate out the staggered fermions $\chi_{i,x}\ \bar{\chi}^i_x$ within Eq. (1.14). Due to the anti-commuting nature of the Grassmann variables, appropriate reordering is necessary:

$$\mathcal{J}_0(\mathcal{M},\mathcal{M}^\dagger) = \sum_{k=0}^{N_\mathrm{c}} \left\{ \frac{(N_\mathrm{c}-k)!}{N_\mathrm{c}!k!} \left((\eta_\nu(x))^2 M_x M_{x+\hat{\nu}} \right)^k \right\} \tag{1.15}$$

$$+\,\kappa \left\{ \rho_\nu(x)^{N_\mathrm{c}} \bar{B}_x B_{x+\hat{\nu}} + \left(-\rho_\nu(x)\bar{\chi}_{x+\hat{\nu}}\chi_x\right)^{N_\mathrm{c}} \right\} \tag{1.16}$$

where the effective degrees of freedom are the meson fields M and baryon fields B:

$$M(x) = \bar{\chi}(x)\chi(x), \qquad B(x) = \frac{1}{N_\mathrm{c}!}\epsilon_{i_1\ldots i_{N_\mathrm{c}}}\chi_{i_1}(x)\ldots\chi_{i_{N_\mathrm{c}}}(x). \tag{1.17}$$

The Grassmann integration on each lattice site introduces the quark mass dependence

$$\int \prod_{i=1}^{N_\mathrm{c}} [d\chi_{i,x} d\bar{\chi}_{i,x}] e^{2am_q\bar{\chi}_x\chi_x} (\bar{\chi}_x\chi_x)^k = \frac{N_\mathrm{c}!}{m_x!}(2am_q)^{m_x} \tag{1.18}$$

with m_x the monomer number on that site. Since there are only N_c quarks and N_c anti-quarks per site available, $k + m_x = N_\mathrm{c}$, with k the sum of all dimers attached to x.

1.3.4 Dual partition function

The previous steps allow for an exact rewriting of the staggered partition function in terms of a discrete system:

$$Z_F(m_q,\mu) = \sum_{\{k,n,\ell\}} \underbrace{\prod_{b=(x,\mu)} \frac{(N_\mathrm{c}-k_b)!}{N_\mathrm{c}!k_b!}}_{\text{meson hoppings } M_xM_y} \underbrace{\prod_x \frac{N_\mathrm{c}!}{m_x!}(2am_q)^{m_x}}_{\text{chiral condensate } \bar{\chi}\chi} \underbrace{\prod_\ell w(\ell,\mu)}_{\text{baryon hoppings } \bar{B}_xB_y}$$

$$w(\ell, a\mu) = \left(\prod_{x\in\ell} N_\mathrm{c}! \right)^{-1} \sigma(\ell) e^{N_\mathrm{c}N_t\omega_l a\mu}$$

$$k_b \in \{0,\ldots N_\mathrm{c}\}, \qquad m_x \in \{0,\ldots N_\mathrm{c}\}, \qquad \ell_b \in \{0,\pm 1\} \tag{1.19}$$

with ω_ℓ the winding number of the baryonic loop ℓ in temporal direction and $N_\mathrm{c} = 3$ for QCD. The partition function is subject to the so-called Grassmann constraint resulting from Eq. (1.18):

$$m_x + \sum_{\hat{\mu}=\pm\hat{0},\ldots\pm\hat{d}} \left(k_{\hat{\mu}}(x) + \frac{N_\mathrm{c}}{2}|\ell_{\hat{\mu}}(x)| \right) = N_\mathrm{c}, \tag{1.20}$$

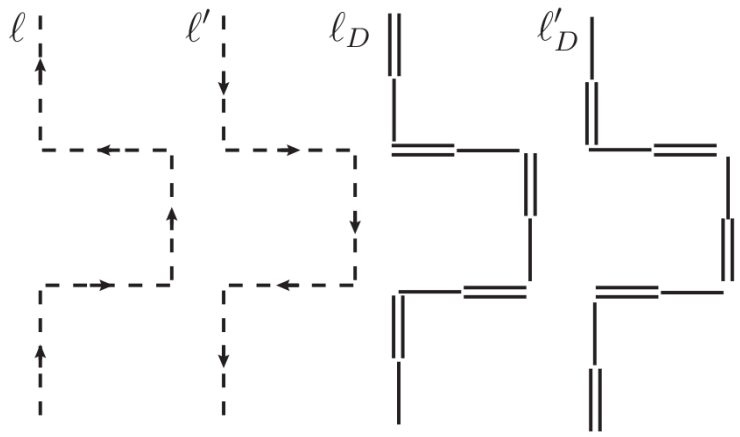

FIGURE 1.5: The resummation of baryonic world-lines with dimer chains that cancel the negative signs completely. From [91].

which implies that the lattice is a disjoint union of baryons and mesons, baryons form self-avoiding loops ℓ, and mesons (both dimers and monomers) attached to a site add up to N_c. The sign $\sigma(C) \in \{-1, +1\}$ of a configuration C factorizes and depends on the geometry of the baryonic loops:

$$\sigma(C) = \prod_{\ell} \sigma(\ell), \quad \sigma(\ell) = (-1)^{1+w(\ell)+N_-(\ell)} \prod_{\tilde{\ell}} \eta_\mu(x). \tag{1.21}$$

The origin of the residual sign problem is four-fold: a minus is associated with each fermionic loop (Fermi statistics), for each backward hopping $U^\dagger$ in Eq. (1.2) with $N_-(\ell)$ the total number of backward hoppings per loop ℓ, for each winding $w(\ell)$ (anti-periodic boundary conditions), and from the product of staggered phases. Compared to lattice QCD based on the fermion determinant, the dual representation has a much milder sign problem: $\Delta_f \simeq 10^{-5}$ for most temperatures and densities, which allows sign reweighting for sufficiently large volumes, see Chap. 2. This is because there are no fluctuations from the gauge fields (as they are integrated out), and because baryons are rather heavy even in the chiral limit. They are non-relativistic, spatial baryon hoppings are hence suppressed. This makes most of the baryon loops geometries trivial, with $\sigma(\ell) = 1$, see Sec. 4.1. Further resummations of meson and baryon world lines are possible to cancel sign completely [84], see Fig. 1.5.

Lattice gauge theory with compact gauge group is always confining in the strong coupling limit, even in the chiral limit: the effective degrees of freedom are hadronic. For gauge group SU(3) with $N_f = 1$ flavor, the hadronic degrees of freedom are mesons and baryons. Beyond the strong coupling limit, as discussed in Chap. 3, the dual partition function is still in terms of color singlet link states, but those in general are not purely fermionic and receive contributions from the gauge corrections. Hence the color singlets

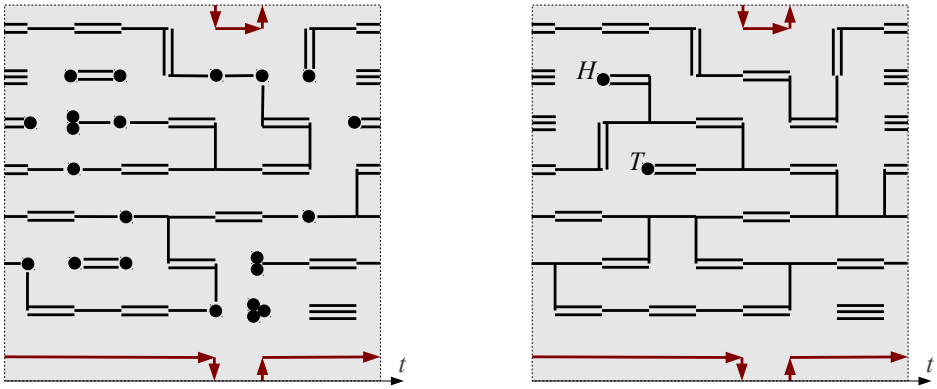

FIGURE 1.6: Typical 2-dimensional configurations. *Left*: the configuration is subject to the Grassmann constraint. *Right:* the configuration relaxes the constraint at the worm head H and tail T to sample to 2-point function.

will no longer correspond to hadronic states and deconfinement can be discussed in this context.

In the strong coupling regime of lattice QCD, chiral symmetry is spontaneously broken at low temperatures (see Chap. 2). In addition, chiral symmetry is broken explicitly by the quark mass, which in terms of dual variables is due to the presence of monomers: the number of monomers on even sites equals its number on odd sites. In the chiral limit we expect O(2) critical exponents for the chiral phase transition. This is also the case away from the strong coupling limit, as long as the lattice spacing is finite.

1.4 Monte Carlo methods for the dual representation

Many lattice models, in particular spin models, can be reformulated in a way that allow for global updates to improve drastically on critical slowing down: local updates suffer from a large autocorrelation time, i.e. $\tau \sim L^z$ with L the system size in lattice units and z a rather large exponent. There are two types of global updates that have much smaller z: the cluster algorithms [93,94] based on a low temperature expansion, and the worm algorithms based on a high temperature expansion of the partition function. Since the strong coupling expansion of lattice QCD in β corresponds to a high temperature expansion, a worm algorithm is natural in this context. Even at $\beta = 0$, the hopping parameter expansion is well suited for a worm algorithm. The partition function Eq. (1.19) together with the Grassmann constraint Eq. (1.20) calls for an update that modifies the bond variables and baryon world lines of the dual representation.

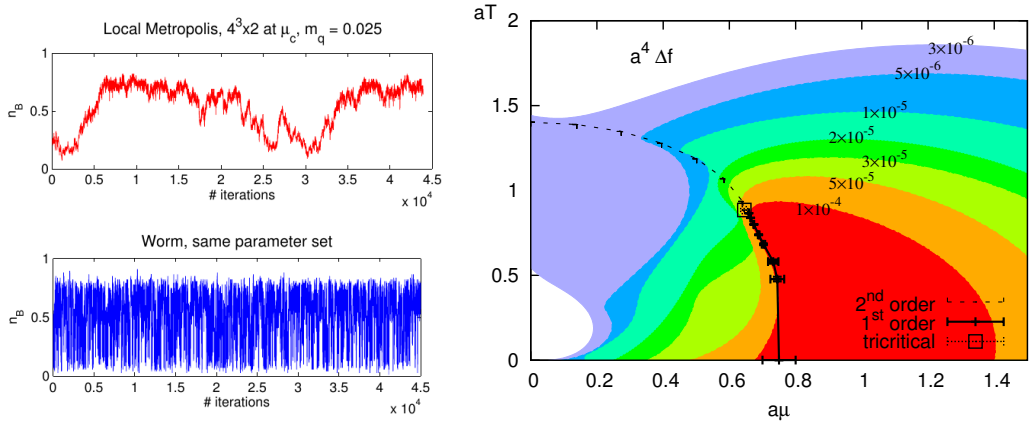

FIGURE 1.7: *Left:* Monte Carlo history of the baryon density, illustrating that the worm algorithm explores the configuration space much faster. *Right:* Residual sign problem of the worm algorithm for strong coupling QCD in the chiral limit, before any resummation.

1.4.1 Worm algorithm

Strong coupling lattice QCD in the dual formulation has been revisited in the last decade due to the applicability of the worm algorithm. The previously used MDP algorithm was found to have severe convergence problems due to the insufficient ergodicity [95]. The worm algorithm could solve these issues, and samples the configuration space considerably faster, see Fig. 1.7 (*left*). As a consequence, the first study of strong coupling QCD with the worm algorithm [96] found sizeable corrections to the older results [84].

The basic idea of a worm algorithm is to enlarge the configuration space by relaxing the constraint on the dual variables by inserting two sources (worm head and tail) and sample the 2-point correlation functions. Worm algorithms are applicable whenever the partition function could be written in terms of dual variables that can be interpreted as world-line or flux representation. The worm algorithm has been invented in [97] and consists of two types of updates:

Move update: the worm head x_H and tail x_T are moved to a new site and accepted depending on a local weight, given by the monomer number m_x.

Shift update: the worm head x_H is shifted away from the worm tail x_T and increments or decrements the dual degrees of freedom such as the bond occupation numbers or fluxes, depending on the bond weights.

Shift updates are repeated until both head and tail are at the same position ($x_H = x_T$) and the sources can recombine, which results in a global update. In the context of strong coupling lattice QCD, the worm head and tail corresponds to additional monomers, and

during the shift updates, the 2-point function $G_2(x_H, x_T)$ is sampled. The larger the volume and the lower the temperature, the longer it takes for these sources to recombine.

The first application of the worm algorithm to lattice gauge theory was for the strong coupling limit with U(3) gauge group in [90], which was generalized to SU(3) in [96]. Whereas for U(N_c) a mesonic worm that modifies the dimer networks is sufficient, for SU(N_c) a baryonic worm algorithm is required that creates or annihilates baryonic loops. The residual sign problem of that algorithm shown in Fig. 1.7 (*right*), with $\Delta F \sim 10^{-5}$ is indeed mild enough to study the full μ_B - T phase diagram, as discussed in Sec. 2.4. In Sec. 4.1 also some resummations are applied that combine mesonic and baryonic worm updates and are sign problem-free.

A generalization of the worm algorithm was also developed for the Abelian Gauge-Higgs model [98], where a surface worm algorithm was constructed. No such strategy is known for non-Abelian gauge theories.

For Monte Carlo simulations beyond the strong coupling limit, as discussed in Chap. 3, it is not sufficient to have a worm algorithm to update all dual variables. We also need an update scheme for the plaquette occupation number introduced in Sec. 3.2. This requires an additional update which is based on the Metropolis-Hastings algorithm [99].

1.4.2 Remarks on the software development

All Monte Carlo simulations have been carried out with a code library I developed for spin models and lattice field theories. These libraries are written in `C++` and compiled as shared libraries that can be imported to `python`. The underlying d-dimensional lattice can be combined with a statistical model, and with any available Monte Carlo algorithm for that model (Metropolis, heatbath, cluster, worm). For most models, visualizations as those shown in between the appendices exit. The source code is available as a git repository, accessible to all members of the CRC-TR 211. Students in my Emmy Noether group used this code extensively and on computer clusters, mainly at PC^2 in Paderborn.

Chapter 2

The phase diagram in the strong coupling limit

2.1 Many-flavored QCD and conformality

Chiral Symmetry breaking induces a mass scale, rendering the theory non-conformal. The transition temperature for chiral symmetry restoration depends on the quark masses and the number of flavors. It is well known that the transition temperature gets smaller as the chiral limit is approached, and it also gets smaller with increasing number of flavors. A larger number of Goldstone modes reduces the chiral transition temperature. This is also the case at strong coupling [100].

The phase diagram of SU(N_c) gauge theory with N_f fundamental fermions as a function of N_f has been predicted by Miransky [101]. Based on mean-field in the 1/d expansion it has been argued that for staggered fermions, chiral symmetry is always broken at zero temperature even as the number of flavors grows and the chiral limit is taken [102, 103]. That this is not the case but that there is a finite N_{fc} at which chiral symmetry becomes restored has been discovered by us for the first time in the publication [A1] together with Ph. de Forcrand and S. Kim. I wrote substantial parts of the paper (discussing the interpretation intensely with Ph. de Forcrand), wrote the multi-flavor HMC code and contributed most of the numerical data.

We found that in the strong coupling limit with staggered fermions, chiral symmetry is restored at zero temperature if the number of flavors is above a critical value ${\tilde{N_f}}^c = 13$ in the chiral limit (which corresponds to ${N_f}^c = 4\tilde{N}_f^c = 52$ in the continuum due to taste partners), contrary to common wisdom. The chiral condensate for various quark masses is shown in Fig. 2.1 and exhibits a strong first order transition with N_f for small quark

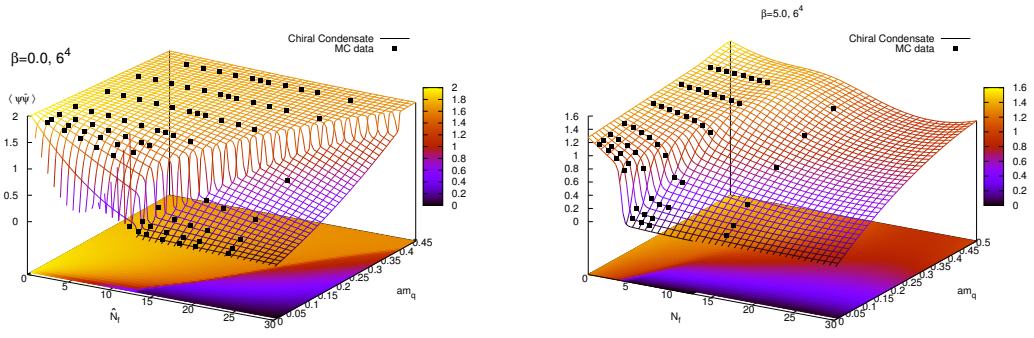

FIGURE 2.1: The chiral condensate on a 6^4 volume for various N_f and quark masses: *left*: at $\beta = 0$, *right*: at $\beta = 5$. Towards the chiral limit, the transition becomes strongly first order.

masses. We have investigated whether this chirally restored phase is IR-conformal, which requires the existence of an infrared fixed point. We found numerical evidence by by measuring the (1) torelon mass, (2) the integrated eigenvalue density of the Dirac spectrum, which exhibits a spectral gap in the chirally restored phase, and (3) the pion and ρ masses. Indeed we find conformal behaviour above ${N_\mathrm{f}}^c$, with the system size L the only infrared scale. Also we have not observed an additional transition as a function of β, which leads us to the speculation that the conformal phase persists towards the continuum limit, see Fig. 2.2. Whereas the details of ${N_\mathrm{f}}^c(\beta)$ will depend on the fermion discretization, the qualitative features remain: fermions generically have an ordering effect on the gauge fields [104].

In the continuum, it is believed that there is a conformal window, which is expected to start below $N_\mathrm{f} = 12$ and ends at $N_\mathrm{f} = 16.5$ flavors where asymptotic freedom is lost and the theory is trivial. Various groups have attempted to study this conformal window via lattice QCD [105, 106, 107] and the consensus is that QCD with $N_\mathrm{f} = 12$ is likely to be conformal. These studies are challenging as it is required to take the chiral limit and to probe the infrared properties of the theory to answer whether there is an infrared fixed point. The flavor-dependence of the chiral transition and Miransky scaling has also been investigated via the functional renormalization group [108, 109].

The search for a conformal window is motivated by physics beyond the standard model of particle physics: it is a requirement for certain models to work, in particular technicolor theories [110, 111], which may imply that the Higgs boson is composite.

There have been attempts to explain the N_f-induced chiral restoration at $T = 0$ analytically in the strong coupling limit [112, 113], with extensions to other gauge groups, but no prediction for $N_{\mathrm{f}c}$.

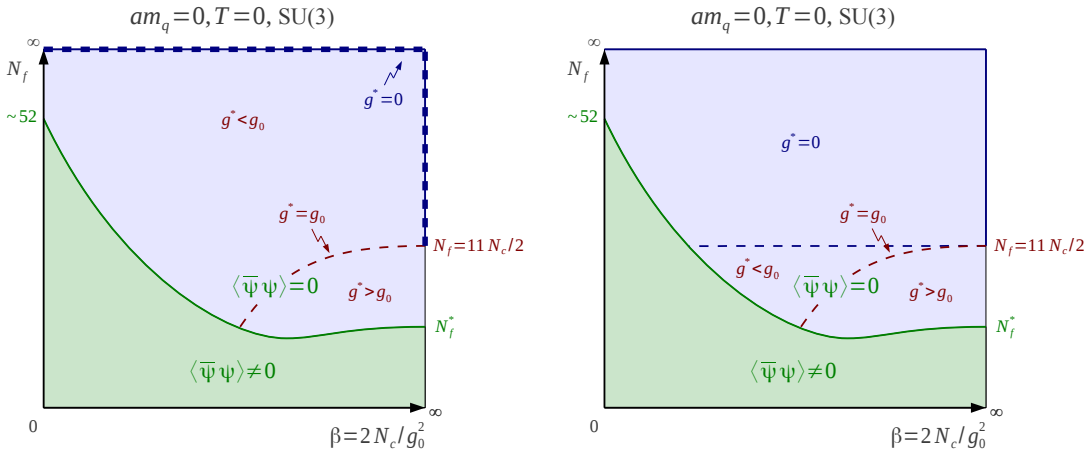

FIGURE 2.2: Two scenarios on the connection of the IR-conformal phase at strong coupling with the conformal window in the continuum. From [A1].

A dual representation valid for any number of flavors could help to understand chiral restoration beyond $N_{\mathrm{f}c}$ but is difficult to attain (see Sec. 4.2 for the two-flavor formulation).

2.2 Combinatorial identities

The structure of strong coupling lattice gauge theory can be studied analytically in low dimensions. In [A2] I derived some identities for the strong coupling limit in one temporal dimensions, since in the high temperature limit, $Z = (Z_1)^{V_s}$ with Z_1 the partition function of one spatial site and V_s the spatial lattice volume. I devised a group-theoretical approach to determine the SU(3) invariants $\langle L^n L^{*m}\rangle$ with arbitrary $n, m \geq 0$ via so-called 3-step Lucas polynomials that can be generalized to other gauge groups as well:

$$C_{n,m} = \int dL\, L^n L^{*m} = \begin{cases} C_3(|a-b|/3, \min(n,m)) & \text{for} \quad |n-m| \mod 3 = 0 \\ 0 & \text{else} \end{cases}$$

$$C_3(n_B, n_M) = \sum_{\lambda \vdash n_M;3} f^{\lambda+n_B} f^{\lambda} \tag{2.1}$$

with $L = \mathrm{tr}[U]$, $L^* = \mathrm{tr}[U^\dagger]$ the traces of any $U, U^\dagger \in \mathrm{SU}(3)$ along a closed contour such as a Polyakov loop. The $C_{n,m}$ invaraints are listed for small n, m in Tab. 2.1, which are a generalization of the Catalan numbers obtained for the corresponding SU(2) invariants The same result has been obtained in [114] via Ward identities rather than group theory. The coefficients $C^{n,m}$ can be identified in the expansion of the fundamental character

	1 (mesonic)	L^3	L^6	L^9	L^{12}
1 (baryonic)	1	1	5	42	462
(LL^*)	**1**	3	21	210	2574
$(LL^*)^2$	**2**	11	98	1122	15015
$(LL^*)^3$	**6**	47	498	6336	91091
$(LL^*)^4$	**23**	225	2709	37466	571428

TABLE 2.1: Invariants $C_{n,m}$ given in Eq. (2.1) for various n, m. In red are the invariants for $n = m$ which is the sector for U(N_c) gauge group. From [A2].

coefficient $u(\beta)$ for SU(3), see Sec. 1.2.4, which can be expressed as a Schur polynomial

$$u(\beta) = \frac{1}{3}\frac{\sum_{n=-\infty}^{\infty} D_n^{(3,f)}(2x)}{\sum_{n=-\infty}^{\infty} D_n^{(3,e)}(2x)} = \frac{\frac{1}{0!1!}x + \frac{1}{0!2!}x^2 + \frac{2}{1!2!}x^3 + \frac{5}{8}x^4 + \frac{2\times 6+1}{24}x^5 + \frac{77}{240}x^6 + \dots}{1 + \frac{1}{1!^2}x^2 + \frac{1+1}{3!}x^3 + \frac{2}{2!^2}x^4 + \frac{1}{4}x^5 + \frac{2\times 6+1}{72}x^6 + \dots} \tag{2.2}$$

In [A2] the 1-dim. partition functions for both Staggered and Wilson fermions are compared for any number of flavors and colors. The static limit $Z = Z_1^{V_s}$ (no spatial pions and baryons) is the starting point of the hopping parameter expansion for both the 3-dim. effective theory [50] and the dual representation. An explicit result for staggered fermions, which is an extension of [115, 116], is:

$$Z_{N_f}(\mu, T) = \sum_{k=-N_f}^{N_f} \prod_{a=0}^{N_c-1} \frac{a!(2N_f + a)!}{(N_f + a - k)!(N_f + a + k)!} e^{k\mu/T}. \tag{2.3}$$

The special case $N_f = 2$ is discussed in Sec. 4.2.

2.3 Anisotropic lattices

The standard definition of the temperature $T = \frac{1}{N_t a(\beta)}$ is not applicable to study the phase diagram in the strong coupling limit, as for $\beta = 0$ the lattice spacing a cannot be varied with β and the chiral transition turns out to be of the order $aT \simeq 1.5$, hence for any N_t the temperature is in the chirally broken phase. To study the phase boundary, it is necessary to vary the temperature continuously by introducing a bare anisotropy γ in the Dirac couplings:

$$\mathcal{L}_F = \sum_x \Big[\sum_\nu \gamma^{\delta_{\nu 0}} \eta_\nu(x) \left(e^{a_t \mu \delta_{\nu 0}} \bar{\chi}(x) U_\nu(x) \chi(x+\hat{\nu}) - e^{-a_t \mu \delta_{\nu 0}} \bar{\chi}(x+\hat{\nu}) U_\mu^\dagger(x) \chi(x) \right) + 2\hat{m}\bar{\chi}\chi(x) \Big], \tag{2.4}$$

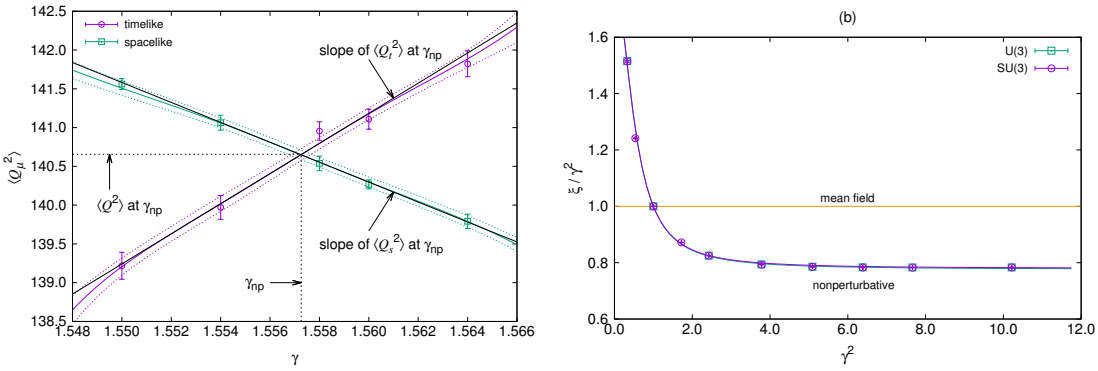

FIGURE 2.3: *Left*: Anisotropy calibration, determining γ_0 for given ξ which makes the lattice physically isotropic. *Right*: The resulting correction factor $\frac{\xi}{\gamma^2}$ and its deviation from the mean-field result. From [A4].

which results in the γ-dependent dual strong coupling partition function

$$Z_F(\hat{m}, a_t\mu, \gamma) = \sum_{\{k,n,\ell\}} \prod_{b=(x,\mu)} \frac{(N_c - k_b)!}{N_c! k_b!} \gamma^{2k_b\delta_{\mu 0}} \prod_x \frac{N_c!}{m_x!} (2\hat{m})^{m_x} \prod_\ell w(\ell, a_t\mu),$$
$$w(\ell, a_t\mu) = \gamma^{N_c N_0(\ell)} \left(\prod_{x\in\ell} N_c! \right)^{-1} \sigma(\ell) e^{N_c N_t \omega_l a_t \mu}, \tag{2.5}$$

with $a_t\mu$ the bare chemical potential, $N_0(\ell)$ the number temporal baryon segments in loop ℓ, and $\hat{m}$ the bare mass which only for $\gamma = 1$ corresponds to am_q. The bare anisotropy γ is related to the physical anisotropy $\xi \equiv \frac{a}{a_t}$ Whereas the weak coupling analysis of Eq. (2.4) yields $\xi(\gamma) = \gamma$, the mean-field analysis at strong coupling yields $\xi(\gamma) = \gamma^2$ [100]. The precise relation in the strong coupling regime is not known a priori, hence for an unambiguous definition of the temperature it is important to determine the non-perturbative relationship between the bare anisotropy γ and the renormalized physical anisotropy ξ. The first study to measure $\xi(\gamma)$ or equivalently $\gamma(\xi)$ I have carried out in [A3] together with my colleagues Ph. de Forcrand and H. Vairinhos (and a mean-field result provided by P. Romatschke), and in the publication [A4], which also contains some further applications. I provided the program, performed all simulations on anisotropic lattices and wrote substantial parts of the publication.

The idea to obtain the relation $\gamma(\xi)$ is by identifying conserved currents that allow to instantiate a physically isotropic lattice. It has been realized in [117] that the Grassmann constraint Eq. (1.20) implies locally conserved pion current:

$$j_\mu(x) = \epsilon(x) \left(k_\mu(x) - \frac{3}{2}|b_{x,\mu}| - \frac{3}{2d} \right) \quad \rightarrow \quad \sum \pm\hat{\mu}(j_\mu(x) - j_\mu(x-\hat{\mu})) = 0,$$
$$Q_\mu = \sum_{x\perp\mu} j_\mu(x), \tag{2.6}$$

with $\epsilon(x)$ the parity of site x and Q_μ the conserved charges for direction μ. Whereas the charge vanishes on average $\langle Q_\mu \rangle = 0$, its variance remains non-zero: $\langle Q_\mu^2 \rangle \neq 0$ This allows to define the following calibration procedure via a renormalization condition for a physically isotropic box:

$$N_s a_s = N_t a_t, \quad \xi = \frac{N_t}{N_s} \quad \Leftrightarrow \quad \langle Q_t^2 \rangle (\gamma_0) \stackrel{!}{=} \langle Q_s^2 \rangle (\gamma_0), \qquad \frac{a_s}{a_t} = \frac{N_t}{N_s} = \xi(\gamma_0). \tag{2.7}$$

The determination of γ_0 is shown in Fig. 2.3 (*left*), with multi-histogram reweighting applied to $\langle Q_0^2 \rangle$ and $\langle Q_s^2 \rangle$ to pinpoint the intersection point γ_0 and the slopes with high precision. The result of this calibration for various ξ and extrapolation to the thermodynamic limit (see [A4]) is shown in Fig. 2.3 (*right*). The data has been parameterized to yield the anisotropy correction factor, converting the mean-field assignment to the non-perturbative result:

$$\frac{\xi(\gamma)}{\gamma^2} \simeq \kappa + \frac{1}{1 + \lambda \gamma^4}. \tag{2.8}$$

The condition $\xi = 1$ for $\gamma = 1$ implies $\lambda = \kappa/(1-\kappa)$. With this fit Ansatz we obtain $\kappa \simeq 0.7815$. For large ξ, i.e. small a_t (towards the continuous time limit), $\xi = \kappa\gamma^2$. Further analysis of κ is discussed in Sec. 4.1, as it can be directly measured in the continuous time limit.

At finite quark mass, the current is no longer conserved as it receives a contribution $-am_q\bar{\psi}\gamma_5\psi$. But it turns out that this contribution cancels, as monomers on even sites act as sources ($\epsilon_x = 1$), and monomers on odd sites act as sinks ($\epsilon_x = -1$). Due to the even/odd decomposition for staggered fermions, on each configuration, the number of monomers on even sites equals those on odd sites. In [A5] I have shown that for any bare quark mass $m_1 = am(\xi = 1)$, the anisotropy calibration still works. The additional difficulty addressed there is that the bare quark mass enters the Lagrangian via the term $a_s^3 a_t \hat{m}\bar{\psi}\psi$ and a line of constant physics is required to obtain the function $\xi(\gamma, \hat{m})$, with $\hat{m}(\gamma)$ fixed such that $\hat{m}_1 = am_q$ for values as given in Fig. 2.4 (*right*). Possible conditions are $M_\pi L = \text{const.}$ or $[m_q \langle \bar{\psi}\psi \rangle]_L = \text{const.}$ For simplicity we chose the second conditions, as it can be expressed in terms of the number of monomers:

$$a_s^4 m_q \langle \bar{\psi}\psi \rangle = a_s^3 a_t \xi \hat{m}(\xi) \langle \bar{\psi}\psi \rangle = \xi \langle m_x \rangle = \text{const.} \tag{2.9}$$

Fig. 2.4 (*left*) shows the function $\gamma(\xi, \hat{m})$, where along the grey curves the physical quark mass is kept constant. These curves were obtained by scanning for γ_0 for various ξ and $\hat{m}$, with a controlled interpolation, for details see [A5]. Fig. 2.4 (*right*) shows the resulting parametrization of the correction factor $[\xi/\gamma^2](\hat{m})$ required to set aT and $a\mu_B$ unambiguously also for finite quark masses. From this figure it is also evident that the

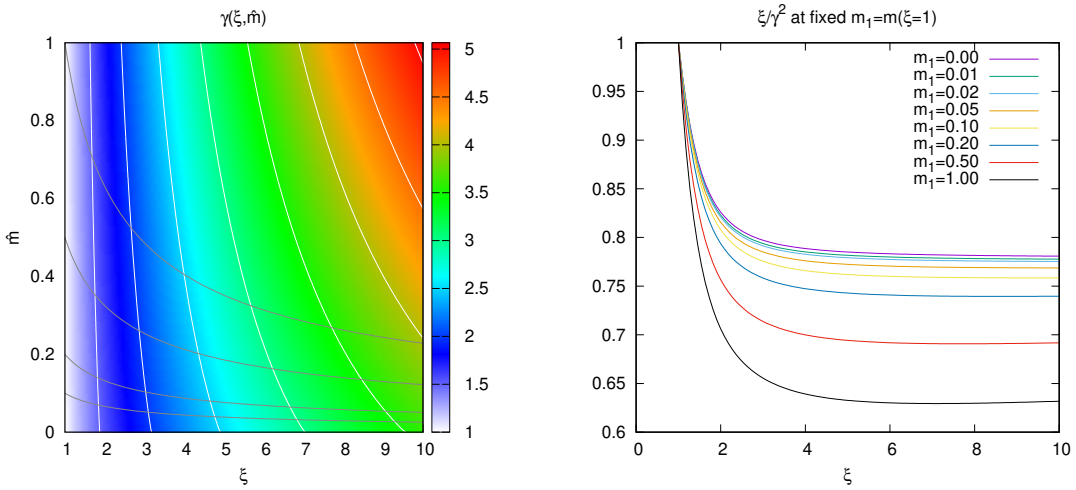

FIGURE 2.4: *Left:* Result of the anisotropy calibration, bare anisotropy γ for various ξ and quark masses and $\hat{m}$. The dark grey curves show the lines of constant physics which correspond to fixed physical mass. The white curves are lines of constant γ. *Right:* the anisotropy correction factor ξ/γ^2 for various masses. From [A5].

continuous time limit $\xi \to \infty$, $a_t \to 0$ is also defined for finite m_q, and $\kappa(\hat{m})$ is well described by the Ansatz

$$\kappa(\hat{m}_1) = \frac{\kappa_0}{1 + c_1\hat{m}_1 + c_2\hat{m}_1^2}, \qquad \hat{m}_1 = \hat{m}(\xi = 1), \tag{2.10}$$

with κ_0 the value determined in the chiral limit, Eq. (2.8).

An extension $\gamma(\xi, \beta)$ to finite values of β is addressed in Sec. 3.2. The interpretation of the locally conserved current as pion current becomes evident in the Hamiltonian formulation in Sec. 4.2. Anisotropic lattices have been used to study thermodynamics, and in particular the equation of state above the transition temperature. An analysis in the standard formulation can be found in [118].

2.4 Thermodynamic observables and phase diagram

From the partition function Eq. (2.5) and with the defintions

$$N_q = 2N_{Dt} + N_c N_{Bt}, \quad N_{Dt} = \sum_x |k_0(x)|, \quad N_{Bt} = \sum_x |b_0(x)|, \quad N_M = \sum_x m(x) \tag{2.11}$$

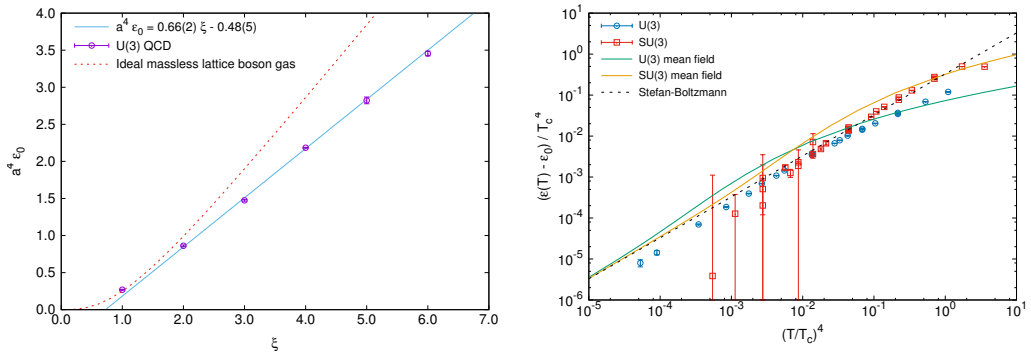

FIGURE 2.5: *Left*: Energy density at zero temperature ϵ_0 for various ξ. *Right*: Temperature-dependence of the energy and comparison with the Stefan-Boltzmann law. From [A3].

the dimensionless thermodynamic observables in terms of dual variables are:

$$\text{baryon density:} \quad a_s^3\rho_B = a_s^3 \frac{T}{V}\frac{\partial \log Z}{\partial \mu_B}\bigg|_{V,T} = \frac{\langle\Omega\rangle}{N_\sigma^3} = \langle\omega\rangle \tag{2.12}$$

$$\text{chiral condensate:} \quad a_s^3\langle\bar{\chi}\chi\rangle = a_s^3 \frac{\langle N_M\rangle}{N_\sigma^3 N_t a_s^3 a_t} = \frac{1}{a_t m_q}\langle n_M\rangle \tag{2.13}$$

$$\text{energy density:} \quad a^3 a_t \epsilon = \mu_B\rho_B - \frac{a^3 a_t}{V}\frac{\partial \log Z}{\partial T^{-1}}\bigg|_{V,\mu_B} = \frac{\xi}{\gamma}\frac{d\gamma}{d\xi}\langle n_q\rangle - \langle n_M\rangle \tag{2.14}$$

$$\text{pressure:} \quad a_s^3 a_t p = -a_s^3 a_t T \frac{\partial \log Z}{\partial V}\bigg|_{T,\mu_B} = \frac{\xi}{3\gamma}\frac{d\gamma}{d\xi}\langle n_q\rangle \tag{2.15}$$

$$\tag{2.16}$$

$$\text{interaction measure:} \quad \epsilon - 3p = -\frac{\langle n_M\rangle}{a_s^3 a_t} = -m_q\langle\bar{\chi}\chi\rangle \tag{2.17}$$

$$\text{entropy density:} \quad s = \frac{1}{T}\left(\frac{4\epsilon}{3} - \mu_B\rho_B\right) \tag{2.18}$$

The derivative $d\gamma/d\xi$ in the energy-like observables can be related to the slopes $\langle Q_\mu^2\rangle'$ of the conserved charges as shown in Fig. 2.3 (*left*):

$$\frac{1}{\xi}\frac{d\xi}{d\gamma}\bigg|_{\gamma_0} = \frac{\langle Q_t^2\rangle|'_{\gamma_0} - \langle Q_t^2\rangle|_{\gamma_0}}{\langle Q^2\rangle|_{\gamma_0}}, \tag{2.19}$$

which can be regarded as the strong coupling analogue of the Karsch coefficients [119]. The prefactor for the energy and pressure on isotropic lattices is

$$\frac{1}{\xi}\frac{d\xi}{d\gamma}\bigg|_{\gamma=1} = 2 + 4\kappa(\kappa - 1) \simeq 1.315 \tag{2.20}$$

In [A3] we investigated the temperature dependence of the energy density over many orders of magnitude based on simulations for $\xi = 2, 3, 4, 5, 6$ and found that over a wide range up to T_c the Stefan-Boltzmann law holds, indicating that the energy density is

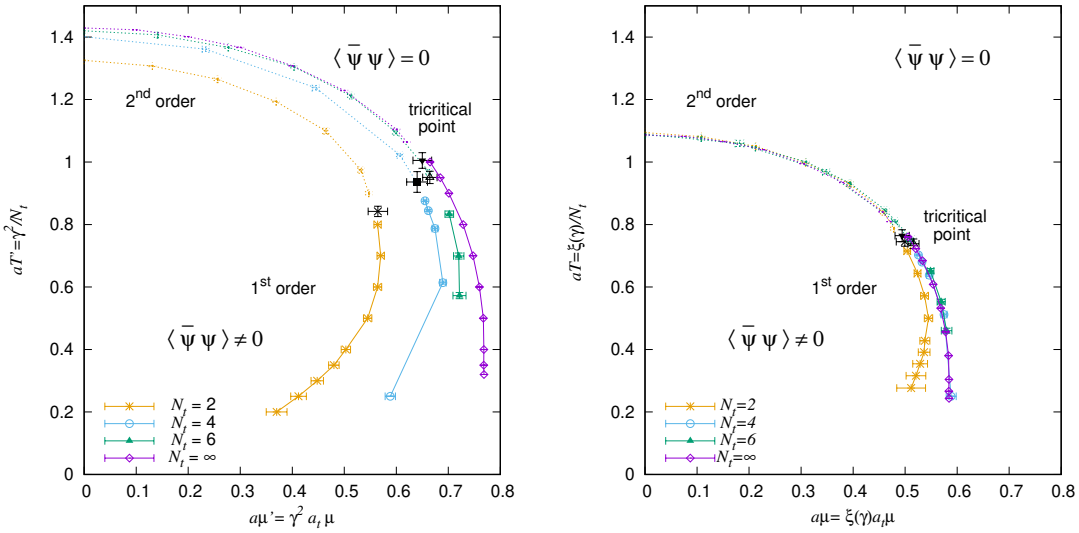

FIGURE 2.6: The phase diagram in the strong coupling limit and chiral limit. *Left:* with the mean-field definitions of the temperature and chemical potential, showing a strong N_t-dependence of the phase boundary. *Right:* with the non-perturbative correction, which results in an unambiguous phase-boundary. From [A4].

dominated by an ideal massless relativistic pion gas. The results are shown in Fig. 2.5, with the left-hand side providing the energy density at zero temperature for various ξ, and the right-hand side the temperature dependence of the subtracted energy density. The deviations at the lowest temperatures may be due to finite size effects, see also [120].

The result of the unambigous definition of the temperature and chemical potential for any N_t immproves on the phase diagram as shown in Fig. 2.6. Whereas the left-hand figure uses the mean-field definitions $aT' = \frac{\gamma^2}{N_t}$ $aT' = \frac{\gamma^2}{N_t}$, $a\mu' = \gamma^2 a_t \mu$, both receive corrections according to

$$aT = \frac{\xi}{N_t} = \frac{\xi}{\gamma^2}[aT'], \qquad a\mu = \xi a_t \mu = \frac{\xi}{\gamma^2}[a\mu'], \tag{2.21}$$

which results in a largely N_t-independent phase boundary. The back-bending of the phase boundaries for small temperatures corresponding to $\gamma < 1$ towards smaller values of $a\mu$ have vanished. For more applications such as the determination of the static baryon mass, the pion decay constant, the chiral condensate obtained from chiral perturbation theory in a finite box [121], see [A4].

Together with my colleague J. Kim I also studied the phase diagram at finite quark mass and applied the anisotropy correction factors [A6], as shown in Fig. 2.7. To obtain precise results we implemented multi-histogram reweighting in the dual variables. These results were obtained for $N_t = 4$, but due to the applied correction ξ/γ^2, the first order lines do again not show any back-bending as it was the case for the mean-field assignments of aT' and $a\mu'$. The fact that the chiral and nuclear first order transitions

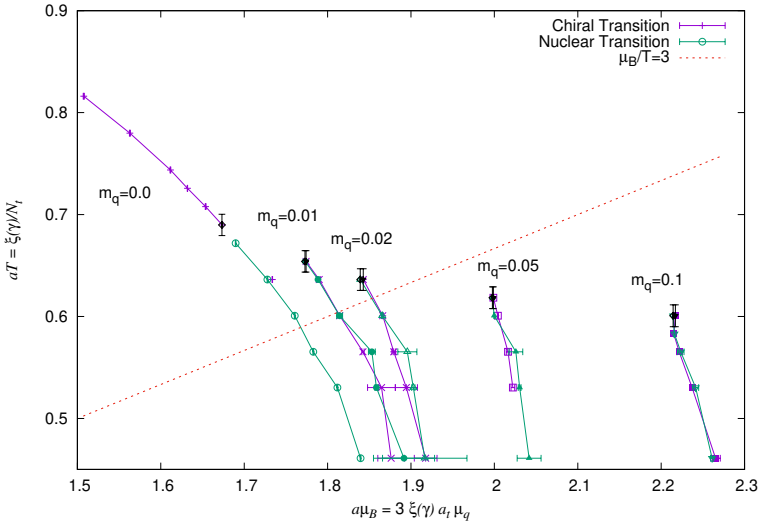

FIGURE 2.7: Phase diagram at finite quark mass [A6]: the second order line turns crossover, and the tricritical point becomes a critical point as soon as the quark mass is non-zero. The determination of the non-perturbative anisotropy used here was investigated in [A3, A4].

coincide in the strong coupling limit at zero temperature is well understood due to Pauli saturation on the lattice. That also the nuclear CEP obtained from finite size scaling of the baryon susceptibility and the chiral CEP obtained from the chiral susceptibility match for any quark mass is a numerical finding. Also the first order lines match for any temperature below the CEP. The line $\mu_B/T = 3$ roughly indicates the range of validity of the indirect methods discussed in Sec. 1.2.3. Already at rather small mass $am_q = 0.05$, corresponding to $M_\pi \simeq 0.15 M_B$, the CEP moves outside of the region available with the indirect methods.

It is however an open question what happens towards the continuum limit: it is possible that the chiral and nuclear transition at zero temperature are not well separated. Our finding rules out the possibility that the difference μ_c^{nuclear} and μ_c^{chiral} grows with the quark mass. The corresponding results away from the strong coupling limit are reported in Sec. 3.2.

2.5 Equation of state and nuclear potential at strong coupling

One of the key questions in QCD is on the nature of interactions between either hadrons (in the confined phase) or quarks and gluons (in the deconfined phase). There are several observables which give insight into such interactions:

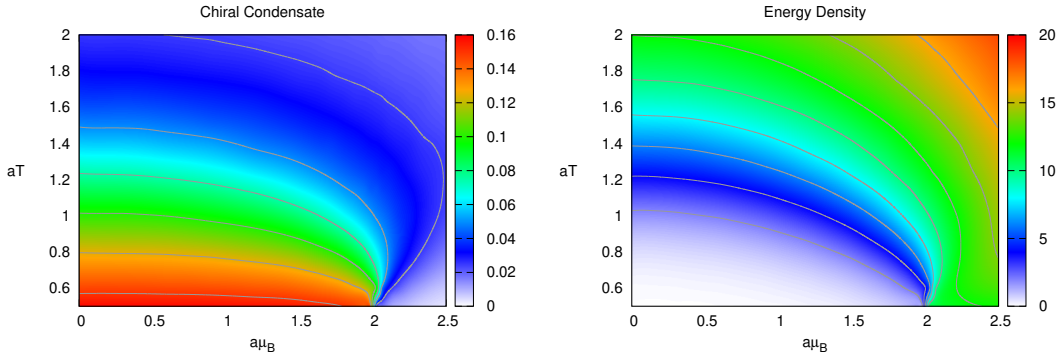

FIGURE 2.8: The chiral condensate (*left*) and the energy density (*right*) at finite quark mass ($am_q = 0.1$). From [A5]

(1) The QCD equation of state, i.e. the energy density ϵ and pressure p, and the interaction measure $\epsilon - 3p$,

(2) The nuclear equation of state and the nuclear potential.

The QCD equation of state simplifies drastically in the strong coupling limit as it does not receive any contributions from the gauge action. In fact, the interaction measure is simply given by the chiral condensate, see Eq. (2.17). In the chiral limit this implies that the pressure is proportional to the energy density as discussed in Sec. 2.4. At finite quark mass, the equation of state for all values of the temperatures and chemical potential, characterized by the energy density and the chiral condensate, is shown in Fig. 2.8. The equation of state has been analyzed together with my former student D. Bollweg and is discussed in [A5]. We find that the pressure as calculated according to Eq. (2.16) also shows a discontinuity across the first order line, as the derivative with the volume with respect to the grand-canonical potential Ω requires fixed T. This is in contrast to the expectation in the continuum, where the homogeneity of Ω implies the equivalence of the definitions for the pressure:

$$\Omega(T, \alpha V, \mu) = \alpha\Omega(T, V, \mu) = -T \log Z \qquad \rightarrow \qquad p = -\left.\frac{\partial\Omega}{\partial V}\right|_{T,\mu} \stackrel{!}{=} \frac{\Omega}{V}. \tag{2.22}$$

Homogeneity and hence the equivalence do not hold on the lattice. We have resolved this puzzle in the continuous time limit, see Sec. 4.1.

The nuclear potential, which has a long range Yukawa interaction mediated by the pion, also receives additional contributions for small distances from multi-pions and heavy mesons such as the ρ. It has been studied on the lattice [122] via the equal-time Bethe-Salpeter wave function, with ongoing efforts to study nuclear physics from first principles [123].

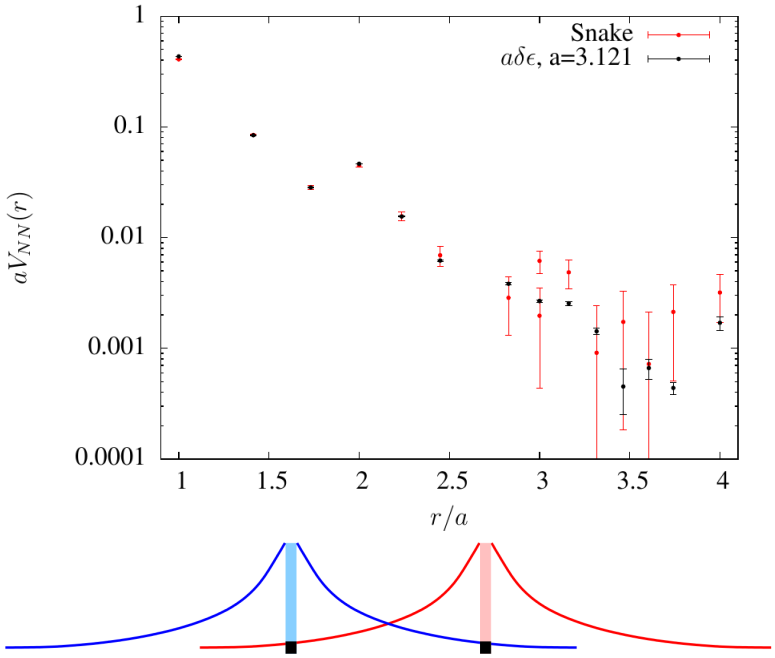

FIGURE 2.9: Nuclar potential $V_{NN}(r)$ at strong coupling with $r = |\vec{r}$ a spatial distance between two static baryons. Unpublished.

In the dual representation at strong coupling, there is a direct way to study the nuclear potential by putting two static baryon world-lines into the ensemble at some distance given by the lattice vector $\vec{r}$. I have studied V_{NN} together with D. Bollweg to extend on [96], but this work so far remained unpublished. We applied the Snake algorithm [124] to build up a static baryon at distance $\vec{r}$ from the origin, and extracted V_{NN} from $\Delta F = F_2 - F_0$, i.e. F_2 has two static baryons. We found it proportional to the pion cloud surrounding a static baryon, and to the ρ-meson correlator:

$$aV_{NN}(r) \sim \delta a^4 \epsilon(r) \sim \frac{e^{-m_\rho r}}{r}, \tag{2.23}$$

$$a^4 \delta\epsilon(r) = \left\langle 2k_0(r) + N_c|b_0(r)| - \frac{Nc}{4} \right\rangle. \tag{2.24}$$

The potential shows an attractive force, in agreement with a binding energy per nucleon, which has already determined in [96] to be $[E/A]_{SC} \simeq 0.26 m_B$ in the limit $A \to \infty$, which is much larger than its continuum value $[E/A]_{\text{cont}} \simeq 0.017 m_B$. The nuclear potential exponentially decays with the distance according to the ρ-meson mass. We find that the profile is indeed proportional to the pion cloud $\delta\epsilon(r)$ and also to the ρ-meson correlator, but the proportionality factor differs from $a = 2$ expected from a simple overlap of the pion clouds of each individual baryon. We tried to address this obstacle by measuring $\Delta E = \Delta F + TS$ directly, given we now have full control over the anisotropy according to Eq. (2.14), and that both definitions are equivalent for $T = 0$. Fig. 2.9 (*top*) shows a preliminary result of that new strategy, where the proportionality

turns out to be $a = 3.121$ rather than $a = 2$ as expected from the overlap argument illustrated in Fig. 2.9 (*bottom*).

The nuclear transition is further discussed in Sec. 4.3.

Chapter 3

Phase Diagram in the strong coupling regime, $\beta > 0$

While the strong coupling limit shares important features with full QCD and is a great laboratory to study new methods, it is necessary to incorporate gauge corrections and extend the validity of this effective theory into the strong coupling regime to learn more about the QCD phase diagram. Lattice QCD in the strong coupling regime should be considered as a 1-parameter deformation of QCD, and the larger the lattice coupling β can be made, the finer the corresponding lattices.

The long term questions we want to answer is whether the chiral critical point survives on finer lattices, and what the nature of the nuclear liquid gas transition is.

3.1 Reweighting approach

The leading order gauge corrections $\mathcal{O}(\beta)$ to the strong coupling limit are obtained by expanding the Wilson gauge action Eq. (1.2) before integrating out the gauge links. A formal expression is obtained by changing the order of integration (first gauge links, then Grassmann-valued fermions) within the QCD partition function:

$$Z_{QCD} = \int d\chi d\bar{\chi} DU e^{-S_G[U]-S_F[U]} = \int d\chi d\bar{\chi} Z_F \left\langle e^{-S_G[U]} \right\rangle_{Z_F}, \quad Z_F = \int DU e^{-S_F[U]}. \tag{3.1}$$

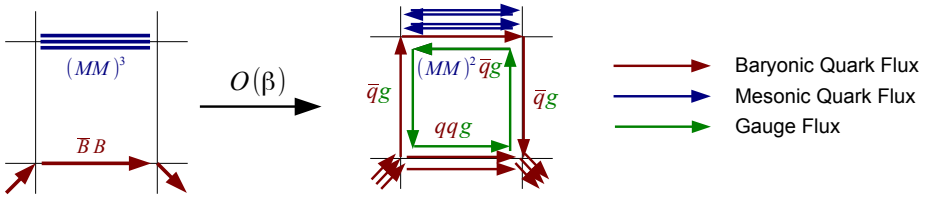

FIGURE 3.1: Reweighting of a diagram at strong coupling to a diagram with an excited plaquette. From [B1].

With this the $\mathcal{O}(\beta)$ partition function is

$$Z^{(1)} = \int d\chi d\bar{\chi} Z_F \left\langle -S_G[U] \right\rangle_{Z_F}, \tag{3.2}$$

$$\left\langle -S_G[U] \right\rangle_{Z_F} = \frac{\beta}{2N_c} \frac{\int DU \sum_P \left(\mathrm{tr}[U_P + U_P^\dagger] \right) e^{-S_F[U]}}{Z_F}. \tag{3.3}$$

The challenge in computing $Z^{(1)}$ is to address the $\mathrm{SU}(N_c)$ integrals that receive contributions from the elementary plaquette U_P. Link integration no longer factorizes, however the $\mathrm{tr}[U_P]$ can be decomposed before integration:

$$\int DU \, \mathrm{tr}[U_P] e^{-S_F[U]} = J_{ab} J_{bc} J_{cd} J_{da}, \quad J_{ij}(\mathcal{M}, \mathcal{M}^\dagger) = \int DU \, e^{\mathrm{tr}[U\mathcal{M}^\dagger + \mathcal{M}U^\dagger]} U_{ij} \tag{3.4}$$

Integrals of the type J_{ij} with two open color indices - as compared to J_0 defined in Eq. (1.14) - have been derived from generating functions

$$Z^{a,b}[K,J] = \int_G DU \, \mathrm{tr}[UK]^a \, \mathrm{tr}[U^\dagger J]^b \tag{3.5}$$

for either $J = 0$ [92] or for $G = \mathrm{U}(N_c)$ [125, 126]. My former colleague J. Langelage addressed the integral for $G = \mathrm{SU}(3)$ with staggered fermions by additionally computing $I_{4,1} = \int dU U_{i_1 j_1} U_{i_2 j_2} U_{i_3 j_3} U_{i_4 j_4} U^\dagger_{kl}$ and together we reordered the staggered fields to simplify the integral further, resulting in [B2]

$$J_{ij} = -\sum_{k=1}^{3} \frac{3-k}{3!(k-1)!} [M_\psi M_\phi]^{k-1} \bar{\phi}_j \psi_j + \frac{1}{2} \epsilon_{i i_2 i_3} \epsilon_{j j_2 j_3} \bar{\phi}_{i_2} \psi_{j_2} \bar{\phi}_{i_3} \psi_{j_3} - \frac{1}{3} \bar{B}_\psi B_\phi \bar{\phi}_j \psi_i. \tag{3.6}$$

A more general expression that we obtained via group theory rather recently is discussed in Sec. 3.3. In terms of the dual variables, neglecting rotation and reflection symmetries, there are 19 distinct diagrams to be considered, see Fig. 3.1 for an example. The resulting

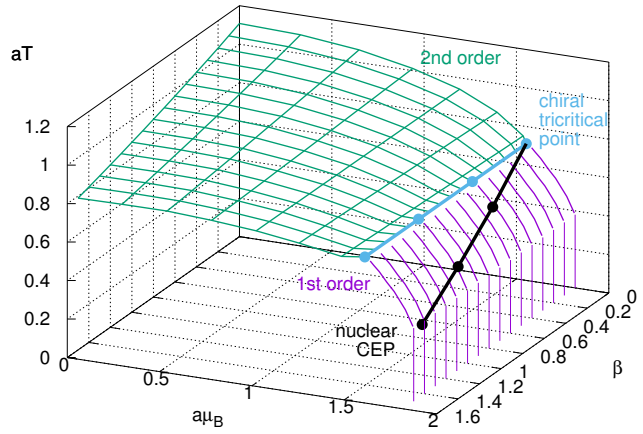

FIGURE 3.2: The staggereed lattice QCD phase diagram in the strong coupling regime from reweighting in the chiral limit: the chiral tricritical point is invariant under β and the nuclear critical point remains within the first order surface of the chiral transition. From [B2].

partition function, valid to $\mathcal{O}(\beta)$, is

$$Z(\beta) = \sum_{\{n,k,\ell,q_P\}} \prod_x \hat{w}_x \prod_b \hat{w}_b \prod_\ell \hat{w}_\ell \prod_P \hat{w}_P \tag{3.7}$$

$$\hat{w}_x = w_x v_x, \qquad \hat{w}_b = w_b k_b^{q_b}, \qquad \hat{w}_\ell = w_\ell \prod_\ell w_{B_i}(\ell), \qquad \hat{w}_P = \left(\frac{\beta}{2N_c}\right)^{q_P}, \tag{3.8}$$

where the site weights $w_x \mapsto \hat{w}_x$, bond weights $w_b \mapsto \hat{w}_b$ and baryon loop weights $w_\ell \mapsto \hat{w}_\ell$ receive modifications compared to the strong coupling limit Eq. (1.19) for sites and bonds adjacent to an excited plaquette $q_P = 1$. The weights are given in [B2], and are re-derived for any gauge group in Sec. 3.3. The configurations $\{n, k, \ell\}$ must satisfy at each site x the constraint inherited from Grassmann integration:

$$n_x + \sum_{\hat{\nu}=\pm\hat{0},\ldots,\pm\hat{d}} \left(k_{\hat{\nu}}(x) + \frac{N_c}{2} |\ell_{\hat{\nu}}(x)| \right) = N_c + q_x, \tag{3.9}$$

which is the modified version of Eq. (1.20) with $q_x = 1$ if located at the corner of an excited plaquette, otherwise $q_x = 0$.

Together with M. Fromm, J. Langelage, Ph. de Forcrand and O. Philipsen I have developed the reweighting technique to address the leading order gauge corrections for any observable $\mathcal{O}$ from simulations of the strong coupling ensemble:

$$\langle O \rangle_\beta = \frac{\langle O e^{-\beta S_g} \rangle_0}{\langle e^{-\beta S_g} \rangle_0} \simeq \frac{\langle O \,\mathrm{tr}[U_p] \rangle_0}{\langle \mathrm{tr}[U_p] \rangle_0}.$$

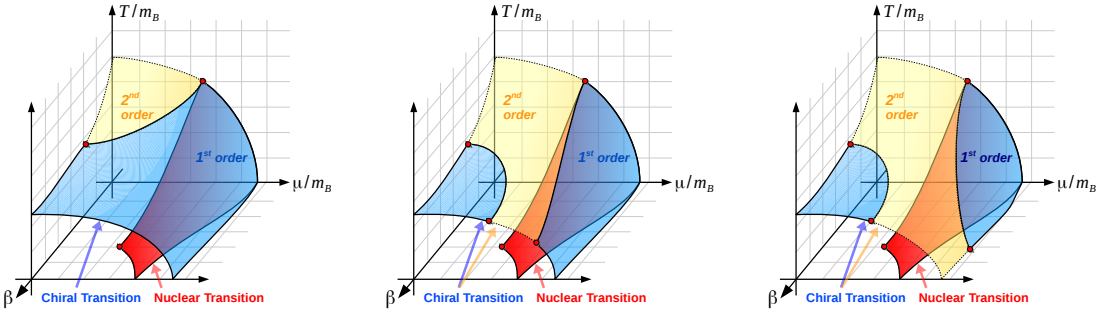

FIGURE 3.3: Various scenarios on how the strong coupling phase diagram could be extended towards the continuum, $\beta \to \infty$, valid for the chiral limit. It is expected that the nuclear and chiral transition eventually split. It is an open question how the location of the tricritical point found at $\beta = 0$ depends on β. From [B3].

The first results of Monte Carlo simulations on the phase diagram were reported in [B1], followed by the publication [B2], which can be considered the proof of concept for the working program on which the research in my Emmy Noether group was based. This paper illustrates the power of our method to obtain the phase boundary at non-zero values of the inverse gauge coupling β. The phase boundary for finite β (see Fig. 3.2) was obtained via finite size scaling of the reweighted chiral susceptibilities. At $\mu_B = 0$, the transition temperature aT_c decreases according to:

$$aT_c|_{\beta=0} = 1.4021(7), \qquad \frac{d}{d\beta} aT_c(\beta)\bigg|_{\beta=0} = -0.46(1). \tag{3.10}$$

This is also the case for small chemical potential, $aT_c(a\mu_B)$ decreases with increasing β as the lattice spacing becomes smaller. In contrast, the critical chemical potential $a\mu_B^c \simeq 1.78(1)$ at zero temperature has no β-dependence. For the ratio, we found $T/\mu_B = 0.787$ for $\beta = 0$ and $T/\mu_B = 0.529$ for $\beta = 1$, which should be compared to $\frac{T_c}{m_B} \simeq \frac{154\text{MeV}}{0.93\text{GeV}} = 0.165$ for full QCD [17], as μ_B is almost equal to the baryon mass m_B. A linear extrapolation beyond $\beta = 1$ renders aT_c negative for $\beta > 3$, but we found numerical evidence that at an exponential extrapolation

$$\frac{aT_c(\beta)}{aT_c(\beta = 0)} \approx \exp\left(\beta \, \frac{d}{d\beta} aT_c\bigg|_{\beta=0}\right) \tag{3.11}$$

produces better agreement with Monte Carlo data, see Fig. 3.4, resulting in $aT_c \to 0$ as $\beta \to \infty$. Additional aspects are discussed in [B3], in particular the various scenarios on how this phase diagram can be extended towards the continuum, see Fig. 3.3. However, since reweighting cannot be fully trusted across a first order boundary, direct simulations at non-zero β are necessary, which are discussed in the next section.

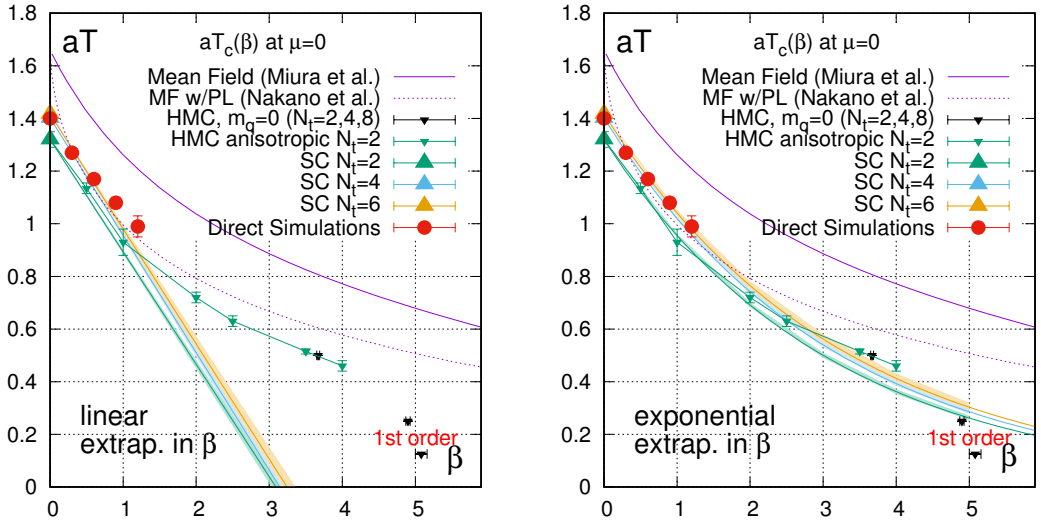

FIGURE 3.4: Phase boundary in $\beta - aT$ plane at $\mu_B = 0$, comparing direct simulations with (1) conventional HMC, (2) reweighting in β and (3) mean-field results, without [88] and with Polyakov loop effects [127]. *Left:* linear extrapolation of reweighting. *Right:* exponential extrapolation of reweighting. The direct simulations favor the exponential extrapolation, which also reproduces the HMC data on isotropic lattices. From [B4].

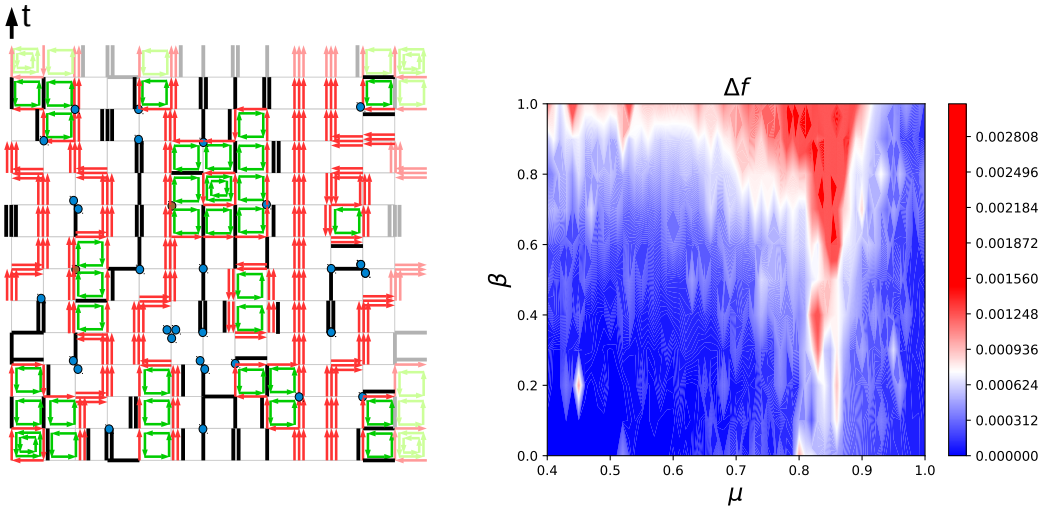

FIGURE 3.5: *Left:* Illustration of a 2-dim configuration in terms of the dual variables at finite β, m_q and μ_B, from [B4]. *Right:* Severity of the sign problem in the μ - β at low $aT = 0.25$, from [B5]. We can extract observables reliably for up to $\beta \simeq 1$.

3.2 Direct sampling based on plaquette occupation numbers

Whereas the reweighting result could not answer the question about the β-dependence of the chiral and nuclear critical point, direct simulations at finite β could in principle resolve this issue. This required to implement a plaquette update based on the plaquette and anti-plaquette occupation numbers n_p, $\bar{n}_p$, which is essentially a Metropolis-Hasting

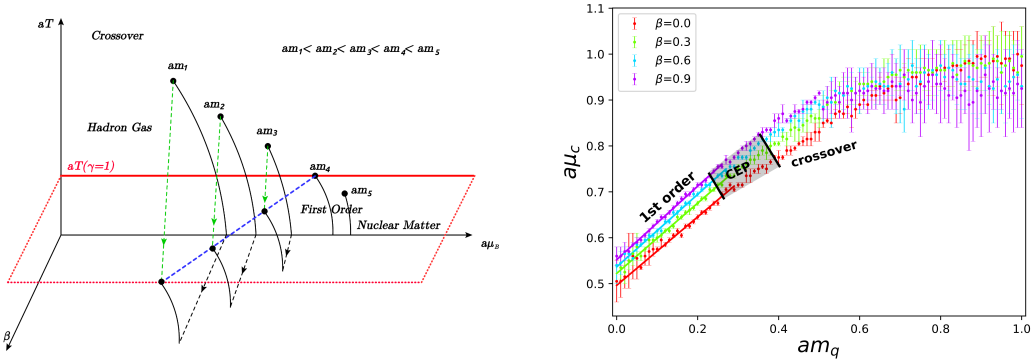

FIGURE 3.6: *Left:* Scheme for scanning the nuclear transition at fixed temperature $aT = 0.25$ for various quark masses and baryon chemical potential, resulting in a location $a\mu_B^c(am_q)$ (blue line). *Right:* Monte Carlo result for the phase boundaries, and an estimate of the nuclear critical endpoint $\frac{1}{3}a\mu_B^c(am_q)$ as a function of the quark mass for various values of β. From [B5].

algorithm, see Sec. 1.4.1. The mesonic and baryonic Worm algorithms need to be mixed with plaquette updates sufficiently to have an ergodic algorithm valid for sufficiently large β. In practice, after the worm closes, a plaquette update is proposed on random plaquette coordinates p. Typical configurations in terms of monomers, dimers, fermion world-lines and plaquette excitations as shown in Fig. 3.5 (*left*) are based on Eq. (3.8), but now at each plaquette coordinate there can be a non-zero plaquette excitation of either positive orientation ($\mathrm{tr}[U_P]$) or negative orientation ($\mathrm{tr}[U_P^\dagger]$). The crosscheck with HMC and reweighting for $\mu_B = 0$ is shown in Fig. 3.4. In practice, such simulations are limited by the sign problem which already becomes severe for $\beta > 1$, see Fig. 3.5 (*right*): baryons that are point-like in the strong coupling limit become resolved as fermions split around plaquettes with non-zero plaquette occupation number. The fermion world-lines no longer have simple geometries.

Our results on the partition function and its numerical investigation was published in [B4] together with my colleague J. Kim and my former PhD student G. Gagliardi. The algorithm was implemented by me, J. Kim helped with carrying out the simulations, and G. Gagliardi provided some analytic improvements. The phase boundaries were obtained via finite size scaling with MC simulations carried out on large spatial volumes and $N_t = 4, 6$. We found that in the chiral limit the chiral transition at small chemical potential moves to lower temperature, but the nuclear and chiral transition at low temperatures are still on top for moderate values of β, i.e. $\mu_c^{\mathrm{nuclear}} \approx \mu_c^{\mathrm{chiral}}$. There is no evidence for a nuclear phase with the chiral symmetry still broken. Note that a similar result of the invariance of the critical chemical potential with increasing β was also found in a mean-field study [88].

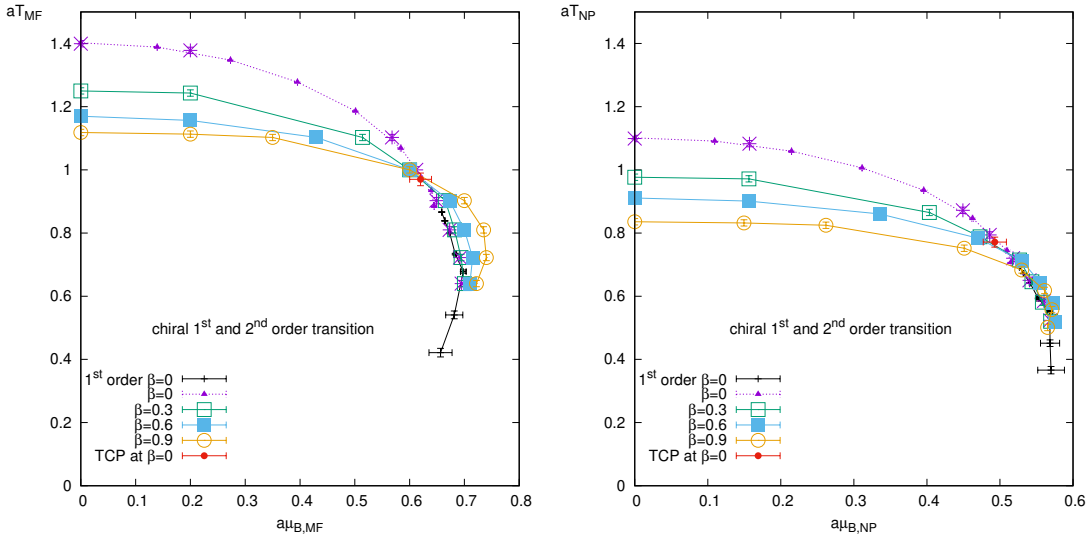

FIGURE 3.7: The phase diagram for the chiral transition from direct simulations. *Left:* According to mean-field definitions of aT an $a\mu_B$. *Right:* According to the non-perturbative determination of aT an $a\mu_B$ via the anisotropy calibration procedure. From [B6].

Together with J. Kim we also investigated the β-dependence of the nuclear transition for a large range of quark masses, aiming for an overlap with the 3-dim effective theory investigated in the group of O. Philipsen in Frankfurt, see Sec. 1.2.3 and Sec. 5.2. We chose a fixed rather small temperature $aT = 1/N_t$ with $N_t = 4$, corresponding to an isotropic lattice, $\gamma = 1$, $\xi = 1$, to simplify the analysis. The strategy to scan for the first order transition and the critical point $a\mu_B^c(am_q)$ is shown in Fig. 3.6 (*left*). The numerical results obtained from the peak of the baryon susceptibility are shown in Fig. 3.6 (*right*), which is an extension of Fig. 2.7 discussed in Sec. 2.4. We found that the phase boundary only has a very weak β-dependence, and that it is first order up to the quark mass $am_q^c \simeq 0.3 - 0.4$, slightly depending on β. At larger quark masses the nuclear CEP has dropped below $aT = 0.25$, rendering the nuclear transition to a crossover.

In Fig. 3.7 the results on the chiral phase transition for various values of β are shown before (*left*) and after (*right*) applying the anisotropy correction factor ξ/γ^2. The unphysical back-bending towards smaller chemical potential with decreasing temperature has therefore vanished also at finite β. This illustrates the importance of the anisotropy calibration, as discussed in Sec. 2.3. The same strategy has been successfully applied by my colleague J. Kim and me also at finite values of β [B6], i.e. we have determined $\xi = \xi(\gamma, \beta)$. Although there are actually two distinct bare anisotropies, $\gamma \equiv \gamma_F$ from the fermion action, and $\gamma_G \equiv \sqrt{\beta_t/\beta_s}$ from the gauge action, in the strong coupling regime, $a_s/a_t \propto \gamma_G^2$, which implies $\gamma_G = \gamma_F$. This is no longer the case at weak coupling [128, 119].

3.3 Tensor network representation

The first steps towards a dual representation based on the strong coupling expansion, valid for all orders in β have been discussed in [B7]: Together with G. Gagliardi I have generalized the link integration from $\mathrm{U}(N_\mathrm{c})$ to $\mathrm{SU}(N_\mathrm{c})$, for any q with $a = qN_\mathrm{c} + p$ the number of color indices $\boldsymbol{i} = (i_1, \dots i_a)$, $\boldsymbol{j} = (j_1, \dots j_a)$ and $b = p$ the number of color indices $\boldsymbol{k} = (k_1, \dots k_b)$, $\boldsymbol{l} = (l_1, \dots l_b)$:

$$\begin{aligned}\mathcal{I}^{a,b}_{\boldsymbol{i}\boldsymbol{j},\boldsymbol{k}\boldsymbol{l}} &= \int_{\mathrm{SU}(N_\mathrm{c})} DU\; U^{j_1}_{i_1} \cdots U^{j_a}_{i_a}\, U^{\dagger\, l_1}_{k_1} \cdots U^{\dagger\, l_b}_{k_b} \\ &\propto \sum_{(\alpha,\beta)} \sum_{\pi,\sigma\in S_p} \epsilon^{\otimes q}_{i_{\{\alpha\}}} \delta^{l_\pi}_{i_{\{\beta\}}}\, \tilde{\mathrm{Wg}}^{q,p}_N(\pi\circ\sigma^{-1}) \epsilon^{\otimes q, j_{\{\alpha\}}} \delta^{j_{\{\beta\}}}_{k_\sigma}. \end{aligned} \tag{3.12}$$

Here, $\epsilon^{\otimes q}$ is a shortcut for the $q-$fold product of Levi-Civita epsilon tensors and $\delta_i^{\,l_\pi}$, $\delta^{\,j}_{k_\sigma}$ are the generalized Kronecker deltas where the indices are reordered according to the permutations $\pi, \sigma \in S_p$, and $\tilde{\mathrm{Wg}}^{q,p}_{N_\mathrm{c}}$ is our generalization of the Weingarten functions, with $\mathrm{Wg}^{p}_{N_\mathrm{c}} = \tilde{\mathrm{Wg}}^{0,p}_{N_\mathrm{c}}$ the usual Weingarten functions [129], see the Appendix in [B8]. Essentially, these relate the irreducible representations of $\mathrm{SU}(N_\mathrm{c})$ with those of the symmetric group S_p, as both can be expressed by the integer partitions λ. This result goes beyond previously published expressions for $q = 0$ [130, 131] (which corresponds to $\mathrm{U}(N_\mathrm{c})$) and $q = 1$ [132], and was also derived later by Borisenko *et al.* [133]. Based on Eq. (3.12), we have evaluated the partition function for pure Yang-Mills theory on the lattice, see [B7] for details:

$$Z_{\mathrm{Y.M.}} = \sum_{\{n_p,\bar{n}_p\}} \frac{(\beta/2N)^{\sum_p n_p+\bar{n}_p}}{\prod_p n_p!\bar{n}_p!} \underbrace{\prod_\ell \prod_p \int_{\mathrm{SU}(N_\mathrm{c})} \mathrm{tr}[U_p]^{n_p}\, \mathrm{tr}[U_p^\dagger]^{\bar{n}_p}}_{W(\{n_p,\bar{n}_p\})}, \tag{3.13}$$

$$W(\{n_p,\bar{n}_p\}) = \sum_{\substack{\{\lambda_\ell \vdash d_\ell\} \\ \mathrm{len}(\lambda_\ell)\le N_\mathrm{c}}} W(\{n_p,\bar{n}_p,\lambda_\ell\}) \tag{3.14}$$

with $W(\{n_p,\bar{n}_p\},\{\lambda_\ell\})$ the weight of a plaquette configuration with the links $\ell = (x,\mu)$ in the irreducible representation $\lambda_\ell \vdash d_\ell$, which is a partition of the dimer number

$$d_\ell = \min\left(\sum_{\nu\neq\mu} n_{x,\mu,\nu} + \bar{n}_{x-\hat{\nu},\mu,\nu}, \sum_{\nu\neq\mu} n_{x,\mu,\nu} + \bar{n}_{x-\hat{\nu},\mu,\nu} \right), \tag{3.15}$$

see Fig. 3.8 (*left*), and the number of parts of the partition λ is limited by N_c as explained in Sec. 2.2. These weights are all positive, in contrast to the Weingarten basis, where half of the weights are negative. The partition function Eq. (3.14) incorporates λ_ℓ as auxiliary

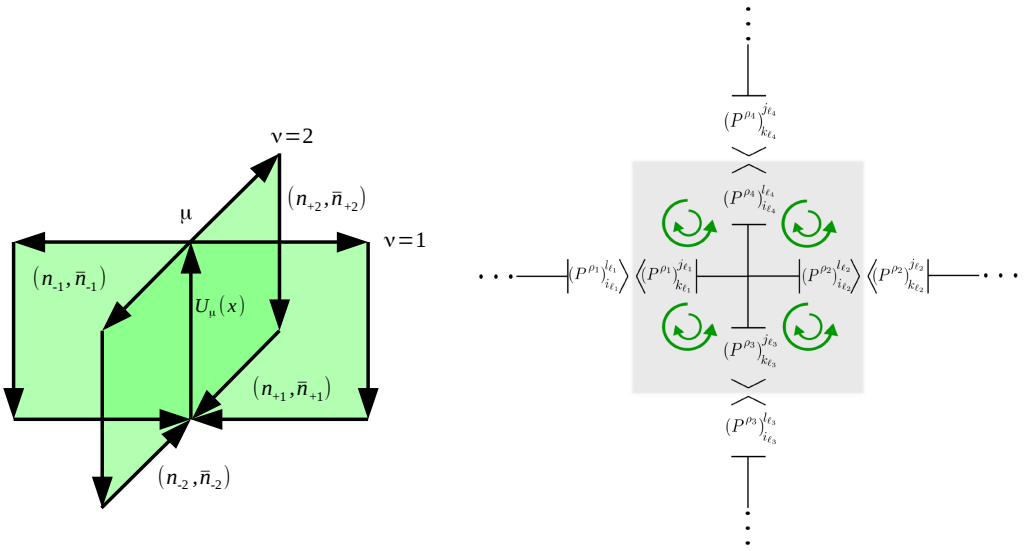

FIGURE 3.8: *Left*: Plaquette occupation numbers n, $\bar{n}$ participating in link weights. *Right*: Graphical picture of the local tensors that are defined via the dual variables attached to a site, decoupling from nearst neighbors. From [B4, B8]

degrees of freedom, and can be simulated via Monte Carlo in the strong coupling regime, which requires a non-local evaluation of $W(\{n_p, \bar{n}_p\}, \{\lambda_\ell\})$. In the Abelian case U(1), this simplifies to the random surface ensemble that can be simulated also in the weak coupling regime [134].

Encouraged by the improvements concerning the sign problem we applied this group-theoretic strategy to obtain an all-order strong coupling expansion including staggered fermions, published in [B8]. This work is a breakthrough towards a dualization of full QCD. The first step was to simplify Eq. (3.12) further by decoupling the weights to make them local. We managed to do so by introducing new dual variables, which we called decoupling operator indices ρ, that are multi-indices describing the group-theoretic structure of Eq. (3.12):

$$\mathcal{I}^{qN_c+p,p}_{\boldsymbol{i}\boldsymbol{j},\boldsymbol{k}\boldsymbol{l}} = \prod_{r=1}^{N_c-1} \frac{r!}{(r+q)!} \sum_\rho (P^\rho)_{\boldsymbol{i}}^{\boldsymbol{l}} \, (P^\rho)_{\boldsymbol{k}}^{\boldsymbol{j}} \,, \tag{3.16}$$

$$(P^\rho)_{\boldsymbol{i}}^{\boldsymbol{l}} = \sum_\pi \frac{1}{p!} \frac{f_\lambda}{\sqrt{D_{\lambda,N+q}}} M^\lambda_{mn}(\pi) \epsilon^{\otimes q}_{i_{\{\alpha\}}} \delta_{i_{\{\beta\}}}^{\,l_\pi} \,. \tag{3.17}$$

The orthongonal matrices M^λ are chosen such that $\chi^\lambda(\pi \circ \sigma^{-1}) \equiv \mathrm{Tr}\left(M^\lambda(\pi) M^\lambda(\sigma^{-1})\right)$, with $\chi^\lambda(\pi \circ \sigma^{-1})$ the characters of the symmetric group S_p [135] which occurs in $\tilde{\mathrm{Wg}}^{q,p}_{N_c}$. The operators P^ρ decouple the colour indices $\boldsymbol{i}$, $\boldsymbol{l}$ and $\boldsymbol{k}$, $\boldsymbol{j}$ in the integral, and its computation has been automatized. The decoupling operator index ρ can be cast into

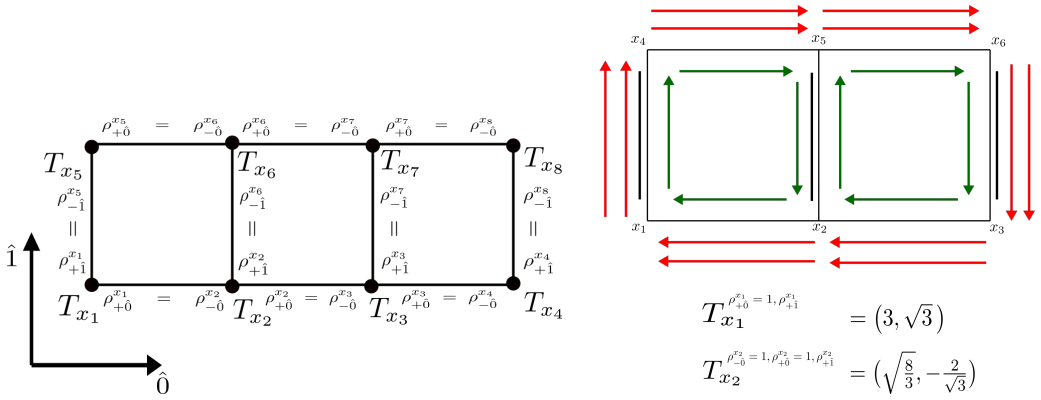

FIGURE 3.9: *Left*: Scheme for the evaluation of the tensor network. *Right*: Example of a tensor contraction for two adjacent plaquettes, with bond dimension 2. From [B8].

an integer. We have collected all P^{ρ} connected to a site x into a local tensor:

$$T_x^{\rho^x_{-d}\cdots\rho^x_d}(\mathcal{D}_x) \equiv \mathrm{Tr}_{\mathcal{D}_x}\left[\prod_{\pm\mu} P^{\rho^x_\mu}\right], \qquad \mathcal{D}_x = \{m_x, d_{x,\pm\mu}, n_{x,\mu\nu}, \bar{n}_{x,\mu\nu}\}, \tag{3.18}$$

with $\mathcal{D}_x$ the set of participating dual variables, illustrated in Fig. 3.8 (*right*). The resulting dual representation, taking into account ρ as an additional dual variable, has the form of tensor network:

$$\mathcal{Z}(\beta,\mu_q,\hat{m}_q) = \sum_{\substack{\{n_p,\bar{n}_p\}\\ \{k_\ell,f_\ell,m_x\}}} \sigma_f \sum_{\{\rho^x_{\pm\mu}\,|\,\rho^x_\mu=\rho^{x+\mu}_{-\mu}\}} \prod_p \frac{\tilde{\beta}^{n_p+\bar{n}_p}}{n_p!\bar{n}_p!} \prod_{\ell=(x,\mu)} \frac{e^{\mu_q\delta_{\mu,0}f_{x,\mu}}}{k_\ell!(k_\ell+|f_\ell|)!} \prod_x \frac{(2\hat{m}_q)^{m_x}}{m_x!} T_x^{\rho^x_{-d},\ldots,\rho^x_d}(\mathcal{D}_x), \tag{3.19}$$

This partition function is valid to any order in β, and we could compute the tensorial weights up to $\mathcal{O}(\beta^5)$, which already has 360525 distinct tensors. Its evaluation requires tensor network contractions on those sub-lattices where the plaquette occupation numbers are non-zero, as shown in Fig. 3.9. The partition function in the strong coupling limit Eq. (1.19) and the partition function at $\mathcal{O}(\beta)$ Eq. (3.8) can be re-derived from Eq. (3.19). We have analyzed the result of tensor network contractions for various gauge groups on 2×2 and 4×4 lattices via exact enumeration. Results for SU(3), evaluating the chiral condensate, the chiral susceptibility and the average sign, are shown in Fig. 3.10, comparing the various truncations of Eq. (3.19) at $\mathcal{O}(\beta^n)$ with HMC simulations. For $\beta < 1$ there are only small deviations, but for $\beta > 1$ higher orders are indeed necessary. The sign problem only mildly depends on β, but the situation will certainly be different in 3+1 dimensions, where exact enumeration is not feasible.

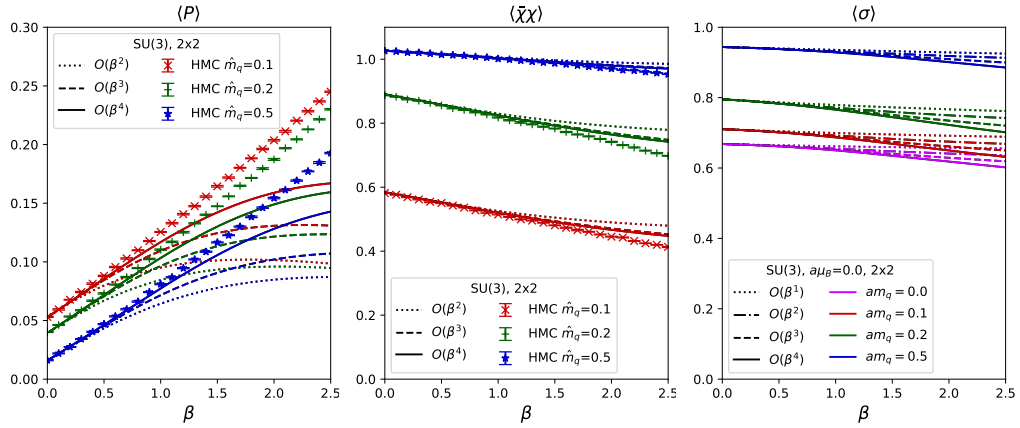

FIGURE 3.10: Comparison between exact enumeration and HMC on a 2×2 lattice for SU(3), (*left*) for the average plaquette and (*center*) for the chiral susceptibility. Sign problem on a 2×2 lattice as a function of β for various quark masses. *Right:* average sign $\langle \sigma \rangle$, including the geometric sign of fermion lines and the sign from the tensorial weights: it only depends weakly on β up to $\beta = 1$. From [B8].

We have discussed two methods to perform Monte Carlo simulations of this new dual representation:

(1) the tensor contractions are re-computed on the fly for connected plaquette surfaces, whenever these are modified,

(2) the tensors are mapped to vertex weights, which are updated with a worm algorithm, generalizing the worm at strong coupling.

Whereas method (1) is feasible for small β, the computational costs for large β to evaluate plaquette surfaces grow dramatically as they eventually fill the whole lattice. The method (2) extends on existing vertex models for which worm algorithms exist, such as the Schwinger model [136, 137, 138], but the increasing number of vertices for higher orders in β slows down the evolution of the worm.

Further ideas and new developments to evaluate Eq. (3.19) are outlined in Sec. 5.2.

Chapter 4

Hamiltonian formulation of strong coupling lattice QCD

The Hamiltonian formulation of lattice QCD was already considered in [139] and has been used for some analytical computations [140, 141]. In this chapter I present a Hamiltonian formulation for strong coupling lattice QCD with staggered fermions, which can also be studied numerically via Quantum Monte Carlo (QMC).

This formulation is based on the Euclidean continuous time limit, which will have several advantages: (1) the ambiguities arising from the functional dependence of observables on the anisotropy $\xi(\gamma)$ as discussed in Sec. 2.4 will be circumvented, (2) there is no need to perform the continuum extrapolation $N_t \to \infty$ (see Sec. 4.1), which will (3) allow to measure the phase boundaries unambiguously (see Sec. 4.3), and (4) for all temperatures of interest, the Quantum Monte Carlo algorithm is considerably faster than its discrete version. Moreover, temporal correlation functions as discussed in Sec. 4.4 can be measured with high resolution.

4.1 The Euclidean continuous time limit

The first step towards a Hamiltonian formulation is to consider the continuous time limit. This idea goes back to [142], where the continuous time limit was derived via the Trotter-Suzuki decomposition [143] for the Heisenberg quantum anti-ferromagnet. Since then, continuous time methods have been widely used in condensed matter [144, 145].

That the continuous time limit is also well defined in strong coupling lattice QCD was already discussed in Sec. 2.3. The continuous time limit is a joint limit $N_t \to \infty$, and $a_t \to 0$ such that the physical temporal extent $\beta = \frac{1}{aT}$ is fixed. This implies that

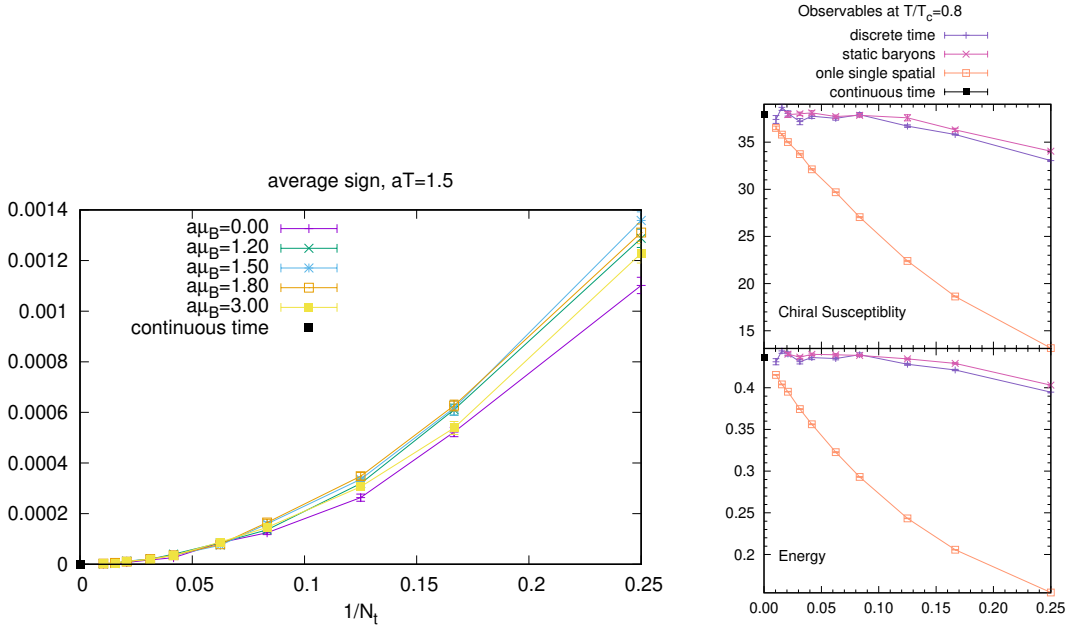

FIGURE 4.1: *Left*: The sign problem vanishes in the continuous time limit $N_t \to \infty$. *Right*: all observables have a well-defined continuous time limit. From [C2].

both the bare anisotropy γ and the renormalized anisotropy $\xi = a_s/a_t$ diverge. However, as was pointed out in Eq. (2.8), the ratio ξ/γ^2 remains finite: the non-perturbative functional dependence $\xi(\gamma)$ has been determined by matching conserved current fluctuations in spatial and temporal direction. Extrapolating to the continuous time limit gives $\xi/\gamma^2 = \kappa$.

Prior to the determination of κ, I have considered the continuous time limit for the first time in [C1], assuming $\kappa = 1$. Together with Ph. de Forcrand I developed the formalism, I implemented a worm algorithm operating directly in continuous time and performed the simulations in the μ_B - T plane to identify the chiral phase boundary, comparing results for both finite and infinite N_t. The important finding was that baryons become static in the continuous time limit: they are non-relativistic and the baryon mass is rather large even in the chiral limit, which leads to a suppression of spatial baryon hoppings with $1/\gamma$ and eventually become absent in the limit $\gamma \to \infty$. As a consequence, the sign problem completely vanishes in the continuous time limit, as shown in Fig. 4.1 (*left*). Also multiple spatial dimers on the same bond, corresponding to multiple meson exchange, become expressed: they are resolved into single spatial dimers as $a_t \to 0$. The results subject to various constraints are shown in Fig. 4.1 (*right*), and they all approach the same continuous time limit for all observables (here shown for energy and chiral susceptibility). This holds for all temperatures and chemical potential. Moreover, we found non-monotonic behaviour in several observables and also in the extrapolation

of T_c. An extrapolation based on only $N_t \leq 16$ would give sizeable deviations, at least $N_t = 64$ is required to get T_c correct in three decimal places.

The partition function in the continuous time limit is derived in detail in [C2], and the final result for gauge group SU(3) expressed via an all-order high temperature expansion in $1/\mathcal{T}$ (with $\mathcal{T}$ the bare temperature) is

$$\mathcal{Z}_{\mathrm{CT}}(\mathcal{T}, \mu_{\mathcal{B}}) = \sum_{\{\Lambda_\sigma^M, \Lambda_\sigma^B\}} \sum_{\{\omega\}|_{\Lambda_\sigma^B}} e^{\omega_{\vec{x}} \mu_B / T} \sum_{n \in 2\mathbb{N}} \frac{1}{n!} \frac{1}{(2\mathcal{T})^n} \sum_{\mathcal{G} \in \Gamma_n^{\Lambda_\sigma^M}} v_{\mathbf{T}}^{N_{\mathbf{T}}(\mathcal{G})}, \tag{4.1}$$

$$N_{\mathbf{T}} = \sum_{\vec{x} \in \Lambda_\sigma^M} \int_0^{1/\mathcal{T}} d\tau \, n_{\mathbf{T}}(\vec{x}, \tau), \tag{4.2}$$

where $\Gamma_n = \{n_{\mathbf{L}}(\vec{x}, \tau), n_{\mathbf{T}}(\vec{x}, \tau)\}$ is the set of all valid configurations on the mesonic sub-lattice Λ_σ^M with $n \equiv N_{Ds}$ spatial dimers and $N_{\mathbf{T}} \leq 2n$ is the total number of non-trivial vertices (so-called $\mathbf{T}$-vertices with $v_{\mathbf{T}} = \frac{2}{\sqrt{3}}$). The decomposition into a disjoint spatial mesonic and baryonic sub-volume $\Lambda = N_s^3 \times N_t = \Lambda_M \dot{\cup} \Lambda_B$ is a consequence of the Grassmann constraint Eq. (1.20). The prefactor $1/n!$ is due to time-ordering. In Sec. 4.2 this result will be reformulated as a Hamiltonian, where we obtain a meaningful expression for Γ_n.

The continuous time worm algorithm discussed in [C1] acts in Euclidean time as a Poisson process with a space-dependent decay constant $\lambda_{\vec{x}}$:

$$P(\Delta_t) = e^{-\lambda_{\vec{x}} \Delta_t}, \quad \Delta_t \in [0, 1], \quad \lambda_{\vec{x}} = \frac{d_M(\vec{x})}{4\mathcal{T}}, \quad d_M(\vec{x}) = 2d - \sum_{\langle \vec{x}, \vec{y} \rangle} |B(\vec{y})|. \tag{4.3}$$

Here, $d_M(\vec{x})$ is the number of non-baryonic neighbors to which a spatial dimer can be emitted, due to the Grassmann constraint Eq. (1.20). The baryonic loops ℓ simplify to be purely temporal, denoted by $B(\vec{x})$, with winding number $\omega = 1$ for baryons and $\omega = -1$ for anti-baryons. The mesonic continuous time worm is based on the directed path algorithm introduced for discrete lattices and gauge group U(3) in [90]. In contrast to discrete time simulations considered in the previous chapters, the baryonic worm simplifies: since only static baryons survive in the limit, it is sufficient to have a heatbath for baryons on those sites that have no spatial dimers attached.

The unambiguous identification of the chiral and nuclear phase boundary in the continuous time limit requires to define the temperature and chemical potential non-perturbatively as discussed for discrete time, see Eq. (2.21). In particular the bare temperature $\mathcal{T}$ used in the partition function Eq. (4.2) needs to be renormalized to yield aT, whereas the chemical potential enters the continuous time partition function via the

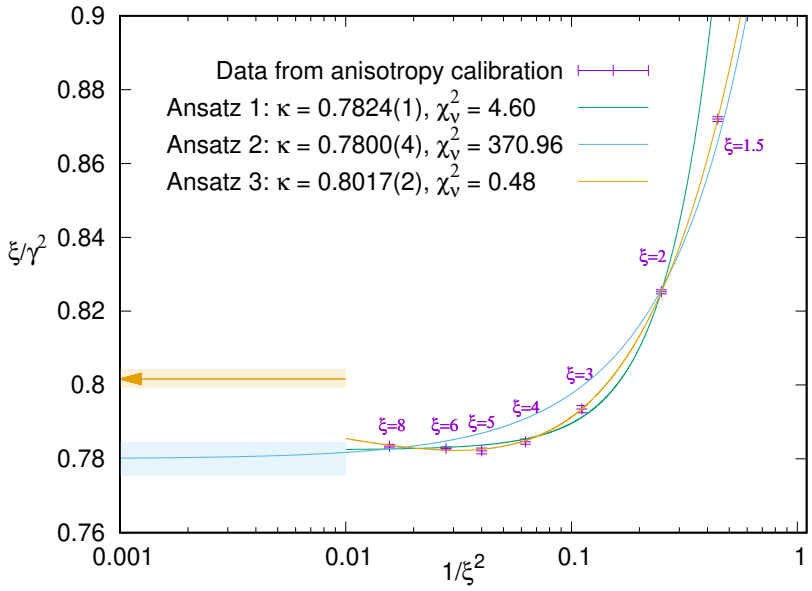

FIGURE 4.2: Result of the anisotropy correction factor ξ/γ^2 and its extrapolation to $\xi \to \infty$ for different fit Ansätze, see [C2], which have an impact on κ. The best fit reflects the non-monotonicity as found in the data.

ratio μ_B/T. I have improved the fit of the anisotropy calibration to yield $\kappa = 0.8017(2)$, based on a 3-parameter Ansatz (including also $\xi < 1$ into the fit) that reflects the symmetry of small anisotropy $\xi \to 0$ and large anisotropy $\xi \to \infty$, as shown in Fig. 4.2. The anisotropy calibration can also be implemented directly in the continuous time limit: this yields $\kappa = 0.7971(3)$, which is much closer to the result of the improved fit Ansatz compared to the Ansatz Eq. (2.8)

4.2 The Quantum Hamiltonian

In order to rewrite the partition function Eq. (4.2) in terms of a Hamiltonian $\mathcal{H} = \mathcal{H}_0 + \mathcal{H}_i$, we make use of a diagrammatic expansion in $\mathcal{H}_i$. After summing over all configurations Γ_n of a given order $n \in 2\mathbb{N}$ in the expansion parameter $1/\mathcal{T}$, one integrates over all possible times at which spatial dimers occur. To this aim we replace the temporal dimers $k_0(x)$ by meson occupation number $\mathfrak{m}(x)$:

$$k_0(x) \mapsto \mathfrak{m}(x) = \epsilon(x)\left(k_0(x) - \frac{N_c}{2}\right) + \frac{N_c}{2} \qquad \mathfrak{m}(x) \in \{0, 1, \dots N_c\} \tag{4.4}$$

with $\epsilon(x) = \pm 1$ the parity of a site introduced in Eq. (1.3). As a consequence, explained in detail in [C2], the alternating dimer chains will be replaced by meson occupation numbers $\mathfrak{m}(x)$ which are constant on the interval between attached spatial dimers. The spatial dimers change the meson state by one unit: $\mathfrak{m}(x) \mapsto \mathfrak{m}'(x) = \mathfrak{m}(x) \pm 1$. In

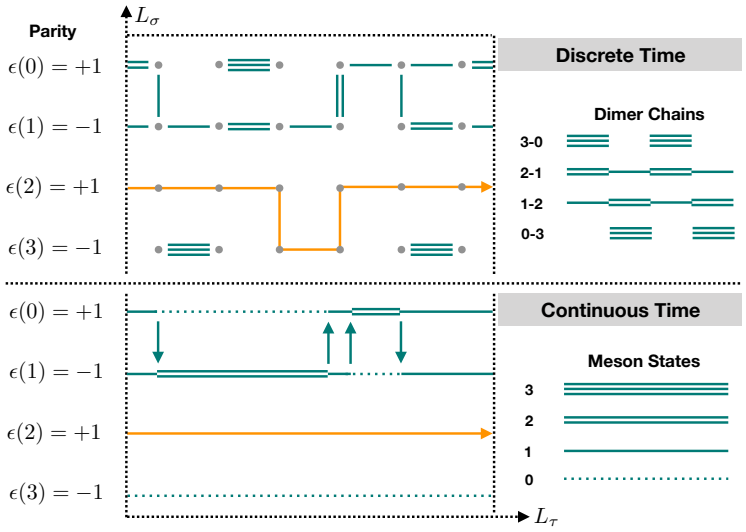

FIGURE 4.3: Typical configurations at discrete time and continuous time, with spatial dimers represented meson raising and lowering operators that can occur at any location in time. From [C2].

fact there is a conservation law: if a quantum number $\mathfrak{m}(x)$ is raised/lowered by a spatial dimer, then at the site connected by the spatial dimer the quantum number is lowered/raised, see Fig. 4.3. This is a direct consequence of its definition in Eq. (4.4): the parity of the two sites connected by a spatial dimer is opposite. We therefore can replace the vertices by meson raising and lowering operators $\hat{J}^+$, $\hat{J}^-$:

$$\mathcal{Z}_{\mathrm{CT}}(\mathcal{T},\mu_{\mathcal{B}},V)=\mathrm{Tr}_{\mathfrak{h}^{\otimes V}}\left[e^{(\hat{\mathcal{H}}+\hat{\mathcal{N}}\mu_{\mathcal{B}})/\mathcal{T}}\right],\quad \hat{\mathcal{H}}=\hat{\mathbb{1}}+\hat{\mathcal{H}}_i,\quad \hat{\mathcal{H}}_i=\frac{1}{2}\sum_{\langle\vec{x},\vec{y}\rangle}\left(\hat{J}^+_{\vec{x}}\hat{J}^-_{\vec{y}}+\hat{J}^-_{\vec{x}}\hat{J}^+_{\vec{y}}\right),$$

$$|\mathfrak{h}\rangle=|\mathfrak{m},\mathfrak{b}\rangle=\left(\begin{array}{c}0\\ \pi\\ 2\pi\\ 3\pi\\ \hline B^+\\ B^-\end{array}\right),\qquad \hat{J}^+=\left(\begin{array}{cccc|cc}0&0&0&0&&\\1&0&0&0&&\\0&\hat{v}_{\mathsf{T}}&0&0&&\\0&0&1&0&&\\ \hline &&&&0&0\\&&&&0&0\end{array}\right),\qquad \hat{J}^-=(\hat{J}^+)^T,$$

$$\hat{\mathcal{N}}=\sum_{\vec{x}}\hat{\omega}_x,\qquad \hat{\omega}=\left(\begin{array}{cccc|cc}0&0&0&0&&\\0&0&0&0&&\\0&0&0&0&&\\0&0&0&0&&\\ \hline &&&&1&0\\&&&&0&-1\end{array}\right).\tag{4.5}$$

This result is valid for $N_{\mathrm{c}}=3$ (but has been formulated for arbitrary N_{c}) and $N_{\mathrm{f}}=1$. Here, $\hat{\mathcal{N}}$ is the baryon number operator and $|\mathfrak{h}\rangle$ is the local Hilbert space at each spatial

lattice site $\vec{x} \in V$. The block-diagonal structure expresses the fact that the Hilbert space of hadrons is a direct sum of mesonic states and baryonic states, $|\mathfrak{h}\rangle = |\mathfrak{m}\rangle \oplus |\mathfrak{b}\rangle$, which results in the vanishing commutator $[\hat{\mathcal{H}}, \hat{\mathcal{N}}] = 0$. The meson states $|\mathfrak{m}\rangle$ count pseudoscalars, and we denote them as pions π (despite the fact they are flavorless for $N_\mathrm{f} = 1$ and they cannot be distinguished from the η or η' mesons). The pion current is conserved, but only in the chiral limit, see Sec. 2.3. Since Pauli saturation holds on the level of the quarks and pions have a fermionic substructure, we cannot have more than N_c pions per spatial site. If we omitted the additive constant $N_\mathrm{c}/2$ from Eq. (4.4), a particle-hole symmetry becomes evident. For arbitrary N_c we can identify the following algebra (see [C2]):

$$\hat{J}_1 = \frac{\sqrt{N_\mathrm{c}}}{2}\left(\hat{J}^+ + \hat{J}^-\right), \qquad \hat{J}_2 = \frac{\sqrt{N_\mathrm{c}}}{2i}\left(\hat{J}^+ - \hat{J}^-\right), \tag{4.6}$$

$$\hat{J}_3 = i[\hat{J}_1, \hat{J}_2] = \frac{N_\mathrm{c}}{2}[\hat{J}^+, \hat{J}^-] \qquad \hat{J}^2 = \frac{N_\mathrm{c}(N_\mathrm{c}+2)}{4}\mathbb{1} \tag{4.7}$$

The "spin"-representation is $d = N_\mathrm{c} + 1$-dimensional, with $S = N_\mathrm{c}/2$. For $N_\mathrm{c} = 1$, $\hat{J}_\pm = \frac{1}{2}(\sigma_x \pm i\sigma_y)$ is expressed in terms of the Pauli matrices, and the continuous time partition function becomes that of the quantum XY model. By shifting the pion occupation numbers by its average value $\mathfrak{m} \mapsto \mathfrak{s} = \mathfrak{m} - \frac{N_\mathrm{c}}{2}$ we can identify the quantum state corresponding to this algebra:

$$\hat{J}_3 \left|\frac{N_\mathrm{c}}{2}, \mathfrak{s}\right\rangle = \mathfrak{s}\left|\frac{N_\mathrm{c}}{2}, \mathfrak{s}\right\rangle, \quad \hat{J}^2 \left|\frac{N_\mathrm{c}}{2}, \mathfrak{s}\right\rangle = \frac{N_\mathrm{c}\,(N_\mathrm{c}+2)}{4}\left|\frac{N_\mathrm{c}}{2}, \mathfrak{s}\right\rangle, \quad [\hat{J}^2, \hat{J}_3] = 0. \tag{4.8}$$

This remarkable result is due to the fact that pion occupation numbers on the lattice are not just bounded from below but also from above. The pion dynamics encoded in the Hamiltonian is that of a relativistic pion gas as reviewed in Sec. 2.4. The fact that baryon becomes static is due to its non-relativistic nature. Its restmass is large but finite, and it has been determined in continuous time in [C2] to be $am_B^{\mathrm{CT}} = 3.628(22)$ which is consistent with the extrapolated value $am_B^{\mathrm{extrap}} = 3.649(20)$ ($\xi \to \infty$). We will use this mass to set the temperature and baryon chemical potential in Sec. 4.3.

4.3 Grand-canonical and canonical phase diagram

In this section I will review the results on the phase diagram obtained from Quantum Monte Carlo in the continuous time limit, described in detail in [C2]. This systematically improves on the results discussed in Sec. 2.4. Here, we have studied both the chiral and nuclear transition. To obtain the nuclear transition and both the grand-canonical phase diagram in the μ_B - T plane and the canonical phase diagram in the n_B - T plane with $a^3 n_B$ the baryon density (the continuous time counterpart of Eq. (2.12)), we

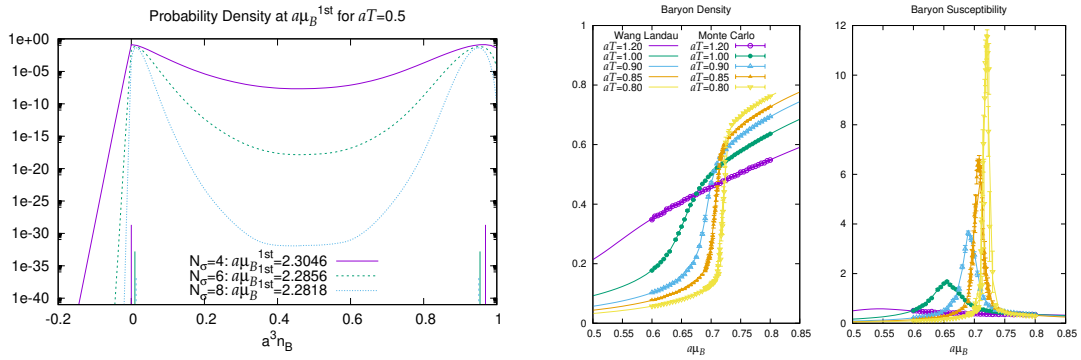

FIGURE 4.4: *Left*: The probability density, obtained from reweighting the density of states to $a\mu_B^{1^{st}}(N_s)$ such that the two maxima are of the same height, for various volumes and at a fixed temperature $\mathcal{T} = 0.5$. The first maximum denotes the baryon density $a^3 n_B^{(1)}$ where the mixed phase in the canonical phase diagram begins, the second maximum denotes the baryon density $a^3 n_B^{(2)}$ where the mixed phase ends. *Right:* Comparison of the Wang Landau method with QMC data for the baryon density $a^3 \langle n_B \rangle$ and the baryon susceptibility $a^6 \Lambda_\sigma (\langle n_B^2 \rangle - \langle n_B \rangle^2)$, as a function of $\mu_\mathcal{B}$ for various temperatures $\mathcal{T}$ and on a $6^3 \times$ CT lattice. The data are in perfect agreement. From [C2].

have introduced a resummation of baryon world-lines with mesonic world-lines, called polymers (the continuous time analogue of the Karsch-Mütter resummation [84]). This is advantageous as (1) it allows to both simulate at real and imaginary chemical potential, (2) we are able to adapt the Wang-Landau method [55] to obtain also the canonical phase diagram from the density of states at high precision. The $\mathcal{Q}$-polymers are related to the baryon density:

$$|\mathcal{Q}\rangle_{\vec{x}} = |B^+\rangle_{\vec{x}} + |B^-\rangle_{\vec{x}} + \sum_{\mathfrak{m}=0}^{N_c} |\mathfrak{m}\rangle_{\vec{x}}, \qquad Q(C) = \sum_{\vec{x}} q_{\vec{x}}(C), \tag{4.9}$$

where for a given configuration C, the single site weights and total distribution of baryon number in terms of the polymer number $|B| \leq Q \leq V$ are related via:

$$q_{\vec{x}} = |b_{\vec{x}}| + m_{\vec{x}} \in \{0, 1\}, \qquad w_\mathcal{Q}(\mu_B/T) = N_c + 1 + 2\cosh\left(\frac{\mu_B}{T}\right), \tag{4.10}$$

$$D^{\mathcal{QB}}_{\mu_B/T}(Q, B) = \sum_{P=|B|}^{Q} \binom{Q}{\frac{P+B}{2}, \frac{P-B}{2}, Q-P} \frac{e^{B\mu_B/T}(N_c+1)^{Q-P}}{w_q(\mu_B/T)^Q}. \tag{4.11}$$

For some observables we need higher moments of the baryon number. We have measured the histograms for $\mathcal{Q}$-polymers, $H^\mathcal{Q}_{V,\mathcal{T},\mu_\mathcal{B}}(Q)$, and get the histogram in the baryon number $H^\mathcal{B}_{V,\mathcal{T},\mu_\mathcal{B}}(B)$ from the above distributions and higher moments or cumulants given by some function $f(B)$:

$$H^\mathcal{B}_{V,\mathcal{T},\mu_\mathcal{B}}(B) = \sum_{Q=B}^{V} D^{\mathcal{QB}}_{\mu_B/T}(Q, B)\, H^\mathcal{Q}_{V,\mathcal{T},\mu_\mathcal{B}}(Q), \qquad \langle f(B) \rangle = H^\mathcal{B}_{V,\mathcal{T},\mu_\mathcal{B}}(B)\, f(B). \tag{4.12}$$

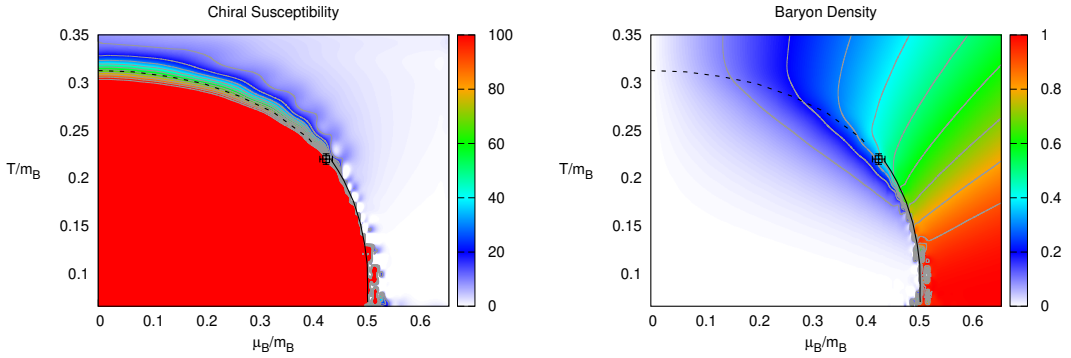

FIGURE 4.5: *Left:* The chiral susceptibility in the μ_B - T plane in units of the baryon mass m_B. The chiral susceptibility in the μ_B - T plane in units of the baryon mass m_B. *Right:* The baryon density in the μ_B - T plane in units of the baryon mass m_B.

As for large spatial volumes V, the distributions in Eq. (4.11) involve large numbers. In practice we use its logarithmic version.

One method to determine the canonical partition sum $\mathcal{Z}_C(\mathcal{T}, B)$ is to obtain the $\mathcal{Z}_{GC}$ for imaginary chemical potential and reweighting for the resulting Fourier coefficient [146]. In the dual representation it can be determined directly by the Wang-Landau method, which measures numerically the histogram $g(\mathcal{T}, Q)$ up to the target precision and

$$\mathcal{Z}_{GC}(\mathcal{T}, \mu_{\mathcal{B}}) = \sum_{B=-V}^{V} \mathcal{Z}_C(\mathcal{T}, B) e^{B\mu_B/T}, \quad \mathcal{Z}_C(\mathcal{T}, B) = \sum_{P=|B|}^{Q} \binom{Q}{\frac{P+B}{2}, \frac{P-B}{2}, Q-P} g(\mathcal{T}, Q) \tag{4.13}$$

This histogram method improves drastically over the usual measurement of higher moments. We performed simulations at a set of fixed temperatures and reweight the obtained density of states to the critical $a\mu_B^{1^{st}}$, which is characterized by equal probability of the low and high density phase, see Fig. (4.4) (*left*).

The QMC simulations allow to determine the chiral and nuclear transition, which also coincide (as discussed for finite N_t in Sec. 2.4) in the continuous time limit. In Fig. 4.5 the chiral susceptibility and baryon density are shown in the μ_B - T plane, where we have used the previously measured baryon mass to rescale into dimensionless ratios. All results are obtained for the chiral limit (see Sec. 5.2 for the prospects on QMC for finite quark mass), where the chiral condensate is strictly zero in a finite volume (the ϵ-regime). We also determined the chiral condensate via chiral perturbation theory in a finite box [121], see [A4], [C2]. The second order phase boundary of the chiral transition is determined via finite size scaling of the chiral susceptibility $\lim_{L\to\infty} \chi(L, T_c) \propto L^{\gamma/\nu}$

(with $\chi \propto \langle(\bar{\psi}\psi)^2\rangle$ in the chiral limit) with critical exponents of the 3-dim. O(2) universality class [147], up to the chiral tricritical point.

With $m_B \simeq 938\text{GeV}$ and the pseudo-critical crossover temperature $T_{pc} \simeq 154\text{MeV}$ [17] we find that the ratio at strong coupling and in the chiral limit is more than twice as large:

$$\left.\frac{T_c}{m_B}\right|_{CT-SC} = 0.379(1), \qquad \left.\frac{T_{pc}}{m_B}\right|_{\text{cont.}} = 0.164(9). \tag{4.14}$$

The comparison improves for $\beta > 0$, as the pseudo-critical transition temperature drops while the baryon mass is quite insensitive [B2]. The determination of $T_c(\mu_B)$ at finite chemical potential is straight forward up to the tricritical point $(a\mu_B^{\text{TCP}}, aT^{\text{TCP}})$, beyond which both the chiral susceptibility χ and the baryon density n_B develops a gap, see Fig. 4.5 (*left*).

The nuclear liquid gas transition and its critical end-point agrees with the chiral first order transition and its tricritical point in the strong coupling limit (but see Sec. 3.1 for $\beta > 0$). This phase boundary is measured from the baryon density and its susceptibility, both by QMC simulations at finite chemical potential, Fig. 4.5 (*right*), and by the Wang-Landau method, see Fig. 4.4 (*right*) for the comparison. Monte Carlo simulations at low temperatures across the strong first order transition are challenging: for $\mu_B < \mu_B^{1st}$, the phase is described as an ideal pion gas, for $\mu_B > \mu_B^{1st}$ the phase is that of a baryon crystal (liquid), associated with a large change in entropy. At zero temperature, the baryon density jumps at $a\mu_B^{1st}$ from $\langle n_B = 0\rangle$ to $\langle n_B = 1\rangle$ (as it is a quark saturated phase). This challenge is overcome by the Wang-Landau method: a zero temperature extrapolation yields $a\mu_B^{1st} = 1.86(2)$. The binding energy between baryons in the continuous time limit is even stronger as for discrete simulations ($\gamma = 1$ [96]):

$$\left[\frac{m_B - \mu_B^{1st}}{m_B}\right]_{\text{CT}} \simeq 0.489(6), \qquad \left[\frac{m_B - \mu_B^{1st}}{m_B}\right]_{\gamma=1} \simeq 0.381(3). \tag{4.15}$$

The phase boundaries of both the grand-canonical and canonical phase diagram are shown in Fig. 4.6. In the grand-canonical phase diagram, one can clearly see that the chiral first order phase boundary and the nuclear transition are on top. In the canonical phase diagram, a mixed phase of nucleons and nuclei exists, with its low and high density boundaries $n_B^{(1)}(aT)$, $n_B^{(2)}(aT)$. The low density boundary $a^3 n_B^{(1)}$ tends to zero, whereas the high density boundary $a^3 n_B^{(2)}$ tends to one. A meaningful density of nuclear matter cannot be assigned at strong coupling.

The nuclear end point is characterized by the vanishing of the mixed phase, resulting in $n_B^{(1)} = n_B^{(2)}$, at which the density of states becomes flat as the double peak structure

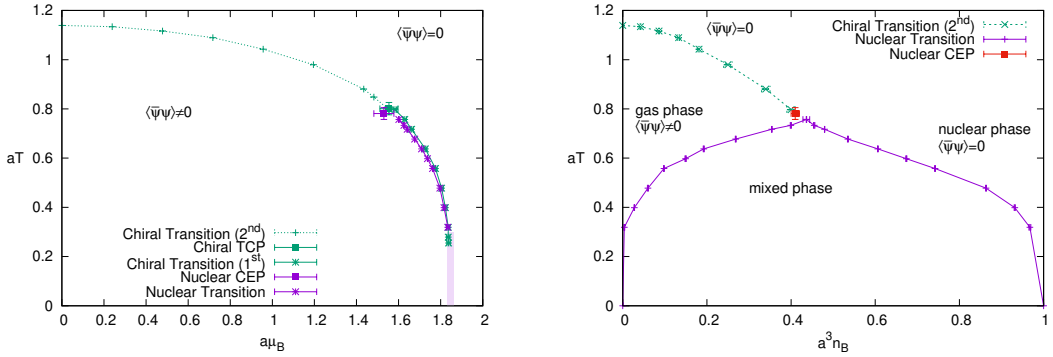

FIGURE 4.6: *Left:* The grand-canonical phase diagram, with the chiral transition obtained from Quantum Monte Carlo and the nuclear transition obtained from the Wang-Landau method. *Right:* The canonical phase diagram, with the phase boundary of the mixed phase obtained from the Wang-Landau method.

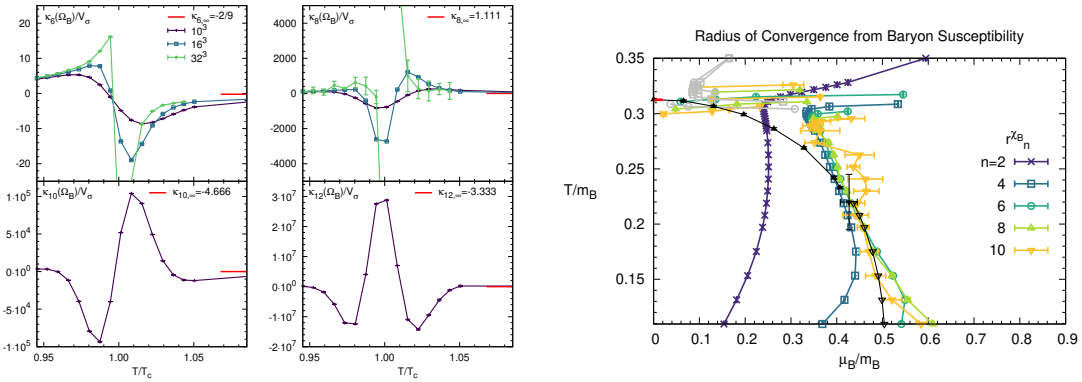

FIGURE 4.7: *Left:* Measurement of the cumulant κ_6 to κ_12 as a function of the temperature in the vicinity of T_c for volume 10^3 or greater. *Right:* The radius of convergence as estimated from the Taylor coefficients for the baryon susceptibility, compared to the actual phase boundary obtained from QMC. From [C2].

vanishes. The chiral tricritical point coincides with the nuclear critical endpoint (which can be made plausible via a percolation analysis, see [C2]), and is located at

$$aT^{\mathrm{TCP}} = 0.78(2), \qquad a\mu_B^{\mathrm{TCP}} = 1.53(5), \qquad a^3 n_B^{TCP} = 0.43(2). \tag{4.16}$$

This deviates substantially from the mean field value: $\mathcal{T}_{\mathrm{MF}}^{\mathrm{TCP}} = 0.866$, $\mu_{\mathcal{B}\,\mathrm{MF}}^{\mathrm{TCP}} = 1.731$ [86]. Our results also eliminate systematic uncertainties in previous findings for fixed N_t [96]. In the chiral limit, the chiral critical point may in principle be within reach with indirect methods, see Sec. 1.2.3, as $\mu_B^{\mathrm{TCP}}/T^{\mathrm{TCP}} = 1.96(7)$, but as discussed in Sec. 2.4, with increasing m_q this ratio increases rapidly.

The dual representation of SC-LQCD is a great laboratory to benchmark other methods to circumvent the sign problem, such as the Taylor expansion method [32], which might allow to estimate the location of a possible chiral critical endpoint based on estimate for

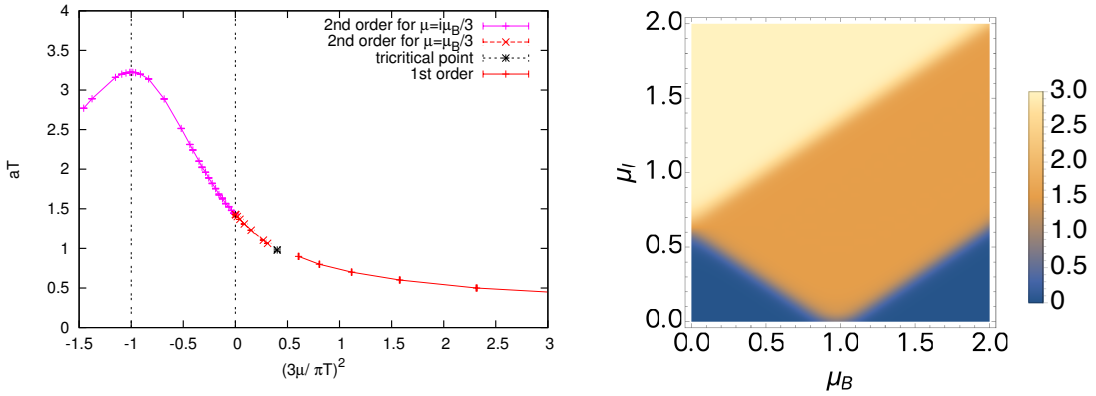

FIGURE 4.8: *Left:* Extension of the grand-canonical phase diagram to imaginary chemical potential, with the chiral transition temperature maximal at the Roberwe-Weiss point $i\mu_B = \pi T$ From [C1] *Right:* Isospin density at finite baryon and isospin chemical potential at zero temperature, showing strong phase boundaries form pion condensation. From [C2]

the radius of convergence of the Taylor series of the pressure or the baryon susceptibility. Whereas the current state of the art is limited to $\mathcal{O}((\mu_B/T)^6)$ with improved action [148] and $\mathcal{O}((\mu_B/T)^8)$ for unimproved action [149], in the dual representation via QMC, using the histogram methods Eq. (4.12), we were able to determine higher orders of Taylor coefficients, both for the pressure and the baryon susceptibility up to $\mathcal{O}((\mu_B/T)^{12})$. These are obtained from the cumulants κ_{2n} in terms of the total baryonic winding numbers $\Omega_B = \sum_{\vec{x}} \omega(\vec{x})$:

$$p(T,\mu_B) = p(T,\mu_B=0) + \sum_{n=1}^{\infty} c_{2n} \left(\frac{\mu_B}{T}\right)^{2n}, \qquad \chi_B = \sum_{n=2}^{\infty} n(n-1) c_{2n} \left(\frac{\mu_B}{T}\right)^{2n-2},$$
$$c_{2n} = \frac{T}{V}\frac{1}{(2n)!}\frac{\partial^{2n}\log\mathcal{Z}}{\partial(\mu_B/T)^{2n}} = \frac{T}{(2n)!}\frac{\kappa_{2n}(\Omega_B)}{V}. \tag{4.17}$$

The cumulants $\frac{\kappa_{2n}(\Omega_B)}{V}$ are shown in Fig. 4.7 (*left*) which oscillate around T_c, developing n inflection points from which aT_c can be estimated, extrapolating into the thermodynamic limit. From the Taylor coefficients we obtain an estimate for the phase boundary from the radius of convergence [150], shown in Fig. 4.7 (*right*):

$$r^\alpha = \lim_{n\to\infty} r_n^\alpha, \quad r_n^\alpha = \sqrt{\left|\alpha_x \frac{\kappa_n}{\kappa_{n+2}}\right|}, \quad \alpha_p = \sqrt{(n+2)(n+1)}, \quad \alpha_{\chi_B} = \sqrt{(n-1)n}. \tag{4.18}$$

We find that the actual phase boundary measured via QMC is approximated well already from $r_n^{\chi_B}$ with $n = 10$.

The finite density phase diagram can be extended in two ways:

(1) Based on the $\mathcal{Q}$-polymer resummation Eq. (4.9) we can simulate also at imaginary

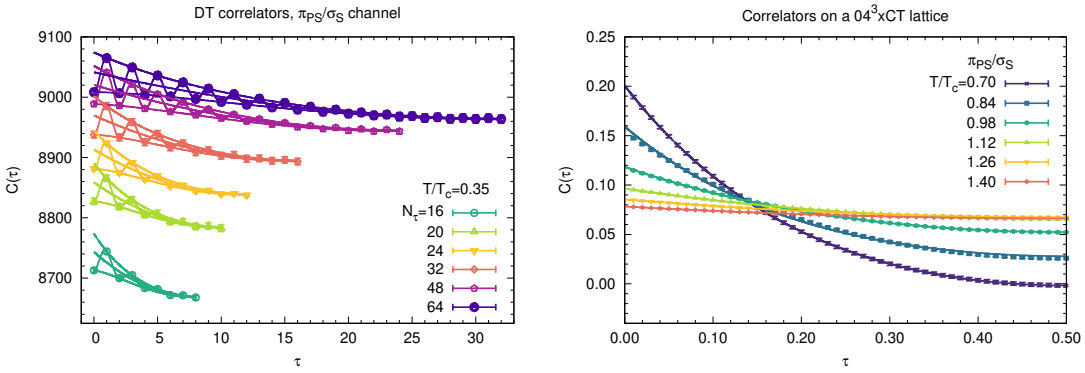

FIGURE 4.9: *Left:* Pion correlators at discrete time for various N_t, showing that the oscillatory behavior persists for larger N_t, with a well behaved continuous time limit. *Right:* Pion correlator at continuous time for various temperatures, for $N = 100$ bins. This is sufficient to extract the pole masses $M_\pi(T)$ to high precision. From [C2].

chemical potential, which is interesting in its own right due to the Roberge-Weiss periodicity [151] and the Roberge-Weiss transition [152]. The result for the strong coupling, chiral and continuous time limit is shown in Fig. 4.8 (*left*).

(2) Based on the $N_\mathrm{f} = 2$ Hamiltonian formulation we can extend the phase diagram into finite isospin chemical potential. First steps of the formulation were considered in [C3] for gauge theory U(2) and in [C2] for gauge group SU(3). Here, the corresponding Hamiltonian has a 92-dimensional Hilbert space per site, preliminary results exist so far for 1-dim QCD, see Fig. 4.8 (*right*).

4.4 Meson pole masses

The 2-point correlation function is sampled during worm evolution, see Sec. 1.4.1. Together with my former PhD student M. Klegrewe we have studied temporal correlation functions, from which we can extract the ground state energy corresponding to the meson pole mass [C4, C2] We were able to determine its dependence on temperature and baryon chemical potential. M. Klegrewe helped to implement the measurements of the correlators into the Quantum Monte Carlo code and performed most of the simulations and data analyis.

The definition of the temporal correlators at zero momentum $\vec{p} = 0$ for staggered fermions $\bar{\chi}$, χ, based on the local single-time-slice operators [153] is:

$$C_S(\tau) = \sum_{\vec{x}} C_S(\vec{x}, \tau), \qquad C_S(\vec{x}, \tau) = \langle \bar{\chi}_{\vec{0},0} \chi_{\vec{0},0} \bar{\chi}_{\vec{x},\tau} \chi_{\vec{x},\tau} \rangle g^S_{\vec{x},\tau}, \tag{4.19}$$

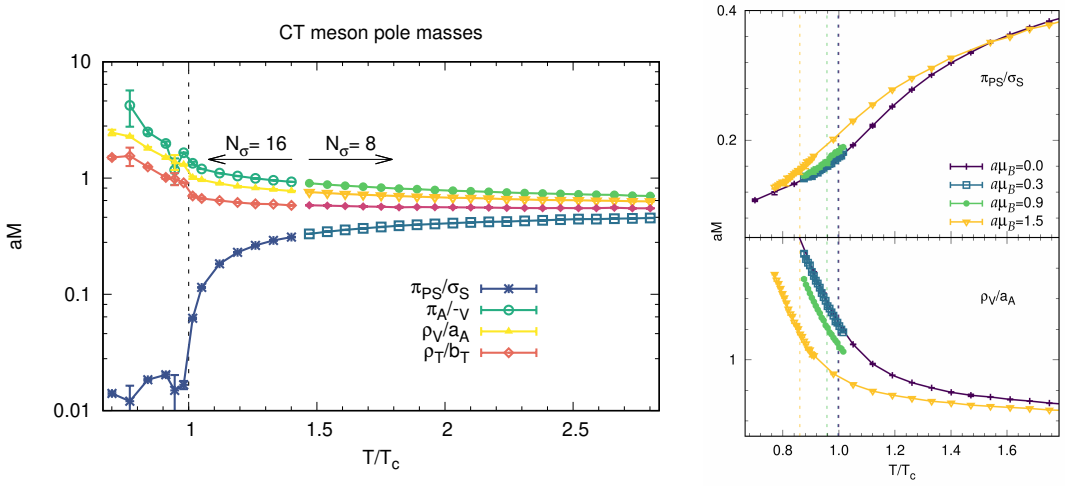

FIGURE 4.10: Meson pole masses aM *left:* for various quantum numbers J^{PC} as a function of the temperature, *right:* for various chemical potentials $\mu_{\mathcal{B}}$, as a function of the temperature. The vertical dashed lines indicate the transition temperatures, wich has an imprint on the meson masses. From [C2].

where the spin S of the meson is given by the kernel operators Γ^S in terms of phase factors $g^S_{\vec{x},\tau} \in \{\pm 1\}$. We only consider operators diagonal in spin-taste space: $\Gamma^S \otimes \Gamma^T$ with $\Gamma^T = \Gamma^{S*}$ and do not consider any flavor structure as $N_{\rm f} = 1$ (but see the Appendix in [C2] for $N_{\rm f} = 2$). In every mesonic correlator specified by Γ^S, there is a non-oscillating part and oscillating part with additional phase factor $(-1)^\tau$, which is due to the even-odd decomposition for staggered fermions. This parity partner has opposite spin, parity and taste content. Thus the non-oscillating and oscillating part correspond to different physical states. Of particular interest is the pion π_{PS} which is the Goldstone boson for the residual chiral symmetry, Eq. (1.3). Throughout the worm evolution, monomer two-point correlation functions are accumulated whenever head and tail are at opposite parities. This book-keeping also works in the continuous time limit (see [C4] for details):

$$C_S(\vec{x}_H - \vec{x}_T, \tau_H - \tau_T) = C_S(\vec{x}, \tau) = N_c \frac{H(C_S(\vec{x}, \tau))}{Z} \tag{4.20}$$

$$O(C_S(\vec{x}, \tau)) \;\to\; H(C_S(\vec{x}, \tau)) + f(\mathcal{T}) g^S_{\vec{x},\tau}\, \delta_{x_T, x_1} \delta_{x_H, x_2}, \tag{4.21}$$

with Z the number of worm updates and H the histogram for the 2-point function incremented during worm updates. Summing over the correlators yields immediately the corresponding susceptibilities:

$$a^6 \chi_S^{\rm CT} = \frac{\mathcal{T}}{N_s^3} \sum_{\vec{x}} \int_0^{1/\mathcal{T}} d\tau\; C_S(\vec{x}, \tau). \tag{4.22}$$

The non-oscillating and oscillating parts of the correlators are related to the corresponding meson masses:

$$C_{\mathrm{NO}}(\tau) = A_{\mathrm{NO}} \cosh(a_t M_{\mathrm{NO}}(\tau - N_t/2)), \quad C_{\mathrm{O}}(\tau) = A_{\mathrm{O}} \cosh(a_t M_{\mathrm{O}}(\tau - N_t/2). \quad (4.23)$$

It is advantageous to consider the linear combinations

$$C_{\mathrm{Odd}}(\tau) = C_{\mathrm{NO}} + C_{\mathrm{O}}, \qquad C_{\mathrm{Even}}(\tau) = C_{\mathrm{NO}} - C_{\mathrm{O}}, \qquad (4.24)$$

as it can be measured in the continuous time limit, where we can distinguish even and odd τ via emission and absorption events, see Fig. 4.3. In Fig. 4.9 the discrete time correlators (*left*) and the continuous time correlators for various temperature (*right*) are shown for the pion with $g^{\pi}_{\vec{x}} = (-1)^{x+y+z}$.

Even in the continuous time limit, it is necessary to discretize the temporal correlators due to memory limitations and finite statistics. The histograms depend on the bin size $\Delta\tau = \frac{1}{\mathcal{T}N}$, with N the number of bins. In principle one could measure the continuous time correlators without introducing a binning [154], but in practice this seems not necessary as our measurements for $N = 100, 200, 400$ lead to almost identical results.

The groundstate masses are meson pole masses: $E_0(\vec{p} = 0) = M$, extracted via the dimensionless quantity M/T by multi-state fits (see [C2] for details) and converted via $aM = \kappa\mathcal{T}\, M/T$ with κ as determined in Sec. 4.1. The errors for pole masses extracted from CT-correlators are much smaller than those from corresponding DT-correlators, and uncertainties about 3% in the extrapolation are circumvented.

As a function of the temperature, Fig. 4.10 (*left*), the pion becomes massless below T_c in the thermodynamic limit and heavy at the chiral transition. The pion and all other mesons do not acquire a thermal mass, rather, they all tend to the same high temperature value $aM = 0.411(1)$. We suspect that this is an artifact of the strong coupling limit: even at high temperatures, in the chirally restored phase, the quarks are still confined into mesons. Hence, they do not experience the anti-periodic boundary conditions [155] and will not receive contributions from the lowest Matsubara frequencies πT above T_c. The extension to finite chemical potential $\mu_{\mathcal{B}}$ is straight forward, the temperature dependence of the pole masses for various chemical potentials below $\mu_{\mathcal{B}}{}^{\mathrm{TCP}}$ is shown in Fig. 4.10 (*right*): as T_c drops with increasing chemical potential, the pole masses have a correspondingly modified temperature dependence.

Chapter 5

Summary and Outlook

5.1 Summary

In the previous chapters and within the publications attached, I have illustrated that the strong coupling regime of lattice QCD is a promising approach to study finite density lattice QCD in a regime where the finite density sign problem is under control. This was achieved by a dual formulation that was extended to finite inverse gauge coupling β via the strong coupling expansion for staggered fermions in Chap. 3, and to the Euclidean continuous time limit that could be studied via Quantum Monte Carlo in Chap. 4. Many techniques to circumvent the sign problem could be combined with the dual formulation which makes it a powerful tool that can benchmark results obtained from other methods.

In the publications, new methods were proposed and various results obtained: the grand-canonical and canonical phase diagram, bulk thermodynamics, and the evaluation of the baryon mass and nuclear interactions. These results cannot yet be compared to full lattice QCD, but the diagrammatic nature gives additional insights that standard HMC cannot give. For unambiguous results on anisotropic lattices that are needed for thermodynamics in the strong coupling regime, a lot of effort was put into the renormalization of the temperature and baryon chemical potential.

It was expected from the start that the sign problem is the greatest challenge within dual formulations beyond the strong coupling limit. Every method that has been proposed by using some sort of dual variables to solve sign problems only does so for very specific models, such as bosonic matter fields, Abelian gauge groups [98], or low dimensions. There is no generic solution to the sign problem, and every method has its caveats. For QCD at finite baryon density, there is no feasible method yet that works for any quark mass and any value of β.

In our approach, it was expected that as soon as the plaquette surfaces (world-sheets) would grow sufficiently to allow for non-trivial geometries, the sign problem is reintroduced. At what value of β this would occur could not be known a priori, but required Monte Carlo simulations including the higher order gauge corrections. It turned out that in the plaquette occupation number basis we were using, the sign problem already became severe for $\beta > 1$. Hence the splitting of the nuclear and chiral first order lines, if it occurs at all, has not yet been observed.

Despite these numerical limitations, we were able to write down the partition function of the dual representation to arbitrary orders in β by computing the intricate group-theoretical weights. Invariant integration over SU(N), i.e. over class functions obtained from the expansion of the staggered Dirac operator and the Wilson gauge action resulted in tensorial weights that compose a tensor network. We introduced operators (we called them decoupling operators) that could map the permutations of color indices on each link connected to a site into multi-indices that defines the tensors. The weights are still local, but can no longer be decompose into site weight and link weight beyond $\mathcal{O}(\beta^2)$. These findings, published in [B8], are valid to any order in β and we have explicitly computed all tensorial weights up to $\mathcal{O}(\beta^6)$. On small volumes, where exact enumeration is feasible, we have checked that up to this order we have agreement with hybrid Monte Carlo data for all observables considered (chiral condensate and susceptibility, average plaquette and Polyakov loop). In theory, even higher orders can be addressed, in practice the list of tensors rapidly increases with the order in β and limits the applicability of the worm algorithm. Our strategy has a lot of potential for the future developments. At the moment we explore machine learning techniques to simplify the large list of vertices to a smaller list of weights suitable for a worm algorithm.

Other groups have made some progress in the last years that however were not applicable to full QCD yet: The group at Universität Graz led by C. Gattringer has developed a formulation in terms of Abelian color cycles [156] and Abelian color fluxes [157], which is however only sign problem-free for gauge group SU(2) and requires a larger set of dual variables. O. Borisenko and colleagues have also considered invariant SU(N) integration [133] and recently obtained results for the Polyakov effective theory based on Wilson fermions [158, 159]. The group of O. Philipsen in Frankfurt that pioneered the so-called 3-dim. effective theory based on Wilson fermions [50] are now computing observables analytically via a linked cluster expansion. We have an ongoing collaboration to extend the range of validity for both effective theories to establish an overlap in quark mass and temperature. A recent review of the strong coupling methods including results of the 3-dim. effective theory is [160].

5.2 Future research

All publications discussed here make use the staggered fermion discretization, which has some limitations besides the sign problem: so far, all results are valid for unrooted staggered fermions, which in the continuum corresponds to 4 flavors ($N_{\rm f} = 1$ at strong coupling) or 8 flavors ($N_{\rm f} = 2$ at strong coupling). There is no direct way to implement rooting in the dual representation as this is applied to the fermion determinant and would yield non-local interactions. Hence it is natural to also consider the dual representation for Wilson fermions, which can be done at least in this respect: (1) The dual representation in terms of a tensor network can equally be evaluated for Wilson fermions. (2) The density of states used to obtain the canonical phase diagram could be also applied to the results in the 3-dim. effective theory used by the group of O. Philipsen.

To extend our tensor network approach [B8] to much larger values of $\beta \lesssim 6$, we attempted to incorporate the character expansion for staggered fermions. This is highly non-trivial (in contrast to pure Yang Mills theory or Wilson fermions). We managed to incorporate the fundamental and adjoint characters (which is not yet published but is contained in the PhD thesis of my former student G. Gagliardi).

With my former student T. Kaya I have explored alternative monomer updates that could lead to the Hamiltonian formulation at finite quark masses. That this limit is well defined has been discussed in [C2]. The Hamiltonian formulation is then planned to be extended to $N_{\rm f} = 2$ and to study the $T - \mu_B - \mu_I$ phase diagram in 3+1 dimensions.

References

Articles reviewed in Chapter 2

[A1] Philippe de Forcrand, Seyong Kim, and Wolfgang Unger. Conformality in many-flavour lattice QCD at strong coupling. *JHEP*, 02:051, 2013.
Link to reprint: Sec. A.1.

[A2] Wolfgang Unger. Combinatorics of Lattice QCD at Strong Coupling. *PoS*, LATTICE2014:192, 2014.
Link to reprint: Sec. A.2.

[A3] Philippe de Forcrand, Paul Romatschke, Wolfgang Unger, and Helvio Vairinhos. Thermodynamics of strongly-coupled lattice QCD in the chiral limit. *PoS*, LATTICE2016:086, 2017.
Link to reprint: Sec. A.3.

[A4] Philippe de Forcrand, Wolfgang Unger, and Helvio Vairinhos. Strong-Coupling Lattice QCD on Anisotropic Lattices. *Phys. Rev.*, D97(3):034512, 2018.
Link to reprint: Sec. A.4.

[A5] W. Unger, Dennis Bollweg, and Marc Klegrewe. Thermodynamics at Strong Coupling on Anisotropic Lattices. *PoS*, LATTICE2018:181, 2018.
Link to reprint: Sec. A.5.

[A6] Jangho Kim and Wolfgang Unger. Quark Mass Dependence of the QCD Critical End Point in the Strong Coupling Limit. *PoS*, LATTICE2016:035, 2016.
Link to reprint: Sec. A.6.

Articles reviewed in Chapter 3

[B1] Wolfgang Unger. The Phase Diagram of Lattice QCD in the Strong Coupling Limit and Away from It. *Acta Phys. Polon. Supp.*, 7(1):127–136, 2014.
Link to reprint: Sec. B.1.

[B2] Philippe de Forcrand, Jens Langelage, Owe Philipsen, and Wolfgang Unger. Lattice QCD Phase Diagram In and Away from the Strong Coupling Limit. *Phys. Rev. Lett.*, 113(15):152002, 2014.
Link to reprint: Sec. B.2.

[B3] Philippe de Forcrand, Owe Philipsen, and Wolfgang Unger. QCD phase diagram from the lattice at strong coupling. *PoS*, CPOD2014:073, 2015.
Link to reprint: Sec. B.3.

[B4] Giuseppe Gagliardi, Jangho Kim, and Wolfgang Unger. Dual Formulation and Phase Diagram of Lattice QCD in the Strong Coupling Regime. *EPJ Web Conf.*, 175:07047, 2018.
Link to reprint: Sec. B.4.

[B5] Jangho Kim, Owe Philipsen, and Wolfgang Unger. On the β- and Quark Mass Dependence of the Nuclear Transition in the Strong Coupling Regime. *PoS*, LATTICE2019:064, 2019.
Link to reprint: Sec. B.5.

[B6] Jangho Kim, Marc Klegrewe, and Wolfgang Unger. Gauge Corrections to Strong Coupling Lattice QCD on Anisotropic Lattices. In *37th International Symposium on Lattice Field Theory*, 2019.
Link to reprint: Sec. B.6.

[B7] Giuseppe Gagliardi and Wolfgang Unger. Towards a Dual Representation of Lattice QCD. *PoS*, LATTICE2018:224, 2018.
Link to reprint: Sec. B.7.

[B8] Giuseppe Gagliardi and Wolfgang Unger. New dual representation for staggered lattice QCD. *Phys. Rev. D*, 101(3):034509, 2020.
Link to reprint: Sec. B.8.

Articles reviewed in Chapter 4

[C1] Wolfgang Unger and Philippe de Forcrand. Continuous Time Monte Carlo for Lattice QCD in the Strong Coupling Limit. *PoS*, LATTICE2011:218, 2011.
Link to reprint: Sec. C.1.

[C2] Marc Klegrewe and Wolfgang Unger. Strong Coupling Lattice QCD in the Continuous Time Limit. *Phys. Rev. D*, 102(3):034505, 2020.
Link to reprint: Sec. C.2.

[C3] Wolfgang Unger and Philippe de Forcrand. New algorithms and new results for strong coupling LQCD. *PoS*, LATTICE2012:194, 2012.
Link to reprint: Sec. C.3.

[C4] Marc Klegrewe and Wolfgang Unger. Temporal Correlators in the Continuous Time Formulation of Strong Coupling Lattice QCD. *PoS*, LATTICE2018:182, 2018.
Link to reprint: Sec. C.4.

Further References

[1] Jean-Michel Drouffe and Jean-Bernard Zuber. Strong Coupling and Mean Field Methods in Lattice Gauge Theories. *Phys. Rept.*, 102:1, 1983.

[2] R. Hagedorn. Statistical thermodynamics of strong interactions at high-energies. *Nuovo Cim. Suppl.*, 3:147–186, 1965.

[3] H. Fritzsch, Murray Gell-Mann, and H. Leutwyler. Advantages of the Color Octet Gluon Picture. *Phys. Lett. B*, 47:365–368, 1973.

[4] David J. Gross and Frank Wilczek. Ultraviolet Behavior of Nonabelian Gauge Theories. *Phys. Rev. Lett.*, 30:1343–1346, 1973.

[5] H. David Politzer. Reliable Perturbative Results for Strong Interactions? *Phys. Rev. Lett.*, 30:1346–1349, 1973.

[6] N. Cabibbo and G. Parisi. Exponential Hadronic Spectrum and Quark Liberation. *Phys. Lett. B*, 59:67–69, 1975.

[7] John C. Collins and M. J. Perry. Superdense Matter: Neutrons Or Asymptotically Free Quarks? *Phys. Rev. Lett.*, 34:1353, 1975.

[8] T. Matsui and H. Satz. J/ψ Suppression by Quark-Gluon Plasma Formation. *Phys. Lett. B*, 178:416–422, 1986.

[9] Ulrich W. Heinz and Maurice Jacob. Evidence for a new state of matter: An Assessment of the results from the CERN lead beam program. 1 2000.

[10] John Adams et al. Experimental and theoretical challenges in the search for the quark gluon plasma: The STAR Collaboration's critical assessment of the evidence from RHIC collisions. *Nucl. Phys. A*, 757:102–183, 2005.

[11] K Aamodt et al. Elliptic flow of charged particles in Pb-Pb collisions at 2.76 TeV. *Phys. Rev. Lett.*, 105:252302, 2010.

[12] Anton Andronic, Peter Braun-Munzinger, Krzysztof Redlich, and Johanna Stachel. Decoding the phase structure of QCD via particle production at high energy. *Nature*, 561(7723):321–330, 2018.

[13] A. Chodos, R. L. Jaffe, K. Johnson, Charles B. Thorn, and V. F. Weisskopf. A New Extended Model of Hadrons. *Phys. Rev. D*, 9:3471–3495, 1974.

[14] Kenneth G. Wilson. Confinement of Quarks. *Phys. Rev. D*, 10:2445–2459, 1974.

[15] Larry D. McLerran and Benjamin Svetitsky. A Monte Carlo Study of SU(2) Yang-Mills Theory at Finite Temperature. *Phys. Lett. B*, 98:195, 1981.

[16] Szabolcs Borsanyi, Zoltan Fodor, Christian Hoelbling, Sandor D Katz, Stefan Krieg, Claudia Ratti, and Kalman K. Szabo. Is there still any T_c mystery in lattice QCD? Results with physical masses in the continuum limit III. *JHEP*, 09:073, 2010.

[17] A. Bazavov et al. The chiral and deconfinement aspects of the QCD transition. *Phys. Rev. D*, 85:054503, 2012.

[18] A. I. Ivanytskyi, K. A. Bugaev, V. V. Sagun, L. V. Bravina, and E. E. Zabrodin. Influence of flow constraints on the properties of the critical endpoint of symmetric nuclear matter. *Phys. Rev. C*, 97(6):064905, 2018.

[19] Larry McLerran and Robert D. Pisarski. Phases of cold, dense quarks at large N(c). *Nucl. Phys. A*, 796:83–100, 2007.

[20] Mark G. Alford, Andreas Schmitt, Krishna Rajagopal, and Thomas Schäfer. Color superconductivity in dense quark matter. *Rev. Mod. Phys.*, 80:1455–1515, 2008.

[21] Misha A. Stephanov, K. Rajagopal, and Edward V. Shuryak. Signatures of the tricritical point in QCD. *Phys. Rev. Lett.*, 81:4816–4819, 1998.

[22] O. Kaczmarek, F. Karsch, E. Laermann, C. Miao, S. Mukherjee, P. Petreczky, C. Schmidt, W. Soeldner, and W. Unger. Phase boundary for the chiral transition in (2+1) -flavor QCD at small values of the chemical potential. *Phys. Rev. D*, 83:014504, 2011.

[23] Claudio Bonati, Massimo D'Elia, Francesco Negro, Francesco Sanfilippo, and Kevin Zambello. Curvature of the pseudocritical line in QCD: Taylor expansion matches analytic continuation. *Phys. Rev. D*, 98(5):054510, 2018.

[24] A. Bazavov et al. Chiral crossover in QCD at zero and non-zero chemical potentials. *Phys. Lett. B*, 795:15–21, 2019.

[25] H.B. Nielsen and M. Ninomiya. A no-go theorem for regularizing chiral fermions. *Physics Letters B*, 105(2):219–223, 1981.

[26] Leonard Susskind. Lattice Fermions. *Phys. Rev. D*, 16:3031–3039, 1977.

[27] P. Hasenfratz and F. Karsch. Chemical Potential on the Lattice. *Phys. Lett. B*, 125:308–310, 1983.

[28] R. V. Gavai. Chemical Potential on the Lattice Revisited. *Phys. Rev. D*, 32:519, 1985.

[29] Owe Philipsen. Lattice QCD at non-zero temperature and baryon density. In *Les Houches Summer School: Session 93: Modern perspectives in lattice QCD: Quantum field theory and high performance computing*, 9 2010.

[30] S. Duane, A. D. Kennedy, B. J. Pendleton, and D. Roweth. Hybrid Monte Carlo. *Phys. Lett. B*, 195:216–222, 1987.

[31] Matthias Troyer and Uwe-Jens Wiese. Computational complexity and fundamental limitations to fermionic quantum Monte Carlo simulations. *Phys. Rev. Lett.*, 94:170201, 2005.

[32] C. R. Allton, M. Doring, S. Ejiri, S. J. Hands, O. Kaczmarek, F. Karsch, E. Laermann, and K. Redlich. Thermodynamics of two flavor QCD to sixth order in quark chemical potential. *Phys. Rev.*, D71:054508, 2005.

[33] Philippe de Forcrand and Owe Philipsen. The QCD phase diagram for three degenerate flavors and small baryon density. *Nucl. Phys.*, B673:170–186, 2003.

[34] Massimo D'Elia and Maria-Paola Lombardo. Finite density QCD via imaginary chemical potential. *Phys. Rev.*, D67:014505, 2003.

[35] R. Bellwied, S. Borsanyi, Z. Fodor, J. Günther, S. D. Katz, C. Ratti, and K. K. Szabo. The QCD phase diagram from analytic continuation. *Phys. Lett. B*, 751:559–564, 2015.

[36] Z. Fodor and S. D. Katz. A New method to study lattice QCD at finite temperature and chemical potential. *Phys. Lett.*, B534:87–92, 2002.

[37] Z. Fodor and S. D. Katz. Critical point of QCD at finite T and mu, lattice results for physical quark masses. *JHEP*, 04:050, 2004.

[38] G. Parisi and Yong-shi Wu. Perturbation Theory Without Gauge Fixing. *Sci. Sin.*, 24:483, 1981.

[39] Poul H. Damgaard and Helmuth Huffel. Stochastic Quantization. *Phys. Rept.*, 152:227, 1987.

[40] J. Berges and I. O. Stamatescu. Simulating nonequilibrium quantum fields with stochastic quantization techniques. *Phys. Rev. Lett.*, 95:202003, 2005.

[41] Dénes Sexty. Simulating full QCD at nonzero density using the complex Langevin equation. *Phys. Lett.*, B729:108–111, 2014.

[42] Gert Aarts, Felipe Attanasio, Benjamin Jäger, and Dénes Sexty. The QCD phase diagram in the limit of heavy quarks using complex Langevin dynamics. *JHEP*, 09:087, 2016.

[43] Gert Aarts, Erhard Seiler, and Ion-Olimpiu Stamatescu. The Complex Langevin method: When can it be trusted? *Phys. Rev. D*, 81:054508, 2010.

[44] Marco Cristoforetti, Francesco Di Renzo, and Luigi Scorzato. New approach to the sign problem in quantum field theories: High density QCD on a Lefschetz thimble. *Phys. Rev.*, D86:074506, 2012.

[45] Christian Schmidt and Felix Ziesché. Simulating low dimensional QCD with Lefschetz thimbles. *PoS*, LATTICE2016:076, 2017.

[46] F. Di Renzo and G. Eruzzi. One-dimensional QCD in thimble regularization. *Phys. Rev.*, D97(1):014503, 2018.

[47] Stefan Bluecher, Jan M. Pawlowski, Manuel Scherzer, Mike Schlosser, Ion-Olimpiu Stamatescu, Sebastian Syrkowski, and Felix P. G. Ziegler. Reweighting Lefschetz Thimbles. *SciPost Phys.*, 5(5):044, 2018.

[48] Shailesh Chandrasekharan and Uwe-Jens Wiese. Meron cluster solution of a fermion sign problem. *Phys. Rev. Lett.*, 83:3116–3119, 1999.

[49] Shailesh Chandrasekharan. The Fermion bag approach to lattice field theories. *Phys. Rev. D*, 82:025007, 2010.

[50] Michael Fromm, Jens Langelage, Stefano Lottini, Mathias Neuman, and Owe Philipsen. Onset Transition to Cold Nuclear Matter from Lattice QCD with Heavy Quarks. *Phys. Rev. Lett.*, 110(12):122001, 2013.

[51] Jonas Glesaaen, Mathias Neuman, and Owe Philipsen. Equation of state for cold and dense heavy QCD. *JHEP*, 03:100, 2016.

[52] Hélvio Vairinhos and Philippe de Forcrand. Integrating out lattice gauge fields. *PoS*, CPOD2014:061, 2015.

[53] Bastian B. Brandt, Robert Lohmayer, and Tilo Wettig. Induced QCD I: Theory. *JHEP*, 11:087, 2016.

[54] Bastian B. Brandt, Robert Lohmayer, and Tilo Wettig. Induced QCD II: Numerical results. *JHEP*, 07:043, 2019.

[55] Fugao Wang and D. P. Landau. Efficient, multiple-range random walk algorithm to calculate the density of states. *Phys. Rev. Lett.*, 86:2050–2053, Mar 2001.

[56] Kurt Langfeld, Biagio Lucini, and Antonio Rago. The density of states in gauge theories. *Phys. Rev. Lett.*, 109:111601, 2012.

[57] Simon Hands, John B. Kogut, Maria-Paola Lombardo, and Susan E. Morrison. Symmetries and spectrum of SU(2) lattice gauge theory at finite chemical potential. *Nucl. Phys. B*, 558:327–346, 1999.

[58] J. B. Kogut and D. K. Sinclair. Lattice QCD at finite isospin density at zero and finite temperature. *Phys. Rev. D*, 66:034505, 2002.

[59] B. B. Brandt, G. Endrodi, and S. Schmalzbauer. QCD phase diagram for nonzero isospin-asymmetry. *Phys. Rev. D*, 97(5):054514, 2018.

[60] Jangho Kim, Anh Quang Pham, Owe Philipsen, and Jonas Scheunert. The SU(3) spin model with chemical potential by series expansion techniques. *JHEP*, 10:051, 2020.

[61] R. Balian, J. M. Drouffe, and C. Itzykson. Gauge Fields on a Lattice. 3. Strong Coupling Expansions and Transition Points. *Phys. Rev. D*, 11:2104, 1975. [Erratum: Phys.Rev.D 19, 2514 (1979)].

[62] Gernot Munster. Strong Coupling Expansions for the Mass Gap in Lattice Gauge Theories. *Nucl. Phys. B*, 190:439–453, 1981. [Addendum: Nucl.Phys.B 200, 536–538 (1982), Erratum: Nucl.Phys.B 205, 648–648 (1982)].

[63] K. Seo. GLUEBALL MASS ESTIMATE BY STRONG COUPLING EXPANSION IN LATTICE GAUGE THEORIES. *Nucl. Phys. B*, 209:200–216, 1982.

[64] Ulli Wolff. Simulating the All-Order Strong Coupling Expansion III: $O(N)$ sigma/loop models. *Nucl. Phys. B*, 824:254–272, 2010. [Erratum: Nucl.Phys.B 834, 395–397 (2010)].

[65] F. J. Wegner. Duality in Generalized Ising Models and Phase Transitions Without Local Order Parameters. *J. Math. Phys.*, 12:2259–2272, 1971.

[66] Jens Langelage and Owe Philipsen. The deconfinement transition of finite density QCD with heavy quarks from strong coupling series. *JHEP*, 01:089, 2010.

[67] Michael Fromm, Jens Langelage, Stefano Lottini, and Owe Philipsen. The QCD deconfinement transition for heavy quarks and all baryon chemical potentials. *JHEP*, 01:042, 2012.

[68] Ulli Wolff. Strong coupling expansion Monte Carlo. *PoS*, LATTICE2010:020, 2010.

[69] Falk Bruckmann, Christof Gattringer, Thomas Kloiber, and Tin Sulejmanpasic. Dual lattice representations for O(N) and CP(N-1) models with a chemical potential. *Phys. Lett.*, B749:495–501, 2015. [Erratum: Phys. Lett.B751,595(2015)].

[70] Christof Gattringer and Thomas Kloiber. Lattice study of the Silver Blaze phenomenon for a charged scalar ϕ^4 field. *Nucl. Phys.*, B869:56–73, 2013.

[71] Ydalia Delgado Mercado, Christof Gattringer, and Alexander Schmidt. Dual Lattice Simulation of the Abelian Gauge-Higgs Model at Finite Density: An Exploratory Proof of Concept Study. *Phys. Rev. Lett.*, 111(14):141601, 2013.

[72] Christof Gattringer. Baryon bags in strong coupling QCD. *Phys. Rev.*, D97(7):074506, 2018.

[73] Christof Gattringer, Daniel Göschl, and Carlotta Marchis. Kramers–Wannier duality and worldline representation for the SU(2) principal chiral model. *Phys. Lett.*, B778:435–441, 2018.

[74] Falk Bruckmann and Jacob Wellnhofer. Diagrammatic representation of scalar QCD and sign problem at nonzero chemical potential. *Phys. Rev.*, D97(1):014501, 2018.

[75] Ulli Wolff. Simulating the All-Order Strong Coupling Expansion I: Ising Model Demo. *Nucl. Phys.*, B810:491–502, 2009.

[76] Ulli Wolff. Simulating the All-Order Hopping Expansion. II. Wilson Fermions. *Nucl. Phys.*, B814:549–572, 2009.

[77] Christof Gattringer, Thomas Kloiber, and Vasily Sazonov. Solving the sign problems of the massless lattice Schwinger model with a dual formulation. *Nucl. Phys.*, B897:732–748, 2015.

[78] Daniel Göschl, Christof Gattringer, Alexander Lehmann, and Christoph Weis. Simulation strategies for the massless lattice Schwinger model in the dual formulation. *Nucl. Phys. B*, 924:63–85, 2017.

[79] N. Kawamoto and J. Smit. Effective Lagrangian and Dynamical Symmetry Breaking in Strongly Coupled Lattice QCD. *Nucl. Phys.*, B192:100, 1981. [,556(1981)].

[80] Hannah Kluberg-Stern, Andre Morel, and Bengt Petersson. Spectrum of Lattice Gauge Theories with Fermions from a 1/D Expansion at Strong Coupling. *Nucl. Phys.*, B215:527–554, 1983.

[81] Goran Faldt and Bengt Petersson. Strong Coupling Expansion of Lattice Gauge Theories at Finite Temperature. *Nucl. Phys.*, B265:197–222, 1986.

[82] Pietro Rossi and Ulli Wolff. Lattice QCD With Fermions at Strong Coupling: A Dimer System. *Nucl. Phys.*, B248:105–122, 1984.

[83] Ulli Wolff. Baryons in Lattice {QCD} at Strong Coupling. *Phys. Lett. B*, 153:92–96, 1985.

[84] F. Karsch and K. H. Mutter. Strong Coupling QCD at Finite Baryon Number Density. *Nucl. Phys.*, B313:541–559, 1989.

[85] G. Boyd, J. Fingberg, F. Karsch, Leo Karkkainen, and B. Petersson. Critical exponents of the chiral transition in strong coupling QCD. *Nucl. Phys. B*, 376:199–217, 1992.

[86] Yusuke Nishida. Phase structures of strong coupling lattice QCD with finite baryon and isospin density. *Phys. Rev.*, D69:094501, 2004.

[87] N. Kawamoto, K. Miura, A. Ohnishi, and T. Ohnuma. Phase diagram at finite temperature and quark density in the strong coupling limit of lattice QCD for color SU(3). *Phys. Rev.*, D75:014502, 2007.

[88] Kohtaroh Miura, Takashi Z. Nakano, Akira Ohnishi, and Noboru Kawamoto. Phase diagram evolution at finite coupling in strong coupling lattice QCD. *Phys. Rev. D*, 80:074034, 2009.

[89] Kohtaroh Miura, Noboru Kawamoto, Takashi Z. Nakano, and Akira Ohnishi. Polyakov loop effects on the phase diagram in strong-coupling lattice QCD. *Phys. Rev.*, D95(11):114505, 2017.

[90] David H. Adams and Shailesh Chandrasekharan. Chiral limit of strongly coupled lattice gauge theories. *Nucl. Phys.*, B662:220–246, 2003.

[91] Michael Fromm. *Lattice QCD at strong coupling.* PhD thesis, Zurich, ETH, 2010.

[92] Michael Creutz. ON INVARIANT INTEGRATION OVER SU(N). *J. Math. Phys.*, 19:2043, 1978.

[93] Robert H. Swendsen and Jian-Sheng Wang. Nonuniversal critical dynamics in Monte Carlo simulations. *Phys. Rev. Lett.*, 58(2):86–88, January 1987.

[94] Ulli Wolff. Collective Monte Carlo Updating for Spin Systems. *Phys. Rev. Lett.*, 62:361, 1989.

[95] R. Aloisio, V. Azcoiti, G. Di Carlo, A. Galante, and A. F. Grillo. Three colors and two colors finite density QCD at strong coupling: A New look. *Nucl. Phys. B*, 564:489–499, 2000.

[96] Philippe de Forcrand and Michael Fromm. Nuclear Physics from lattice QCD at strong coupling. *Phys. Rev. Lett.*, 104:112005, 2010.

[97] Nikolay Prokof'ev and Boris Svistunov. Worm Algorithms for Classical Statistical Models. *Phys. Rev. Lett.*, 87:160601, 2001.

[98] Ydalia Delgado Mercado, Christof Gattringer, and Alexander Schmidt. Surface worm algorithm for abelian Gauge-Higgs systems on the lattice. *Comput. Phys. Commun.*, 184:1535–1546, 2013.

[99] W. K. Hastings. Monte Carlo Sampling Methods Using Markov Chains and Their Applications. *Biometrika*, 57:97–109, 1970.

[100] Neven Bilic, Frithjof Karsch, and Krzysztof Redlich. Flavor dependence of the chiral phase transition in strong coupling QCD. *Phys. Rev.*, D45:3228–3236, 1992.

[101] V. A. Miransky and Koichi Yamawaki. Conformal phase transition in gauge theories. *Phys. Rev. D*, 55:5051–5066, 1997. [Erratum: Phys.Rev.D 56, 3768 (1997)].

[102] Hannah Kluberg-Stern, Andre Morel, and Bengt Petersson. Spectrum of Lattice Gauge Theories with Fermions from a 1/D Expansion at Strong Coupling. *Nucl. Phys. B*, 215:527–554, 1983.

[103] P. H. Damgaard, D. Hochberg, and N. Kawamoto. Effective Lagrangian Analysis of the Chiral Phase Transition at Finite Density. *Phys. Lett. B*, 158:239–244, 1985.

[104] Anna Hasenfratz and Thomas A. DeGrand. Heavy dynamical fermions in lattice QCD. *Phys. Rev. D*, 49:466–473, 1994.

[105] A. Deuzeman, M. P. Lombardo, and E. Pallante. Evidence for a conformal phase in SU(N) gauge theories. *Phys. Rev. D*, 82:074503, 2010.

[106] Anqi Cheng, Anna Hasenfratz, and David Schaich. Novel phase in SU(3) lattice gauge theory with 12 light fermions. *Phys. Rev. D*, 85:094509, 2012.

[107] Yasumich-i Aoki, Tatsumi Aoyama, Masafumi Kurachi, Toshihide Maskawa, Kei-ichi Nagai, Hiroshi Ohki, Akihiro Shibata, Koichi Yamawaki, and Takeshi Yamazaki. Lattice study of conformality in twelve-flavor QCD. *Phys. Rev. D*, 86:054506, 2012.

[108] Jens Braun and Holger Gies. Chiral phase boundary of QCD at finite temperature. *JHEP*, 06:024, 2006.

[109] Jens Braun, Christian S. Fischer, and Holger Gies. Beyond Miransky Scaling. *Phys. Rev. D*, 84:034045, 2011.

[110] Francesco Sannino. Conformal Dynamics for TeV Physics and Cosmology. *Acta Phys. Polon. B*, 40:3533–3743, 2009.

[111] Francesco Sannino. Jumping Dynamics. *Mod. Phys. Lett. A*, 28:1350127, 2013.

[112] E. T. Tomboulis. Absence of chiral symmetry breaking in multi-flavor strongly coupled lattice gauge theories. *Phys. Rev. D*, 87(3):034513, 2013.

[113] Alexander S. Christensen, Joyce C. Myers, Peter D. Pedersen, and Jan Rosseel. Calculating the chiral condensate of QCD at infinite coupling using a generalised lattice diagrammatic approach. *JHEP*, 03:068, 2015.

[114] S. Uhlmann, R. Meinel, and A. Wipf. Ward identities for invariant group integrals. *J. Phys. A*, 40:4367–4390, 2007.

[115] Neven Bilic and Kresimir Demeterfi. One-dimensional QCD With Finite Chemical Potential. *Phys. Lett. B*, 212:83–87, 1988.

[116] L. Ravagli and J. J. M. Verbaarschot. QCD in One Dimension at Nonzero Chemical Potential. *Phys. Rev. D*, 76:054506, 2007.

[117] Shailesh Chandrasekharan and Fu-Jiun Jiang. Chiral limit of strongly coupled lattice QCD at finite temperatures. *Phys. Rev.*, D68:091501, 2003.

[118] Ludmila Levkova, Thomas Manke, and Robert Mawhinney. Two-flavor QCD thermodynamics using anisotropic lattices. *Phys. Rev.*, D73:074504, 2006.

[119] F. Karsch and I. O. Stamatescu. QCD Thermodynamics With Light Quarks: Quantum Corrections to the Fermionic Anisotropy Parameter. *Phys. Lett.*, B227:153–160, 1989.

[120] J. Engels, F. Karsch, and H. Satz. Finite Size Effects in Euclidean Lattice Thermodynamics for Noninteracting Bose and Fermi Systems. *Nucl. Phys. B*, 205:239–252, 1982.

[121] P. Hasenfratz and H. Leutwyler. Goldstone Boson Related Finite Size Effects in Field Theory and Critical Phenomena With O(N) Symmetry. *Nucl. Phys. B*, 343:241–284, 1990.

[122] N. Ishii, S. Aoki, and T. Hatsuda. The Nuclear Force from Lattice QCD. *Phys. Rev. Lett.*, 99:022001, 2007.

[123] Michael L. Wagman, Frank Winter, Emmanuel Chang, Zohreh Davoudi, William Detmold, Kostas Orginos, Martin J. Savage, and Phiala E. Shanahan. Baryon-Baryon Interactions and Spin-Flavor Symmetry from Lattice Quantum Chromodynamics. *Phys. Rev. D*, 96(11):114510, 2017.

[124] Philippe de Forcrand, Massimo D'Elia, and Michele Pepe. A Study of the 't Hooft loop in SU(2) Yang-Mills theory. *Phys. Rev. Lett.*, 86:1438, 2001.

[125] K. E. Eriksson, N. Svartholm, and B. S. Skagerstam. On Invariant Group Integrals in Lattice QCD. *J. Math. Phys.*, 22:2276, 1981.

[126] S. I. Azakov and E. S. Aliev. ONE LINK INTEGRAL IN THE LATTICE QCD: STRONG COUPLING. *Phys. Scripta*, 38:769, 1988.

[127] Takashi Z. Nakano, Kohtaroh Miura, and Akira Ohnishi. Effective Potential in the Strong-coupling Lattice QCD with Next-to-Next-to-Leading Order Effects. *Prog. Theor. Phys.*, 123:825–851, 2010.

[128] G. Burgers, F. Karsch, A. Nakamura, and I. O. Stamatescu. QCD ON ANISOTROPIC LATTICES. *Nucl. Phys.*, B304:587–600, 1988.

[129] Don Weingarten. Asymptotic Behavior of Group Integrals in the Limit of Infinite Rank. *J. Math. Phys.*, 19:999, 1978.

[130] Benoît Collins and Piotr Śniady. Integration with Respect to the Haar Measure on Unitary, Orthogonal and Symplectic Group. *Communications in Mathematical Physics*, 264(3):773–795, Jun 2006.

[131] Benoît Collins and Sho Matsumoto. Weingarten calculus via orthogonality relations: new applications, 2017.

[132] Jean-Bernard Zuber. Revisiting SU(n) integrals. *Journal of Physics A: Mathematical and Theoretical*, 50(1):015203, nov 2016.

[133] O. Borisenko, S. Voloshyn, and V. Chelnokov. SU(N) polynomial integrals and some applications. 2018.

[134] Tomasz Korzec and Ulli Wolff. Simulating the Random Surface representation of Abelian Gauge Theories. *PoS*, LATTICE2013:038, 2014.

[135] K. M. R. Audenaert. 2006.

[136] Manfred Salmhofer. Equivalence of the strongly coupled lattice Schwinger model and the eight vertex model. *Nucl. Phys. B*, 362:641–648, 1991.

[137] K. Scharnhorst. The Exact equivalence of the two flavor strong coupling lattice Schwinger model with Wilson fermions to a vertex model. *Nucl. Phys. B*, 479:727–745, 1996.

[138] Urs Wenger. Efficient simulation of relativistic fermions via vertex models. *Phys. Rev.*, D80:071503, 2009.

[139] John B. Kogut and Leonard Susskind. Hamiltonian Formulation of Wilson's Lattice Gauge Theories. *Phys. Rev. D*, 11:395–408, 1975.

[140] Xiang-Qian Luo, Qi-Zhou Chen, Guo-cai Xu, and Jun-Qin Jiang. Improved Hamiltonians for lattice gauge theory with fermions. *Phys. Rev. D*, 50:501–508, 1994.

[141] Eric B. Gregory, Shuo-Hong Guo, Helmut Kroger, and Xiang-Qian Luo. Hamiltonian lattice QCD at finite chemical potential. *Phys. Rev. D*, 62:054508, 2000.

[142] B. B. Beard and U. J. Wiese. Simulations of discrete quantum systems in continuous Euclidean time. *Phys. Rev. Lett.*, 77:5130–5133, 1996.

[143] M. Suzuki. Generalized Trotter's Formula and Systematic Approximants of Exponential Operators and Inner Derivations with Applications to Many Body Problems. *Commun. Math. Phys.*, 51:183–190, 1976.

[144] Emanuel Gull, Andrew J. Millis, Alexand er I. Lichtenstein, Alexey N. Rubtsov, Matthias Troyer, and Philipp Werner. Continuous-time Monte Carlo methods for quantum impurity models. *Reviews of Modern Physics*, 83(2):349–404, Apr 2011.

[145] Lode Pollet. Recent developments in quantum monte carlo simulations with applications for cold gases. *Reports on Progress in Physics*, 75(9):094501, aug 2012.

[146] Philippe de Forcrand and Slavo Kratochvila. Finite density QCD with a canonical approach. *Nucl. Phys. Proc. Suppl.*, 153:62–67, 2006. [,62(2006)].

[147] Massimo Campostrini, Martin Hasenbusch, Andrea Pelissetto, Paolo Rossi, and Ettore Vicari. Critical behavior of the three-dimensional XY universality class. *Phys. Rev. B*, 63:214503, May 2001.

[148] A. Bazavov, H.-T. Ding, P. Hegde, O. Kaczmarek, F. Karsch, E. Laermann, Y. Maezawa, Swagato Mukherjee, H. Ohno, P. Petreczky, H. Sandmeyer, P. Steinbrecher, C. Schmidt, S. Sharma, W. Soeldner, and M. Wagner. Qcd equation of state to $\mathcal{O}(\mu_B^6)$ from lattice qcd. *Phys. Rev. D*, 95:054504, Mar 2017.

[149] Saumen Datta, Rajiv V. Gavai, and Sourendu Gupta. Quark number susceptibilities and equation of state at finite chemical potential in staggered qcd with $N_t = 8$. *Phys. Rev. D*, 95:054512, Mar 2017.

[150] Frithjof Karsch, Bernd-Jochen Schaefer, Mathias Wagner, and Jochen Wambach. Towards finite density QCD with Taylor expansions. *Phys. Lett. B*, 698:256–264, 2011.

[151] Andre Roberge and Nathan Weiss. Gauge Theories With Imaginary Chemical Potential and the Phases of QCD. *Nucl. Phys.*, B275:734–745, 1986.

[152] Christopher Czaban, Francesca Cuteri, Owe Philipsen, Christopher Pinke, and Alessandro Sciarra. Roberge-Weiss transition in $N_{\mathrm{f}} = 2$ QCD with Wilson fermions and $N_\tau = 6$. *Phys. Rev.*, D93(5):054507, 2016.

[153] Thomas DeGrand and Carleton E. Detar. *Lattice methods for quantum chromodynamics*. 2006.

[154] Bernd A. Berg and Robert C. Harris. From data to probability densities without histograms. *Computer Physics Communications*, 179(6):443–448, Sep 2008.

[155] G. Boyd, Sourendu Gupta, F. Karsch, and E. Laermann. Spatial and temporal hadron correlators below and above the chiral phase transition. *Z. Phys. C*, 64:331–338, 1994.

[156] Christof Gattringer and Kurt Langfeld. Approaches to the sign problem in lattice field theory. *Int. J. Mod. Phys.*, A31(22):1643007, 2016.

[157] Carlotta Marchis and Christof Gattringer. Dual representation of lattice QCD with worldlines and worldsheets of abelian color fluxes. *Phys. Rev. D*, 97(3):034508, 2018.

[158] O. Borisenko, V. Chelnokov, and S. Voloshyn. Dual formulations of Polyakov loop lattice models. *Phys. Rev. D*, 102(1):014502, 2020.

[159] Oleg Borisenko, Volodymyr Chelnokov, Emanuele Mendicelli, and Alessandro Papa. Dual simulation of a Polyakov loop model at finite baryon density: Phase diagram and local observables. *Nucl. Phys. B*, 965:115332, 2021.

[160] Owe Philipsen. Strong coupling methods in QCD thermodynamics. 4 2021.

Appendix A

Reprint of articles reviewed in Chapter 2

A.1 Conformality in many-flavour lattice QCD at strong-coupling [A1]

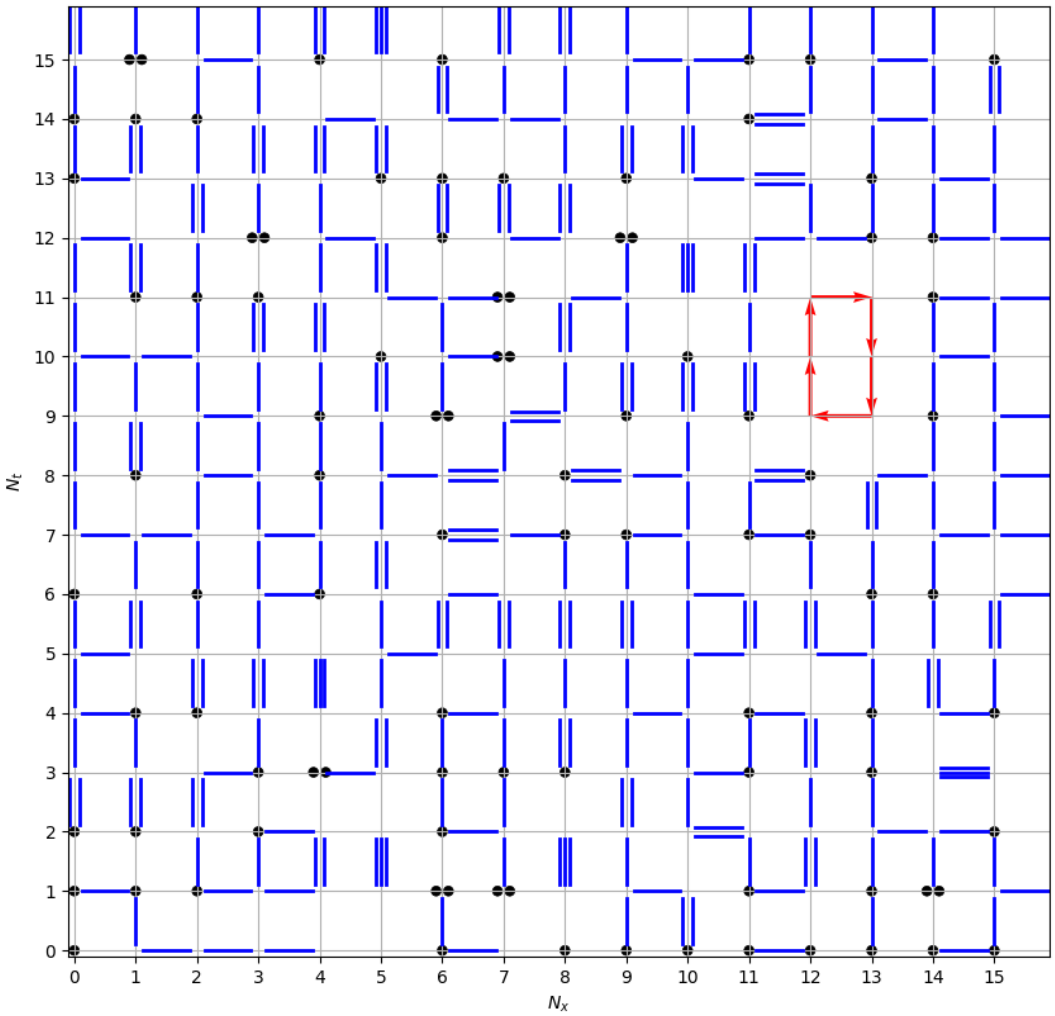

JHEP

Published for SISSA by Springer

Received: August 20, 2012
Revised: January 7, 2013
Accepted: January 9, 2013
Published: February 8, 2013

Conformality in many-flavour lattice QCD at strong coupling

Ph. de Forcrand,[a,b] **S. Kim**[c] **and W. Unger**[a,d]

[a] *Institut für Theoretische Physik, ETH Zürich, CH-8093 Zürich, Switzerland*
[b] *CERN, Physics Department, TH Unit, CH-1211 Geneva 23, Switzerland*
[c] *Department of Physics, Sejong University, Seoul 143-747, Korea*
[d] *Institut für Theoretische Physik, Goethe-Universität Frankfurt, 60438 Frankfurt am Main, Germany*

E-mail: forcrand@phys.ethz.ch, skim@sejong.ac.kr, unger@th.physik.uni-frankfurt.de

Abstract: It is widely believed that chiral symmetry is spontaneously broken at zero temperature in the strong coupling limit of staggered fermions, for any number of colors and flavors. Using Monte Carlo simulations, we show that this conventional wisdom, based on a mean-field analysis, is wrong. For sufficiently many fundamental flavors, chiral symmetry is restored via a bulk, first-order transition. This chirally symmetric phase appears to be analytically connected with the expected conformal window of many-flavor continuum QCD. We perform simulations in the chirally symmetric phase at zero quark mass for various system sizes L, and measure the torelon mass, the Dirac spectrum and the hadron spectrum. All masses go to zero with $1/L$. L is hence the only infrared length scale. Thus, the strong-coupling chirally restored phase appears as a convenient laboratory to study IR-conformality. Finally, we present a conjecture for the phase diagram of lattice QCD as a function of the bare coupling and the number of quark flavors.

Keywords: Lattice QCD, Lattice Gauge Field Theories, Conformal and W Symmetry, Technicolor and Composite Models

ArXiv ePrint: 1208.2148

doi:10.1007/JHEP02(2013)051

JHEP02(2013)051

Contents

1 Introduction 1

2 Monte Carlo results 2

3 Looking for conformality in the chirally symmetric phase 4

3.1 Characterizing the chirally restored phase: (I) The Torelon mass 5

3.2 Characterizing the chirally restored phase: (II) Dirac spectrum 7

3.3 Characterizing the chirally restored phase: (III) Hadron masses 9

4 The conjectured phase diagram 10

5 Conclusion 12

1 Introduction

The possibility that the Higgs boson could be a composite bound-state in a high-energy Technicolor theory [1–3] has generated considerable interest, especially in the lattice community. In particular, the requirement that the Technicolor theory be "walking" [4–6], in order to accommodate stringent bounds on flavor-changing neutral currents, has been the driving motivation behind several large-scale computer simulation efforts to determine the possible combinations of gauge groups and fermion contents leading to a conformal window.

To determine via lattice Monte Carlo simulations whether a given theory is inside the conformal window is particularly challenging, because it involves a triple difficulty: in order to identify (or not) an infrared fixed point (IRFP) which is the signature of a theory inside the conformal window, one must probe the extreme infrared properties of the theory, while at the same time taking the continuum limit of the lattice discretization, and controlling the limit when the quarks become massless. This compounded difficulty may explain why, in spite of considerable efforts, there is no consensus yet on the minimum number $N_f{}^*$ of quark flavors needed for QCD to be inside the conformal window [7]. A numerical demonstration of walking has been provided only recently, in a toy model, the 2-d $O(3)$ model at vacuum angle $\theta \approx \pi$ [8].

Here, we relax the demand that results should be obtained in the continuum limit. On a coarse lattice, long-distance properties can be studied more economically. While such properties may differ from those of the corresponding continuum theory, it may still be instructive to consider the possible existence of an IRFP for a discretized lattice theory. The phase diagram of SU(N_c) gauge theory with N_f fundamental fermions, as a function of N_f and the bare gauge coupling, has been predicted in the celebrated ref. [9], which serves as a guide to understand the results of Monte Carlo simulations performed at finite

JHEP02(2013)051

bare coupling. It is important to confront these predictions with uncontroversial numerical evidence. Therefore, we start our investigation by considering the strong coupling limit, where the lattice is maximally coarse.

Note that we consider standard staggered fermions, and (away from the strong-coupling limit) the standard plaquette action. Other discretizations could lead to different results, since only the continuum limit is universal.

The conventional wisdom for strong coupling QCD with staggered fermions is that chiral symmetry remains always broken at zero temperature, regardless of the number of colors and flavors. This belief is based on mean-field analyses performed in some of the earliest papers on lattice QCD. In particular, it was shown in [10] that at leading order in a $1/d$ expansion, the chiral condensate has a value independent of the number of colors N_c and of the number of staggered fields $\hat{N}_f = N_f/4$, where N_f would be the corresponding number of degenerate fermion flavors in the weak-coupling limit, but depends only on the number d of spatial dimensions:

$$\langle \psi\bar{\psi}\rangle(T=0) = \sqrt{\frac{2}{d}}\left(1 - \frac{1}{4d}\right) \tag{1.1}$$

Chiral symmetry may be restored by increasing the temperature T. Following the approach of [11], where explicit results are provided for a few small values of N_c and $\hat{N}_f$, we calculated the chiral restoration temperature aT_c and found that it is indeed non-zero for all $\hat{N}_f$, and independent of N_c to leading order in $1/\hat{N}_f$:

$$aT_c = \frac{d}{4} + \frac{d}{32}\frac{N_c}{\hat{N}_f} + \mathcal{O}\left(\frac{1}{\hat{N}_f{}^2}\right) \tag{1.2}$$

Hence chiral symmetry will never be restored at zero temperature, according to the mean-field analysis. Since mean-field theory is expected to work well when the number of d.o.f. per site is large (e.g. providing exact results in the Gross-Neveu model for $N_f \to \infty$), there was no reason to doubt the validity of this finding. Besides, it is in accord with the intuition that the gauge field is maximally disordered in the strong-coupling limit, and that this disorder will drive chiral symmetry breaking.

On the other hand, one naively should expect the above disorder to be modified by dynamical fermions, which have an ordering effect. Indeed, the loop expansion of the determinant shows that the fermionic effective action induced by dynamical fermions, $S_{\text{eff}} = -\log\det(\not{D} + m_q)$, starts with a positive plaquette coupling $\Delta\beta$, proportional to $1/m_q^4$ for heavy quarks, which has been studied numerically in [12]. Clearly, for N_f flavors the effective action is proportional to N_f, and $\Delta\beta$ grows proportionally. This plaquette term suppresses fluctuations in the gauge field, which suggests that chiral symmetry restoration might take place for sufficiently large N_f.

2 Monte Carlo results

The only way to resolve this puzzle is to perform Monte Carlo simulations in the strong coupling limit of staggered fermions, to detect a possible chiral symmetry restoration for

JHEP02(2013)051

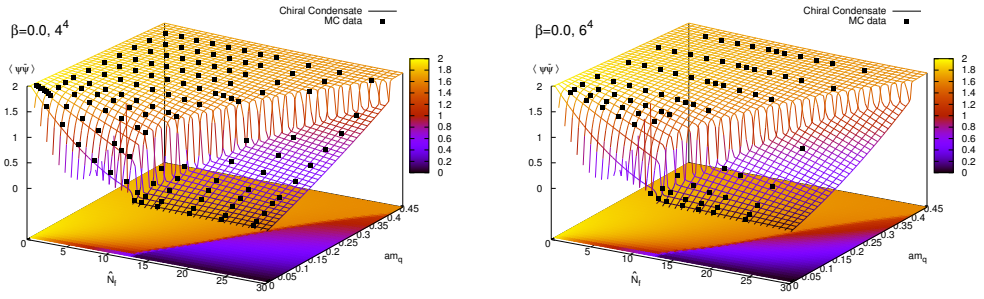

Figure 1. The chiral condensate at strong coupling, $\beta = 0$, in the $(\hat{N}_f, am_q)$ plane, for 4^4 (left) and 6^4 (right) lattices.

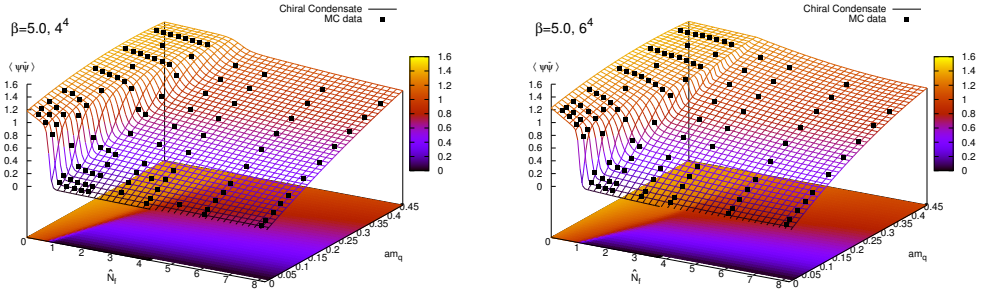

Figure 2. The chiral condensate at weaker coupling, $\beta = 5$, in the $(\hat{N}_f, am_q)$ plane, for 4^4 (left) and 6^4 (right) lattices.

sufficiently large $\hat{N}_f$. These simulations are straightforward, using the standard Hybrid Monte Carlo algorithm. As expected, the effect of increasing $\hat{N}_f$ on the chiral condensate is to reduce its magnitude. But it came as a surprise to find that the chiral condensate vanishes via a strong first-order transition at $\hat{N}_f{}^c \simeq 13$ staggered fields in the chiral limit (i.e. $N_f{}^c \simeq 52$ continuum fermion flavors). In the broken phase, the chiral condensate remains almost constant. It vanishes in the chiral limit due to finite-size effects only. In contrast, in the chirally restored phase the condensate is caused by explicit symmetry breaking and is proportional to the quark mass. This is illustrated figure 1, where the condensate is shown as a function of $\hat{N}_f$ and bare quark mass (am_q). Moreover, this N_f-driven transition turns out to be a bulk, zero-temperature transition, which can be seen by the fact that finite-size effects on the phase boundary are small when comparing two different system sizes 4^4 and 6^4, as shown figure 1 (left and right).

One also observes in these figures that the critical number of flavors increases with the quark mass. This is easy to understand: heavier quarks have a weaker ordering effect, so that the induced plaquette coupling $\Delta\beta$ decreases if one keeps $\hat{N}_f$ fixed. It takes more flavors to keep the system chirally symmetric. Hence, $\hat{N}_f{}^c$ increases, and for heavy quarks should obey $\hat{N}_f{}^c \propto (am_q)^4$.

One can now go back to the mean-field treatment and trace the origin of its failure. Two kinds of terms at least are neglected: (i) multiple meson hopping along a given

JHEP02(2013)051

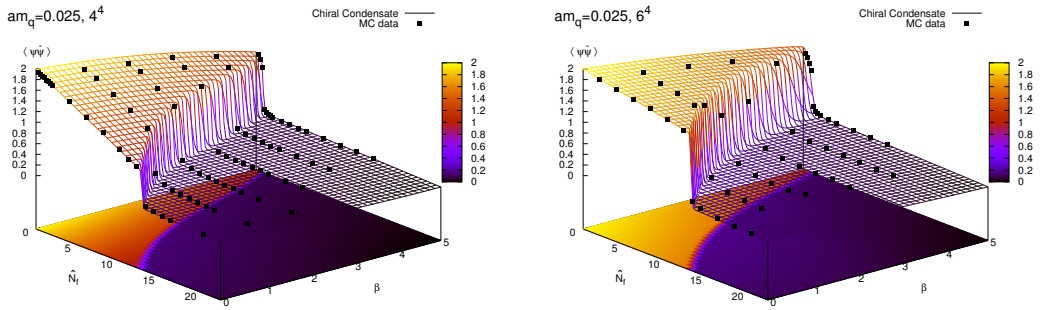

Figure 3. The chiral condensate at $am_q = 0.025$ in the $(\hat{N}_f, \beta)$ plane, for 4^4 (left) and 6^4 (right) lattices. The phase transition remains strongly first order at weaker coupling. The contour plot indicates the qualitative behaviour of the phase boundary, extending to weaker coupling.

link, and (ii) baryon loops. These terms amount to corrections $\mathcal{O}(\hat{N}_f/N_c)$ and $\mathcal{O}(\hat{N}_f/d^2)$, respectively, where $\hat{N}_f = N_f/4$ is the number of staggered fields, and is normally set to 1 in the mean-field treatment. Here, we consider $\hat{N}_f \gtrsim 13$, and the previously neglected corrections become dominant. The conventional wisdom that chiral symmetry is always broken at $T = 0$ in the strong-coupling limit comes from mistakenly applying the lowest-order mean-field approximation in a regime where it is invalid.

Having established an $\hat{N}_f$-driven phase transition in the strong-coupling limit, we may consider its impact on the lattice theory at non-zero lattice gauge coupling β as well. Since the transition is strongly first order, it has to persist for some range in β at least. Hence we have compared the strong coupling phase diagram with the phase diagram at weaker coupling $\beta = 5$, illustrated figure 2. We find a similar qualitative behavior, but with $\hat{N}_f{}^c$ drastically reduced to $\mathcal{O}(2)$. Finite-size effects are more pronounced, but the transition still seems to be a first-order bulk transition.

In fact, we find a smooth variation of the $\hat{N}_f$-driven transition with β at a given small quark mass $am_q = 0.025$, as shown figure 3. The transition extends to weak coupling, at least to $\beta = 5$, and remains strongly first-order. Thus, it is plausible that this transition, which separates a chirally broken (small N_f) and a chirally symmetric (large N_f) phase, persists all the way to the $\beta \to \infty$ continuum limit, where it is to be identified with the transition at $N_f = N_f{}^*$ between the chirally broken and the IR-conformal, chirally symmetric phase. In other words, our chirally restored phase may be analytically connected to the conformal window in the continuum limit, because we do not observe any additional non-analyticity as β is increased.

This possibility motivates our study of the properties of the strong-coupling chirally symmetric phase, looking for tests of IR-conformality.

3 Looking for conformality in the chirally symmetric phase

It is natural to ask whether the chirally restored phase is connected to the conformal window, i.e. whether the chirally restored phase at strong coupling is also IR-conformal.

JHEP02(2013)051

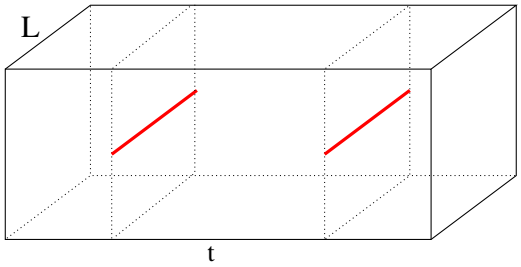

Figure 4. Torelon correlator.

And if this is indeed the case, the next obvious question is whether this IR-conformal phase is trivial, ie. whether the IR fixed point coupling is zero or not. In this section we present measurements of gluonic and fermionic observables chosen to address these questions: the torelon mass from which we define a running coupling, the Dirac eigenvalue spectrum, and the hadron spectrum. Our results support the following conclusion: the strong-coupling chirally symmetric phase is indeed IR-conformal, and it is non-trivial.

The simulations performed here are all in the chirally symmetric phase at zero plaquette coupling, with $\hat{N}_f = 14$ and 24 staggered fields, which would correspond, in the weak-coupling limit, to $N_f = 56$ and 96 continuum flavors, and with lattices of size $4^3 \times 16$, $6^3 \times 16$, $8^3 \times 16$, $10^3 \times 20$ and $12^3 \times 24$. The quark mass is set exactly to zero unless specified otherwise. We will see below that the Dirac operator has a spectral gap in the symmetric phase, which makes a study of the massless theory within reach of modest computer resources. Moreover, having one infrared scale, the system size L, rather than two scales (L and $1/m_q$) is of great advantage when analyzing the results.

Let us mention the average plaquette values which we measure: ≈ 0.35 and ≈ 0.52 for $\hat{N}_f = 14$ and 24, respectively (normalized to 1 for the free field). So we are very far from a plaquette value of 0, corresponding to maximally disordered gauge fields and achieved for $N_f = 0$: the ordering effect of the dynamical fermions plays a dominant role in our case, and the vanishing of the plaquette coupling is not associated with special properties.

3.1 Characterizing the chirally restored phase: (I) The Torelon mass

The "torelon" is a gluonic excitation which is topologically non-trivial: it is excited by any Wilson loop which wraps around the spatial boundary in one direction, for instance, as illustrated figure 4,

$$T_i(t) = \mathrm{Tr} \prod_{k=0}^{L-1} U_i(\vec{x} + k\hat{i}, t), \tag{3.1}$$

where $i = 1, 2, 3$ is one of the spatial directions and $\hat{i}$ the unit vector in that direction.[1] We extract the mass of this excitation from the exponential decay of the correlator $\langle T_i(0)^* T_i(t) \rangle$.

[1] We initially adopted periodic boundary conditions in space and anti-periodic in time for the fermion fields. However, the dynamical fermions drive T_i to negative values in this case, with a Z_2 degeneracy between the two complex Z_3 sectors. We occasionally observed tunneling of T_i between these two sectors, and long metastabilities. For this reason, we changed the spatial boundary conditions to anti-periodic, which makes $\langle T_i \rangle$ real positive.

JHEP02(2013)051

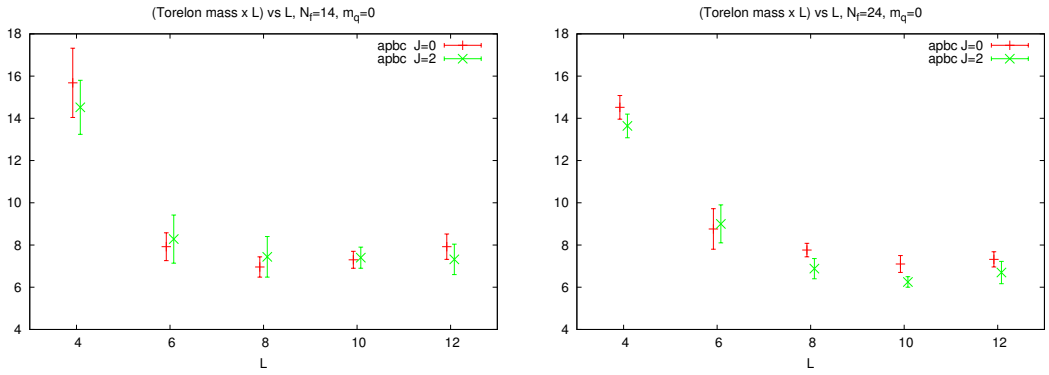

Figure 5. The torelon mass $m_T(L)$ multiplied by L versus L, left: $\hat{N}_f = 14$, right: $\hat{N}_f = 24$ (for anti-periodic boundary conditions).

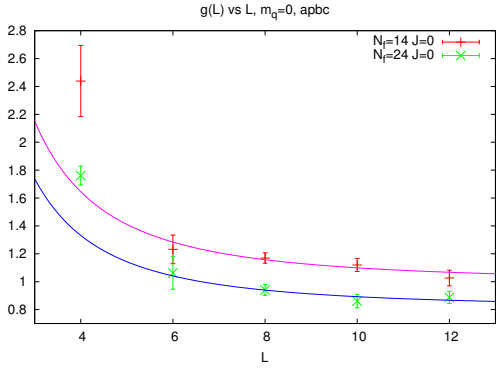

Figure 6. The running coupling $g(L)$ defined via the temperature-dependence of the Debye mass, which is identified with the torelon mass, for $\hat{N}_f = 14$ and 24. For each $\hat{N}_f$, the curve is a fit to a constant plus $(a/L)^2$ corrections of the 4 largest volumes. The larger $\hat{N}_f$ has a smaller coupling.

To suppress excited states, we smear the links within each time-slice before constructing T_i. This observable has been used for a long time to extract the string tension σ in Yang-Mills theories [13]: it can be viewed as a loop of gluonic string, whose energy $m_T(L)$ grows with its length as σL. So our initial, naive expectation was to measure a mass $m_T(L)$ growing with L, until perhaps the string would break due to fermion-pair creation.

This is not at all what we observed. The dimensionless quantity which we measure, $am_T(L)$, *decreases* on larger lattices corresponding to a larger ratio L/a. Clearly, our theory is not confining. Moreover, as shown figure 5, the combination $Lm_T(L)$ is approximately constant as L is increased. So the torelon mass varies as $1/L$ (actually, for small L it initially decreases even faster with L as seen in the figure). Thus, there is no intrinsic mass scale which appears in this channel: the torelon mass is set by the system size L. This remarkable result is our first evidence that our theory is IR-conformal.

We actually combined the $T_i(t), i \in \{1, 2, 3\}$ into two representations of the cubic discrete rotation group: the A_1^+ (corresponding to a 0^+ representation of $O(3)$) and the E^+ (corresponding to a 2^+ representation of $O(3)$). The mass of the E^+ seems to be slightly smaller, as observed in small-volume analytic Yang-Mills calculations [14].

JHEP02(2013)051

Now, by relabelling the spatial direction i as the imaginary time direction, one realizes that we are measuring the correlation of two time-like Polyakov loops, whose decay rate is governed by the Debye mass, given perturbatively at lowest order by

$$m_D(T) = 2gT\sqrt{\frac{N_c}{3} + \frac{N_f}{6}} \tag{3.2}$$

This expression allows us to *define* a running coupling $g(L)$ via

$$g(L) \equiv \frac{m_T(L)L}{2\sqrt{\frac{N_c}{3} + \frac{N_f}{6}}} \tag{3.3}$$

and we see that, in this scheme, our running coupling seems to go to a non-zero constant as L increases (although one cannot exclude, of course, that it slowly goes to zero). Therefore, we have numerical evidence supporting the view that our strong-coupling, chirally symmetric theory is IR-conformal and non-trivial.

Interestingly, the extracted value of $g(L)$ approaches ~ 0.95 and ~ 0.80 for $\hat{N}_f = 14$ and 24 respectively. So the IR fixed-point coupling value decreases as $\hat{N}_f$ increases. This is what one would expect: as $\hat{N}_f$ keeps increasing, the ordering effect of the fermions increases, and all Wilson loops are driven towards 1, their free field value. At the same time, any definition of a running coupling will approach zero. The theory becomes trivial for $\hat{N}_f \to \infty$, even in the strong-coupling limit. We will come back to this point in section 4.

3.2 Characterizing the chirally restored phase: (II) Dirac spectrum

We now turn to fermionic properties, starting with the spectrum of the Dirac operator. We have analyzed the Dirac eigenvalue spectrum of the configurations in our Monte Carlo ensembles, using a Lanczos algorithm to obtain an approximation of the whole spectral density and an Arnoldi method to extract the smallest eigenvalues to high accuracy. The observable shown in figure 7 is the integrated eigenvalue density, defined as:

$$\int_0^\lambda \rho(\bar{\lambda})d\bar{\lambda} = \frac{\text{rank}(\lambda)}{\text{rank(Dirac matrix)}} \in [0,1]. \tag{3.4}$$

This function of λ counts the fraction of eigenvalues smaller than λ. Its derivative is simply the eigenvalue density $\rho(\lambda)$. We first compare this observable on quenched configurations ($N_f = 0$) and in the chirally symmetric phase ($\hat{N}_f = 14$). In figure 7 (left), 10 curves for 10 configurations are superimposed: variations in the spectrum are very small. We observe that $N_f = 0$ and $\hat{N}_f = 14$ spectra are similar in the ultraviolet, but differ in the infrared, as illustrated in the inset. The $N_f = 0$ curve starts linearly from the origin, reflecting an eigenvalue density approximately constant near $\lambda = 0$. On the contrary, the integrated eigenvalue density for $\hat{N}_f = 14$ shows a spectral gap for small eigenvalues, which is of course consistent with chiral symmetry restoration according to the Banks-Casher relation, since $\rho(0) = 0$.

The crucial question is on which scale does this spectral gap depend. To answer this question, in figure 7 (right) we compare the integrated eigenvalue density at $\hat{N}_f = 14$ for various lattice volumes, $L = 4, 6, 8, 10$ and 12. As evidenced in the inset, we find that the

JHEP02(2013)051

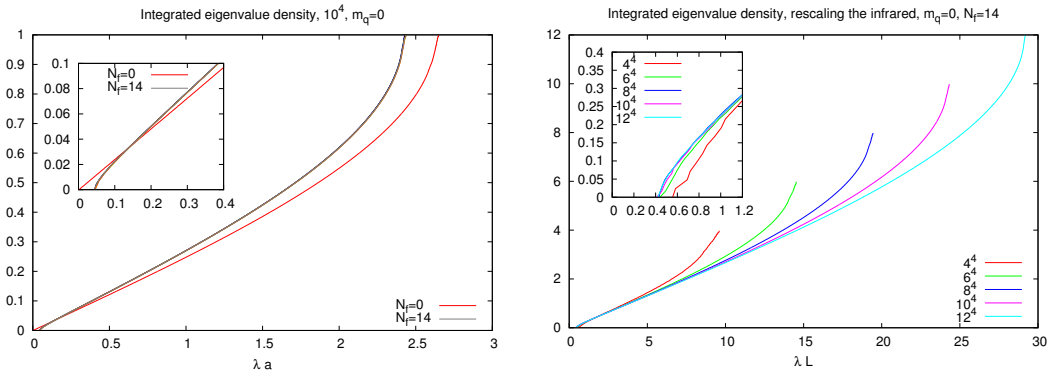

Figure 7. The integrated eigenvalue density. Left: comparison of $N_f = 0$ (quenched) with $\hat{N}_f = 14$ in the chirally restored phase, where only the latter shows a spectral gap. Right: the rescaled spectral gap, indicating $1/L$ scaling.

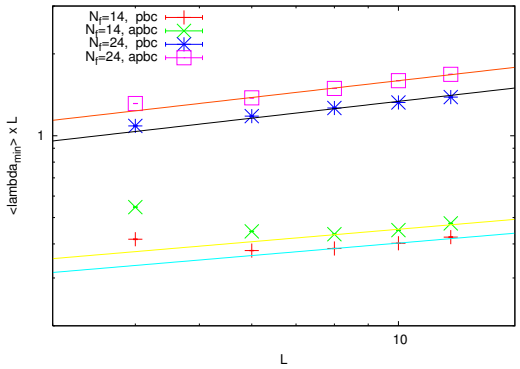

Figure 8. The anomalous dimension from fits to the spectral gap for $\hat{N}_f = 14, 24$ with periodic and anti-periodic boundary conditions. Fitted exponents to the three largest volumes are $\gamma^* \sim 0.26$ for $\hat{N}_f = 14$ and $\gamma^* \sim 0.38$ for $\hat{N}_f = 24$.

spectral gap scales $\propto 1/L$ to a good approximation, which is a strong indication that our theory is IR-conformal:[2] there does not seem to be any length scale in the chirally restored phase other than the box size L.

Actually, small deviations from $1/L$ scaling allow us, in principle, to extract the anomalous mass dimension γ^*. We make such an attempt in figure 8, where the gap has been multiplied by L already: deviations from a constant are indicative of anomalous dimension, *provided* other corrections $\mathcal{O}((a/L)^2)$ are negligible. The effect of a finite system size L on the Dirac spectrum has not been analyzed yet. We have simply considered that the infrared conformal symmetry is explicitly broken by the infrared scale $1/L$, which is the analogue of an explicit breaking by a quark mass m_q. Consequently, we expect the mass gap to behave as $(1/L)^{1/(1+\gamma^*)}$. A crude, 2-parameter fit based on our 3 largest volumes gives $\gamma^* \sim 0.26$ and 0.38 for $\hat{N}_f = 14$ and 24, respectively. Simulations on larger volumes should be performed to bring under control the systematic error in these estimates. The true, infinite volume value of γ^* seems to be approached from below.

[2]If one would take the limits $L \to \infty$ first, then $m_q \to 0$, the expected spectral density for a conformal theory would be $\rho(\lambda) \sim \lambda^{(3-\gamma^*)/(1+\gamma^*)}$. Here, we take the opposite order of limits.

JHEP02(2013)051

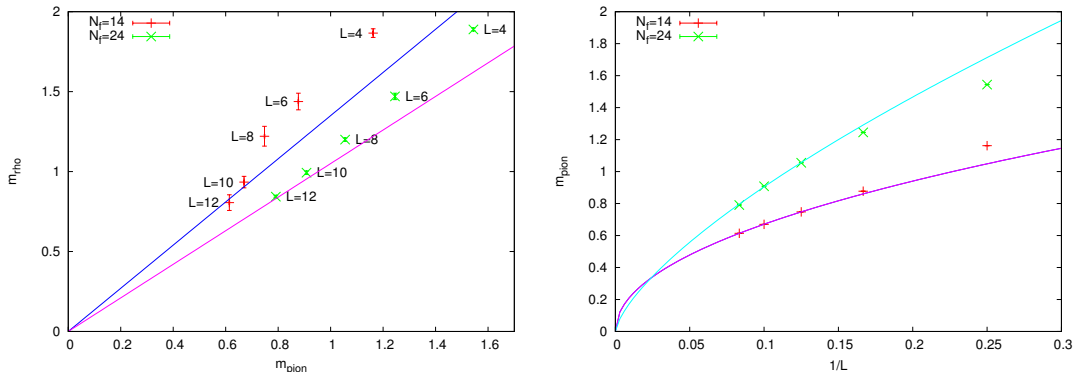

Figure 9. Left: meson masses m_π and m_ρ for various system sizes L, showing a fast decrease of the masses as L increases, while the mass ratio remains more or less constant. Right: pion mass as a function of $1/L$, with the three largest volumes fitted by the ansatz $(1/L)^{1/(1+\gamma^*)}$, yielding $\gamma^* \sim 1.0$ and 0.4 for $\hat{N}_f = 14$ and 24, respectively.

3.3 Characterizing the chirally restored phase: (III) Hadron masses

Finally, we turn to hadron masses measured on our $\hat{N}_f = 14$ and $\hat{N}_f = 24$ Monte Carlo ensembles. Even though the quark mass is zero in these ensembles, we observe non-zero hadron masses. As expected, parity partners are degenerate since chiral symmetry is restored. Now, if our theory is IR-conformal, the masses which we measure are exclusively due to finite-size effects: all masses should go to zero as the lattice size L is increased. This is what we observe, as shown in figure 9 (left): the "pion" and "rho" masses both decrease by a factor ~ 2 as the lattice size is increased from $L = 4$ to 12. Notice however that the smallest mass is still > 0.6, which is not very light.

Furthermore, one generally expects that the approach to zero should be the same for all hadrons, so that mass ratios should remain constant as $L \to \infty$. Note that there may be exceptions to this "rule": in the $2d$ $O(3)$ sigma model near $\theta = \pi$, the mass of the $O(3)$ singlet state approaches zero faster than that of the $O(3)$ triplet as θ approaches π [15]. Here, our figure 9 (left) would show all data points aligned on "rays" going through the origin if mass ratios were constant. One can see deviations from this behavior, which perhaps are caused by the not-too-light masses which we measure. Another possible cause is technical: as L is increased, the groundstate masses in each channel decrease, but so do also the mass differences between groundstate and excited states. It becomes more difficult to extract the groundstate mass, and our lattices are likely too short to properly control this source of systematic error.

Nevertheless, we show in figure 9 (right) the mass of the "pion", in which we have the most confidence, as a function of $1/L$. Since $1/L$ breaks the conformal symmetry much like a quark mass m_q would, we expect that the pion mass should scale the same way, namely as $(1/L)^{1/(1+\gamma^*)}$, if L is large enough. A 2-parameter fit to our three largest system sizes gives $\gamma^* \sim 1.0$ and 0.4 for $\hat{N}_f = 14$ and 24, respectively. As with the estimates of γ^* from the Dirac spectrum, simulations on larger volumes are needed to bring the systematic error under control.

JHEP02(2013)051

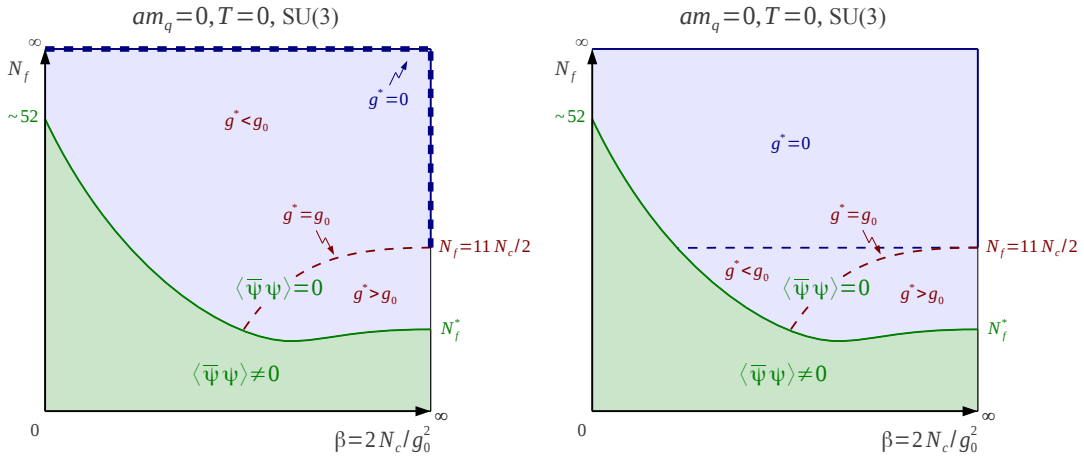

Figure 10. Left: conjectured phase diagram in the (β, N_f) plane. A single phase transition line separates the chirally broken phase from the chirally symmetric, IR-conformal phase. The thick dotted line indicates trivial theories. Right: alternative scenario, where the trivial theories extend to the area above $N_f = 11N_c/2$. It is not favored by our measurements.

4 The conjectured phase diagram

Using both gluonic and fermionic observables, we have presented evidence that the chirally restored phase at strong coupling is IR-conformal and non-trivial, and speculated about a connection to the conformal window in the continuum. We now want to propose a phase diagram sketched in figure 10 (left), as a function of the plaquette coupling $\beta = 6/g_0^2$ and of the number of would-be fundamental flavors N_f in the weak-coupling limit $\beta = \infty$. That is, we simply convert the number $\hat{N}_f$ of staggered fields to $N_f = 4\hat{N}_f$. Moreover, we promote N_f to a real, continuous parameter: while N_f must be integer for a well-defined continuum theory, one may let it take any value in the statistical model defined by the lattice partition function. Our conjectured phase diagram can be compared with, e.g., those of ref. [9, 16]: one can see substantial differences. The essential feature of our phase diagram is that the $\beta = 0$ IR-conformal phase is analytically connected with the weak-coupling, continuum IR-conformal phase. This is the simplest scenario, supported by our exploratory scan in β shown figure 3. A single phase transition line ${N_f}^c(\beta)$ separates the region of broken chiral symmetry at small N_f from the chirally symmetric region at large N_f. The transition is first-order, at least for some range of β starting from zero. Moreover, the number $\hat{N_f}^c$ of staggered fields which bring enough order to restore chiral symmetry at $\beta = 0$, $\hat{N_f}^c(\beta = 0) = 1/4{N_f}^c(\beta = 0) = 13(1)$, is remarkably close to the expected number ${N_f}^*$ of continuum quark fields which achieve the same effect.[3] This may be more than a numerical accident. At strong coupling, taste symmetry breaking is maximal, and $\hat{N}_f = 13$ staggered fields can be viewed as $\hat{N}_f$ massless fields, plus $3\hat{N}_f$ fields with mass $\mathcal{O}(a^{-1})$. Only the former have a significant effect toward chiral symmetry restoration.

In the chirally symmetric phase, we see no evidence for a dynamically generated mass scale of any sort. Then, based on our results for the running coupling figure 6, we conjecture

[3] Different groups place $N_f = 12$ above or below ${N_f}^*$.

JHEP02(2013)051

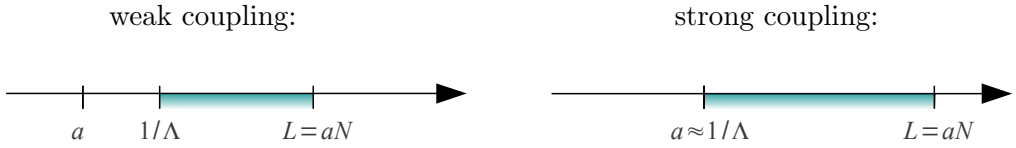

Figure 11. The ordering of scales at weak coupling (left) and strong coupling (right), showing that the range of conformal invariance is larger in the latter case.

that for any finite β and $N_f > N_f{}^c(\beta)$, large-N_f lattice QCD is IR-conformal, with a non-trivial fixed-point coupling $g^* > 0$. This value changes continuously with (β, N_f), reaching the value zero for $\beta = \infty, N_f > 33/2$ and for $N_f = \infty\ \forall\beta$, as indicated figure 10 (left) by a thick dotted line. g^* grows as one moves away from this dotted boundary towards the phase transition line.

An alternative scenario would be that the running coupling in figure 6 slowly approaches zero, and $g^* = 0$ for $N_f > 33/2$ for any β in the chirally symmetric phase. This is sketched in figure 10 (right). If the basin of attraction of the weak coupling trivial fixed point would extend all the way to the strong coupling limit, one should observe for the running coupling $g^2(L) \sim 1/\log(L/L_0)$, with $L_0 \sim \mathcal{O}(a)$. Whether or not this happens depends on the marginal operators induced by our lattice action. Our numerical results figure 6 for the running coupling are indeed consistent with this possibility. But we should also observe in this case an anomalous mass dimension $\gamma^* = 0$, which is not favored by our other measurements. More careful, large-scale simulations are necessary to settle this issue.

Finally, one may consider the line $g^* = g_0$, with $g_0 = (2N_c/\beta)^{1/2}$, where the IR fixed-point coupling has the same value as the bare coupling, so that the coupling does not run as a function of the renormalization scale. This line starts at the point $(\beta = \infty, N_f = 33/2)$ where $g^* = g_0 = 0$. Its precise location depends on the chosen renormalization scheme. It is not associated with any kind of singularity of the free energy. There is no phase transition along this line: simply, on the left (resp. on the right) of that line, the coupling increases (resp. decreases) from g^* as one reduces the distance scale. Since there is a lower distance cutoff a no divergence is observed as one crosses this [scheme-dependent] line.

We have determined the phase diagram in the strong-coupling region only. Studying the continuum limit is of course much more difficult, due to the large lattices that have to be used in order to control the finite size effects and the difficult control of lattice artifacts. We would like to suggest that the strong-coupling limit may represent an advantageous "poor man's laboratory" for the study of $4d$ IR-conformal gauge theories. In particular, as illustrated figure 11, the range of scales over which conformal invariance applies for a given computing effort is greatly reduced at weak coupling: there, for a given lattice size N^4, the scales are ordered as follows:

$$a \ll 1/\Lambda \ll L = Na. \tag{4.1}$$

where Λ is the scale generated by the asymptotically free gauge dynamics and Yang-Mills perturbation theory applies at distances $\lesssim 1/\Lambda$. In contrast, at strong coupling, where the lattice becomes maximally coarse, there is no small distance where Yang-Mills perturbation

JHEP02(2013)051

theory applies, and the hierarchy is:

$$a \sim 1/\Lambda \ll L = Na. \tag{4.2}$$

Hence the dynamical range of conformal invariance, characterized by the product $L\Lambda$, is maximized at $\beta = 0$ for a given lattice size $N = L/a$.

5 Conclusion

We have shown that for $\beta = 0$, contrary to common wisdom, there exists a strongly first-order, N_f-driven bulk transition to a chirally symmetric phase. In the chiral limit, the transition occurs for $\hat{N_f}^c = 13(1)$ staggered fields, i.e. ${N_f}^c = 52(4)$ *continuum* flavors. This finding is in contrast to the mean-field prediction, whose failure can be traced back to approximations relying on N_f being small. Clearly, the conventional, automatic association of the strong-coupling limit with confinement and chiral symmetry breaking is too naive. Furthermore, the chirally restored phase extends to weak coupling.

We have also shown numerical evidence that the $\beta = 0$ chirally restored phase of "large-N_f QCD" is IR-conformal, with a non-trivial, N_f-dependent value of the IR fixed-point coupling. We conclude that the strong-coupling limit is the laboratory of choice to study a 4d IR-conformal gauge theory. Simulations at large N_f and *zero* quark mass can be performed without too much computational effort since a gap appears in the Dirac spectrum. As N_f increases, the spectral gap increases, the average plaquette approaches 1, and the fixed-point coupling approaches 0. Setting the quark mass to zero eliminates one IR scale, leaving the system size L as the only remaining one. This greatly simplifies the analysis of simulation results.

Since we have not observed any evidence for an additional $T = 0$ phase transition as β is increased, we speculate that the strong coupling chirally symmetric, IR-conformal phase is analytically connected with the continuum IR-conformal phase.

One may ask how robust these statements are with respect to the particular discretization of the Dirac operator and the gauge action. While the quantitative details of the phase transition ${N_f}^c(\beta)$ will surely change, we think that the qualitative features will remain. Chiral symmetry breaking at strong coupling, for small N_f, is a general consequence of the disorder in the gauge field. The ordering effect of fermions also is generic. So we do expect a bulk transition, generically of first-order, as a function of N_f in the strong-coupling limit. Actually, such a transition was observed for Wilson fermions in ref. [17, 18]. At intermediate coupling, additional transitions may appear depending on the lattice action. Interestingly, a first-order transition to a chirally broken phase as β is reduced has been observed many times, for various lattice actions [19–23]. These transitions were observed for some fixed value of N_f. Here, we simply put all these earlier observations together. It is interesting that this phase transition is consistently of first-order. If the first-order nature persists all the way to the continuum limit, then walking dynamics will not be observed, and the transition to the conformal window will be characterized by "jumping dynamics", as proposed by Sannino [24].

JHEP02(2013)051

One may also wonder what happens to the (β, N_f) phase diagram as the gauge group or the fermion content is changed. For $4d$ compact U(1), the change would not be dramatic, because the strong-coupling behavior is much the same as for SU(3): our first-order transition line would end at $(\beta \approx 1.01, N_f = 0)$ on the horizontal axis rather than on the vertical axis, and the region of triviality would cover the whole chirally symmetric phase, except for $N_f = 0$. For SU(2) or SU(3) with adjoint fermions, the change would be more significant: in the strong-coupling limit, increasing N_f would order the plaquette in the adjoint representation, not in the fundamental. Center monopoles would likely condense [25], and might delay or prevent the restoration of chiral symmetry.

Finally, there are many directions in which to extend this exploratory study. To buttress the claim that the chirally symmetric phase is IR conformal, more observables, like the static potential and the Fredenhagen-Marcu order parameter, should be studied. Also, and to make contact with other numerical studies, a mass deformation could be introduced. As a first step in this direction, we show in figure 12 the quark mass dependence of the chiral condensate. This figure shows all the technical difficulties associated with extracting the anomalous dimension γ^*: Heavier fermions have less ordering effect, which triggers a phase transition back into the chirally broken phase for some critical fermion mass. Finite-size effects associated with that transition should not be included in the determination of γ^*. Moreover, the non-anomalous contributions $\langle\bar{\psi}\psi\rangle = c_1 m_q + c_2 m_q^3$ easily overwhelm the anomalous $m_q^{(3-\gamma^*)/(1+\gamma^*)}$. Actually, fits based on the ansatz

$$\langle\bar{\psi}\psi\rangle = c_1 m_q + c_2 m_q^{\frac{3-\gamma^*}{1+\gamma^*}} \ , \tag{5.1}$$

or including an m_q^3 term [26], favor negative values for γ^*, which crucially depend on the fitting range and the included analytic contributions. We believe that extracting γ^* from the Dirac spectrum provides better control of the systematics, as emphasized in [27]. In any case, larger system sizes are required before reliable estimates of γ^* can be obtained. This is beyond the scope of this work. Here, we have argued that such reliable estimates can be obtained *in principle* from the L-dependence of the Dirac spectrum and of the meson spectrum, both measured at zero quark mass.

Acknowledgments

We are grateful for stimulating discussions with P. Damgaard, L. Del Debbio, A. Hasenfratz, A. Kovner, A. Patella, K. Rummukainen, F. Sannino, K. Splittorff, B. Svetitsky and R. Zwicky. Computations have been carried out on the Brutus cluster at the ETH Zürich and on a small cluster in the Sejong University physics department. Ph. de F. thanks the Institute for Nuclear Theory at the University of Washington for its hospitality and the Department of Energy for partial support during the completion of this work. S. K. is supported by Korea Foundation for International Cooperation of Science & Technology (KICOS). W. U. is supported by the Swiss National Science Foundation under grant 200020-122117.

JHEP02(2013)051

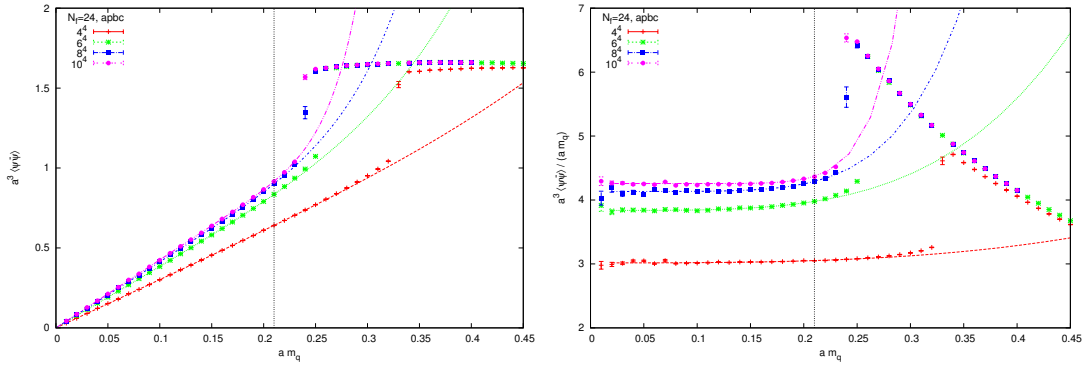

Figure 12. Left: the chiral condensate as a function of the quark mass, showing clearly a linear relation as appropriate for the chirally symmetric phase. Deviations from linearity can be used to determine the mass anomalous dimension according to eq. 5.1. Right: the same data, now divided by (am_q) to emphasize deviations from linear behaviour. The fitted values of γ^* depend on the fitting range (delimited by the vertical line), but tend to be negative (e.g. $\gamma^* \sim -0.5$ for $L = 10$).

References

[1] S. Weinberg, *Implications of dynamical symmetry breaking*, *Phys. Rev.* **D 13** (1976) 974 [INSPIRE].

[2] L. Susskind, *Dynamics of spontaneous symmetry breaking in the Weinberg-Salam theory*, *Phys. Rev.* **D 20** (1979) 2619 [INSPIRE].

[3] E. Farhi and L. Susskind, *A technicolored G.U.T.*, *Phys. Rev.* **D 20** (1979) 3404 [INSPIRE].

[4] B. Holdom, *Raising the sideways scale*, *Phys. Rev.* **D 24** (1981) 1441 [INSPIRE].

[5] T. Appelquist and L. Wijewardhana, *Chiral hierarchies and chiral perturbations in technicolor*, *Phys. Rev.* **D 35** (1987) 774 [INSPIRE].

[6] D.D. Dietrich, F. Sannino and K. Tuominen, *Light composite Higgs from higher representations versus electroweak precision measurements: Predictions for CERN LHC*, *Phys. Rev.* **D 72** (2005) 055001 [hep-ph/0505059] [INSPIRE].

[7] L. Del Debbio, *The conformal window on the lattice*, arXiv:1102.4066.

[8] P. de Forcrand, M. Pepe and U.-J. Wiese, *Walking near a conformal fixed point: the 2D $O(3)$ model at θ near π as a test case*, *Phys. Rev.* **D 86** (2012) 075006 [arXiv:1204.4913] [INSPIRE].

[9] V. Miransky and K. Yamawaki, *Conformal phase transition in gauge theories*, *Phys. Rev.* **D 55** (1997) 5051 [*Erratum ibid.* **D 56** (1997) 3768] [hep-th/9611142] [INSPIRE].

[10] H. Kluberg-Stern, A. Morel and B. Petersson, *Spectrum of lattice gauge theories with fermions from a $1/D$ expansion at strong coupling*, *Nucl. Phys.* **B 215** (1983) 527 [INSPIRE].

[11] P.H. Damgaard, D. Hochberg and N. Kawamoto, *Effective lagrangian analysis of the chiral phase transition at finite density*, *Phys. Lett.* **B 158** (1985) 239 [INSPIRE].

JHEP02(2013)051

[12] A. Hasenfratz and T.A. DeGrand, *Heavy dynamical fermions in lattice QCD*, *Phys. Rev.* **D 49** (1994) 466 [hep-lat/9304001] [INSPIRE].

[13] C. Michael, *Torelons and unusual ground states*, *Phys. Lett.* **B 232** (1989) 247 [INSPIRE].

[14] M. Lüscher and G. Munster, *Weak coupling expansion of the low lying energy values in the* SU(2) *gauge theory on a torus*, *Nucl. Phys.* **B 232** (1984) 445 [INSPIRE].

[15] D. Controzzi and G. Mussardo, *On the mass spectrum of the two-dimensional* $O(3)$ σ*-model with* θ *term*, *Phys. Rev. Lett.* **92** (2004) 021601 [hep-th/0307143] [INSPIRE].

[16] T. Banks and A. Zaks, *On the phase structure of vector-like gauge theories with massless fermions*, *Nucl. Phys.* **B 196** (1982) 189 [INSPIRE].

[17] Y. Iwasaki, K. Kanaya, S. Sakai and T. Yoshie, *Quark confinement and number of flavors in strong coupling lattice QCD*, *Phys. Rev. Lett.* **69** (1992) 21 [INSPIRE].

[18] K.-i. Nagai, G. Carrillo-Ruiz, G. Koleva and R. Lewis, *Exploration of* SU(N_c) *gauge theory with many Wilson fermions at strong coupling*, *Phys. Rev.* **D 80** (2009) 074508 [arXiv:0908.0166] [INSPIRE].

[19] J. Kogut and D. Sinclair, SU(2) *and* SU(3) *lattice gauge theories with many fermions*, *Nucl. Phys.* **B 295** (1988) 465 [INSPIRE].

[20] P. Damgaard, U.M. Heller, A. Krasnitz and P. Olesen, *On lattice QCD with many flavors*, *Phys. Lett.* **B 400** (1997) 169 [hep-lat/9701008] [INSPIRE].

[21] A. Deuzeman, M. Lombardo and E. Pallante, *Evidence for a conformal phase in* SU(N) *gauge theories*, *Phys. Rev.* **D 82** (2010) 074503 [arXiv:0904.4662] [INSPIRE].

[22] X.-Y. Jin and R.D. Mawhinney, *Lattice QCD with* 12 *degenerate quark flavors*, PoS(LATTICE 2011)066 [arXiv:1203.5855] [INSPIRE].

[23] A. Cheng, A. Hasenfratz and D. Schaich, *Novel phase in* SU(3) *lattice gauge theory with* 12 *light fermions*, *Phys. Rev.* **D 85** (2012) 094509 [arXiv:1111.2317] [INSPIRE].

[24] F. Sannino, *Jumping dynamics*, arXiv:1205.4246 [INSPIRE].

[25] P. de Forcrand and O. Jahn, *Comparison of* SO(3) *and* SU(2) *lattice gauge theory*, *Nucl. Phys.* **B 651** (2003) 125 [hep-lat/0211004] [INSPIRE].

[26] H. Leutwyler and A.V. Smilga, *Spectrum of Dirac operator and role of winding number in QCD*, *Phys. Rev.* **D 46** (1992) 5607 [INSPIRE].

[27] A. Patella, *A precise determination of the psibar-psi anomalous dimension in conformal gauge theories*, *Phys. Rev.* **D 86** (2012) 025006 [arXiv:1204.4432] [INSPIRE].

JHEP02(2013)051

A.2 Combinatorics of Lattice QCD at Strong Coupling [A2]

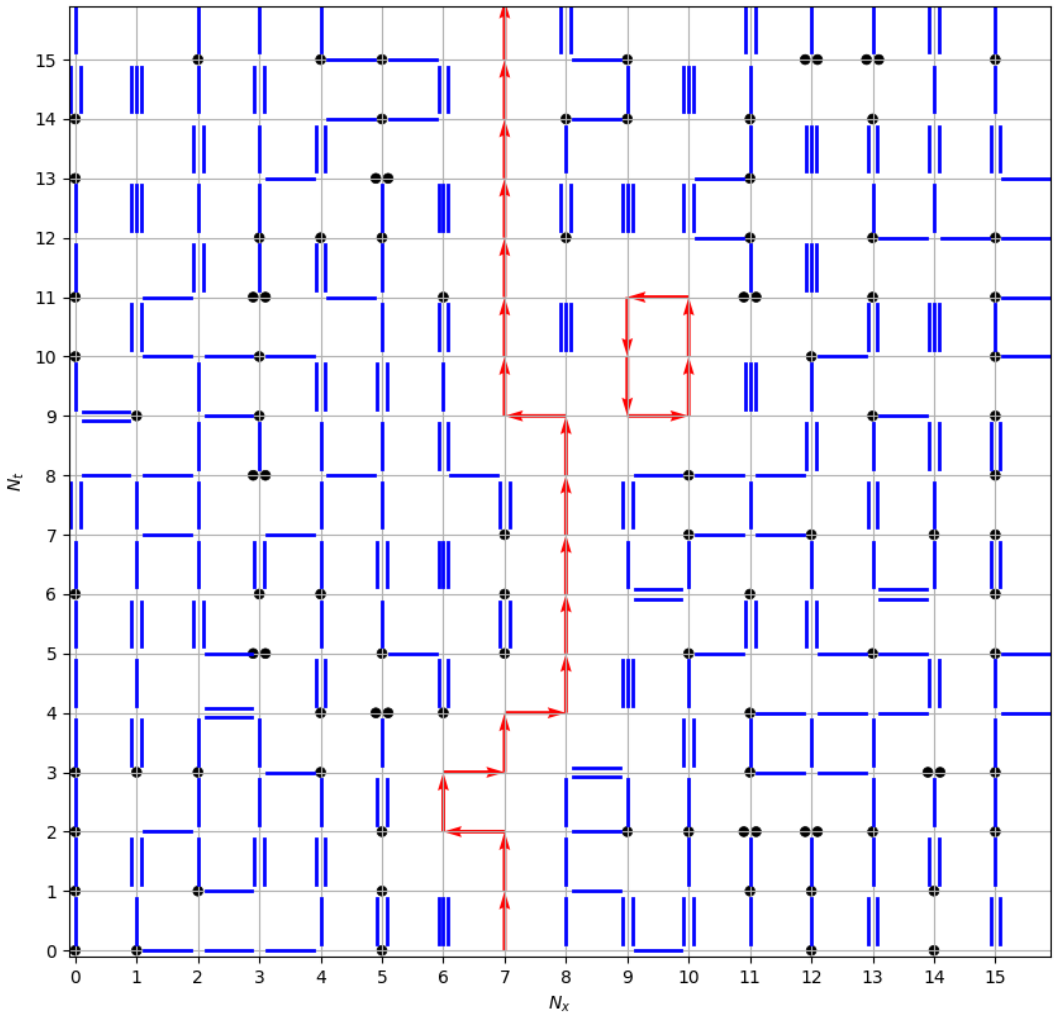

PROCEEDINGS OF SCIENCE

Combinatorics of Lattice QCD at Strong Coupling

Wolfgang Unger*
Institut für Theoretische Physik, Goethe-Universität Frankfurt,
60438 Frankfurt am Main, Germany
E-mail: unger@th.physik.uni-frankfurt.de

Thermodynamics in the strong coupling limit of lattice QCD has features which may be similar to those of continuum QCD, such as a chiral critical end point and a nuclear liquid gas transition. Here I compare the combinatorics of staggered and Wilson fermions in the strong coupling limit for arbitrary number of colors and flavors. The partition functions can be considered as an expansions in hadronic spatial hoppings from the static limit, where both discretizations can be expressed via formulae with coefficients of distinct combinatorial interpretation. The corresponding multiplicites of hadronic states are evaluated using generalizations of Catalan numbers and Lucas polynomials. I outline how quantum Monte Carlo simulations can be carried out in general, and summarize recent results on the gauge corrections to the strong coupling limit.

The 32nd International Symposium on Lattice Field Theory
23-28 June, 2014
Columbia University New York, NY

*Speaker.

1. Motivation

The QCD phase diagram is conjectured to have a rich phase structure, but only little is known from lattice QCD due to the sign problem. The available Monte Carlo methods are all limited to $\mu/T \lesssim 1$. Lattice QCD in the strong coupling limit, $\beta = \frac{2N_c}{g^2} \to 0$, and in a dual representation is a model where the sign problem is mild enough to study the full μ-T phase diagram. This virtue crucially depends on the order of integration. The following three orders are common: (1) Integrating out fermions first. This results in the fermion determinant $\det M[U]$. The Monte Carlo simulation is over gauge fields, β can be varied continuously. However, there is the severe sign problem at finite μ, and it is expensive to approach the chiral limit. (2) Integrating out spatial gauge links first then the fermions. The remaining temporal gauge links are mapped on Polyakov loops to obtain a 3-dim. heavy quark effective theory [1, 2]. This is applicable to Wilson fermions, where backtracking of fermion world lines is prohibited. The fermion determinant is factorized into a kinetic and a static part. Corrections to the static limit are treated analytically (expansion in hopping parameter and gauge action up to some order $\mathscr{O}(\kappa^n u(\beta)^m)$). (3) Integrating out all gauge links first, then the fermions. For staggered fermions, this leads to the Monomer-Dimer-System [3], which has a mild sign problem, and the chiral limit is cheap. There is no fermion determinant and it can be studied e.g. via Worm algorithms [4]. For Wilson fermions, results only consist for the Schwinger model so far [5, 6]. Moreover, incorporating the gauge action requires additional gauge integrals and introduces plaquette occupation numbers [7].

I will focus here on strategy (3) and explain its combinatorial interpretation. Lattice QCD at strong coupling (SC-LQCD) shares important features with continuum QCD: it is "confining" in the sense that only color singlet d.o.f. survive gauge integration, the mesons and baryons. These are point-like objects in the strong coupling limit, but become extended objects away from the strong coupling limit and mix with gluons. SC-LQCD also has a (nuclear) liquid gas transition from the vacuum to a baryonic crystal, where all lattice sites are occupied by baryons. Since the lattice spacing at strong coupling is maximally coarse, the degrees of freedom are on a hypercubic crystal and saturation is due to the Pauli principle. For staggered fermions, there is also spontaneous chiral symmetry breaking and its restoration at some critical temperature aT_c. In contrast to Wilson fermions, there is a remnant chiral symmetry $U_{55}(1) \subset SU_L(N_f) \times SU_R(N_f)$ that is not broken by the finite lattice spacing. The ultimate goal is to study the QCD phase diagram and the nuclear transition away from the strong coupling limit. A first step into that direction, the $O(\beta)$ corrections to the strong coupling phase diagram, has already been undertaken [7].

A dimer/flux representation is possible for both lattice actions, but they differ qualitatively. For staggered fermions: a partition function in the monomer-dimer representation is valid for any quark mass; there is an exact chiral symmetry, hence it is adequate to study chiral properties (also, simulations in the chiral limit are cheap); however, staggered fermions are spinless in the strong coupling limit. Contrast this with Wilson fermions: the flux representation involves spin, but since backtracking of fermions is not allowed, $(\mathbb{1}-\gamma_\mu)(\mathbb{1}+\gamma_\mu) = 0$, it poses a complicated combinatorial problem and expansion in spatial hadronic hoppings is required. Both discretizations have very different lattice artifacts. The main motivation for this analysis is the question whether they share a "physical" content at strong coupling or at $\mathscr{O}(\beta)$ which could be isolated from lattice artifacts. The combinatorial perspective may help to shed light on this question.

2. Gauge Integrals, Invariants and Combinatorics

Combinatorics can give additional insight into lattice QCD, when formulated in a dual, color singlet representation based on integer variables. The combinatorial paradigm I want to utilize is the question of how many ways there are to put n balls into k boxes. Many combinatorial problems reduce to this question, and the answer will depend on the permutation symmetries in the problem, i.e. whether balls or boxes are distinguishable or not, and which restrictions on the placements are made (e.g. the 12 canonical answers known as "twelvefold way"). Combinatorial formulae amount to integer sequences, which are listed in the On-Line Encyclopedia of Integer Sequences [8]. In the following I quote the A numbers from OEIS for further explanations and proofs.

First consider the SU(N_c) one-link integral [9, 10] which can be evaluated both for staggered and Wilson fermions:

$$z(x,\mu) = \int dU_\mu(x) e^{\mathrm{tr}_c\left[U_\mu(x)M^\dagger + U_\mu(x)^\dagger M\right]}, \tag{2.1}$$

$$(M^{\text{stagg.}})_{ij} = \chi_i^f(x)\bar{\chi}_j^f(x+\hat{\mu}), \qquad (M^{\text{Wilson}})_{ij} = \psi_i^{\beta,f}(x)(\mathbb{1}-\gamma_\mu)_{\alpha\beta}\bar{\psi}_j^{\alpha,f}(x+\hat{\mu}), \tag{2.2}$$

with $i,j \in \{1,\dots N_c\}$, $f \in \{1,\dots N_f\}$ and α, β Dirac indices. In both cases, the link integrals are gauge invariants, which can be expressed by linear combinations of traces and determinants.

$$z(x,\mu) = \sum_{k_1,\dots k_{N_c+1}} \alpha_{k_1\dots k_{N_c+1}} \det_c[M]^{k_1} \det_c\left[M^\dagger\right]^{k_2} \mathrm{tr}_c\left[MM^\dagger\right]^{k_3} \dots \mathrm{tr}_c\left[(MM^\dagger)^{N_c-1}\right]^{k_{N_c+1}} \tag{2.3}$$

The prefactors $\alpha_{k_1\dots k_{N_c+1}}$ can be determined via Grassmann identities, e.g. for $N_f = 1$ staggered fermions (with $y = x+\hat{\mu}$ and $B(x) = \frac{1}{N_c!}\varepsilon_{i_1\dots i_{N_c}}\chi_{i_1}(x)\dots\chi_{i_{N_c}}(x)$):

$$e^{\bar{\chi}_y\chi_y} = \int d\chi_x d\bar{\chi}_x \int dU e^{\bar{\chi}_x\chi_x + \bar{\chi}_x U\chi_y - \bar{\chi}_y U^\dagger\chi_x} = \sum_{l=0}^{N_c} \alpha_k \frac{N_c!}{(N_c-k)!}(\bar{\chi}_x\chi_x\bar{\chi}_y\chi_y)^k \tag{2.4}$$

$$\Rightarrow \qquad z(x,y) = \sum_{k=0}^{N_c} \frac{(N_c-k)!}{N_c!k!}(M_xM_y)^k + \bar{B}(x)B(y) + (-1)^{N_c}\bar{B}(y)B(x). \tag{2.5}$$

The prefactors can also be determined via combinatorics (labeled balls into labeled boxes, see Fig. 1). This strategy can be generalized to also apply to $N_f > 1$ and for Wilson fermions, where meson hoppings $(M_xM_{x+\hat{\mu}})$ and baryon hoppings $\bar{B}(x)B(x+\hat{\mu})$ carry flavor and spin. The corresponding integrals have been determined for $N_c \leq 3$ in [10] and are in agreement with the combinatorial determination.

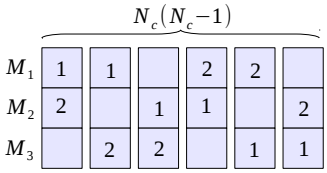

Figure 1: $k = 2$ balls $(\bar{\chi}\chi)$ into $N_c = 3$ boxes (mesons).

Another type of gauge integrals are those over the trace of closed loops of gauge links: let $P = \prod_{(x,\mu)\in\mathscr{C}} U_\mu(x) = \mathrm{diag}\left(e^{i\phi_1},\dots e^{i\phi_{N_c-1}}, e^{i\phi_{N_c}}\right)$ with $\phi_{N_c} = -\sum_{k=1}^{N_c-1}\phi_k$ be any closed loop of gauge links along contour $\mathscr{C}$ (e.g. Polyakov loop, Wilson loop), then, for SU(N_c) there are N_c-1 gauge invariants, such as $L = \mathrm{tr}_c[P]$ and L^*. Only the mesonic $\mathscr{M} = LL^*$, baryonic $\mathscr{B} = L^{N_c}$, and mixed operators $\mathscr{O} = \mathscr{M}^n\mathscr{B}^m$ for $n,m \in \mathbb{N}$) have non-vanishing expectation values:

$$\langle\mathscr{O}(L,L^*\dots)\rangle = \frac{1}{(2\pi)^{N_c-1}}\int d\phi_1\dots d\phi_{N_c-1} V(L,L*,\dots)\mathscr{O}(L,L^*,\dots), \tag{2.6}$$

	1 (mesonic)	L^3	L^6	L^9	L^{12}
1 (baryonic)	1	1	5	42	462
(LL^*)	1	3	21	210	2574
$(LL^*)^2$	2	11	98	1122	15015
$(LL^*)^3$	6	74	498	6336	91091
$(LL^*)^4$	23	225	2709	37466	571428

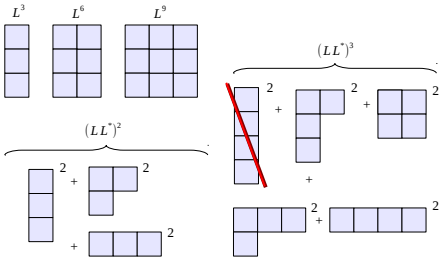

Table 1: List of SU(3) gauge integrals $\langle (LL^*)^n (L^3)^m \rangle$, which enumerate the number of restricted permutations patterns, which is the number representations of bounded height, see Eq. (2.8).

where $V(L,L^*\ldots)$ is obtained from the invariant Haar measure: $d\mu(\phi) = \prod_{i>j} |e^{i\phi_i} - e^{i\phi_j}|^2 \prod_i d\phi_i$. The result for SU(2), where $L^* = L$, gives rise to the so-called Catalan numbers (A000108), which play a prominent role in combinatorics, e.g. as the number of 123-avoiding permutation patterns:

$$\left\langle L^{2n} \right\rangle = \frac{1}{2\pi} \int_0^{2\pi} d\phi 2\sin^2\phi (2\cos\phi)^{2n} = \frac{1}{2\pi} \int_{-2}^{2} dL \sqrt{4-L^2} L^{2n} = C_n \equiv \frac{1}{n+1} \binom{2n}{n} \tag{2.7}$$

For SU(3), where $\mathrm{tr}[P^2] = L^2 - 2L^{*2}$, the various results listed in Tab. 1 can be mapped on representations of the permutation group. The invariants of higher moments in L, L^*, which are needed to express the static limit of Wilson fermions (see below), can be characterized as restricted permutation patterns, which correspond to dimensions of standard young tableaux of bounded height.

$$m_{N_c}(n) = \sum_{h(\lambda_n) \le N_c} d^2_{\lambda_n}, \qquad b_{N_c}(n) = d_{n \times N_c}, \qquad mix_{N_c}(n_m, n_b) = \sum_{h(\lambda_{n_m}) \le N_c} d_{n_b \times N_c, \lambda_{n_m}} d_{\lambda_{n_m}}. \tag{2.8}$$

To compute these invariants in the general case of SU(N_c) or U(N_c) and $N_f > 1$, one needs to evaluate $\mathrm{tr}[P^n]$, where $n = 1, \ldots, N_c N_f$. These can be obtained via generalized Lucas polynomials. The Lucas n-step numbers are $F_k^{(n)} = \sum_{i=1}^{n} F_{k-i}^{(n)}$ (which is Fibonacci-like for $n = 2$). Related to SU(3) are the 3-step Lucas numbers $F_k^{(3)} = F_{k-1}^{(3)} + F_{k-2}^{(3)} + F_{k-3}^{(3)}$ with seeds $F_0^{(3)} = 3$, $F_1^{(3)} = 1$, $F_2^{(3)} = 3$, from which the following 3-step polynomials F in the variables x, y, z are obtained :

$$F_n^{(3)}(x,y,z) = \mathrm{tr}\left[\begin{pmatrix} x & y & z \\ 1 & 0 & 0 \\ 0 & 1 & 0 \end{pmatrix}^n \right], \quad \tilde{F}_n^{(3)}(x,y,z) = \mathrm{tr}\left[\begin{pmatrix} x & y & z \\ -1 & 0 & 0 \\ 0 & -1 & 0 \end{pmatrix}^n \right]. \tag{2.9}$$

It turns out that the signed verison $\tilde{F}_n$ is directly related to $\mathrm{tr}[P^n] = \tilde{F}_n(P)$ by identifiying $x \equiv L = \mathrm{tr}[P]$, $y \equiv L^* = \mathrm{tr}[P^\dagger]$, $z \equiv D = \det[P]$ (=1 for SU(N_c)). The first orders are

$$\begin{aligned} &\mathrm{tr}[P^0] = 3, && \mathrm{tr}[P^1] = L, \\ &\mathrm{tr}[P^2] = L^2 - 2L^*, && \mathrm{tr}[P^3] = L^3 - 3LL^* + 3D, \\ &\mathrm{tr}[P^4] = L^4 - 4L^2L^* + 2L^{*2} + 4LD, && \mathrm{tr}[P^5] = L^5 - 5L^3L^* + 5LL^{*2} + 5L^2D - 5L^*D. \end{aligned}$$

The corresponding versions for arbitrary N_c is obtained by considering the signed $N_c \times N_c$ matrix $\tilde{F}(x_1, \ldots, x_{N_c})$. I have used the generalized Lucas polynomials to determine the flavor dependence of the static limit.

3. Strong Coupling Partition Functions

The final partition functions at strong coupling are obtained after Grassmann integration, which introduces site weights w_x. For staggered fermions:

$$w_x = \int \prod_c [d\chi_{c,x} d\bar{\chi}_{c,x}] e^{2am_q \bar{\chi}_{c,x}\chi_{c,x}} (\bar{\chi}_{c,x}\chi_{c,x})^{k_x} = \frac{N_c!}{n_x!}(2am_q)^{n_x}, \tag{3.1}$$

with monomers $n_x = N_c - k_x$, determined by the Grassmann constraint $k_x = \sum_{\pm\hat{\mu}} k_{\pm\hat{\mu}}(x)$, hence $n_x \in \{0,\dots N_c\}$, and no monomers at baryonic sites. The well-known staggered partition function ($N_f = 1$) valid to all orders in the hopping parameter $\kappa = \frac{1}{2am_q}$ is

$$Z_{SC}^{\text{stagg.}}(m_q,\mu,\gamma) = \sum_{\{k_b,n_x,\ell\}} \underbrace{\prod_{b=(x,\mu)} \frac{(N_c-k_b)!}{N_c!k_b!}\gamma^{2k_b\delta_{\mu 0}}}_{\text{meson hoppings } M_xM_y} \underbrace{\prod_x \frac{N_c!}{n_x!}(2am_q)^{n_x}}_{\text{chiral condensate } M_x} \underbrace{\prod_\ell w(\ell,\mu)}_{\text{baryon hoppings } \bar{B}_xB_y}, \tag{3.2}$$

with $k_b \in \{0,\dots N_c\}$, $n_x \in \{0,\dots N_c\}$, $\ell_b \in \{0,\pm 1\}$. The weight $w(\ell,\mu)$ and sign $\sigma(\ell) = \pm 1$ for an oriented loop ℓ depend on loop geometry. The anisotropy $\gamma = a/a_t$ is needed to vary the temperature continuously at $\beta = 0$ [11].

For Wilson fermions, Grassmann integration amounts to spin and flavor conservation. The site weights (almost) cancel link weights. Only when spatial hoppings of color neutral states occur, the site weights are non-trivial. The partition function can generally be mapped on a vertex model. This has been done for the Schwinger model, which maps on a 7-vertex model for $N_f = 1$ [5] and on a modified 3-state 20-vertex model for $N_f = 2$ [6]. Grassmann integration for $N_c > 1$ is too complicated to do by hand but can be automatized using computer algebra. The Wilson fermion partition function has the general structure

$$Z_{SC}^{\text{Wilson}}(\kappa,\mu) = \sum_{\{k_b,n_x,\ell_j\}} N(\{k_b,\ell_j\}) v_i^{C_i} \prod_x \frac{1}{(2\kappa)^{n_x}} \prod_{\ell_j} w(\ell_j,\mu). \tag{3.3}$$

C_i counts how often vertices of type i occur and $N(\{k_b,\ell_j\})$ counts multiplicities of loops. There are various baryonic loops ℓ_j (depending on spin and flavor). The Grassmann constraint allows mesonic and baryonic world lines to intersect even for $N_f = 1$. The vertex weights v_i still need to be determined in general via Grassmann integration.

In the static limit, i.e. in the absence of spatial fermion hoppings, the strong coupling partition function is $Z_{SC}^{\text{static}} = \prod_{\vec{x}} Z_1(\vec{x})$, where Z_1 is the sum over all possible hadronic quantum states $|\psi\rangle$. This describes SC-LQCD in the high temperature and/or high density regime, see Fig. 2. For staggered fermions, the chiral restoration takes place when the number of spatial dimers reaches a critical value. The nuclear and chiral transition coincide, because $\langle\bar{\chi}\chi\rangle$ vanishes as a baryonic crystal forms. The number of hadronic states $|\psi\rangle = |P_u, P_d, \dots P_{N_f}, Q_{\pi^+}, Q_{K^+}, \dots\rangle$ is

$$Z_1(\mu,T) = \binom{2N_f}{N_cN_f}_{N_c} + \sum_{n=1}^{N_tN_c/2} t_n(2am_q)^{2n} + 2\binom{N_c+N_f-1}{N_f-1}\cosh(\mu_B/T), \tag{3.4}$$

where the terms $\mathcal{O}(2am_q)$ are suppressed at high T (for $N_c = 3$ in the chiral limit, the prefactors t_n are related to Tribonacci numbers (A000073), a generalization of Fibonacci). The degeneracies of

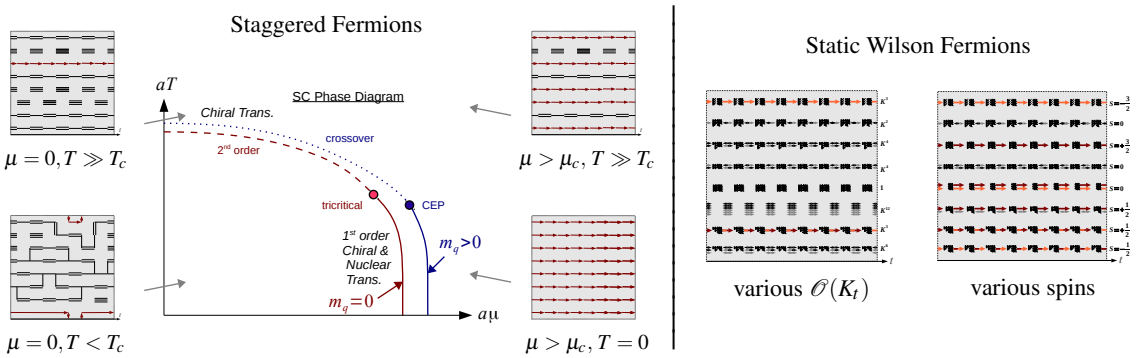

Figure 2: At $\beta=0$, both staggered and Wilson fermions become static at large T and/or μ. Left: The staggered SC phase diagram, it has been measured in [4,7]. Right: Static Wilson fermions described by monomers/dimers/fluxes, multiplicities are due to spin and K_t.

the mesonic states are given by central polynomial coefficients (see A077042) which number the possibilities to put n unlabeled balls into k labeled boxes, allowing at most N_c balls in each box.

For Wilson fermions, with $K_t=(2\kappa)^{N_\tau}$ and hopping parameter $\kappa=\frac{1}{2d+2am_q}$, for $N_f=1$:

$$Z_1(\mu,T)=\sum_{k=0}^{2N_c}T(k)K_t^{2k}+\sum_{k=0}^{N_c}P(k)K_t^{(2k+N_c)}2\cosh(\mu_B/T)+K_t^{2N_c}2\cosh(2\mu_B/T). \tag{3.5}$$

The combinatorics of the mesonic sector is given by the so-called tetrahedal numbers (A133826) $T(k)=\sum_{q=0}^{k}d_{D^{0q}}=\binom{3+\min(k,2N_c-k)}{3}$, with D^{0q} the mesonic irreducible representations of SU(N_c), and product numbers $P(k)=(1+k)(1+N_c-k)$. This can be generalized for $N_f>1$, e.g. $T(k)=\binom{(2N_f)^2-1+\min(k,2N_c-k)}{(2N_f)^2-1}$, and Eq. (3.5) contains $2N_f+1$ sums $\sim K_t^{2k+nN_c}$. To conclude, the quantum number degeneracies of all static states can be listed via combinatorial formulae.

There are two kinds of corrections to the static limit, which can be both addressed systematically via an expansion: (1) The (spatial) hopping parameter expansion in κ_s allows to approach the chiral limit, with the number of spatial mesonic and baryonic hoppings being controlled by the quark mass. In a finite volume, this expansion always terminates due to the Grassmann constraint! (2) The expansion in β (the inverse gauge coupling) allows to approach the continuum limit. The staggered strong coupling partition function is in fact valid for all quark masses (with the chiral limit being cheapest when addressed with a worm algorithm), whereas the Wilson partition function is restricted to rather large quark masses. In both lattice discretizations, the gauge action can be incorporated order by order, which gives rise to higher order link integrals.

The strategy to study both lattice discretizations on a par is to expand around the static limit by making use of the Hamiltonian formulation that can be derived in the continuous time limit, $N_\tau\to\infty$ [11]. In this limit, the partition function simplifies further as only single meson hoppings need to be considered. The static lines are the in and out states of the transfer matrix:

$$Z=\mathrm{Tr}[e^{\beta\mathscr{H}}],\qquad \mathscr{H}=\frac{1}{2}\sum_{\langle x,y\rangle}\sum_{Q_i}J^+_{Q_i(x)}J^-_{Q_i(y)},\qquad J^-_{Q_i}=(J^+_{Q_i})^\dagger, \tag{3.6}$$

where the generalized quantum numbers Q_i (spin, parity, flavor) are globally conserved, and spatial dimers represented by $J^+_{Q_i(x)}J^-_{Q_i(y)}$ raise quantum number Q_i at site x and lower them at a neighboring site y (see [11] for the case of $N_f=1,2$ for staggered fermions). For both staggered and Wilson

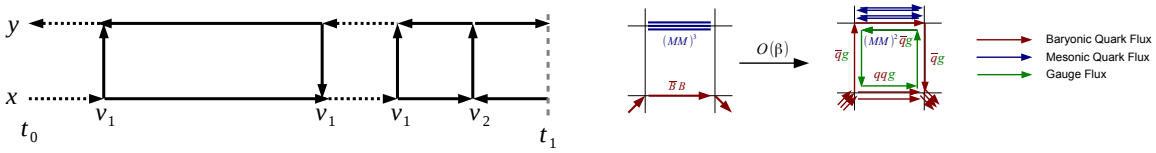

Figure 3: *Left:* Systematic expansion in the spatial hoppings in the Hamiltonian formulation, where hadrons are emitted/absorbed at events in continuous time, depending on vertex weights v_i. *Right:* Example of a gauge correction to the SC-limit, hadrons become extended objects.

fermions, the matrices $J^{\pm}_{Q_i}$ contain vertex weights. They are the crucial input to sample the corresponding partition function with a quantum Monte Carlo algorithm to all orders in κ_s, e.g. via a continuous time Worm algorithm. However, whether also for Wilson fermions in four dimensions all vertex weights are positive to evade the sign problem is still an open question, although due to the continuous time limit, only a small set of vertices need to be considered. For the simulation of the Schwinger model with Wilson fermions at strong coupling with the Worm algorithm see [12].

Also the gauge corrections could be included in this Hamiltonian formulation. So far, the gauge corrections have been studied for finite $N_\tau = 4$ and for $N_f = 1$ staggered fermions. In a collaboration with J. Langelage, P. de Forcrand and O. Philipsen, we have determined the phase diagram of SC-LQCD at $\mathcal{O}(\beta)$ [7], where the gauge action is linearized and a new set of one-link integrals (those along an excited plaquette) have to be evaluated and new invariants with a combinatorial interpretation arise. We find that the second order phase boundary in the μ-T plane is shifted to lower temperatures with increasing β, but that the tricritical point and the first order transition is invariant at $\mathcal{O}(\beta)$. In contrast, the critical endpoint of the first order nuclear transition, which coincides with the chiral transition at $\beta = 0$, moves down along the chiral first order line.

Acknowledgement - I would like to thank Philippe de Forcrand and Owe Philipsen for numerous discussions. This works was supported by the Helmholtz International Center for FAIR within the LOEWE program launched by the State of Hesse.

References

[1] De Pietri *et al.*, *Phys. Rev. D* **76** (2007) 114501.

[2] Fromm *et al.*, *Phys. Rev. Lett.* **110** (2013) 122001.

[3] P. Rossi and U. Wolff, *Nucl. Phys. B* **258** (1984) 105.

[4] P. de Forcrand, M. Fromm, *Phys. Rev. Lett.* **104** (2010) 112005.

[5] M. Salmhofer, *Nucl. Phys. B* **362** (1991) 641.

[6] K. Scharnhorst, *Nucl. Phys. B* **479** (1996) 727.

[7] P. de Forcrand, J. Langelage, O. Philipsen and W. Unger, *Phys. Rev. Lett.* **113** (2014) 152002.

[8] N. J. A. Sloane, On-Line Encyclopedia of Integer Sequences `http://www.oeis.org`.

[9] M. Creutz, *J. Math. Phys.* **19** (1978) 2043.

[10] K. E. Eriksson, N. Svartholm and B. S. Skagerstam, *J. Math. Phys.* **22** (1981) 2276.

[11] W. Unger and P. de Forcrand, *PoS LATTICE* **2012** (2012) 194 [arXiv:1211.7322 [hep-lat]].

[12] U. Wenger, *Phys. Rev. D* **80** (2009) 071503 [arXiv:0812.3565 [hep-lat]].

A.3 Thermodynamics of strongly-coupled lattice QCD in the chiral limit [A3]

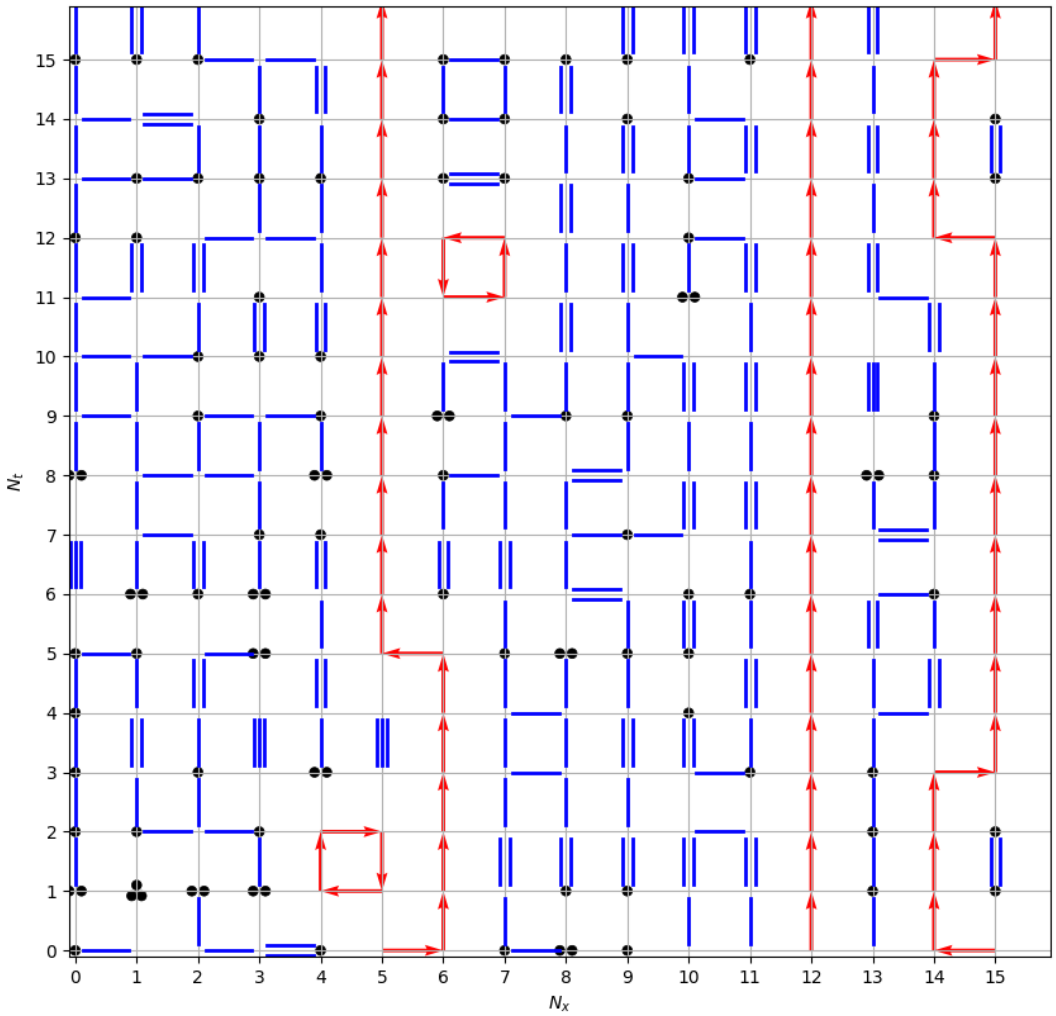

CERN-PH-TH-2017-012

PROCEEDINGS OF SCIENCE

Thermodynamics of strongly-coupled lattice QCD in the chiral limit

Philippe de Forcrand
Institut für Theoretische Physik, ETH Zürich, CH-8093 Zürich, Switzerland
CERN, TH Division, CH-1211 Geneva 23, Switzerland
E-mail: forcrand@phys.ethz.ch

Paul Romatschke
Department of Physics, 390 UCB, University of Colorado at Boulder, Boulder, CO, USA
E-mail: paul.romatschke@colorado.edu

Wolfgang Unger
Fakultät für Physik, Universität Bielefeld, Universitätstasse 25, D33619 Bielefeld, Germany
E-mail: wunger@physik.uni-bielefeld.de

Hélvio Vairinhos*
Institut für Theoretische Physik, ETH Zürich, CH-8093 Zürich, Switzerland
E-mail: helviov@phys.ethz.ch

In the strong coupling limit, n-point functions in lattice QCD with staggered fermions can be rewritten exactly as sums over constrained configurations of monomers, dimers, and baryon loops covering the spacetime lattice. Worm algorithms provide efficient global sampling methods over such ensembles, and are particularly efficient in the chiral limit. We study the thermodynamics of strongly-coupled $U(3)$ and $SU(3)$ lattice QCD with one massless staggered fermion using such methods, and compare the results with the relativistic pion gas down to low temperatures $O(15\ \mathrm{MeV})$.

34th annual International Symposium on Lattice Field Theory
24-30 July 2016
University of Southampton, UK

*Speaker.

1. Introduction

Consider $U(N)$ or $SU(N)$ lattice QCD with a single staggered fermion flavour, at finite temperature. At low temperatures, the chiral U(1) symmetry of the massless staggered fermion is spontaneously broken, to which a single massless Goldstone boson is associated: the pion.

The pion is interacting, but at sufficiently low temperatures the strength of the effective interactions vanishes, i.e. $\frac{T}{F_\pi} \to 0$, and the pion is effectively free. In such a regime, the physics is that of an ideal pion gas, whose energy density, ε, satisfies the Stefan-Boltzmann law (SB) for a single bosonic degree of freedom:

$$\varepsilon(T) = \varepsilon(0) + \frac{\pi^2}{30} T^4 \tag{1.1}$$

Here we summarize our numerical study of the thermal properties of $U(3)$ and $SU(3)$ lattice QCD with a single staggered fermion, in the chiral limit, where we test the hypothesis of a (near) ideal pion gas below the critical temperature of the chirally-restoring phase transition.

We choose to perform simulations in the strong coupling limit, $\beta = 0$, for there we have access to Monte Carlo algorithms of the worm type, which are very efficient, even in the chiral limit and at low temperatures. This allows us to determine the equation of state of lattice QCD with high precision, at unprecedentedly low temperatures.

2. Thermodynamics of a free massless boson on the lattice

First, it is instructive to understand the behavior of an ideal gas of massless bosons on a lattice. Lattice corrections to the ideal gas regime of a free massless boson, on a $N_s^3 \times N_t$ lattice with anisotropy $\xi = a/a_t$, have been studied in [1]. The energy density ε of such a gas is given by:

$$a^4 \varepsilon(T) = -\frac{\xi^3}{N_s^3 N_t} \sum_{\vec{j} \neq \vec{0}} \frac{\sin^2(\pi j_0/N_t)}{b^2 + \xi^2 \sin^2(\pi j_0/N_t)}, \qquad b^2 = \sum_{i=1}^{3} \sin^2(\pi j_i/N_s) \tag{2.1a}$$

$$a^4 \varepsilon(0) = -\frac{\xi^3}{N_s^3} \sum_{\vec{j} \neq \vec{0}} \left(b^2 + \xi^2 + b\sqrt{b^2 + \xi^2} \right)^{-1} \tag{2.1b}$$

where the lattice temperature is given by $aT = \xi/N_t$. Similar expressions can be obtained for the pressure p. In particular, they imply that the trace anomaly vanishes on any finite lattice [1]:

$$\Delta\varepsilon - 3\Delta p = 0 \tag{2.2}$$

where $\Delta\varepsilon(T) = \varepsilon(T) - \varepsilon(0)$, and $\Delta p(T) = p(T) - p(0)$.

In this system, discretization effects are quite significant (see Fig. 1): from [1], we learn that lattice corrections are small for $N_s \geq 2N_t$ and $\xi \geq 2$. Actually, the ideal gas behavior is only exact in the continuous time limit, $\xi \to \infty$.

We keep this in mind when simulating lattice QCD in the regime where the $U(1)$ chiral symmetry is spontaneously broken, and the pion is massless. Even though pions are not free ($F_\pi \neq 0$), their interactions should be negligible in the regime $T \ll F_\pi$ (or in the large N limit), and the picture of an ideal pion gas should become a good approximation.

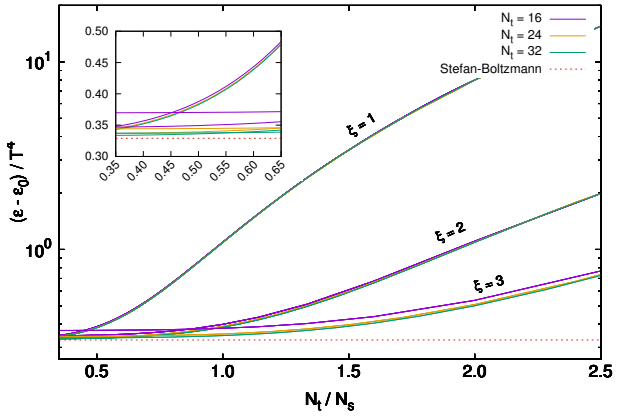

Figure 1: Energy density of a free massless boson on the lattice: the finite-size effects induce very large deviations from the Stefan-Boltzmann limit (dotted line), but are significantly suppressed (less than 10%) when $N_s \gtrsim 3N_t$ for $\xi = 1$, or $N_s \gtrsim 2N_t$ for $\xi \geq 2$.

3. Dimer representation of lattice QCD in the strong coupling limit

The partition function of $SU(3)$ lattice QCD with $N_f = 1$ staggered fermions, at $\beta = 0$, is:

$$Z = \int \mathscr{D}U \mathscr{D}\psi \mathscr{D}\bar{\psi}\, e^{2a_t m_q \sum_x \bar{\psi}_x \psi_x + \sum_{x,\mu} \gamma^{\delta_{\mu 0}} \eta_{x\mu} \left(e^{a_t \mu_q} \bar{\psi}_x U_{x\mu} \psi_{x+\hat{\mu}} - e^{-a_t \mu_q} \bar{\psi}_{x+\hat{\mu}} U^\dagger_{x\mu} \psi_x \right)} \tag{3.1}$$

where μ_q is the quark chemical potential, γ is the bare anisotropy, m_q is the bare quark mass, a_t (a) is the temporal (spatial) lattice spacing, and $\eta_{x\mu} = \pm 1$ are the staggered phases.

Analytic integration of the link variables, followed by the integration of the Grassmann variables, yields the partition sum of a system of monomers, dimers, and baryon loops [2]:

$$Z = \sum_{\{n,k,\ell\}} \frac{\sigma(\ell)}{3!^{|\ell|}} \left(\prod_x \frac{3!}{n_x!} \right) \left(\prod_{x,\mu} \frac{(3-k_{x\mu})!}{3! k_{x\mu}!} \right) (2a_t m_q)^{N_M} \gamma^{2N_{Dt} + 3N_{\ell t}} e^{3N_t a_t \mu_q w_\ell} \tag{3.2}$$

where $n_x, k_{x\mu} \in \{0,1,2,3\}$ are occupation numbers of monomers and dimers, $\ell_{x\mu} \in \{0, \pm 1\}$ are occupation numbers of oriented baryonic dimers, and $N_M, N_{Dt}, N_{\ell t}$ denote, respectively, the total number of monomers, timelike dimers, and timelike baryonic links:

$$N_M = \sum_x n_x, \qquad N_{Dt} = \sum_x k_{x0}, \qquad N_{\ell t} = \sum_x |\ell_{x0}| \tag{3.3}$$

w_ℓ counts the number of times baryon loops wrap around the thermal direction, and $\sigma(\ell) = \pm 1$ is a sign which depends on the shape of the baryon loops (and introduces a sign problem).

Due to the Grassmann integration, the configurations which contribute to the partition function are constrained, on each site, to have either exactly 3 monomers and/or dimers, or be traversed by a non-self-intersecting oriented baryon loop:

$$n_x + \sum_{\pm\mu} k_{x\mu} \stackrel{!}{=} 3, \qquad \sum_{\pm\mu} \ell_{x\mu} \stackrel{!}{=} 0, \qquad \forall x \tag{3.4}$$

Such constrained configurations can be efficiently sampled using variants of the worm algorithm: a "mesonic worm", which updates the monomer-dimer sector [3], and a "baryonic worm", which updates the baryonic loops and the 3-dimer sector [4, 5].

The partition function for $U(3)$ QCD is obtained from (3.2) by removing the baryons, i.e. $\ell_{x\mu} = 0, \forall x, \mu$. In this case, only the mesonic worm is needed to simulate it.

4. Thermodynamics of lattice QCD in the strong coupling and chiral limits

The energy density and pressure in $SU(3)$ lattice QCD, in the strong coupling limit ($\beta = 0$) and chiral limit ($m_q = 0$), are related to the density of hadrons hopping in the time direction (i.e. timelike dimers and timelike baryon links):

$$a^3 a_t \, \Delta\varepsilon = \mu_B \rho_B - \frac{a^3 a_t}{V} \left. \frac{\partial \log Z}{\partial T^{-1}} \right|_{V,\mu_B} = \frac{\xi}{\gamma} \frac{d\gamma}{d\xi} \langle 2n_{Dt} + 3n_{\ell t} \rangle \tag{4.1a}$$

$$a^3 a_t \, \Delta p = a^3 a_t T \left. \frac{\partial \log Z}{\partial V} \right|_{T,\mu_B} = \frac{\xi}{3\gamma} \frac{d\gamma}{d\xi} \langle 2n_{Dt} + 3n_{\ell t} \rangle \tag{4.1b}$$

where μ_B is the baryon chemical potential, $\rho_B = \langle w_\ell \rangle / N_s^3$ is the baryon density, and $\xi(\gamma) = \frac{a}{a_t}$ is the renormalized anisotropy, which parameterizes the physical anisotropy of the lattice. In order to obtain the corresponding expressions in $U(3)$ QCD, it suffices to take $\rho_B = 0$ and $n_{\ell t} = 0$.

Eqs. (4.1a) and (4.1b) imply that the trace anomaly vanishes for any lattice spacing, cf. (2.2).

5. Anisotropy calibration

An accurate determination of the energy density (4.1a), or pressure (4.1b), requires a precise knowledge of the renormalized anisotropy ξ as a function of the bare anisotropy γ, and also of its running, $d\xi/d\gamma$. For this purpose, we use the fluctuations of certain conserved charges, labelled by spacetime directions, as probes for the calibration of the lattice anisotropy.

In the chiral limit, Grassmann constraints (3.4) imply the existence of conserved currents [6]:

$$j_{x\mu} = \pi_x \left(k_{x\mu} - \frac{3}{2} |\ell_{x\mu}| - \frac{3}{8} \right) \quad \Rightarrow \quad \sum_{\pm\mu} j_{x\mu} = 0, \ \forall x \tag{5.1}$$

where $\pi_x = (-1)^{\sum_\mu x_\mu} = \pm 1$ is the parity (bipartite color) of the site x. We can also define conserved charges by integrating the currents along codim-1 hyperslices $\mathscr{S}_\mu$ perpendicular to the direction $\hat{\mu}$:

$$Q_\mu = \sum_{x \in \mathscr{S}_\mu} j_{x\mu} \tag{5.2}$$

Due to parity symmetry, $\langle Q_\mu \rangle = 0$, $\forall \mu$. We consider lattices with the same size N_s in all spatial directions, and thus compare variations of the timelike charge, $Q_t^2 = Q_0^2$, and of the average of the spacelike charges, $Q_s^2 = \frac{1}{3} \sum_{i=1}^3 Q_i^2$.

Our non-perturbative renormalization criterion requires the fluctuations of the conserved charges to be isotropic when the physical volume is hypercubic (in the thermodynamic limit):

$$\langle Q_t^2 \rangle (\gamma_{\text{np}}) = \langle Q_s^2 \rangle (\gamma_{\text{np}}) \quad \Rightarrow \quad \frac{a N_s}{a_t N_t} = \xi(\gamma_{\text{np}}) \frac{N_s}{N_t} = 1 \tag{5.3}$$

where γ_{np} is the nonperturbative, finely tuned value of the bare anisotropy for which fluctuations of the conserved charges coincide. Using scaling arguments, it is also easy to relate the running of the renormalized anisotropy to expectation values associated with these conserved charges:

$$\xi \frac{d\gamma}{d\xi} = \frac{\langle Q^2 \rangle_{\gamma_{\text{np}}}}{\left(\frac{d}{d\gamma} \langle Q_t^2 \rangle - \frac{d}{d\gamma} \langle Q_s^2 \rangle \right) \Big|_{\gamma_{\text{np}}}} \tag{5.4}$$

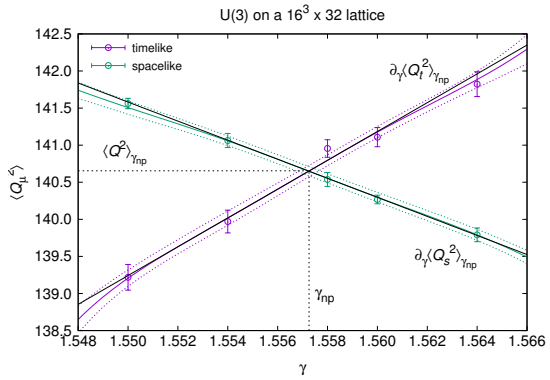

Figure 2: Fluctuations of the conserved charges in the timelike (purple) and spacelike (green) directions, as a function of the bare anisotropy γ, in $U(3)$ QCD. The intersection point corresponds to the critical value of γ for which the physical box is hypercubic, while the lattice has an anisotropy $\xi(\gamma_{\text{np}}) = \frac{N_t}{N_s} = 2$.

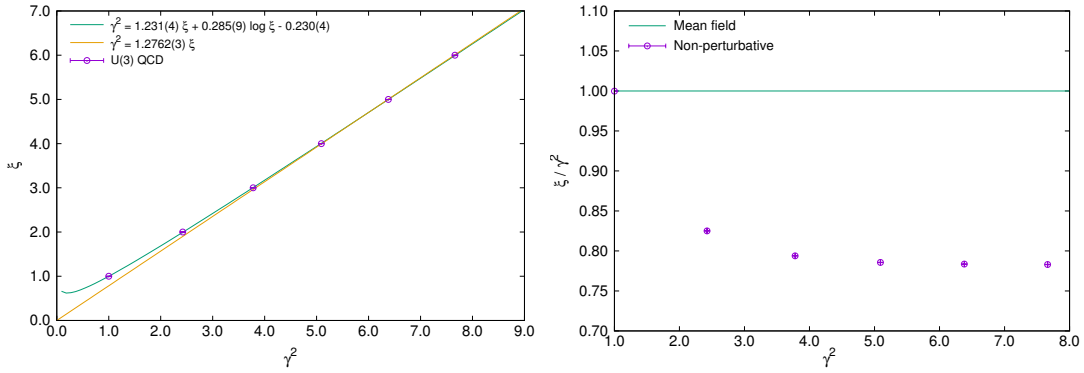

Figure 3: Nonperturbative relation between the bare and renormalized anisotropy in $U(3)$ QCD (left), and its deviation from the mean field prediction (right).

where $\langle Q^2 \rangle_{\gamma_{\text{np}}}$ is the variance at $\gamma = \gamma_{\text{np}}$, and the denominator depends only on the difference of their slopes at $\gamma = \gamma_{\text{np}}$. We determine all these quantities by finding the intersection point of the curves of Q_t^2 and Q_s^2, which are constructed using multi-histogram reweighting (Fig. 2).

We determine γ_{np} for several aspect ratios, $\frac{N_t}{N_s} = \xi \in \{2,3,4,5,6\}$, and for different spatial sizes, in $U(3)$ and $SU(3)$ QCD. In the thermodynamic limit, the functional dependence $\xi(\gamma)$ appears to be quadratic for large γ (Fig. 3, left). Mean field arguments also predict a quadratic dependence in the large γ limit: $\xi(\gamma) = \gamma^2$ [7], but the non-perturbative prefactor differs from the mean-field one by $\approx 25\%$ (Fig. 3, right).

6. Energy density vs. temperature

Given the relation between the bare and renormalized anisotropies, and the corresponding running (Fig. 3), the remaining ingredient for an accurate determination of the energy density (4.1a) in $U(3)$ QCD is a precise measurement of the density of timelike dimers, n_{Dt}.

In order to determine the dependence of the energy density ε on the temperature T, we first need to accurately subtract from it the $T = 0$ contribution, ε_0. We compute ε_0 by taking the thermodynamic limit of the density of timelike dimers evaluated on a hypercubic lattice:

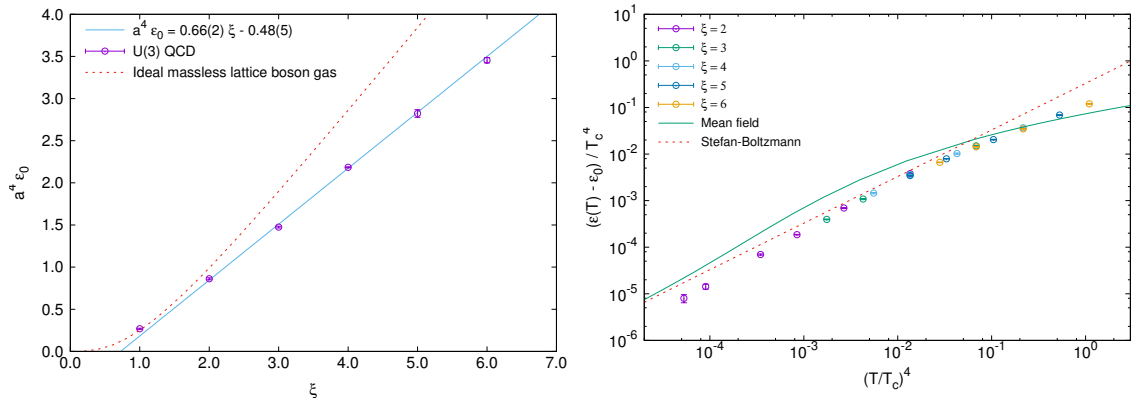

Figure 4: Scaling of the energy density with the physical anisotropy, at $T = 0$ (left), and the subtracted energy density $(\varepsilon(T) - \varepsilon_0)$ as a function of the temperature (right), both for $U(3)$ QCD. There are significant deviations to the equation of state of an ideal pion gas, for low temperatures and for temperatures near T_c. Note that the lowest temperature reached is $O(15\text{ MeV})$.

$$a^4\varepsilon_0(\xi) = \lim_{N_s\to\infty} \frac{\xi^2}{\gamma}\frac{d\gamma}{d\xi}\langle 2n_{Dt}\rangle\Big|_{N_t=\xi N_s} \tag{6.1}$$

We observe that ε_0 scales approximately linearly with ξ, for large ξ (Fig. 4, left), similarly to an ideal gas of massless scalar bosons on the lattice [1], but with a different non-universal prefactor.

At finite temperature, we compute the energy density $a^4\Delta\varepsilon(N_s, N_t, \xi)$, with the ε_0 contribution subtracted, on $N_s^3 \times N_t$ lattices, for fixed $aT = \frac{\xi}{N_t}$, and for several spatial sizes. We then take the thermodynamic limit of $a^4\Delta\varepsilon$, assuming $O(N_s^{-3})$ corrections.[1] We express both energy density and temperature in units of the critical temperature of the chiral phase transition, which for $U(3)$ is $aT_c = 1.466$ and for $SU(3)$ is $aT_c = 1.089$.[2]

The dependence of the energy density on the temperature, in $U(3)$ QCD, is given in Fig. 4 (right). The data points seem to fall on an universal curve, which deviates from SB (dotted line) at temperatures near T_c, and also at low temperatures. It is qualitatively consistent with the (analytical) mean field prediction in the large N limit (solid line).[3]

The surprising deviation from SB at low temperatures may be due to finite size effects: the data points at the lowest temperatures require large N_t, but are computed for possibly not large enough values of N_s. Simulations with larger spatial volumes are required for a better control of the thermodynamical limit. On the other hand, the deviation from SB at high temperatures may be due to an UV cutoff effect, and simulations with larger values of ξ are required in order to increase N_t, at fixed temperature. At intermediate values of the temperature, the energy density is the closest to SB, with a small discrepancy which may be due to a finite-ξ effect: SB scaling is only expected to be exact in the $\xi \to \infty$ (continuous time) limit.

[1] Inspired by the lessons of the ideal gas of massless scalar bosons on the lattice (Section 2), we take the thermodynamic limit, $N_s \to \infty$, by only using lattices for which $N_s \geq 2N_t$, in order to minimize the finite-size corrections.

[2] In the literature, the values of the critical temperature, namely $aT_c = 1.8843(1)$ for $U(3)$ [5] and $aT_c = 1.402(2)$ for $SU(3)$ [8], are determined assuming the mean field relation between the bare and renormalized anisotropy couplings, i.e. $aT_c = \gamma^2 a_t T_c$. Using our non-perturbative method for setting the anisotropy scale, the corresponding values for the $U(3)$ and $SU(3)$ critical temperatures, $aT_c = \xi(\gamma)a_t T_c$, deviate from those in the literature by $\approx 25\%$.

[3] In this mean field approach, the critical temperature is not easy to fix. For comparison with the $U(3)$ and $SU(3)$ data, we set the critical temperature to the $U(3)$ mean field value: $aT_c = 5/2$ [7].

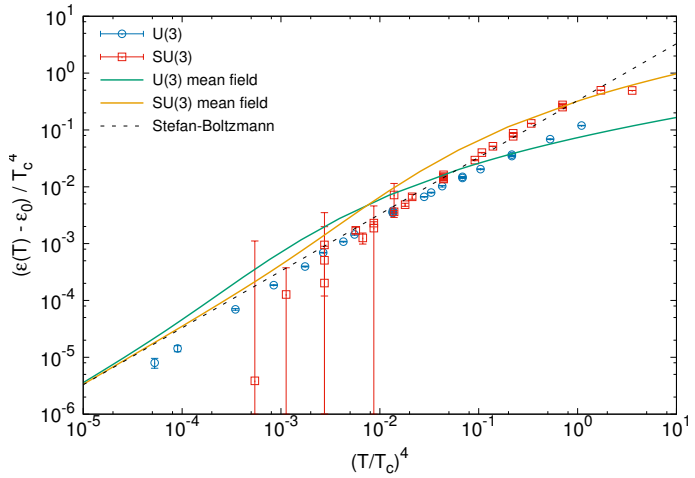

Figure 5: Comparison of the energy densities in $U(3)$ QCD (blue) and $SU(3)$ QCD (red), as a function of the temperature, in units of the critical temperatures of the respective chiral phase transitions. The large error bars in $SU(3)$ QCD, at low temperatures, are due to large fluctuations in the baryonic sign. The mean field curves are computed analytically in the large N limit, and we set $aT_{c,U(3)} = 5/2$ and $aT_{c,SU(3)} = 5/3$ [7].

Using the same approach, we have also computed the energy density as a function of the temperature in $SU(3)$ lattice QCD. A comparison between the $U(3)$ and $SU(3)$ theories is shown in Fig. 5. The difference between the two cases is the additional contribution of baryon loops to the $SU(3)$ theory, which also introduces a sign problem, thus increasing the statistical error, especially for the large volumes required at low temperatures.

At high temperatures, up to T_c, the $SU(3)$ energy density is consistent with SB, and consistently higher than that for $U(3)$, which we understand as being due to the thermal excitation of the extra baryonic modes, which contribute to the total pressure (and energy density).

In conclusion, the ideal pion gas is a reasonably good approximation for the low T regime of $U(3)$ and $SU(3)$ lattice QCD. Deviations from it, associated with pion interactions and with the thermal excitation of massive hadrons, can be quantified and deserve further study. The study of the equation of state can also be extended to the cases of non-zero quark mass and of non-zero chemical potential.

References

[1] J. Engels, F. Karsch, H. Satz, Nucl. Phys. B **205** (1982) 239.

[2] P. Rossi, U. Wolff, *Nucl. Phys.* **B248** (1984) 105; F. Karsch, K. Mutter, *Nucl. Phys.* **B313** (1989) 541.

[3] D. H. Adams, S. Chandrasekharan, *Nucl.Phys.* **B662** (2003) 220. [hep-lat/0303003].

[4] P. de Forcrand, M. Fromm, Phys. Rev. Lett. **104** (2010) 112005. [arXiv:0907.1915].

[5] W. Unger, P. de Forcrand, PoS LATTICE **2011** (2011) 218. [arXiv:1111.1434].

[6] S. Chandrasekharan, F.-J. Jiang, *Phys.Rev.* **D74** (2006) 014506.

[7] N. Bilic, F. Karsch, K. Redlich, *Phys. Rev.* **D45** (1992) 3228.

[8] P. de Forcrand, J. Langelage, O. Philipsen, W. Unger, *Phys. Rev. Lett.* **113** (2014) 15, 152002. [arXiv:1406.4397].

A.4 Strong-coupling lattice QCD on anisotropic lattice [A4]

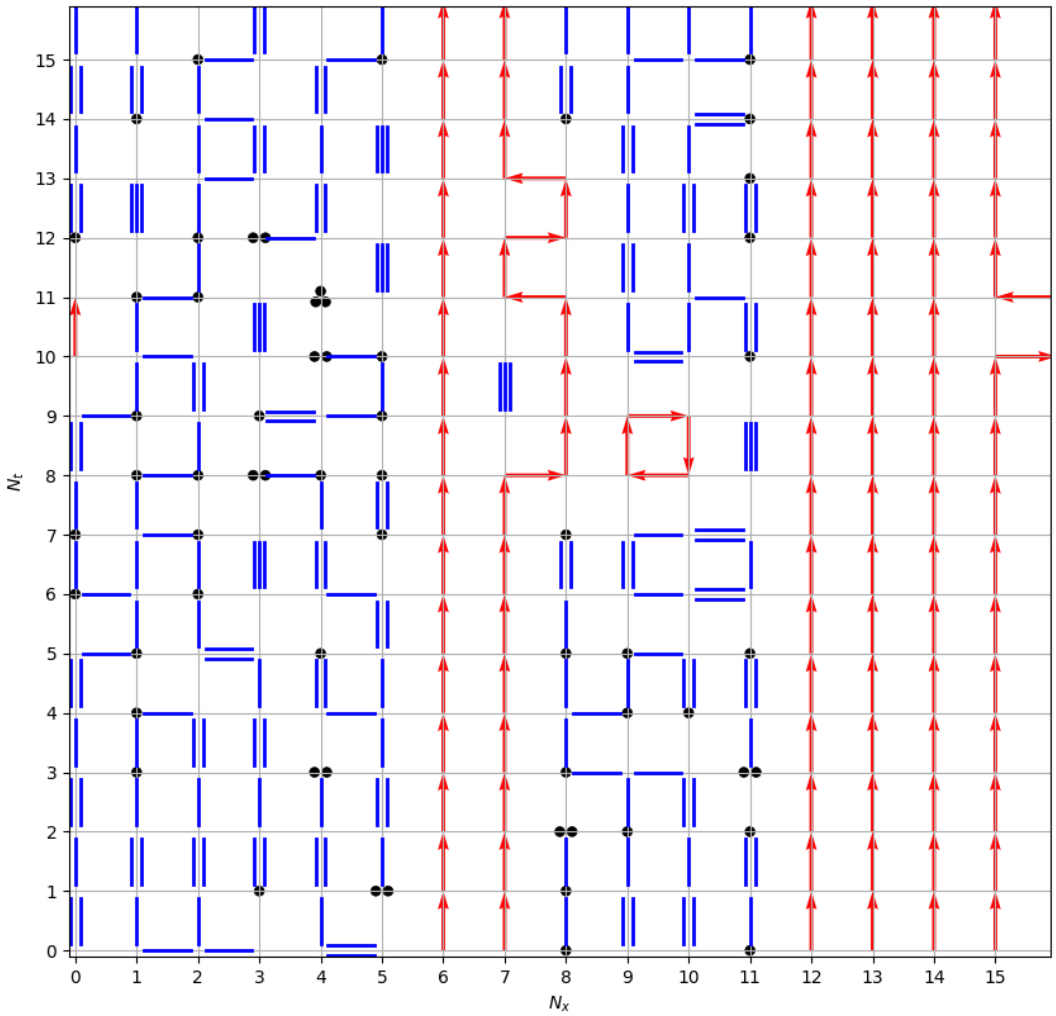

Strong-coupling lattice QCD on anisotropic lattices

Philippe de Forcrand,[1,2,*] Wolfgang Unger,[3,†] and Hélvio Vairinhos[‡]
[1]Institut für Theoretische Physik, ETH Zürich, CH-8093 Zürich, Switzerland
[2]CERN, TH Department, CH-1211 Geneva 23, Switzerland
[3]Fakultät für Physik, Universität Bielefeld, Universitätstrasse 25, D33619 Bielefeld, Germany

(Received 9 November 2017; published 28 February 2018)

Anisotropic lattice spacings are mandatory to reach the high temperatures where chiral symmetry is restored in the strong-coupling limit of lattice QCD. Here, we propose a simple criterion for the nonperturbative renormalization of the anisotropy coupling in strongly coupled $\mathrm{SU}(N_c)$ or $\mathrm{U}(N_c)$ lattice QCD with massless staggered fermions. We then compute the renormalized anisotropy, and the strong-coupling analogue of Karsch's coefficients (the running anisotropy), for $N_c = 3$. We achieve high precision by combining diagrammatic Monte Carlo and multihistogram reweighting techniques. We observe that the mean field prediction in the continuous time limit captures the nonperturbative scaling, but receives a large, previously neglected correction on the unit prefactor. Using our nonperturbative prescription in place of the mean field result, we observe large corrections of the same magnitude to the continuous time limit of the static baryon mass and of the location of the phase boundary associated with chiral symmetry restoration. In particular, the phase boundary, evaluated on different finite lattices, has a dramatically smaller dependence on the lattice time extent. We also estimate, as a byproduct, the pion decay constant and the chiral condensate of massless SU(3) QCD in the strong-coupling limit at zero temperature.

DOI: 10.1103/PhysRevD.97.034512

I. INTRODUCTION

For all practical purposes, the sign problem in lattice QCD with staggered fermions at finite density has been solved at strong coupling. By integrating out the gauge degrees of freedom exactly—which allows replacing Grassmann integration by a sum over fermionic color singlets—the sign problem becomes mild enough to allow for controlled numerical results at moderate volumes, by combining importance sampling and reweighting methods. As a result, the phase diagram of lattice QCD in the strong-coupling limit [1] and at first order in the strong-coupling expansion [2] can be completely mapped.

In practice, however, it is not sufficient to simulate the strongly coupled theory directly on rectangular lattices because the critical temperature of chiral symmetry restoration is higher than what can be reached using the smallest lattice time extent.[1] In order to study the thermodynamical properties of staggered lattice QCD, in particular across the chiral phase transition, it is therefore necessary to simulate the theory on anisotropic lattices.

On anisotropic lattices, one assigns independent lattice spacings to the spatial and temporal directions, respectively, a and a_t. The corresponding physical extents of the lattice can then be varied continuously and independently. A more useful parametrization of the lattice geometry uses the spatial lattice spacing, a, and the anisotropy parameter ξ,

$$\xi = \frac{a}{a_t}, \tag{1}$$

which becomes unity when the lattice is isotropic and diverges in the continuous time limit $a_t \to 0$. In this parametrization, the lattice temperature is given by

$$aT = \frac{\xi}{N_t}, \tag{2}$$

where N_t is the lattice time extent. Hence, the lattice temperature can be varied continuously, through ξ.

*forcrand@phys.ethz.ch
†wunger@physik.uni-bielefeld.de
‡helvio.vairinhos@gmail.com

[1]With staggered fermions, the spacetime lattice is necessarily bipartite. In particular, on a rectangular lattice it has an even number of lattice points in each direction. In this case, the lattice time extent is $N_t \geq 2$, hence the lattice temperature is $aT = \frac{1}{N_t} \leq 0.5 < aT_c$.

In lattice gauge theory, the physical parameters a and ξ can only be varied implicitly, through independent bare parameters: the bare gauge coupling β and the bare anisotropy coupling γ. These bare parameters couple differently to the spatial and temporal plaquettes in the Wilson action of $\mathrm{SU}(N_c)$ or $\mathrm{U}(N_c)$ pure lattice gauge theory in $d+1$ dimensions [3]:

$$S_g = \frac{\beta}{\gamma}\sum_x \sum_{1\le i<j\le d}\left(1-\frac{1}{N_c}\mathrm{ReTr}(U_{x,ij})\right) + \beta\gamma\sum_x\sum_{i=1}^{d}\left(1-\frac{1}{N_c}\mathrm{ReTr}(U_{x,i0})\right), \tag{3}$$

where $U_{x,\mu\nu}$ is the ordered product of link variables around a plaquette parallel to the $\hat{\mu}$ and $\hat{\nu}$ directions.

For a single flavor of staggered fermions in the strong-coupling limit ($\beta = 0$), the anisotropic lattice action is given by

$$S_f = 2a_t m_q \sum_x \bar{\psi}_x\psi_x + \sum_x\sum_{\mu=0}^{d}\gamma^{\delta_{\mu 0}}\eta_{x\mu}\left(e^{a_t\mu_q\delta_{\mu 0}}\bar{\psi}_x U_{x\mu}\psi_{x+\hat{\mu}} - e^{-a_t\mu_q\delta_{\mu 0}}\bar{\psi}_{x+\hat{\mu}}U^{\dagger}_{x\mu}\psi_x\right), \tag{4}$$

where $a_t m_q$ and $a_t\mu_q$ are the bare quark mass and quark chemical potential, respectively, and $\eta_{x\mu} = \pm 1$ are the staggered phases. In the case of $\mathrm{U}(N_c)$, gauge invariance dictates that color singlets are independent of $a_t\mu_q$, hence we may set $a_t\mu_q$ to zero without loss of generality.

How a and ξ depend on the bare parameters of the theory is unknown *a priori*. This knowledge is, however, essential for precision measurements on anisotropic lattices, e.g. bulk thermodynamic quantities, and any uncontrolled approximation can easily be the main source of systematic errors.

In the weak gauge coupling regime ($\beta \to \infty$) of the $\mathrm{SU}(N_c)$ pure gauge theory Eq. (3), perturbation theory and the nonrenormalization of the speed of light can be used to calibrate the anisotropy coupling [4]. In that regime, it is found that $\xi_{\mathrm{pert}}(\gamma) = \gamma$ (as expected classically).

Using mean field techniques, the behavior of the renormalized anisotropy at strong coupling ($\beta \ll 1$) and at large values of γ is predicted to be quadratic, with unit prefactor [5]:

$$\xi_{\mathrm{mf}}(\gamma) = \gamma^2. \tag{5}$$

In the nonperturbative regime, however, the relation between bare and renormalized anisotropy couplings can only be determined numerically. This has been done, for example, in pure gauge theory [3,6], in lattice QCD with staggered fermions [7] or Wilson fermions [8]. The nonperturbative renormalization of the bare parameters requires fine-tuning, guided by some physical criterion which controls the recovery of Euclidean symmetry.

In this Letter we present a simple, precise, and nonperturbative method to calibrate the anisotropy coupling in lattice QCD with massless staggered fermions, in the limit of strong gauge coupling.

II. DIAGRAMMATIC REPRESENTATION OF LATTICE QCD

The partition function of $\mathrm{SU}(N_c)$ or $\mathrm{U}(N_c)$ QCD on a bipartite $N_t \times N_s^d$ lattice, with a single flavor of staggered fermions, in the strong-coupling limit ($\beta \to 0$) factorizes into a product of solvable fermionic one-link integrals:

$$Z = \int \mathcal{D}\psi\mathcal{D}\bar{\psi}\exp\left(2a_t m_q\sum_x\bar{\psi}_x\psi_x\right) \times \prod_{x,\mu}\int dU_{x\mu}\exp(\gamma^{\delta_{\mu 0}}\eta_{x\mu}(e^{a_t\mu_q\delta_{\mu 0}}\bar{\psi}_x U_{x\mu}\psi_{x+\hat{\mu}} - e^{-a_t\mu_q\delta_{\mu 0}}\bar{\psi}_{x+\hat{\mu}}U^{\dagger}_{x\mu}\psi_x)). \tag{6}$$

In the $\mathrm{SU}(N_c)$ case, the group integration of the link variables, followed by the Grassmann integration of the fermionic degrees of freedom, yields the partition function of a monomer-dimer-loop system [9]:

$$Z = \sum_{\{n,k,\ell\}}\prod_x\frac{N_c!}{n_x!}\prod_{x,\mu}\frac{(N_c-k_{x\mu})!}{N_c!k_{x\mu}!}\frac{\sigma(\ell)}{N_c!^{|\ell|}}(2a_t m_q)^{N_M} \times \gamma^{2N_{Dt}+N_c N_{\ell t}}e^{N_c N_t a_t\mu_q w(\ell)}. \tag{7}$$

This partition function is a constrained sum over integer occupation numbers of monomers and dimers, $n_x,\ k_{x\mu} \in \{0,1,\ldots,N_c\}$, and of oriented baryon links, $\ell_{x\mu} \in \{0,\pm 1\}$, which combine to form oriented baryon loops. The global quantities,

$$N_M = \sum_x n_x, \tag{8a}$$

$$N_{Dt} = \sum_x k_{x0}, \tag{8b}$$

$$N_{\ell t} = \sum_x |\ell_{x0}|, \tag{8c}$$

enumerate the monomers, temporal dimers, and temporal baryon links on the lattice, respectively. $\sigma(\ell) = \pm 1$ is a geometric sign associated with the configuration of baryon loops ℓ; $|\ell|$ is their length, and $w(\ell)$ is their winding number around the Euclidean time direction.

The monomers represent fermion condensates, $M_x^{n_x}$, dimers represent meson hoppings, $(M_x M_{x+\hat{\mu}})^{k_{x\mu}}$, and baryon links represent baryon hoppings, $\bar{B}_x B_{x+\hat{\mu}}$ or $\bar{B}_{x+\hat{\mu}}B_x$, where M_x is a meson and B_x is a baryon:

$$M_x = \bar{\psi}_x \psi_x, \tag{9a}$$

$$B_x = \frac{1}{N_c!} \varepsilon_{i_1 \ldots i_{N_c}} \psi_x^{i_1} \ldots \psi_x^{i_{N_c}}. \tag{9b}$$

In order for a configuration of occupation numbers to contribute nontrivially to the partition function Eq. (7), the Grassmann integrals over the corresponding fermionic degrees of freedom must be nontrivial on each lattice site.

Due to their Grassmann nature, such configurations must necessarily represent arrangements of exactly N_c fermions and N_c antifermions on each lattice site.[2] This imposes the following local constraints on the integer occupation numbers:

$$n_x + \sum_{\pm\mu} \left(k_{x\mu} + \frac{N_c}{2} |\ell_{x\mu}| \right) \stackrel{!}{=} N_c, \tag{10a}$$

$$\sum_{\pm\mu} \ell_{x\mu} \stackrel{!}{=} 0. \tag{10b}$$

Equation (10b) is a local discrete conservation law for baryon links, which formalizes our statement above that baryon links in admissible configurations form closed oriented loops.

In the $\mathrm{U}(N_c)$ case, since $\ell_{x\mu} = 0$, the partition function Eq. (7) reduces to a sum over monomer-dimer configurations:

$$Z = \sum_{\{n,k\}} \prod_x \frac{N_c!}{n_x!} \prod_{x,\mu} \frac{(N_c - k_{x\mu})!}{N_c! k_{x\mu}!} (2a_t m_q)^{N_M} \gamma^{2N_{Dt}}, \tag{11}$$

with the same Grassmann constraint for monomers and dimers on each site:

$$n_x + \sum_{\pm\mu} k_{x\mu} \stackrel{!}{=} N_c. \tag{12}$$

Likewise, the $\mathrm{U}(N_c)$ observables are defined in the same way as the observables (in the mesonic sector) of the $\mathrm{SU}(N_c)$ theory.

III. CONSERVED CURRENTS AND CONSERVED CHARGES

Let $\sigma_x = \pm 1$ be the parity of the site x on a bipartite lattice. From Eq. (10b), it is easy to construct baryonic currents:

$$j^B_{x\mu} = \sigma_x \ell_{x\mu}, \tag{13}$$

which are conserved at every site:

$$\sum_{\mu=0}^{d} (j^B_{x\mu} - j^B_{x-\hat{\mu},\mu}) = 0. \tag{14}$$

The corresponding conserved charges are integrals of the baryonic currents Eq. (13) over a codimension-1 lattice slice $\mathcal{S}_\mu$, perpendicular to $\hat{\mu}$:

$$Q^B_\mu = \sum_{x \in \mathcal{S}_\mu} j^B_{x\mu}. \tag{15}$$

Similarly, by rewriting Eq. (10a) as

$$\sum_{\pm\mu} \left(k_{x\mu} + \frac{N_c}{2} |\ell_{x\mu}| - \frac{N_c}{2d} \right) = -n_x, \tag{16}$$

it is easy to construct the corresponding (pion) currents:

$$j_{x\mu} = \sigma_x \left(k_{x\mu} + \frac{N_c}{2} |\ell_{x\mu}| - \frac{N_c}{2d} \right), \tag{17}$$

from which a local discrete Gauss' law for dimers results:

$$\sum_{\mu=0}^{d} (j_{x\mu} - j_{x-\hat{\mu},\mu}) = -\sigma_x n_x. \tag{18}$$

Thus, monomers are sources of the pion currents. Using Grassmann variables, the source term on the right-hand side of Eq. (18) corresponds to $-a_t m_q \bar{\psi}_x \gamma_5 \psi_x$. Only in the chiral limit, i.e. in the absence of monomers, are the pion currents conserved. In the chiral limit, the corresponding conserved charges are integrals of the pion currents over a lattice slice $\mathcal{S}_\mu$:

$$Q_\mu = \sum_{x \in \mathcal{S}_\mu} j_{x\mu}. \tag{19}$$

In the $\mathrm{U}(N_c)$ theory, since $\ell_{x\mu} = 0$, the pion currents simplify to

$$j_{x\mu} = \sigma_x \left(k_{x\mu} - \frac{N_c}{2d} \right). \tag{20}$$

IV. NONPERTURBATIVE ANISOTROPY CALIBRATION

In this section, we show how the conserved pion charges can be used to calibrate the anisotropy coupling in lattice QCD with staggered fermions, at zero temperature, in the strong-coupling limit.

In the strong-coupling limit, the partition functions of $\mathrm{SU}(N_c)$ and $\mathrm{U}(N_c)$ lattice QCD with staggered fermions have monomer-dimer-loop representations, Eqs. (7) and (11), with no dependence on the spatial lattice spacing, a. In order for the pion charges Q_μ to be conserved, we take the lattice fermions to be massless, $a_t m_q = 0$. In the

[2] If the gauge group is $\mathrm{SU}(N_c)$, the ordering of the Grassmann variables in such arrangements contributes with the geometric sign $\sigma(\ell) = \pm 1$, which introduces a (baryonic) sign problem in the system. See Eq. (7).

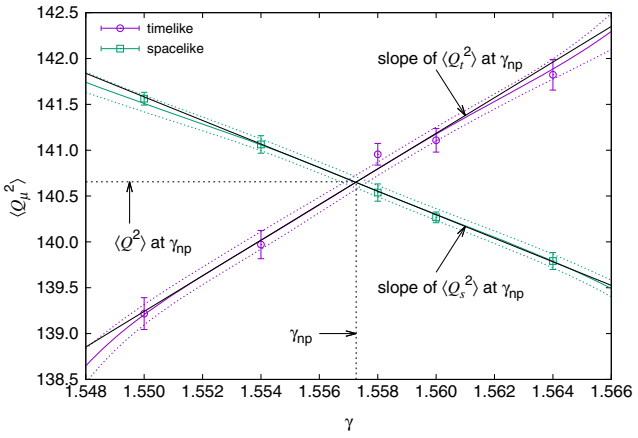

FIG. 1. Measurements of the fluctuations of the conserved pion charges in a numerical simulation of U(3) lattice QCD on a 32×16^3 lattice. The measurements are interpolated using Ferrenberg-Swendsen multihistogram reweighting. The intersection of the two curves provides a precise nonperturbative estimate of the bare parameter $\gamma_{\rm np}$ associated with the renormalized anisotropy: $\xi = 2$. It also provides an estimate of the value of such fluctuations in the hypercubic lattice, $\langle Q^2\rangle$, which, together with the estimates of the slopes of the tangents to the curves at the intersection point, allows an estimation of the running anisotropy, $\frac{1}{\xi}\frac{d\xi}{d\gamma}$.

$\mathrm{SU}(N_c)$ case, we only consider the case of zero chemical potential, $a_t\mu_q = 0$.[3] The corresponding partition functions thus depend only on a single parameter: the bare anisotropy coupling γ.

Let us consider the theories to be defined on anisotropic $N_t \times N_s^d$ lattices. In order to calibrate the anisotropy, we compare the fluctuations of the conserved pion charges in different directions.

Due to spatial isotropy, the expectation values of fluctuations of the spatial pion charges Q_i, $i = 1, \ldots, d$ must coincide. Therefore, it is convenient to quantify spatial fluctuations using the expectation value of

$$Q_s^2 = \frac{1}{d}\sum_{i=1}^{d} Q_i^2, \tag{21}$$

while the temporal fluctuations are quantified using the expectation value of $Q_t^2 = Q_0^2$.

Now, when the lattice is hypercubic, i.e. $N_t = \xi N_s$, the fluctuations of the spatial and temporal conserved charges must be equal. This provides a simple, nonperturbative criterion for the renormalization of the anisotropy coupling: the value of the bare parameter, $\gamma_{\rm np}$, corresponding to the renormalized value, $\xi(\gamma_{\rm np}) = N_t/N_s$, is that for which the fluctuations of the spatial and temporal conserved charges are equal:

$$\langle Q_t^2\rangle_{\gamma_{\rm np}} \stackrel{!}{=} \langle Q_s^2\rangle_{\gamma_{\rm np}}. \tag{22}$$

In Fig. 1, we give a practical example. In a numerical simulation of U(3) lattice QCD on a 32×16^3 lattice, we evaluate $\langle Q_s^2\rangle$ and $\langle Q_t^2\rangle$ for a few values of the bare parameter γ, about the correct nonperturbative value $\gamma_{\rm np}$ associated with the renormalized anisotropy parameter, $\xi = 2$. Using Ferrenberg-Swendsen multihistogram reweighting, we interpolate the measurements of the fluctuations and estimate with high precision the value of the bare parameter for which the two curves intersect, i.e. when the lattice is hypercubic. In this particular case, $\gamma_{\rm np} = 1.55725(29)$. This value is to be compared with the commonly accepted mean field prediction, $\gamma_{\rm mf} = \sqrt{\xi = 2} \approx 1.41421$.

V. RUNNING ANISOTROPY

It is also possible to estimate the running of the anisotropy parameter, $\frac{1}{\xi}\frac{d\xi}{d\gamma}$, using extra information from the intersection point in Fig. 1. This quantity—the strong-coupling analogue of Karsch's coefficients [4]—is important for computing e.g. bulk thermodynamic quantities, like the energy density and pressure [10].

The fluctuations of the conserved charges scale with the volume of the lattice slices on which the corresponding conserved currents are integrated over

$$\langle Q_t^2\rangle \propto (N_s a)^3, \tag{23a}$$

$$\langle Q_s^2\rangle \propto (N_s a)^2 N_t a_t. \tag{23b}$$

The ratio of temporal and spatial fluctuations then becomes directly related to the renormalized anisotropy:

$$\frac{\langle Q_t^2\rangle}{\langle Q_s^2\rangle} = \frac{N_s}{N_t}\xi. \tag{24}$$

We have already explained the fact that this ratio is 1 when the lattice is hypercubic.

Now, taking the derivative of Eq. (24) with respect to the bare parameter γ, at the intersection of the curves in Fig. 1, yields the value of the running anisotropy at that point:

$$\left.\frac{d}{d\gamma}\frac{\langle Q_t^2\rangle}{\langle Q_s^2\rangle}\right|_{\gamma_{\rm np}} = \frac{\langle Q_t^2\rangle'_{\gamma_{\rm np}} - \langle Q_s^2\rangle'_{\gamma_{\rm np}}}{\langle Q^2\rangle_{\gamma_{\rm np}}} = \left.\frac{N_s}{N_t}\frac{d\xi}{d\gamma}\right|_{\gamma_{\rm np}} = \left.\frac{1}{\xi}\frac{d\xi}{d\gamma}\right|_{\gamma_{\rm np}}. \tag{25}$$

[3]The chemical potential only modifies the temporal boundary conditions, which is irrelevant at $T = 0$. A nonzero quark mass, on the other hand, modifies the dynamics, and so the renormalization prescription must take this into account (we discuss the massive case in the Conclusion).

Therefore, in order to estimate the value of the running anisotropy at $\gamma_{\rm np}$, we also need the value of the fluctuation of the conserved pion charges on a hypercubic lattice:

$$\langle Q^2\rangle_{\gamma_{\rm np}} \equiv \langle Q_t^2\rangle_{\gamma_{\rm np}} \stackrel{!}{=} \langle Q_s^2\rangle_{\gamma_{\rm np}}, \tag{26}$$

and the values of the slopes of the tangents to the curves at the intersection point: $\langle Q_t^2\rangle'_{\gamma_{\rm np}}$ and $\langle Q_s^2\rangle'_{\gamma_{\rm np}}$.

VI. NUMERICAL RENORMALIZATION

The Monte Carlo sampling of the $\mathrm{U}(N_c)$ partition function Eq. (11) is highly efficient when using directed path algorithms [11]. In the $\mathrm{SU}(N_c)$ case, observables must be reweighted because of the occurrence of negative-weight baryonic configurations, even at zero chemical potential. However, this sign problem is mild and controllable for moderate lattice volumes [1,2,10].

We simulate massless U(3) and SU(3) lattice QCD in the strong-coupling limit, using the directed path algorithm [11], for several values of the renormalized anisotropy ξ. For each ξ, we estimate the corresponding value of the bare parameter $\gamma_{\rm np}$ on a $(\xi N_s)\times N_s^3$ lattice, for several values of N_s, using the method described in Sec. IV. We also measure the running of the anisotropy coupling Eq. (25). The results for U(3) and SU(3) are summarized in Tables I and II, respectively.

In these tables, rather than storing the estimators of Eq. (25), we instead store the estimators of its reciprocal, the reason being that the latter enters linearly in the definition of important bulk thermodynamic quantities, e.g. the energy density:

$$a^4\varepsilon = \frac{a^4}{V}\frac{\partial \log Z}{\partial T^{-1}} = \frac{\xi}{\gamma}\frac{d\gamma}{d\xi}\frac{2\xi\langle N_{Dt}\rangle}{N_s}. \tag{27}$$

The nonperturbative relation between the renormalised and bare anisotropy parameters, in the thermodynamic limit, is presented in Fig. 2(a). At large anisotropies, the renormalized parameter depends quadratically on the bare parameter. Such a behavior is expected from mean field arguments. However, the corresponding prefactor differs significantly (≈25%) from that of the mean field relation Eq. (5). This introduces a significant systematic error in any numerical study of strongly coupled lattice QCD.

We find that the whole range of measurements is well described by a simple, one-parameter rational Ansatz (see Fig. 2(b)):

$$\frac{\xi(\gamma)}{\gamma^2} \approx \kappa + \frac{1}{1+\lambda\gamma^4}, \tag{28}$$

where κ is a constant, and $\lambda \stackrel{!}{=} \kappa/(1-\kappa)$, from the requirement that $\xi(1)\stackrel{!}{=}1$. The approach to the continuous time limit is better captured by Taylor expanding Eq. (28) to quadratic order in $1/\xi^2$ (see Fig. 2(c)):

TABLE I. Values of the bare anisotropy coupling $\gamma_{\rm np}$ associated with the renormalized anisotropy ξ, from numerical simulations of massless U(3) lattice QCD on $(\xi N_s)\times N_s^3$ lattices. Corresponding values of the running anisotropy (derivative), the helicity modulus $a^2\Upsilon$, and the chiral susceptibility density $a^6\chi/N_s^4$. The quantity $\gamma_{\rm np}$ exhibits small finite-volume corrections and is consistent (within errors) with its thermodynamic limit, even on the smallest lattices. This rapid convergence justifies using small lattice measurements as thermodynamic estimators for $\gamma_{\rm np}$. This is particularly useful in simulations at large ξ, for which significant statistics can only be obtained on small volumes.

ξ	N_s	$\gamma_{\rm np}$	$\left.\frac{\xi}{\gamma}\frac{d\gamma}{d\xi}\right\vert_{\gamma_{\rm np}}$	$a^2\Upsilon$	$a^6\chi/N_s^4$
1/2	8	0.5741(2)	0.435(9)	0.27470(7)	0.283789(5)
	12	0.5745(2)	0.453(8)	0.27491(2)	0.282628(8)
	16	0.5743(2)	0.43(1)	0.274795(8)	0.282207(4)
	20	0.5743(4)	0.44(2)	0.27479(2)	0.282092(3)
	24	0.5744(5)	0.44(3)	0.27469(2)	0.282157(7)
1	4	1.00000(5)	0.357(2)	0.433247(7)	0.489464(1)
	6	1.0001(5)	0.39(2)	0.43388(2)	0.485824(9)
	8	0.9998(5)	0.34(2)	0.43408(2)	0.484272(6)
	10	1.0000(5)	0.36(3)	0.43418(2)	0.483406(5)
2	4	1.55745(7)	0.284(2)	0.548979(9)	0.683806(2)
	6	1.5570(4)	0.28(2)	0.54933(2)	0.67935(1)
	8	1.557(1)	0.37(5)	0.54945(3)	0.67775(2)
	10	1.5565(9)	0.27(3)	0.54889(3)	0.67696(2)
	12	1.5566(8)	0.26(3)	0.54914(4)	0.67636(2)
3	4	1.9446(1)	0.261(4)	0.582224(1)	0.761084(2)
	6	1.9431(8)	0.31(2)	0.58265(3)	0.75674(2)
	8	1.9445(7)	0.23(3)	0.58247(3)	0.75382(2)
	10	1.9442(9)	0.25(2)	0.58206(4)	0.75309(2)
4	4	2.2573(1)	0.254(2)	0.594889(1)	0.798407(2)
	6	2.2566(3)	0.257(6)	0.595057(7)	0.793426(6)
	8	2.2568(4)	0.274(6)	0.59514(2)	0.791196(4)
	10	2.2566(6)	0.268(8)	0.59497(2)	0.79023(1)
5	4	2.5273(2)	0.248(3)	0.600789(6)	0.819251(2)
	6	2.5267(3)	0.264(6)	0.600829(7)	0.814061(4)
	8	2.5266(5)	0.26(2)	0.60085(2)	0.81195(1)
	10	2.531(3)	0.5(3)	0.6011(2)	0.80865(7)
6	4	2.7692(2)	0.247(2)	0.603881(5)	0.832205(3)
	6	2.7682(3)	0.27(2)	0.604074(7)	0.827064(5)
	8	2.7683(6)	0.23(2)	0.60390(2)	0.824761(9)
	10	2.7683(8)	0.31(2)	0.60388(2)	0.82384(1)
8	4	3.1954(2)	0.255(4)	0.606741(4)	0.847192(2)
	6	3.1943(5)	0.238(4)	0.60697(2)	0.841938(4)
	8	3.1946(7)	0.25(2)	0.60665(2)	0.83959(2)
	10	3.194(2)	0.21(3)	0.60687(4)	0.83889(1)

$$\frac{\xi(\gamma)}{\gamma^2} \approx \kappa\left(1+\frac{c_1}{\xi^2}+\frac{c_2}{\xi^4}\right). \tag{29}$$

The fitted values of κ using the Ansatz Eq. (29), consistent with those obtained using the Ansatz Eq. (28), are

$$\kappa = \begin{cases} 0.7795(4), & \mathrm{U}(3) \\ 0.7810(8), & \mathrm{SU}(3), \end{cases} \tag{30}$$

where errors are statistical only. This prefactor is significantly different from the mean field value 1.

Values for U(3) and SU(3) are statistically consistent with each other. This is to be expected: in the continuous

TABLE II. Values of the bare anisotropy coupling $\gamma_{\rm np}$ associated with the renormalized anisotropy ξ, from numerical simulations of massless SU(3) lattice QCD on $(\xi N_s) \times N_s^3$ lattices. Corresponding values of the running anisotropy (derivative), the helicity modulus $a^2\Upsilon$, the chiral susceptibility density $a^6\chi/N_s^4$, and the average baryonic sign. The quantity $\gamma_{\rm np}$ exhibits small finite-volume corrections and is consistent (within errors) with its thermodynamic limit, even on the smallest lattices. This rapid convergence justifies using small lattice measurements as thermodynamic estimators for $\gamma_{\rm np}$. This is particularly useful in simulations at large ξ, for which significant statistics can only be obtained on small volumes. In the continuous time limit, the baryons become increasingly static, which explains the lack of fluctuations that contribute to the sign problem at large ξ.

ξ	N_s	$\gamma_{\rm np}$	$\frac{\xi}{\gamma}\frac{d\gamma}{d\xi}\Big\vert_{\gamma_{\rm np}}$	$a^2\Upsilon$	$a^6\chi/N_s^4$	average sign
1/2	8	0.5743(2)	0.43(1)	0.27445(2)	0.283424(6)	0.99657(7)
	12	0.5745(2)	0.450(6)	0.274509(6)	0.282271(4)	0.9833(2)
	16	0.5744(2)	0.436(6)	0.274417(6)	0.281835(2)	0.9475(8)
	20	0.5744(4)	0.43(2)	0.274471(6)	0.281640(4)	0.818(4)
	24	0.5746(7)	0.44(3)	0.27459(2)	0.28152(2)	0.63(2)
2/3	6	0.7324(2)	0.405(6)	0.34033(2)	0.362517(3)	0.99863(2)
	12	0.7327(4)	0.38(1)	0.34040(2)	0.359782(8)	0.9777(4)
1	4	0.99993(5)	0.356(2)	0.432995(9)	0.489211(1)	0.991260(3)
	6	1.0000(3)	0.36(2)	0.43384(2)	0.485553(5)	0.99830(2)
	8	1.0002(3)	0.36(2)	0.43400(1)	0.483803(6)	0.99543(7)
	10	0.9999(3)	0.369(5)	0.433984(8)	0.483086(6)	0.9876(2)
3/2	4	1.3117(2)	0.309(5)	0.510010(1)	0.610195(3)	0.996258(6)
	8	1.3115(5)	0.30(2)	0.51024(2)	0.603968(9)	0.9933(2)
2	4	1.5573(2)	0.291(5)	0.548483(8)	0.683098(2)	0.998044(7)
	6	1.5571(4)	0.28(2)	0.54882(2)	0.678474(8)	0.99815(3)
	8	1.5568(6)	0.29(2)	0.54884(2)	0.676714(8)	0.99162(2)
	10	1.5569(5)	0.28(2)	0.54873(3)	0.67565(2)	0.97084(8)
	12	1.5572(6)	0.24(2)	0.54870(2)	0.67518(2)	0.942(3)
3	4	1.9449(2)	0.263(4)	0.581568(5)	0.760045(5)	0.999186(4)
	6	1.944(1)	0.31(6)	0.58200(3)	0.75514(2)	0.99787(8)
	8	1.944(2)	0.32(4)	0.58200(3)	0.75323(2)	0.9921(4)
	10	1.945(1)	0.26(2)	0.58170(4)	0.75143(3)	0.979(2)
4	4	2.2581(6)	0.262(8)	0.59431(2)	0.79686(2)	0.999682(4)
	6	2.2578(9)	0.27(2)	0.59455(3)	0.79164(2)	0.99885(5)
	8	2.258(1)	0.24(3)	0.59433(5)	0.78914(4)	0.9964(2)
	10	2.2569(6)	0.27(1)	0.59455(3)	0.78899(1)	0.9898(5)
5	4	2.5288(6)	0.25(3)	0.6002(2)	0.81777(2)	0.999770(9)
	6	2.527(1)	0.21(2)	0.60071(4)	0.81291(2)	0.99885(7)
	8	2.528(2)	0.23(3)	0.60024(6)	0.81009(4)	0.9983(2)
	10	2.5272(9)	0.25(4)	0.60022(4)	0.80927(3)	0.9870(7)
6	4	2.7702(2)	0.248(5)	0.60354(2)	0.830977(4)	0.999816(1)
	6	2.7693(4)	0.241(7)	0.603662(8)	0.825741(7)	0.99958(2)
	8	2.7685(8)	0.30(3)	0.60375(2)	0.82393(1)	0.99857(6)
	10	2.769(2)	0.3(1)	0.60362(4)	0.82234(5)	0.985(1)
8	4	3.1968(3)	0.257(5)	0.60656(2)	0.845910(3)	0.999891(1)
	6	3.1958(5)	0.275(8)	0.60671(2)	0.840645(7)	0.999808(6)
	8	3.196(1)	0.25(3)	0.60669(3)	0.83855(2)	0.99902(5)
	10	3.195(2)	0.22(3)	0.60539(7)	0.8370(1)	0.9935(7)

time limit, baryons become increasingly static, and their effect on pion currents vanishes at $T = 0$.

The Ansatz Eq. (28) is also consistent, after differentiation, with the Monte Carlo data for the running anisotropy. In particular, for the isotropic case, instead of the mean field value,

$$\frac{1}{\xi_{\rm mf}}\frac{d\xi_{\rm mf}}{d\gamma}\bigg|_{\gamma=1} = 2, \tag{31}$$

we find nonperturbative corrections consistent with

$$\frac{1}{\xi}\frac{d\xi}{d\gamma}\bigg|_{\gamma=1} \approx 2 + 4\kappa(\kappa - 1). \tag{32}$$

VII. APPLICATIONS

In this section, we use the nonperturbative relation between ξ and γ, determined above, in order to control the convergence of several physical quantities to their continuous time limits.

First, we examine the N_t dependence of the phase boundary of the (μ_q, T) phase diagram of massless SU(3) lattice QCD and its sensitivity to the anisotropy prescription. Then, we estimate the continuous time values of the static baryon mass am_B, the pion decay constant aF_π, and the infinite-volume chiral condensate $a^3\Sigma$, in massless U(3) or SU(3) lattice QCD. We use a quadratic Ansatz in $1/\xi^2$, consistent with $O(a^2)$ discretization errors of staggered fermions, to model the anisotropy corrections to the continuous time limit:

$$\mathcal{O} \approx \mathcal{O}^{\rm CT}\left(1 + \frac{c_1}{\xi^2} + \frac{c_2}{\xi^4}\right), \tag{33}$$

where $\mathcal{O}$ is one of the physical quantities listed above, and $\mathcal{O}^{\rm CT}$ is the corresponding continuous time value.

For the computation of the pion decay constant and of the chiral condensate, we use the fact that U(3) and SU(3) lattice QCD with massless staggered fermions have an exact $O(2)$ chiral symmetry. At $T = 0$ this symmetry is spontaneously broken, and the dynamics of the resulting Goldstone degrees of freedom (pions) are well described by an O(2) sigma model in $d = 4$ dimensions. From a finite-size scaling analysis of the discrete O(2) model, it is then possible to extract low-energy quantities like F_π and Σ.

For example, the pion decay constant at $T = 0$ can be shown to be related to the helicity modulus Υ [12]:

$$a^2F_\pi^2 = \lim_{N_s\to\infty} a^2\Upsilon, \tag{34}$$

which corresponds, in the diagrammatic representation, to the variance of the conserved pion charges Q_μ on a hypercubic lattice [13]:

$$a^2\Upsilon = \frac{1}{N_s^2}\langle Q^2\rangle_{\gamma_{\rm np}}. \tag{35}$$

In turn, the chiral condensate Σ at $T = 0$ can be estimated from the finite-size scaling of the chiral susceptibility χ, evaluated on hypercubic lattices. This has been done in $d = 3 + 1$ at finite temperature [13]. In our case where $T = 0$, chiral perturbation theory of the O(2) model predicts the leading finite-size corrections to be of the form [12]:

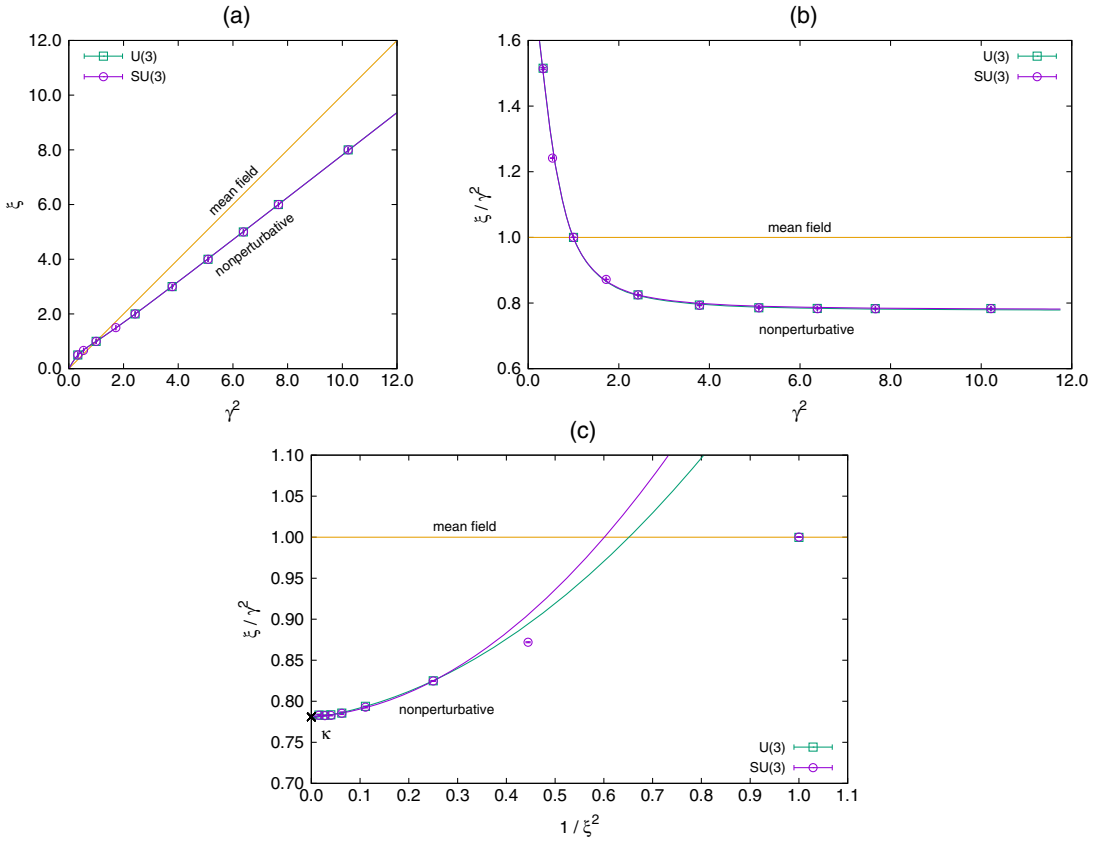

FIG. 2. Nonperturbative relation between the bare and renormalized anisotropy parameters, for U(3) (green) and SU(3) (purple) massless lattice QCD, in the thermodynamic limit, presented in 3 different ways. Figure 2(a) shows that, as predicted by mean field, the renormalized anisotropy at large γ is $\xi(\gamma) \propto \gamma^2$, but with a smaller prefactor than predicted. Figure 2(b) shows the ratio ξ/γ^2 for a wide range of γ, larger and smaller than 1. A simple one-parameter Ansatz Eq. (28) describes the data well. Figure 2(c) shows the approach to the continuous time limit, i.e. $\xi \to \infty$. In that regime, ξ/γ^2 approaches a constant κ, with quadratic corrections in $1/\xi^2$. The behaviors of U(3) and SU(3) are almost undistinguishable because baryons are heavy and describe small loops only.

$$a^6\chi \approx \frac{1}{2}a^6\Sigma^2 N_s^4\left(1+\frac{\beta_1}{a^2F_\pi^2N_s^2}+\frac{\alpha}{2a^4F_\pi^4N_s^4}\right), \quad (36)$$

where $\beta_1 = 0.140461$ and α is given by

$$\alpha = \beta_1^2+\beta_2+\frac{1}{8\pi^2}\log\frac{a\Lambda_\Sigma^2 N_s}{\Lambda_M}, \quad (37)$$

with $\beta_2 = -0.020305$, and $\Lambda_\Sigma, \Lambda_M$ are renormalization group invariant scales. The average value of the chiral susceptibility is estimated using intermediate configurations—generated with the directed path algorithm—which sample the mesonic two-point function, as described in [11].

A. Phase diagram

An example of a study that is sensitive to the choice of an anisotropy prescription is the mapping of the phase diagram of massless SU(3) lattice QCD, in the strong-coupling limit [1].

The phase boundary separating the chirally broken phase at low (μ_q, T) and the chirally symmetric phase at high (μ_q, T) is determined by monitoring the chiral condensate $a^3\Sigma$ during Monte Carlo simulations, using directed path algorithms and sign reweighting for importance sampling on moderate volumes (see Fig. 3).

For fixed N_t, the temperature is varied implicitly through the bare coupling γ [2]. Assuming the mean field relation Eq. (5), the observed phase boundary has a strong dependence on N_t (see Fig. 3, top), which makes its interpretation questionable. This systematic error is dramatically reduced by using the nonperturbative prescription Eq. (28) for the renormalized anisotropy (see Fig. 3, bottom). Note that, under the nonperturbative prescription, the tricritical couplings on the temperature and chemical potential axes both decrease by $\approx 25\%$.

Moreover, analytic studies of the phase diagram generally consider Euclidean time as continuous [15] and should be compared with the $N_t = \infty$ data only.

B. Static baryon mass

The static baryon mass am_B is another observable for which the inexact calibration of anisotropy can have a strong effect. This observable can be determined using the

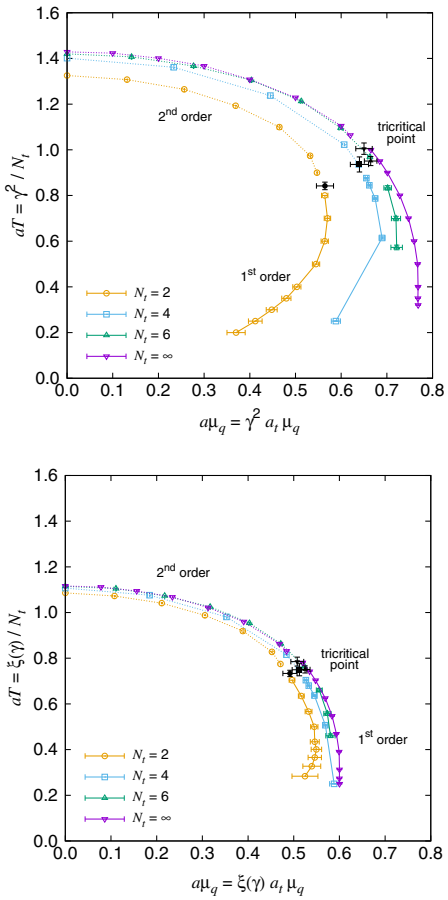

FIG. 3. Phase diagram of SU(3) lattice QCD with massless staggered fermions, in the strong-coupling limit, in which the anisotropy is set using mean field (top) [2], or using the present nonperturbative prescription (bottom). Under the nonperturbative prescription Eq. (28), the N_t dependence of the phase boundary and of the tricritical point decreases substantially. Also, the tricritical couplings on the horizontal and vertical axes both decrease by ≈25%. The $N_t = \infty$ data are produced from simulations directly in the continuous time limit [14].

"snake algorithm" [16], which samples partition functions Z_k describing the system with an open baryonic segment of length k:

$$am_B = \frac{\xi}{N_t} \sum_{k=0}^{N_t-2} \log \frac{Z_{k+2}}{Z_k}. \tag{38}$$

We simulate massless SU(3) lattice QCD for different anisotropies using the snake algorithm and estimate am_B as a function of ξ (see Fig. 4). Under the two anisotropy prescriptions, Eqs. (5) and (28), baryon masses differ by ≈25% at large ξ. In this regime, the fitting Ansatz Eq. (33) describes the data well. The vertical intercepts give the values of the static baryon mass in the continuous time (CT) limit:

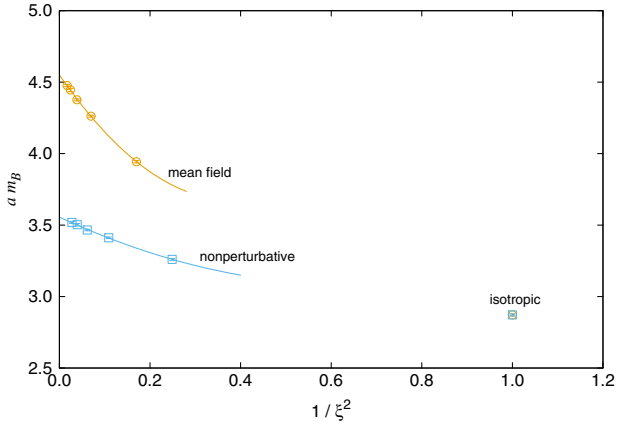

FIG. 4. Effect of the physical anisotropy on the static baryon mass, in massless SU(3) lattice QCD. The anisotropy corrections to the continuous time limit ($\xi \to \infty$) are well described by a quadratic Ansatz in $1/\xi^2$. The baryon mass is heavier on anisotropic lattices than on isotropic lattices, where its value is $am_B \approx 2.88$ [1]. With the anisotropy set using mean field, the baryon mass receives an ≈50% correction in the continuous time limit with respect to the isotropic case, while under the present nonperturbative prescription it only receives an ≈20% correction.

$$(am_B)^{\mathrm{CT}} = \begin{cases} 4.550(8), & \text{mean field} \\ 3.556(6), & \text{nonperturbative.} \end{cases} \tag{39}$$

On an isotropic lattice, static baryons have mass $am_B \approx 2.88$ [1] and become heavier with anisotropy. In the continuous time limit, the baryon mass is only ≈20% heavier than the isotropic case, when using the nonperturbative prescription for the anisotropy, as compared with the ≈50% difference when using mean field.

C. Pion decay constant

Using our nonperturbative prescription for ξ, we can obtain reliable estimates of several physical quantities in the continuous time limit, e.g. the pion decay constant, aF_π. In order to estimate this quantity, we measure the helicity modulus Eq. (35) for several finite hypercubic lattices and values of ξ. The results are summarized in Tables I and II and displayed in Fig. 5 (top). The pion decay constant (squared) corresponds to the thermodynamic limit of the helicity modulus, in accordance with Eq. (34).

Again, the numerical data can be suitably fitted using the Ansatz Eq. (33). At large ξ, the anisotropy corrections are rather small. The vertical intercepts give the values of the pion decay constant in the continuous time limit at $T = 0$[4]:

$$(aF_\pi)^{\mathrm{CT}} = \begin{cases} 0.7820(2), & \mathrm{U}(3) \\ 0.78171(4), & \mathrm{SU}(3). \end{cases} \tag{40}$$

[4]New, direct measurements of aF_π in the continuous time limit [17] are consistent with our extrapolation.

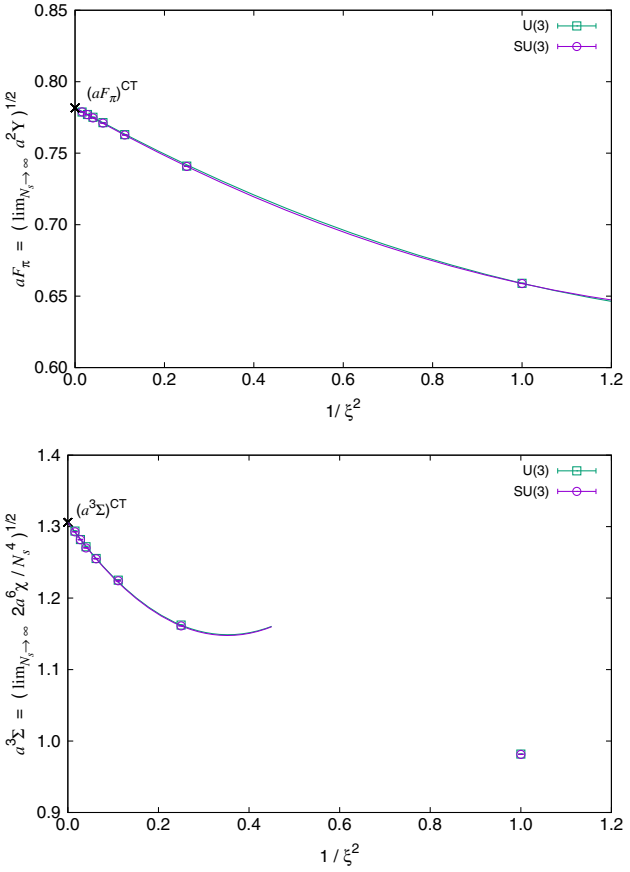

FIG. 5. Effect of the physical anisotropy on the pion decay constant (top) and on the chiral condensate (bottom), in massless U(3) and SU(3) lattice QCD. The anisotropy corrections to the continuous time limit ($\xi \to \infty$) are rather small and well described by a quadratic Ansatz in $1/\xi^2$. The baryonic corrections to the U(3) helicity modulus are negligible. In both graphs, the isotropic points $\xi = 1$ are not included in the quadratic fits: the intersection of the fitting curves with the isotropic point in the top graph is accidental.

Again, U(3) and SU(3) are equivalent in the thermodynamic and continuous time limits, within errors.

D. Chiral condensate

We also estimate accurate values for the infinite-volume chiral condensate $a^3\Sigma$, by analyzing the finite-size scaling of the chiral susceptibility $a^6\chi$, using chiral perturbation theory, and by using our nonperturbative prescription for the lattice anisotropy.

To this end, we estimate the chiral susceptibility density $a^6\chi/N_s^4$ (as in [11]) for several finite hypercubic lattices and values of ξ (see Tables I and II). We estimate $a^6\Sigma^2$ at finite ξ by extrapolating $a^6\chi/N_s^4$ to the thermodynamic limit, modeling the finite-size corrections in accordance with chiral perturbation theory; see Eq. (36).

The dependence of $a^3\Sigma$ on ξ is again well described by the Ansatz Eq. (33) (see Fig. 5, bottom). The vertical intercepts give the values of the chiral condensate in the continuous time limit at $T = 0$:

$$(a^3\Sigma)^{\mathrm{CT}} = \begin{cases} 1.3063(9), & \mathrm{U}(3) \\ 1.306(1), & \mathrm{SU}(3). \end{cases} \tag{41}$$

As before, U(3) and SU(3) are equivalent in the thermodynamic and continuous time limits, within errors. We also observe that, when keeping β_1 as a free parameter in Eq. (36), the finite-size fits are consistent with its theoretical value.

VIII. CONCLUSION

It is very important to have a precise scale for the lattice anisotropy. Even though mean field captures the correct power scaling of the renormalized anisotropy for asymptotically large values of the bare anisotropy, namely $\xi \sim \gamma^2$, it fails to predict the nonperturbative prefactor. The discrepancy between the mean field and nonperturbative prefactors introduces systematic errors of the same magnitude in many physical quantities of interest, particularly in the continuous time limit. This should be kept in mind when comparing strong-coupling Monte Carlo results and analytic mean field results, since the latter are usually formulated in continuous time.

In the dimer representation of the strong-coupling limit of lattice QCD with massless staggered fermions, we have proposed a simple method to determine the nonperturbative dependence $\xi(\gamma)$ between the bare and renormalized anisotropy couplings. The method is amenable to Monte Carlo simulations using very efficient directed path algorithms which, together with the multihistogram reweighting method, allows us to determine $\xi(\gamma)$ with high precision. In the end, the nonperturbative prefactor is observed to be off by $\approx 25\%$ with respect to the mean field prefactor.

As an application, we revisit the phase diagram of SU(3) lattice QCD [1] and update it using our nonperturbative relation $\xi(\gamma)$. A strong dependence of the phase boundary on N_t, introduced by the mean field anisotropy, essentially vanishes. The new locations of the phase boundary and of the tricritical point reveal corrections of $\approx 25\%$, in the chemical potential and temperature, compared with the old mean field values. We also compute the mass of the static baryon in the continuous time limit, which again receives corrections of $\approx 25\%$ compared with the mean field value. These corrections are the direct consequence of the $\approx 25\%$ correction to the mean field prefactor to $\xi(\gamma)$ mentioned above.

We also estimate the values of the pion decay constant, aF_π, and of the infinite-volume chiral condensate, $a^3\Sigma$, in massless lattice QCD in the strong-coupling limit at $T = 0$. The anisotropy corrections to these quantities are small and provide a reliable extrapolation to their continuous time limits.

Even though the strong-coupling limit of lattice QCD is unphysical, it may still be of interest to compare its predictions with those of continuum QCD, in the regime where chiral symmetry is spontaneously broken. For example, the strong-coupling SU(3) lattice value of the pion decay constant Eq. (40), in units of the critical temperature $aT_c \approx 1.089$ [10], is $F_\pi/T_c \approx 0.72$, which is about 15% above the continuum QCD value.

Our approach can be generalized to the case of massive quarks. As before, in a hypercubic box the variances of the spatial and the temporal pion charges Eq. (19) can be required to be equal. Since they still scale as in Eqs. (23a) and (23b), the renormalization criterion Eq. (22) is justified. What changes is that the pion charges are no longer conserved as per Eq. (18), i.e. have different values on parallel codimension-1 lattice slices. A sensible observable is the average over such parallel slices of the variance of the pion charge on each slice. Thus, the setting of the anisotropy should be performed in a fixed volume L^4, characterized by the value of $m_\pi L$. This implies a fine-tuning of the quark mass, in order to keep fixed $m_\pi L$ while the bare anisotropy γ is varied. Alternatively, the anisotropy may also be set by keeping ξ and $m_q L = N_t a_t m_q$ fixed while varying γ [17].

It may also be possible to extend the present study to finite β, in the framework of the $O(\beta)$ partition function defined in [2]. The new occupation numbers (associated with plaquettes) introduce new Grassmann constraints on the extended configuration space. Such constraints may be used to construct analogues of the pion current, which would include plaquette corrections. In the chiral limit, we expect such currents to be conserved. The associated conserved charges could then be used to define non-perturbative renormalization criteria for the (independent) spatial and temporal gauge couplings. An extension of this program to finite quark mass would be similar to the above proposal for $\beta = 0$.

ACKNOWLEDGMENTS

We are very grateful to Oscar Åkerlund, Tobias Rindlisbacher, and Paul Romatschke for many useful discussions. We are also grateful to the Mainz Institute for Theoretical Physics (MITP) for its hospitality and its partial support during the completion of this work. Numerical simulations were performed on the Brutus and Euler clusters at ETH Zürich, and on the OCuLUS cluster at PC2 (Universität Paderborn). This work is supported by the Swiss National Science Foundation under the Grant No. 200020_162515. W. U. acknowledges support by the Deutsche Forschungsgemeinschaft (DFG) through the Emmy Noether Program under Grant No. UN 370/1 and through the Grant No. CRC-TR 211 "Strong-interaction matter under extreme conditions".

[1] P. de Forcrand and M. Fromm, Phys. Rev. Lett. **104**, 112005 (2010).
[2] P. de Forcrand, J. Langelage, O. Philipsen, and W. Unger, Phys. Rev. Lett. **113**, 152002 (2014).
[3] J. Engels, F. Karsch, H. Satz, and I. Montvay, Nucl. Phys. **B205**, 545 (1982); G. Burgers, F. Karsch, A. Nakamura, and I. O. Stamatescu, Nucl. Phys. **B304**, 587 (1988).
[4] F. Karsch, Nucl. Phys. **B205**, 285 (1982); F. Karsch and I. O. Stamatescu, Phys. Lett. B **227**, 153 (1989).
[5] G. Faldt and B. Petersson, Nucl. Phys. **B265**, 197 (1986); N. Bilic, F. Karsch, and K. Redlich, Phys. Rev. D **45**, 3228 (1992).
[6] G. Boyd, J. Engels, F. Karsch, E. Laermann, C. Legeland, M. Lutgemeier, and B. Petersson, Nucl. Phys. **B469**, 419 (1996); F. Karsch, J. Engels, and T. Scheideler, Nucl. Phys. B, Proc. Suppl. **63**, 427 (1998); T. R. Klassen, Nucl. Phys. **B533**, 557 (1998); S. Ejiri, Y. Iwasaki, and K. Kanaya, Phys. Rev. D **58**, 094505 (1998); J. Engels, F. Karsch, and T. Scheideler, Nucl. Phys. **B564**, 303 (2000); M. G. Alford, I. T. Drummond, R. R. Horgan, H. Shanahan, and M. J. Peardon, Phys. Rev. D **63**, 074501 (2001).
[7] L. Levkova and T. Manke, Nucl. Phys. B, Proc. Suppl. **106**, 218 (2002); L. Levkova, Nucl. Phys. B, Proc. Suppl. **119**, 520 (2003); K. Nomura, T. Umeda, and H. Matsufuru, Nucl. Phys. B, Proc. Suppl. **129**, 390 (2004); K. Nomura, H. Matsufuru, and T. Umeda, Prog. Theor. Phys. **111**, 245 (2004).
[8] R. Morrin, A. O. Cais, M. Peardon, S. M. Ryan, and J. I. Skullerud, Phys. Rev. D **74**, 014505 (2006); H. W. Lin *et al.* (Hadron Spectrum Collaboration), Phys. Rev. D **79**, 034502 (2009).
[9] P. Rossi and U. Wolff, Nucl. Phys. **B248**, 105 (1984); F. Karsch and K. H. Mutter, Nucl. Phys. **B313**, 541 (1989).
[10] P. de Forcrand, P. Romatschke, W. Unger, and H. Vairinhos, Proc. Sci., LATTICE2016 (**2017**) 086.
[11] D. H. Adams and S. Chandrasekharan, Nucl. Phys. **B662**, 220 (2003).
[12] P. Hasenfratz and H. Leutwyler, Nucl. Phys. **B343**, 241 (1990).
[13] S. Chandrasekharan and F. J. Jiang, Phys. Rev. D **68**, 091501 (2003).
[14] W. Unger and P. de Forcrand, Proc. Sci. LATTICE2011 (**2011**) 218.
[15] P. H. Damgaard, N. Kawamoto, and K. Shigemoto, Phys. Rev. Lett. **53**, 2211 (1984); P. H. Damgaard, D. Hochberg, and N. Kawamoto, Phys. Lett. **158B**, 239 (1985); P. H. Damgaard, N. Kawamoto, and K. Shigemoto, Nucl. Phys. **B264**, 1 (1986); Y. Nishida, Phys. Rev. D **69**, 094501 (2004).
[16] P. de Forcrand, M. D'Elia, and M. Pepe, Phys. Rev. Lett. **86**, 1438 (2001).
[17] W. Unger and M. Klegewe (to be published).

A.5 Thermodynamics at strong coupling on anisotropic lattices [A5]

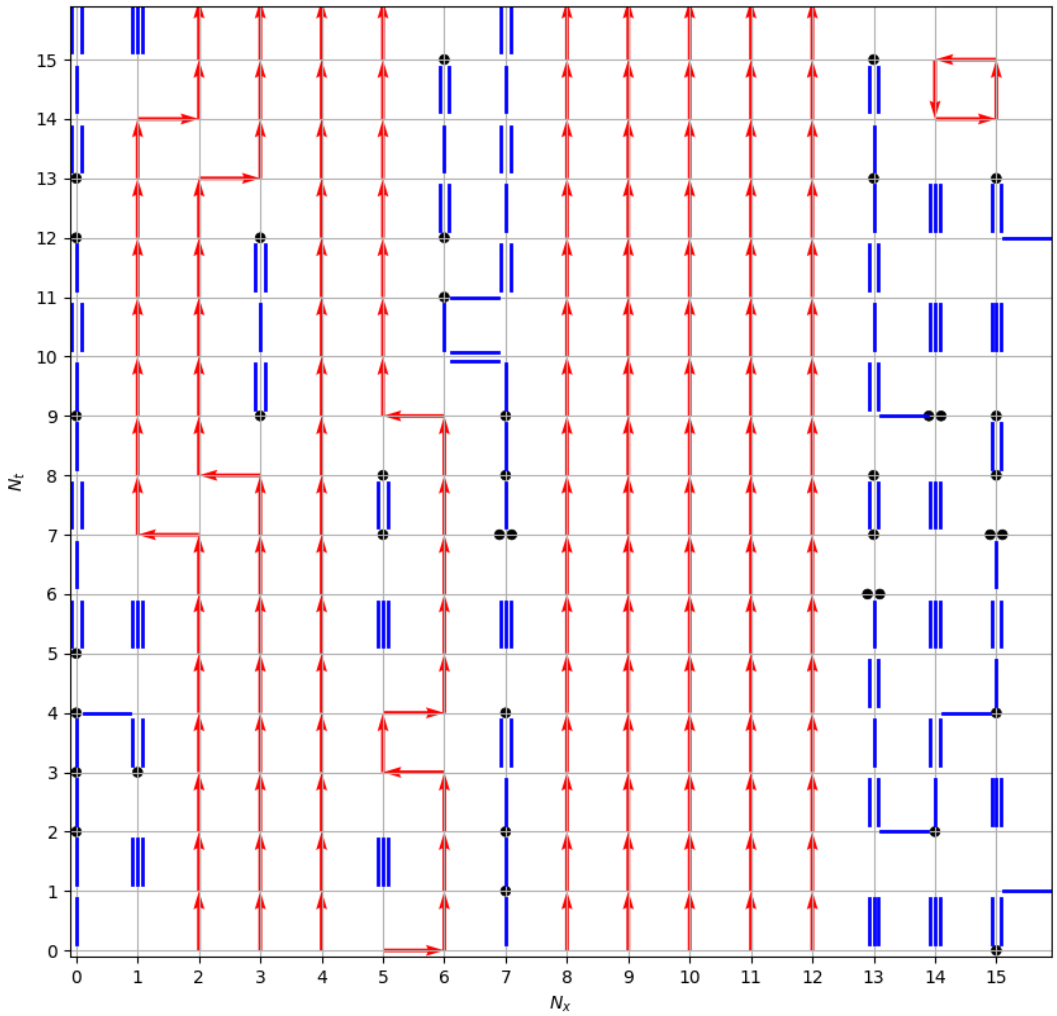

PROCEEDINGS OF SCIENCE

Thermodynamics at Strong Coupling on Anisotropic Lattices

Wolfgang Unger*
Bielefeld University
E-mail: wunger@physik.uni-bielefeld.de

Dennis Bollweg
Bielefeld University
E-mail: dbollweg@physik.uni-bielefeld.de

Marc Klegrewe
Bielefeld University
E-mail: mklegrewe@physik.uni-bielefeld.de

Lattice QCD with staggered fermions at strong coupling has long been studied in a dual representation to circumvent the finite baryon density sign problem. Monte Carlo simulations at finite temperature and density require anisotropic lattices. Recent results that established the non-perturbative functional dependence between the bare anisotropy γ and the physical anisotropy a_s/a_t in the chiral limit are now extended to finite quark mass. We illustrate how the calibration of the anisotropy works and discuss the consequences of the anisotropy on thermodynamic observables. We also show first results on the energy density and pressure in the QCD phase diagram in the strong coupling regime.

The 36th Annual International Symposium on Lattice Field Theory - LATTICE2018
22-28 July, 2018
Michigan State University, East Lansing, Michigan, USA.

*Speaker.

1. Introduction: Sign Problem

Lattice QCD at finite baryon density suffers from the numerical sign problem: no direct simulations based on the fermion determinant (such as RHMC) are feasible, due to the fact that the fermion determinant becomes complex for $\mu_B > 0$. Hence, with the well established methods, a possible critical endpoint is still out of reach. Methods based on a complexified parameter space (Complex Langevin, Lefschetz Thimbles) are promising, but not (yet) applicable to full QCD. Since the sign problem is representation-dependent, the partition sum can also be rewritten in new degrees of freedom which are closer to the physical states. Then the sign problem can be milder or even be absent. Here, we will make use of so-called dual representations,. These have been proven useful in many models which have severe sign problems in the original formulation (e. g. [1]). For lattice QCD, a dual representation is well known in the strong coupling limit in terms of a monomer-dimer system [2, 3, 4]. In this limit $\beta = \frac{2N_c}{g^2} \to 0$, it is possible to reverse the order of integration and integrate out all gauge fields $U_\mu(x)$ before the Grassman variables since link integration factorizes due to the absence of the plaquette contributions of the gauge action. The resulting color singlet degrees of freedom are mesons and baryons. This system has been studied since decades both via Monte Carlo and mean field and has proven to be a great laboratory for finite density QCD. The advantage of the dual formulation of strong coupling LQCD is twofold: (1) the very mild sign problem (which is even absent in the continuous time limit) and (2) the applicability of Worm algorithms that enable fast simulations. This allows to study the full phase diagram in the μ_B - T plane.

2. The Dual Representation of Strong Coupling Lattice QCD

The strong coupling partition function is obtained from the fermionic action of staggered fermions by an exact rewriting of the path integral by integrating out the gluons first. Followed by Grassmann integration, it can be mapped on a discrete system of monomers $n_x \in \{0,\dots N_c\}$, dimers $k_b \in \{0,\dots N_c\}$, and world lines $\ell_b \in \{0,\pm 1\}$ [2, 3]:

$$Z_F(m_q,\mu) = \sum_{\{k,n,\ell\}} \prod_{b=(x,\mu)} \frac{(N_c-k_b)!}{N_c!k_b!} \prod_x \frac{N_c!}{n_x!} (2am_q)^{n_x} \prod_\ell \left(\frac{1}{N_c!^{|\ell|}} \sigma(\ell) e^{3N_t r_l a_\tau \mu} \right) \tag{2.1}$$

The Grassmann integration imposes the following constraint on the sum over configurations in the above partition sum:

$$n_x + \sum_{\hat{\mu}=\pm\hat{0},\dots\pm\hat{d}} \left(k_{\hat{\mu}}(x) + \frac{N_c}{2} |\ell_{\hat{\mu}}(x)| \right) = N_c, \tag{2.2}$$

which is a remnant of the gauge group and entails that mesonic degrees of freedom (monomers and dimers) do not touch baryon world lines, The latter form oriented self-avoiding loops ℓ of length $|\ell|$, and its sign $\sigma(\ell) \in \{-1,+1\}$ depends on loop geometry.

The caveat of this formulation is that the lattice is very coarse, and it requires $\beta > 0$ to make the lattice finer. In principle it is possible to include the effects of the gauge action by expanding it in terms of plaquette occupation numbers before integrating out the gauge links. This gives rise to a strong coupling expansion. Here, we do not include such corrections, but they have been addressed

to next to leading order [5, 6] and have also been presented at this conference in the contribution [7] "Towards a Dual Representation of Lattice QCD" by G. Gagliardi. Alternative strategies with dual variables have been proposed in [8, 9]. The leading order gauge correction $\mathcal{O}(\beta)$ to the SC-LQCD phase diagram in the chiral limit has been first addressed via reweighting in β from the ensemble at $\beta = 0$ [5]. Here it was found that although the nuclear liquid gas critical end point splits from the chiral tri-critical point, the first order line from the nuclear transition and the chiral transition did not split. An immediate question one can ask is: do the nuclear and chiral transition split at sufficiently large β? New simulations obtained by sampling plaquette contributions directly via world sheets did not indicate any splitting [6]. We may have to consider the possibility that in the chiral limit, both transitions are on top even in the continuum limit. Hence it might be necessary to address simulations at finite quark mass for the splitting to be sizeable. This motivates the study presented here.

3. Thermodynamics of Strong Coupling Lattice QCD

In order to vary the temperature in the strong coupling limit, where the lattice spacing $a(\beta)$ cannot be modified at fixed $\beta = 0$, we need to introduce the bare anisotropy γ in the Dirac couplings. This is in particular necessary since $aT = 1/N_t$ is discrete (with N_t even): it turns out that the chiral transition temperature is about $aT_c \simeq 1.5$, hence we cannot address the phase transition on isotropic lattices. The bare anisotropy will change the temporal lattice spacing a_t continuously at fixed $a_s \equiv a$. :

$$\mathscr{L}_{\rm F}(\hat{m}, a_t\mu, \gamma) = \sum_x \left\{ \sum_\nu \gamma^{\delta_{\nu 0}} \eta_\nu(x) \left(e^{a_t\mu\delta_{\nu 0}} \bar{\psi}_x U_\nu(x) \psi_{x+\hat{\nu}} - e^{-a_t\mu\delta_{\nu 0}} \bar{\psi}_{x+\hat{\nu}} U_\nu^\dagger(x) \psi_x \right) + 2\hat{m}\bar{\psi}_x\psi_x \right\}$$

$$Z_F(\hat{m}, a_t\mu, \gamma) = \sum_{\{k,n,\ell\}} \prod_{b=(x,\nu)} \frac{(N_c - k_b)!}{N_c! k_b!} \gamma^{2k_b\delta_{\nu 0}} \prod_x \frac{N_c!}{n_x!} (2\hat{m})^{n_x} \prod_\ell w(\ell, a_t\mu) \tag{3.1}$$

The anisotropy $\frac{a_s}{a_t} \equiv \xi(\gamma)$ is a non-perturbative function of the bare anisotropy γ which allows to define the temperature $aT = \frac{\xi(\gamma)}{N_t}$. At weak coupling one expects $\xi(\gamma) = \gamma$, however, at strong coupling, where the degrees of freedom are not quarks but hadrons, this is not the case. Mean field theory at strong coupling implies $\xi(\gamma) = \gamma^2$, since the square of the critical bare coupling is proportional to N_t: $\gamma_c^2 = N_t \frac{(d-1)(N_c+1)(N_c+2)}{6(N_c+3)}$ [10]. However, modifications are expected beyond mean field, hence we need to determine the precise correspondence between $\xi \equiv a_s/a_t$ and γ.

Consider the SU(3) partition function Eq. (3.1), in terms of the extensive quantities: $N_M = \sum_x n_x$ the total monomer number, $N_q = 2N_{Dt} + 3N_{Bt}$ (with $N_{Dt} = \sum_x k_{x,0}$ and $N_{Bt} = \sum_x |b_{x,0}|$ the total number of temporal dimer and temporal baryon segments), and Ω the total winding number of all baryon world lines. The dimensionless thermodynamic observables in terms of these dual variables are:

$$\text{baryon density:} \qquad a_s^3\rho_B = a_s^3 \frac{T}{V} \frac{\partial \log Z}{\partial \mu_B}\bigg|_{V,T} = \frac{\langle\Omega\rangle}{N_\sigma^3} = \langle\omega\rangle \tag{3.2}$$

$$\text{energy density:} \qquad a_s^3 a_t \varepsilon = \mu_B\rho_B - \frac{a^3 a_t}{V} \frac{\partial \log Z}{\partial T^{-1}}\bigg|_{V,\mu_B} = \frac{\xi}{\gamma}\frac{d\gamma}{d\xi}\langle n_q\rangle - \langle n_M\rangle \tag{3.3}$$

$$\text{pressure:} \qquad a_s^3 a_t p = -a_s^3 a_t T \frac{\partial \log Z}{\partial V}\bigg|_{T,\mu_B} = \frac{\xi}{3\gamma}\frac{d\gamma}{d\xi}\langle n_q\rangle \tag{3.4}$$

$$\text{chiral condensate:} \qquad a_s^4 \langle \bar{\psi}\psi \rangle = a_s^4 \frac{\langle N_M \rangle}{N_\sigma^3 N_t a_s^4 a_t} = \frac{\xi}{\hat{m}} \langle n_M \rangle \tag{3.5}$$

$$\text{interaction measure:} \qquad \varepsilon - 3p = -\frac{\langle n_M \rangle}{a_s^3 a_t} = -m_q \langle \bar{\psi}\psi \rangle \tag{3.6}$$

Clearly, most of these observables explicitly depend on $\xi(\gamma)$ and its derivative. They have been measured in the full μ_B - T plane after having determined $\xi(\gamma)$ non-perturbatively.

4. Anisotropy Calibration and Results

The determination of $\xi(\gamma)$ in the chiral limit has already been addressed in [11, 12]. The non-perturbative result deviates from the mean field assignment $\xi_{\text{mf}}(\gamma) = \gamma^2$ considerably:

$$\xi(\gamma) \approx \kappa\gamma^2 + \frac{\gamma^2}{1+\lambda\gamma^4} \qquad \text{with} \qquad \kappa = 0.781(1) \tag{4.1}$$

As an application, the dependence of observables on the anisotropy was studied: the pion decay constant, the chiral condensate and the baryon mass. With this result, it is also possible to define unambiguously the continuous time limit $a_t \to 0$ via $N_t \to \infty$ and $\gamma \to \infty$ at fixed aT, which is further elaborated in [13] and in a contribution to this conference "Temporal Correlators in the Continuous Time Limit of Lattice QCD" my M. Klegrewe [14]. The anisotropy calibration can also directly be performed in the continuous time limit.

In this proceedings, we want to extend these results to finite quark, i. e. we address the anisotropy calibration and its difficulties for $m_q > 0$. In order to determine $\xi(\gamma)$ the idea is to consider the following current that is implied by the Grassmann constraint [15]:

$$j_\mu(x) = \sigma(x)\left(k_\mu(x) - \frac{N_c}{2}|b_{x,\mu}| - \frac{N_c}{2d}\right) \quad \to \quad \sum_{\pm\hat{\mu}} (j_\mu(x) - j_\mu(x-\hat{\mu})) = -\sigma(x)n(x) \tag{4.2}$$

In the chiral limit, where $n(x) = 0$, the current $j_\mu(x)$ is locally conserved. The conserved charge $Q_\mu = \sum_{x \perp \mu} j_\mu(x)$ has $\langle Q_\mu \rangle = 0$, but non-zero variance: $\langle Q_\mu^2 \rangle \neq 0$. The calibration of $\xi(\gamma)$ is then obtained via a renormalization condition on demanding a physically isotropic box:

$$a_t N_t = a_s N_s \quad \Leftrightarrow \quad \langle Q_t^2 \rangle(\gamma_0) \stackrel{!}{=} \langle Q_s^2 \rangle(\gamma_0), \qquad \frac{a_s}{a_t} = \frac{N_t}{N_s} = \xi(\gamma_0). \tag{4.3}$$

To extend this method to finite quark mass, there is yet a difficulty: $j_\mu(x)$ is no longer a conserved current, i.e. on a given configuration, $Q_t(t_1) \neq Q_t(t_2)$ (and $Q_z(z_1) \neq Q_t(z_2)$). This is expected because the monomers are sources of a pion current $-m_q\bar{\psi}\gamma_5\psi$. However, due to the even/odd decomposition for staggered fermions, there are as many monomers on even as on odd sites. Hence, when averaging over parallel hypersurfaces,

$$Q_t = \frac{1}{N_t}\sum_t (Q_t(t)), \qquad Q_z = \frac{1}{N_s}\sum_z (Q_z(z)), \tag{4.4}$$

the monomers of opposite parity $\sigma(x)$ cancel each other, such that the total charge and its fluctuations can still be used for anisotropy calibration. Again, we demand the fluctuations to be equal,

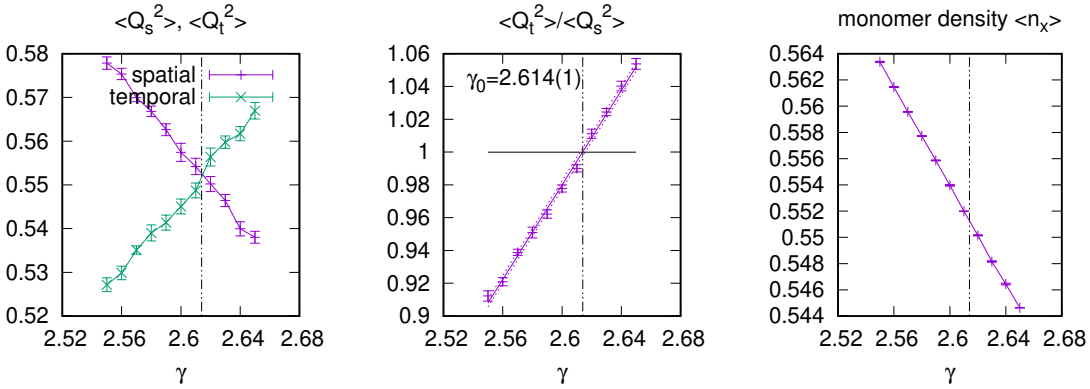

Figure 1: Anisotropy calibration at bare mass $\hat{m} = 0.1$, $\xi = 5$ on a lattice $10^3 \times 50$. *Left:* Spatial and temporal charge fluctuations. *Center:* Ratio, from which γ_0 is obtained. *Right:* Monomer density around γ_0.

$\langle Q_t^2 \rangle(\gamma_0) \stackrel{!}{=} \langle Q_s^2 \rangle(\gamma_0)$. However, at finite dimensionless bare quark mass $\hat{m}$, we need to keep the physics constant e. g. $M_\pi L = \text{const}$ or $[m_q \langle \bar{\psi}\psi \rangle]_L = \text{const}$. Hence we need to determine $\hat{m}(\xi)$ as well (see also [16]). We implement the second condition:

$$a^4 m_q \langle \bar{\psi}\psi \rangle = a^3 a_t \xi \hat{m}(\xi) \langle \bar{\psi}\psi \rangle = \xi \langle n_x \rangle = \text{const}, \tag{4.5}$$

which is related to the monomer density. Note that it is not possible to identify $\hat{m}$ with either am_q nor $a_t m_q$ as $\hat{m}$ depends on ξ ($\hat{m}$ is the bare mass in Eq. (3.1)). In Fig. 1 an example of the anisotropy calibration is shown. Fig. 2 shows the final result obtained by scanning through various bare quark masses $\hat{m} \in [0,1]$ and lattices $10^3 \times N_t$ with aspect ratio $\frac{N_t}{N_s} = \xi \in \{1,2,3,4,5,6,8,10\}$. With the calibration results, the continuous time limit $N_t \to \infty$ is well defined also for finite m_q with

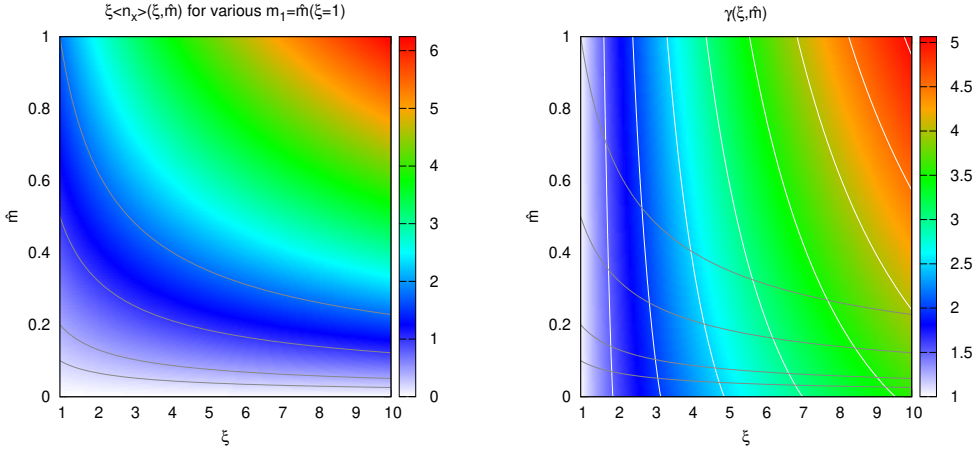

Figure 2: Anisotropy calibration at finite quark mass: *Left:* Lines of constant physics: fixed $m_q \bar{\psi}\psi$, which defines $\hat{m}(\xi)$ with $\hat{m}_1 = \hat{m}(\xi = 1) = am_q$. *Right:* bare anisotropy γ as a function of ξ and $\hat{m}$.

m_q/T fixed. The extrapolation towards continuous time is shown in Fig. 3. The non-perturbative correction factor turns out to have a simple quark mass dependence, such that the temperature and chemical potential are uniquely specified and have a well defined continuous time limit also at

finite quark mass $\hat{m}_1 = am_q$:

$$\kappa(\hat{m}_1) = \frac{\kappa_0}{1 + c_1\hat{m}_1 + c_2\hat{m}_1^2} \qquad aT = \kappa(\hat{m}_1)[aT]_{\rm mf} \qquad a\mu_B = \kappa(\hat{m}_1)[a\mu_B]_{\rm mf} \tag{4.6}$$

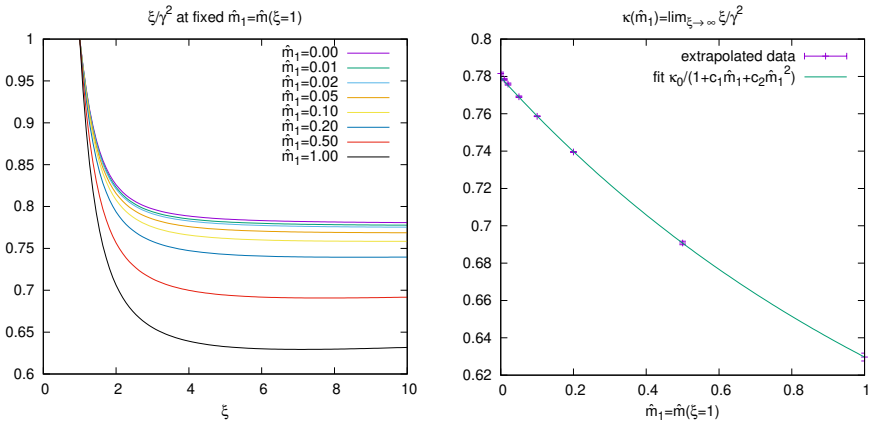

Figure 3: Example on how to obtain the continuous time limit at finite quark mass. *Left:* Correction factor $\xi(\gamma)/\gamma^2$ at fixed $\hat{m}_1$. *Right:* Dependence of the correction factor κ in the continuous time limit on m_q.

By fixing the temperature aT on a lattice specified by N_t, and the isotropic bare quark mass $\hat{m}_1 = am_q$, one can determine via $\xi = aTN_t$ the corresponding $\hat{m}(\xi)$ and $\gamma_0(\xi, \hat{m}(\xi))$ for the Monte Carlo simulations. With this it is possible to measure various thermodynamic observables at fixed mass in the μ_B-T plane. Results on the phase boundary at $m_q > 0$ have already been addressed in [17], but here the mass-independent mean field definitions aT and $a\mu_B$ were used. The new results for the thermodynamic observables Eqs. (3.2)-(3.5), are shown in Fig. (4) for $am_q = 0.1$.

5. Conclusions

We have shown how to extend the anisotropy calibration to finite quark mass to obtain the bare anisotropy $\gamma_0(\xi, \hat{m}(\xi))$ given $\xi = \frac{a_s}{a_t}$ corresponds to a physically isotropic lattice: $a_sN_s = a_tN_t$. Here, the difficulty was addressed that γ_0 now also depends on $\hat{m}$, which requires an additional condition that keeps the physics constant and yields $\hat{m} = \hat{m}(\xi)$. This allows us to define the temperature/chemical potenital and measure thermodynamic observables such as energy and pressure unambiguously. Simulations in the continuous time limit $\xi \to \infty$ confirm the extrapolated results (see also the contribution to this conference [14]). In the future, we want to address the anisotropy calibration also for $\beta > 0$: Here, the non-perturbative determination of $a_s/a_t \equiv \xi(\gamma, \hat{m}, \beta)$ now also involves β, and it might be necessary to introduce an additional bare anisotropy β_s/β_t as well.

6. Acknowledgment

We thank Philippe de Forcrand and Hélvio Vairinhos for useful discussions. Numerical simulations were performed on the OCuLUS cluster at PC^2 (Universität Paderborn). We acknowledge support by the Deutsche Forschungsgemeinschaft (DFG) through the Emmy Noether Program under Grant No. UN 370/1 and through the Grant No. CRC-TR 211 "Strong-interaction matter under extreme conditions".

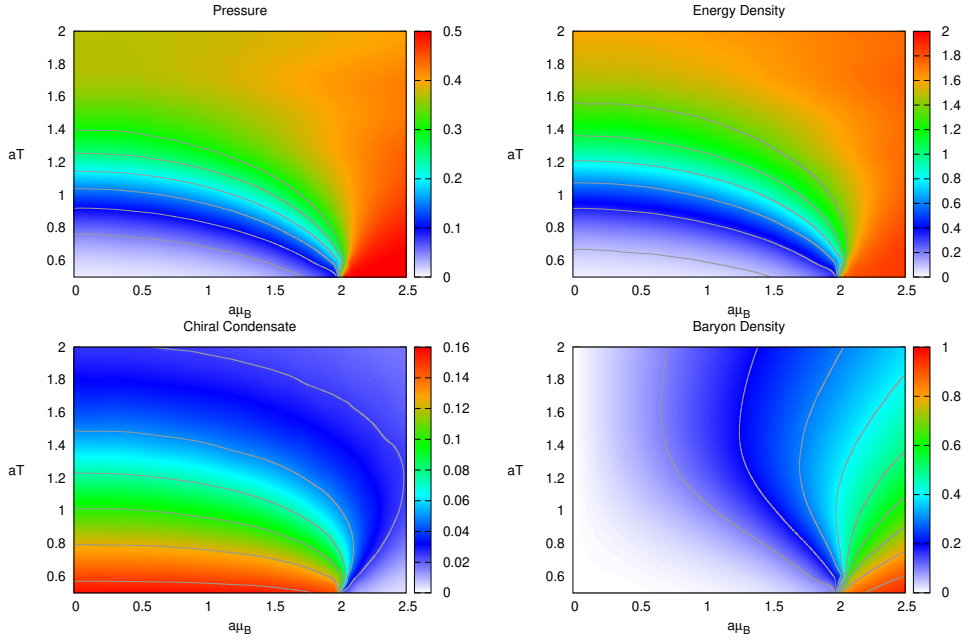

Figure 4: Various thermodynamic observables in the μ_B - T plane at quark mass $am_q = 0.1$. The imprint of the chiral critical endpoint at around $(aT, a\mu_B) \simeq (0.6, 2.0)$ can clearly be seen in all observables.

References

[1] C. Gattringer, T. Kloiber and V. Sazonov, *Nucl. Phys.* **B897** (2015) 732 [1502.05479].

[2] P. Rossi and U. Wolff, *Nucl. Phys.* **B248** (1984) 105.

[3] F. Karsch and K. H. Mutter, *Nucl. Phys.* **B313** (1989) 541.

[4] P. de Forcrand and M. Fromm, *Phys. Rev. Lett.* **104** (2010) 112005 [0907.1915].

[5] P. de Forcrand, J. Langelage, O. Philipsen and W. Unger, *Phys. Rev. Lett.* **113** (2014) 152002 [1406.4397].

[6] G. Gagliardi, J. Kim and W. Unger, *EPJ Web Conf.* **175** (2018) 07047 [1710.07564].

[7] G. Gagliardi and W. Unger, *PoS* **LATTICE2018** (2018) 224 [1811.02817].

[8] C. Gattringer and C. Marchis, *Nucl. Phys.* **B916** (2017) 627 [1609.00124].

[9] O. Borisenko, V. Chelnokov and S. Voloshyn, *EPJ Web Conf.* **175** (2018) 11021 [1712.03064].

[10] N. Bilic, F. Karsch and K. Redlich, *Phys. Rev.* **D45** (1992) 3228.

[11] P. de Forcrand, P. Romatschke, W. Unger and H. Vairinhos, *PoS* **LATTICE2016** (2017) 086 [1701.08324].

[12] P. de Forcrand, W. Unger and H. Vairinhos, *Phys. Rev.* **D97** (2018) 034512 [1710.00611].

[13] W. Unger and P. de Forcrand, *PoS* **LATTICE2012** (2012) 194 [1211.7322].

[14] M. Klegrewe and W. Unger, *PoS* **LATTICE2018** (2018) 182 [1811.01614].

[15] S. Chandrasekharan and F.-J. Jiang, *Phys. Rev.* **D68** (2003) 091501 [hep-lat/0309025].

[16] L. Levkova, T. Manke and R. Mawhinney, *Phys. Rev.* **D73** (2006) 074504 [hep-lat/0603031].

[17] J. Kim and W. Unger, *PoS* **LATTICE2016** (2016) 035 [1611.09120].

A.6 Quark Mass Dependence of the QCD Critical End Point in the Strong Coupling Limit [A6]

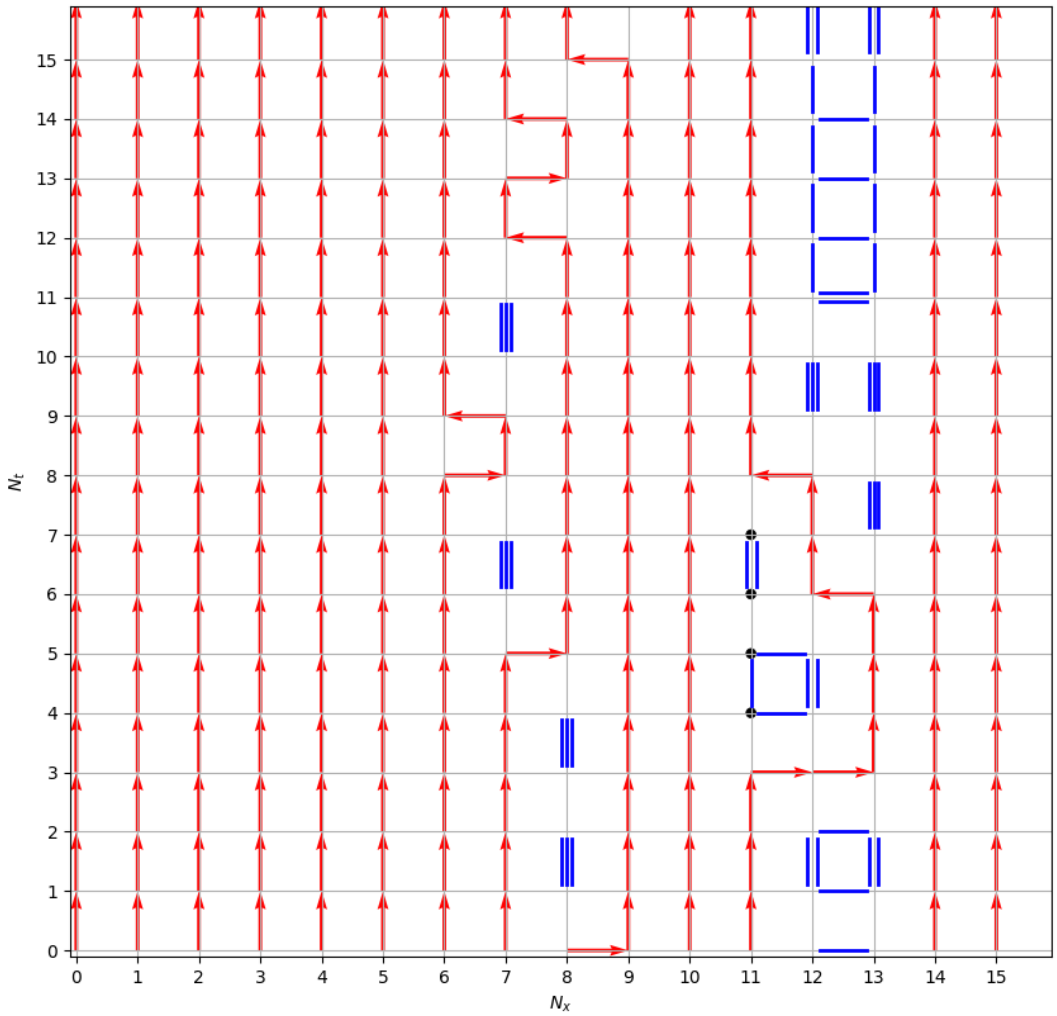

PROCEEDINGS OF SCIENCE

Quark Mass Dependence of the QCD Critical End Point in the Strong Coupling Limit

Jangho Kim*
Fakultät für Physik, Universität Bielefeld, Universitätstasse 25, D33619 Bielefeld, Germany
E-mail: jangho@physik.uni-bielfeld.de

Wolfgang Unger
Fakultät für Physik, Universität Bielefeld, Universitätstasse 25, D33619 Bielefeld, Germany
E-mail: wunger@physik.uni-bielfeld.de

Strong coupling lattice QCD in the dual representation allows to study the full μ-T phase diagram, due to the mildness of the finite density sign problem. Such simulations have been performed in the chiral limit, both at finite N_t and in the continuous time limit. Here we extend the phase diagram to finite quark masses, with an emphasis on the low temperature first order transition. We present our results on the quark mass dependence of the critical end point and the first order line obtained by Monte Carlo via the worm algorithm.

34th annual International Symposium on Lattice Field Theory
24-30 July 2016
University of Southampton, UK

*Speaker.

1. Introduction

It is possible to investigate the full μ-T phase diagram using strong coupling lattice QCD in the dual representation due to its mild sign problem. The sign problem depends on the representation of the partition function. It is well known that in the strong coupling limit $\beta \equiv \frac{2N_c}{g^2} \to 0$, i. e. in the absence of the gauge action, one can make use of a dual representation due to the factorization of one-link gauge integrals [1]. This dual representation is well suited for Monte Carlo simulations via the worm algorithm [2, 3]. Such simulations on the μ-T phase diagram have been carried out in the chiral limit [4, 5]. Simulation at finite quark masses have been studied in [3]. Here we extend on these studies and focus on the phase boundary for finite quark masses. Also we obtain the critical end points (CEP) for finite quark masses.

The Lagrangian for staggered fermions χ including an anisotropy γ, favoring temporal gauge links in order to continuously vary the temperature, is:

$$\mathscr{L}_F = \sum_\nu \frac{\gamma^{\delta_{\nu 0}}}{2} \eta_\nu(x) \left(e^{\mu \delta_{\nu 0}} \overline{\chi}(x) U_\nu(x) \chi(x+\hat{\nu}) - e^{-\mu \delta_{\nu 0}} \overline{\chi}(x+\hat{\nu}) U_\nu^\dagger(x) \chi(x) \right). \tag{1.1}$$

From the Eq. (1.1), one can derive the partition function in the dual representation by integrating out the gauge links and Grassmann variables:

$$Z = \sum_{\{k,n,\ell\}} \underbrace{\prod_{b=(x,\hat{\mu})} \frac{(N_c-k_b)!}{N_c! k_b!} \gamma^{2k_b \delta_{\hat{0},\hat{\mu}}}}_{\text{meson hoppings}} \underbrace{\prod_x \frac{N_c!}{n_x!} (2am_q)^{n_x}}_{\text{chiral condensate}} \underbrace{\prod_\ell w(\ell,\mu)}_{\text{baryon hoppings}} . \tag{1.2}$$

This partition function describes a system of mesons and baryons. The mesons live on the bonds $b \equiv (x,\hat{\mu})$, where they hop to a nearest neighbor $y = x+\hat{\mu}$, and the hopping multiplicity are given by so-called dimers $k_b \in \{0,\dots,N_c\}$. The baryon must form self-avoiding loops.

$$w(\ell,\mu) = \frac{1}{\prod_{x\in\ell}} \sigma(\ell) \gamma^{3N_{\hat{0}}} \exp\left(3N_t r_\ell a_t \mu\right), \quad \sigma(\ell) = (-1)^{r_\ell + N_-(\ell)+1} \prod_{b=(x,\hat{\mu})\in\ell} \eta_{\hat{\mu}}(x), \tag{1.3}$$

where ℓ denotes a baryon loop, $N_{\hat{0}}$ is the number of baryons in temporal direction. N_t is the number of lattice sites in temporal direction and r_ℓ is the baryon winding number in temporal direction. $\sigma(\ell)$ is the sign. The sign is related to staggered phase factor $\eta_{\hat{\mu}}(x)$ and the geometry of the baryon loop ℓ: the winding number r_ℓ and the number of baryons in negative direction $N_-(\ell)$. $N_-(\ell)$ comes from the negative sign in front of the second term in Eq. (1.1). By the Grassmann constraint, the summation over configurations $\sum_{\{k,n,\ell\}}$ in Eq. (1.1) is restricted by the following condition.

$$n_x + \sum_{\mu=\pm 0,\cdots,\pm d} \left(k_\mu(x) + \frac{N_c}{2} |\ell_\mu(x)| \right) = N_c \tag{1.4}$$

In the chiral condensate part, m_q is the quark mass and n_x is the number of monomers at site x. In the chiral limit, monomers are absent to avoid that the partition function becomes zero. On the contrary, for finite quark masses, monomers are present.

2. Chiral and Nuclear Transition

2.1 Symmetries and phase diagram

The chiral symmetry at strong coupling is $\chi'(x) = e^{i\alpha\varepsilon(x)}\chi(x)$, where $\varepsilon(x) = (-1)^{\sum_\mu x_\mu}$. It is spontaneously broken ($\langle\overline{\chi}\chi\rangle \neq 0$) at low temperatures and densities. At high temperatures and densities, the chiral symmetry is restored ($\langle\overline{\chi}\chi\rangle = 0$). Between these two phases, there is a 2nd order phase transition line with $O(2)$ critical exponents at small chemical potential ($\mu < \mu_{\rm tric}$) and a 1st order line $\mu_{\rm 1st}(T) > \mu_{\rm tric}$. The tricritical point (TCP) is located between the 2nd and 1st order lines point. On the other hand, nuclear transition between vacuum phase and nuclear matter phase does not have the 2nd order line. They have the 2nd order CEP that is similar to the CEP of a liquid gas transition, and the 1st order line is located below the CEP. The 1st order line $\mu_{\rm 1st}(T)$ separates the hadronic phase where the baryon density $\langle n_B\rangle = 0$ from the nuclear matter phase. At $T = 0$ and above $\mu > \mu_{\rm 1st}$, where $\langle n_B\rangle = 1$, Pauli saturation occurrs: Due to the finite lattice spacing, the baryons form a crystal in this nuclear matter phase, i. e. every lattice site is filled by a baryon. Because of the Pauli principle, the mesons and the baryons can not intersect with each other. Hence, in the nuclear matter phase, the chiral condensate $\langle\overline{\chi}\chi\rangle$ vanishes. On the contrary, in the hadronic phase, the baryons are rare and the mesons are common.

2.2 Observables

Our observables for the chiral transition are the chiral condensate $\langle\overline{\chi}\chi\rangle$ and the chiral susceptibility χ_{ch}.

$$\langle\overline{\chi}\chi\rangle = \frac{1}{2m_qV}\langle N_M\rangle\,, \quad \chi_{ch} = \frac{1}{V}\frac{\partial^2}{\partial(2m_q)^2}\log Z = \frac{1}{(2m_q)^2V}\left(\langle N_M^2\rangle - \langle N_M\rangle^2 - \langle N_M\rangle\right), \tag{2.1}$$

where $N_M \equiv \sum_x n_x$. In the chiral limit, $\langle\overline{\chi}\chi\rangle = 0$ because $N_M = 0$. For the nuclear transition, we measure the baryon density $\langle n_B\rangle$ and the baryon susceptibility χ_B, which are given by the winding numbers $r_\ell \in \mathbb{Z}$.

$$\langle n_B\rangle = \frac{1}{V_sN_t}\frac{\partial}{\partial(3a_t\mu)}\log Z = \frac{1}{V_s}\langle\sum_\ell r_\ell\rangle\,, \quad \chi_B = \frac{N_t}{V_s}\left(\langle(\sum_\ell r_\ell)^2\rangle - \langle\sum_\ell r_\ell\rangle^2\right) \tag{2.2}$$

The general reweighting method with the average sign is applied in our study.

$$\langle O\rangle = \frac{\langle O\sigma\rangle}{\langle\sigma\rangle}\,, \quad \langle\sigma\rangle = \exp(-L^3N_t\Delta f)\,, \tag{2.3}$$

where Δf is the difference between full and sign-quenched free energy density.

2.3 Anisotropy and finite temperature

We introduce the anisotropy γ in the Dirac couplings in order to vary the temperature in the strong coupling limit $\beta = 0$, where a does not vary, but a_t does vary in Eq. (1.1). The ratio of the lattice spacing in spatial and temporal direction can be written as a general function $\frac{a}{a_t} = \xi(\gamma)$. Mean field theory of Eq. (1.2) suggests [6] that $\xi'(\gamma) = \gamma^2$, it is an N_t-independent choice. $\xi(\gamma)$ is obtained from non-perturbative calculation [7]. Hence, we use the following notations to distinguish $\xi(\gamma)$ and $\xi'(\gamma)$.

$$a\mu' = a_t\mu\xi'(\gamma)\,, \quad aT' = \frac{\xi'(\gamma)}{N_t}\,, \qquad a\mu = a_t\mu\xi(\gamma)\,, \quad aT = \frac{\xi(\gamma)}{N_t} \tag{2.4}$$

3. Results

3.1 Average sign

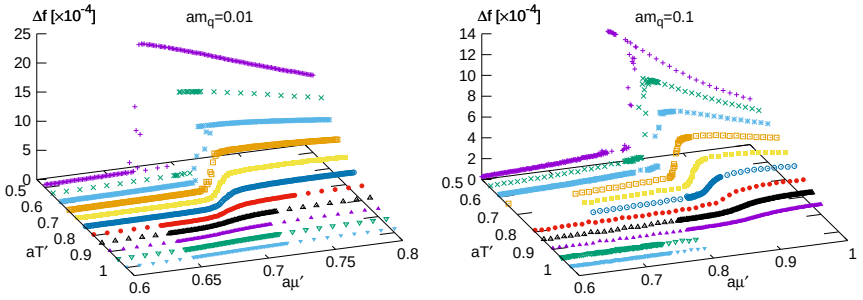

Figure 1: The average sign in the range of $0.5 < aT' < 1$, and $0.6 < a\mu' < 0.8$ for $am_q = 0.01, 0.1$. Here, $\Delta f = -\frac{1}{V}\log\langle \text{sign} \rangle$

In order to show the mildness of the sign problem in the dual the representation, we plot Δf in Fig. 1 which is defined in Eq. (2.3). In the area of $0.5 < aT' < 1$, and $0.6 < a\mu' < 0.8$, where our simulation is done, the average sign is quite small for various quark masses $am_q = 0.01, 0.1$.

3.2 Finite size scaling at finite density

We use finite size scaling to the chiral and nuclear susceptibilities to find the temperature of CEP. The finite size scaling is carried out using the following critical exponents. In the chiral limit ($m_q = 0$), the $O(2)$ exponents with $L^{\rho(\equiv\gamma/\nu)}$, $\gamma = 1.3177$ and $\nu = 0.67155$ are used for the 2nd order line in chiral transition and CEP in nuclear transition. For the crossover region in the nuclear transition, $\rho = 1$ is applied. We use the exponents with $\gamma = 1$ and $\nu = 0.5$ at the TCP for the chiral transition. For the finite quark masses, we apply the $Z(2)$ exponents with $\gamma = 1.237$ and $\nu = 0.613$ at the CEP for both chiral and nuclear transitions. $\rho = 3$ is applied for the first order lines.

We scan the parameter space along the μ-direction for various temperatures in the range of $0.5 \leq aT \leq 1.0$ with the step size 0.05 to find the CEP and phase boundary. We analyse a peak of the chiral and baryon susceptibilities. In the chiral limit, the chiral susceptibility does not have a peak. Hence, we use the baryon susceptibility to find the TCP temperature because the location of the TCP in the chiral transition is same as that of the CEP for the nuclear transition in the strong coupling limit ($\beta = 0$). For finite quark masses, the chiral susceptibility has a peak. So, we obtain the CEPs and phase boundaries separately from the chiral and nuclear transitions. We use the standard finite scaling method to find the temperature of the CEP. We compare the peak heights of the different lattice volumes, they are rescaled by the CEP exponents. By the standard method, the peak heights of the different lattice volumes become equal at the temperature (aT_E') of the CEP.

To obtain the critical chemical potential $a_t\mu_c'$, we analyse the peak position of the chiral and baryon susceptibilities. For the chiral transition in the chiral limit, we obtain the critical chemical potential $a_t\mu_c'$ from the crossing points between the different lattice volumes because the chiral susceptibility does not have a peak. For other cases, we obtain the peak position using the following

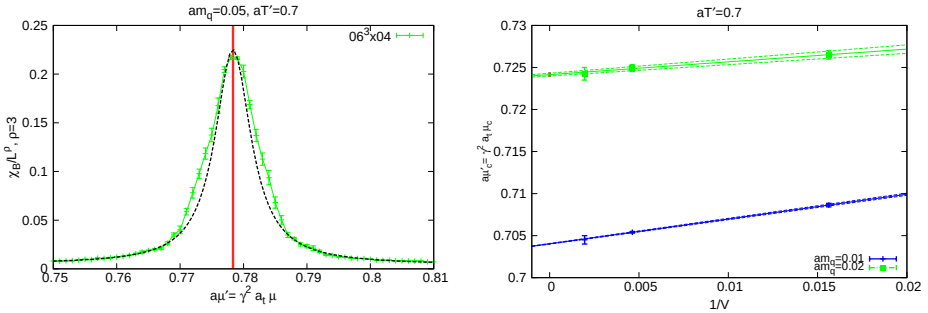

(a) Fit to the Breit-Wigner with polynomial (b) Extrapolation to Thermodynamic limit

Figure 2: The left panel shows the Breit-Wigner fit to find the peak position. The right panel shows the extrapolation to the thermodynamic limit for various quark masses in fixed temperature $aT' = 0.7$.

way. First, we fit a peak of the susceptibility using the Breit-Wigner function with polynomial to find the peak position. The red lines in Fig. 2(a) are the peak position with fitting errors. After we get the $a_t\mu'_c$, we do the extrapolation to the thermodynamic limit to eliminate the volume dependency. The results of extrapolations have very linear behavior with respect to $1/V$ as shown in Fig. 2(b).

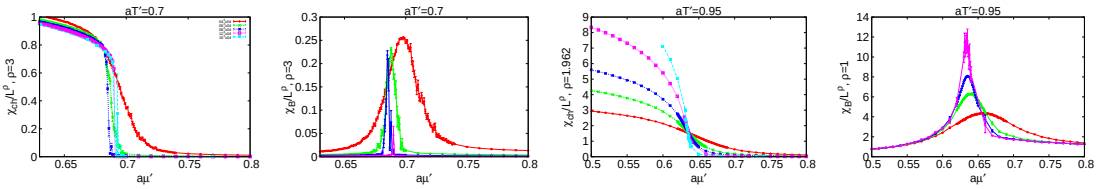

Figure 3: The chiral and baryon susceptibilities in the chiral limit. In the case of chiral susceptibility, we apply the finite size scaling with $\rho = 1.962$ for the 2nd order in the third panel, and $\rho = 3$ for the 1st order transition in the first panel. For the baryon susceptibility, we apply $\rho = 1$ for crossover transition in the forth panel, and $\rho = 3$ for the 1st order transition in the second panel.

First, we address the results in the chiral limit comparing the 1st order lines from the nuclear and chiral transition. We plot the chiral and nuclear susceptibilities in Fig. 3. For the chiral transition at $aT' = 0.95$, we use the $O(2)$ exponents for 2nd line. But the case of nuclear transition at $aT' = 0.95$, crossover scaling $\rho = 1$ is applied. We apply finite size scaling with $\rho = 3$ at $aT' = 0.7$ for both chiral and nuclear transitions because they are belonged in the temperature of 1st order transition.

If we turn on the quark mass, the chiral susceptibility has a peak. We plot the chiral condensate and susceptibility for finite quark mass in Fig. 4(a). The baryon density and susceptibility for finite quark mass are plotted in Fig. 4(b). For the lower panels in Fig. 4(a) and Fig. 4(b), the $Z(2)$ exponents are applied. Then, the order of peak heights at $aT' = 0.725$ and those at $aT' = 0.75$ are opposite. Hence, we find that the temperature of the CEP is located between $0.725 < aT' < 0.75$. The phase boundaries for finite quark masses are obtained from the peak analysis explained above. In the Table 1, our results of CEPs are agree with the previous Monte Carlo results for various

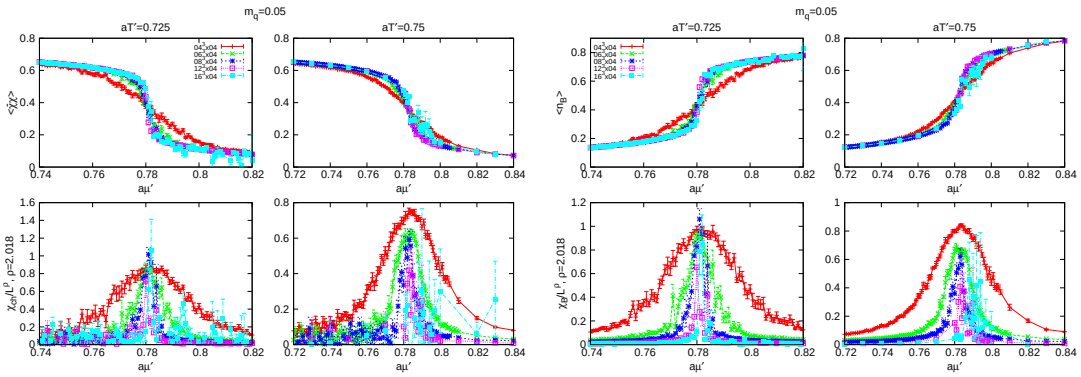

(a) Chiral transition (b) Nuclear transition

Figure 4: The figure (a) shows the chiral condensate and the chiral susceptibility for finite quark mass $m_q = 0.05$ near the critical end point temperature. The data is more noisy than those of nuclear transition due to the monomer fluctuations. The figure (b) shows the baryon density and the baryon susceptibility for finite quark mass $m_q = 0.05$ near the critical end point temperature.

quark masses. We also compare the results to the Mean Field results in Table 1.

am_q	Previous MC(aT'_E, $a\mu'_E$)	MeanField(aT'_E, $a\mu'_E$)	Ours(aT'_E, $a\mu'_E$)	Ours(aT_E, $a\mu_E$)
0.00	0.94(7), $0.64^{+0.02}_{-0.04}$	0.866, 0.577	0.83(3), 0.6671(2)	0.69(3), 0.5563(2)
0.01	0.77(3), 0.70(2)	0.764, 0.583	0.78(3), 0.7005(5)	0.66(3), 0.5906(4)
0.02	N/A	N/A	0.75(3), 0.7234(14)	0.64(3), 0.6137(12)
0.05	N/A	0.690, 0.617	0.73(3), 0.7808(5)	0.62(3), 0.6653(4)
0.10	0.69(1), 0.86(1)	0.646, 0.653	0.70(3), 0.8606(10)	0.60(3), 0.7386(9)

Table 1: We compare our results of CEPs for various quark masses to the previous Monte Carlo results [3] and Mean Field results [8]. The forth column shows the results when we apply the correct anisotropy $\xi(\gamma)$.

3.3 Phase diagram for finite quark masses

Finally, we obtain the phase diagram for finite quark masses. We plot the phase diagrams applied $\xi'(\gamma) = \gamma^2$ and $\xi(\gamma)$ in the first and second panels in Fig. 5. When we apply the $\xi'(\gamma)$, they have back-bending in the low temperature region. This is because for $\gamma < 1$ spatial dimers are favored, which results in an unphysical phase boundary. However, the back-bending disappears when the correct non-perturbative result $\xi(\gamma)$ is applied. The third panel shows the trajectory of CEPs and those of mean-field theory [8]. The x-axis $(am_q)^{2/5}$ in this panel is suggested by tricritical scaling. Due to the correct non-perturbative anisotropy $\xi(\gamma)$, the mismatch with mean-field theory has been enlarged. Just as aT_c differs between Monte Carlo and mean-field theory, also the slope in $(am_q)^{2/5}$ differs.

4. Conclusion

We obtain the phase boundary and critical end points for various quark masses using Monte Carlo simulation in the dual representation. We extend the 1st order phase boundary to the lower

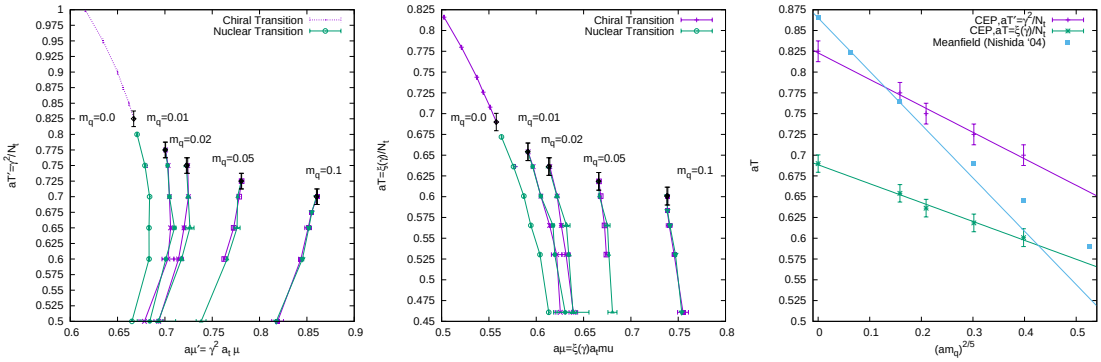

Figure 5: The first and second panels are the phase boundary of chiral and nuclear transition for finite quark masses. In the first panel, we apply the $\xi'(\gamma) = \gamma^2$ for anisotropy. They have back-bending at the low temperature region. In the second panel, we apply $\xi(\gamma)$ obtained from non-perturbative calculation. After we apply the correct anisotropy, the back-bending has disappeared. The third panel is the trajectory of critical end points (from $\xi(\gamma)$ and $\xi'(\gamma)$) and those of mean-field theory.

temperature than the previous Monte Carlo results. As expected, both the nuclear and chiral 1st order transitions are on top also for $m_q > 0$. By applying the non-perturbative results for $\frac{a}{a_t} \equiv \xi(\gamma)$, we confirm the disappearance of back-bending for all quark masses.

Acknowledgments

Calculations leading to the results presented here were performed on resources provided by the Paderborn Center for Parallel Computing. We would like to thank Philippe de Forcrand and Helvio Vairinhos for helpful discussions.

References

[1] P. Rossi and U. Wolff, *Lattice QCD With Fermions at Strong Coupling: A Dimer System*, *Nucl. Phys.* **B248** (1984) 105–122.

[2] D. H. Adams and S. Chandrasekharan, *Chiral limit of strongly coupled lattice gauge theories*, *Nucl. Phys.* **B662** (2003) 220–246, [hep-lat/0303003].

[3] M. Fromm, *Lattice QCD at string coupling: thermodynamics and nuclear physics*, *Thesis* (2010).

[4] P. de Forcrand and M. Fromm, *Nuclear Physics from lattice QCD at strong coupling*, *Phys. Rev. Lett.* **104** (2010) 112005, [0907.1915].

[5] W. Unger and P. de Forcrand, *Continuous Time Monte Carlo for Lattice QCD in the Strong Coupling Limit*, *PoS* **LATTICE2011** (2011) 218, [1111.1434].

[6] G. Faldt and B. Petersson, *Strong Coupling Expansion of Lattice Gauge Theories at Finite Temperature*, *Nucl. Phys.* **B265** (1986) 197–222.

[7] P. de Forcrand, P. Romatschke, W. Unger, and H. Vairinhos, *Thermodynamics of strongly-coupled lattice QCD in the chiral limit*, *PoS* **LATTICE2016** (2016) 086.

[8] Y. Nishida, *Phase structures of strong coupling lattice QCD with finite baryon and isospin density*, *Phys. Rev.* **D69** (2004) 094501, [hep-ph/0312371].

Appendix B

Reprint of articles reviewed in Chapter 3

B.1 The Phase Diagram of Lattice QCD in the Strong Coupling Limit and Away from It [B1]

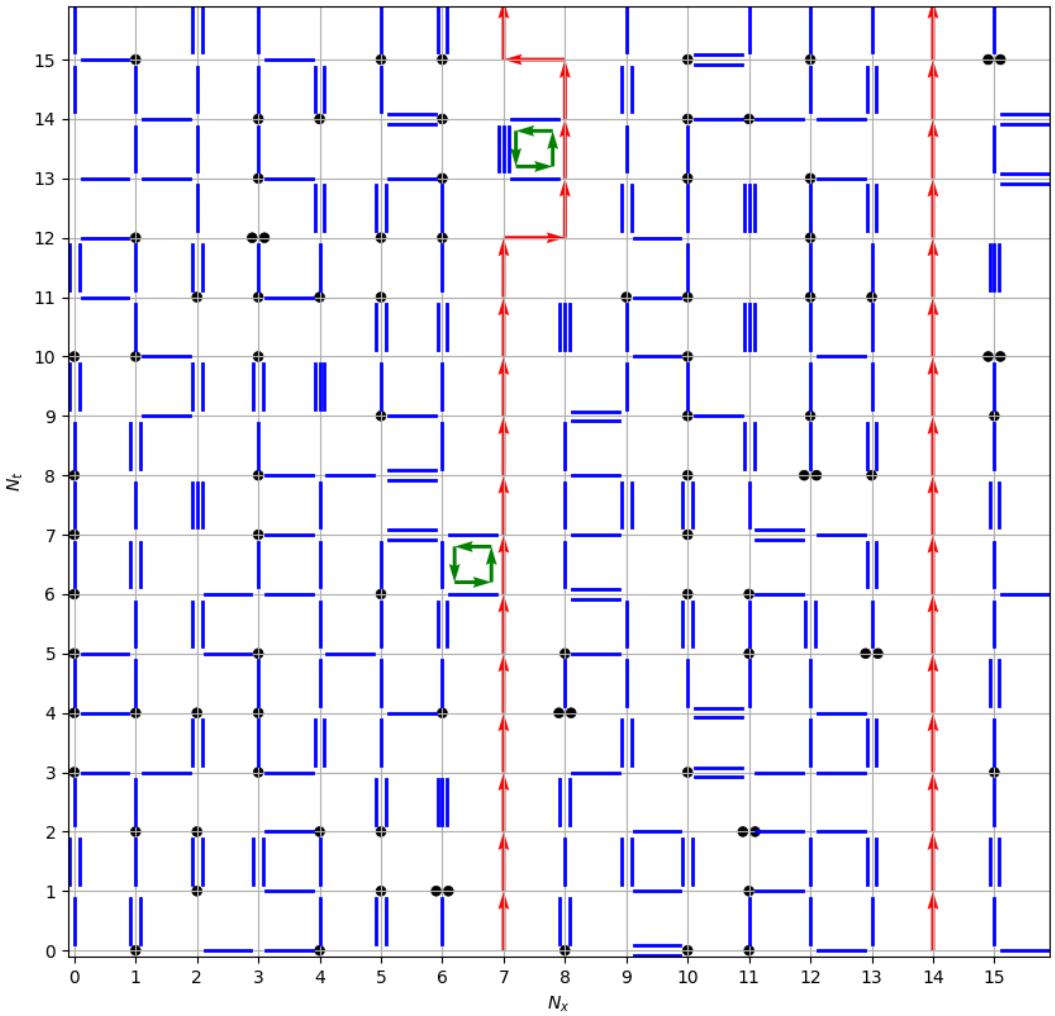

THE PHASE DIAGRAM OF LATTICE QCD IN THE STRONG COUPLING LIMIT AND AWAY FROM IT*

Wolfgang Unger

Institut für Theoretische Physik, Goethe-Universität Frankfurt
60438 Frankfurt am Main, Germany

(Received February 14, 2014)

The strong coupling limit of staggered lattice QCD has been studied for decades, both via Monte Carlo and mean field. In this model, the finite density sign problem is mild and the full phase diagram can be studied, even in the chiral limit. However, in the strong coupling limit the lattice is maximally coarse. Here, we propose a method to go beyond the strong coupling limit with first results and discuss the consequences on the QCD phase diagram in the μ–T plane, in particular the existence of chiral critical end point which is sought in heavy ion collisions. We explain how to construct an effective theory for non-zero lattice coupling, valid to $\mathcal{O}(\beta)$, and present Monte Carlo results incorporating these corrections.

DOI:10.5506/APhysPolBSupp.7.127
PACS numbers: 12.38.Gc, 13.75.Cs, 21.10.Dr, 21.65.–f

1. Introduction

It is one of the main goals of lattice QCD at finite temperature and density to map the phase boundary and the order of the transition as a function of the quark chemical potential μ and the temperature T. However, due to the sign problem of fermion determinant based Hybrid Monte Carlo, little progress has been made in this field. All the methods at hand are limited to small μ/T [1]. Here, we propose to study the phase diagram from a strong coupling perspective, where simulations are feasible also at finite chemical potential. The basic idea of strong coupling lattice QCD is to perform the link integrals analytically before integrating out the Grassmann variables, hence no fermion determinant arises. The sign problem does not

* Lecture presented at the XXXI Max Born Symposium and HIC for FAIR Workshop "Three Days of Critical Behaviour in Hot and Dense QCD", Wrocław, Poland, June 14–16, 2013.

pose a problem in practice, because at high temperatures or densities the sign problem vanishes and is still mild across the phase boundary. We adopt the staggered fermion discretization, where a reformulation in "dual variables" can be obtained ([2, 3], see also [4] for the dual variable approach in another model with chemical potential). The full QCD partition function is given by

$$Z_{\mathrm{QCD}} = \int d\psi d\bar{\psi} dU e^{S_{\mathrm{G}}+S_{\mathrm{F}}}, \qquad S_{\mathrm{G}} = \frac{\beta}{2N_{\mathrm{c}}} \sum_P \mathrm{tr}\left[U_P + U_P^\dagger\right], \tag{1}$$

$$\begin{aligned} S_{\mathrm{F}} &= am_q \sum_x \bar{\psi}_x \psi_x \frac{1}{2} \sum_{x,\nu} \eta_\nu(x) \gamma^{\delta_{\nu 0}} \\ &\quad \times \left[\bar{\psi}_x e^{a_{\mathrm{t}}\mu\delta_{\nu 0}} U_\nu(x) \psi_{x+\hat{\nu}} - \bar{\psi}_{x+\hat{\nu}} e^{-a_{\mathrm{t}}\mu\delta_{\nu 0}} U_\nu^\dagger(x) \psi_x\right] \end{aligned} \tag{2}$$

with m_q the quark mass and $\mu = \frac{1}{3}\mu_{\mathrm{B}}$ the quark chemical potential. The anisotropy in the Dirac couplings γ is introduced to vary the temperature continuously. At strong coupling, the ratio of spatial and temporal lattice spacing is $\frac{a}{a_{\mathrm{t}}} \simeq \gamma^2(1 + \mathcal{O}(1/N_\tau))$ [5]. The action in the strong coupling limit is simply given by the fermionic action, as the lattice gauge coupling $\beta = 2N_{\mathrm{c}}/g^2$ vanishes in the strong coupling limit $g \to \infty$. Since the link integration factorizes in the absence of the gauge action, the gauge links $\mathrm{U}_\nu(x)$ can be integrated out analytically [6]. After performing the Grassmann integration, the final partition function, introduced in [2], is obtained by an analytic rewriting in terms of hadronic degrees of freedom (mesons and baryons)

$$Z_{\mathrm{SC}} = \sum_{\{k,n,\ell\}} \prod_b \frac{(N_{\mathrm{c}} - k_b)!}{N_{\mathrm{c}}! k_b!} \prod_x \frac{N_{\mathrm{c}}!}{n_x!} (2am_q)^{n_x} \prod_\ell w(\ell, \mu)\,. \tag{3}$$

The mesons are represented by monomers $n_x \in \{0, \dots N_{\mathrm{c}}\}$ on sites x, and dimers $k_b \in \{0, \dots N_{\mathrm{c}}\}$ (with $b = (x, \mu)$ the bonds), whereas the baryons are represented by oriented self-avoiding loops ℓ. The weight $w(\ell, \mu) = \left(\prod_{b\in\ell} N_{\mathrm{c}}!\right)^{-1} \sigma(\ell) e^{N_{\mathrm{c}} N_\tau r_\ell a_\tau \mu}$ for a baryonic loop ℓ and its sign $\sigma(\ell) \in \{+1, -1\}$ depends on the loop geometry. The essential constraint on the admissible configuration $\{k, n, \ell\}$ is the Grassmann constraint

$$n_x + \sum_{\hat{\mu}=\pm\hat{0},\cdots\pm\hat{d}} \left(k_{\hat{\mu}}(x) + \frac{N_{\mathrm{c}}}{2} |\ell_{\hat{\mu}}(x)|\right) = N_{\mathrm{c}}\,. \tag{4}$$

Due to this constraint, mesonic degrees of freedom (monomers and dimers) cannot occupy baryonic sites. This system has been studied both via mean field [7–10] and Monte Carlo methods [5, 11, 13]. In recent years, Monte

Carlo simulations of this system have undergone a revival due to the applicability of the Worm algorithm [5, 12, 13]. The idea is to violate the Grassmann constraint in order to sample the monomer two-point function $G(x, y)$ from which the chiral susceptibility is computed. These techniques have been applied to obtain all lattice data presented in this paper. In Fig. 1, we show the (μ, T) phase diagram in the strong coupling limit and for $m_q = 0$, where $\langle \bar{\psi}\psi \rangle$ is an exact order parameter for spontaneous chiral symmetry breaking. It is qualitatively similar to the expected phase diagram of QCD in the chiral limit: the transition is of second order at $a\mu = 0$, up to the tricritical point at $(a\mu_{\rm tcp}, aT_{\rm tcp})$, and turns to first order. At finite quark mass, the second order line turns into a crossover, the tricritical point into a second order critical end point. At low temperatures, in contrast to QCD, the chiral transition coincides with the nuclear transition. This is because above the critical chemical potential a baryonic crystal forms, which restores chiral symmetry. This saturation effect is a lattice artifact.

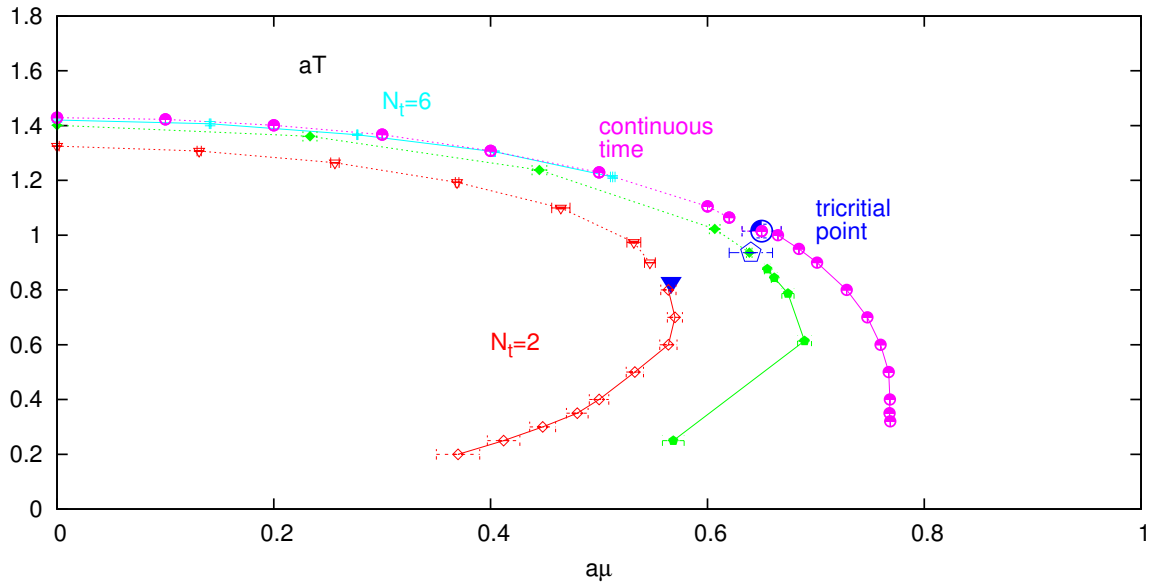

Fig. 1. SC phase diagram from Worm algorithm with identifications: $aT = \frac{\gamma^2}{N_\tau}$, $a\mu = \gamma^2 a_\tau \mu$. Note that the re-entrance at low temperatures vanishes in continuous time $(N_\tau \to \infty)$.

Since strong coupling lattice QCD can be thought of as a one-parameter deformation of continuum QCD, an important question is how both phase diagrams are connected. Due to the sign problem, only the plane at $\mu = 0$ and the plane at $\beta = 0$ is known. The QCD phase diagram in the (μ, T) plane in the continuum limit is largely unknown. If the tricritical point persists in the continuum limit, this is strong evidence for the existence of a chiral critical end point in full QCD at physical quark mass. In order to go beyond the strong coupling limit, we derive a partition function valid at $\mathcal{O}(\beta)$, from

which we compute the slope of the chiral transition temperature. There are two questions we want to address: What is the slope of the tricritical line with respect to β, and do the chiral and nuclear transition split as expected? Two of various possible scenarios are sketched in Fig. 2.

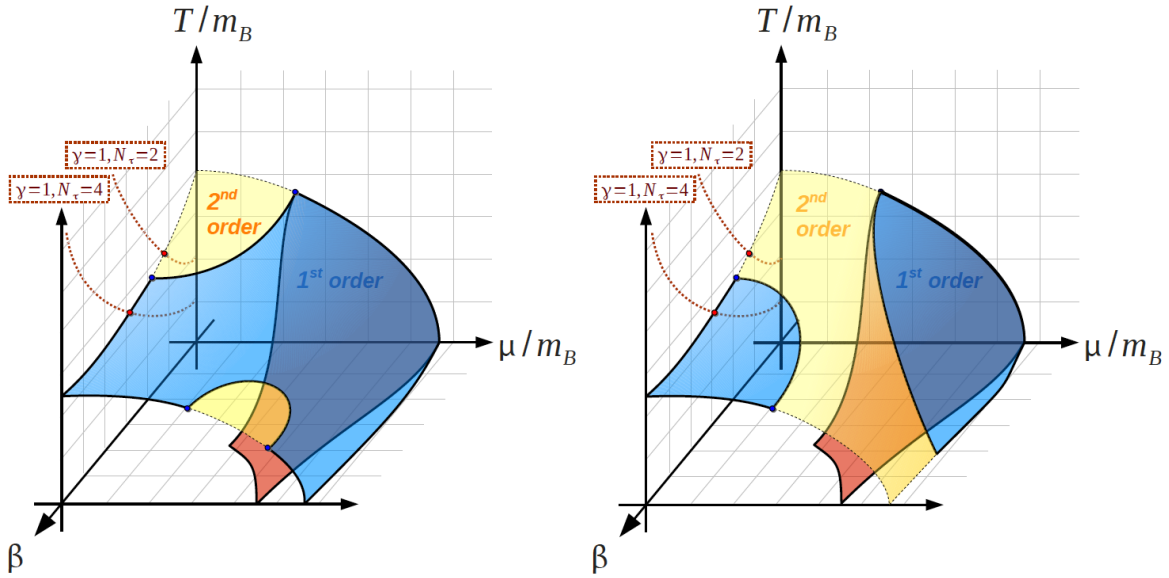

Fig. 2. Two scenarios of the extension of the chiral transition to finite β. It is expected that the chiral transition and the nuclear transition will split. The first and second order regions are separated by tricritial lines. Of special interest is whether the tricritical point at strong coupling will move to smaller (left) or larger (right) values of μ_c as a function of β.

2. Corrections to the strong coupling limit

To go beyond the strong coupling limit, a systematic expansion of the QCD partition function in β is needed. Here, we derive the effective action valid to the leading order $\mathcal{O}(\beta)$. The SC partition function including the gauge part can be written in terms of a fermionic path integral

$$Z_{\mathrm{QCD}} = \int d\chi d\bar{\chi} dU e^{S_{\mathrm{G}}+S_{\mathrm{F}}} = \int d\chi d\bar{\chi} Z_{\mathrm{F}} \left\langle e^{S_{\mathrm{G}}} \right\rangle_{Z_{\mathrm{F}}} , \tag{5}$$

where $Z_{\mathrm{F}} = \int dU e^{-S_{\mathrm{F}}}$ is the fermionic partiton function, which is related to the strong coupling partition function via $Z_{\mathrm{SC}} = \int d\chi d\bar{\chi} Z_{\mathrm{F}}$. The gauge action can then be expressed as an expectation value which we linearize to obtain the $\mathcal{O}(\beta)$ contribution

$$\left\langle e^{S_{\mathrm{G}}} \right\rangle_{Z_{\mathrm{F}}} \simeq 1 + \langle S_{\mathrm{G}} \rangle_U = 1 + \frac{\beta}{2N_{\mathrm{c}}} \sum_P \left\langle \mathrm{tr} \left[U_P + U_P^\dagger \right] \right\rangle_{Z_{\mathrm{F}}} . \tag{6}$$

Evaluating the expectation value of the elementary plaquette $\mathrm{tr}[U_P]$ in the strong coupling ensemble, we need to compute the link integrals with an additional gauge link coming from the plaquette. Before Grassmann integration, the plaquette is given by $P = J_{ij}J_{jk}J_{kl}J_{li}$ with the link integrals at the edge of an elementary plaquette [14–16]

$$\begin{aligned} J_{ij} &= \sum_{k=1}^{N_\mathrm{c}} \frac{(N_\mathrm{c}-k)!}{N_\mathrm{c}!(k-1)!}(M_\chi M_\varphi)^{k-1}\bar{\chi}_j\varphi_i \\ &\quad + \frac{1}{N_\mathrm{c}!(N_\mathrm{c}-1)!}\epsilon_{ii_1i_2}\epsilon_{jj_1j_2}\bar{\varphi}_{i_1}\bar{\varphi}_{i_2}\chi_{j_1}\chi_{j_2} - \frac{1}{3}\bar{B}_\chi B_\phi \bar{\phi}_j\chi_i \end{aligned} \tag{7}$$

with M and B representing the mesons and baryons. From these link integrals, we can compute the weight for inserting a plaquette or a Polyakov loop into the strong coupling configuration. At the corners of the plaquette, the Grassmann variables ϕ, χ are bound into baryons and mesons to fulfill a modified Grassmann constraint: here, the degrees of freedom add up to $N_\mathrm{c}+1$. For $N_\mathrm{c}=3$, there are 19 diagrams contributing to the plaquette P [16], one of them given in Fig. 3. We can summarize the generalized link weights w and site weights v as follows

$$\begin{aligned} v_\mathrm{M} &= (N_\mathrm{c}-1)\,, \qquad v_\mathrm{B} = N_\mathrm{c}!\,, \qquad w_{D_k} = \frac{(N_\mathrm{c}-k)!}{N_\mathrm{c}!k!}k\,, \\ w_{B_0} &= \frac{1}{N_\mathrm{c}!}\,, \qquad w_{B_1} = \frac{1}{N_\mathrm{c}!(N_\mathrm{c}-1)!}\,, \qquad w_{B_2} = \frac{(N_\mathrm{c}-1)!}{N_\mathrm{c}!}\,, \end{aligned} \tag{8}$$

where at v_B the external leg is baryonic, whereas at v_M the external leg is mesonic, B_1 is an oriented link where one quark flux is replaced by a gauge flux and B_2 the link state of a baryon dressed with oppositely oriented gauge and quark flux. We can insert a new set of variables, the plaquette occupation numbers $q_p \in \{0,1\}$ (and derived from it a bond-plaquette number $q_b \in \{0,1\}$), to include a Metropolis update allowing to sample the partition function

$$\begin{aligned} Z &= \sum_{\{k,n,q,\ell\}} \prod_x w_x \prod_b w_b \prod_\ell w_\ell \prod_P w_P\,, \\ w_x &= \frac{N_\mathrm{c}!}{n_x!}(2am_q)^{n_x} v_i(x)\,, \qquad w_b = \frac{(N_\mathrm{c}-k_b)!}{N_\mathrm{c}!(k_b-q_b)!}\,, \\ w_\ell &= \prod_\ell w_{B_i}(\ell)\sigma(\ell)e^{3N_\tau r_\ell a_\tau \mu}\,, \qquad w_P = \left(\frac{\beta}{2N_\mathrm{c}}\right)^{-2q_p} \end{aligned} \tag{9}$$

at finite β. Qualitatively new aspects of the $\mathcal{O}(\beta)$ contributions are (1) that mesons and baryons are now allowed to interact and (2) that baryons become

extended objects, in contrast to their pointlike nature in the strong coupling limit. There is no strict decomposition of the lattice into mesonic and baryonic sites due to the plaquettes. The $\mathcal{O}(\beta)$ corrections allow to measure the zero-th order of gauge observables (average plaquette, Polyakov loop), and the first order of fermionic observables (slope of the chiral suceptibility, baryon density).

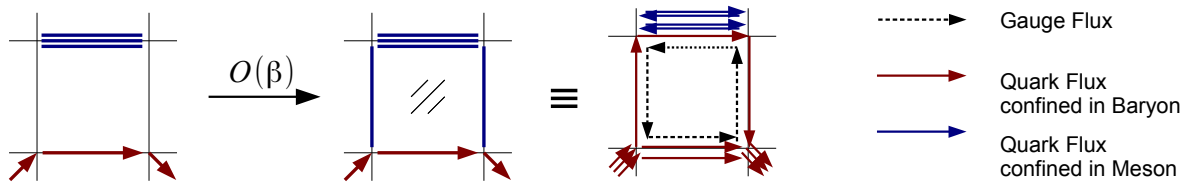

Fig. 3. Illustration of reweighting from the strong coupling ensemble: insertion of two parallel dimers produces one of the 19 plaquette diagrams. The dimer and flux variables adjacent to the plaquette are composed of quark flux and gauge flux: black/blue lines represent mesonic content, gray/red lines represent baryonic content. The baryon becomes an extended object.

3. Gauge observables

We obtain gauge observables via reweighting from the strong coupling ensemble, instead of sampling at finite β. This is because the average plaquette, given by

$$\langle P \rangle = \frac{2}{Vd(d-1)} \frac{\partial}{\partial \beta} \log(Z) = \frac{1}{\beta} \langle n_P \rangle \ , \qquad n_P = \frac{2}{Vd(d-1)} \sum_P q_P \quad (10)$$

is very noisy for small β due to the division of two small numbers. In Fig. 4 we show a detailed comparison of the strong coupling algorithm (making use of both the worm algorithm and reweighting in the plaquette number, abbreviated SC-algorithm) with conventional hybrid Monte Carlo (HMC). Both the Polyakov loop and the average plaquette are consistent in the whole parameter space in quark mass and temperature. In Fig. 5 the volume dependence of the Polyakov loop and average plaquette is shown, both are sensitive to the chiral transition. This cusp-like behaviour should not be interpreted as deconfinement, but is an imprint of the chiral transition. We have reported this finding for U(3) gauge theory in [17], and similar behaviour is also found in the opposite limit of non-confining models, discussed in [18].

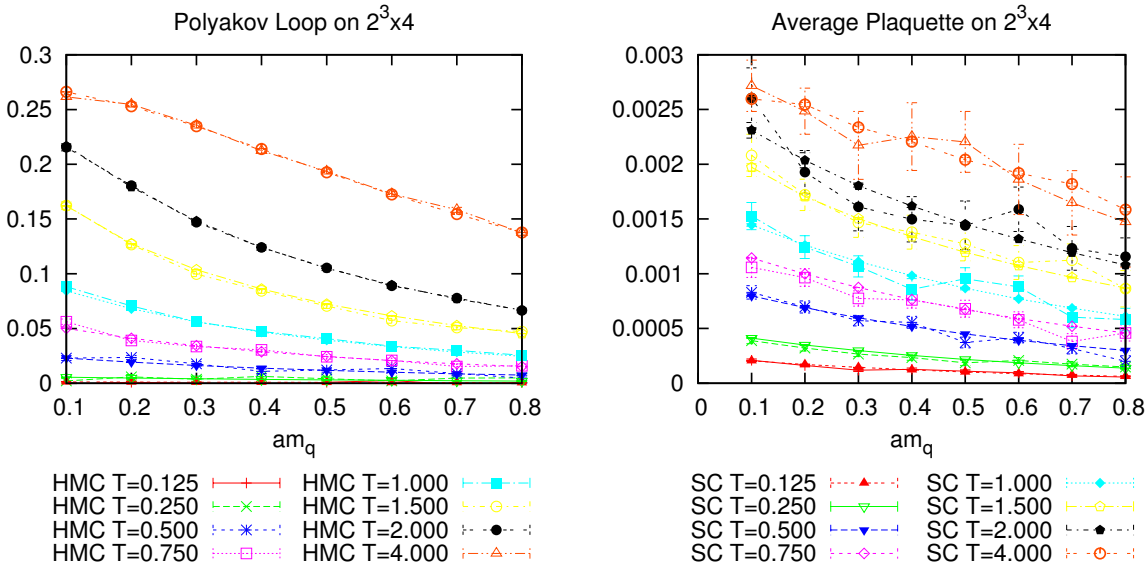

Fig. 4. Comparison of gauge observables measured both with SC-algorithm and Hybrid Monte Carlo. Perfect agreement is found for the Polyakov loop (left). The average plaquette (right) is very noisy in HMC, but in good agreement with the results from the SC-algorithm.

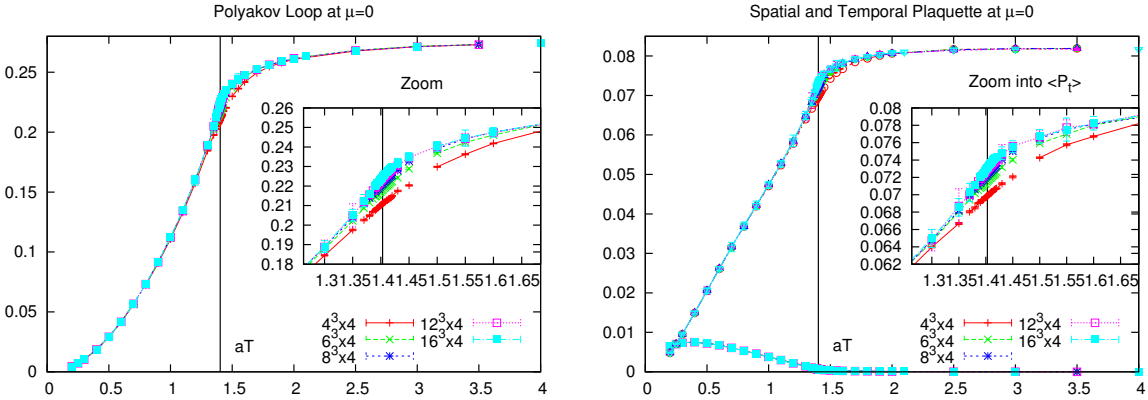

Fig. 5. Volume dependence of gauge observables: both the Polyakov loop (left) and the average plaquette (right) show an L-dependence at the transition region, close to $aT_c = 1.402(1)$.

4. Phase diagram as a function of β

For fermionic observables, such as the chiral susceptibility or the baryon density, we can extract the leading order corrections (the slope with respect to β). This allows us to compute the gauge corrections to the strong coupling phase diagram. We now address the chiral susceptibility, which in terms of the monomer number N_M is given by

$$\chi = \frac{1}{(2am_q)^2 L^3 N_\mathrm{t}} \left(\langle N_\mathrm{M}^2 \rangle - \langle N_\mathrm{M} \rangle^2 - \langle N_\mathrm{M} \rangle \right) . \tag{11}$$

In the following, we consider the chiral limit, where $\langle N_\mathrm{M} \rangle = 0$ due to the finite system size. The worm algorithm samples the 2-point correlation function in the 2-monomer sector, its integral is

$$\chi = \frac{1}{V} \sum_{x_1, x_2} G(x_1, x_2) \equiv \left\langle \left(\bar{\psi}\psi\right)^2 \right\rangle . \tag{12}$$

The leading order Taylor coefficient of χ is given by the derivative of the chiral susceptibility w.r.t. β.

$$\begin{aligned} \chi(\beta) &= \chi_0 + c_\chi \beta + \mathcal{O}\left(\beta^2\right) , \\ c_\chi &= \frac{\partial}{\partial \beta} \left\langle \left(\bar{\psi}\psi\right)^2 \right\rangle = N_\mathrm{s}^3 N_\mathrm{t} \left(\left\langle \left(\bar{\psi}\psi\right)^2 P \right\rangle - \left\langle \left(\bar{\psi}\psi\right)^2 \langle P \rangle \right\rangle \right) . \end{aligned} \tag{13}$$

At finite temperature, we need in fact to measure both spatial and temporal plaquette expectation values as well as their joint expectation value with $(\bar{\psi}\psi)^2$. This results in two Taylor coefficients, c_s, c_t. However, c_s is largely suppressed with temperature, just as the spatial plaquette itself (see Fig. 5), so that we did not need to consider any anistropy in the gauge coupling $\beta_\mathrm{s}/\beta_\mathrm{t}$ at the phase boundary. We determine the chiral transition temperature via critical scaling with $3d$ O(2) critical exponents γ, ν

$$\chi_\mathrm{L}(T, \beta) / L^{\gamma/\nu} = A + BtL^{1/\nu} , \qquad t = \frac{T - T_\mathrm{c}(\beta = 0)}{T_\mathrm{c}(\beta = 0)} \tag{14}$$

that is the chiral susceptibility collapses on a universal scaling function when rescaled in this way, which is almost linear in the scaling window with non-universal coefficients $A \simeq 1.001(1)$ and $B \simeq -0.982(1)$ for SU(3) at zero density. Our strategy is to determine the shift in aT_c induced by a finite value of β. For this to be the case, the Taylor coefficient also has to obey critical scaling. We indeed find that c_χ can well be fitted by a linear function in t

$$\frac{c_\chi}{\chi} \simeq c_1 + c_2 L^{1/\nu} + c_3 t , \tag{15}$$

with $c_2 = -0.397(2)$ for SU(3) at $\mu = 0$. The coefficient c_3 drops out since the term is of higer order in β. The slope of the critical temperature is

$$s \equiv \frac{d}{d\beta} aT_c(\beta) \bigg|_{\beta=0} = -aT_\mathrm{c} \frac{A}{B} c_2 . \tag{16}$$

For SU(3), where $aT_c = 1.402(1)$ at $\mu = 0$, we obtain $s = -0.446(7)$, as shown in Fig. 6, so we indeed find that the transition temperature drops. The slope can be compared to the mean field result of Miura *et al.* [19], who get $s \approx 0.4$, which is quite compatible

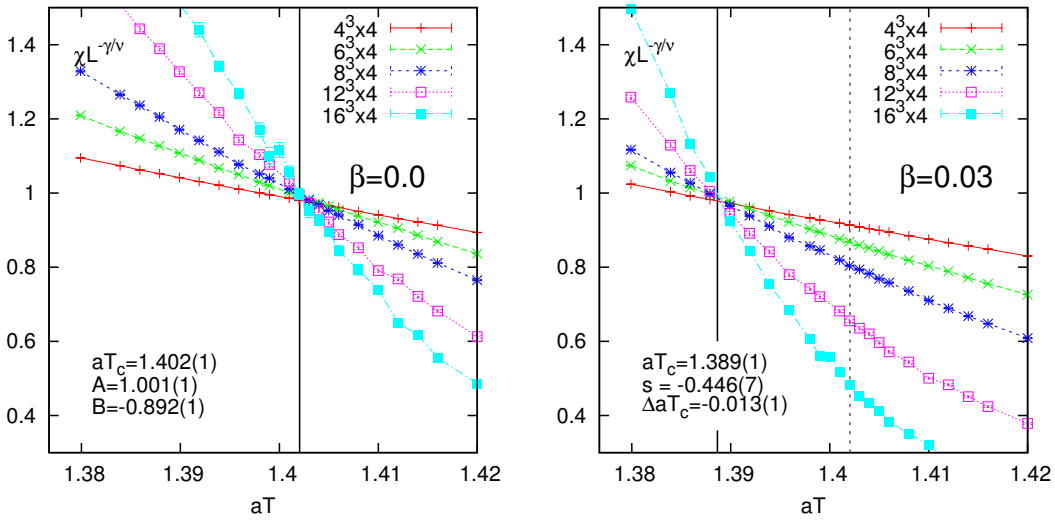

Fig. 6. The transition temperature from critical scaling of the chiral susceptibility. Left: for $\beta = 0$, $aT_c = 1.402(1)$. Right: for $\beta = 0.03$, the transition temperature shifts to $aT_c = 1.389(1)$.

The drop in aT_c is expected since the lattice spacing $a(\beta)$ shrinks as β is increased. Also, in the strong coupling limit, the ratio $\frac{T_c(\mu=0)}{3\mu_c(T=0)} \approx \frac{1.403}{1.71} = 0.82$ is much too large compared to the continuum result (in the chiral limit) $\frac{T_c}{3\mu_c} \approx \frac{154\,\mathrm{MeV}}{0.93\,\mathrm{GeV}} = 0.165$. Hence it is expected that the phase boundary at small μ decreases more drastically with β than at large μ. Due to the mild sign problem of the dimer representation, our method to determine the slope of aT_c can be readily extended to finite density. Numerical results for the phase boundary as a function of β will be presented in a forthcoming publication.

5. Conclusion

We have presented a method to compute gauge corrections to the QCD phase diagram at strong coupling. The correct average plaquette and Polyakov loop are reproduced at $\beta = 0$ and can be measured at high precision. This allows us to obtain the leading order gauge corrections to the chiral susceptibilty via reweighting. Via a second order scaling analysis we were able to get the slope of the chiral transition temperature $\frac{d}{d\beta} aT_c$, which is in good agreement with the expected value.

The author would like to thank Ph. de Forcrand, J. Langelage and O. Philipsen for helpful discussions. This work was supported by the Helmholtz International Center for FAIR.

REFERENCES

[1] P. de Forcrand, *PoS* **LAT2009**, 010 (2009).
[2] P. Rossi, U. Wolff, *Nucl. Phys.* **B248**, 105 (1984).
[3] U. Wolff, *Phys. Lett.* **B153**, 92 (1985).
[4] Y.D. Mercado, C. Gattringer, A. Schmidt, *Phys. Rev. Lett.* **111**, 141601 (2013) [arXiv:1307.6120 [hep-lat]].
[5] W. Unger, P. de Forcrand, *PoS* **LATTICE2011**, 218 (2011).
[6] K.E. Eriksson, N. Svartholm, B.S. Skagerstam, *J. Math. Phys.* **22**, 2276 (1981).
[7] N. Bilic, F. Karsch, K. Redlich, *Phys. Rev.* **D45**, 3228 (1992).
[8] N. Bilic, K. Demeterfi, B. Petersson, *Nucl. Phys.* **B377**, 651 (1992).
[9] Y. Nishida, *Phys. Rev.* **D69**, 094501 (2004).
[10] A. Ohnishi, K. Miura, T. Nakano, N. Kawamoto, *PoS* **LAT2009**, 160 (2009).
[11] F. Karsch, K.H. Mütter, *Nucl. Phys.* **B313**, 541 (1989).
[12] D.H. Adams, S. Chandrasekharan, *Nucl. Phys.* **B662**, 220 (2003).
[13] P. de Forcrand, M. Fromm, *Phys. Rev. Lett.* **104**, 112005 (2010).
[14] M. Creutz, *J. Math. Phys.* **19**, 2043 (1978).
[15] S.I. Azakov, E.S. Aliev, *Phys. Scr.* **38**, 769 (1988).
[16] J. Langelage, Ph.D. Thesis (2009).
[17] M. Fromm *et al.*, *PoS* **LATTICE2011**, 212 (2011).
[18] S. Benić, *Phys. Rev.* **D88**, 077501 (2013).
[19] K. Miura, T.Z. Nakano, A. Ohnishi, N. Kawamoto, *Phys. Rev.* **D80**, 074034 (2009).

B.2 Lattice QCD Phase Diagram In and Away from the Strong Coupling Limit [B2]

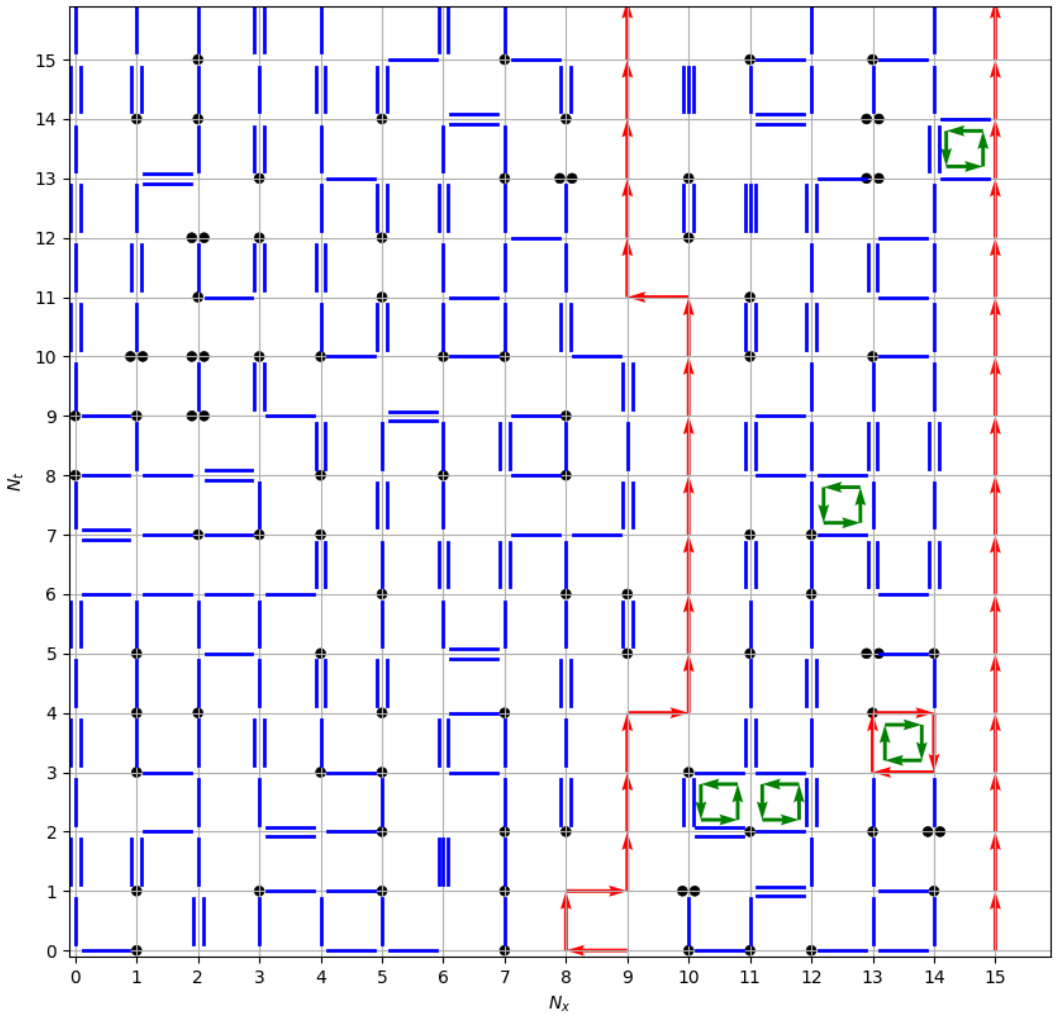

Lattice QCD Phase Diagram In and Away from the Strong Coupling Limit

Ph. de Forcrand,[1,2] J. Langelage,[1] O. Philipsen,[3] and W. Unger[3]
[1]*Institut für Theoretische Physik, ETH Zürich, CH-8093 Zürich, Switzerland*
[2]*CERN, Physics Department, TH Unit, CH-1211 Geneva 23, Switzerland*
[3]*Institut für Theoretische Physik, Goethe-Universität Frankfurt, 60438 Frankfurt am Main, Germany*
(Received 17 June 2014; published 6 October 2014)

We study lattice QCD with four flavors of staggered quarks. In the limit of infinite gauge coupling, "dual" variables can be introduced, which render the finite-density sign problem mild and allow a full determination of the $\mu - T$ phase diagram by Monte Carlo simulations, also in the chiral limit. However, the continuum limit coincides with the weak coupling limit. We propose a strong-coupling expansion approach towards the continuum limit. We show first results, including the phase diagram and its chiral critical point, from this expansion truncated at next-to-leading order.

DOI: 10.1103/PhysRevLett.113.152002 PACS numbers: 12.38.Gc, 12.38.Aw, 21.65.-f

The properties of QCD as a function of temperature T and matter density are summarized by its phase diagram, whose determination is a major goal of heavy-ion experiments. Although the quark-gluon plasma has been observed at high temperature, further features of the phase diagram, especially a possible QCD critical point, have not been identified yet. Heroic efforts have been devoted to numerical lattice simulations, which are the appropriate tool for nonperturbative phenomena like phase transitions. However, the fermion determinant becomes complex upon turning on a chemical potential μ coupled to the quark number. This so-called "sign problem" requires prohibitively large computer resources growing exponentially with the lattice 4-volume. Approaches to circumvent this problem are applicable when $\mu/T \lesssim 1$ only [1], and results on the QCD critical point are inconclusive. We want to make progress on this problem by means of a strong coupling expansion as applied to zero density in the early days of lattice gauge theory or, recently, to finite temperature and density with heavy quarks [2,3]. Here we want to address the opposite, chiral limit with a different strategy [4,5]. Note that both for heavy and chiral quarks, the strong coupling approach gives access also to the cold and dense regime of nuclear matter [3,6,7].

The sign problem occurs when elements $\langle\psi_i|\exp(-\delta\tau H)|\psi_j\rangle$ of the transfer matrix between states $|\psi_i\rangle$ and $|\psi_j\rangle$ sampled by Monte Carlo simulations become negative. This problem is representation dependent: in an eigenbasis of the Hamiltonian, all matrix elements would be non-negative. Thus, the sign problem will become milder if we can express the partition function in terms of approximate eigenstates. We know that QCD eigenstates are color singlets. Therefore, instead of performing Monte Carlo calculations on colored gauge links, as in the usual approach, we integrate the gauge links *first*, and work with the resulting color singlets. This strategy becomes particularly practical in the strong coupling limit. Here, we reexpress the partition function as a sum over configurations of hadron worldlines, similar to the "dual variables" used in [8]. The resulting sign problem is extremely mild, allowing us to simulate large lattices at arbitrarily large chemical potentials, and reliably obtain the full phase diagram. Of course, in the strong coupling limit $g \to \infty, \beta = 2N_c/g^2 \to 0$ (for N_c colors), the lattice is maximally coarse, whereas the continuum limit coincides with the weak coupling limit $g \to 0, \beta \to \infty$. In this Letter, we first summarize the $\beta = 0$ phase diagram and then explain how to include the first $\mathcal{O}(\beta)$ corrections, which allows us to measure Wilson loops at $\beta = 0$ and fermionic observables at $\mathcal{O}(\beta)$. We then present the QCD phase diagram for small $\beta > 0$. For $\mu = 0$, where we can cross-check with the full Monte Carlo approach, perfect agreement is found for small β.

We adopt the staggered fermion discretization and the Wilson plaquette action with the partition function

$$Z_{\mathrm{QCD}} = \int d\psi d\bar{\psi} dU e^{S_G + S_F},$$
$$S_G = \frac{\beta}{2N_c}\sum_P \mathrm{tr}[U_P + U_P^\dagger], \tag{1}$$

$$S_F = am_q \sum_x \bar{\psi}_x \psi_x + \frac{1}{2}\sum_{x,\nu} \eta_\nu(x)\gamma^{\delta_{\nu 0}} \times [\bar{\psi}_x e^{a_t\mu\delta_{\nu 0}} U_\nu(x)\psi_{x+\hat{\nu}} - \bar{\psi}_{x+\hat{\nu}} e^{-a_t\mu\delta_{\nu 0}} U_\nu^\dagger(x)\psi_x], \tag{2}$$

with a and a_t the spatial and temporal lattice spacings, γ the anisotropy by which one may tune a/a_t, m_q the quark mass, and μ the quark chemical potential. The η's are the usual ± 1 staggered phases. In the continuum limit $g \to 0$, our action describes QCD with 4 mass-degenerate quark species. In the opposite limit $g \to \infty$, the plaquette, four-link coupling β vanishes and so does the gauge action S_G. Then, the integration over the links $U_\nu(x)$ factorizes into a

product of one-link integrals which can be carried out analytically [9]. Finally, one performs the Grassmann integration over the fermion fields $\psi(x), \bar{\psi}(x)$, and obtains the partition function in terms of color-singlet degrees of freedom (mesons and baryons) [4], as a sum over discrete graphs on the lattice (with $N_c = 3$ for QCD):

$$Z_{SC} = \sum_{\{n,k,\ell\}} \prod_x w_x \prod_b w_b \prod_\ell w_\ell \tag{3}$$

$$w_x = \frac{N_c!}{n_x!}(2am_q)^{n_x}; \qquad w_b = \frac{(N_c - k_b)!}{N_c! k_b!}. \tag{4}$$

The mesons are represented by monomers $n_x \in \{0, \ldots, N_c\}$ on sites x and dimers $k_b \in \{0, \ldots, N_c\}$ on bonds $b = (x, \hat{\nu})$, whereas the baryons are represented by oriented self-avoiding loops ℓ. The weight w_ℓ of a baryonic loop ℓ and its sign depend on the loop geometry [10]. Configurations $\{n, k, \ell\}$ must satisfy at each site x the constraint inherited from Grassmann integration:

$$n_x + \sum_{\hat{\nu}=\pm\hat{0},\ldots,\pm\hat{d}} \left(k_{\hat{\nu}}(x) + \frac{N_c}{2} |\ell_{\hat{\nu}}(x)| \right) = N_c, \tag{5}$$

which implies that mesonic degrees of freedom cannot occupy baryonic sites.

This system has been studied for decades, both via mean field [11–16] and by Monte Carlo methods [5,7,10]. In recent years, the latter have undergone a revival using the worm algorithm [7,17,18], which violates the Grassmann constraint in order to sample the monomer two-point function $G(x, y)$, from which the chiral susceptibility can be obtained. These techniques have been applied to obtain all lattice data presented here. We study the chiral limit $m_q = 0$, which does not incur a penalty in computer cost, contrary to the usual determinantal approach. The staggered action S_F Eq. (2) then satisfies a $U(1)$ "remnant" chiral symmetry, which is spontaneously broken at low temperature and density, with order parameter $\langle\bar{\psi}\psi\rangle$. In Fig. 1 left, we show the (μ, T) phase diagram in the strong-coupling limit. It is qualitatively similar to the expected phase diagram of QCD in the chiral limit: the transition is of second order from $a\mu = 0$ up to a tricritical point $(a\mu_T, aT_T)$, then turns first order. At finite quark mass, the second order line turns into a crossover and the tricritical point into a second order critical endpoint. Note the different phase boundaries obtained from lattices with different numbers N_t of time slices: they converge to the continuous-time phase boundary as $N_t \to \infty$. The $1/N_t$ corrections can be absorbed in a parametrization of $a/a_t = f(\gamma)$, with γ the anisotropy needed to reach temperatures $aT > 1/2$ [18], resulting in Fig. 1, right [19].

A crucial question is whether this phase diagram develops new features as β is increased from 0 to ∞. At low temperature especially, things may change: when $\beta = 0$,

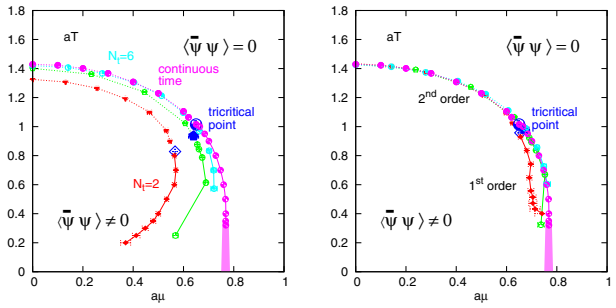

FIG. 1 (color online). Left: Lattice QCD phase diagram in the strong coupling limit, setting $a/a_t = \gamma^2$ following mean field. Different results are obtained for different numbers N_t of time slices $N_t = 2$, $N_t = 4$ [7], $N_t = 6$, and $N_t = \infty$ (i.e., continuous Euclidean time) [18]. Right: Same, with corrected anisotropy [19].

the transition at $\mu_c(T = 0)$ separates a chirally broken, baryon-free vacuum and a chirally symmetric, baryon-saturated state with one static baryon per lattice site. That is a very crude cartoon of a nuclear matter phase: in the continuum limit, depending on μ, it may evolve into a nuclear liquid, a crystalline phase, a color superconductor, etc. A first insight may be gained by considering $\mathcal{O}(\beta)$ corrections to the $\beta = 0$ phase diagram. At the same time, we can also address an interesting quantitative issue: the ratio $T_c(\mu = 0)/\mu_c(T = 0)$ is about $(160\,\mathrm{MeV})/(300\,\mathrm{MeV})$ $\sim$0.53 in nature, but about $1.402/0.75 \approx 1.87$ when $\beta = 0$. How does it vary with β?

Corrections to the strong coupling limit.—To go beyond the strong coupling limit, a systematic expansion in β of the partition function is needed, which we perform to first order. Writing the $\beta = 0$ partition function as $Z_{SC} = \int d\psi d\bar{\psi} Z_F$, with $Z_F(\psi, \bar{\psi}) = \int dU e^{S_F}$ the fermionic partition function, the $\beta \neq 0$ partition function Eq. (1) becomes

$$Z_{\mathrm{QCD}} = \int d\psi d\bar{\psi} dU e^{S_F + S_G} = \int d\psi d\bar{\psi} Z_F \langle e^{S_G} \rangle_{Z_F}, \tag{6}$$

$$\langle e^{S_G} \rangle_{Z_F} \simeq 1 + \langle S_G \rangle_{Z_F} = 1 + \frac{\beta}{2N_c} \sum_P \langle \mathrm{tr}[U_P + U_P^\dagger] \rangle_{Z_F}, \tag{7}$$

where Eq. (7) is an $\mathcal{O}(\beta)$ truncation. We thus need the expectation value of the elementary plaquette $\mathrm{tr}[U_P]$ in the strong coupling ensemble Z_F. The plaquette is composed of 4 links representing gluons, which provide new possibilities to make color singlets together with $\bar{\psi}_x \psi_{x\pm\hat{\mu}}$ propagating fermions. The modifications to the partition function are computed from the product $U_P = J_{ij} J_{jk} J_{kl} J_{li}$ of the one-link integrals $J_{ij} \equiv \int dU U_{ij} \exp(\bar{\psi} U \phi - \bar{\phi} U^\dagger \psi)$ around an elementary plaquette [20–22]

$$J_{ij} = -\sum_{k=1}^{3} \frac{(3-k)!}{3!(k-1)!} [M_\psi M_\phi]^{k-1} \bar{\phi}_j \psi_i + \frac{1}{12} \varepsilon_{i i_2 i_3} \varepsilon_{j j_2 j_3} \bar{\psi}_{i_2} \phi_{j_2} \bar{\psi}_{i_3} \phi_{j_3} - \frac{1}{3} \bar{B}_\psi B_\phi \bar{\phi}_j \psi_i, \quad (8)$$

where M and B represent mesons and baryons. The first term describes the propagation of a $(\bar{q}g)$ antiquark plus gluon together with 0 to 2 mesons, the second term describes a (qqg), the third term is a $(\bar{q}g)$ together with a baryon. From these, we compute the weight associated with a plaquette source term in the strong coupling configuration.

At the corners of the plaquette, the Grassmann variables ψ, ϕ are bound into baryons and mesons. Introducing a variable $q_P \in \{0, 1\}$ to mark the "excited" plaquettes P associated with the second term of Eq. (7), and corresponding variables q_b and $q_x = q_P$ for the links and the corners of such plaquettes, we can write the $\mathcal{O}(\beta)$ partition function in the same form as Eq. (3) with modified weights $\hat{w}$:

$$Z(\beta) = \sum_{\{n,k,\ell,q_P\}} \prod_x \hat{w}_x \prod_b \hat{w}_b \prod_\ell \hat{w}_\ell \prod_P \hat{w}_P \quad (9)$$

$$\hat{w}_x = w_x v_x, \qquad \hat{w}_b = w_b k_b^{q_b}, \quad (10)$$

$$\hat{w}_\ell = w_\ell \prod_\ell w_{B_i}(\ell), \qquad \hat{w}_P = \left(\frac{\beta}{2N_c}\right)^{q_P}, \quad (11)$$

where $v_x = (N_c - 1)!$ if x is the corner of an excited plaquette attached to an external meson line, $N_c!$ if it is attached to an external baryon line, 1 otherwise. Likewise, the weight of each baryon loop segment l is modified by a factor $w_{B_1} = 1/(N_c - 1)!$, $w_{B_2} = (N_c - 1)!$, where B_1 and B_2 correspond to the second and third expression in Eq. (8). We can sample this partition function by the same worm algorithm as for $\beta = 0$, adding a Metropolis step to update the plaquette variables q_P. In practice, we found it simpler to reweight from the $\beta = 0$ ensemble.

Qualitatively new features from $\mathcal{O}(\beta)$ contributions are as follows: (i) The constituent quarks of baryons and mesons can now separate; hadrons are no longer pointlike, but acquire a size $\sim a$. (ii) The baryon-baryon interaction can now proceed by quark exchange: it is no longer limited to the on-site Pauli exclusion principle. (iii) Chiral symmetry breaking becomes possible even in the dense phase similar to nuclear matter.

Wilson loops at $\beta = 0$.—Figure 2 illustrates the dependence of the Polyakov loop and of the plaquette (timelike and spacelike) on the chemical potential μ and the temperature T, at $\beta = 0$. The x axis represents the "distance" $a\sqrt{\mu^2 + T^2}$ from the vacuum, and different symbols are used for different values of μ/T. Several features are noticeable. (i) The plaquette has a nonzero value caused by the ordering effect of the fermions. Indeed, increasing

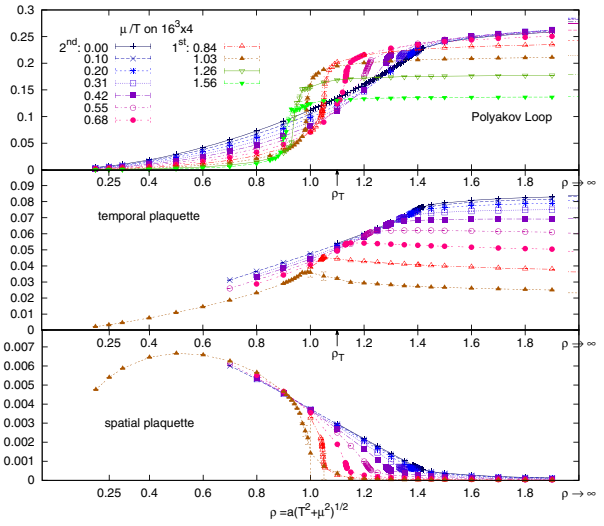

FIG. 2 (color online). Polyakov loop $\frac{1}{3}\langle \mathrm{tr} L \rangle$ and average spatial and temporal plaquette $\frac{1}{3}\langle \mathrm{tr} P_s \rangle$, $\frac{1}{3}\langle \mathrm{tr} P_t \rangle$ as a function of (μ, T) on a $16^3 \times 4$ lattice at $\beta = 0$. The colors label successive values of μ/T, and the x axis is $\rho \equiv a\sqrt{\mu^2 + T^2}$. At the tricritical point, $\rho_T = 1.10(2)$. Wilson loops are sensitive to the chiral transition and develop a discontinuity as the transition turns first order. $\langle \mathrm{tr} P_s \rangle$ varies oppositely to $\langle \mathrm{tr} P_t \rangle$, and remains very small.

the number of quark fields from 1 to 13 triggers restoration of the chiral symmetry [23]. (ii) The first-order phase transition is visible at large μ/T through a discontinuity in all Wilson loops, although it is associated with chiral symmetry. This can be assigned to the nonzero latent heat. (iii) Even in the regime of small μ/T, where the chiral transition is second order, the Polyakov loop is clearly sensitive to the transition as already found in U(3) gauge theory [24], reflecting the "entanglement" of confinement and chiral symmetry seen in effective models [25].

Phase diagram as a function of β.—We now show how to obtain the derivative $d(aT_c)/d\beta|_{\beta=0}$ of the chiral transition temperature aT_c with respect to β. Since the worm algorithm samples the two-point correlation function $G(x_1, x_2)$, we can measure its integral, which is equal to the chiral susceptibility χ (there is no disconnected piece $\langle \bar{\psi}\psi \rangle^2$ at $m_q = 0$ and in a finite volume, since $\langle \bar{\psi}\psi \rangle = 0$ also in the chirally broken phase),

$$\chi \equiv \langle (\bar{\psi}\psi)^2 \rangle = \frac{1}{L^3 N_t} \sum_{x_1, x_2} G(x_1, x_2). \quad (12)$$

At $\beta = 0$ and for some $\mu < \mu_T$, the critical temperature $aT_c(\mu)$ can be obtained from finite-size scaling: the curves $\chi(aT, L)L^{-\gamma/\nu}$ obtained on several lattice sizes L all intersect at $T = T_c(\mu)$, with a slope $\propto L^{1/\nu}$ at the intersection, as illustrated Fig. 3, left. The transition is in the $3dO(2)$ universality class with known critical exponents, which facilitates the analysis. In the region of a first-order

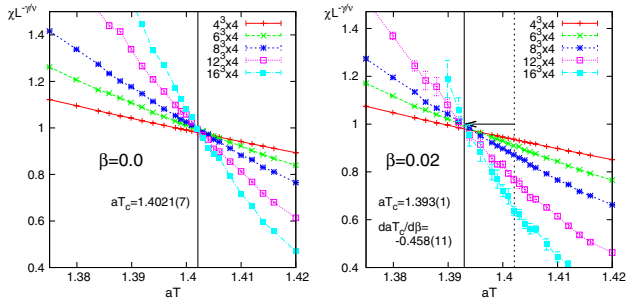

FIG. 3 (color online). The $\mu = 0$ transition temperature aT_c from finite-size scaling of the chiral susceptibility on $N_t = 4$ lattices. Left: $\beta = 0$. Right: $\beta = 0.02$. The arrow marks the shift in aT_c.

transition, $\mu > \mu_T$, this ansatz is modified following Ref. [26]. When we turn on β, the chiral susceptibility changes and we can measure its derivative

$$\frac{d\chi}{d\beta} = 3L^3 N_t(\langle(\bar{\psi}\psi)^2 P_t\rangle - \langle(\bar{\psi}\psi)^2\rangle\langle P_t\rangle). \tag{13}$$

While both the temporal and the spatial plaquettes formally enter in this expression, the latter is a factor $\gtrsim 10$ smaller than the former; cf. Fig. 2. The effect of β, to linear order, is illustrated in Fig. 3, right. At temperature aT_c, the rescaled chiral susceptibility $\chi L^{-\gamma/\nu}$ changes by $\beta(d\chi/d\beta)L^{-\gamma/\nu}$ [19], which produces a horizontal shift of the intersection point. At $\mu = 0$ (on $N_t = 4$ lattices), $aT_c|_{\beta=0} = 1.4021(7)$, $(d/d\beta)aT_c(\beta)|_{\beta=0} = -0.46(1)$.

We find that aT_c decreases as β increases: this is expected since a decreases. Our result agrees rather well with mean-field predictions [27,28]; see Fig. 4. More importantly, we can compare with the finite-β Hybrid Monte Carlo simulations at $\mu = 0$ (which are sign-problem free) performed on $N_t = 2$ and $N_t = 4$ [29–31] lattices with isotropic actions (i.e., $aT = 1/2$ and $1/4$) and extrapolated to zero quark mass. These data points are

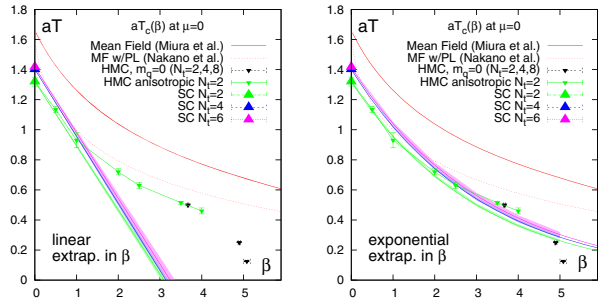

FIG. 4 (color online). Phase boundary in $\beta - aT$ plane at $\mu = 0$. Left: linear extrapolation. Right: exponential extrapolation. The boundary coincides very well with conventional Hybrid Monte Carlo data at large β. Also, the phase boundary is rather similar to the one obtained via a mean field theory approach without [27] and with Polyakov loop effects [28].

marked in black in Fig. 4. We have also computed $aT_c(\mu = 0)$ ourselves, using HMC on anisotropic lattices. As Fig. 4 left shows, our $\mathcal{O}(\beta)$ determination of $aT_c(\mu = 0)$ agrees perfectly with the linear approximation to the HMC determination. But the latter shows significant curvature. To better approximate the exact result, we perform an empirical, exponential extrapolation $aT_c(\mu = 0, \beta)/aT_c(\mu = 0, \beta = 0) \approx \exp(\beta(d/d\beta)aT_c|_{\beta=0})$. As seen in Fig. 4 right, it turns out that this approximation, which includes a resummation of higher-order β contributions, follows the exact HMC result up to $\beta \sim 5$ (or $a \sim 0.3$ fm), where the lattice theory is much closer to continuum physics. We have applied the same procedure to determine $aT_c(\beta)$ at nonzero chemical potential. $d(aT_c)/d\beta$ is clearly not as large as when $\mu = 0$. In fact, $d(aT_c)/d\beta$ becomes consistent with zero as μ approaches μ_T. The tricritical point and the first order line seem to only weakly depend on β. Thus, $T_c(\mu = 0)/\mu_c(T = 0)$ decreases at $\mathcal{O}(\beta)$ towards its continuum value.

The resulting phase diagram is illustrated Fig. 5 for $\beta = 0.5$, 1.0, and 1.5. We show the phase boundary obtained by linear reweighting, based on Eq. (7), and that obtained by exponential extrapolation, which works so well at $\mu = 0$. In both cases, the phase boundary becomes more "rectangular" at weaker coupling: the second-order transition line becomes "flatter" (less μ dependent), and the first-order transition line remains almost "vertical," leaving the tricritical point at the "corner of the rectangle." From the chiral susceptibility, no clear shift of $(a\mu_T, aT_T) = (0.65(2), 0.91(5))$ could be detected; however, from the baryon density n_B [19], we have evidence that the critical

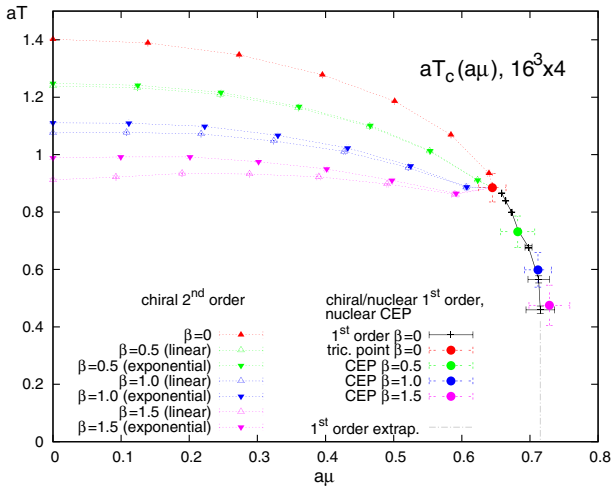

FIG. 5 (color online). Phase boundary in the $\mu - T$ plane in the strong coupling limit and extrapolated to finite β, comparing linear and exponential extrapolation. We do not observe a shift of the chiral tricritical point. The nuclear critical end point (CEP), determined from the reweighted baryon density, moves down along the first order line (extrapolated to $T = 0$ to guide the eye) as β is increased.

end point of the nuclear transition, which coincides with the chiral transition at $\beta = 0$, moves along the first order line, to smaller values of T. This is expected: as β increases, the lattice spacing a shrinks, and (aM_B) also, where M_B is the baryon mass. If $(a\mu_c)$ stays approximately constant as we observe, then the nuclear attraction responsible for the difference $[M_B - 3\mu_c(T = 0)]$, of about 300 MeV when $\beta = 0$ [7], becomes weaker. The weakening of the associated first-order transition brings the nuclear critical end point down in temperature.

We plan to study $\mathcal{O}(\beta^2)$ corrections next.

We would like to thank K. Miura and A. Ohnishi for helpful discussions. This work is supported by the Swiss National Science Foundation under Grant No. 200020-149723 and the Helmholtz International Center for FAIR within the LOEWE program launched by the State of Hesse.

[1] P. de Forcrand, *Proc. Sci.*, LATT2009 (2009) 010 [arXiv:1005.0539].
[2] M. Fromm, J. Langelage, S. Lottini, and O. Philipsen, J. High Energy Phys. 01 (2012) 042.
[3] M. Fromm, J. Langelage, S. Lottini, M. Neuman, and O. Philipsen, Phys. Rev. Lett. **110**, 122001 (2013).
[4] P. Rossi and U. Wolff, Nucl. Phys. **B248**, 105 (1984).
[5] U. Wolff, Phys. Lett. **153B**, 92 (1985).
[6] J. Langelage, M. Neuman, and O. Philipsen, arXiv:1403.4162.
[7] P. de Forcrand and M. Fromm, Phys. Rev. Lett. **104**, 112005 (2010).
[8] Y. Delgado Mercado, C. Gattringer, and A. Schmidt, Phys. Rev. Lett. **111**, 141601 (2013).
[9] K. E. Eriksson, N. Svartholm, and B. S. Skagerstam, J. Math. Phys. (N.Y.) **22**, 2276 (1981).
[10] F. Karsch and K. H. Mütter, Nucl. Phys. **B313**, 541 (1989).
[11] N. Kawamoto and J. Smit, Nucl. Phys. **B192**, 100 (1981).
[12] P. H. Damgaard, D. Hochberg, and N. Kawamoto, Phys. Lett. **158B**, 239 (1985).
[13] N. Bilic, F. Karsch, and K. Redlich, Phys. Rev. D **45**, 3228 (1992).
[14] N. Bilic, K. Demeterfi, and B. Petersson, Nucl. Phys. **B377**, 651 (1992).
[15] Y. Nishida, Phys. Rev. D **69**, 094501 (2004).
[16] A. Ohnishi, K. Miura, T. Nakano, and N. Kawamoto, *Proc. Sci.*, LATT2009 (2009) 160 [arXiv:0910.1896].
[17] D. H. Adams and S. Chandrasekharan, Nucl. Phys. **B662**, 220 (2003).
[18] W. Unger and P. de Forcrand, *Proc. Sci.*, LATT2011 (2011) 218 [arXiv:1111.1434].
[19] See Supplemental Material at http://link.aps.org/supplemental/10.1103/PhysRevLett.113.152002 for details on the anisotropy, the scaling analysis, and the baryon density.
[20] S. I. Azakov and E. S. Aliev, Phys. Scr. **38**, 769 (1988).
[21] M. Creutz, J. Math. Phys. (N.Y.) **19**, 2043 (1978).
[22] J. Langelage, Ph.D. thesis, Westfälische Wilhelms-Universität Münster, 2009.
[23] P. de Forcrand, S. Kim, and W. Unger, J. High Energy Phys. 02 (2013) 051.
[24] M. Fromm, J. Langelage, O. Philipsen, P. de Forcrand, W. Unger, and K. Miura, *Proc. Sci.*, LATT2011 (2011) 212 [arXiv:1111.4677].
[25] T. Hell, K. Kashiwa, and W. Weise, Phys. Rev. D **83**, 114008 (2011).
[26] C. Borgs and R. Kotecky, J. Stat. Phys. **61**, 79 (1990).
[27] K. Miura, T. Z. Nakano, A. Ohnishi, and N. Kawamoto, Phys. Rev. D **80**, 074034 (2009).
[28] T. Z. Nakano, K. Miura, and A. Ohnishi, Phys. Rev. D **83**, 016014 (2011).
[29] S. A. Gottlieb, W. Liu, D. Toussaint, R. L. Renken, and R. L. Sugar, Phys. Rev. D **35**, 3972 (1987).
[30] R. V. Gavai, S. Gupta, A. Irbäck, F. Karsch, S. Meyer, B. Petersson, H. Satz, and H. W. Wyld (MT(c) Collaboration), Phys. Lett. B **241**, 567 (1990).
[31] M. D'Elia and M.-P. Lombardo, Phys. Rev. D **67**, 014505 (2003).

Supplemental Material for "The lattice QCD phase diagram in and away from the strong coupling limit"

Ph. de Forcrand,[1,2] J. Langelage,[1] O. Philipsen,[3] and W. Unger[3]

[1] *Institut für Theoretische Physik, ETH Zürich, CH-8093 Zürich, Switzerland*
[2] *CERN, Physics Department, TH Unit, CH-1211 Geneva 23, Switzerland*
[3] *Institut für Theoretische Physik, Goethe-Universität Frankfurt, 60438 Frankfurt am Main, Germany*

(Dated: July 31, 2014)

PACS numbers: 12.38.Gc, 13.75.Cs, 21.10.Dr, 21.65.-f

ANISOTROPY

The anisotropy γ in the Dirac coupling of the fermionic action needs to be introduced in order to reach temperatures $aT > 1/2$. At $\mu = 0$, $aT_c \simeq 1.402$, hence the chiral transition at strong coupling can only be studied if the temporal lattice spacing a_t is much smaller than the spatial lattice spacing a. However, the precise correspondence between a/a_t and γ is not known. At weak coupling, $a/a_t = \gamma$, but there is no reason why this should hold at strong coupling. Indeed, mean field theory predicts that $a/a_t = \gamma^2$. This implies that $aT = \frac{\gamma^2}{N_t}$. With this assignment, we found (Fig. 1 left of the main text) that the N_t-dependence of the phase boundary is still strong, in particular for large chemical potential. Indeed, for every N_t, the phase boundary bends back toward the origin $(aT, a\mu) = (0, 0)$ when $\gamma \lesssim 1$, i.e. $aT \lesssim 1/N_t$. This re-entrance at low temperature is supported by mean-field calculations [1]. It only disappears in the continuous-time limit $N_t \to \infty$, $\gamma^2 \to \infty$ with γ^2/N_t fixed. There are two contributions to the observed $\mathcal{O}(1/N_t)$ corrections: (i) chiral observables are subject to non-monotonic corrections, as studied (at $\mu = 0$) in [2]; (ii) a coarse ($\gamma < 1$) temporal lattice spacing has little effect on the dense phase, which consists of static baryon lines; but it causes a systematic underestimate of the entropy of the vacuum phase, which consists of dimers branching in all directions (temporal and spatial) at each site. That is why the phase boundary shows re-entrance and $a\mu_c$ decreases in proportion with aT. Assuming the form $a/a_t = \gamma^2 \exp(c/\gamma^2)$ (with $c \simeq 0.29$) and allowing for small $\mathcal{O}(1/N_t)$ corrections (Fig. 1 right of the main text) produces much more consistent results.

At finite β, additionally to the anisotropy in the Dirac couplings, also the anisotropy $\gamma_G \equiv \sqrt{\beta_t/\beta_s}$ in the gauge action has to be taken into account. In the strong coupling regime, $a/a_t = \gamma_G^2$, which implies $\gamma_G = \gamma$. We have adopted this assignment to determine aT_c on anisotropic lattices in HMC simulations at $\mu = 0$.

β-DEPENDENCE OF CRITICAL TEMPERATURE

We determine the chiral transition temperature via critical scaling with 3d O(2) critical exponents γ, ν:

$$\chi_L(T,\beta)/L^{\gamma/\nu} = A + BtL^{1/\nu}, \quad t = \frac{T - T_c}{T_c} \qquad (1)$$

i.e. the chiral susceptibility data, when rescaled in this way, collapse on a universal scaling function, which is almost linear in the scaling window with non-universal coefficients $A \simeq 0.997(3)$ and $B \simeq -0.867(8)$ at $\mu = 0$. The shift in aT_c induced by a finite value of β is related to the L-dependence of the Taylor coefficient of χ, $\frac{d\chi}{d\beta}\Big|_{\beta=0}$. We indeed find that that this Taylor coefficient satisfies

$$\frac{1}{\chi}\frac{d\chi}{d\beta}\bigg|_{\beta=0} \simeq c_1 + c_2 L^{1/\nu} + c_3 t, \qquad (2)$$

with $c_2 = -0.283(2)$ at $\mu = 0$. The coefficient c_3 contributes at $\mathcal{O}(\beta^2)$ only. The variation of the critical temperature with β is then

$$\frac{d(aT_c)}{d\beta} = \frac{d\chi}{d\beta} L^{-\gamma/\nu} [d\chi/d(aT)]^{-1} = -aT_c \frac{A}{B} c_2, \qquad (3)$$

which characterizes the new intersection point. The L-independence of the shift $\Delta(aT_c) = \beta \frac{d(aT_c)}{d\beta}$ is a consistency check of our analysis.

BARYON DENSITY

We have measured the $\beta = 0$ baryon density n_B and reweighted towards finite β from the strong coupling ensemble via

$$\frac{dn_B}{d\beta} = 3L^3 N_t \left(\langle n_B P_t \rangle - \langle n_B \rangle \langle P_t \rangle \right), \qquad (4)$$

where, as in Eq. (13) of the main text, we can safely neglect the contribution of spatial plaquettes. This observable allows us to study the nuclear transition separately from the chiral transition. There is no reason to expect the two transitions to coincide for non-zero β. Although

we do not find that the first order lines of both transitions separate at $\mathcal{O}(\beta)$, we observe that the critical end point of the nuclear transition moves down along the first order line as β is increased. This is evident from the reweighted baryon density shown in Fig. 1. In contrast, we see no evidence that the chiral tricritical point varies with β at leading order.

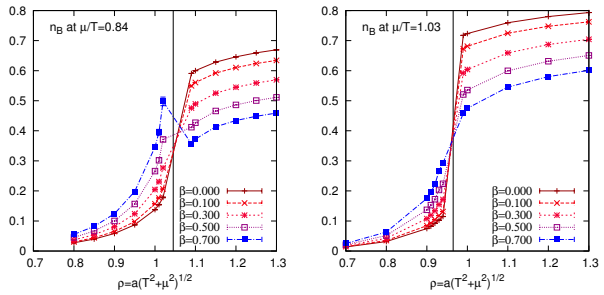

FIG. 1: Reweighted baryon density n_B for $\mu/T > \mu_T/T_T \approx 0.71$, i.e. in the first-order regime. The nuclear transition weakens as β is increased. At some β_c it turns from first order to second order, when the jump in the baryon density vanishes. The larger μ/T, the stronger the first order transition, and the larger β_c. *Left:* μ/T is close to the tricritical point, $\beta_c \approx 0.3$. *Right:* μ/T is larger and $\beta_c \approx 0.7$.

[1] Y. Nishida, *Phys. Rev. D* **69** (2004) 094501.
[2] W. Unger and P. de Forcrand, *PoS LATTICE* **2011** (2011) 218.

B.3 QCD phase diagram from the lattice at strong coupling [B3]

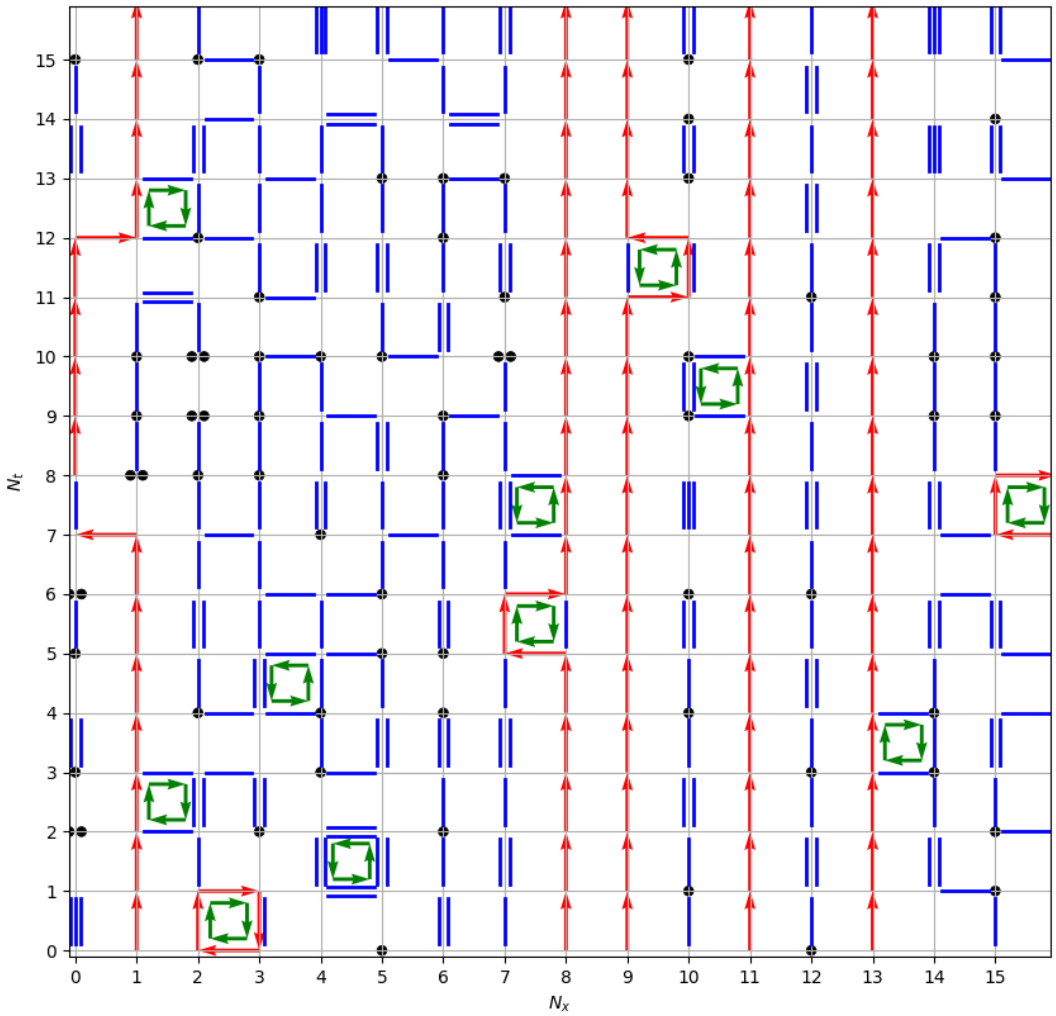

PROCEEDINGS OF SCIENCE

CERN-PH-TH-2015-067

QCD phase diagram from the lattice at strong coupling

Philippe de Forcrand
Institute for Theoretical Physics, ETH Zürich, CH-8093 Zürich, Switzerland and
CERN, Physics Department, TH Unit, CH-1211 Geneva 23, Switzerland
E-mail: forcrand@phys.ethz.ch

Owe Philipsen, Wolfgang Unger*
Institut für Theoretische Physik, Goethe-Universität Frankfurt,
60438 Frankfurt am Main, Germany
E-mail: philipsen@th.physik.uni-frankfurt.de
unger@th.physik.uni-frankfurt.de

The phase diagram of lattice QCD in the strong coupling limit can be measured in the full μ-T plane, also in the chiral limit. In particular, the phase diagram in the chiral limit features a tricritical point at some (μ_c, T_c). This point may be related to the critical end point expected in the QCD phase diagram. We discuss the gauge corrections to the phase diagram at strong coupling and compare our findings with various possible scenarios in continuum QCD. We comment on the possibility that the tricritical point at strong coupling is connected to the tricritical point in the continuum, massless QCD.

9th International Workshop on Critical Point and Onset of Deconfinement
17-21 November, 2014
ZiF (Center of Interdisciplinary Research), University of Bielefeld, Germany

*Speaker.

1. Motivation

The QCD phase diagram is conjectured to have a rich phase structure. At low temperatures, QCD has a vacuum and nuclear matter phase; at high temperatures and/or densities, QCD matter develops a qualitatively different phase where quarks are liberated from confinement - the so-called quark gluon plasma (QGP). While there is strong evidence for a crossover transition from the hadronic phase to the QGP for zero baryon chemical potential μ_B, there is no evidence for a true phase transition at higher densities. Lattice studies of QCD have aimed to extend the simulations to finite quark chemical potential $\mu = \frac{1}{3}\mu_B$, but the available methods are limited to $\mu/T \lesssim 1$ due to the sign problem: Monte Carlo simulations sample a probability distribution and hence rely on the condition that the statistical weights are positive. In the conventional approach to lattice QCD based on the fermion determinant, the weight for the fermion determinant becomes complex as soon as the chemical potential is non-zero. The sign problem (more precisely in this context: the complex phase problem) is severe, prohibiting direct simulations for $\mu > 0$ - which is also due to the fact that Monte Carlo is performed on the colored gauge fields.

However, there is a representation of lattice QCD which does not suffer severely from the sign problem: in this representation, the lattice degrees of freedom are color singlets. The complex phase problem is reduced to a mild sign problem induced by geometry-dependent signs of fermionic world lines. Such a "dual" representation of lattice QCD has been derived for staggered fermions in the strong coupling limit, that is in the limit of infinite gauge coupling $g \to \infty$ [7]. In this limit, only the fermionic action contributes to the path integral, whereas the action describing gluon propagation is neglected. QCD at strong coupling has been studied extensively since 30 years, both with mean field methods [1, 2, 3, 4, 5, 6] and by Monte Carlo simulations [7, 8, 9, 10, 11, 12]. Those studies have been limited to the strong coupling limit, which corresponds to rather coarse lattices. However, recently [13] we were able to include the leading order gauge corrections to the partition function. The effects of these gauge corrections on the phase diagram will be discussed below.

2. The chiral and nuclear transition in the strong coupling limit

The path integral of staggered fermions in the strong coupling limit can be rewritten exactly as a partition function of a monomer+dimer+flux system. The reformulation proceeds in two steps: first the gauge links (gluons) are integrated out, which confines the quark fields $\psi(x)$ into color singlets, the hadrons: those are the mesons $M(x) = \bar{\psi}(x)\psi(x)$ and the baryons $B(x) = \frac{1}{6}\varepsilon_{i_1 i_2 i_3}\psi_{i_1}(x)\psi_{i_2}\psi_{i_3}(x)$. In the second step, also the quarks are integrated out, which allows to express the partition function via integer variables:

$$Z_{SC}(m_q,\mu) = \sum_{\{k_b,n_x,\ell\}} \underbrace{\prod_{b=(x,\mu)} \frac{(3-k_b)!}{3!k_b!}}_{\text{meson hoppings } M_x M_y} \underbrace{\prod_x \frac{3!}{n_x!}(2am_q)^{n_x}}_{\text{chiral condensate } M_x} \underbrace{\prod_\ell w(\ell,\mu)}_{\text{baryon hoppings } \bar{B}_x B_y} \tag{2.1}$$

with $k_b \in \{0,\ldots 3\}$, $n_x \in \{0,\ldots 3\}$, $\ell_b \in \{0,\pm 1\}$. Since the quark fields are treated as anti-commuting Grassmann variables in the path integral, the integration realizes a Pauli exclusion principle called

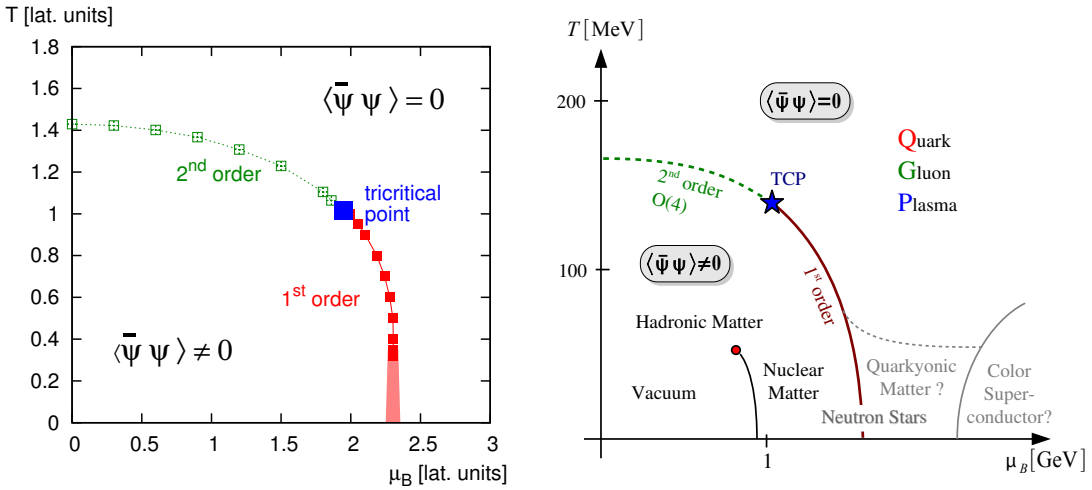

Figure 1: The Phase diagram in the strong coupling limit (*left*), as measured in a Monte Carlo simulation, compared to the standard expectation of the continuum QCD phase diagram (*right*). Both diagrams are for massless quarks.

the Grassmann constraint:

$$n_x + \sum_{\hat{v}=\pm\hat{0},\ldots,\pm\hat{d}} \left(k_{\hat{v}}(x) + \frac{N_c}{2} |\ell_{\hat{v}}(x)| \right) = 3. \tag{2.2}$$

This constraint restricts the number of admissible configurations $\{k_b, n_x, \ell\}$ in Eq. (2.1) such that mesonic degrees of freedom always add up to 3 and baryons form self-avoiding loops not in contact with the mesons. The weight $w(\ell,\mu)$ and sign $\sigma(\ell) = \pm 1$ for an oriented baryonic loop ℓ depend on the loop geometry. The partition function Eq. (2.1) describes effectively only one quark flavor, which however corresponds to four flavors in the continuum (see Sec. 4). It is valid for any quark mass. We will however restrict here to the theoretically most interesting case of massless quarks, $m_q = 0$. In fact, in this representation the chiral limit is very cheap to study via Monte Carlo, in contrast to conventional determinant-based lattice QCD where the chiral limit is prohibitively expensive.

For staggered fermions in the strong coupling limit, there is a remnant of the chiral symmetry $U_{55}(1) \subset SU_L(N_f) \times SU_R(N_f)$. This symmetry is spontaneously broken at $T = 0$ and is restored at some critical temperature T_c with the chiral condensate $\langle \bar{\psi}\psi \rangle$ being the order parameter of this transition. As shown in Fig. 1 (*left*), we find that this transition is of second order. This is analogous to the standard expectation in continuum QCD with $N_f = 2$ massless quarks, where the transition is also believed to be of second order. Moreover, both for our numeric finding at strong coupling and for the expectation in the continuum, the transition turns into first order as the chemical potential is increased. Thus the first order line ends in a tricritical point, which is the massless analogue of the chiral critical endpoint sought for in heavy ion collisions.

In fact, at strong coupling, the zero temperature nuclear transition at $\mu_{B,c} \simeq m_B$ is intimately connected to the chiral transition, and they coincide as long as the transition is first order. The reason for this is the saturation on the lattice due to the Pauli principle: in the nuclear matter

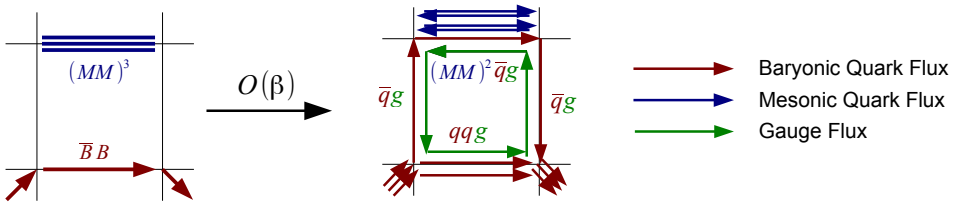

Figure 2: Example of an $\mathcal{O}(\beta)$ diagram. On an excited plaquette, color singlets can also be composed of quark-quark-gluon or antiquark-gluon combinations. Whereas in the strong coupling limit baryons are pointlike, they become extended objects due to the gauge corrections.

phase at $T = 0$, the lattice is completely filled with baryons, leaving no space for a non-zero chiral condensate to form (in terms of the dual variables, there is no space for monomers on the lattice). This is certainly a lattice artifact which disappears in the continuum limit, where the nuclear phase behaves like a liquid rather than a crystal.

The ultimate question is whether the tricritical point at strong coupling is related to the hypothetical tricritical point in continuum massless QCD. If we can establish such a connection numerically, this would be strong evidence for the existence of a chiral critical endpoint in the μ-T phase diagram of QCD. To answer this question, it is necessary to go away from the strong coupling limit and incorporate the gauge corrections, which will lower the lattice spacing and eventually allow to make contact to the continuum.

3. Gauge Corrections to the strong coupling phase diagram

Lattice QCD in the strong coupling limit is defined by the the lattice coupling $\beta = \frac{6}{g^2} \to 0$ as $g \to \infty$. Going away from the strong coupling limit is realized by making use of strong coupling expansions in β. We have recently shown how to incorporate the leading order gauge corrections $\mathcal{O}(\beta)$ [13]. In a nutshell, the strategy is to compute link integrals at the boundary of "excited" plaquettes, which correspond to gluonic excitations. Introducing a variable $q_P \in \{0,1\}$ to mark the "excited" plaquettes P, the $\mathcal{O}(\beta)$ partition function can be expressed in a similar fashion as Eq. (2.1) with modified weights $\hat{w}$ (for details see [13]):

$$Z(\beta) = \sum_{\{n,k,\ell,q_P\}} \prod_x \hat{w}_x \prod_b \hat{w}_b \prod_\ell \hat{w}_\ell \prod_P \hat{w}_P, \qquad \hat{w}_P = \left(\frac{\beta}{6}\right)^{q_P}. \tag{3.1}$$

We can sample this partition function by the same algorithm (variant of the worm algorithm) as for $\beta = 0$, adding a Metropolis accept/reject step to update the plaquette variables q_P. These simulations have been carried out for $N_\tau = 4$ and various lattice volumes $N_\sigma = 4, 6, 8, 12, 16$ to perform finite size scaling and to measure the phase boundary as a function of the chemical potential. In contrast to the strong coupling limit, where the color singlets are entirely composed of quarks and antiquarks, including the gauge corrections allows color singlets to be composed of quark-quark-gluon or antiquark-gluon color singlet states, as shown in Fig. 2. There are two qualitatively new features that arise when incorporating the $\mathcal{O}(\beta)$ corrections:

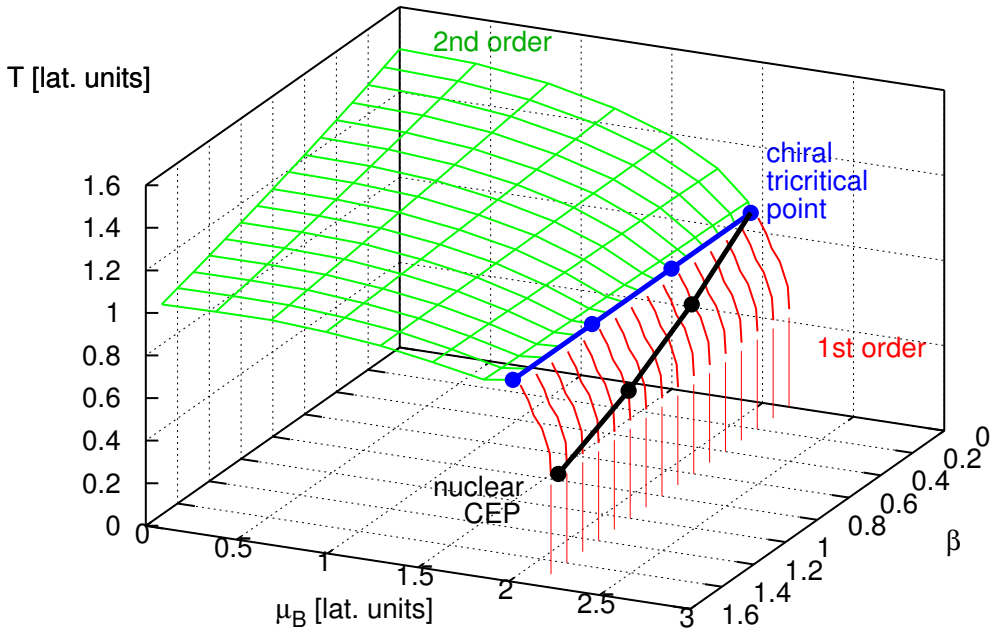

Figure 3: Phase boundary in the μ-T plane extended to finite β. The backplane corresponds to the strong coupling limit $\beta = 0$. The second order phase boundary is lowered by increasing β. We do not observe a shift of the chiral tricritical point. However, the nuclear critical endpoint (CEP), determined from the baryon density, moves down along the first order line (extrapolated to $T = 0$ to guide the eye) as β is increased.

1. Baryons are point-like in the strong coupling limit, the lattice spacing is too coarse to resolve the internal structure of the baryon. Including the gauge correction, baryons become extended objects, spread over one lattice spacing.

2. The nuclear potential in the strong coupling limit is of entropic nature, where two static baryons interact merely by the modification of the pion bath. With the leading order gauge correction, pion exchange is possible as the Grassmann constraint is relaxed: on excited plaquettes, the degrees of freedom in Eq. (2.2) add up to 4 instead of 3.

These features will have an impact on the phase boundary. In Fig. 3, the effect of the gauge corrections is shown. We find that the second order phase boundary is lowered, as expected because the critical temperature in lattice units drops as the lattice spacing is decreased with increasing β. However, we find the chiral tricritical point and the first order transition to be invariant under the $\mathcal{O}(\beta)$ corrections. We want to stress that there are actually two end points, which split due to the gauge corrections: the second order end point of the nuclear liquid-gas transition is traced by looking at the nuclear density as an order parameter. We expect the nuclear and the chiral first order transition to split, such that at $T = 0$ there are three different phases instead of two phases (as

shown in Fig. 1 *right*). The nuclear phase is in the continuum distinct from the chirally restored phase. As a first evidence for this splitting, we find that the nuclear critical end point separates from the chiral tricritical point.

4. Relation between the strong coupling phase diagram and continuum QCD

In Fig. 4 we speculate how the separation of the first order transitions could be realized at larger values of β. Moreover, we can distinguish at least three scenarios (A,B,C) on how the chiral tricritical point depends on β. These scenarios start from the same phase diagram in the strong coupling limit, but have different continuum limits at $\beta \to \infty$ ($a \to 0$). In all three scenarios, a tricritical point exists at $\mu = 0$, $\beta > 0$: it must exist because the finite-temperature $\mu = 0$ transition, which is of second order for $\beta = 0$, is of first order for $\beta = \infty$, following the argument of [14] which applies to the continuum, $N_f = 4$ theory.

1. In scenario (A) the chiral transition remains first order for all values of μ_B. Hence the tricritical line turns towards $\mu = 0$ at some finite $\beta_{\rm tric}^{(\mu=0)}$.

2. In scenario (B) the chiral transition weakens and hence turns second order, but strengthens again to turns first order at larger μ_B.

3. In scenario (C) the chiral transition weakens and remains second order. In that case the tricritical line bends towards larger μ and eventually vanishes at some finite $\beta_{tric}^{(T=0)}$.

In order to discuss the relation between the phase diagram in the μ-T plane for $N_f = 4$ massless quarks with the more physical scenario $N_f = 2+1$ with 2 massless up and down quarks and one physical strange quark, we show phase diagrams in the N_f-μ plane. Interpolating between integer numbers of massless flavors N_f and $N_f + 1$ can be realized by decreasing the mass of an additional flavor from infinity to zero. In all scenarios it is assumed that for $N_f = 2$, the chiral transition is second order, and that there is a tricritical strange quark mass m_s^{tric} separating it from the $N_f = 3$ first order transition, as shown in the so-called Columbia plot, Fig. 5. Note that whether $N_f = 2$ is indeed second order and thus whether m_s^{tric} exists and also whether it is larger or smaller than the physical strange quark mass is still under debate [15]. The standard scenario of QCD in the chiral limit, as shown in Fig. 1 (right), corresponds to scenario (B) in Fig 4. However, the non-standard scenario (C) is supported by Monte Carlo simulations for imaginary chemical potential and analytic continuation [15, 16]: these studies suggest (at least for small chemical potential) that the chiral transition weakens with chemical potential, making the $N_f = 3$ first order region in Fig. 5 to shrink with increasing μ_B. This should also be the case for $N_f = 4$.

A last comment on staggered fermions is in order: one of the lattice artifacts is due to the way this discretization solves the so-called fermion doubling problem: At strong coupling, there is effectively only one quark flavor, whereas in the continuum limit the same action describes 4 flavors due to the fermion doubling. Instead of 15 Goldstone bosons that are present in the $N_f = 4$ continuum theory, there is only one Goldstone boson at strong coupling, since the others 14 receive masses from lattice artifacts (called taste-splitting). In the determinant-based approach, the problem is solved by "rooting": taking the root of the fermion determinant to reduce the number of flavors from 4 to 2 (and the number of Goldstone bosons from 15 to 3). This strategy is not available

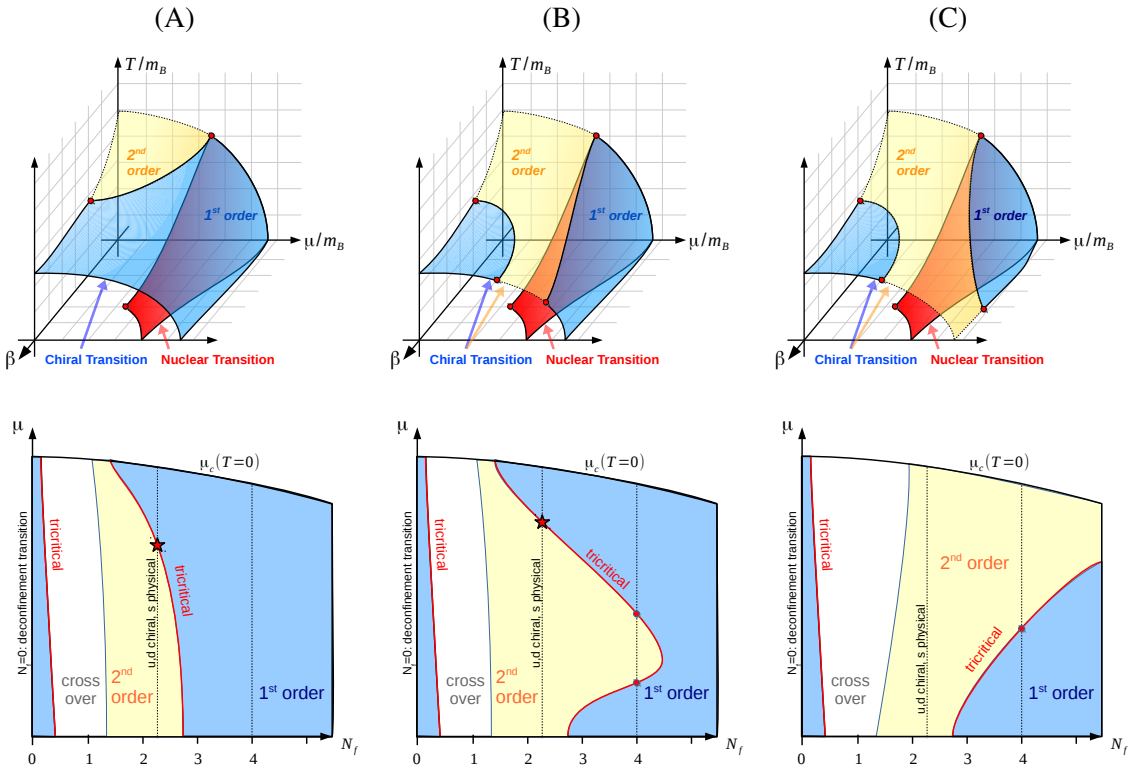

Figure 4: *Top row:* Various scenarios for extending the phase diagram in the strong coupling limit ($\beta = 0$) toward the the continuum limit ($\beta \to \infty$). All three scenarios assume that the nuclear and chiral transition split, and that at $\mu = 0$ the chiral transition is of first order (since in the continuum $N_f = 4$). In the strong coupling limit, the chiral transition at $\mu = 0$ is second order (corresponding to $N_f = 1$ and the doublers decoupled), hence there must be a tricritical point at some $\beta_{tric}^{(\mu=0)}$. It is an open question whether the tricritical point at strong coupling is connected to this tricritical point at $\beta_{tric}^{(\mu=0)}$ (*left*), or connected to the speculated tricritical point in the continuum (*center*) or terminates at some finite β at $T = 0$ (*right*).
Bottom row: the corresponding scenarios for the finite temperature chiral transition in the $\mu - N_f$ phase diagram, showing the possible relation of the tricritical point at $N_f = 4$ with those at $N_f = 2+1$, assuming the chiral limit for the light quarks and a physical strange quark mass. The μ-N_f is limited by the line $\mu_c(T = 0)$, beyond which chiral symmetry is restored. *Left:* For $N_f = 4$, the transition is of first order for all values of μ. *Center:* The tricritical point at $N_f = 4$ is is connected to the tricritical point at $N_f = 2+1$. This would be evidence for the existence of the critical end point in the QCD phase diagram for physical quark masses. *Right:* The $N_f = 4$ first order region does not extend to $N_f = 2+1$, where it remains second order. This second order transition turns into a crossover immediately as $m_u, m_d > 0$, so in this scenario there is no chiral critical end point at physical quark masses.

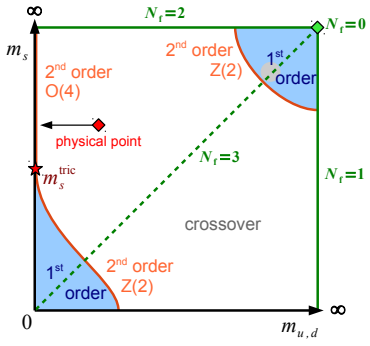

Figure 5: The Columbia plot with the assumption $m_s^{phys} > m_s^{tric}$, which implies that the chiral transition is second order for $N_f = 2$. The arrow points towards the $N_f = 2+1$ chiral light quark masses and physical strange quark mass as denoted in the bottom row of Fig. 4 in between $N_f = 2$ and $N_f = 3$.

in our dual-variable approach. Although the strong coupling limit has effectively only one flavor, the residual chiral symmetry is that of a $N_f = 4$ continuum theory, with one true Goldstone boson which even persists when the chiral anomaly $U_A(1)$ is present for $\beta > 0$. This is in contrast to a genuine $N_f = 1$ theory in the continuum which has no Goldstone bosons at all. The chiral anomaly breaks the chiral symmetry explicitly, driving the chiral transition into a crossover (corresponding to the lower right corner of the Columbia plot Fig. 5). Hence the deconfinement transition at $N_f = 0$ is most likely completely separate from the chiral transition for $N_f \geq 2$, as shown in all three scenarios Fig. 4 (bottom).

5. Outlook for future investigations

There are various ways to discretize fermions on the lattice, with staggered fermions and Wilson fermions the most widely used for thermodynamics studies. They describe the same physics in the continuum limit only. At finite lattice spacing, and in particular at strong coupling, both discretizations are quite different. In particular, the spin and the kinetic term of the fermion action are treated very differently. A dimer+flux representation is also possible for Wilson fermions. Such a representation was so far only determined for lattice QED [17, 18], since the Grassmann integration is much more involved for $N_c > 1$.

As a matter of principle, for both lattice discretizations, the gauge action can be incorporated order by order in β. There are however technical difficulties that remain to be solved. A new strategy to study both lattice discretizations on a par is to expand both in systematically in β and the inverse quark mass by making use of a Hamiltonian formulation [19]. The partition function is then expressed by a Hamiltonian composed by operators:

$$Z = \mathrm{Tr}[e^{\beta \mathscr{H}}], \qquad \mathscr{H} = \frac{1}{2} \sum_{\langle x,y \rangle} \sum_{Q_i} J^{+}_{Q_i(x)} J^{-}_{Q_i(y)}, \qquad J^{-}_{Q_i} = (J^{+}_{Q_i})^{\dagger} \tag{5.1}$$

where the generalized quantum numbers Q_i (spin, parity,flavor) are globally conserved, and nearest neighbor interactions are characterized by the operators $J^{+}_{Q_i(x)} J^{-}_{Q_i(y)}$, which raise the quantum number Q_i at site x and lowers it at a neighboring site y (see [19] for the case of $N_f = 1, 2$ for staggered fermions). For both staggered fermions and Wilson fermions, the matrices $J^{\pm}_{Q_i}$ contain vertex weights which are the crucial input to sample the corresponding partition function. The plan for the future is to do so with a quantum Monte Carlo algorithm. Comparing both fermion discretizations order by order in the strong coupling expansion will help to discriminate lattice discretization errors from the genuine physics, in particular with respect to QCD at finite density.

Acknowledgement - This works was supported by the Helmholtz International Center for FAIR within the LOEWE program launched by the State of Hesse.

References

[1] N. Kawamoto and J. Smit, Nucl. Phys. B **192** (1981) 100.

[2] P. H. Damgaard, D. Hochberg and N. Kawamoto, Phys. Lett. B **158** (1985) 239.

[3] N. Bilic, F. Karsch, K. Redlich, *Phys. Rev. D* **45** (1992) 3228.

[4] N. Bilic, K. Demeterfi, B. Petersson, *Nucl. Phys. B* **377** (1992) 3651.

[5] Y. Nishida, *Phys. Rev. D* **69** (2004) 094501.

[6] K. Miura, T. Z. Nakano, A. Ohnishi and N. Kawamoto, *Phys. Rev. D* **80** (2009) 074034.

[7] P. Rossi, U. Wolff, *Nucl. Phys. B* **258** (1984) 105;

[8] U. Wolff, *Phys. Lett. B* **153** (1985) 92.

[9] F. Karsch, K. H. Mütter, *Nucl. Phys. B* **313** (1989) 541.

[10] D. H. Adams and S. Chandrasekharan, *Nucl. Phys. B* **662** (2003) 220.

[11] P. de Forcrand and M. Fromm, Phys. Rev. Lett. **104** (2010) 112005 [arXiv:0907.1915 [hep-lat]].

[12] W. Unger and P. de Forcrand, PoS LATTICE **2011** (2011) 218 [arXiv:1111.1434 [hep-lat]].

[13] P. de Forcrand, J. Langelage, O. Philipsen and W. Unger, *Phys. Rev. Lett.* **113** (2014) 152002.

[14] R. D. Pisarski and F. Wilczek, Phys. Rev. D **29** (1984) 338.

[15] C. Bonati, P. de Forcrand, M. D'Elia, O. Philipsen and F. Sanfilippo, Phys. Rev. D **90** (2014) 7, 074030 [arXiv:1408.5086 [hep-lat]].

[16] P. de Forcrand and O. Philipsen, JHEP **0811** (2008) 012 [arXiv:0808.1096 [hep-lat]].

[17] M. Salmhofer, Nucl. Phys. B **362** (1991) 641.

[18] K. Scharnhorst, Nucl. Phys. B **479** (1996) 727 [hep-lat/9604024].

[19] W. Unger and P. de Forcrand, PoS LATTICE **2012** (2012) 194 [arXiv:1211.7322 [hep-lat]].

B.4 Dual Formulation and Phase Diagram of Lattice QCD in the Strong Coupling Regime [B4]

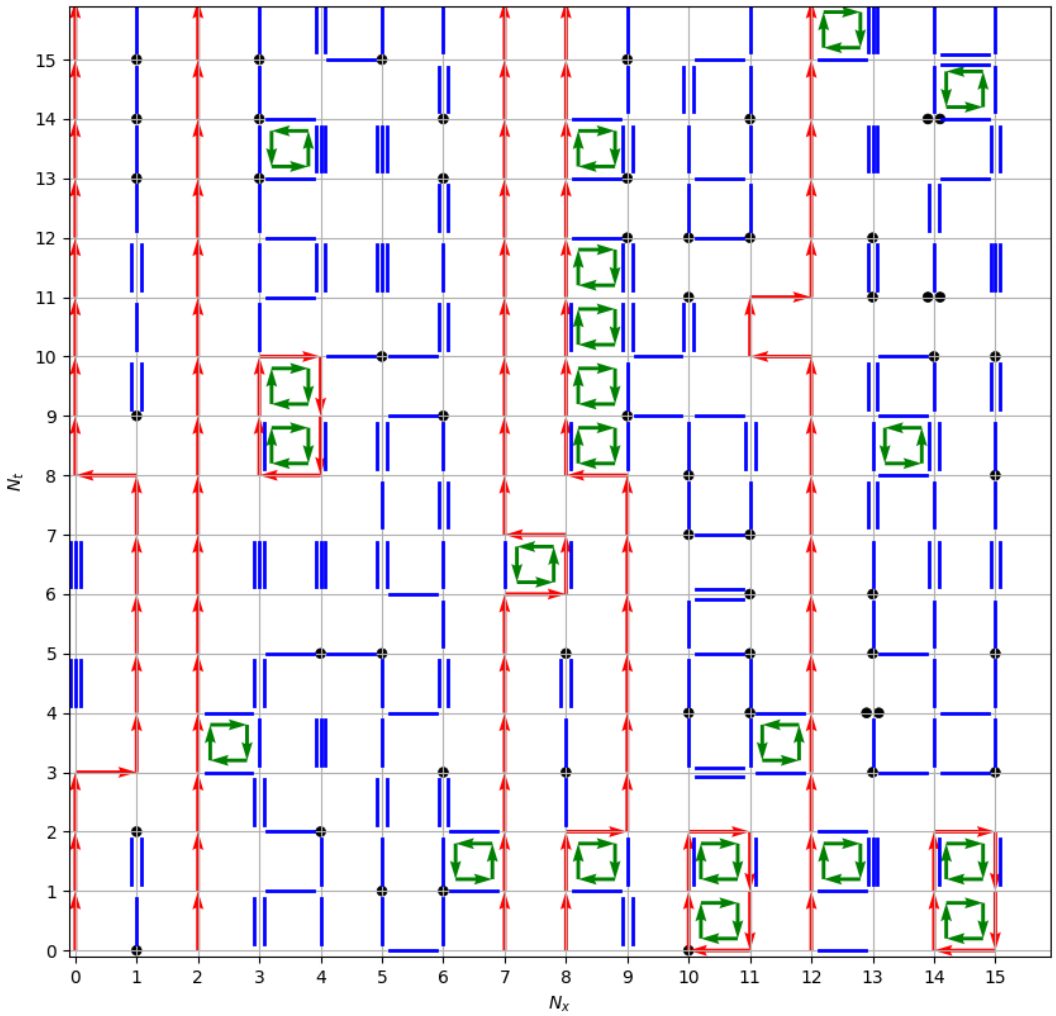

EPJ Web of Conferences **175**, 07047 (2018) https://doi.org/10.1051/epjconf/201817507047
Lattice 2017

Dual Formulation and Phase Diagram of Lattice QCD in the Strong Coupling Regime

Giuseppe Gagliardi[1], *Jangho* Kim[1,2⋆], and *Wolfgang* Unger[1⋆⋆]

[1] *Fakultät für Physik, Universität Bielefeld, D-33615 Bielefeld, Germany*
[2] *National Superconducting Cyclotron Laboratory and Department of Physics and Astronomy, Michigan State University, East Lansing, Michigan 48824, USA*

Abstract. We present the computation of invariants that arise in the strong coupling expansion of lattice QCD. These invariants are needed for Monte Carlo simulations of Lattice QCD with staggered fermions in a dual, color singlet representation. This formulation is in particular useful to tame the finite density sign problem. The gauge integrals in this limiting case $\beta \to 0$ are well known, but the gauge integrals needed to study the gauge corrections are more involved. We discuss a method to evaluate such integrals.
The phase boundary of lattice QCD for staggered fermions in the $\mu_B - T$ plane has been established in the strong coupling limit. We present numerical simulations away from the strong coupling limit, taking into account the higher order gauge corrections via plaquette occupation numbers. This allows to study the nuclear and chiral transition as a function of β.

1 Introduction

The finite baryon density sign problem in lattice QCD hinders a direct evaluation of the phase structure of QCD in the $\mu_B - T$ plane. In particular, the existence of a critical end-point (CEP) that is sought for in heavy ion collision experiments at RHIC and LHC could not be established yet via lattice simulations. Although the well established methods for small μ_B/T, such as Taylor expansion, reweighting and analytic continuation from imaginary chemical potential can in principle make statements about the existence of the CEP, it is likely that the CEP, if it exists, has a quite large μ_B^{crit}, such that it is not within reach with the aforementioned methods.

In recent years, many alternative methods have been proposed and tested to circumvent the finite density sign problem. Most notably, the complex Lagenvin method together with gauge cooling could address full QCD in the deconfined phase [1, 2]. Another method based on complexified QCD, the Lefschetz thimbles, are currently applied to QCD-inspired models with few degrees of freedom, but the method is far from being applicable to full lattice QCD [3–5].

A promising alternative strategy is to change the degrees of freedom of the original partition function. Since the sign problem is representation dependent, it may be possible to find a different set of

⋆ Speaker, e-mail: jangho@physik.uni-bielefeld.de
⋆⋆ Speaker, e-mail: wunger@physik.uni-bielefeld.de

variables that are closer to the true eigenstates of the Hamiltonian. Finding such a basis would reduce the sign problem significantly, or even solve it. Changing the degrees of freedom can be for example obtained by a Hubbard-Stratonovich transformation [6], or by introducing auxiliary fields. Another way is to integrate out some of the degrees of freedom to obtain a "dual" representation in terms of world lines. This strategy has been successfully applied to address sign problems in models with an abelian gauge group (such as the massless Schwinger model [7], and the gauge-Higgs models [8]) It is however quite non-trivial to find a dual representation for non-abelian gauge groups. A recent attempt is to decompose the non-abelian components into abelian "color cycles" [9].

Our attempt to perform Monte Carlo simulations on the QCD phase diagram is based on the strong coupling expansion. The starting point is the well-established partition function of staggered fermions in the strong coupling limit. Here, the phase diagram is well established. We then propose a dual representation in terms of world lines and world sheets that incorporates some contributions of the gauge action. For small β, we are able to determine the phase boundary between the chirally broken and chirally restored phase. The leading order correction has been addressed via reweighting from the strong coupling ensemble to $\beta > 0$ in [10]. We go beyond this scope by directly sampling the partition function including next to leading order gauge corrections.

2 Link Integration

2.1 Lattice Action and Partition Function

We consider the standard lattice action for staggered fermions (no rooting, no improvement) together with the Wilson gauge action:

$$S_{\mathrm{F}} = \sum_x \left(\sum_\mu \gamma^{\delta_{\mu 0}} \eta_\nu(x) \left(e^{a_t \mu \delta_{\mu 0}} \bar{\chi}_x U_\mu(x) \chi_{x+\hat{\mu}} - e^{-a_t \mu \delta_{\mu 0}} \bar{\chi}_{x+\hat{\mu}} U_\mu^\dagger(x) \chi_x \right) + 2am_q \bar{\chi}_x \chi_x \right), \tag{1}$$

$$S_{\mathrm{G}} = \frac{\beta}{2N_{\mathrm{c}}} \sum_{P=(x,\mu<\nu)} \mathrm{tr}[U_P + U_P^\dagger], \qquad U_P = U_\mu(x) U_\nu(x+\hat{\mu}) U_\mu(x+\hat{\nu})^\dagger U_\nu(x)^\dagger, \tag{2}$$

with $a_t\mu = \frac{1}{N_{\mathrm{c}}} a_t \mu_B$ the quark chemical potential. The only modification is that we introduced a bare anisotropy γ, favoring temporal fermion hoppings over spatial fermion hoppings, giving rise to an anisotropy of the lattice spacings $\frac{a}{a_t} = \xi(\gamma)$. This will allow us later to vary the temperature continuously in the strong coupling regime.

The standard approach for lattice simulations is to integrate out the Grassmann-valued staggered fermions χ and $\bar{\chi}$ to obtain the fermion determinant. However, the fermion determinant becomes complex for finite quark chemical potential, resulting in the finite density sign problem. Our strategy is to expand the action $S = S_F + S_G$ both in the fermion hoppings and in $\beta = \frac{2N_{\mathrm{c}}}{g^2}$. Then we exchange the order of integration, i.e. integrate out the link variables analytically first, and afterwards the Grassmann variables. The remaining degrees of freedom will be color singlets on the links, and the plaquette occupation numbers n_P (from the moments of the fundamental plaquettes $\mathrm{tr}[U_P]^{n_P}$) and $\bar{n}_P$ (from the moments of the anti-fundamental plaquettes $\mathrm{tr}[U_P^\dagger]^{\bar{n}_P}$).

The fermions can be gathered into matrices

$$\mathcal{M}^\dagger{}_j^{\ i} = \eta_\mu(x) \bar{\chi}^i_x \chi_{x+\hat{\mu},j}, \qquad \mathcal{M}_l^{\ k} = -\eta_\mu(x) \bar{\chi}^k_{x+\hat{\mu}} \chi_{x,l} = \eta_\mu(x) \chi_{x,l} \bar{\chi}^k_{x+\hat{\mu}}. \tag{3}$$

All elementary plaquettes P from the expansion of S_{G} that share a given link $U_\mu(x)$ need to be taken into account when integrating out the link $U \equiv U_\mu(x)$:

$$P_U = \{P \mid U \in U_P\} = P_U^+ \cup P_U^-. \tag{4}$$

with P_+ the subsets of plaquettes in forward and P_- in backward direction, as illustrated in Fig. 1. Hence the one-link integral over gauge group $G = \mathrm{SU}(N_c), U(N_c)$ that we will consider has the fermion matrices $\mathcal{M}$, $\mathcal{M}^\dagger$ and the set of staples S_P with $U_P = U_\mu(x)S_P$ as external sources:

$$\begin{aligned}
\mathcal{J}(\mathcal{M},\mathcal{M}^\dagger,\{S_P,S_P^\dagger\}) &= \int_G dU\, e^{\mathrm{tr}[\mathcal{M}^\dagger U]+\mathrm{tr}[\mathcal{M}U^\dagger]} e^{\frac{\beta}{2N_c}\sum_{P\supset U}(\mathrm{tr}[US_P]+\mathrm{tr}[U^\dagger S_P^\dagger])} \\
&= \int_G dU \sum_{\kappa,\bar\kappa} \frac{\mathrm{tr}[\mathcal{M}^\dagger U]^\kappa \mathrm{tr}[\mathcal{M}U^\dagger])^{\bar\kappa}}{\kappa!\bar\kappa!} \prod_{P\supset U}\sum_{n_P,\bar n_P}\left(\frac{\beta}{2N_c}\right)^{n_P+\bar n_P} \frac{\mathrm{tr}[US_P]^{n_P}\mathrm{tr}[U^\dagger S_P^\dagger]^{\bar n_P}}{n_P!\bar n_P!} \\
&= \sum_{\kappa,\bar\kappa}\prod_{P\supset U}\sum_{n_P,\bar n_P}\frac{1}{\kappa!\bar\kappa!}\frac{\left(\frac{\beta}{2N_c}\right)^{n_P+\bar n_P}}{n_P!\bar n_P!}\int_G dU \mathrm{tr}[\mathcal{M}^\dagger U]^\kappa \mathrm{tr}[\mathcal{M}U^\dagger]^{\bar\kappa}\mathrm{tr}[US_P]^{n_P}\mathrm{tr}[U^\dagger S_P^\dagger]^{\bar n_P} \\
&= \sum_{m,\bar m} C(\beta,\{S_P,S_P^\dagger\})^{m,\bar m}_{\boldsymbol{j}\boldsymbol{i},\boldsymbol{l}\boldsymbol{k}} \sum_{\kappa,\bar\kappa}\frac{1}{\kappa!\bar\kappa!}\mathcal{K}^{m,\bar m}_{\boldsymbol{i}\boldsymbol{j},\boldsymbol{k}\boldsymbol{l}}(\mathcal{M},\mathcal{M}^\dagger), \qquad \mathrm{tr}[US_P] = \sum_{i,j=1}^{N_c} U_i{}^j S_P{}_j{}^i
\end{aligned} \tag{5}$$

where we expand in the forward hoppings κ, backward hoppings $\bar\kappa$, and plaquette and anti-plaquette occupation numbers n_P, $\bar n_P$. In the last line, we have decomposed the traces to separate the staples from the gauge link and summation over the set of indices $\boldsymbol{i}$, $\boldsymbol{j}$, $\boldsymbol{k}$,$\boldsymbol{l}$ is implied. It is the tensor $C(\beta,\{S_P,S_P^\dagger\})_{\boldsymbol{j}\boldsymbol{i},\boldsymbol{l}\boldsymbol{k}}$ which leads to non-local color contractions and can be related to the set of plaquette occupation numbers $\{n_P,\bar n_P\}$ when contracting the m open color indices from U and $\bar m$ open color indices from $U^\dagger$ with the one-link integrals from the neighbor links:

$$m = \sum_{P\in P_U^+} n_P + \sum_{P\in P_U^-}\bar n_P, \qquad \bar m = \sum_{P\in P_U^+}\bar n_P + \sum_{P\in P_U^-} n_P. \tag{6}$$

The remaining integral can be related to integrals over the link matrices only [12]:

$$\mathcal{I}^{a,b}_{\boldsymbol{i}\boldsymbol{j},\boldsymbol{k}\boldsymbol{l}} = \int_G dU \prod_{\alpha=1}^{a} U_{i_\alpha}{}^{j_\alpha}\prod_{\beta=1}^{b}(U^\dagger)_{k_\beta}{}^{l_\beta}, \qquad \begin{matrix}\boldsymbol{i}=i_1,\dots i_a & \boldsymbol{k}=k_1,\dots k_b\\ \boldsymbol{j}=j_1,\dots j_a & \boldsymbol{l}=l_1,\dots l_b\end{matrix} \tag{7}$$

$$\begin{aligned}
\mathcal{K}^{m,\bar m}_{\boldsymbol{i}\boldsymbol{j},\boldsymbol{k}\boldsymbol{l}}(\mathcal{M},\mathcal{M}^\dagger) &= \int_G dU \mathrm{tr}[\mathcal{M}^\dagger U]^\kappa \mathrm{tr}[\mathcal{M}U^\dagger]^{\bar\kappa}\prod_{\alpha=1}^{m} U_{i_\alpha}{}^{j_\alpha}\prod_{\beta=1}^{\bar m} U^\dagger{}_{k_\beta}{}^{l_\beta} \\
&= \sum_{\{i_\alpha,j_\alpha,k_\beta,l_\beta\}}\left(\prod_{\alpha=1}^{\kappa}\prod_{\beta=1}^{\bar\kappa}\mathcal{M}_{j_\alpha}{}^{i_\alpha}\mathcal{M}^\dagger{}_{l_\beta}{}^{k_\beta}\right)\mathcal{I}^{\kappa+m,\bar\kappa+\bar m}_{\boldsymbol{i}\boldsymbol{j},\boldsymbol{k}\boldsymbol{l}}.
\end{aligned} \tag{8}$$

Here, $a = \kappa + m$ and $b = \bar\kappa + \bar m$ is the number of U-matrix and $U^\dagger$-matrix elements. In this one-link integral, only the color indices from the quark matrices will be contracted. The contraction of the remaining indices can in general not be carried out easily, however in certain cases link integration on the complete lattice will be possible to give rise to a color singlet partition function:

$$Z(\beta) = \sum_{\mathcal{G}=\{n_P,\bar n_P,\kappa,\bar\kappa\}} w(\mathcal{G})\prod_P\left(\frac{\beta}{2N_c}\right)^{n_P+\bar n_P}, \tag{9}$$

where the admissible graphs $\mathcal{G}$ are such that they fulfill the constraint

$$\kappa-\bar\kappa+m-\bar m = \begin{cases} 0 & \text{for} \quad \mathrm{U}(N_c) \\ 0 \mod N_c & \text{for} \quad \mathrm{SU}(N_c)\end{cases}. \tag{10}$$

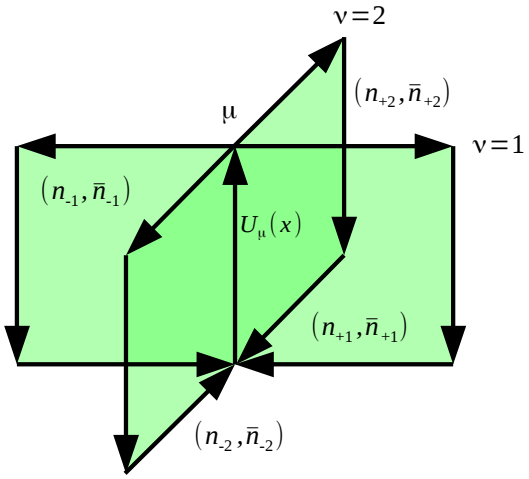

Figure 1. Staples and corresponding plaquette occupation numbers $(n_P, \bar{n}_P)$ for directions perpendicular to the link $U_\mu(x)$ to be integrated out: the moment of $U_\mu(x)$ from the moments of the Wilson gauge action is $m = \sum_{\nu\perp\mu} n_{+\nu} + \bar{n}_{-\nu}$ and $\bar{m} = \sum_{\nu\perp\mu} n_{-\nu} + \bar{n}_{+\nu}$, see Eq. (6).

2.2 Link Integration in the Strong Coupling Limit

For $\beta = 0$, link integration factorizes:

$$Z_0(am_q, a_t\mu, \gamma) = \prod_x \int d\chi_x d\bar{\chi}_x e^{2am_q\bar{\chi}_x\chi_x} \prod_\mu \int dU_\mu(x) \left(e^{\gamma^{\delta_{\mu 0}}\eta_\nu(x)e^{a_t\mu\delta_{\mu 0}}(\bar{\chi}_x U_\mu(x)\chi_{x+\hat{\mu}} - \bar{\chi}_{x+\hat{\mu}}U^\dagger_\mu(x)\chi_x)} \right). \tag{11}$$

The corresponding one-link integrals $\mathcal{K}_0$ will not depend on any external gauge links:

$$\mathcal{K}_0(\mathcal{M},\mathcal{M}^\dagger) = \int_G dU \mathrm{tr}[\mathcal{M}^\dagger U]^\kappa \mathrm{tr}[\mathcal{M}U^\dagger]^{\bar{\kappa}} = \sum_{\{i_\alpha,j_\alpha,k_\beta,l_\beta\}} \left(\prod_{\alpha=1}^{\kappa}\prod_{\beta=1}^{\bar{\kappa}} \mathcal{M}_{j_\alpha}^{\ i_\alpha} \mathcal{M}^\dagger_{\ l_\beta}^{\ k_\beta} \right) \mathcal{I}^{\kappa,\bar{\kappa}}_{\boldsymbol{i}\boldsymbol{j},\boldsymbol{k}\boldsymbol{l}}. \tag{12}$$

Hence, link integration can be carried out analytically. Only a finite number of integrals have to be evaluated due to the Grassmann nature of the fermions: since they come in N_c colors, $0 \le \kappa,\bar{\kappa} \le N_\mathrm{c}$. Moreover, integral Eq. (7) will only be non-zero if $\kappa - \bar{\kappa} = qN_\mathrm{c}$ with $q = 0, \pm 1$ (see next section). The corresponding result for Eq. (5) was first addressed in [13] when deriving the strong coupling partition function for $N_\mathrm{f} = 1$:

$$\begin{aligned} \mathcal{J}_0(\mathcal{M},\mathcal{M}^\dagger) &= \int_G dU e^{\mathrm{tr}[U\mathcal{M}^\dagger + \mathcal{M}U^\dagger]} \\ &= \sum_{k=0}^{N_\mathrm{c}} \frac{(N_\mathrm{c}-k)!}{N_\mathrm{c}!k!} \left(M_x M_{x+\hat{\mu}}\right)^k + \frac{q}{N_\mathrm{c}!}\left\{(\rho_\nu(x)^{N_\mathrm{c}}\bar{B}_x B_{x+\hat{\mu}}) + (-\rho_\nu(x))^{N_\mathrm{c}}\bar{B}_{x+\hat{\mu}}B_x)\right\} \\ \text{with} \quad q = \begin{cases} 0 & \text{for} \quad G = \mathrm{U}(N_\mathrm{c}) \\ 1 & \text{for} \quad G = \mathrm{SU}(N_\mathrm{c}) \end{cases} \quad &\text{and} \quad \rho_\nu(x) = \eta_\nu(x) \begin{cases} e^{\pm a_t\mu} & \nu = 0 \\ 1 & \text{else} \end{cases} . \end{aligned} \tag{13}$$

Here, $M_x = \bar{\chi}_x \chi_x$ are the mesonic and $B_x = \frac{1}{N_c!}\epsilon_{i_1 \dots i_{N_c}} \chi_{x,i_1} \dots \chi_{x,i_{N_c}}$ are the baryonic degrees of freedom. After the final Grassmann integration, where also the expansion of $e^{2am_q \bar{\chi}\chi}$ enters, the partition function is exactly rewritten in terms of integer variables:

$$Z_0(am_q, a_t\mu_B, \gamma) = \sum_{\{k,n,\ell\}} \prod_{b=(x,\mu)} \frac{(N_c - k_b)!}{N_c! k_b!} \gamma^{2k_b \delta_{\mu 0}} \prod_x \frac{N_c!}{n_x!} (2am_q)^{n_x} \prod_\ell w(\ell, a_t\mu_B) \tag{14}$$

where $k_b \in \{0, \dots, N_c\}$ are the so-called dimers, i.e. multiplicities of bonds b that represent meson hoppings, $n_x \in \{0, \dots, N_c\}$ are the so-called monomers and represent $\bar{\chi}_x \chi_x$ not being part of dimers, and the baryon world lines ℓ form oriented self-avoiding loops, with loop weight

$$w(\ell, a_t\mu_B) = \frac{1}{N_c!} \sigma(\ell) \gamma^{N_c N_{0,\ell}} e^{N_\tau a_t \mu_B r_\ell}, \qquad \sigma(\ell) = (-1)^{1 + r_\ell + N_{-,\ell}} \prod_{(x,\mu)\in\ell} \eta_\mu(x). \tag{15}$$

Here, $N_{0,\ell}$ is the number of temporal baryon segments on ℓ. The sign $\sigma(\ell)$ of a baryon loop ℓ is due to geometry: number of backward directions $N_{-,\ell}$, winding number r_ℓ and staggered phases along the loop. The sign of a configuration is the product of the signs of all baryonic loops. The sign problem of sampling this partition function is however very mild for any value of the chemical potential, because the baryons are heavy and hence tend to have simple geometries which contribute with positive signs.

2.3 Weingarten Functions

In order to obtain the partition function away from the strong coupling limit, we will make use of Weingarten functions [14, 15]. This is particularly useful since when some of the link matrices emerge from the Wilson gauge action, we also need contributions to Eq. (7) for $a > 0$ and $b > 0$. For $n \equiv a = b$, the result is expressed via permutations $\sigma, \tau \in S_n$ on the color indices that go into $2n$ Kronecker deltas, and are multiplied by the Weingarten functions, which sums over all irreducible representations (irreps) λ of SU(N_c) that are tensors of n fundamental irreps:

$$\mathcal{I}^{n,n}_{\boldsymbol{i}\boldsymbol{j},\boldsymbol{k}\boldsymbol{l}} = \sum_{\sigma,\tau\in S_n} \prod_{r=1}^{n} \left(\delta^{l_r}_{i_{\sigma(r)}} \delta^{j_{\tau(r)}}_{k_r}\right) \mathrm{Wg}^{n,N_c}([\sigma \circ \tau^{-1}]), \tag{16}$$

$$\mathrm{Wg}^{n,N}(\rho) = \frac{1}{(n!)^2} \sum_{\lambda\vdash n, l(\lambda)\le N_c} \frac{(f^\lambda)^2}{D_\lambda(N)} \chi^\rho_\lambda, \tag{17}$$

with $D_\lambda(N)$ the dimension of the irrep λ of U(N) and f^λ the dimension of the irrep λ of S_n. The irreps of both the unitary and the symmetric groups are labeled by integer partitions

$$\lambda \vdash n, \qquad \lambda = (\lambda_1, \dots \lambda_{l(\lambda)}), \qquad n = \sum_{i=1}^{l(\lambda)} \lambda_i, \qquad \lambda_i \ge \lambda_{i+1}, \tag{18}$$

and due to the finite number of available color indices, the corresponding partitions have a finite number of parts, $l(\lambda) \le N$. The Weingarten functions contain the character χ^ρ_λ of the symmetric group S_n, which only depends on the conjugacy class $\rho = [\pi]$ of a permutation $\pi \in S_n$, given by the cycle structure of π. The conjugacy class $\rho \vdash n$ is also labeled by an integer partition. Some examples of Weingarten functions are:

$$\mathrm{Wg}^{3,N}(21) = \frac{-1}{(N^2-1)(N^2-4)}, \qquad \mathrm{Wg}^{3,N}(1^3) = \frac{N^2-2}{N(N^2-1)(N^2-4)}. \tag{19}$$

The Weingarten functions for $a - b = qN_c$ with $q = 1$ has been addressed in [16]. For $q \neq 0$, also epsilon tensors enter Eq. (17), which leads to lengthy expressions. The generalization for $q > 1$ will be addressed in a forthcoming publication. Here we simply want to illustrate that we recover the strong coupling limit and the leading order gauge correction within this formalism.

2.4 Link Integration via Weingarten Functions

The Weingarten functions are a powerful tool to address gauge corrections and integrals for many flavors, given that the matrices $\mathcal{M}$, $\mathcal{M}^\dagger$ are generalized to $N_f > 1$. Depending on how many fermion hoppings contribute to the link integral, we restrict the sum over irreps within the Weingarten function to those consistent with the fermion content:

$$\mathrm{Wg}^{n,N}{}_\lambda(\rho) = \frac{1}{(n!)^2}\frac{(f^\lambda)^2}{D_\lambda}\chi^\rho_\lambda, \qquad \mathrm{Wg}^{n,N}{}_\Lambda(\rho) = \sum_{\substack{\lambda\vdash n\\ \lambda\in\Lambda}} \mathrm{Wg}^{n,N}{}_\lambda(\rho) \tag{20}$$

This restriction is possible due to the orthogonality of characters: for any $\lambda \neq [n]$ (i.e. with the exception of the completely symmetric irrep which has $\chi^\rho_{[n]} = 1$ for all ρ) it holds that

$$\sum_{\rho\vdash n} h_\rho \chi^\rho_\lambda = 0, \qquad \sum_{\rho\vdash n} h_\rho = n! \tag{21}$$

with h_ρ the number of elements in the conjugacy class ρ. However, due to the additional minus signs from the ordering of the Grassmann variables, there are other irreps $\lambda \in \Lambda$ which are non-zero. At strong coupling, where all sources are fermionic, only the completely anti-symmetric irrep is non-zero, $\Lambda = \{[1^n]\}$, with $n \leq N_c$. Here, $\chi^\rho_{[1^n]} = \mathrm{sgn}(\rho)$, resulting in

$$\mathcal{I}^{n,n}_{\boldsymbol{i}\boldsymbol{j},\boldsymbol{k}\boldsymbol{l}}(\Lambda) = \sum_{\sigma,\tau\in S_n}\prod_{r=1}^{n}\left(\delta^{l_r}_{i_{\sigma(r)}}\delta^{j_{\tau(r)}}_{k_r}\right)\frac{1}{(n!)^2}\frac{(N_c-n)!}{N_c!}\mathrm{sgn}(\rho), \qquad \rho = [\sigma\tau^{-1}] \tag{22}$$

$$J_0(\mathcal{M},\mathcal{M}^\dagger) = \sum_{k=0}^{N_c}\sum_{\rho\vdash k} h_\rho \mathrm{tr}_\rho[\mathcal{M}\mathcal{M}^\dagger]\frac{(N_c-k)!}{N_c!(k!)^2}\mathrm{sgn}(\rho), \tag{23}$$

$$\mathrm{tr}_\rho[\ldots] = \prod_i \mathrm{tr}[(\ldots)^i]^{\rho_i}, \qquad \sum_i i\rho_i = n. \tag{24}$$

This agrees for $N_f = 1$ with the result in Eq. (13) since $\mathrm{sgn}(\rho)$ is canceled by the anti-commutativity of the Grassmann variables.

For the leading order gauge corrections, the additional gauge link from the plaquette allows partial symmetrization, $\Lambda = \{[1^n], [21^{n-2}]\}$:

$$\mathcal{I}^{n,n}_{\boldsymbol{i}\boldsymbol{j},\boldsymbol{k}\boldsymbol{l}}(\Lambda) = \sum_{\sigma,\tau\in S_n}\prod_{r=1}^{n}\left(\delta^{l_r}_{i_{\sigma(r)}}\delta^{j_{\tau(r)}}_{k_r}\right)\frac{1}{(n!)^2}\frac{(N_c-n)!}{(N_c+1)!}\left((N_c+1)\mathrm{sgn}(\rho)+(N_c+1-n)\chi^\rho_{[21^{n-2}]}\right), \tag{25}$$

$$J_{i^j}(\mathcal{M},\mathcal{M}^\dagger) = \sum_{k=0}^{N_c}\frac{1}{(k-1)!k!}\sum_{\rho\vdash k} h_\rho \mathrm{tr}_\rho[\mathcal{M}\mathcal{M}^\dagger\mathcal{M}_{i^j}]$$
$$\frac{(N_c-k)!k!}{(N_c+1)!}\left((N_c+1)\mathrm{sgn}(\rho)+(N_c+1-n)\chi^\rho_{[21^{n-2}]}\right) \tag{26}$$

For $N_\mathrm{f} = 1$ this reproduces the known result [10, 11]:

$$J_{i^j}(\mathcal{M}, \mathcal{M}^\dagger) = \sum_{k=0}^{N_\mathrm{c}} \frac{(N_\mathrm{c}-k)!}{N_\mathrm{c}!(k-1)!} (M_x M_{x+\hat{\mu}})^k \mathcal{M}_{i^j} \tag{27}$$

With this result, one address gauge corrections as shown in Fig. 3. Similarly, other gauge corrections can be addressed, which we plan to do in a forthcoming publication.

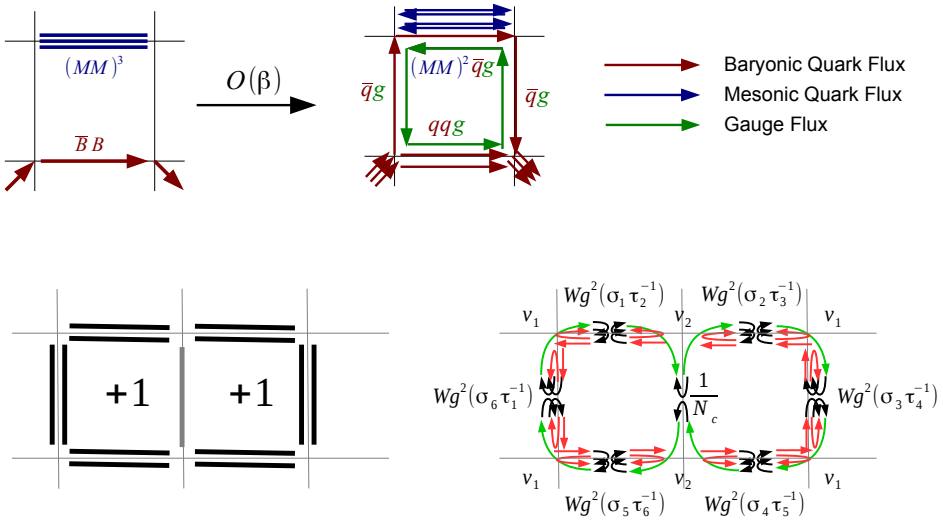

Figure 2. Gauge corrections to the strong coupling limit. Top: the effect of gauge corrections to world lines: a baryon along an excited plaquette, smearing the previously point-like baryons over a lattice spacing. Bottom: Two excited adjacent plaquettes, displayed as dimer covering, and with internal structure of dimers. Contributions from plaquettes, dimers via Weingarten functions, green: plaquette contributions, red: fermion hoppings, black: permutations that enter the Weingarten functions and are summed over. The vertex weights $v_1 = v_2 = 1$ are trivial in that example.

3 Dual Formulation

3.1 Grassmann Integration

Given that all link integrals $\mathcal{K}_{i^j,k^l}$ are computed, the remaining task is to organize the fermions such that they can be integrated out. If the integrals $\mathcal{K}_{i^j,k^l}$ have more than two open indices, the Grassmann integration gives rise to a tensor network that is difficult to evaluate. For U(N_c) gauge theory, the contractions are however possible as there are exact cancellations, as shown in Fig. 3. Only integrals with two open indices $\mathcal{K}^{1,0}_{i_1^{j_1}}$ or $\mathcal{K}^{0,1}_{k_1^{l_1}}$ give non-zero contributions. Since Grassmann integration results in one incoming and one outgoing loop per site if the site is on the boundary of a plaquette surface, these have to be contracted along loops. The resulting simplifying constraint, exact for U(N_c) and valid for the $q = 0$ sector of SU(N_c), is that plaquette surfaces are bound by quarks which form self-avoiding loops. However, for $q \neq 0$, quark loops can intersect such that the constraint is no longer valid. We will nevertheless apply this constraint, resulting in systematic errors for fermionic observables at $O(\beta^{N_\mathrm{c}})$.

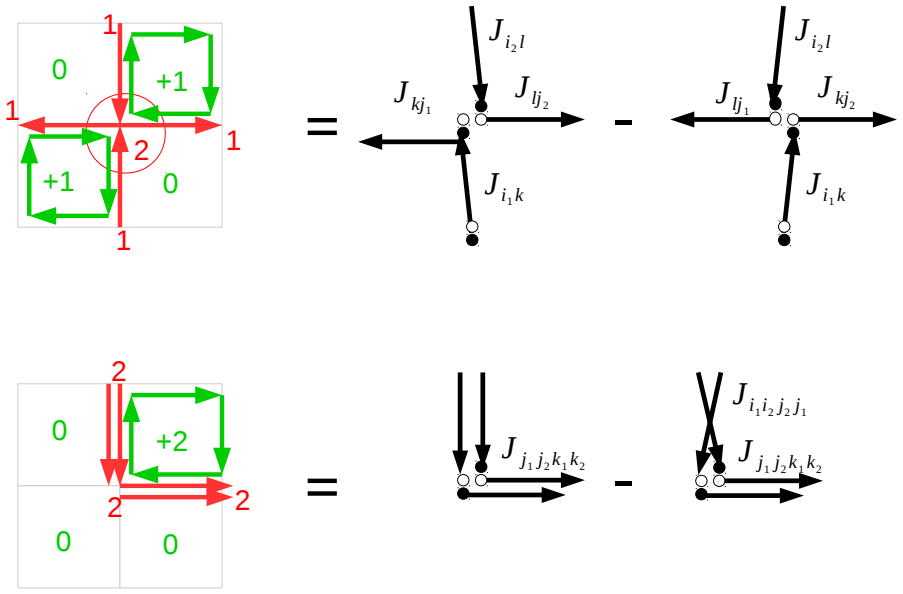

Figure 3. Simplification due to Grassmann integration within the U(N_c) sector due to exact cancellations. Top: plaquette configurations that result in $f_x > 1$. Bottom: plaquette configurations that result in $f_b > 1$. Hence, in U(N_c), the quark fluxes around the plaquette surfaces form self-avoiding loops. We will also restrict to that in SU(N_c), where this simplification is no longer applicable and introduces systematic errors at $O(\beta^{N_c})$.

3.2 The Partition Function

With the above simplification, the resulting partition sum is a sum over monomers, dimers, world lines and world sheets defined as surfaces of constant plaquette occupation numbers. To do so, we have to introduce two auxiliary variables which are completely determined by the plaquette configuration:

$$f_b = \sum_{P\in P_b^+} (n_P - \bar{n}_P) + \sum_{P\in P_b^-} (\bar{n}_P - n_P) \in \{0, \pm 1\}, \qquad f_x = \frac{1}{2}\sum_b |f_b| \in \{0, 1\}, \tag{28}$$

$$\ell_f = \{b = (x,\mu)\,|\, f_b = \pm 1 \text{ are connected}\} \equiv \partial\{n_P, \bar{n}_P\}, \tag{29}$$

where f_b counts the number of fermion fluxes through a bond b, f_x counts the number of fermion fluxes through a site x, and ℓ_f are the self-avoiding loops that are defined on the boundary of the plaquette surfaces of constant plaquette occupation numbers. With this, the partition function reads

$$Z(am_q, a_t\mu, \gamma) = \sum_{\{k_b, n_x, \ell_{N_c}, n_P, \bar{n}_P\}} \prod_{b=(x,\mu)} \frac{(N_c - k_b)!}{N_c!(k_b - |f_b|)!} \gamma^{(2k_b - f_b)\delta_{\mu 0}} \prod_x \frac{N_c!}{n_x!}(2am_q)^{n_x}$$
$$\times \prod_{\ell_{N_c}, \ell_f} w(\ell_{N_c}, \ell_f, \mu) \prod_P \frac{\left(\frac{\beta}{2N_c}\right)^{n_P + \bar{n}_P}}{n_P!\bar{n}_P!} \tag{30}$$

$$k_b \in \{0, \dots N_c\}, \qquad n_x \in \{0, \dots N_c\}, \qquad \ell_{N_c} \in \{0, \pm 1\}, \qquad n_P, \bar{n}_P \in \mathbb{N}. \tag{31}$$

Due to restriction discussed Sec. 3.1, we however only sample plaquette surfaces where either $\bar{n}_P = 0$ or $n_P = 0$, resulting in a net plaquette occupation number $n_P - n_P = 0 \in \mathbb{Z}$.

The color constraint, a modification of the Grassmann constraint, is

$$n_x + \sum_{\hat{\mu}=\pm\hat{0},\ldots\pm\hat{d}} \left(k_{\hat{\mu}}(x) + \frac{N_c}{2} |\ell_{N_c,\hat{\mu}}(x)| \right) = N_c + f_x. \tag{32}$$

The N_c-flux loops ℓ_{N_c} have the same role as baryon loops at strong coupling, but they are now not necessarily made up of N_c quarks. Likewise, also dimers are not necessarily mesons, but can be composed of a quark-gluon combination. The bond weights are modified in case a bond is both part of a loop ℓ_{N_c} and a loop ℓ_f :

$$w(B_1) = \frac{1}{N_c!(N_c-1)!}, \qquad w(B_2) = \frac{(N_c-1)!}{N_c!} \tag{33}$$

with B_1 a N_c-flux bond without and B_2 with an additional dimer. Also the site weights are modified in case fermion flux is reoriented, i.e. when $f_x = 1$, with $v_1 = (N_c - 1)!$ the weight when it merges into a dimer, and $v_2 = N_c!$ when it merges with a N_c-flux.

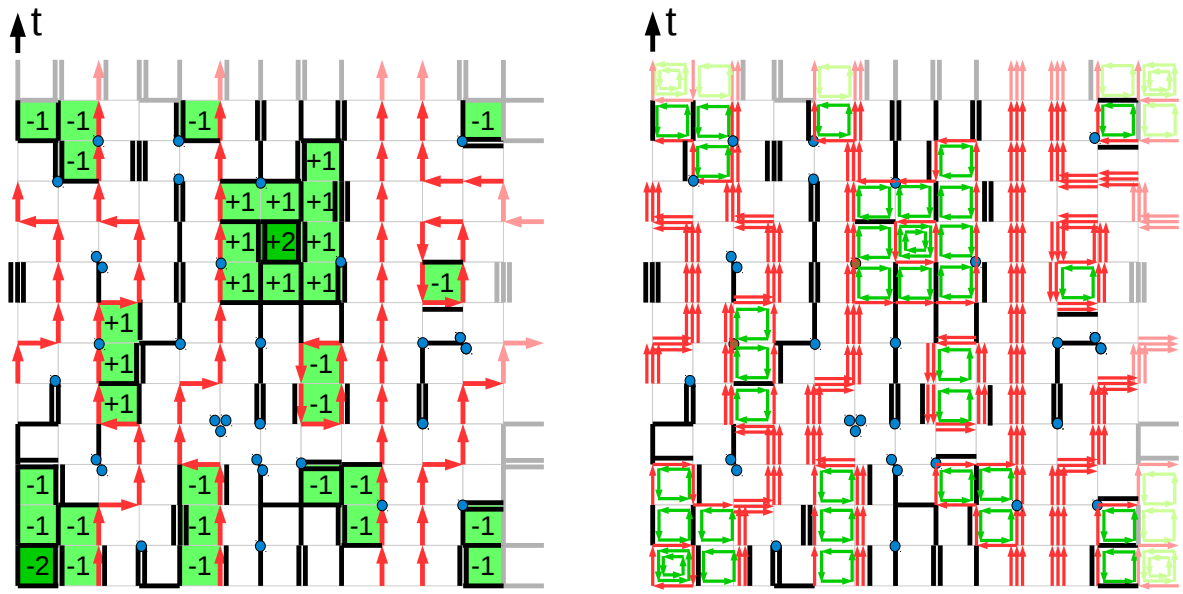

Figure 4. Typical 2-dimensional configuration at finte β, $a_t\mu$ and am_q. Left: degrees of freedom that are sampled: monomers (blue), dimers (black), 3-fluxes (red) and plaquette occupation numbers (green). Right: the same configuration but with the substructure of color singlets and triplets along excited plaquettes: quarks (red) and gauge fluxes (green). Baryons becomes extended objects.

We sample the partition function Eq. (31) by extending the mesonic and baryonic worm algorithm used at strong coupling. In particular, we update the plaquette occupation numbers on closed loop configurations, and the 0-flux and N_c-flux worms take modified weights on edges with $f_b \neq 0$. A detailed discussion of the algorithm will be left for a forthcoming publication.

3.3 Sign Problem

Although the finite density sign problem has been made very mild in the strong coupling limit, this is not necessarily the case away from the strong coupling limit, as fermion hoppings on the boundary of

plaquette surfaces take place. Single fermion hoppings are however not suppressed by a large mass. In fact, the sign problem in the dual representation due to finite β even arises for the U(N_c) gauge theory, which is sign problem-free in the conventional fermion determinant representation, as the depenence on the chemical potential drops out.

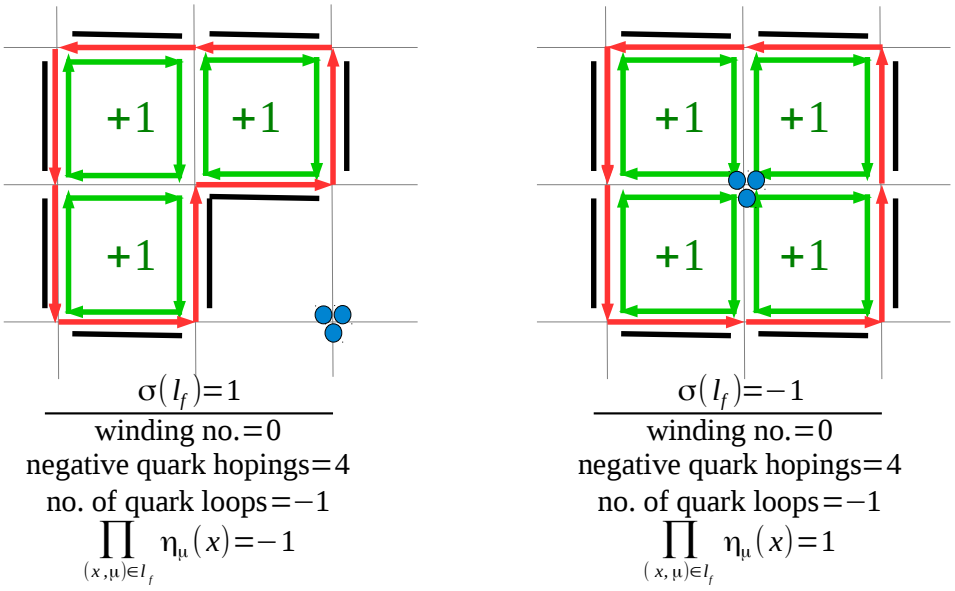

Figure 5. The plaquette-induced sign problem: example of two configurations with opposite signs.

The sign of a configuration factorizes in the N_c-flux sign and the fermion flux sign:

$$\sigma(C) = \prod_{\ell_f} \sigma(\ell_f) \prod_{\ell_{N_c}} \sigma(\ell_{N_c}), \qquad \sigma(\ell) = (-1)^{1+w(\ell)+N_-(\ell)} \prod_{\tilde{\ell}} \eta_\mu(x). \tag{34}$$

For $N_c = 3$, the combination of fermion loops and 3-flux loops lead to the following identification, as shown in Fig. 4: dimers on bonds with fermion $f_b \neq 0$ are fermionic, whereas 3-fluxes on bonds with fermion $f_b \neq 0$ are bosonic.

The example of a negative configuration, Fig. 5 (right), illustrates that in two dimensions, negative contributions are related to frustration of monomers: a loop trapping an odd number of monomers has negative sign. This is known from the dual representation of the Schwinger model at finite quark mass. But for dimensions $d > 2$, even without monomers, a sign problem is induced as dimers and N_c-fluxes can be perpendicular on a plaquette surface, giving rise to topologically inequivalent configurations with opposite signs.

3.4 Crosschecks

We have made extensive crosschecks on small 2-dimensional volumes where exact enumeration is possible. In Fig. 6 some gauge observables, the average plaquette and the Polyakov loop, are shown as obtained from the dual representation, as a function of am_q for $\mu = 0$, and for various gauge groups. They agree well both with the exact result and with hybrid Monte Carlo (HMC).

Another important crosscheck where HMC and Meanfield results [19] are available is the phase boundary in the β-T plane for SU(3) at $\mu = 0$. Fig. 7 shows that the results from direct sampling agree well with extrapolations of HMC.

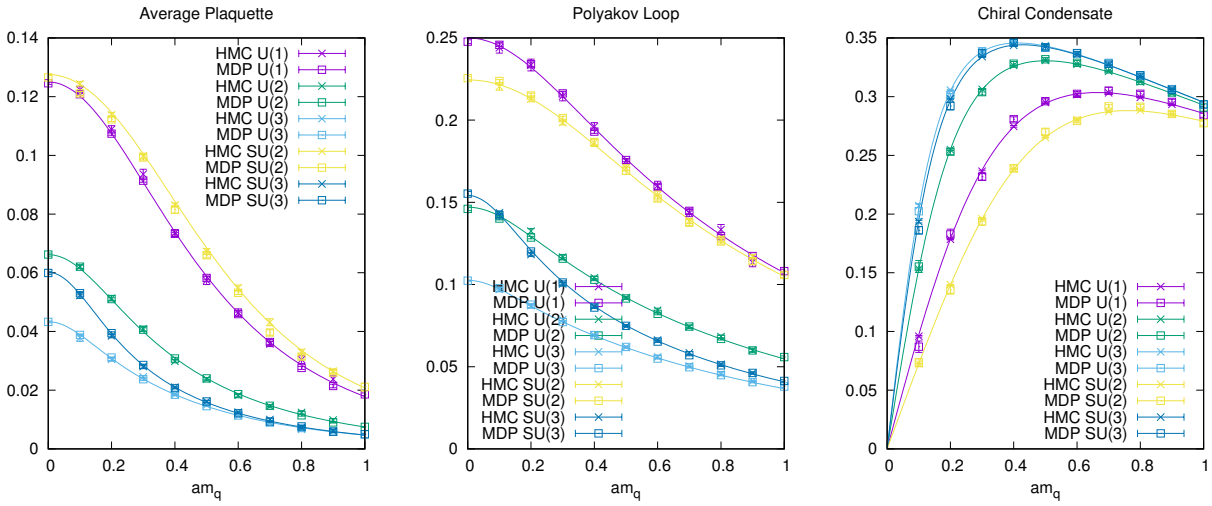

Figure 6. Crosschecks for various gauge groups at $\mu_B = 0$ on small lattices where both analytic results from exact enumeration and hybrid Monte Carlo data were obtained. The average plaquette, Polyakov loop and chiral susceptibility are shown as a function of the quark mass.

4 Results on the Phase Diagram

4.1 Strong Coupling Regime at Finite Temperature

We have derived the dual representation in the strong coupling limit by taking into account the bare anisotropy γ in order to continuously vary the temperature independent of β. In a recent publication [17], one of us has determined with collaborators the non-perturbative anisotropy a/a_t as a function of the bare anisotropy in order to unambiguously define the temperature:

$$aT = \frac{\xi(\gamma)}{N_\tau}, \qquad \frac{a}{a_t} \equiv \xi(\gamma) \simeq \kappa + \frac{1}{1+\lambda\gamma^4}, \qquad \lambda = \kappa/(1-\kappa), \qquad \kappa \simeq 0.7810(8) \tag{35}$$

We adopt this non-perturbative definition of the temperature, which differs significantly from the previously used mean field result $aT = \frac{\gamma^2}{N_t}$. Likewise we convert the chemical potential: $a\mu_B = \xi(\gamma) a_t \mu_B$.

4.2 Phase Diagram in the Strong Coupling Regime

Lattice QCD with staggered fermions has a residual chiral symmetry even in the strong coupling regime, since there is an exact Goldstone mode in the spin⊗taste basis $\gamma_5 \otimes \gamma_5$. The lattice action at zero quark mass, and likewise partition function Eq. (31) has the symmetry

$$U(1)_V \times U(1)_{55} : \qquad \chi(x) \mapsto e^{i\epsilon(x)\theta_A + i\theta_V}\chi(x), \quad \epsilon(x) = (-1)^{x_1+x_2+x_3+x_4}, \tag{36}$$

i.e. even and odd sites transform independently. The chiral symmetry is spontaneously broken at low temperatures, but restored at some phase boundary $aT_c(a\mu_B)$. The transition in the chiral limit is second order for small and intermediate $a\mu_B$ and turns into a first order transition at low temperatures, separated by a tri-critical point. This point at $(a\mu_B^{\rm tric}, aT^{\rm tric}) = (1.56(4), 0.73(4))$ turns into a critical

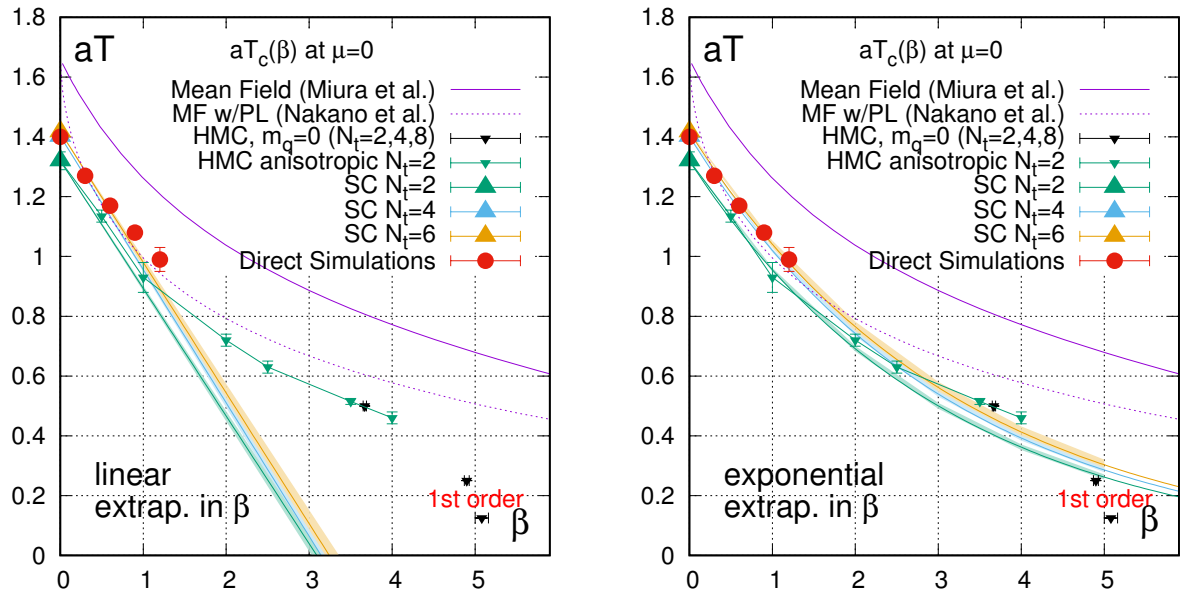

Figure 7. The phase boundary for SU(3) at $\mu_B = 0$. The comparison of direct sampling (red dots) with reweighting and mean field theory. This results makes use of the mean field value of $a/a_t = \gamma^2$ for better comparison. The direct simulations favor the scenario of extrapolating the phase boundary via an exponential ansatz (right) rather than a linear ansatz (left), as has been discussed in [10].

end point as soon as the quark mass becomes finite. The ratio $\mu_B^{\rm CEP}/T^{\rm CEP} > 2$ becomes even larger as a function of the quark mass. The phase boundary for the chiral transition in the strong coupling regime can be measured by finite size scaling of the chiral susceptibility, as shown in Fig. 9 (top). The nuclear transition can be obtained from the position of the gap in the baryon density. In the strong coupling limit, the first order chiral and nuclear transition coincide. The reason is that the nuclear liquid phase is actually a Pauli saturated phase of a baryon crystal, such that no quarks are left for the formation of a chiral condensate. This finding seems to be independent of the quark mass [18]. We restrict in the following to the chiral limit, where simulation via the Worm algorithm are even faster than with finite quark mass, in contrast to HMC.

Via reweighting from the $\beta = 0$ ensemble, Fig. 8 (left), it was found that the chiral transition $aT_c(a\mu_B)$ for small chemical potential indeed decreases, as expected since the lattice spacing $a(\beta)$ becomes smaller. However, the chiral and nuclear first order transition still coincide with the strong coupling result for small β. This may be very likely a reweighting artifact, as it is impossible to reweight from one phase to another phase across a first order transition. We only found that the nuclear critical end point separates from the chiral tri-critical point, but does not split from the first order line. The expectation is however that the chiral and nuclear transition split, a possible scenario is shown in Fig. 8 (right). It is however a priori not clear how much $\mu_c^{\rm nuclear}$ and $\mu_c^{\rm chiral}$ are separated in nature, and how large β needs to be to observe that splitting.

In order to understand the relation between nuclear and chiral transition, we need to sample the partition function Eq. (31) directly at finite β. With the direct simulations at finite β, based on local plaquette updates together with the worm to update the dimers and 3-flux world lines, we find that the chiral first order transition indeed depends on β, as shown in Fig. 9 (bottom). Our lattices were $N_s times 4$ with $N_s = 4, 6, 8$, and for various temperatures and baryon chemical potentials, which

suffices to determine the chiral phase boundary quite accurately. These preliminary results still needs to be reconciled with the first order nuclear transition, which requires larger volumes.

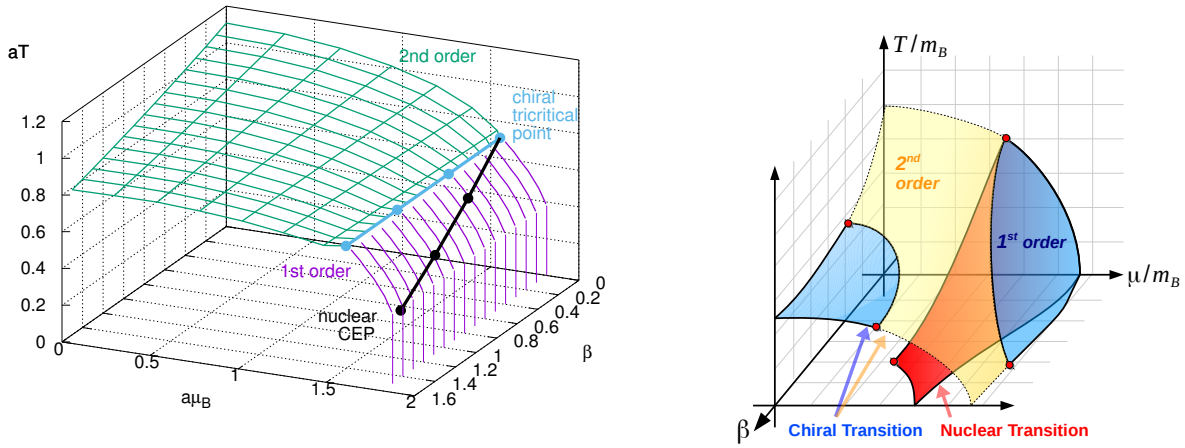

Figure 8. Left: The phase boundary for SU(3) in the chiral limit as a function of small β, obtained from reweighting [10] but with the non-perturbative anisotropy a/a_t to convert to aT and $a\mu_B$. Contrary to the expectation, the nuclear and chiral transition did not split, which is likely an artifact from reweighting. Right: one of several possible scenarios on the β-dependence of the chiral and nuclear transition for unrooted staggered fermions in the chiral limit.

5 Conclusion

We have presented a partition function that includes higher order gauge corrections with the constraint that the plaquette world sheets are bound by fermion loops. Plaquette occupation numbers are in principle unbounded, such that we sample contributions of the gauge action at arbitrarily large order in β. However, due to the complicated non-local structure of the tensors $C(\beta, \{S_P, S_P^\dagger\})_{j,l}^{i,k}$, it is not yet possible to write down a partition function that is correct for all orders in β. Hence we restrict to the limit where plaquettes form surfaces bounded by quark flux. This restriction is no longer valid for SU(N_c), and our approximation will result in systematic errors in fermionic observables at $O(\beta^{N_c})$. However, in the strong coupling regime with $\beta \ll 2N_c$, these systematic errors are expected to be small.

Due to the sign problem induced by the boundaries of the plaquette surfaces, simulations are restricted to $\beta \lesssim 1$. We presented first direct measurements at non-zero β and μ, which are consistent with the previous results from reweighting. It will be essential to improve on the sign problem further to apply these methods for $\beta > 1$.

A systematic error on the phase boundary as shown in Fig. 9 is due to the anisotropy $\xi = \frac{a}{a_t}$. We only considered the bare anisotropy $\gamma_F \equiv \gamma$ in the Dirac coupling, but one should also introduce an anisotropy in the Wilson action, $\gamma_G = \beta_t/\beta_s$. Then the lattice anisotropy is a non-perturbative function of both bare anisotropies, $\xi(\gamma_F, \gamma_G)$, that can in principle be determined in a similar way as in [17].

In this work we have only studied the gauge corrections of the phase diagram in the chiral limit. We plan to study the gauge corrections also at finite quark mass.

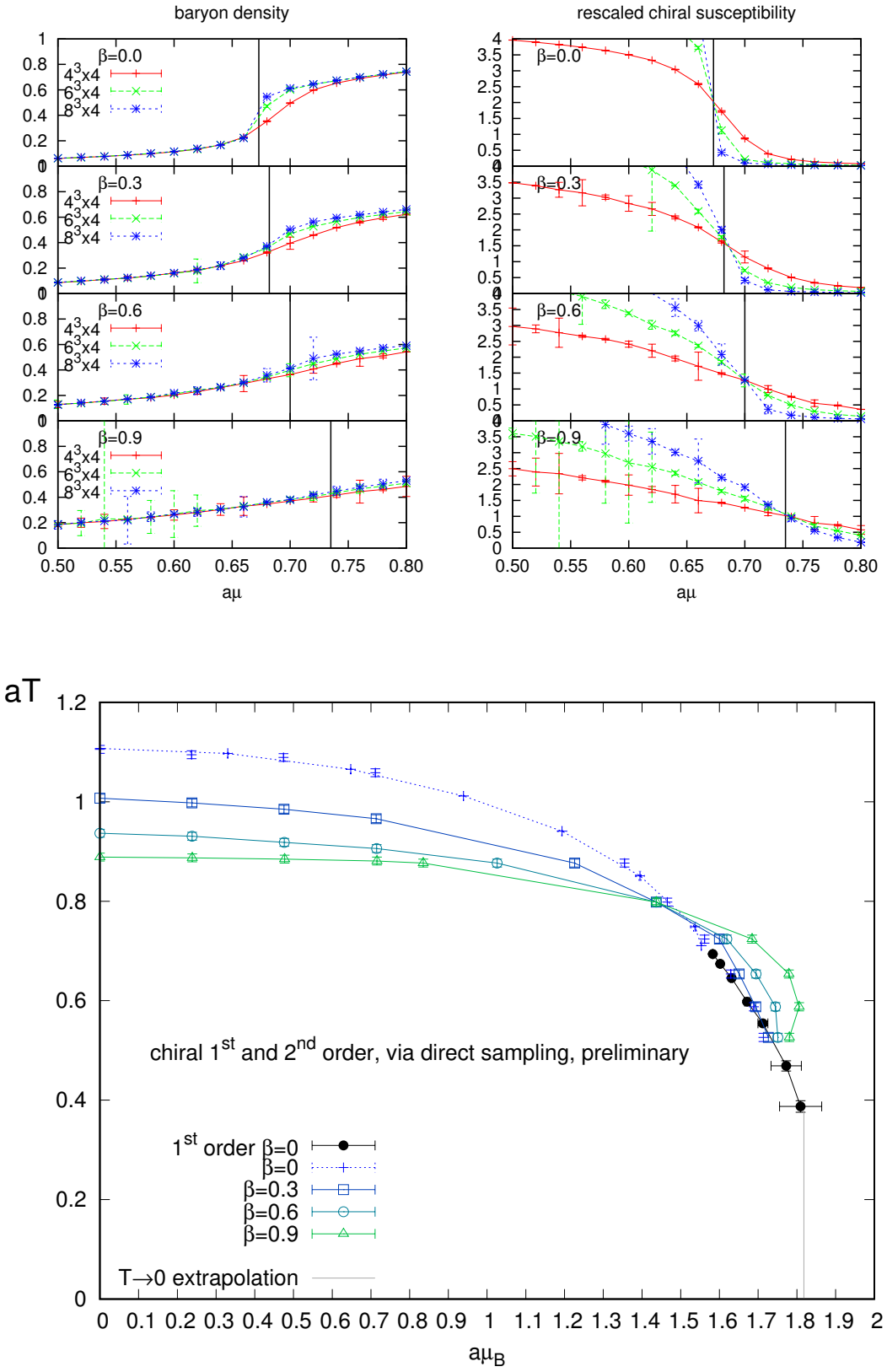

Figure 9. Top: baryon density and rescaled chiral susceptibility at $aT = 0.7$ (in the vicinity of the tri-critical point) from direct simulations for various β. Bottom: The phase boundary for SU(3) at $\mu_B = 0$. For $\mu_B = 0$ up to the tri-critcial point, the direct simulations agree well with the results from reweighting, but a different behaviour is observed along the first order line.

5.1 Acknowledgement

We would like to thank Philippe de Forcrand and Hélvio Vairinhos for stimulating discussions. This work is supported by the Emmy Noether Program under the grant UN 370/1-1. Computations have been carried out on the OCuLUS cluster at PC2 (Universität Paderborn).

References

[1] D. Sexty, Phys. Lett. B **729** (2014) 108 [arXiv:1307.7748 [hep-lat]].
[2] G. Aarts, L. Bongiovanni, E. Seiler, D. Sexty and I. O. Stamatescu, Eur. Phys. J. A **49** (2013) 89 doi:10.1140/epja/i2013-13089-4 [arXiv:1303.6425 [hep-lat]].
[3] A. Alexandru, G. Basar, P. F. Bedaque, G. W. Ridgway and N. C. Warrington, JHEP **1605** (2016) 053 doi:10.1007/JHEP05(2016)053 [arXiv:1512.08764 [hep-lat]].
[4] C. Schmidt and F. Ziesché, PoS LATTICE **2016** (2017) 076 [arXiv:1701.08959 [hep-lat]].
[5] F. Di Renzo and G. Eruzzi, arXiv:1709.10468 [hep-lat].
[6] H. Vairinhos and P. de Forcrand, JHEP **1412** (2014) 038 [arXiv:1409.8442 [hep-lat]].
[7] C. Gattringer, T. Kloiber and V. Sazonov, Nucl. Phys. B **897** (2015) 732 [arXiv:1502.05479 [hep-lat]].
[8] Y. Delgado Mercado, C. Gattringer and A. Schmidt, Comput. Phys. Commun. **184** (2013) 1535 [arXiv:1211.3436 [hep-lat]].
[9] C. Gattringer and C. Marchis, Nucl. Phys. B **916** (2017) 627 [arXiv:1609.00124 [hep-lat]].
[10] P. de Forcrand, J. Langelage, O. Philipsen and W. Unger, Phys. Rev. Lett. **113** (2014) no.15, 152002 [arXiv:1406.4397 [hep-lat]].
[11] K. E. Eriksson, N. Svartholm and B. S. Skagerstam, J. Math. Phys. **22** (1981) 2276.
Phys. Rev. Lett. **113** (2014) no.15, 152002 [arXiv:1406.4397 [hep-lat]].
[12] M. Creutz, J. Math. Phys. **19** (1978) 2043.
[13] P. Rossi and U. Wolff, Nucl. Phys. B **248** (1984) 105.
[14] D. Weingarten, J. Math. Phys. **19** (1978) 999.
[15] B. Collins, Int. Math. Res. Notices **17** (2003) 953
[16] J. B. Zuber, J. Phys. A **50** (2017) no.1, 015203 [arXiv:1611.00236 [math-ph]].
[17] P. de Forcrand, W. Unger and H. Vairinhos, arXiv:1710.00611 [hep-lat].
[18] J. Kim and W. Unger, PoS LATTICE **2016** (2016) 035 [arXiv:1611.09120 [hep-lat]].
[19] K. Miura, N. Kawamoto, T. Z. Nakano and A. Ohnishi, Phys. Rev. D **95** (2017) no.11, 114505 [arXiv:1610.09288 [hep-lat]].

B.5 On the β- and quark mass dependence of the nuclear transition in the strong coupling regime [B5]

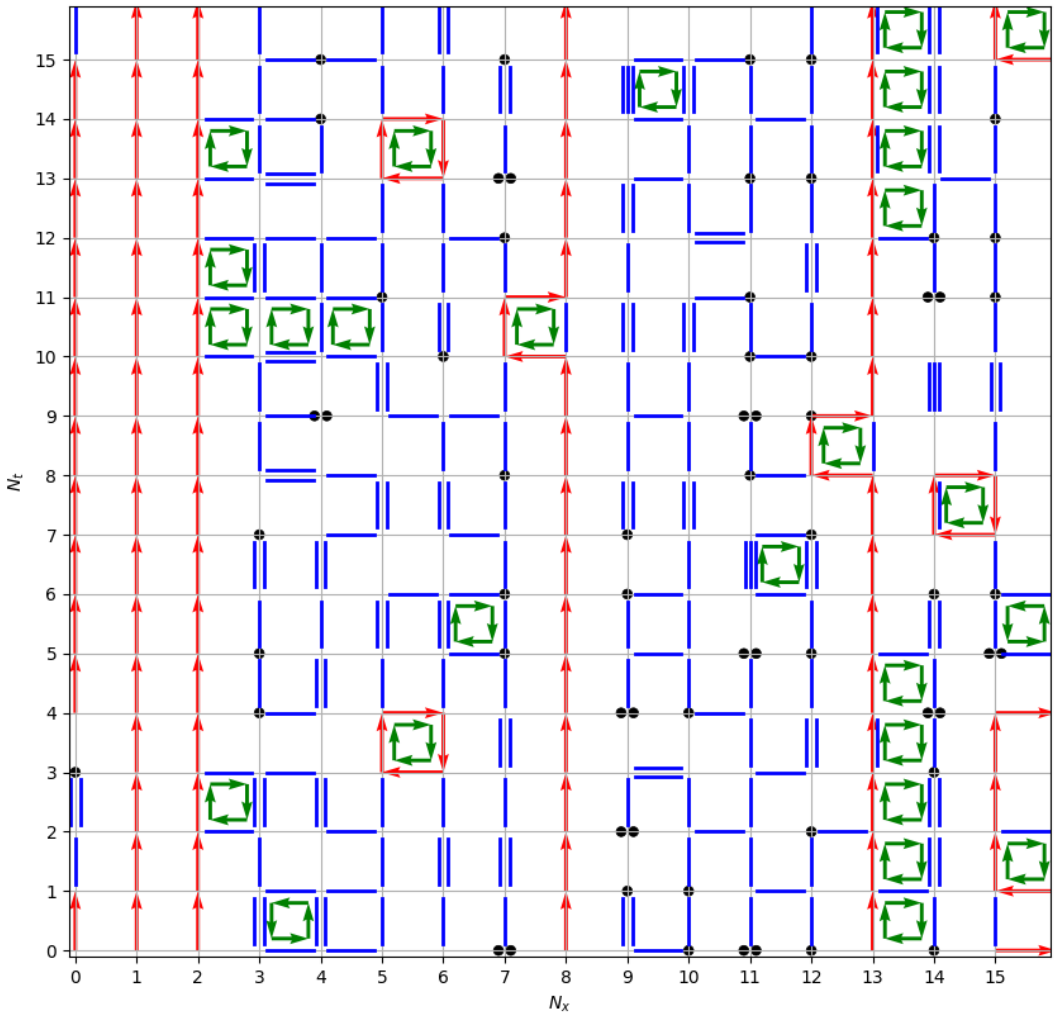

PROCEEDINGS OF SCIENCE

On the β- and quark mass dependence of the nuclear transition in the strong coupling regime

Jangho Kim*
Institut für Theoretische Physik, Goethe-Universität Frankfurt am Main, Max-von-Laue-Str. 1, 60438 Frankfurt am Main, Germany
E-mail: jkim@th.physik.uni-frankfurt.de

Owe Philipsen
Institut für Theoretische Physik, Goethe-Universität Frankfurt am Main, Max-von-Laue-Str. 1, 60438 Frankfurt am Main, Germany
E-mail: philipsen@th.physik.uni-frankfurt.de

Wolfgang Unger
Fakultät für Physik, Universität Bielefeld, Universitätstasse 25, D33619 Bielefeld, Germany
E-mail: wunger@physik.uni-bielefeld.de

Lattice QCD in a dual formulation with staggered fermions is well established in the strong coupling limit and allows to perform Monte Carlo simulations at finite baryon chemical potential. We have recently addressed the dependence of the nuclear critical end point as a function of the quark mass am_q, and separately as a function of the lattice gauge coupling β in the chiral limit. Here we proceed to determine the dependence of the nuclear transition on both, am_q and β, on isotropic lattices and attempt to pinpoint the critical end point for various β where the sign problem is still manageable.

37th International Symposium on Lattice Field Theory - Lattice2019
16-22 June 2019
Wuhan, China

*Speaker.

1. Introduction

The finite density sign problem hinders the direct Monte Carlo simulation of QCD at finite baryon chemical potential. As an alternative method, we adopt the dual representation which is changing degrees of freedom of the original theory to integer variables. The dual representation in the strong coupling regime allows us to investigate the full $\mu_B - T$ phase diagram. We have studied the dependence of the nuclear critical end point (CEP) as a function of the quark mass am_q in the strong coupling limit ($\beta = 0$) [1]. If quark mass increases, the critical baryon chemical potential increases and the critical temperature decreases. Hence, as shown in Fig. 1, the critical end point moves to the bottom right direction. We also have presented the β dependence in the chiral limit in our previous study [2]. In these proceedings, we present the β dependence of the critical end line at finite quark masses in the strong coupling regime. We sketch the expected behavior of the critical line in Fig. 1. If β increases, the critical end point of a certain quark mass is expected to move to lower temperature but the critical baryon chemical potential does not change much. Hence, the first order line shortens with increasing β.

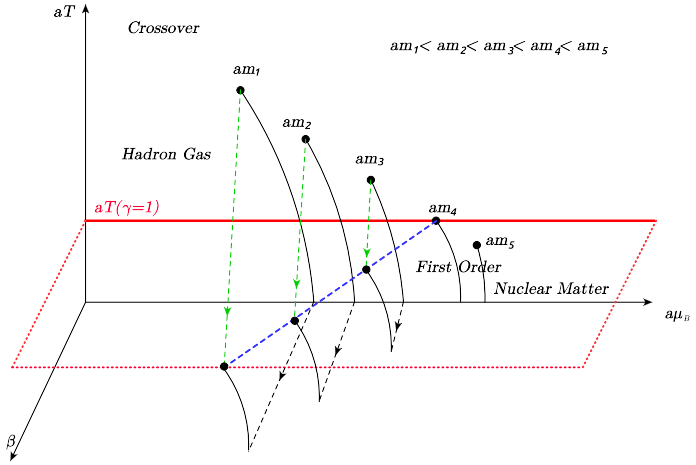

Figure 1: Sketch of β and quark mass dependence of the CEP on anisotropic lattices. The red plane denotes fixed temperature in lattice units $aT = 1/N_t$, and the dotted blue line is the expected critical end line in the $aT = 1/N_t$ plane. The dotted green lines are the expected behavior of CEP at fixed quark mass in $aT > 1/N_t$, as a function of β.

2. Setup

We use staggered fermions in the dual formulation [3, 4, 5] with gauge corrections $O(\beta)$ [6, 2, 7].

$$Z(m_q,\mu,\gamma) =$$

$$\sum_{\{k,n,\ell,n_p\}} \underbrace{\prod_{b=(x,\mu)} \frac{(N_c-k_b)!}{N_c!(k_b-|f_b|)!}\gamma^{2k_b\delta_{0,\hat{\mu}}}}_{\text{singlet hoppings}} \underbrace{\prod_x \frac{N_c!}{n_x!}(2am_q)^{n_x}}_{\text{chiral condensate}} \underbrace{\prod_{\ell_3} w(\ell_3,\mu)}_{\text{triplet hoppings}} \underbrace{\prod_{\ell_f} \tilde{w}(\ell_f,\mu)}_{\text{weight modification}} \underbrace{\prod_P \frac{\left(\frac{\beta}{2N_c}\right)^{n_P+\bar{n}_P}}{n_P!\bar{n}_P!}}_{\text{gluon propagation}}, \tag{2.1}$$

$$w(\ell_3,\mu) = \frac{1}{\prod_{x\in\ell_3}}\sigma(\ell_3)\gamma^{N_c N_{\hat{0}}}\exp\left(N_c N_t r_{\ell_3} a_t \mu\right), \quad \sigma(\ell_3) = (-1)^{r_{\ell_3}+N_-(\ell_3)+1}\prod_{b=(x,\hat{\mu})\in\ell_3}\eta_{\hat{\mu}}(x), \tag{2.2}$$

where k_b and f_b are the number of dimers and gauge fluxes at bond b, n_x is the number of monomers at site x, and ℓ_3 denotes a 3-fermion fluxes loop and ℓ_f is a single fermion loop. n_P and $\bar{n}_P$ are plaquette (counterclockwise and clockwise) occupation number. $N_{\hat{0}}$ is the number of 3-fermion fluxes in temporal direction, r_{ℓ_3} is the winding number in temporal direction. N_- is the number of 3-fermion fluxes in negative direction and $\eta_{\hat{\mu}}$ is the staggered phase factor. In this simulation, we fix the temporal lattice extent to $N_t = 4$ and an anisotropy $\gamma = 1$. The lattices temperature is fixed to $aT = \frac{1}{N_t}$. If we change β, the lattice spacing a is changed but aT is invariant. We simulate for $\beta = 0.0, 0.1, \cdots, 0.9, 1.0$ and am_q from 0.0 to 0.5 with step size 0.01. We scan the baryon chemical potential $a\mu_B$ for each (β, am_q) and find the critical baryon chemical potential $a\mu_c$. On the $\mu - T$ plane in Fig.1, if the quark mass becomes heavy, the critical end point moves to the large $a\mu$ and low aT region. Because we fix the temperature and vary the quark mass, the first order phase transition occurs at lighter quark masses in our simulation. By contrast, a crossover transition is expected for heavy quark mass. At a certain critical quark mass (am_4 in Fig.1), the transition turns into a second order transition.

3. Analysis and results

3.1 Sign problem

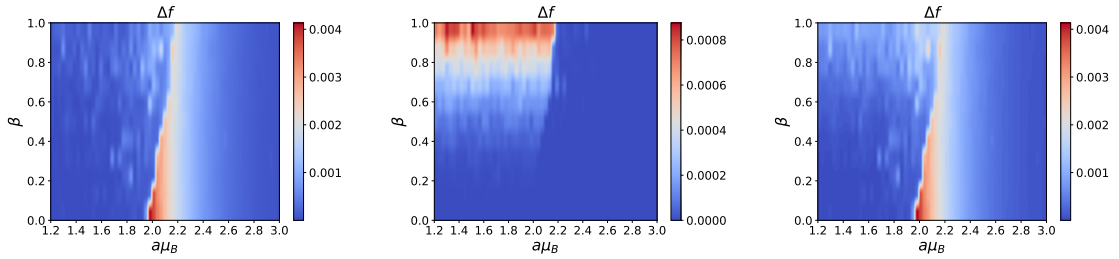

(a) From 3 fermion fluxes (b) From Single fermion flux (c) Total sign problem

Figure 2: Sign problems from two difference sources.

First, let us consider the sign problem at finite β and am_q. The sign problem comes from the odd number of fermion flux. In $O(\beta)$, only single and 3 fermion fluxes cause the sign problem and they are distinguishable. Single fermion flux and 3 fermion fluxes make fermion loops like baryon world lines in the strong coupling limit, and the sign problems is related to their geometries [2]. We distinguish these two types of sign problems and show in the Fig. 2(a) and Fig. 2(b). Here Δf is a difference between full and sign quenched free energy density and sign is $\sigma = \exp\left(-N_s^3 N_t \Delta f\right)$. In the Fig. 2(a), the sign problem from 3 fermion fluxes mainly occurs near the phase transition region. We will see in the next section that the first order transition weakens when increasing β. So, the phase transition area gets wide in $a\mu$. The single fermion flux sign problem increases with β as expected, but only occurs in the hadronic gas phase as shown in Fig. 2(b). We present the combined sign problem in Fig. 2(c).

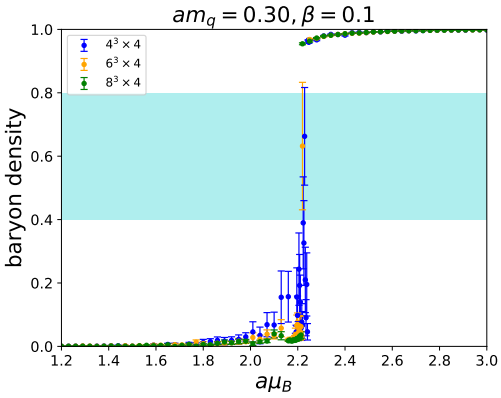

(a) $\beta = 0.1$, $am_q = 0.3$

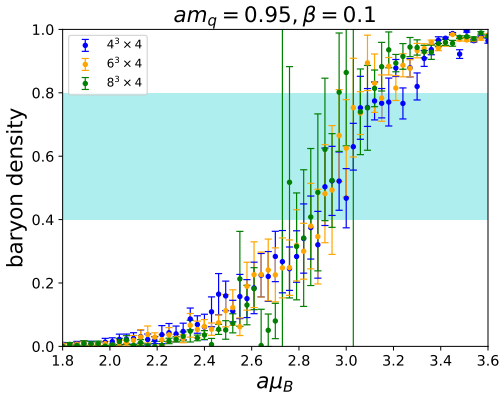

(b) $\beta = 0.1$, $am_q = 0.95$

Figure 3: Baryon density at $\beta = 0.1$

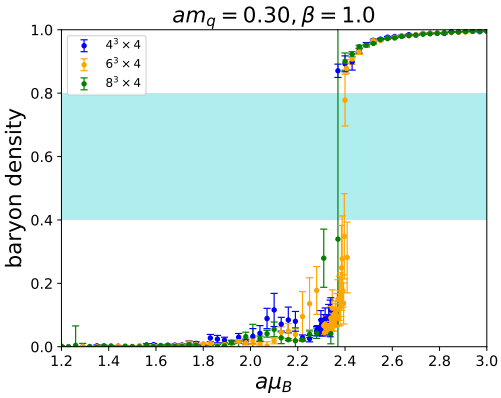

(a) $\beta = 1.0$, $am_q = 0.3$

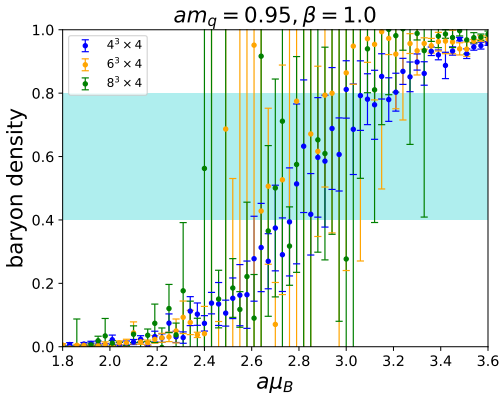

(b) $\beta = 1.0$, $am_q = 0.95$

Figure 4: Baryon density at $\beta = 1.0$

3.2 Analysis of baryon density

Now let us consider the baryon density $\langle n_B \rangle = \frac{1}{V_s N_t} \frac{\partial}{\partial (N_c a_t \mu)} \log Z = \frac{1}{V_s} \langle \sum_{\ell_3} r_{\ell_3} \rangle$ which is our observable to determine the critical end points, where V_s is a spatial volume. We present our results of baryon density in Fig. 3 and Fig. 4. In a first step, the critical $a\mu_c$ is determined by data points crossing the blue band, which was chosen by eye to be sufficiently distinct from both zero and saturation. In Fig. 3 we compare the onset of the nuclear transition for $\beta = 0.1$ for two different quark masses and various volumes. At small quark mass, the transition is consistent with first order, and large quark mass weakens the phase transition. This also holds for Fig. 4. If we fix the quark mass and change β, comparing Fig. 3(a) and Fig. 4(a) or Fig. 3(b) and Fig. 4(b), we can see increasing β diminishes the phase transition. From the above analysis, we choose the $a\mu_c$ and plot them with respect to am_q in Fig. 5. The small quark mass region results in a first order phase transition and the large quark region results in a crossover. As β increases, the first order region shrinks and the crossover is extended. Between these first order and crossover transitions, there is

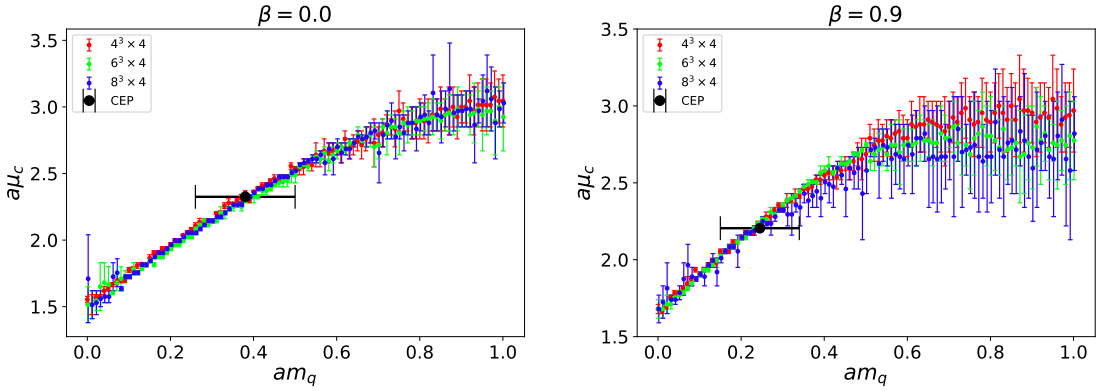

(a) $\beta = 0.0$ (b) $\beta = 0.9$

Figure 5: Critical chemical potential ($a\mu_c$) as a function of quark mass (am_q).

a critical end point. Hence, the critical end point is moving to the smaller quark masses when β is increased.

3.3 Critical end point analysis using histograms

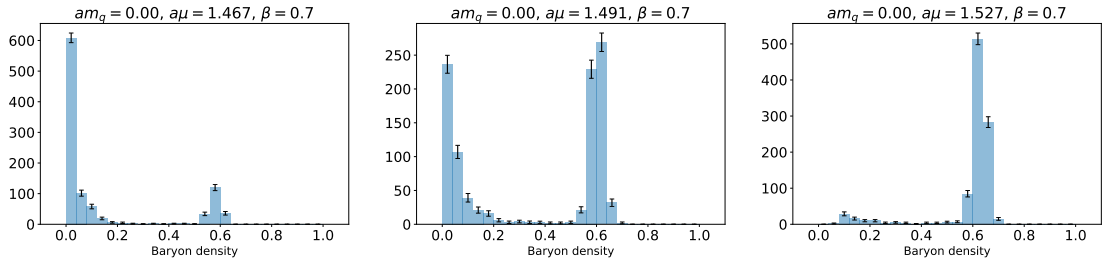

Figure 6: Baryon density histogram at small quark mass $am_q = 0.0$

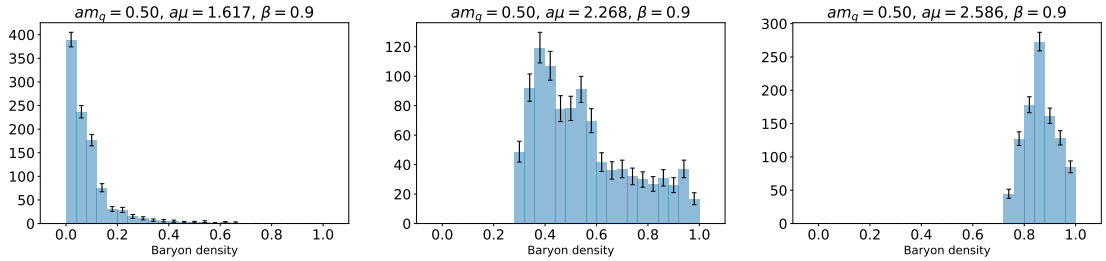

Figure 7: Baryon density histogram at large quark mass $am_q = 0.5$

Because of the huge statistical errors near the critical chemical potential μ_c, the analysis of the baryon susceptibility is difficult. So, we analyse the data using histograms to bound the critical end points. We use the data of a $8^3 \times 4$ volume for the histograms and the errors are computed by the bootstrap resampling method. In the Fig. 6 and Fig. 7, we plot histograms around $a\mu_c$. At small

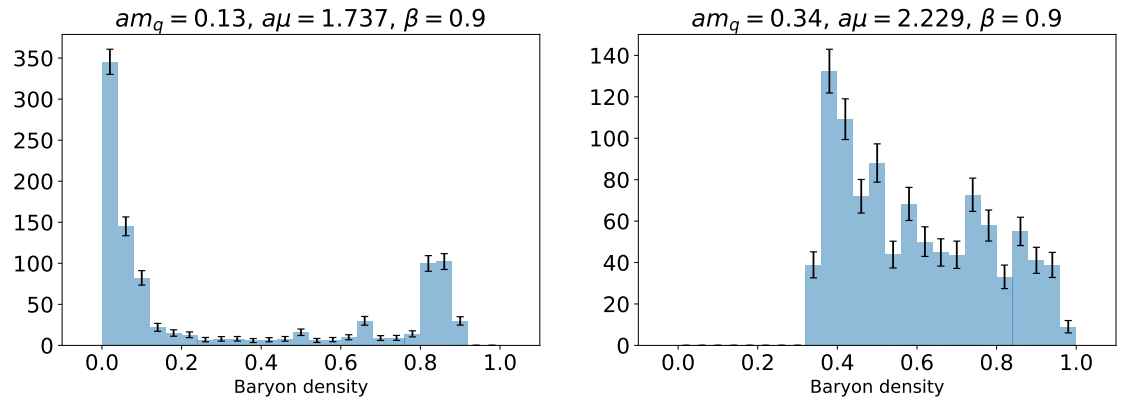

(a) Lower bound on CEP

(b) Upper bound on CEP

Figure 8: Baryon density histogram of lower and upper limit of am_q at $a\mu_c$ for critical end point at $\beta = 0.5$.

quark masses, the histograms have a two-peak distribution. Clearly at this quark mass, the phase transition is of first order. For large quark mass, there is no two-peak distribution and the peak moves smoothly from one state to the other state with increasing $a\mu$. There is no perfect two-peak distributions in the first order transition histogram because of finite volume effects, so we choose the lower bound for the CEP when two-peak distribution is clear that is shown in Fig. 8(a). The upper bound for the CEP is selected when two-peak vanishes and a peak starts to move smoothly. This is presented in Fig. 8(b). From the histogram analysis we can determine the upper limit of quark mass for the first order phase transition and the lower limit of that for crossover. Between those upper and lower limits, the second order end point is located. The critical line as a function of β is presented in Fig. 9(a). In this plot, the left lower corner corresponds to the first order region and the right upper corner is crossover. As β increases, the quark mass of the CEP decreases slightly. This is similar for the baryon chemical potential as shown in Fig. 9(b). To determine the error bars in Fig. 9(b), we take the smallest and largest quark masses in Fig. 9(a) for each β. Then there are corresponding $a\mu_c$ for quark masses. We use the range of these $a\mu_c$ values to the errors of critical line in Fig. 9(b). We determine the error bars from the histograms very conservatively. The huge errors in Fig. 9 are caused by the uncertainty and small statistics. The β dependence of both am_q and $a\mu$ are linear in β in the small $\beta \lesssim 1$ region.

4. Conclusion

We simulate the dual representation with finite quark mass and lattice gauge coupling β. Because this simulation takes into account only $O(\beta)$, we restrict to the range of β smaller than one. In this parameter space, the sign problem is still mild enough to use a sign reweighting method. We obtain the β dependence of the critical line using a histogram analysis. In the small β region, the critical line looks like linear, but still has large errors. Hence, the higher corrections of β are essential to extend this study to β larger than one and an important step in this direction has been addressed in Ref. [7].

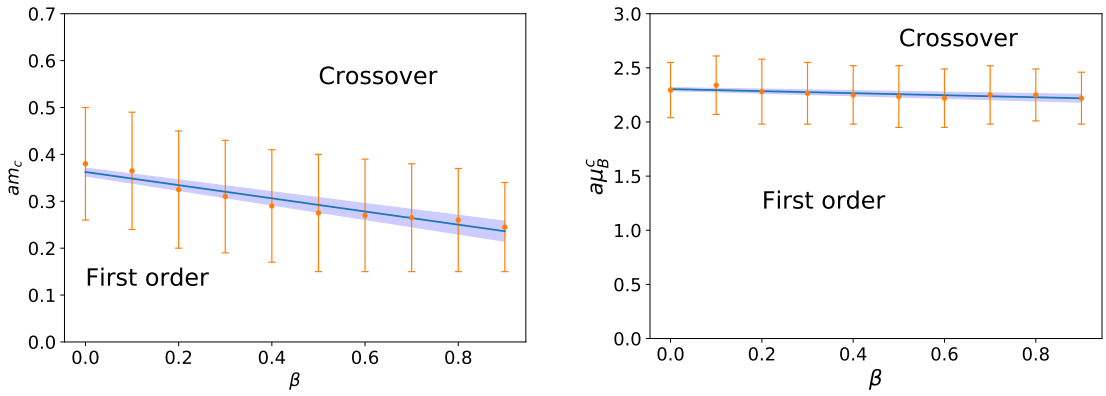

(a) Quark mass critical line

(b) Baryon chemical potential critical line

Figure 9: Critical line of end points as a function of β.

Acknowledgments

The authors J.K., O.P. and W.U. acknowledge support by the Deutsche Forschungsgemeinschaft (DFG, German Research Foundation) through the CRC-TR 211 'Strong-interaction matter under extreme conditions'– project number 315477589 – TRR 211. J.K. would like to thank the Center for Scientific Computing, University of Frankfurt for making their High Performance Computing facilities available. W.U. acknowledges support by the Deutsche Forschungsgemeinschaft (DFG) through the Emmy Noether Program under Grant No. UN 370/1.

References

[1] J. Kim and W. Unger, *Quark Mass Dependence of the QCD Critical End Point in the Strong Coupling Limit*, *PoS* **LATTICE2016** (2016) 035, [1611.09120].

[2] G. Gagliardi, J. Kim, and W. Unger, *Dual Formulation and Phase Diagram of Lattice QCD in the Strong Coupling Regime*, *EPJ Web Conf.* **175** (2018) 07047, [1710.07564].

[3] P. Rossi and U. Wolff, *Lattice QCD With Fermions at Strong Coupling: A Dimer System*, *Nucl. Phys.* **B248** (1984) 105–122.

[4] D. H. Adams and S. Chandrasekharan, *Chiral limit of strongly coupled lattice gauge theories*, *Nucl. Phys.* **B662** (2003) 220–246, [hep-lat/0303003].

[5] M. Fromm, *Lattice QCD at string coupling: thermodynamics and nuclear physics*, *Thesis* (2010).

[6] P. de Forcrand, J. Langelage, O. Philipsen, and W. Unger, *Lattice QCD Phase Diagram In and Away from the Strong Coupling Limit*, *Phys. Rev. Lett.* **113** (2014), no. 15 152002, [1406.4397].

[7] G. Gagliardi and W. Unger, *A new dual representation for staggered lattice QCD*, 1911.08389.

B.6 Gauge Corrections to Strong Coupling Lattice QCD on Anisotropic Lattices [B6]

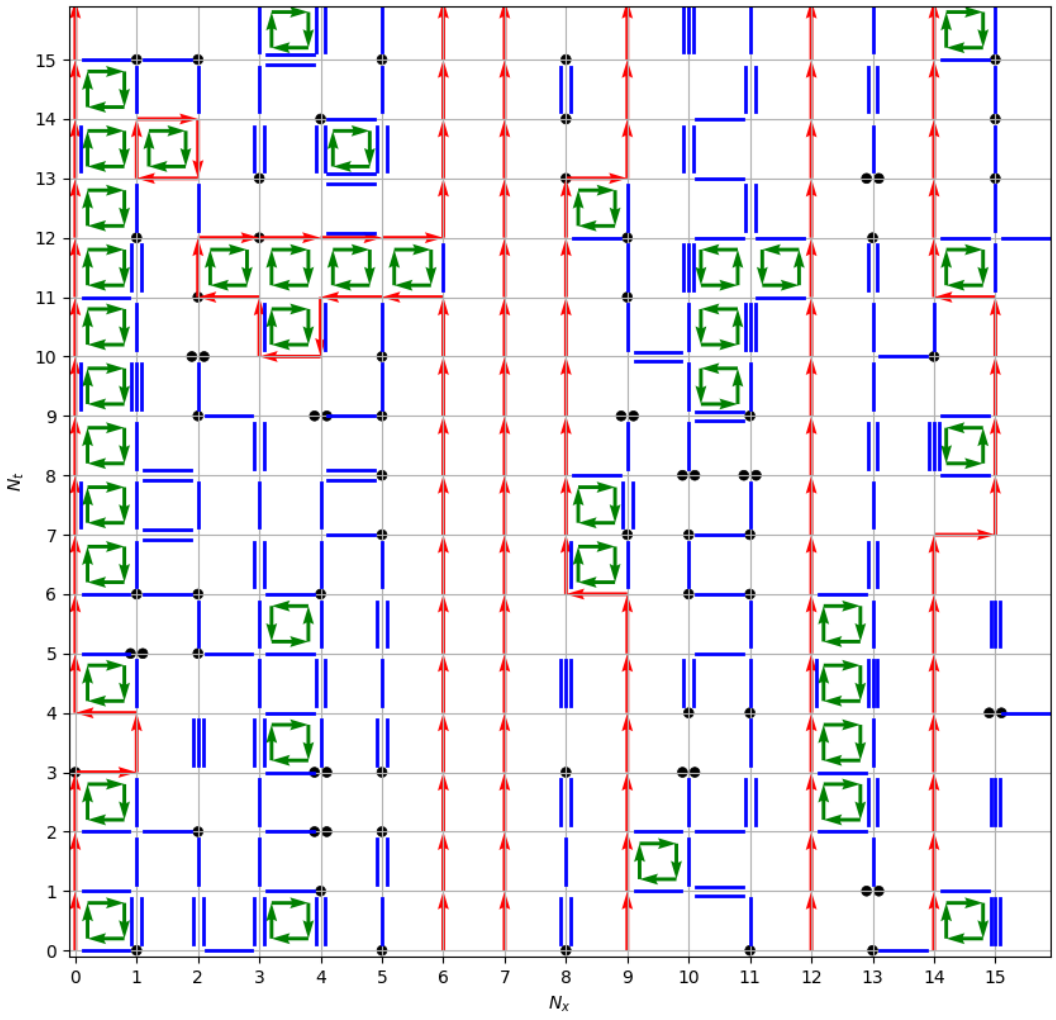

PROCEEDINGS OF SCIENCE

Gauge Corrections to Strong Coupling Lattice QCD on Anisotropic Lattices

Jangho Kim
Institut für Theoretische Physik, Goethe-Universität Frankfurt am Main, Max-von-Laue-Str. 1, 60438 Frankfurt am Main, Germany
E-mail: jkim@th.physik.uni-frankfurt.de

Marc Klegrewe
Fakultät für Physik, Universität Bielefeld, Universitätstasse 25, D33619 Bielefeld, Germany
E-mail: mklegrewe@physik.uni-bielefeld.de

Wolfgang Unger*
Fakultät für Physik, Universität Bielefeld, Universitätstasse 25, D33619 Bielefeld, Germany
E-mail: wunger@physik.uni-bielefeld.de

Lattice QCD with staggered fermions can be formulated in dual variables to address the finite baryon density sign problem. In the past we have performed simulations in the strong coupling regime, including leading order gauge corrections. In order to vary the temperature for fixed β it was necessary to introduce a bare anisotropy. In this talk we will extend our work to include results from a non-perturbative determination of the physical anisotropy $a_\sigma/a_\tau = \xi(\gamma,\beta)$, which is necessary to unambiguously locate the critical end point and the first order line of the chiral transition.

37th International Symposium on Lattice Field Theory - Lattice2019
16-22 June 2019
Wuhan, China

*Speaker.

1. Introduction

Despite many attempts and partial successes to address the finite density sign problem in lattice QCD, a solution applicable to the full parameter space (temperature T, baryon chemical potential μ_B, quark mass m_q and lattice gauge coupling β) has not yet been established. Here we report on the incremental progress to unravel the phase diagram in the strong coupling regime of lattice QCD with staggered fermions, based on a leading order strong coupling expansion valid to $\mathcal{O}(\beta)$ [1, 2, 3]. The recent progress to address higher order corrections [4] are not yet considered in full Monte Carlo simulations.

The phase diagram of lattice QCD in the strong coupling limit has been investigated since more than 30 years [5, 6, 7, 8] and is by now well known, with the Worm algorithm as a main Monte Carlo tool to investigate its features [9, 10, 11]. Beyond the strong coupling limit, the leading order gauge corrections have been included as well, but ambiguities on the phase boundary arising when using different N_τ have not yet been addressed. These ambiguities have so far only been successfully resolved in the strong coupling limit (both in the chiral limit [12] and at finite quark mass [13]).

The long-term goal is to extend the validity of the strong coupling expansion to answer an important question on the existence of the critical end point (CEP): At strong coupling, the CEP has been located at $(a\mu_B^c, aT^c) = (1.56(3), 0.80(2))$ in the chiral limit (where the CEP turns into a tri-critical point TCP), and its quark mass dependence has been investigated, with tri-critical scaling $\propto m_q^{2/5}$ for small quark masses [14]. The dependence of the location of the CEP as a function of β has not yet been determined. Whether the CEP also exists in the continuum limit remains an open question. First hints can be obtained by monitoring the β-dependence of the CEP for small β: if it moves to smaller μ_B (and if this behaviour is monotonous), it may exist; if it moves to larger μ_B, it may even vanish in the continuum limit and the chiral transition is for all values of μ_B just a crossover.

The main difficulty when mapping out the phase diagram is that we need to introduce a bare anisotropy γ in the strong coupling regime in order to vary the temperature continuously at fixed values of β. The temperature and chemical potential are however determined by the physical anisotropy $\xi \equiv \frac{a_\sigma}{a_\tau}$, which depends non-perturbatively on γ and the lattice gauge coupling β. Here we will report on how the β-dependence of ξ is determined, and present preliminary results when applied to the phase diagram in the strong coupling regime.

2. Dual formulation of lattice QCD

The strong coupling regime of lattice QCD can be formulated in a dual representation and it was generalized recently to include in principle any order in β [4]. In this proceedings however, we only incorporate the leading order gauge correction $\mathcal{O}(\beta)$ as outlined in [2] and re-derived in the appendix of [4]. It is based on a series expansion in terms of the (anti-) quark hopping $\bar{d}_\mu(x)$ from the staggered Dirac operator, and plaquette occupation numbers $n_p, \bar{n}_p$ on plaquette coordinates $p = (x, \mu, \nu)$ from the Wilson gauge action. In contrast to previous formulations of the

dual partition sum, we now adopt the notation:

$$k_\mu(x) = \min\left\{d_\mu(x), \bar{d}_\mu(x)\right\}, \qquad f_\mu(x) = d_\mu(x) - \bar{d}_\mu(x), \tag{2.1}$$

where $k_\mu(x) \in \{0, \dots N_c\}$ is the *dimer number* and $f_\mu(x) \in \{-N_c, \dots N_c\}$ is the *net quark flux*. The $k_\mu(x)$ are always quark-antiquark combinations, and color singlets formed by a quark and gluon are no longer regarded as dimers (in contrast to our previous formulation - the new convention is advantageous when higher order corrections are considered). The dual degrees of freedom $\{k, f, m, \bar{n}, n\}$ fulfill the gauge constraint at each link:

$$f_\mu(x) + \sum_{\nu>\mu}\Big[\delta n_{\mu,\nu}(x) - \delta n_{\mu,\nu}(x-\nu)\Big] - \sum_{\nu<\mu}\Big[\mu \leftrightarrow \nu\Big] = N_c\, q_\mu(x), \tag{2.2}$$

where for the $\mathscr{O}(\beta)$ partition function, $q_\mu(x) \in \{-1, 0, 1\}$ and $\delta n_{\mu,\nu}(x) \equiv \delta n_p = n_p - \bar{n}_p \in \{-1, 0, 1\}$. The Grassmann constraint at each lattice site is:

$$m_x + \sum_{\pm\mu}\left(k_\mu(x) + \frac{|f_\mu(x)|}{2}\right) = N_c, \qquad \sum_{\pm\mu} f_\mu(x) = 0. \tag{2.3}$$

In terms of the above dual variables, and including a bare anisotropy γ, the partition function can be rewritten as:

$$Z(\beta, \gamma, \mu_q, \hat{m}_q) = \sum_{C=\{n_p, \bar{n}_p, k_\ell, f_\ell, m_x\}} \sigma(C) \prod_p \frac{\tilde{\beta}^{n_p+\bar{n}_p}}{n_p!\bar{n}_p!} \prod_{\ell=(x,\mu)} \frac{e^{\mu_q \delta_{\mu,0} f_\mu(x)} \gamma^{\delta_{\mu,0}\left(|f_\mu(x)| + 2k_\mu(x)\right)}}{k_\ell!(k_\ell + |f_\ell|)!} \prod_x \frac{(2\hat{m}_q)^{m_x}}{m_x!} T_i(C_x) \tag{2.4}$$

with $\tilde{\beta} = \frac{\beta}{2N_c}$, the quark chemical potential $\mu_q = \frac{1}{N_c}\mu_B$. The three non-trivial vertex weights

$$T_1 = \frac{N_c!}{\sqrt{N_c}}, \qquad T_2 = (N_c - 1)!, \qquad T_3 = \frac{N_c!}{\sqrt{N_c}} \tag{2.5}$$

depend on the local degrees of freedom $C_x = \{m_x, k_\mu(x), f_\mu(x), n_{\mu\nu}(x), \bar{n}_{\mu\nu}(x)\}$ and are employed whenever some $n_{\mu\nu}(x) > 0$ ($\bar{n}_{\mu\nu}(x) > 0$) and some $f_\mu(x) > 1$. For $N_c = 3$, the sign

$$\sigma(C) = \prod_{\ell_1} \sigma(\ell_1) \prod_{\ell_3} \sigma(\ell_3), \qquad \sigma(\ell) = (-1)^{1 + w(\ell) + N_-(\ell)} \prod_{\tilde{\ell}} \eta_\mu(x) \tag{2.6}$$

factorizes into single fermion ($|f_\mu(x)| = 1$) and triple fermion loops ($|f_\mu(x)| = 3$). This factorization no longer holds beyond $\mathscr{O}(\beta)$, see [4]. The dual degrees of freedom are color singlets which are no longer just baryons and mesons as in the strong coupling limit: the gauge corrections will resolve the quark structure of the point-like baryons and mesons, making them effectively spread out over one or more lattice spacings. The reason why the sign problem is mild in the strong coupling limit is that baryons are heavy, where $\Delta_f \simeq 10^{-5}$. This is still approximately true for $\beta \lesssim 1$, where the sign problem remains manageable. For details see [3].

In the following we will consider the chiral limit of the partition function Eq. (2.4), which implies $m_x = 0$ and which has the symmetry group :

$$U(1)_V \times U(1)_{55}: \qquad \chi(x) \mapsto e^{i\varepsilon(x)\theta_A + i\theta_V}\chi(x), \qquad \varepsilon(x) = (-1)^{x_1+x_2+x_3+x_4}, \tag{2.7}$$

with $U(1)_V$ the baryon number conservation and $U(1)_{55}$ the remnant chiral symmetry which is broken spontaneously at low temperatures and densities. In Sec. 4 we will address the chiral critical line that terminates in a tri-critical point before turning first order.

3. Anisotropy Calibration at finite β

It is crucial to understand the relationship between the bare anisotropy γ and the non-perturbative anisotropy $\xi \equiv \frac{a_\sigma}{a_\tau}$ (with $a \equiv a_\sigma$ the spatial and a_τ the temporal lattice spacing) in order set the temperature and chemical potential consistently for various N_τ. Anisotropic lattices are necessary in the strong coupling regime since at fixed β this is the only way to vary the temperature continuously [15, 16]. The precise correspondence between ξ and γ has been established in the strong coupling limit and in the chiral limit [12], resulting in

$$\xi(\gamma) \approx \kappa\gamma^2 + \frac{\gamma^2}{1+\lambda\gamma^4}, \qquad \kappa = 0.781(1), \tag{3.1}$$

and at finite quark mass in [13], where it was shown that $\kappa(m_q) = \lim_{\xi\to\infty} \frac{\xi}{\gamma^2}$ has a simple mass dependence in the strong coupling limit. The basic idea of the anisotropy calibration is to identify a conserved current and scan in γ such that the lattice is physically isotropic for a fixed aspect ratio:

$$N_\sigma a_\sigma \stackrel{!}{=} N_\tau a_\tau \qquad \Rightarrow \qquad \xi = \frac{N_\tau}{N_\sigma}. \tag{3.2}$$

The conserved current is related to the pion [17]

$$j_\mu(x) = \varepsilon(x)\left(k_\mu(x) - \frac{1}{2}|f_\mu(x)|\right), \tag{3.3}$$

with $\varepsilon(x) = \pm 1$ the parity of site x. Eq. (3.3) is the generalization of the strong coupling limit (where $f_\mu(x) \in \{-N_c, 0, N_c\}$ is the baryon flux through that link) to incorporate gauge corrections. This allows us to extend the anisotropy calibration to finite β to obtain $\xi(\gamma,\beta)$. Away from the strong coupling limit it is in principle necessary to include a second bare anisotropy γ_G in the gauge part

$$\beta^{n_p+\bar{n}_p} \quad \to \quad \beta_\sigma^{n_{p\sigma}+\bar{n}_{p\sigma}}\beta_\tau^{n_{p\tau}+\bar{n}_{p\tau}}, \qquad \gamma_G = \sqrt{\frac{\beta_\tau}{\beta_\sigma}} \tag{3.4}$$

and then scan in both the fermionic and gauge anisotropy to obtain $\xi(\gamma,\gamma_G,\beta)$. On finer lattices this is indeed necessary [7], but in the strong coupling regime, where we cannot set a scale, it is an unnecessary complication: as β is increased, the lattices needed to study the chiral phase transition will eventually become isotropic, and beyond this point, the temperature is varied via $a(\beta)$. In this proceedings, we will always set $\gamma_G = 1$ and leave the more general setup for the future.

In Fig. 1 (*left*) we show the anisotropy calibration for various fixed β: On lattices ${N_\sigma}^3 \times N_\tau$ with aspect ratios $\xi = 2,3,4,5,6,8$ we obtain the value of $\gamma(\xi)$ where the ratio of the temporal and spatial fluctuations of the conserved charge Q_t, Q_s are equal. This is repeated for various β. Since the partition function Eq. (2.4) depends on γ and N_τ, the bare (mean field) temperature $[aT]_{\rm mf} = \frac{\gamma^2}{N_\tau}$ needs to be corrected by the non-perturbative factor $[\xi/\gamma^2]_\beta$, shown in Fig. 1 (*right*), to yield the correct temperature $aT = \frac{\xi(\gamma)}{N_\tau}$. Our result allows to define the Euclidean continuous time limit $a_\tau \to 0$ unambiguously at fixed β: the temperature and chemical potential are then defined as

$$aT = \kappa(\beta)[aT]_{\rm mf}, \qquad a\mu_B = \kappa(\beta)[a\mu_B]_{\rm mf} \qquad \text{with} \qquad \kappa(\beta) = \lim_{\xi\to\infty}[\xi/\gamma^2]_\beta. \tag{3.5}$$

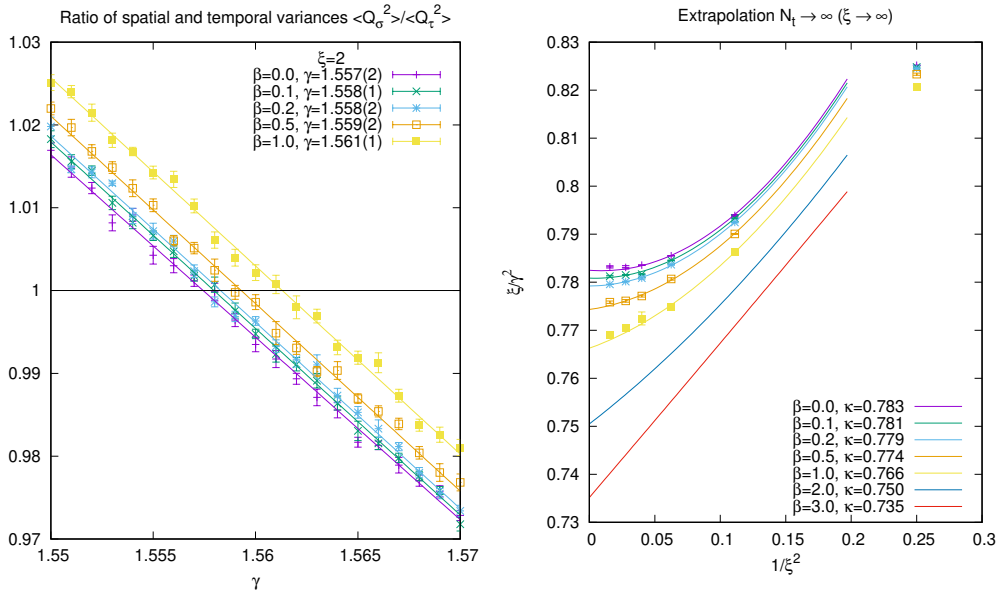

Figure 1: *Left:* Determination of γ for various β by requiring the ratio of charge fluctuations to be equal, shown for $\xi = 2$. *Right:* Extrapolation of the correction factor ξ/γ^2 towards continuous time to yield $\kappa(\beta)$.

4. Gauge Corrections to the Phase Diagram and Density of States

We will now focus on a particularly important application of the previous result: the modification of the chiral transition within the grand-canonical phase diagram, when taking into account the non-perturbative definition of temperature and chemical potential Eq. (3.5). In Fig. 2 we show the effect of applying the β-dependent correction factor $[\xi/\gamma^2]_\beta$ to the phase boundary, for the various β in a regime where the sign problem is manageable. All data have been measured via the Worm algorithm in combination with plaquette updates, on lattices ${N_\sigma}^3 \times 4$ We observe that the back-bending at lower temperatures vanishes. This behaviour meets our expectations, but we require larger lattices and should check that we have the same finding also on lattices with $N_\tau > 4$.

We also investigate the density of states on anisotropic lattices, which can be measured via the Wang-Landau method. Since the quark fluxes $f_\mu(x)$ form world lines, and the total number of quark fluxes wrapping around in temporal direction is a multiple of N_c due to the gauge constraint Eq. (2.2), it is possible to define baryon number sectors $N_B \in \{-{N_\sigma}^3, \ldots, {N_\sigma}^3\}$ and allow updates that modify the baryon number by one unit. We will explain the details of the canonical simulations and the resulting canonical phase diagram is in the $n_B - T$ plane in a forthcoming publication. The analysis of the density of states in N_B as shown in Fig. 3 can yield additional insights concerning the first order phase boundary below the TCP: the density of states is weighted with $e^{N_B \mu_B / T}$ for various β to the critical chemical potential $\mu_B^{1^{\text{st}}}$, where the peak heights are equal. We observe that the first order transition weakens with β, and that the the critical chemical potential $\mu_B^{1^{\text{st}}}$ increases only slightly with β. This is in agreement with the findings of the β-dependence of the nuclear transition at low temperatures on isotropic lattices [3].

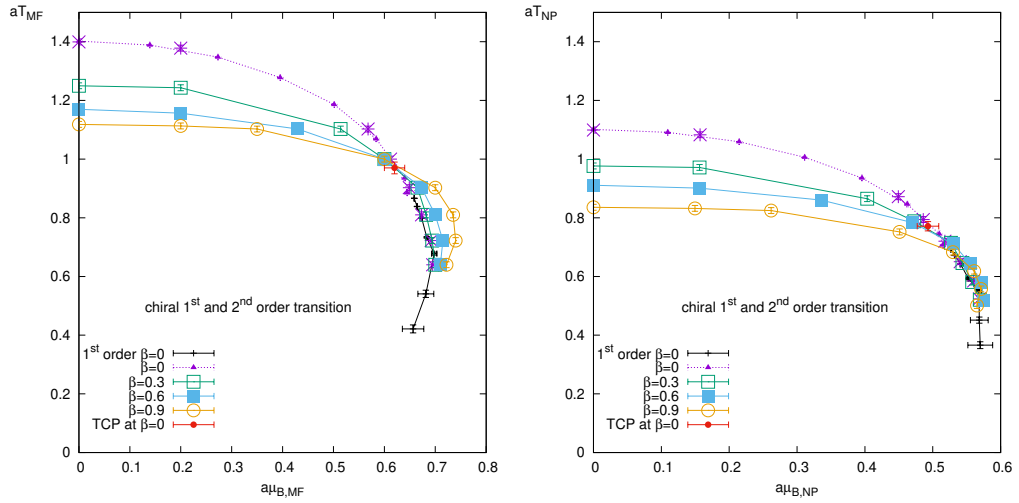

Figure 2: Comparison of the phase boundary with the mean field definition of the temperature *(left)* and its non-perturbative counterpart *(right)*, resulting in a collapse of the first order line for all values of β considered.

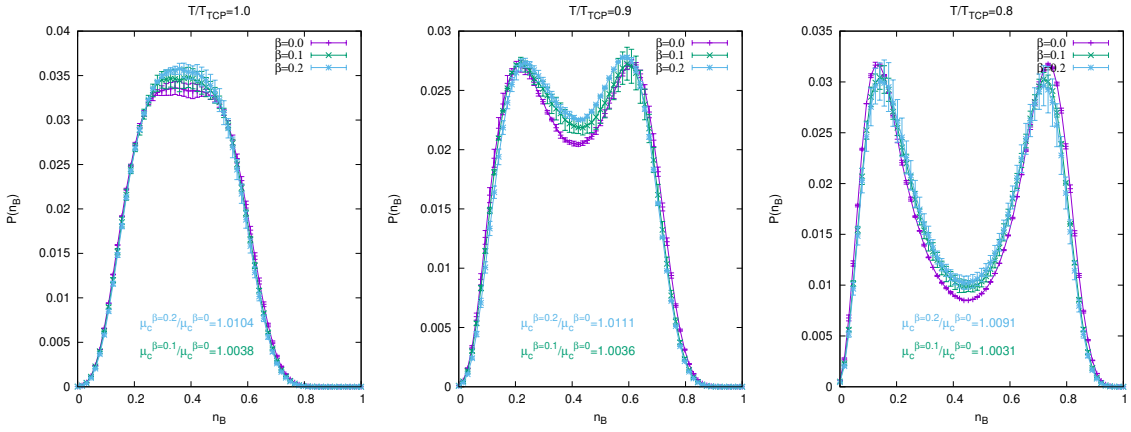

Figure 3: The density of states weighted to the critical chemical potential μ_B^c, showing a double peak structure for $aT < aT_{TCP}$. The value of $\mu_B^{1^{st}}$ only very mildly grows with β.

5. Conclusions

We determined the non-perturbative relation between the bare anisotropy γ and the lattice anisotropy $\xi = \frac{a}{a_t}$ at finite β in the range of validity $\beta \leq 1$, based on the leading order partition function. The results have been used to define the temperature and baryon chemical potential unambiguously. The extrapolation $a_t \to 0$ is under control. This may even allow to extend the existing Monte Carlo simulations in Euclidean continuous time to finite β in the future.

The main (still preliminary) finding on the phase boundary of lattice QCD in in the chiral limit is that the first order line is not β-dependent after the non-perturbative correction of the temperature and chemical potential. This is consistent with mean-field theory [18] and results on isotropic lattices. Whether the first order line is β-dependent for $\beta > 1$ and whether the tri-critical point

moves to larger or smaller chemical potential when β is increased requires further investigation. Most likely higher order corrections need to be included, as outlined in [4].

We have also presented first results on the β-dependence of the density of states in the baryon number, from which the canonical phase diagram can be determined. Even though this dependence is very weak, this method has the potential to discriminate between the chiral and nuclear transition and address the question whether they split, as is expected: in the continuum, chiral symmetry should still be broken in the nuclear phase, resulting in two separate first order transitions at low temperatures.

Acknowledgments

We thank Aaron von Kamen for his contributions to the Wang-Landau method, and Giuseppe Gagliardi for discussions on the partition function. Numerical simulations were performed on the OCuLUS cluster at PC2 (Universität Paderborn). This work is supported by the Deutsche Forschungsgemeinschaft (DFG) through the Emmy Noether Program under grant No. UN 370/1 and through the CRC-TR 211 'Strong-interaction matter under extreme conditions'– project number 315477589 – TRR 211.

References

[1] P. de Forcrand, J. Langelage, O. Philipsen, and W. Unger *Phys. Rev. Lett.* **113** (2014), no. 15 152002, [1406.4397].

[2] G. Gagliardi, J. Kim, and W. Unger *EPJ Web Conf.* **175** (2018) 07047, [1710.07564].

[3] J. Kim, Philipsen, Owe, and W. Unger *PoS* **LATTICE2019** (2019).

[4] G. Gagliardi and W. Unger 1911.08389.

[5] N. Kawamoto and J. Smit *Nucl. Phys.* **B192** (1981) 100. [,556(1981)].

[6] P. Rossi and U. Wolff *Nucl. Phys.* **B248** (1984) 105–122.

[7] F. Karsch and K. H. Mutter *Nucl. Phys.* **B313** (1989) 541–559.

[8] N. Kawamoto, K. Miura, A. Ohnishi, and T. Ohnuma *Phys. Rev.* **D75** (2007) 014502, [hep-lat/0512023].

[9] D. H. Adams and S. Chandrasekharan *Nucl. Phys.* **B662** (2003) 220–246, [hep-lat/0303003].

[10] P. de Forcrand and M. Fromm *Phys. Rev. Lett.* **104** (2010) 112005, [0907.1915].

[11] W. Unger and P. de Forcrand *PoS* **LATTICE2011** (2011) 218, [1111.1434].

[12] P. de Forcrand, W. Unger, and H. Vairinhos *Phys. Rev.* **D97** (2018), no. 3 034512, [1710.00611].

[13] W. Unger, D. Bollweg, and M. Klegrewe *PoS* **LATTICE2018** (2018) 181, [1811.03584].

[14] J. Kim and W. Unger *PoS* **LATTICE2016** (2016) 035, [1611.09120].

[15] L. Levkova, T. Manke, and R. Mawhinney *Phys. Rev.* **D73** (2006) 074504, [hep-lat/0603031].

[16] M. Klegrewe and W. Unger *PoS* **LATTICE2018** (2018) 182, [1811.01614].

[17] S. Chandrasekharan and F.-J. Jiang *Phys. Rev.* **D68** (2003) 091501, [hep-lat/0309025].

[18] K. Miura, N. Kawamoto, T. Z. Nakano, and A. Ohnishi *Phys. Rev.* **D95** (2017), no. 11 114505, [1610.09288].

B.7 Towards a Dual Representation of Lattice QCD [B7]

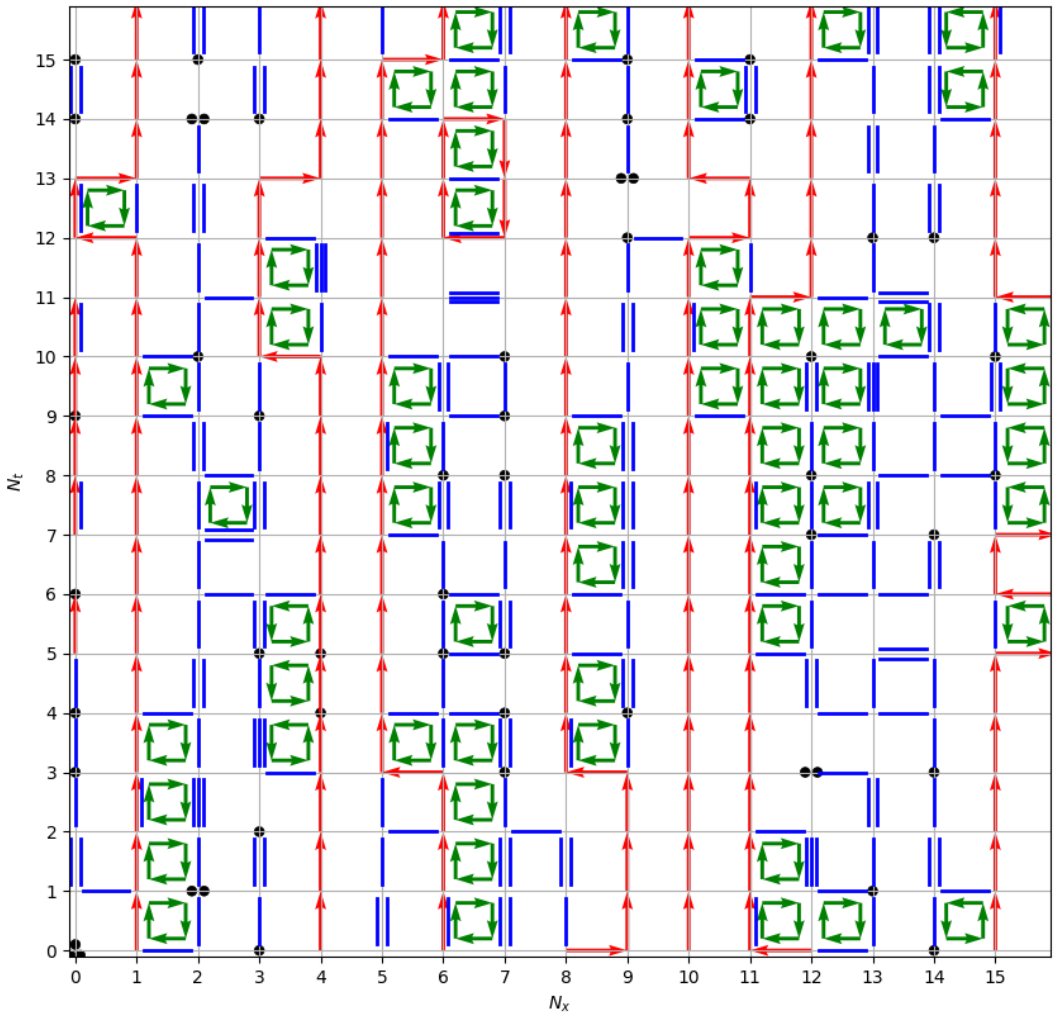

PROCEEDINGS OF SCIENCE

Towards a Dual Representation of Lattice QCD

Giuseppe Gagliardi*
Fakultät für Physik, Universität Bielefeld, D-33615 Bielefeld, Germany
E-mail: giuseppe@physik.uni-bielefeld.de

Wolfgang Unger
Fakultät für Physik, Universität Bielefeld, D-33615 Bielefeld, Germany
E-mail: wunger@physik.uni-bielefeld.de

Our knowledge about the QCD phase diagram at finite baryon chemical potential μ_B is limited by the well known *sign problem*. The path integral measure, in the standard determinantal approach, becomes complex at finite μ_B so that standard Monte Carlo techniques cannot be directly applied. As the sign problem is representation dependent, by a suitable choice of the fundamental degrees of freedom that parameterize the partition function, it can get mild enough so that reweighting techniques can be used. A successful formulation, capable to tame the sign problem, is known since decades in the limiting case $\beta \to 0$, where performing the gauge integration first, gives rise to a dual formulation in terms of color singlets (MDP formulation). Going beyond the strong coupling limit represents a serious challenge as the gauge integrals involved in the computation are only partially known analytically and become strongly coupled for $\beta > 0$. We will present explict formulae for all the integral relevant for SU(N) gauge theories discretised à la Wilson, and will discuss how they can be used to obtain a positive dual formulation, valid for all β, for pure Yang Mills theory.

The 36th Annual International Symposium on Lattice Field Theory - LATTICE2018
22-28 July, 2018
Michigan State University, East Lansing, Michigan, USA.

*Speaker.

1. Introduction

Lattice QCD at finite baryon-chemical potential is affected by the *sign problem*. At non-zero μ_B the LQCD action becomes complex giving rise to an exponentially hard problem. Although various techniques have been developed in the past decades in order to circumvent the sign problem, an ultimate solution is still lacking. A promising approach that we want to discuss here is the dual variables approach. The key point in this approach is realising that the sign problem is representation dependent. This means that by a suitable change of the degrees of freedom, it is possibile to write down the partition function in terms of states that are closer to the true eigenstate of the Hamiltonian, resulting in a much milder sign problem. Dual formulations have been used in the past years to alleviate, or even solve, the sign problem in various model (see for instance [1]-[3]). Here we want to discuss the dual approach in Yang-Mills theory and in full QCD from the perspective of strong coupling expansion. At $\beta = 0$, corresponding to the strong coupling limit, the partition function can be written in terms of dual (integer) degrees of freedom representing mesons and baryons [4]. This dual formulation has the advantage that the sign problem induced by a baryon-chemical potential is mild enough so that the phase boundaries can be mapped out using standard reweighting in the sign. Incorporating leading order β-correction is also possible, by computing the modified weights induced by a single plaquette excitation [5], whereas in [7] gauge contributions produced by plaquette-surfaces have been taken into account. Going beyond these approximations is very challenging. First of all, the link integrals that appear are not completely known for SU(N). In addition, a plaquette induced sign problem can appear at $\beta > 0$, limiting the applicability of this method to small β values. We will discuss these issues. In particular, we will solve the problem of link integration finding explicit formulae for polynomial integrals over SU(N). After analysing the sign problem in SC-LQCD with plaquette surface excitations, we will focus on Yang-Mills theory finding a dual, positive, representation by integrating out the gauge links.

2. Formulation and Link Integration

In the following we will always consider the standard LQCD partition function with gauge action discretised à la Wilson and 1 flavour of unimproved staggered quarks:

$$\begin{aligned} \mathcal{Z} &= \prod_x \int d\chi_x d\bar{\chi}_x e^{2am_q \bar{\chi}_x \chi_x} \prod_\ell \int_G dU_\ell e^{\sum_p \frac{\beta}{N} \mathrm{Re}(\mathrm{Tr} U_p)} \cdot e^{\mathrm{Tr}\left[U_\ell \mathcal{M}_\ell^\dagger + U_\ell^\dagger \mathcal{M}_\ell\right]} \\ \left(\mathcal{M}^\dagger\right)_i^j &= \eta_\mu(x) e^{a\mu_B \delta_{\mu,0}} \bar{\chi}_x^i \chi_{x+\mu,j}, \qquad \mathcal{M}_k^l = -\eta_\mu(x) e^{-a\mu_B \delta_{\mu,0}} \bar{\chi}_{x+\mu}^k \chi_{x,l}, \end{aligned} \tag{2.1}$$

where (ℓ, x, p) label lattice links, sites and plaquettes. After performing a strong coupling expansion in β, Eq. (2.1) can be written as:

$$\prod_x \int d\chi_x d\bar{\chi}_x \, e^{2am_q \bar{\chi}_x \chi_x} \sum_{\{n_p, \bar{n}_p\}} \prod_{\ell,p} \frac{(\beta/2N)^{n_p + \bar{n}_p}}{n_p! \bar{n}_p!} \int_G dU_\ell \mathrm{Tr}[U_p]^{n_p} \mathrm{Tr}[U_p^\dagger]^{\bar{n}_p} e^{\mathrm{Tr}\left[U_\ell \mathcal{M}_\ell^\dagger + U_\ell^\dagger \mathcal{M}_\ell\right]}$$

and we introduced the new collective variables $\{n_p, \bar{n}_p\}$ called plaquette (anti-plaquette) occupation numbers. As usual for dual formulations, we wish to integrate out some of the original degrees of freedom. In this case we want to get rid of the U_ℓ links, by explicitly performing the group integration first. Even though this is quite straightforward in the case $\beta = 0$ [6], plaquette contributions give rise to serious complications. To show this explicitly, let us consider the $O(\beta)$ corrections to SC-LQCD by Taylor expanding the gauge action to first order:

$$\prod_\ell \int_G dU_\ell \, e^{\frac{\beta}{2N}\mathrm{Tr}[U_p + U_p^\dagger]} \cdot e^{\mathrm{Tr}\left[U_\ell \mathcal{M}_\ell^\dagger + U_\ell^\dagger \mathcal{M}_\ell\right]} \approx \prod_\ell \int_G dU_\ell (1 + \underbrace{\frac{\beta}{2N}\mathrm{Tr}[U_p + U_p^\dagger]}_{O(\beta)\text{correction}}) \cdot e^{\mathrm{Tr}\left[U_\ell \mathcal{M}_\ell^\dagger + U_\ell^\dagger \mathcal{M}_\ell\right]}$$

The relevant $O(\beta)$ contribution, after performing a hopping parameter expansion of the fermionic action, is given by:

$$\prod_{\ell \in \mathcal{C}(p)} \int_G dU_\ell \frac{\beta}{2N} \mathrm{Tr}\,[U_p]\, e^{\mathrm{Tr}\left[U_\ell \mathcal{M}_\ell^\dagger + U_\ell^\dagger \mathcal{M}_\ell\right]} = \mathrm{Tr}\Big[\prod_{\ell \in \mathcal{C}(p)} J_\ell\Big], \quad \mathcal{C}(p) = \{(x,\mu) \in \partial p\}$$

$$(J_\ell[\mathcal{M}, \mathcal{M}^\dagger])^n_m = \sum_{\kappa_\ell, \bar{\kappa}_\ell} \frac{1}{\kappa_\ell! \bar{\kappa}_\ell!} \prod_{\alpha=1}^{\kappa_\ell} (\mathcal{M}_\ell)^{i_\alpha}_{j_\alpha} \prod_{\beta=1}^{\bar{\kappa}_\ell} (\mathcal{M}_\ell^\dagger)^{k_\beta}_{l_\beta} \, \mathcal{I}^{k_\ell+1, \bar{k}_\ell}_{m+\boldsymbol{i}\, n+\boldsymbol{j}, \boldsymbol{k}\, l} \tag{2.2}$$

where $\mathcal{I}^{n+1,n}$ is the polynomial gauge integral that must be computed at this order. The open color indices $\{i,j,k,l\}$ must be saturated with fermionic sources $\mathcal{M}, \mathcal{M}^\dagger$ while m, n are contracted along the countour ∂p of the plaquette p so that color singlets are recovered afterwards. Away from strong coupling, where $O(\beta^2), O(\beta^3), ..$, contributions are important, all the integrals $\mathcal{I}^{a,b}$ will in general appear. Having explicit formulae for these integrals is the first step towards a dual representation of non-abelian gauge theories in a strong coupling expansion framework. Their explicit expression is given by:

$$\mathcal{I}^{a,b}_{\boldsymbol{i}\, j, \boldsymbol{k}\, l} = \int_G dU \prod_{\alpha=1}^{a} U^{j_\alpha}_{i_\alpha} \prod_{\beta=1}^{b} (U^\dagger)^{l_\beta}_{k_\beta} \tag{2.3}$$

where dU is the usual invariant Haar measure and depending on the gauge group G the following constraints apply:[1]

$$\mathcal{I}^{a,b} \neq 0 \iff \begin{cases} a = b & \mathrm{U}(N) \\ a = b \bmod N & \mathrm{SU}(N) \end{cases} \tag{2.4}$$

These integrals were studied extensively in the past, mainly in the case $G = \mathrm{U}(N)$, which was completely solved in [8]. Creutz [9] found an explicit formula for the generating functional:

$$\begin{aligned} \mathcal{Z}^{a,b}[K,J] &= \int_{\mathrm{SU}(N)} dU \mathrm{Tr}[UK]^a \mathrm{Tr}[U^\dagger J]^b \\ \mathcal{I}^{a,b}_{\boldsymbol{i}\, j, \boldsymbol{k}\, l} &= \frac{1}{a!b!} \left(\frac{\partial}{\partial K_{j_1 i_1}} \cdots \frac{\partial}{\partial K_{j_a i_a}} \frac{\partial}{\partial J_{l_1 k_1}} \cdots \frac{\partial}{\partial J_{l_b k_b}} \mathcal{Z}^{a,b}[K,J] \right)_{K=J=0} \end{aligned} \tag{2.5}$$

[1] This gives a constraint on the $\{n_p, \bar{n}_p, k_\ell, \bar{k}_\ell\}$ that are allowed. For more details see [7].

for the case $b=0$, whereas recently Zuber computed the generating functional in the case $a=b+N$ [10]. We extended their results in order to cover the most general case ($a-b=q\cdot N$), that we present here without proof:

$$\begin{aligned} Z^{a,b}[K,J] &= \int_{\mathrm{SU}(N)} dU \,\mathrm{Tr}[UK]^a \mathrm{Tr}[U^\dagger J]^b \\ &\overset{n=\min\{a,b\}}{=} (qN+n)! \underbrace{\prod_{i=0}^{N_c-1} \frac{i!}{(i+q)!} (\det K)^q}_{\text{Baryonic contrib.}} \underbrace{\sum_{\rho\vdash n} \tilde{W}_g^{n,q}(\rho,N) t_\rho(JK)}_{\text{Mesonic contrib.}} \\ \tilde{W}_g^{n,q}(\rho,N) &= \sum_{\substack{\lambda\vdash n \\ \mathrm{len}(\lambda)\leq N}} \frac{1}{(n!)^2} \frac{f_\lambda^2 \chi^\lambda(\rho)}{D_{\lambda,N+q}}, \qquad t_\rho(A) = \prod_{\rho_i} \mathrm{Tr}(A^{\rho_i}) \end{aligned} \tag{2.6}$$

where $\lambda\vdash n$ means that λ is an integer partition[2] of size n, $\mathrm{len}(\lambda)$ is its length and $D_{\lambda,N}$, f_λ are respectively the dimension of the irreps of $\mathrm{SU}(N)$ and S_n corresponding to partition λ. Finally, $\chi^\lambda(\rho)$ are the standard S_n irreducible characters. The generating functional is splitted in two parts: the first, baryonic contribution, arises from a non-zero q and, being a power of a determinant, gives rise to epsilon tensors after differentiating with respect to source K. The second part, the mesonic contribution, is written as a sum over integer partitions that select a particular $\mathrm{SU}(N)$ invariant ($\mathrm{Tr}_\rho(JK)$) weighted by the corresponding factor $\tilde{W}_g^{n,q}(\rho,N)$. We called these functions $\tilde{W}_g^{n,q}$, "modified Weingarten functions" as they correspond to a simple generalization of the standard Weingarten functions obtained in [8]. They are all class functions of S_n as the partition ρ can be identified as a conjugacy class of permutations $[\pi]$ using the cycle decomposition. This result for the generating functional can be directly used to systematically obtain gauge corrections to any order by using:[3]

$$\begin{aligned} \mathcal{J}^{a,b}_{\boldsymbol{i}^j,\boldsymbol{k}^l}[\mathcal{M},\mathcal{M}^\dagger] &= \sum_{\{i_\alpha,j_\alpha,k_\beta,l_\beta\}} \left(\prod_{\alpha=1}^{\kappa_a} \mathcal{M}_{j_\alpha}^{\ i_\alpha}\right) \left(\prod_{\beta=1}^{\kappa_b} \mathcal{M}^\dagger{}_{l_\beta}^{\ k_\beta}\right) \mathcal{I}^{a+\kappa_a,b+\kappa_b}_{\boldsymbol{i}^j,\boldsymbol{k}^l} \\ &= \frac{k_a!k_b!}{(a+k_a)!(b+k_b)!} \frac{\partial^{(a+b)} \mathcal{Z}^{a+\kappa_a,b+\kappa_b}[J,K]}{\partial K^{i_1}_{j_1}..\partial K^{i_a}_{j_a} \partial J^{k_1}_{l_1}..\partial J^{k_b}_{l_b}}\Big|_{\substack{K=\mathcal{M}^\dagger \\ J=\mathcal{M}}} \end{aligned} \tag{2.7}$$

3. Sign problem

Although the sign problem is very mild at strong coupling, it could happen that the inclusion of gauge degrees of freedom, in the dual formulation, reintroduce it. This kind of sign problem is absent in the conventional formulation, where a sign problem is only induced by a non-zero μ_B. Our result (2.7) for $\mathcal{J}^{a,b}_{\boldsymbol{i}^j,\boldsymbol{k}^l}$ can be used to understand how the Monte Carlo weights get modified by plaquette excitations (see [7]). By making use of the previous result, we performed simulation at finite β, using an algorithm which is

[2] i.e. $\lambda\vdash n=[\lambda_1,...,\lambda_k]$ with $\sum_{i=1}^{k}\lambda_i=n$ and $\lambda_1\geq\lambda_2\geq...\geq\lambda_k>0$. $\mathrm{len}(\lambda)=k$.

[3] $\mathcal{J}^{a,b}$ is a generalisation, to arbitrary high order, of the integral appearing in Eq. (2.2).

affected by systematic errors only at order β^{N_c}. Results about the phase diagram and details of the simulation can be found in [7]. Here we want to discuss what happens to the sign problem: In Fig. 1 (*Left*), the average sign $\langle\sigma\rangle$ is plotted as a function of μ_B for various β. The sign problem seems to be immediately reintroduced. Reweighting can be applied only for $\beta < 1$, spoiling the possibility of making contact with the low coupling branch. A sign problem is also present at $\mu_B = 0$, making it clear that the gauge degrees of freedom alone, as they appear in the dual formulation, produce negative weights. From a diagrammatic point of view, an example of a configuration with negative sign is shown in Fig. 1 (*Right*). These findings suggest that to go beyond $\beta = 1$, we must study first pure Yang-Mills theory. In particular, we worked on the problem of finding a positive (dual) representation valid for all β, which will be the topic of the next section.

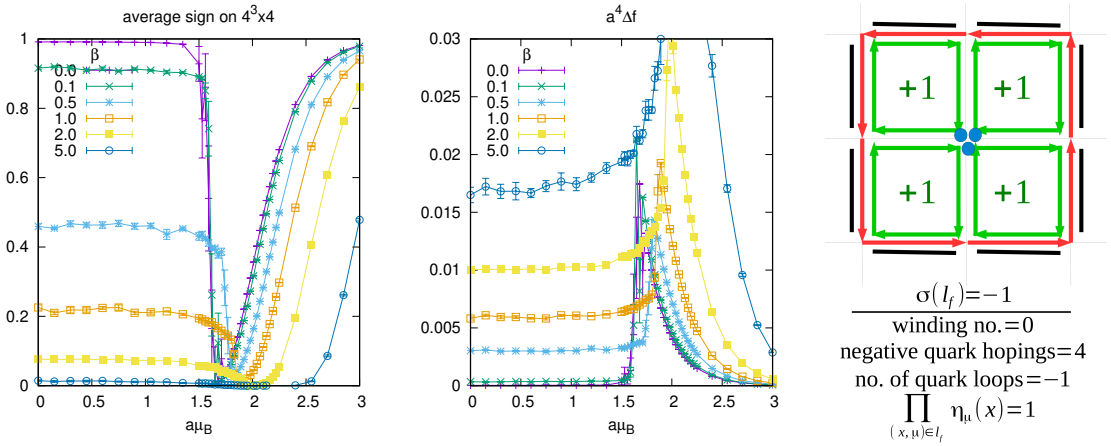

Figure 1: *Left*: The average sign $\langle\sigma\rangle = \frac{Z}{Z_{pq}} = e^{-\frac{V}{T}a^4\Delta f}$ obtained by simulations on a $4^3 \times 4$ lattice is shown as a function of the chemical potential $a\mu$ for various β. *Right*: An example of a configuration with negative sign. An odd number of monomers are trapped in a plaquette surface surrounded by a quark-flux.

4. Dualization of pure Yang Mills theory

Let us consider the partition function for pure Yang-Mills theory and expand it in Taylor series around $\beta = 0$:

$$\mathcal{Z}_{Y.M.} = \sum_{\{n_p,\bar{n}_p\}} \frac{(\beta/2N)^{\sum_p n_p+\bar{n}_p}}{\prod_p n_p!\bar{n}_p!} \underbrace{\prod_\ell \prod_p \int_{\mathrm{SU}(N)} dU_\ell \,(\mathrm{Tr}U_p)^{n_p} \left(\mathrm{Tr}U_p^\dagger\right)^{\bar{n}_p}}_{\mathbf{W}(\{\mathbf{n_p},\bar{\mathbf{n}}_\mathbf{p}\})} \tag{4.1}$$

To successfully dualize the partition function, we must find a way to integrate out the gauge fields U_ℓ, expressing the quantity $W(\{n_p, \bar{n}_p\})$ in terms of auxiliary degrees of freedom. One way to do this is by decomposing the underlying $\mathcal{I}^{a,b}$ integrals by making use

of the Weingarten functions as follows:[4]

$$\mathcal{I}^{n,n}_{\boldsymbol{i}^j,\boldsymbol{k}^l} = \sum_{\sigma,\tau\in S_n} \tilde{W}^{n,0}_g([\sigma\circ\tau^{-1}],N)\delta^{l_\sigma}_i\delta^j_{k_\tau}$$

$$\Rightarrow \quad W(\{n_p,\bar{n}_p\}) = \sum_{\{\sigma_\ell,\tau_\ell\in S_{d_\ell}\}} \prod_\ell \underbrace{\tilde{W}^{d_\ell,0}_g([\sigma_\ell\circ\tau_\ell^{-1}],N)}_{\gtrless 0} \prod_x N^{\mathrm{len}\left(\left[\hat{\sigma}_x\circ\hat{\pi}_x\right]\right)} \tag{4.2}$$

This procedure trades the coloured gauge links U_ℓ, with pair of permutations (σ_ℓ,τ_ℓ). The size of each permutation is determined by the dimer number d_ℓ, defined by:

$$d_{\ell=(x,\mu)} := \min\left\{ \begin{array}{c} \sum_{\nu>\mu} n_{x,\mu,\nu} + \bar{n}_{x-\nu,\mu,\nu} \\ \sum_{\nu>\mu} \bar{n}_{x,\mu,\nu} + n_{x-\nu,\mu,\nu} \end{array} \right\} \tag{4.3}$$

The open color indices of the delta functions appearing in Eq. (4.2) are saturated along the plaquettes to reproduce the traces in Eq. (4.1). This gives rise to powers of N. In Eq. (4.2), the permutation $\hat{\sigma}_x$ depends only on $\{n_p,\bar{n}_p\}$ and tells us how the colour flux is re-oriented at each lattice site, while $\hat{\pi}_x$ permutes the colour flux on the links attached to x and is defined by:

$$\hat{\pi}_x = \bigotimes_{\mu=0}^{d-1} \left(\sigma_{(x,\mu)} \otimes \tau_{(x-\mu,\mu)}\right) \tag{4.4}$$

then $\mathrm{len}\left(\left[\hat{\sigma}_x\circ\hat{\pi}_x\right]\right)$ is the number of colour cycles at site x. This formulation, as it stands, is not suitable for Monte Carlo simulations as almost half of the Weingarten functions appearing in Eq. (4.2) are negative (see [7]). Neverthless, it turned out that is possible to rearrange the terms in Eq. (4.2) in such a way that $W\{n_p,\bar{n}_p\}$ is written as a positive sum:

$$W(\{n_p,\bar{n}_p\}) = \sum_{\substack{\{\lambda_\ell\vdash d_\ell\} \\ \mathrm{len}(\lambda_\ell)\le N}} \sum_{\{\sigma_\ell,\tau_\ell\in S_{d_\ell}\}} \prod_\ell \frac{1}{d_\ell!^2} \frac{f^2_{\lambda_\ell} M^{a_\ell,b_\ell}_{\lambda_\ell}(\sigma_\ell) M^{b_\ell,a_\ell}_{\lambda_\ell}(\tau_\ell^{-1})}{D_{\lambda_\ell,N}} \prod_x N^{\mathrm{len}\left(\left[\hat{\sigma}_x\circ\hat{\pi}_x\right]\right)} \tag{4.5}$$

where $M^{a,b}_\lambda(\pi)$ is a matrix representation of the irrep λ of S_n and $a,b=1,...,f_\lambda$. We will choose M to be orthogonal matrices[5]. After working out the sum over permutations, Eq. (4.5) can be cast in the following form:

$$W(\{n_p,\bar{n}_p\}) = \sum_{\substack{\{\lambda_\ell\vdash d_\ell\} \\ \mathrm{len}(\lambda_\ell)\le N}} \overbrace{\left[\sum_{a_\ell,b_\ell} \prod_\ell \frac{1}{D_{\lambda_\ell,N}} \prod_x w(x)\right]}^{W(\{n_p,\bar{n}_p\},\{\lambda_\ell\})\ge 0} \tag{4.6}$$

$$P^{a,b}_{\lambda\vdash n} = \frac{f_\lambda}{n!}\sum_{\pi\in S_n} M^{a,b}_\lambda(\pi)\delta_\pi, \qquad w(x) = \langle \bigotimes_{\substack{\mu=0 \\ \ell=(x,\pm\hat{\mu})}}^{d-1} P^{a_\ell,b_\ell}_{\lambda_\ell\vdash d_\ell}, \delta_{\hat{\sigma}_x}\rangle_{n_x}, \qquad n_x = \sum_{\mu=0}^{d-1}(d_{x,\mu}+d_{x-\mu,\mu})$$

[4] For simplicity we illustrate the procedure in the U(N) case.

[5] As S_n is a finite group we can always choose unitary irreps. For the specific case of S_n it turns out that the matrix elements are also real.

where $\left\{P^{a,b}_{\lambda\vdash n}\right\}$ are a complete set of orthogonal operators in $(\mathbb{C}^N)^{\otimes n}$ and the inner product $\langle . \rangle_n$ is defined as:

$$\langle A, B\rangle_n := \mathrm{Tr}(A^\dagger B) \qquad\qquad A, B \in \mathrm{End}\big((\mathbb{C}^N)^{\otimes n}\big). \tag{4.7}$$

Therefore, by adding partitions λ_ℓ as an auxiliary degree of freedom, we end up with a partition function that contains only positive terms. However, the possibility of performing Monte Carlo simulations using Eqs. (4.1), (4.6), depends on how fast we can compute the weights in Eq. (4.6). Each term involves a sum over $\prod_\ell f^2_{\lambda_\ell}$ local quantities making a brute force computation infeasible in $d > 2$. To overcome this issue one possible strategy is to tabularize the weights (as they are β-independent) or to make use of Tensor Network methods to speed up the computation, which we plan to do in the future.

5. Conclusion

We have studied dualization in QCD and in pure Yang-Mills theory from the point of view of the strong coupling expansion. We have solved the problem of computing polynomial integrals over SU(N) which appear in the procedure of integrating out the gauge links. We showed that plaquette excitations in a naíve strong coupling expansion of the gauge action, produce a strong sign problem which limits the use of reweighting to $\beta < 1$. As this kind of sign problem is induced by a non-zero β, we focused on pure Yang-Mills theory, finding a basis where the gluon dynamics does not give rise to a sign problem. This dual basis, where the states are labelled by $\{n_p, \bar{n}_p\}$ and by integer partitions λ_ℓ, can reduce the sign problem in full QCD at finite β.

6. Acknowledgement

We acknowledge support by the Deutsche Forschungsgemeinschaft (DFG) through the Emmy Noether Program under Grant No. UN 370/1 and through the Grant No. CRC-TR 211 "Strong-interaction matter under extreme conditions".

References

[1] H. Vairinhos and P. de Forcrand, JHEP **1412** (2014) 038 [arXiv:1409.8442 [hep-lat]].
[2] C. Gattringer, T. Kloiber and M. Müller-Preussker, Phys. Rev. D **92** (2015) no.11, 114508 [arXiv:1508.00681 [hep-lat]].
[3] C. Marchis and C. Gattringer, Phys. Rev. D **97** (2018) no.3, 034508 [arXiv:1712.07546 [hep-lat]].
[4] P. Rossi and U. Wolff, Nucl. Phys. B 248 (1984) 105.
[5] P. de Forcrand, J. Langelage, O. Philipsen and W. Unger, PoS LATTICE **2013** (2014) 142 [arXiv:1312.0589 [hep-lat]].
[6] K. E. Eriksson, N. Svartholm and B. S. Skagerstam, J. Math. Phys. **22** (1981) 2276.
[7] G. Gagliardi, J. Kim and W. Unger, EPJ Web Conf. **175** (2018) 07047 [arXiv:1710.07564 [hep-lat]].
[8] B. Collins, P. Śniady, 2006, Communications in Mathematical Physics, 264, 773.
[9] M. Creutz, J. Math. Phys. **19** (1978), 2043.
[10] J. B. Zuber, J. Phys. A **50** (2017) no.1, 015203 [arXiv:1611.00236 [math-ph]].

B.8 New dual representation for staggered lattice QCD [B8]

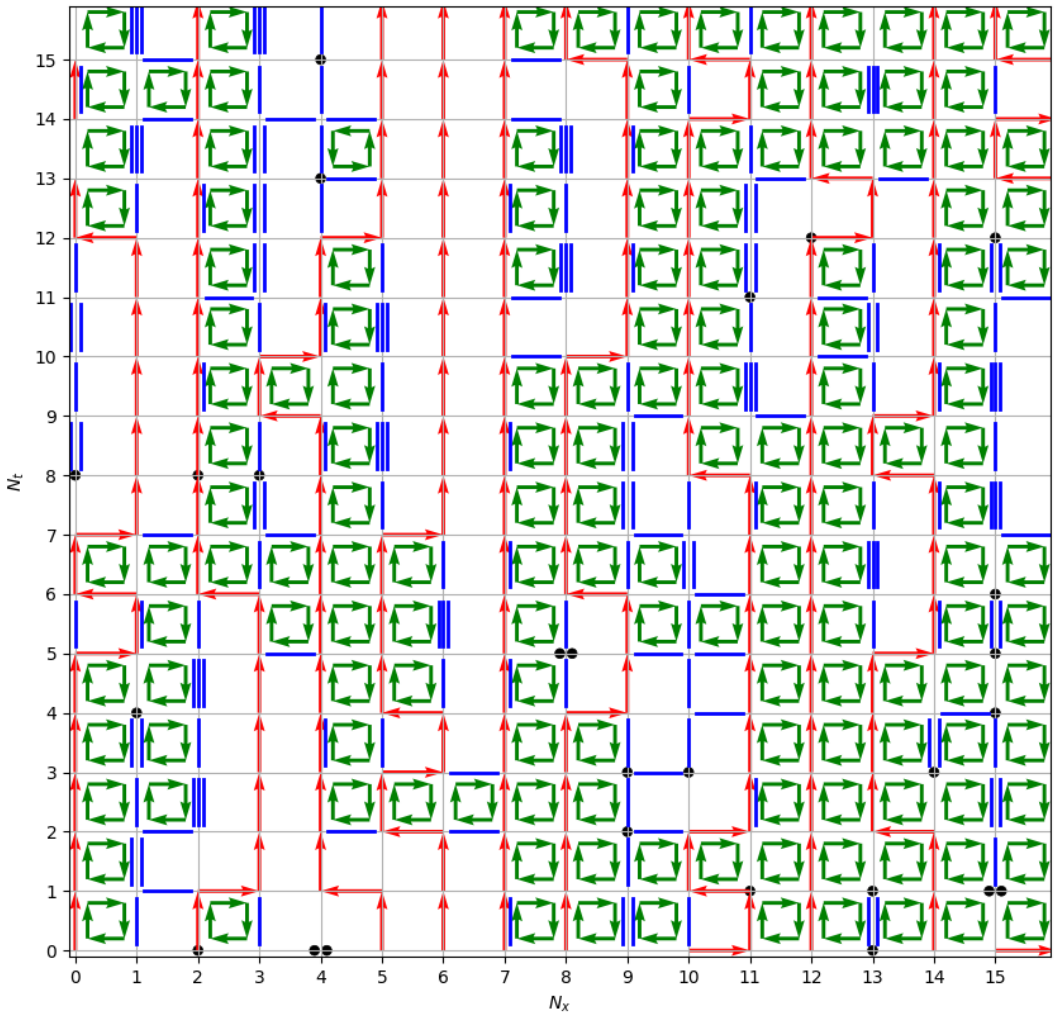

New dual representation for staggered lattice QCD

G. Gagliardi* and W. Unger†

Fakultät für Physik, Bielefeld University, Universitätsstr. 25, D-33615, Germany

(Received 25 November 2019; accepted 9 January 2020; published 12 February 2020)

We propose a new strategy to evaluate the partition function of lattice QCD with Wilson gauge action coupled to staggered fermions, based on a strong coupling expansion in the inverse bare gauge coupling $\beta = 2N/g^2$. Our method makes use of the recently developed formalism to evaluate the SU(N) 1-link integrals and consists in an exact rewriting of the partition function in terms of a set of additional dual degrees of freedom which we call "decoupling operator indices" (DOI). The method is not limited to any particular number of dimensions or gauge group U(N), SU(N). In terms of the DOI, the system takes the form of a tensor network which can be simulated using wormlike algorithms. Higher order β-corrections to strong coupling lattice QCD can be, in principle, systematically evaluated, helping to answer the question whether the finite density sign problem remains mild when plaquette contributions are included. Issues related to the complexity of the description and strategies for the stochastic evaluation of the partition function are discussed.

DOI: 10.1103/PhysRevD.101.034509

I. INTRODUCTION

Lattice QCD at finite baryon density suffers from the notorious sign problem [1]. In a nutshell, the numerical sign problem arises because the weights of the partition function are not positive definite, prohibiting importance sampling in Monte Carlo simulations. One of the several promising approaches to tackle the various sign problems in lattice field theories or spin systems are dual formulations. The basic idea is to rewrite the partition function by replacing the original (possibly continuous) degrees of freedom (d.o.f.) by new discrete d.o.f., such that the numerical sign problem of the new representation is milder or absent [2].

The idea of dual representations is old, and in the last decade, many different sign problems have been solved in this way. Some of the hallmarks in the context of spin models are the O(N) and CP(N-1) models [3–5], and in the context of lattice field theories are the charged scalar ϕ^4 theory [6], the Abelian gauge-Higgs model [7,8], the SU(2) principle chiral model [9], and scalar QCD [10]. The term "dual representation" may seem as a misnomer (they are not duality transformations), but it has been established as an umbrella term for representations of specific type: the representations are obtained by integrating out the original d.o.f. and by introducing discrete variables that encode nearest neighbor interaction, e.g., the so-called bond variables. These are based on a high temperature or strong coupling expansion [11,12] or similar Taylor expansions and can be expressed in terms of oriented fluxes and/or unoriented occupation numbers (usually called monomers and dimers). A dual representation is then oftentimes called a worldline representation, or a dimerization, or is a combination of both. An important feature is that the original symmetries of the system are translated into constraints such as flux conservation or restrictions on the allowed occupation numbers. Typically, these constraints are central in Monte Carlo simulations such as in the worm algorithm [13] or generalizations thereof [14]. Dual representations are in general not unique: a model can have several dual representations which may have different residual sign problems. In some cases, a dual representation can introduce a sign problem that did not exist in the original formulation. An important example is the lattice Schwinger model at finite quark mass.

The focus of this paper is whether dual representations can be successfully applied to lattice QCD at finite baryon density, which has a severe sign problem in the usual representation, where fermions are integrated out, resulting in the fermion determinant. The standard approach is then hybrid Monte Carlo. At finite baryon chemical potential μ_B, the fermion determinant becomes complex, resulting in the sign (complex phase) problem. Many strategies are available to circumvent the sign problem for small values of the chemical potential, like the Taylor expansion method [15], the use of an imaginary chemical potential [16,17], and reweighting [18]. The latter led to a first estimate of the position of the critical end point on a coarse lattice [19]. In general, however, reweighting may suffer from the lack of

*giuseppe@physik.uni-bielefeld.de
†wunger@physik.uni-bielefeld.de

overlap between the sampled $\mu_B = 0$ ensemble and the target ensemble at $\mu_B > 0$. More recently, other approaches that are not limited to small μ_B have been proposed, such as the complex Langevin approach [20,21], the Lefschetz thimble approach [22–24], or the density of states method [25]. To name also some approaches that are in the spirit of a dual representation: the three-dimensional effective theory [26,27] (a joint strong coupling and hopping parameter expansion that can be mapped to SU(3) spin model), decoupling the gauge links using Hubbard-Stratonovich transformations [28], "induced QCD" based on an alternative discretization of Yang Mills Theory [29,30]. All these approaches have their shortcomings, and a method that allows to simulate lattice QCD at finite density has not yet been established.

A dual representation of lattice QCD has only been derived in the strong coupling regime: the classical formulation in terms of a monomer-dimer-polymer system has been both addressed via mean field [31–34] and Monte Carlo [35–38] and is valid only in the strong coupling limit. More recently also the leading order gauge corrections have been included [39,40]. At strong coupling, also the fermion bag approach has been used [41,42] and continuous time methods have been applied [43,44]. Beyond the leading order, a dual formulation for lattice QCD is notoriously difficult. First attempts were made using a character expansion [45,46] and the so-called Abelian color cycles [47]. Our ultimate goal is to find a dual representation for lattice QCD: we propose a new approach based on a combined expansion of the Wilson plaquette action (strong coupling expansion) and of the staggered action (hopping and quark mass expansion) to all orders. The integration order is, as in the case of the strong coupling formulation, swapped, with the gauge integral being performed first while Grassmann integration is carried out after a reparametrization of the link integrals. The strong coupling methods we use go back to the early days of lattice QCD, where computers for large scale simulations were not yet available [48,49]. But only due to recent progress in the computation of one-link integrals (invariant polynomial integration [50,51]), we have complete control on the evaluation of the resulting Boltzmann weight ending up with a fully dualized partition function. The challenge when going beyond the leading order correction is that this dual representation needs to capture nonlocal effects: it is no longer possible to write the partition function as product of site weights and bond weights only. The basic objects of our dual representation have a tensorial structure. In this paper, we show a strategy to compute these tensors. Our method is not restricted to staggered fermions and can readily be applied to Wilson fermions as well.

The paper is organized as follows: in Sec. II, we review the computation of link integrals and introduce the SU(N) decoupling operators which constitute the building blocks of the whole dualization process. In Sec. III, we sketch the steps needed to recover the color singlet Boltzmann weight from the computation of polynomial gauge integrals. In Sec. IV, the dualized partition function will be presented along with the expression of various observables in terms of the dual d.o.f. and a discussion about the sign problem. In Sec. V, numerical crosschecks from exact enumeration in low-dimensional systems will be shown. Finally, in Sec. VI, we draw our conclusions.

II. STRONG COUPLING EXPANSION AND LINK INTEGRATION

We consider the finite density partition function of lattice gauge theory with SU(N) gauge group, using the Wilson gauge action and one flavor of unrooted staggered fermions $\{\bar{\chi},\chi\}$ with lattice quark mass $\hat{m}_q = am_q$,

$$\mathcal{Z} = \int [\mathcal{D}\bar{\chi}\chi] e^{-2\hat{m}_q \bar{\chi}_x \chi_x} \left[\prod_\ell \int_{\mathrm{SU}(N)} DU_\ell\right] e^{-S_g[U] - D_f[\bar{\chi},\chi,U]}, \tag{1}$$

where $\ell = (x,\mu)$ and x stand, respectively, for lattice links and sites and DU is the Haar measure. The gauge links U_ℓ are SU(N) elements, while S_g and D_f are, respectively, the plaquette action and the massless staggered Dirac operator,

$$\begin{aligned} S_g[U] &= -\frac{\beta}{2N}\sum_{x,\mu<\nu} \mathrm{Tr} U_{x,\mu} U_{x+\mu,\nu} U^\dagger_{x+\nu,\mu} U^\dagger_{x,\nu} + \mathrm{H.c.} \\ &= -\frac{\beta}{2N}\sum_p \mathrm{Tr} U_p + \mathrm{Tr} U_p^\dagger, \\ D_f[\bar{\chi},\chi,U] &= \sum_{x,\mu} \eta_\mu(x)\left(e^{+\mu_q \delta_{\mu,0}} \bar{\chi}_x U_{x,\mu} \chi_{x+\mu}\right. \\ &\quad \left. - e^{-\mu_q \delta_{\mu,0}} \bar{\chi}_{x+\mu} U^\dagger_{x,\mu} \chi_x\right) \\ &\equiv \sum_\ell \mathrm{Tr} U_\ell \mathcal{M}^\dagger_\ell + \mathrm{Tr} U^\dagger_\ell \mathcal{M}_\ell, \end{aligned} \tag{2}$$

where $\mu_q = \frac{1}{N}\mu_B$ is the lattice quark chemical potential and $\eta_\mu(x)$ are the usual staggered phases. All traces are intended to be over color indices and in the following we will always use the letter p to label lattice plaquettes.

The first step in the dualization process is to perform a combined Taylor expansion of Eq. (1) in the reduced gauge coupling $\tilde{\beta} \equiv \frac{\beta}{2N} = \frac{1}{g^2}$ and quark mass $\hat{m}_q$,

$$\begin{aligned} \mathcal{Z}(\beta,\hat{m}_q) = &\sum_{\substack{\{n_p,\bar{n}_p\} \\ \{d_\ell,\bar{d}_\ell,m_x\}}} \prod_p \frac{\tilde{\beta}^{n_p+\bar{n}_p}}{n_p!\bar{n}_p!} \prod_\ell \frac{1}{d_\ell!\bar{d}_\ell!} \prod_x \frac{(2\hat{m}_q)^{m_x}}{m_x!} \\ &\times \mathcal{G}_{n_p,\bar{n}_p,d_\ell,\bar{d}_\ell,m_x}, \end{aligned} \tag{3}$$

$$\begin{aligned} \mathcal{G}_{n_p,\bar{n}_p,d_\ell,\bar{d}_\ell,m_x} = &\int \mathcal{D}[\chi\bar{\chi}] (\bar{\chi}_x\chi_x)^{m_x} \prod_{\ell,p} \int DU_\ell \mathrm{Tr}[U_p]^{n_p} \\ &\times \mathrm{Tr}[U_p^\dagger]^{\bar{n}_p} \mathrm{Tr}[U_\ell \mathcal{M}^\dagger_\ell]^{d_\ell} \mathrm{Tr}[U^\dagger_\ell \mathcal{M}_\ell]^{\bar{d}_\ell}. \end{aligned} \tag{4}$$

The sum is over the positive integers that single out a particular term in the expansion: $(\bar{n}_p)\, n_p$ is called the (anti-) plaquette occupation number, m_x the monomer number, and d_ℓ, $\bar{d}_\ell$ stem from the expansion of the massless staggered Dirac operator in forward (d_ℓ) and backward ($\bar{d}_\ell$) directions. The quantity $\mathcal{G}$ contains the nonlocal part of the computation and is given by a Gauge + Grassmann integral over the whole lattice.

Our dualization corresponds to exactly integrate out the gauge links $U_{x,\mu}$ and the Grassmann field $\bar{\chi},\chi$, trading the original d.o.f. with the integer variables appearing in Eq. (3). This can be achieved by splitting the computation of $\mathcal{G}$ in two steps:

(1) The traces appearing in Eq. (4) are written explicitly: we do not perform the matrix multiplication, leaving the color indices uncontracted. As a consequence, the gauge integral $\prod_\ell \int_{\mathrm{SU}(N)} DU_\ell$ becomes a disjoint product of monomial integrals with open color indices and we integrate out every gauge link independently.

(2) After gauge integration, some of the open color indices need to be contracted between links that share a common site such that the plaquette terms are recovered. The remaining indices are contracted with the Grassmann-integrated quark fields. We postpone the description of this step to Sec. III.

If the matrix multiplications are not performed, the link integrals to be computed assume the following general form:

$$\mathcal{I}^{a,b}_{i^j,k^l} = \int_{\mathrm{SU}(N)} DUU^{j_1}_{i_1}\cdots U^{j_a}_{i_a} U^{\dagger l_1}_{k_1}\cdots U^{\dagger l_b}_{k_b}, \qquad (5)$$

where the values a, b depend on the dual d.o.f. $\{n_p, \bar{n}_p, d_\ell, \bar{d}_\ell\}$ and we make use of the multiindex notation,

$$\begin{aligned} i &= (i_1, i_2, \ldots, i_a), \qquad j = (j_1, j_2, \ldots, j_a),\\ k &= (k_1, k_2, \ldots, k_b), \qquad l = (l_1, l_2, \ldots, l_b). \end{aligned} \qquad (6)$$

Due to the properties of the $\mathrm{SU}(N)$ invariant Haar measure, the integrals in Eq. (5) are nonzero only when the difference $a - b$ is an integer multiple of N. As it will be explained in the next section, this corresponds to a (gauge-) constraint for the dual d.o.f. We define

$$q = \frac{|a-b|}{N}, \qquad q \in \mathbb{N}, \qquad (7)$$

and for $\mathrm{U}(N)$ gauge theory $q = 0$. Invariant integration over compact groups has been studied extensively in the last decades [48,49,52–63]. Although many results concerning the $\mathrm{U}(N)$ group are known since many years, only recently the $\mathrm{SU}(N)$ generalization has been found [50,51]. Integrals of the type Eq. (5) are now known in closed form in term of generalized Weingarten functions. The interested reader will find our derivation in the Appendix A. Here we only quote the main result assuming, without loss of generality, $a > b$ ($a = qN + p$, $b = p$),

$$\mathcal{I}^{qN+p,p}_{i^j,k^l} \propto \sum_{(\alpha,\beta)} \sum_{\pi,\sigma\in S_p} \epsilon^{\otimes q}_{i_{\{\alpha\}}} \delta^{l_\pi}_{i_{\{\beta\}}} \tilde{\mathrm{W}}\mathrm{g}^{q,p}_N(\pi\circ\sigma^{-1}) \epsilon^{\otimes q, j_{\{\alpha\}}} \delta^{j_{\{\beta\}}}_{k_\sigma}. \qquad (8)$$

In the previous equation, $\epsilon^{\otimes q}$ is a shortcut for the q-fold product of Levi-Civita epsilon tensors and $\delta^{l_\pi}_i$, $\delta^j_{k_\sigma}$ are the generalized Kronecker deltas where the indices are reordered according to the permutations π and σ. The leftmost sum with

$$\alpha = \{\alpha_1, \ldots, \alpha_q\}, \qquad |\alpha_r| = N, \qquad |\beta| = p \qquad (9)$$

is carried over the $\frac{(qN+p)!}{q!N!^q p!}$ possible ways of partitioning the color indices i, j (which are $qN + p$) into the q epsilon tensors of size N and into the delta function of size p. All the partitions obtained from each other by only permuting the α_r in Eq. (9) are equivalent. Also, note that in Eq. (8), the i and j indices are partitioned in the same way. As in the $\mathrm{U}(N)$ case, a further summation over all possible permutation of indices in the delta functions (sum over π, σ) is present. Every term in the double sum is weighted by the function $\tilde{\mathrm{W}}\mathrm{g}^{q,p}_N$, which is a class function of the symmetric group S_p and represents the natural generalization of the Weingarten functions $\mathrm{W}\mathrm{g}^p_N = \tilde{\mathrm{W}}\mathrm{g}^{0,p}_N$ appearing in the $\mathrm{U}(N)$ result [58,59]. Their expression in terms of the characters χ^λ of the symmetric group is

$$\tilde{\mathrm{W}}\mathrm{g}^{q,p}_N(\pi) = \sum_{\substack{\lambda\vdash p\\ \mathrm{len}(\lambda)\le N}} \frac{1}{(p!)^2} \frac{f_\lambda^2 \chi^\lambda(\pi)}{D_{\lambda,N+q}},$$

$$\lambda\vdash p \equiv \left\{ \lambda_1 \ge \ldots \ge \lambda_{\mathrm{len}(\lambda)} > 0 \,\middle|\, \sum_{i=0}^{\ell(\lambda)} \lambda_i = p \right\}. \qquad (10)$$

The sum is over the irreducible representations (irreps)[1] of the symmetric group S_p, while f_λ is the dimension of the irrep λ of S_p and $D_{\lambda,N+q}$ is the dimension of the $\mathrm{U}(N+q)$ irrep with highest weight $\{\lambda_1, \ldots, \lambda_{\mathrm{len}(\lambda)}, 0, \ldots\}$.

By inspecting Eq. (8), it seems tempting to consider the permutations π, σ as an additional d.o.f. to be evaluated stochastically and to proceed with the index contraction considering single terms in the sum of Eq. (8). Unfortunately, the sign of the generalized Weingarten functions strongly oscillates, preventing the application of standard

[1]The S_n irreps are in 1-1 correspondence with the integer partitions of n. In Eq. (10), only the irreps that correspond to integer partitions with at most N parts contribute.

Monte Carlo methods. Instead, we found it useful to exploit the knowledge of the character expansion in Eq. (10) to reparametrize the $\mathcal{I}$-integral. As a starting point, we write the S_p characters as a matrix product of the corresponding matrix representation,

$$\chi^{\lambda}(\pi\circ\sigma^{-1}) \equiv \mathrm{Tr}(M^{\lambda}(\pi)M^{\lambda}(\sigma^{-1})). \tag{11}$$

Writing the matrix product explicitly, we are able to cast the Weingarten functions and (after summing over the permutations) the $\mathcal{I}$-integrals in the following form:

$$\tilde{\mathrm{Wg}}_N^{q,p}(\pi\circ\sigma^{-1}) = \sum_{\substack{\lambda\vdash p \\ \ell(\lambda)\leq N}} \sum_{m,n=1}^{f_\lambda} \left(\frac{1}{p!}\frac{f_\lambda}{\sqrt{D_{\lambda,N+q}}} M^{\lambda}_{mn}(\pi)\right)\left(\frac{1}{p!}\frac{f_\lambda}{\sqrt{D_{\lambda,N+q}}} M^{\lambda}_{mn}(\sigma)\right), \tag{12}$$

$$\mathcal{I}^{qN+p,p}_{i^l,k^l} \propto \sum_{(\alpha,\beta)} \sum_{\substack{\lambda\vdash p \\ \ell(\lambda)\leq N}} \sum_{m,n=1}^{f_\lambda} \left(\sum_{\pi} \frac{1}{p!}\frac{f_\lambda}{\sqrt{D_{\lambda,N+q}}} M^{\lambda}_{mn}(\pi)\epsilon^{\otimes q}_{i_{\{\alpha\}}}\delta^{l_\pi}_{i_{\{\beta\}}}\right)\left(\sum_{\sigma} \frac{1}{p!}\frac{f_\lambda}{\sqrt{D_{\lambda,N+q}}} M^{\lambda}_{mn}(\sigma)\epsilon^{\otimes q, j_{\{\alpha\}}}\delta^{j_{\{\beta\}}}_{k_\sigma}\right), \tag{13}$$

where the matrices M^{λ} have been chosen to be orthogonal.[2] The quantities in the brackets of Eq. (13) generalize the $\mathrm{U}(N)$ orthogonal operators [64,65] [where the summation over (α,β) and the epsilon tensors are absent] and represent the building blocks of our dualization. The orthogonality property does not generalize to the $\mathrm{SU}(N)$ case; hence, we will refer to them as the $\mathrm{SU}(N)$ decoupling operators. They are identified by a given partition (α,β) and by choosing a given matrix element (m,n) of an irrep λ of S_p. We denote the latter as $(m,n)_\lambda$. Moreover, to make the expression in Eq. (13) more compact, we collect (α,β) and $(m,n)_\lambda$ into a multi-index $\rho = [(\alpha,\beta),(m,n)_\lambda]$ so that we can write the $\mathrm{SU}(N)$ decoupling operators P^ρ and the $\mathcal{I}$-integrals as

$$(P^\rho)^l_i = \sum_{\pi} \frac{1}{p!}\frac{f_\lambda}{\sqrt{D_{\lambda,N+q}}} M^{\lambda}_{mn}(\pi)\epsilon^{\otimes q}_{i_{\{\alpha\}}}\delta^{l_\pi}_{i_{\{\beta\}}}, \tag{14}$$

$$\mathcal{I}^{qN+p,p}_{i^l,k^l} = \prod_{r=1}^{N-1}\frac{r!}{(r+q)!}\sum_{\rho}(P^\rho)_i{}^l(P^\rho)_k{}^j, \tag{15}$$

$$n_\rho = \frac{(qN+p)!}{q!N!^q p!}\sum_{\lambda\vdash p}^{\ell(\lambda)\leq N} f_\lambda^2, \tag{16}$$

where n_ρ is the total number of operator indices. The operators P^ρ decouple the color indices i, l and k, j in the $\mathcal{I}$-integral and its computation has been automatized by using the standard *hook rule* to determine f^λ and $D_{\lambda,N}$. The irreducible matrix elements $M^{\lambda}_{mn}(\pi)$ in the orthogonal representation are computed numerically decomposing the permutation π as a product of adjacent transpositions $\tau^{j,j+1}$ and then using the axial distance formula to compute the matrix representation associated to them (see [64], p. 8).

[2]Every finite group admits a unitary irrep. In the case of the symmetric group, the matrix elements can be also chosen to be real. This basis is known as the Young's orthogonal form.

The quantity ρ, which identifies a given operator in Eq. (15), will play an important role in the following. We will refer to it as decoupling operator index (DOI), which can be cast into an integer in the range $\{1,\ldots,n_\rho\}$.

III. INDEX CONTRACTION AND TENSOR NETWORK

Given the result in Eq. (15), the next step is to perform the contraction of the color indices $\{i,j,k,l\}$ in the $\mathcal{I}$-integrals making use of decomposition in terms of the operators P^ρ obtained in the previous section. This contraction must be performed for every lattice link ℓ. The (anti-)plaquette occupation numbers $(\bar{n}_p)\ n_p$ together with d_ℓ, $\bar{d}_\ell$ determine how the contraction has to be performed in order to recover Eq. (4). We distinguish two types of color indices: those stemming from the expansion of the hopping term and those arising from the expansion of the Wilson gauge action. We will refer to them as the *fermionic* and *gluonic* color indices. The contraction rules for the fermionic color indices are uniquely determined by d_ℓ and $\bar{d}_\ell$. These indices are contracted with the Grassmann fields appearing in the corresponding fermionic matrices $\mathcal{M}_\ell$ and $\mathcal{M}^\dagger_\ell$. Due to the nilpotency of the Grassmann measure, exactly N (for $\mathrm{SU}(N)$) (anti-) fermion fields $(\bar{\chi}_x)\,\chi_x$ have to be present at each site x in order to obtain a nonzero contribution. This property will correspond to a constraint on the allowed d.o.f. d_ℓ, $\bar{d}_\ell, m_x$. Similarly, gluonic color indices are contracted according to the plaquette they correspond to. In this case, the contraction takes place between the color indices of the $\mathcal{I}$-integrals corresponding to links sharing a common site. The contraction rules are determined by the (anti-)plaquette occupation numbers and allow us to recover the plaquette terms in Eq. (4).

The key insight is that fixing the values of the DOI ρ_ℓ for each link ℓ makes the contraction step local. This means that the contraction of the color indices can be carried out independently at different lattice sites. In Fig. 1, we

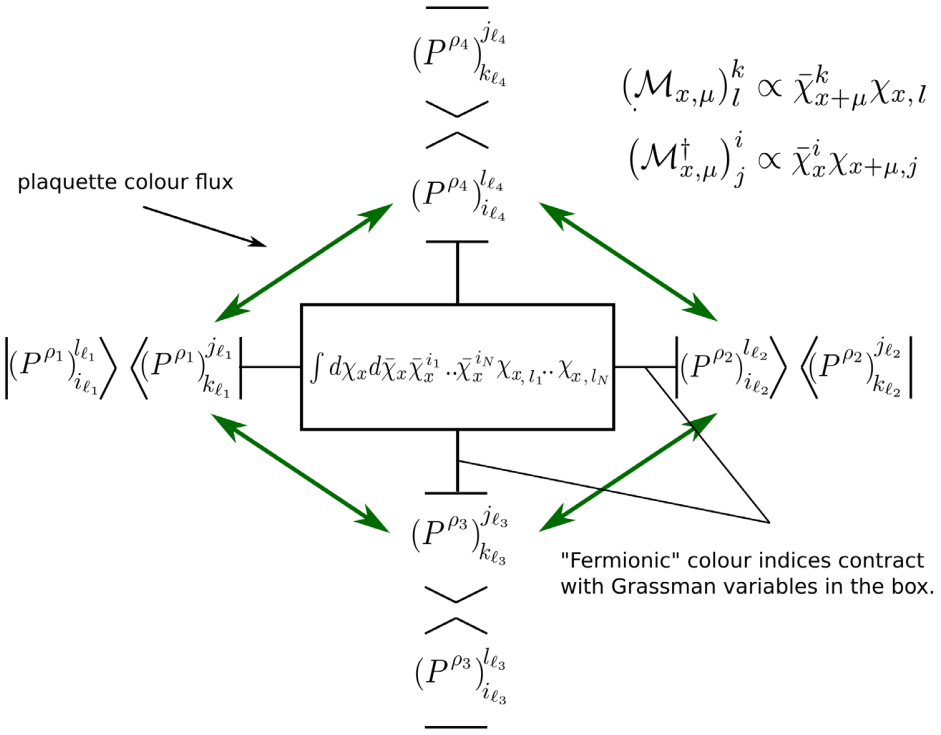

FIG. 1. Illustration of the contraction step in two dimensions: on each of the four links attached to the central lattice site the DOIs $\{\rho_1,\rho_2,\rho_3,\rho_4\}$ have been fixed. Decoupling operators on the same link undergo a disjoined contraction at two different lattice sites. The bra-ket notation only serves to display this feature. At any lattice site (e.g., the central box), the color indices of the four operators are completely saturated. Depending on the plaquette and antiplaquette occupation numbers $\{n_p,\bar{n}_p\}$ on the four plaquettes attached to the site, some of the color indices are contracted between the operators (green arrows). Instead, the color indices stemming from the hopping expansion of the staggered action are contracted with the reordered Grassmann variables at site x. The result is a scalar quantity which only depends on the value of the DOIs and on the dual d.o.f. $\{n_p,\bar{n}_p,d_\ell,\bar{d}_\ell,m_x\}$.

illustrate the procedure in $d=2$. The extension to any number of dimensions is straightforward. To see why the contraction at different lattice sites decouples, let us first consider the case of the gluonic color indices and rewrite explicitly the definition of the plaquette and antiplaquette: for any gauge link U_ℓ with $\ell=(x,\mu)$, the contribution from the product of traces $\mathrm{Tr}U_p,\mathrm{Tr}U_p^\dagger$ for all plaquettes p containing the link ℓ can be gathered into products of matrix elements of U_ℓ and $U_\ell^\dagger$,

$$\begin{aligned}\mathrm{Tr}U_p &= (U_1)^{j_1}_{i_1}(U_2)^{j_2'}_{i_2'}(U_3^\dagger)^{l_3'}_{k_3'}(U_4^\dagger)^{l_4'}_{k_4'}\delta^{i_2'}_{j_1}\delta^{k_3'}_{j_2'}\delta^{k_4'}_{l_3'}\delta^{i_1}_{l_4'},\\ \mathrm{Tr}U_p^\dagger &= (U_1^\dagger)^{l_1}_{k_1}(U_2^\dagger)^{l_2'}_{k_2'}(U_3)^{j_3'}_{i_3'}(U_4)^{j_4'}_{i_4'}\delta^{k_1}_{l_2'}\delta^{k_2'}_{j_3'}\delta^{i_3'}_{j_4'}\delta^{l_1}_{i_4'},\end{aligned}\tag{17}$$

$$\begin{aligned}&\prod_{\{p=(x,\mu,\nu)|\ell\in p\}}^{n}(U_\ell)^{j_1}_{i_1}\cdots(U_\ell)^{j_{n_p}}_{i_{n_p}}(U_\ell^\dagger)^{l_1}_{k_1}\cdots(U_\ell^\dagger)^{l_{\bar{n}_p}}_{k_{\bar{n}_p}}\\ &\hookrightarrow\prod_{\{p=(x,\mu,\nu)|\ell\in p\}}^{n}(\mathrm{Tr}U_p)^{n_p}(\mathrm{Tr}U_p^\dagger)^{\bar{n}_p},\end{aligned}\tag{18}$$

where $U_1,\ldots,U_4$ are the four links contained in the plaquette and summation over repeating color indices is implied. The lhs of Eq. (18) thus contributes to the gluonic color indices $\{i,l\},\{k,j\}$ within $\mathcal{I}_{i^j,k^l}$. Therefore, given the structure of the operators in Eq. (15), $(P^\rho)_i{}^l$ and $(P^\rho)^k_j$ contract, respectively, with the operators attached to site x and $x+\mu$. Fermionic color indices arise instead from terms of the form

$$\mathrm{Tr}[U_\ell\mathcal{M}_\ell^\dagger]^{d_\ell},\qquad \mathrm{Tr}[U_\ell^\dagger\mathcal{M}_\ell]^{\bar{d}_\ell}.\tag{19}$$

They can be written explicitly as $(\ell=(x,\mu))$,[3]

$$\begin{aligned}\mathrm{Tr}[U_\ell\mathcal{M}_\ell^\dagger]^{d_\ell} &\propto \prod_{a=1}^{d_\ell}(U_{x,\mu})_{i_a}^{j_a}\bar{\chi}^{i_a}_x\chi_{x+\mu,j_a},\\ \mathrm{Tr}[U_\ell^\dagger\mathcal{M}_\ell]^{\bar{d}_\ell} &\propto \prod_{b=1}^{\bar{d}_\ell}(U^\dagger_{x,\mu})^{l_b}_{k_b}\bar{\chi}^{k_b}_{x+\mu}\chi_{x,l_b},\end{aligned}\tag{20}$$

and again by inspecting at the index structure of Eq. (15), the indices $\{i,l\}$ of the first operator $(P^\rho)_i{}^l$ are contracted

[3]The dependency of $\mathcal{M},\mathcal{M}^\dagger$ on η_μ and μ_q can be factored out as it will be shown in the dual partition function Eq. (27).

with the Grassmann variables at site x while the indices $\{k, j\}$ of the second operator with the Grassmann variables at site $x+\mu$. This concludes the proof of the locality of the contractions which is schematically shown in Fig. 1. At each site, the corresponding Grassmann integral is replaced with the usual product of two epsilon tensors,

$$\int [d\bar{\chi}_x d\chi_x] \bar{\chi}_x^{i_1} \cdots \bar{\chi}_x^{i_N} \chi_{x,l_1} \cdots \chi_{x,l_N} = \epsilon^{i_1 \cdots i_N} \epsilon_{l_1 \cdots l_N}. \quad (21)$$

On a d-dimensional hypercubic lattice, the operators P^{ρ_ℓ} on the $2d$ links ℓ attached to a site x, together with the epsilon tensors in Eq. (21) are jointly contracted according to the values of the dual d.o.f. This gives a scalar quantity which only depends on the underlying dual d.o.f. and on the values of the DOIs on the links attached to x. The dependency on the dual d.o.f. $\{n_p, \bar{n}_p, d_\ell, \bar{d}_\ell, m_x\}$ is local, in the sense that the contraction at site x is completely determined by the monomer number m_x, by the values of d_ℓ and $\bar{d}_\ell$ on the $2d$ links attached to x, and on the (anti-) plaquette occupation numbers of the $2d(d-1)$ plaquettes attached to x. Different sites communicate only via the common DOI ρ on the shared leg. We can collect the scalar quantities obtained from the contraction of different decoupling operators in a tensor

$$T_x^{\rho_{-d}^x \cdots \rho_d^x}(\mathcal{D}_x) \equiv \mathrm{Tr}_{\mathcal{D}_x}\left[\prod_{\pm\mu} P^{\rho_\mu^x}\right],$$
$$\mathcal{D}_x = \{m_x, d_{x,\pm\mu}, n_{x,\mu\nu}, \bar{n}_{x,\mu\nu}\}, \quad (22)$$

where $\mathrm{Tr}_{\mathcal{D}_x}$ is a "reordered" trace in color space that depends on the local dual d.o.f. $\mathcal{D}_x$ and tells us how to contract the color indices of the operators $P^{\rho_\mu^x}$ according to the rules discussed above. In Eq. (22), the DOIs depend on $\mathcal{D}_x$ implicitly due to the fact that the dual d.o.f. determine the value of (q, p) in the $\mathcal{I}$-integral Eqs. (5) and (8). The tensor elements T_x^ρ can be computed numerically by building up the operators $P^{\rho_\mu^x}$ and saturating their color indices according to the contraction rules from $\mathcal{D}_x$. Given T_x^ρ, the value of $\mathcal{G}$ is given, up to a global fermionic sign (see Sec. IV), by

$$\mathcal{G}_{n_p, \bar{n}_p, d_\ell, \bar{d}_\ell, m_x} = \sum_{\{\rho_{\pm\mu}^x | \rho_\mu^x = \rho_{-\mu}^{x+\mu}\}} \prod_x T_x^{\rho_{-d}^x, \ldots, \rho_d^x}(\mathcal{D}_x), \quad (23)$$

and the constraint $\rho_\mu^x = \rho_{-\mu}^{x+\mu}$ just stems from the fact that DOIs on the same link have to be equal as depicted in Fig. 2. In this form, the system is represented by a tensor network where the value of $\mathcal{G}$ is obtained by contracting the network to a scalar.

In some cases, the contraction of different operators produces the same tensor elements. For instance, two operators with DOIs $[(\alpha, \beta), (m, n)_\lambda]$ and $[(\alpha', \beta'), (m, n)_\lambda]$, where (α, β) and (α', β') only differ by a permutation of fermionic color indices, will produce the same element up to a sign factor. This is clear since the fermionic color indices are always contracted with the Grassmann variables, and a permutation of fermionic color indices only amounts to a reordering of the corresponding indices in the epsilon tensors in Eq. (21). The possible relative minus sign is however unimportant. In fact, it will always cancel when considering the contraction of the operator with same DOI and which lives on the same link. We therefore identify these DOIs taking into account the combinatorial factor from their multiplicity. This reduces the size of the tensor T_x, hence the numerical cost of contracting the network.

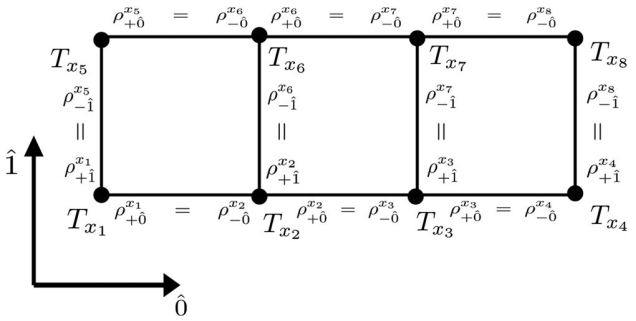

FIG. 2. The tensor network resulting from the dual description: depending on the dual d.o.f. at any lattice site, the tensor T_x is evaluated. Given two neighboring sites x and $x+\mu$, the tensor index on the common link is contracted ($\rho_\mu^x = \rho_{-\mu}^{x+\mu}$). The value of $\mathcal{G}$ is the scalar quantity obtained by contracting all pairs of indices between lattice neighbors. In the figure, the tensor indices have been displaced for visualization purposes.

As we already mentioned, not all sets of dual d.o.f. are allowed. On each lattice link, they have to combine in a way that the corresponding $\mathcal{I}$-integral is nonzero, while at any site exactly N (anti-)fermions carrying different colors must be present. We refer to these two constraints as Gauge and Grassmann constraints. Introducing

$$k_\ell = \min\{d_\ell, \bar{d}_\ell\}, \qquad f_\ell = d_\ell - \bar{d}_\ell, \quad (24)$$

where k_ℓ is the *dimer number* and f_ℓ the *quark flux*, for each link $\ell = (x, \mu)$ the gauge constraint reads

$$f_{x,\mu} + \sum_{\nu>\mu} [\delta n_{\mu,\nu}(x) - \delta n_{\mu,\nu}(x-\nu)]$$
$$- \sum_{\nu<\mu} [\mu \leftrightarrow \nu] = N q_{x,\mu}, \qquad q_{x,\mu} \in Z, \quad (25)$$

where $\delta n_{\mu,\nu}(x) \equiv \delta n_p = n_p - \bar{n}_p$. For each site x, the Grassmann constraint requires in addition

$$m_x + \sum_{\pm\mu} \left(k_{x,\mu} + \frac{|f_{x,\mu}|}{2}\right) = N, \quad \sum_{\mu=0}^{d} (f_{x,+\mu} - f_{x,-\mu}) = 0. \quad (26)$$

Equations (25) and (26) generalize the constraint in the strong coupling limit (where $n_p = \bar{n}_p = 0$ and $f_{x,\mu} = \pm N, 0$). Notice that in contrast to strong coupling QCD,

dimers ($k_{x,\mu} \neq 0$) and fluxes ($f_{x,\mu} \neq 0$) are not mutually exclusive on a given link. The set $\{n_p, \bar{n}_p, f_\ell, k_\ell, m_x\}$ subject to Eqs. (25) and (26) along with the corresponding DOIs define our final dual partition function.

IV. PARTITION FUNCTION IN THE DUAL REPRESENTATION

A. General properties

Using the quantities defined in the previous sections, the partition function Eq. (1) can be rewritten as

$$\mathcal{Z}(\beta,\mu_q,\hat{m}_q) = \sum_{\substack{\{n_p,\bar{n}_p\}\\ \{k_\ell,f_\ell,m_x\}}} \sigma_f \sum_{\{\rho^x_{\pm\mu}|\rho^x_\mu=\rho^{x+\mu}_{-\mu}\}} \prod_p \frac{\tilde{\beta}^{n_p+\bar{n}_p}}{n_p!\bar{n}_p!} \times \prod_{\ell=(x,\mu)} \frac{e^{\mu_q \delta_{\mu,0} f_{x,\mu}}}{k_\ell!(k_\ell+|f_\ell|)!} \times \prod_x \frac{(2\hat{m}_q)^{m_x}}{m_x!} T_x^{\rho^x_{-d},\ldots,\rho^x_d}(\mathcal{D}_x), \tag{27}$$

where the staggered phases η_μ are included in the fermionic sign σ_f whose form will be discussed in the next subsection. In Eq. (27), the dependence of the DOIs ρ^x_μ on $\{n_p, \bar{n}_p, k_\ell, f_\ell, m_x\}$ is implicit, and the constraints in Eqs. (25) and (26) are supposed to be fulfilled. In Fig. 3, we show the typical structure of an allowed configuration in $d = 2$ for $N = 3$. DOIs are not shown. Notice that quark fluxes $f_{x,\mu}$ always form closed loops due to the flux conservation law in Eq. (26). As opposed to the strong coupling limit, the loops can overlap with dimers and can be intersecting. The system is thus an ensemble of unoriented dimers k_ℓ, monomers m_x, closed quark fluxes f_ℓ, and plaquettes. The DOIs instead can be either thought as a mere mathematical tool to automatize the computation of the statistical weights away from strong coupling or as an additional d.o.f. to be also sampled via Monte Carlo. Before discussing these two possibilities, we want to highlight some features of the partition function Eq. (27).

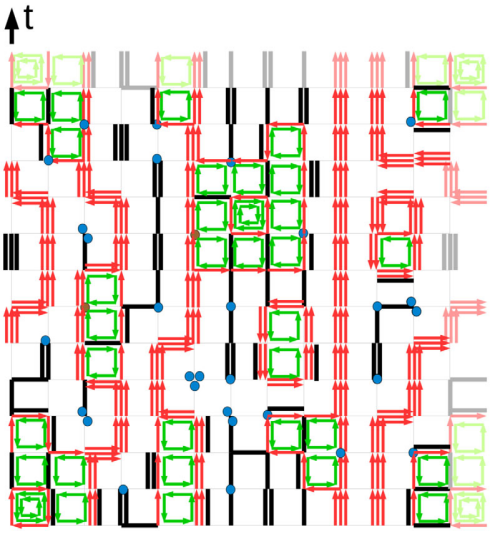

FIG. 3. An allowed configuration in $d = 2$ for SU(3): for each plaquette, a (counter-) clockwise loop corresponds to one unit of (n_p) $\bar{n}_p$. On each site, the monomer number m_x is given by the number of circles, while on each bond the unoriented lines represent dimers (n lines for $k_{x,\mu} = n$). Every arrow represents instead one unit of flux $f_{x,\mu}$. The Grassmann constraint, in agreement with Eq. (26), is satisfied at each site with the net quark flux being always zero. For every link, the difference between the total flux (gluons + quarks) in positive and negative directions is a multiple of $N = 3$. P.B.C. are employed.

A great simplification occurring is that the strong coupling contributions always decouple from those corresponding to nonzero $\{n_p, \bar{n}_p\}$. As we showed in [40], at strong coupling the tensors T^ρ have only one nonzero element. Although for baryon fluxes ($f_{x,\mu} = \pm N$), this is a trivial statement as there is only one possible DOI per link; in the case of dimer contributions, it is a consequence of the structure of the decoupling operators. To show this feature, let us consider the case where only dimers are attached to a given site (Fig. 4, left). Contracting the indices of each delta function appearing in the definitions of the corresponding operators Eq. (15) (for dimer contributions epsilon tensors are absent) with the Grassmann fields, we obtain

$$\int [d\bar{\chi}d\chi] \prod_{\mu<0} [\bar{\chi}^k \chi_j \delta^j_{k_\pi}]_\mu \prod_{\mu>0} [\bar{\chi}^i \chi_l \delta^{l_\pi}_i]_\mu = N! \prod_{\pm\mu} \mathrm{sgn}(\pi_\mu), \tag{28}$$

where $\mathrm{sgn}(\pi_\mu)$ is the parity of the permutation π relative to the operator P in direction μ. Hence, the contraction of single deltas decouples, and due to the *great orthogonality theorem*, the only surviving DOI is the one associated to the totally antisymmetric irrep of the symmetric group,

$$T_x^{\rho^x_{-d},\ldots,\rho^x_d} = N! \prod_{\pm\mu} \left(\sum_{\pi_\mu} \frac{1}{k_{x,\mu}!} \frac{f_{\lambda_\mu}}{\sqrt{D_{\lambda_\mu,N}}} M^{\lambda_\mu}_{m,n}(\pi_\mu)\mathrm{sgn}(\pi_\mu) \right) = N! \prod_{\pm\mu} \frac{1}{\sqrt{D_{\lambda_\mu,N}}} \delta_{\lambda_\mu, \square\!\square\} k_{x,\mu}}, \tag{29}$$

$$D_{\square\!\square\} k_\ell,N} = \frac{N(N-1)\cdots(N-k_\ell+1)}{k_\ell!}, \tag{30}$$

where in this case $\rho^x_\mu = (m,n)_{\lambda_\mu}$ as there are no epsilon tensors. Given this result, one can obtain the usual contributions from monomers and dimers ($f_\ell = 0$) to the strong coupling partition function

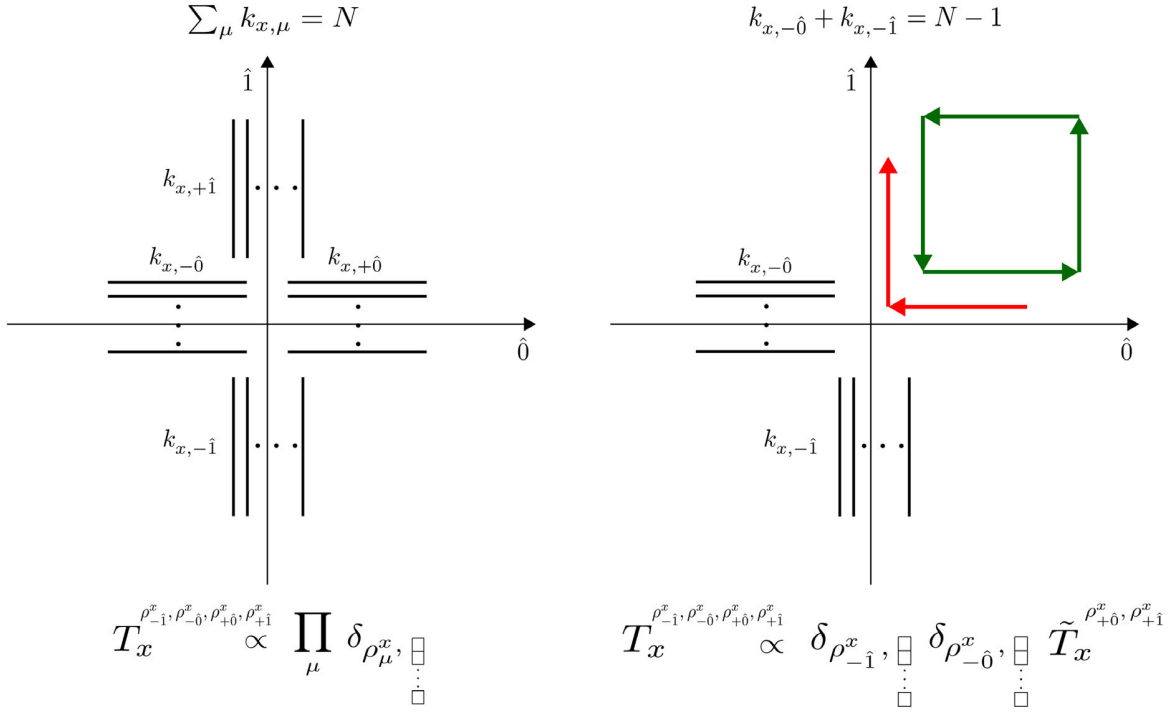

FIG. 4. Left: a typical strong coupling configuration where dimers are attached to a given site. The tensor T^ρ is trivial as only one combination of indices (totally antisymmetric irrep on each leg) contributes. Right: an $O(\beta)$ correction. The tensor T^ρ can be written as external product of a tensor carrying only the DOIs from excited links and delta functions corresponding to the strong coupling legs.

$$\begin{aligned}\mathcal{Z}_{SC} &= \sum_{\{k_\ell,m_x\}} \prod_{\ell=(x,\mu)} \frac{1}{k_\ell!^2} \prod_x \frac{N!}{m_x!} \prod_{\pm\mu} \frac{1}{\sqrt{D_{\lambda_\mu,N}}}\, \delta_{\lambda_\mu,\square\atop\square\}k_{x,\mu}} \\ &= \sum_{\{k_\ell,m_x\}} \prod_{\ell=(x,\mu)} \frac{1}{k_\ell!^2} \frac{1}{D_{\square\atop\square\}k_{\ell},N}} \prod_x \frac{N!}{m_x!} \\ &= \sum_{\{k_\ell,m_x\}} \prod_{\ell=(x,\mu)} \frac{(N-k_\ell)!}{k_\ell!\,N!} \prod_x \frac{N!}{m_x!},\end{aligned} \tag{31}$$

where we dropped the dependency on $\hat{m}_q$ and μ_q in the partition function Eq. (27) at $\beta = 0$. The weight for strong coupling baryon loops can be also easily recovered since the corresponding tensors are of size one by construction. The decoupling Eq. (29) also extends to the case where strong coupling dimers combine on a given site with links carrying a nonzero gauge flux. In this case, the tensor T^ρ can be decomposed as

$$T_x^{\rho^x_{-d},\cdots,\rho^x_d} \propto \prod_{\mu\in s.c.} \delta_{\lambda_\mu,\square\atop\square\}k_{x,\mu}}\, \tilde{T}_x^{\rho^x_{exc.}}, \tag{32}$$

where the proportionality coefficient depends on the external strong coupling dimer legs. An example is provided in Fig. 4 (right), while in Appendix B, we rederive the $\mathcal{O}(\beta)$ partition function. The indices of the tensor in the rhs of Eq. (32) (ρ^x_{exc}) correspond to the DOIs of the links attached to excited plaquettes. A similar decomposition holds in the presence of an external baryon. As a consequence, the value of $\mathcal{G}$ can be written as

$$\mathcal{G} = \mathcal{G}_{\text{s.c.}} \prod_{\text{bubbles i}} \mathcal{G}_{\mathcal{B}_i}, \tag{33}$$

where a bubble $\mathcal{B}_i$ is any *plaquette-connected* region and two bubbles are disconnected if they do not share an excited link (i.e., a link attached to an excited plaquette).

Therefore, to evaluate the total weight of a configuration, it is sufficient to use the more involved structure based on the tensor network contraction on the sublattice where the plaquette occupation numbers are nonzero, exploiting the factorization of the tensor network for disconnected plaquette contributions. The strong coupling part can be evaluated using the standard combinatorial formulae [e.g., Eq. (31)]. This is particularly useful since at small values of β the bubbles $\mathcal{B}_i$ extend over few lattice spacings and the nonlocal effects from the tensor network are manageable.

B. Complexity and sampling strategies

We now want to comment on the complexity of the dual partition function Eq. (27). Given the background $\{n_p, \bar{n}_p, k_\ell, f_\ell, m_x\}$, the weight of the configuration is obtained by contracting the tensor network T^ρ_x. Two different strategies

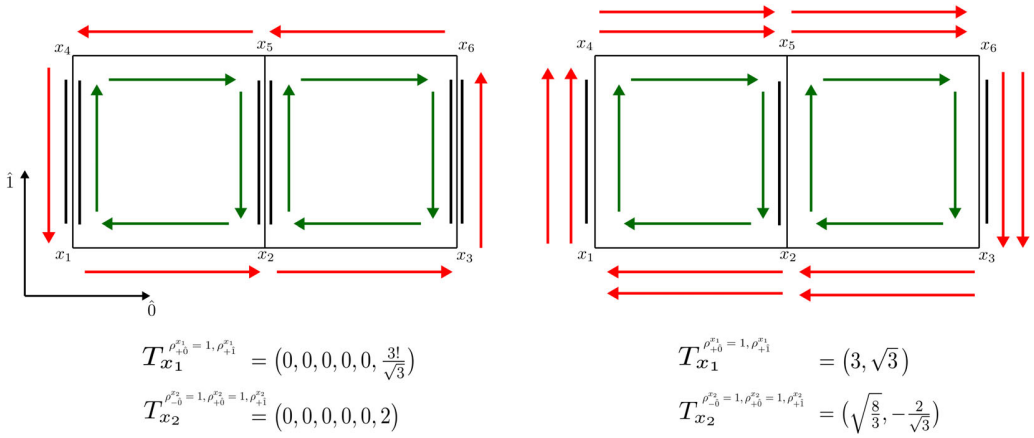

FIG. 5. Two SU(3) bubble contributions at $\mathcal{O}(\beta^2)$ with $(n_p,\bar{n}_p)=(0,1)$ on the two excited plaquettes. At this order, computing the weight corresponding to the bubbles is easy as the tensor network within the bubble is only made up of small vectors. Some external legs are trivial as there is only one possible DOI ($\rho_\mu^x=1$). Oftentimes the tensors T_x are very sparse as a consequence of the great orthogonality theorem (see also Appendix B). In the figures, we only show the tensors associated to x_1 and x_2. The remaining tensors are given by $T_{x_3}=T_{x_4}=T_{x_6}=T_{x_1}$ and $T_{x_5}=T_{x_2}$.

can be used to sample the partition function: one can either exploit the "bubble decomposition" in Eq. (33) to simplify the numerical cost of contracting the network or consider the DOIs as an additional d.o.f. to be evaluated stochastically. In the first case, a relevant question is whether the decomposition Eq. (15) is optimal, meaning that the number of decoupling operators n_ρ in Eq. (16) is the smallest possible. The machine time required to contract the network depends almost completely on the size of the external legs of the tensors. In the U(N) case, we already know that the answer is positive as it can be shown that the operators P^ρ are mutually orthogonal, hence independent. It is therefore not possible to perform a reparametrization of the $\mathcal{I}$-integral that results in a decomposition of the type Eq. (15) with a smaller number of terms within the sum. For SU(N), the situation is not completely clear as we could not prove that the decoupling operators corresponding to the SU(N) contributions (nonzero q) are independent. The question whether the complexity can be reduced using a different parametrization is thus still open. In any case, the lower bound on the number of DOIs provided by the U(N) result already tells that to a certain degree, the complexity is unavoidable. This number grows as a factorial as the (anti-)plaquette occupation numbers increase and contracting the resulting tensors along the excited plaquettes becomes in general too expensive in $d>2$. Even though this description can be used as a starting point for future theoretical development, as it stands, the bubble decomposition and the corresponding tensor network cannot be used for exact calculations in full QCD. Nevertheless, the dual form of the partition function together with the decomposition Eq. (33) can be used to study lattice QCD perturbatively in β, by truncating the expansion of the plaquette action. We remind that this has been done so far, using worldline formulations, only for the leading $\mathcal{O}(\beta)$ corrections [39]. Truncating at $\mathcal{O}(\beta^n)$ means that the allowed configurations are only those corresponding to bubble contributions of at most $\mathcal{O}(\beta^n)$. Making use of this definition, the truncation corresponds to a free energy which is exact up to the same order. For instance, at order $\mathcal{O}(\beta^2)$, the largest allowed bubble contributions are 2×1 rectangles with an elementary (anti-) plaquette excitation ($\bar{n}_p$) $n_p=1$ as sketched in Fig. 5. In the SU(3) case, four of the six tensors T_x^ρ making up the bubble are matrices of sizes at most 6×1, while the other two are rank three tensors of sizes at most $6\times 1\times 1$. Contracting the reduced tensor network within the bubbles is straightforward and can be done on the fly during Monte Carlo evolution without any overhead. Higher order contributions ($n=3,4,5,\ldots$) can be also easily evaluated in $4d$. One possible strategy is to compute and store beforehand all the tensors T^ρ that are compatible with the constraint and the truncation order. This step needs to be performed one time only, as the tensor network does not depend on the simulation parameters. For instance, the computation of all the tensors needed to address the $4d$ N^{3}LO correction to strong coupling QCD took $\approx 10^2 s$ on a single CPU, with the largest tensor having only $\mathcal{O}(10)$ nonzero elements. The tensors are then loaded and used to compute the value of $\mathcal{G}_{B_i}$ when the bubble B_i needs to be updated. We are currently designing an ergodic algorithm capable to sample the bubble contributions which will be illustrated in a forthcoming publication where the higher order β corrections to the strong coupling phase diagram will be addressed.

The second possibility is to consider the DOIs as an additional d.o.f. along with $\{n_p,\bar{n}_p,k_\ell,m_x\}$. The complexity of the tensor network can be thus overcome by

importance sampling. In this case, a given configuration is determined by selecting one tensor element for each lattice site. When doing so, the weight of such configurations is local and an additional metropolis acceptance test can be easily introduced to make sure that the system explores the DOIs configuration space during Monte Carlo. For instance, when a bond, an elementary plaquette or a cube containing six plaquettes is updated, we can propose a quasilocal update by randomly choosing new DOIs on the bonds involved. The feasibility of this approach depends on the minus signs induced by splitting the former configurations in terms of $\{n_p, \bar{n}_p, k_\ell, m_x\}$ into subconfigurations where one selects a single tensor element out of the full tensor T_x^ρ. In fact, the tensor elements are not positive defined and it could happen that without contracting the network an additional source of minus signs is plugged into the system. As mentioned in Sec. I, the main obstacle to the use of the permutation basis was in fact the severe sign problem induced by the Weingarten functions $\tilde{\mathrm{W}}\mathrm{g}$. Using instead the DOIs, the induced sign problem can be much milder. In Sec. V, we will provide preliminary evidences to this statement based on an exact enumeration of the partition function.

C. Sign problem

Having discussed the partition function, we now turn to the computation of σ_f in the dual representation. In general, the fermionic sign of a configuration is determined by the staggered phases, the antiperiodic boundary condition for fermion fields, and by the so-called geometric sign. The latter stems from the fact that, starting from Eqs. (3) and (4), one has to reorder the Grassmann variables contained in the matrices $\mathcal{M}_\ell, \mathcal{M}_\ell^\dagger$ before performing the Grassmann integration at each site. At strong coupling, only baryon loops ($f_\ell = \pm N$) can induce a negative sign and the geometric sign is known in closed form. It combines with the staggered phases and the winding number to produce

$$\sigma_f(\mathcal{C}) = \left[\prod_{\ell\in\mathcal{C}} \eta_\mu(x)\right](-1)^{N_\ell(\mathcal{C})+N_-(\mathcal{C})+\omega(\mathcal{C})} \tag{34}$$

for $\mathrm{SU}(2N+1)$, whereas $\sigma_f = +1$ for $\mathrm{SU}(2N)$. In Eq. (42), $\mathcal{C}$ is the set of links traversed by baryons, $N_\ell(\mathcal{C})$ the number of baryon loops, $N_-(\mathcal{C})$ the number of baryon loop segments in negative directions, and $\omega(\mathcal{C})$ the total winding number in temporal direction. At strong coupling, the baryon-loop induced sign problem is very mild and the finite density phase diagram can be mapped out using sign reweighting [38,43].

At finite β, the structure of the geometric sign gets more complicated as the allowed quark fluxes can also be intersecting and the equality in Eq. (42) does no longer hold true. Specializing to SU(3), a fermionic minus sign is only induced by single and triple quark fluxes while for dimers and diquarks $\sigma_f = +1$.[4] To compute the geometric sign for intersecting loops, as closed formulae are apparently lacking, we explicitly count how many times the Grassmann variables corresponding to odd fluxes need to be commuted to bring them in canonical ordering at each lattice site. Formally, σ_f can be written as

$$\sigma_f(\mathcal{C}_1,\mathcal{C}_3) = \left[\prod_{\ell\in\mathcal{C}_1\cup\mathcal{C}_3} \eta_\mu(x)\right](-1)^{\omega(\mathcal{C}_1,\mathcal{C}_3)}\sigma_G(\mathcal{C}_1,\mathcal{C}_3), \tag{35}$$

where $\mathcal{C}_1$ and $\mathcal{C}_3$ are, respectively, the set of links traversed by single and triple quark fluxes and the winding number $\omega(\mathcal{C}_1,\mathcal{C}_3)$ is given by

$$\omega(\mathcal{C}_1,\mathcal{C}_3) = \sum_{\vec{x}} f_{(\vec{x},N_\tau),\hat{0}}, \tag{36}$$

where N_τ is the temporal extent of the lattice. In Eq. (35), σ_G is the global geometric sign and in general cannot be factorized as a product of two terms depending separately on $\mathcal{C}_1$ and $\mathcal{C}_3$. It is computed after contracting the tensor T_x^ρ at fixed background $\{n_p, \bar{n}_p, d_\ell, f_\ell, m_x\}$, and cannot be cast into a product of local minus signs that can be absorbed with a redefinition of the tensors T_x.

As we already mentioned, another potential source of negative signs, which does not depend on the fermion fields, is caused by the lack of positivity of the tensor elements T_x^ρ. This issue is relevant when considering the DOIs as an additional d.o.f. Strong oscillations of the sign within the tensor network can in fact hinder the application of importance sampling. Although this question can be only answered on the basis of Monte Carlo simulations via sign reweighting, in Sec. V, we will show preliminary results on the interplay between the fermionic and the tensor network induced sign problem, obtained from exact enumeration of the partition function on small volumes.

D. Observables

As both the fermion field and the gauge links have been integrated out, the observables in the dual representation take a different form. The ones defined as derivatives of $\log\mathcal{Z}$ with respect to external parameters can be obtained taking derivatives in Eq. (27). For instance, the chiral condensate $\langle\bar{\psi}\psi\rangle$, baryon number n_B, and average plaquette $\langle P\rangle$ are given by

$$\begin{aligned}
\langle\bar{\psi}\psi\rangle &= \frac{1}{V}\frac{\partial\log\mathcal{Z}}{\partial\hat{m}_q} = \frac{\langle m_x\rangle}{V\hat{m}_q},\\
\langle n_B\rangle &= \frac{1}{V}\frac{\partial\log\mathcal{Z}}{\partial\mu_q} = \frac{\langle f_{x,\hat{0}}\rangle}{V},\\
\langle P\rangle &= \frac{1}{V}\frac{\partial\log\mathcal{Z}}{\partial\beta} = \frac{n_p+\bar{n}_p}{\beta V},
\end{aligned} \tag{37}$$

[4]For SU(2), only single quark fluxes can produce a negative σ_f.

and higher order derivatives (i.e., susceptibilities) can be obtained in a similar fashion, evaluating the various cumulants of m_x, $f_{x,\hat{0}}$, and $n_p + \bar{n}_p$. The definition of nonderivative observables, such as the Polyakov loop, is less trivial in the dual representation as the gauge fields have been already integrated out. Formally, the Polyakov loop can be written as a ratio of partition functions

$$\langle L \rangle = \frac{\mathcal{Z}_L}{\mathcal{Z}}, \tag{38}$$

where $\mathcal{Z}_L$ is the partition function with a Polaykov loop insertion and $\mathcal{Z}$ is given by Eq. (27). $\mathcal{Z}_L$ admits a dual representation similar to Eq. (27) with modified tensors T_x^{ρ} at the sites x crossed by the Polyakov loop. Here, we will not discuss its specific form. The strategy to sample the Polyakov loop will be addressed in a following paper containing the numerical results from Monte Carlo simulations.

To perform finite temperature calculations at nonzero β, we can either vary the temporal lattice extent N_τ at fixed lattice spacing a according to

$$aT = \frac{1}{N_\tau} \tag{39}$$

or perform simulations on anisotropic lattices. The first strategy works well for $\frac{\beta}{2N}$ close to one, where one can meaningfully fix the scale and determine the relations $\beta(a), \hat{m}_q(a)$ imposing a physical constraint on the low-energy mesonic spectrum. Instead, at small enough β (and especially at strong coupling), the scale cannot be fixed as the lattice is too coarse. In this case, the temperature is changed inducing a physical anisotropy $\xi = \frac{a_s}{a_t}$ by using two different β couplings for spatial (β_s) and temporal (β_t) plaquettes and introducing a fermionic bare anisotropy γ that favors hoppings in temporal direction. Implementing this modification in the partition function Eq. (27) is straightforward. The modifications can be summarized in

$$\begin{aligned} \frac{e^{\mu_q \delta_{\mu,0} f_{x,\mu}}}{k_\ell!(k_\ell + |f_\ell|)!} &\to \frac{e^{\mu_q \delta_{\mu,0} f_{x,\mu}}}{k_\ell!(k_\ell + |f_\ell|)!} \gamma^{\delta_{\mu,0}(|f_{x,\mu}| + 2k_{x,\mu})}, \\ \beta^{n_p + \bar{n}_p} &\to \beta_s^{n_{p_s} + \bar{n}_{p_s}} \beta_t^{n_{p_t} + \bar{n}_{p_t}}, \end{aligned} \tag{40}$$

and $(\bar{n}_{p_{s/t}})$ $n_{p_{s/t}}$ are the (anti-)plaquette occupation numbers for spatial and temporal plaquettes. The relation between the bare parameters β_s, β_t, γ and the physical anisotropy ξ has to be determined nonperturbatively via the so-called anisotropy calibration procedure (see [66] and references therein). This has been done so far in the strong coupling limit at zero [66] and nonzero [67] quark mass $\hat{m}_q$. The extension to strong coupling QCD including $\mathcal{O}(\beta)$ is in preparation. In this paper, we will be only interested in the evolution of the observables as a function of $\beta, \hat{m}_q, \mu_q$, hence in comparing the dual observables with the HMC results, we will set $\gamma = 1$ and $\beta_s = \beta_t = \beta$.

V. CROSSCHECKS FROM EXACT ENUMERATION/HMC FOR $N = 2$, $N = 3$ ($\mathrm{U}(N)$ and $\mathrm{SU}(N)$)

In a finite volume, the partition function Eq. (27) truncated at a given order $\mathcal{O}(\beta^n)$ is always a finite polynomial $\mathcal{P}(\beta, \hat{m}_q, z_q)$ in β, quark mass $\hat{m}_q$, and fugacity $z_q = \exp\frac{\mu_q}{T}$. To check the correctness of the dual formulation and the computation of the weights, we performed the exact computation of $\mathcal{P}$ in small two-dimensional volumes, comparing the result from the exact enumeration of $\mathcal{Z}$ with the outcome of standard lattice QCD simulations at zero chemical potential μ_q. We considered as gauge group both $\mathrm{U}(N)$ and $\mathrm{SU}(N)$ for $N = 2, 3$, and obtained the full polynomial $\mathcal{P}$ on 2×2 and 4×4 volumes for various $n \leq 6$, employing periodic boundary conditions in all directions. To enumerate the coefficients of the polynomial, we first precomputed all the tensors $T_x(\mathcal{D}_x)$ compatible with Gauge and Grassmann constraints and with the truncation order. We then generated all possible combinations of $\{n_p, \bar{n}_p, d_\ell, f_\ell, m_x\}$ and contracted the corresponding tensor network to determine its contribution to $\mathcal{P}$. The result of this contraction was then multiplied by the fermionic sign σ_f. In Table I, we show the total number of configurations as a function of the truncation order. At fixed $\mathcal{O}(\beta^n)$, this number grows very large as a function of the number of dimensions; hence, we could not perform the exact enumeration in $d > 2$. Nevertheless, as our dual formulation does not present any fundamental difference when applied to higher dimensions, we believe that this crosscheck gives some hints about its validity in $d = 3, 4$. In Figs. 6 and 7, we show the results of this comparison for the average plaquette $\langle P \rangle$ and for the chiral condensate $\langle \bar{\chi}\chi \rangle$, respectively, for U(2), U(3) and SU(2), SU(3). They were analytically determined from $\mathcal{P}(\beta, \hat{m}_q, z_q)$ by

TABLE I. Number of distinct configurations on a 2×2 lattice for various gauge groups and truncations of $\mathcal{O}(\beta^n)$. All these configurations are taken into account when computing the partition function and its derivatives, as shown in Figs. 6 and 7. The complexity of enumeration rises drastically with n, but can be overcome by importance sampling.

	U(1)	U(2)	U(3)	SU(2)	SU(3)
$\mathcal{O}(\beta^0)$	17	135	695	223	815
$\mathcal{O}(\beta^1)$	25	271	1 775	863	2 495
$\mathcal{O}(\beta^2)$	101	1 839	12 163	14 471	25 259
$\mathcal{O}(\beta^3)$	141	4 119	36 027	152 551	337 503
$\mathcal{O}(\beta^4)$	373	32 107	436 415	4 895 849	4 703 047
$\mathcal{O}(\beta^5)$	497	80 319	1 640 829	106 758 281	182 863 979

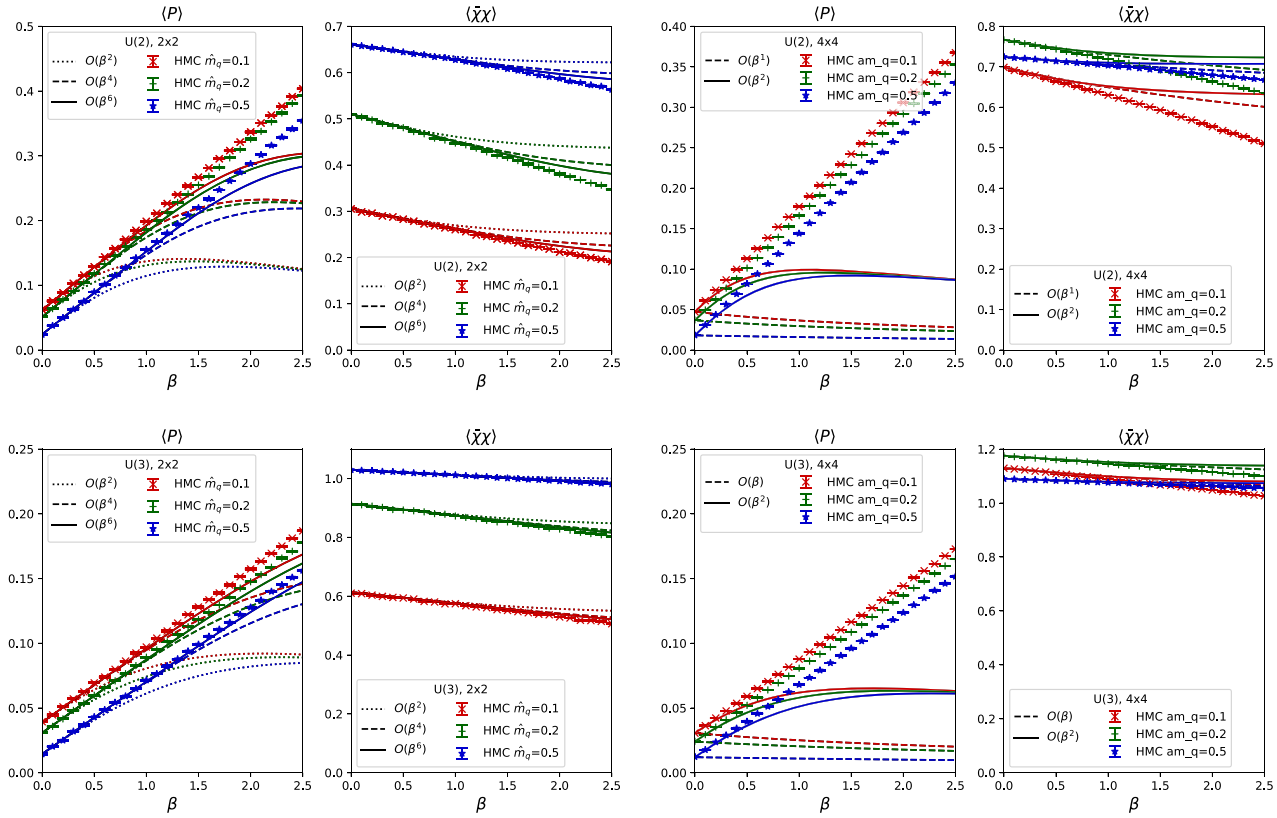

FIG. 6. Comparison between exact enumeration and HMC simulations for U(2) (upper plots) and U(3) (lower plots). For both gauge groups, the average plaquette $\langle P\rangle$ and the chiral condensate $\langle\bar{\chi}\chi\rangle$ are shown on a 2×2 (left) and 4×4 (right) lattice. Data points with different symbols correspond to different quark masses while solid, dashed, and dotted lines correspond to different truncation orders $\mathcal{O}(\beta^n)$.

$$\langle P\rangle = \frac{1}{NL^2}\partial_\beta \mathcal{P}(\beta,\hat{m}_q,0)/\mathcal{P}(\beta,\hat{m}_q,0),$$
$$\langle\bar{\chi}\chi\rangle = \frac{1}{L^2}\partial_{\hat{m}_q}\mathcal{P}(\beta,\hat{m}_q,0)/\mathcal{P}(\beta,\hat{m}_q,0), \tag{41}$$

for $L=2$, 4 and $N=2$, 3. A clear result, emerging from Figs. 6 and 7, is that the strong coupling branch is well described by the polynomials $\mathcal{P}$ for all quark masses, and that the agreement with the HMC results indeed extends to larger and larger β as the truncation order is increased. Notice that at any fixed order $\mathcal{O}(\beta^n)$, the continuum limit $\beta\to\infty$ of the average plaquette is always zero, as it can be seen from its definition in terms of the dual d.o.f. Eq. (37). The value $\beta_{\max}$ that corresponds to a maximum of the

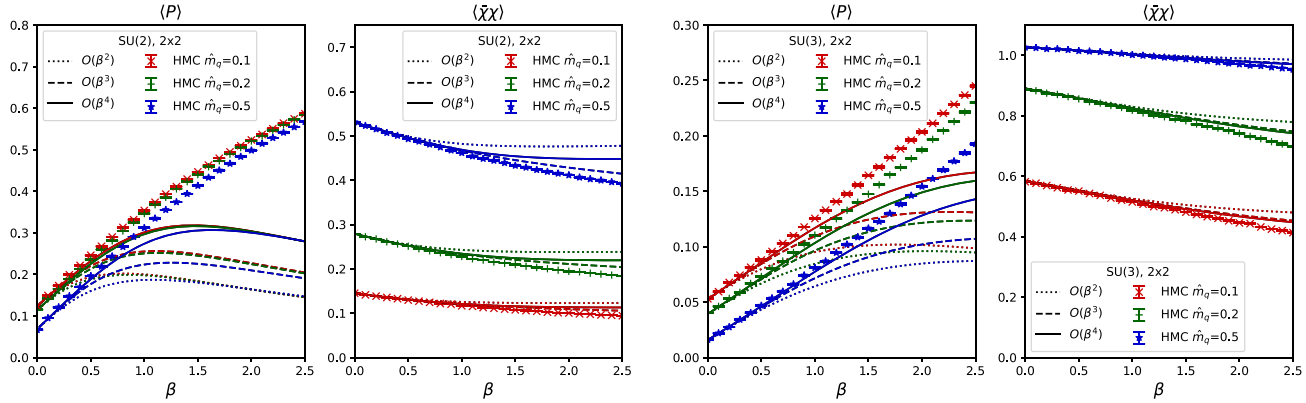

FIG. 7. Similar comparison between exact enumeration and HMC on a 2×2 lattice as in Fig. 6 for SU(2) (left plots) and SU(3) (right plots).

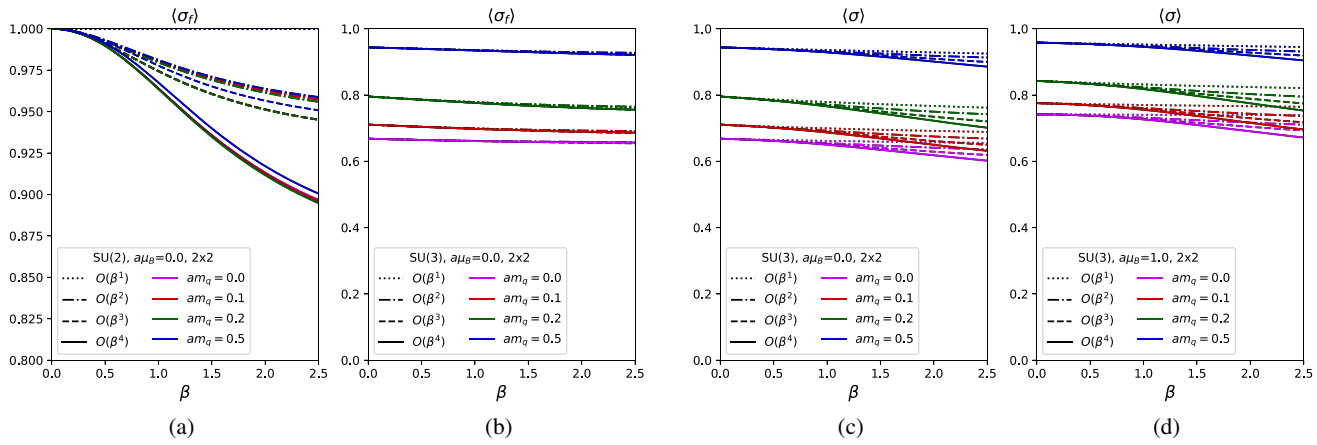

FIG. 8. Sign problem on a 2×2 lattice as a function of β for various quark masses. (a) Fermionic sign $\langle \sigma_f \rangle$ for SU(2) which has no sign problem in the strong coupling limit and only a very mild sign problem for finite β. (b) Fermionic sign $\langle \sigma_f \rangle$ for SU(3): it remains almost constant with β as compared to the strong coupling limit (where the fermionic sign is only due to baryon worldlines). (c) Average sign $\langle \sigma \rangle$ for SU(3). It includes the sign fluctuations within the tensor network. (d) Same as in (c) considering a nonzero value of the baryon chemical potential μ_B.

average plaquette can be used as a strong upper bound for the validity of the expansion at $\mathcal{O}(\beta^n)$.

Another relevant information we can extract from the exact enumeration concerns the magnitude of the sign problem. A measure of its severity is given by the average sign σ. It is defined as the ratio of the full ($\mathcal{Z}$) and the so-called phase quenched ($\mathcal{Z}^{\text{p.q.}}$) partition function

$$\langle \sigma \rangle = \frac{\mathcal{Z}}{\mathcal{Z}^{\text{p.q.}}}. \tag{42}$$

The latter is obtained by taking the norm of each statistical weight in $\mathcal{Z}$. In our case, the partition function is a sum of real quantities; hence, the norm is just the absolute value. From the definition, it follows that $\langle \sigma \rangle \leq 1$ and the equality holds if there is no sign problem. As we want to compare the sign problem in the dual representation with and without the DOIs as an additional d.o.f., we need to employ two different definitions for the phase quenched system. In the first case, we need to set the fermionic sign $\sigma_f = 1$ and take the absolute value of each tensor element

$$T_x^{\rho_{-d}^x \cdots \rho_d^x} \to |T_x^{\rho_{-d}^x \cdots \rho_d^x}|, \tag{43}$$

while in the second case it suffices to set $\sigma_f = 1$ as a configuration is now determined by the contracted tensor network. The two resulting average signs are, respectively, $\langle \sigma \rangle = \langle \sigma_f \sigma_\rho \rangle$ and $\langle \sigma_f \rangle$. In Fig. 8, they are shown in the most relevant cases of SU(2) and SU(3) as a function of the truncation order and in the SU(3) case at nonzero baryon chemical potential as well. In the SU(2) case, the fermionic sign does not play a role on a 2×2 lattice as the allowed loop geometries have $\sigma_f = 1$ and the only source of negative signs is due to the tensor network. In Fig. 8(a), this is shown for various quark masses and for different truncations up to $\mathcal{O}(\beta^4)$. The trend corresponds to a mild deterioration of the sign as β and the truncation order is increased. This deterioration is not dramatic and corresponds to a fall in $\langle \sigma \rangle$ of about 10% at $\beta \approx 2$. In the case of SU(3), the fermionic sign σ_f is not positive [Fig. 8(b)] but remains almost constant as a function of β and truncation order. When considering the sign $\langle \sigma \rangle$, a trend similar to the SU(2) case shows up [Fig. 8(c)]: the sign in this case remains almost constant for $\beta \leq 1$ where it starts to get worse as a function of the truncation order. When a nonzero baryon chemical potential is considered [Fig. 8(d)], this behavior does not change.

Although our numerical results are preliminary and only based on an exact enumeration of the partition function on a 2×2 lattice, we highlight some of the findings that could extend to larger volumes and higher dimensions. First of all, the comparison with the HMC simulations shows that our method provides the correct Boltzmann weights for the dual configurations as the strong coupling branch up to $\beta \leq 0.5$ is well described by the polynomials $\mathcal{P}(\beta, \hat{m}_q, z_q)$ for different gauge groups and quark masses. This is nontrivial: the number of configurations considered already on a small volume is very large (Table I) and the computation is very sensitive to the exact evaluation of the tensor elements T_x^ρ and of the fermionic sign σ_f. The evaluation of the Boltzmann weights away from the strong coupling limit is thus under control and can be used in Monte Carlo simulations if the truncation order $\mathcal{O}(\beta^n)$ is not too large. We considered two main strategies in view of Monte Carlo simulations: the bubble decomposition Eq. (33) and sampling an enlarged configuration space that includes the DOIs. While we are not yet in position to draw general conclusions on the sign problem, when comparing it with the behavior in a permutation based dualization [50], the improvement is drastic. Hence, resumming the permutations as in Eq. (13) effectively reduces the sign problem from the Weingarten functions.

VI. CONCLUSION AND DISCUSSION

In this work, we proposed a new strategy for the evaluation of higher order contributions in the strong coupling expansion of lattice QCD with staggered fermion discretization. The dual representation in terms of local tensorial weights improves on the sign problem as compared to evaluations in a Weingarten function basis. The color constraints from gauge and Grassmann integration combine to yield admissible configurations that after contracting the tensors are intersecting plaquette surfaces that are either closed or bounded by fermion fluxes. The configuration space is thus a worldline and worldsheet representation with the additional multi-indices ρ, which we called decoupling operator indices and that encode the information about the interplay of the unitary and symmetric groups.

The prospects of Monte Carlo simulations of lattice QCD at finite density in the strong coupling regime are encouraging: the weights in the partition functions are local, and various strategies to sample the partition function Eq. (27) are possible. We will be able to obtain results on the phase diagram in the strong coupling regime beyond $\mathcal{O}(\beta)$. One possible way to perform Monte Carlo is via a worm algorithm based on vertices, as was discussed in the context of the Schwinger model [68]. The drawback of this method is that this algorithm slows down drastically with the number of vertices (Table II). This limits in practice the maximal order of β feasible in $3+1$ dimensions. Another intriguing possibility is to perform local metropolis updates that could be parallelized. We can either sample the multi-indices ρ alongside the occupation numbers (monomer, dimer plaquette, and fermion flux) or contract all ρ's on a background of occupation numbers, employing the bubble decomposition discussed in Sec. IV B. Even when including the higher orders, the sign problem might still be manageable if β is not too large. For what values of β simulations are possible in $3+1$ dimensions is only to be seen in practice and will be codetermined by the magnitude of the sign problem, by the numerical cost of evaluating the Boltzmann weights and will also depend crucially on the quark mass. Our representation is also valid for pure Yang Mills theory, which is expected to have a very sign problem after contracting the tensor network.

TABLE II. Number of distinct nonzero tensor elements for various gauge groups and truncations of $\mathcal{O}(\beta^n)$ in two dimensions. These numbers correspond to the total number of vertices that would enter in a corresponding vertex model.

	U(1)	U(2)	U(3)	SU(2)	SU(3)
$\mathcal{O}(\beta^0)$	5	15	35	27	47
$\mathcal{O}(\beta^1)$	13	55	155	155	255
$\mathcal{O}(\beta^2)$	41	215	655	1139	1499
$\mathcal{O}(\beta^3)$	81	639	2279	6995	8939
$\mathcal{O}(\beta^4)$	173	2079	8687	48 957	52 571
$\mathcal{O}(\beta^5)$	293	6007	31 617	338 109	360 525

A finite chemical potential does not introduce an additional sign problem as the zero-density Boltzmann weights get multiplied only by positive factors. Moreover, at fixed values of β, the sign problem becomes milder for large enough temperatures and/or densities: the worldline configurations contributing to the fermionic sign σ_f simplify as the quark fluxes are mainly aligned in temporal direction. A detailed analysis of the sign problem requires, however, large volumes that cannot be obtained via exact enumeration and will be presented in a forthcoming publication.

ACKNOWLEDGMENTS

We thank Jangho Kim for helpful discussions on fast exact enumeration. We acknowledge support by the Deutsche Forschungsgemeinschaft (German Research Foundation) through the Emmy Noether Program under Grant No. UN 370/1 and through the CRC-TR 211 strong-interaction matter under extreme conditions—Project No. 315477589—TRR 211.

APPENDIX A: SU(N) GENERATING FUNCTIONAL AND $\mathcal{I}$-INTEGRALS

Equation (8) for the SU(N) $\mathcal{I}$-integrals can be derived from the generating functional

$$Z^{q,p}[K,J] = \int_{\mathrm{SU}(N)} DU (\mathrm{Tr}[UK])^{qN+p} (\mathrm{Tr}[U^\dagger J])^p \tag{A1}$$

by taking successive derivatives with respect to the sources $J, K \in GL(N,\mathbb{C})$, according to the following equation:

$$\mathcal{I}^{qN+p,p}_{i^j,k^l} = \frac{1}{(qN+p)!p!} \times \frac{\partial^{(qN+2p)} Z^{q,p}[K,J]}{\partial K^{i_1}_{j_1} \cdots \partial K^{i_{qN+p}}_{j_{qN+p}} \partial J^{k_1}_{\ell_1} \cdots \partial J^{k_p}_{\ell_p}} \Big|_{J=K=0}. \tag{A2}$$

To evaluate $Z^{q,p}[K,J]$, we first convert the integral [(A1)] into a U(N) integral, using

$$\frac{1}{\det K^q} \int_{\mathrm{SU}(N)} DU (\mathrm{Tr}[UK])^{qN+p} (\mathrm{Tr}[U^\dagger J])^p = \int_{\mathrm{U}(N)} DU \frac{1}{\det[UK]^q} (\mathrm{Tr}[UK])^{qN+p} (\mathrm{Tr}[U^\dagger J])^p \tag{A3}$$

and assuming for the moment $J, K \in \mathrm{U}(N)$. The equality holds because the last integrand is invariant under multiplication of the U matrix by a complex phase. As a consequence, it gives the same result when integrated using the SU(N) or the U(N) Haar measure. Exploiting this trick, we can make use of the U(N) character expansion to compute the quantity in the rhs of Eq. (A3).

Thanks to the Schur-Weyl duality [69,70], power of traces of U(N) matrices have the following character expansion:

$$(\mathrm{Tr}U)^n = \sum_{\substack{\lambda\vdash n \\ \mathrm{len}(\lambda)\le N}} f_\lambda \hat{\chi}^\lambda(U), \tag{A4}$$

where $\hat{\chi}^\lambda$ are the U(N) characters.[5] Instead, $\det U^q$ are irreducible one-dimensional representations $\forall\, q \in \mathbb{Z}$ (so-called determinantal representations). According to a standard group theory result, the tensor product of the irrep. V_λ with a determinantal representation V^q_{det} gives

$$V_\lambda \otimes V^q_{\mathrm{det}} \cong V_{\lambda+q}, \tag{A5}$$

where $V_{\lambda+q}$ is the $U(N)$ irreducible representation with highest weight $\{\lambda_1+q,\ldots,\lambda_N+q\}$. This gives

$$\hat{\chi}^\lambda(U)\det(U)^q = \hat{\chi}^{\lambda+q}(U). \tag{A6}$$

Substituting Eqs. (A4) and (A6) into the rhs of Eq. (A3), we get

$$\begin{aligned}\frac{Z^{q,p}[K,J]}{\det[K]^q} &= \int_{\mathrm{U}(N)} DU \sum_{\substack{\lambda\vdash qN+p \\ \mathrm{len}(\lambda)\le N}} \sum_{\substack{\lambda'\vdash p \\ \mathrm{len}(\lambda')\le N}} f_\lambda f_{\lambda'} \hat{\chi}^{\lambda-q}(UK)\hat{\chi}^{\lambda'}(U^\dagger J) = \sum_{\substack{\lambda\vdash p \\ \mathrm{len}(\lambda)\le N}} f_{\lambda+q} f_\lambda \frac{\hat{\chi}^\lambda(JK)}{D_{\lambda,N}} \\ &= \frac{(qN+p)!}{p!}\prod_{i=0}^{N-1}\frac{i!}{(i+q)!}\sum_{\substack{\lambda\vdash p \\ \mathrm{len}(\lambda)\le N}}\frac{(f_\lambda)^2}{D_{\lambda,N+q}}\hat{\chi}^\lambda(JK) = \frac{(qN+p)!}{p!^2}\prod_{i=0}^{N-1}\frac{i!}{(i+q)!}\sum_{\substack{\lambda\vdash p \\ \mathrm{len}(\lambda)\le N}}\frac{(f_\lambda)^2}{D_{\lambda,N+q}}\sum_{\rho\vdash p} h_\rho \hat{\chi}^\lambda(\rho) t_\rho(JK) \\ &= (qN+p)!\prod_{i=0}^{N-1}\frac{i!}{(i+q)!}\sum_{\rho\vdash p} h_\rho \tilde{\mathrm{Wg}}^{q,p}_N(\rho) t_\rho(JK),\end{aligned} \tag{A7}$$

where the second equality follows from the orthogonality of characters, the third from the combinatorial identity

$$\frac{f_{\lambda+q}}{D_{\lambda,N}} = \frac{(qN+p)!}{p!}\prod_{i=0}^{N-1}\frac{i!}{(i+q)!}\frac{f_\lambda}{D_{\lambda,N+q}}, \tag{A8}$$

valid for $\mathrm{len}(\lambda)\le N$ and the fourth one from the Frobenius relation (see, for instance, Appendix A of [49]). The last equality is just a rearrangement of terms. The quantities $\tilde{\mathrm{Wg}}^{q,p}_N$ are the generalized Weingarten functions,

$$\tilde{\mathrm{Wg}}^{q,p}_N(\rho) = \frac{1}{(p!)^2}\sum_{\substack{\lambda\vdash p \\ \mathrm{len}(\lambda)\le N}}\frac{(f_\lambda)^2}{D_{\lambda,N+q}}\chi^\lambda(\rho). \tag{A9}$$

They are S_p class functions and therefore depend only on the conjugacy class of a given permutation. Conjugacy classes and irreducible representations are in 1-1 correspondence. This is the reason why the Weingarten functions can also have integer partitions as argument. In Eq. (A7), h_ρ is the number of permutations within the conjugacy class associated to the partition ρ, while $t_\rho(JK)$ is a shortcut for

$$t_\rho(JK) = \prod_{i=0}^{\ell(\rho)}\mathrm{Tr}(JK)^{\rho_i}. \tag{A10}$$

The SU(N) generating functional is

$$\begin{aligned}Z^{q,p}[K,J] &= (qN+p)!\prod_{i=0}^{N-1}\frac{i!}{(i+q)!}\det K^q \\ &\times \sum_{\rho\vdash p} h_\rho \tilde{\mathrm{Wg}}^{q,p}_N(\rho) t_\rho(JK),\end{aligned} \tag{A11}$$

and given the polynomial nature of the expression, it can be extended to any $K,J\in GL(N,\mathbb{C})$. In the limits $q=0$, $q=1$, and $p=0$, the known results [49,63], and [48] are recovered.

Given the expression (A11), the $\mathcal{I}$-integral is obtained by taking derivatives with respect to the sources K, J. We do not need to do this explicitly. In fact, it is sufficient to know the result in the cases $p=0$ and $q=0$ and then use Leibnitz Formula for the derivative of a product. Luckily, these two special cases have already been solved, respectively, by Creutz [48] and by Collins and collaborators in [58,59]. The two results are

$$\begin{aligned}\mathcal{I}^{qN,0}_{i^j,k^l} &= \frac{1}{(qN)!}\frac{\partial^{(qN)}Z^{q,0}[K]}{\partial K_{j_1,i_1}\cdots K_{j_{qN},i_{qN}}}\bigg|_{J=K=0} = \left[\prod_{i=1}^{N-1}\frac{i!}{(i+q)!}\right]\sum_{\{\alpha\}}\epsilon^{\otimes q}_{i_{\{\alpha\}}}\epsilon^{\otimes q,j_{\{\alpha\}}}, \\ \mathcal{I}^{p,p}_{i^j,k^l} &= \frac{1}{p!^2}\frac{\partial^{(2p)}Z^{0,p}[K,J]}{\partial K_{j_1,i_1}J_{l_1,k_1}\cdots K_{j_p,i_p}J_{l_p,k_p}}\bigg|_{J=K=0} = \sum_{\pi,\sigma\in S_p}\delta^{l_\pi}_i\tilde{\mathrm{Wg}}^{0,p}_N(\pi\circ\sigma^{-1})\delta^j_{k_\sigma},\end{aligned} \tag{A12}$$

[5]Not to be confused with the characters χ^λ of the symmetric group.

where $\delta_i^{l_\pi}$ and $\delta_{k_\sigma}^{j}$ are the usual Kronecker deltas where the indices are swapped according to permutations π and σ. The sum in the first line of Eq. (A12) runs over all possible ways $\alpha = \{\alpha_1, \ldots, \alpha_q\}$ of partitioning the qN indices into q epsilon tensors. To get the general $\mathcal{I}$-integral, it is sufficient to exploit the fact that the generating functional (A11) can be decomposed, apart from a trivial combinatorial factor, as a product of $Z^{q,0}$ and a term that resembles the generating functional $Z^{0,p}$. The only difference is in the coefficients $\tilde{\mathrm{W}}\mathrm{g}_N^{0,p}$ that must be substituted with $\tilde{\mathrm{W}}\mathrm{g}_N^{q,p}$. Therefore, by looking at Eq. (A2), when qN derivatives of K act on the power of the determinant $\det K^q$, they will reproduce the result for $I^{qN,0}$. Similarly, when p derivatives of K and p derivatives of J act on the second term, they will reproduce $I^{p,p}$ with the substitution $\tilde{\mathrm{W}}\mathrm{g}_N^{0,p} \to \tilde{\mathrm{W}}\mathrm{g}_N^{q,p}$. Any other combination of derivatives gives zero. Making use of the Leibnitz Formula, we can thus write down the expression of the $\mathcal{I}$-integral as

$$\mathcal{I}_{i^j,k^l}^{qN+p,p} = \left[\prod_{i=1}^{N-1}\frac{i!}{(i+q)!}\right]\sum_{\{\alpha,\beta\}}\sum_{\pi,\sigma\in S_p}\epsilon^{\otimes q}_{i_{\{\alpha\}}}\delta^{l_\pi}_{i_{\{\beta\}}}\tilde{\mathrm{W}}\mathrm{g}_N^{q,p}(\pi\circ\sigma^{-1}) \times \epsilon^{\otimes q, j_{\{\alpha\}}}\delta^{j_{\{\beta\}}}_{k_\sigma}, \tag{A13}$$

where the leftmost sum now runs over all the ways (α, β) of partitioning the i, j indices into the Kronecker deltas and into the q epsilon tensors. This "multiplicity" stems from the fact that we need to take into account every possible way of acting with the K derivatives, on the determinant and on the traces $\mathrm{tr}_\rho(JK)$, and from the Creutz result for $I^{qN,0}$ in Eq. (A12).

APPENDIX B: (RE-)DERIVATION OF THE $\mathcal{O}(\beta)$ PARTITION FUNCTION

The partition function (27) at $O(\beta)$ can be rewritten in terms of site and link (scalar) weights. This is done considering all possible tensors T_x at a corner of the excited plaquette, showing that they can be reduced to scalar objects. In this limiting case, we can perform all steps analytically so as to recover the partition function obtained in [39]. For general SU(N), there are two types of tensors: those corresponding to genuine SU(N) contributions [Figs. 9(b)–9(d)] and the ones that correspond to dimers with a single quark flux oppositely oriented with respect to the plaquette [Fig. 9(a)]. The latter is a pure U(N) contribution as the associated $\mathcal{I}$-integrals have $q = 0$. Let us consider first the second case. Even though the corresponding tensors can be quite large, the same decoupling present at strong coupling holds in this case. Proceeding in a similar fashion as in Eqs. (28), (29), and (31) and with reference to Fig. 9(a), one gets

$$T_{(0)}^{\rho^x_{-d}\cdots\rho^x_d} = N!\prod_{\mu\in s.c.}\frac{1}{\sqrt{D_{\lambda_\mu,N}}}\delta_{\lambda_\mu,\square\}k^{s.c.}_{x,\mu}}\frac{1}{\sqrt{D_{\lambda^{\hat{0}},N}}}\delta_{\lambda^{\hat{0}},\square\}k_{x,+\hat{0}}+1}\frac{1}{\sqrt{D_{\lambda^{\hat{1}},N}}}\delta_{\lambda^{\hat{1}},\square\}k_{x,+\hat{1}}+1}, \tag{B1}$$

where the first product runs over the external (strong coupling) dimers. As in the strong coupling limit, only one element of the tensor is nonzero. The modification of the dimer weight is obtained as in Eq. (31),

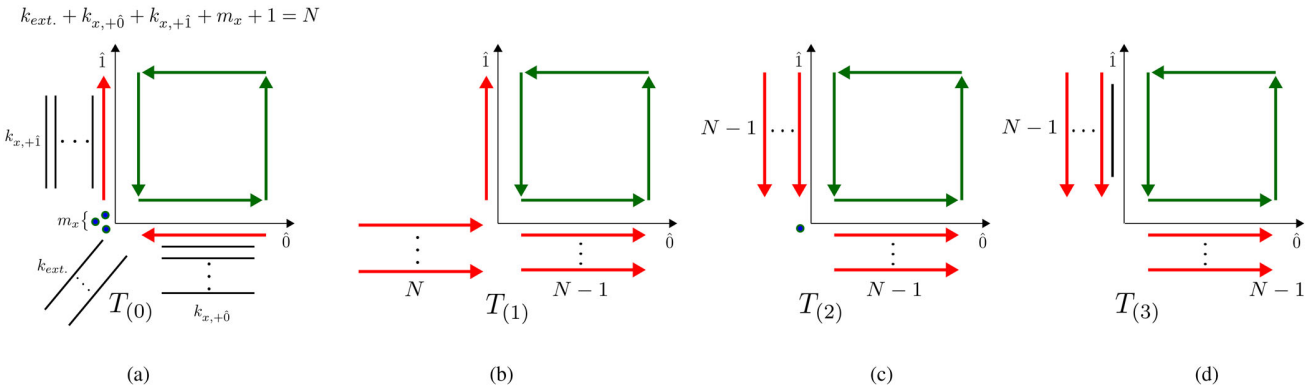

FIG. 9. The four different types of tensor at a corner of the excited plaquette. (a) The two excited links are occupied by dimers and a single quark flux. It represents the most general U(N) contribution to the $\mathcal{O}(\beta)$ partition function. (b) An incoming baryon ($f_\ell = N$) split into a $N-1$ quark flux and a single quark flux. (c) An $N-1$ quark flux travels in the same direction of the gauge flux. A dimer or a monomer must be present to satisfy the Grassmann constraint. (d) As in (c) with a dimer superimposed to the $N-1$ quark flux on one of the two excited links.

$$w_\ell(k_\ell, f_\ell = \pm 1) = \frac{1}{k_\ell!(k_\ell+1)!}\,\frac{1}{D\,\square\!\!\square\!\!\square\,\}\,k_\ell+1,N} = \frac{1}{k_\ell!(k_\ell+1)!}\,\frac{(k_\ell+1)!}{N(N-1)\cdots(N-k_\ell)} = \frac{(N-k_\ell-1)!}{N!k_\ell!}, \tag{B2}$$

and gives the correct link weight to be used when a dimer belongs to an excited link. The genuine SU(N) configurations are instead of three types:

(1) An incoming (strong coupling) baryon splits, at a corner of the plaquette, into a single quark flux and a $N-1$ quark flux. Equivalently, a single quark flux and a $N-1$ quark flux can recombine to form an outcoming (strong coupling) baryon [Fig. 9(b)].
(2) An incoming $N-1$ quark flux exits the site following the gauge flux induced by the plaquette. A monomer or an external dimer is also present in order to fulfill the Grassmann constraint [Fig. 9(c)].
(3) As in (2) with the external dimer or monomer replaced by a dimer on one of the two excited links [Fig. 9(d)].

The first two types of configurations are somewhat trivial as the associated tensors have size one. There is in fact only one DOI associated to the external legs of the two tensors. Their values can be readily computed,

$$T_{(1)} = \frac{N!}{\sqrt{N}} \qquad T_{(2)} = (N-1)!. \tag{B3}$$

In the case of configurations of type (3), the associated tensor has size 2×1. There are in fact two DOIs in direction $+\hat{1}$, where a dimer is superimposed to a $N-1$ quark flux. This tensor is given by

$$T^{1,1}_{(3)} = \frac{N!}{\sqrt{N+1}} \qquad T^{1,2}_{(3)} = \frac{N!}{\sqrt{N(N+1)}}. \tag{B4}$$

To remove this multiplicity, it is sufficient to notice that a link carrying a dimer plus a $N-1$ quark flux can only recombine with a $N-1$ quark flux from another direction. The latter involves an $\mathcal{I}$-integral made up of a single decoupling operator. Therefore, we can perform a resummation of the two DOIs by considering the following modified "tensor" of size 1:

$$\tilde{T}_{(3)} = \sqrt{(T^{1,1}_{(3)})^2 + (T^{1,2}_{(3)})^2} = \frac{N!}{\sqrt{N}}, \tag{B5}$$

and all tensors have been thus reduced to scalar quantities. It is easy to check that the modified dimer weights [Eq. (B2)] and the values of $T_{(1)}, T_{(2)}, \tilde{T}_{(3)}$ together with the usual combinatorial factors from the Taylor expansion are recovered by defining the following link and site weights at the boundary of the excited plaquette:

(1) To each $N-1$, quark flux associates a link weight $\frac{1}{N!(N-1)!}$.
(2) To each $N-1$, quark flux superimposed to a dimer associates a link weight $\frac{(N-1)!}{N!} = \frac{1}{N}$.
(3) For $k_\ell \in \{0,\ldots,N-1\}$, dimers and a single quark flux associate $w_\ell(d_\ell, f_\ell = \pm 1)$.
(4) To each site corresponding to a U(N) configuration, [Fig. 9(a)] associates the usual site weight: $N!/m_x!$.
(5) To each site corresponding to a SU(N) configuration, associate a factor $N!$ if there are no external (strong coupling) dimers or baryons and if $m_x = 0$. Associate a factor $N!(N-1)!$ if there are external dimers or if $m_x = 1$. Finally, associate $N!\sqrt{N}$ if there is an external baryon.

The rules (1)–(5) together with the usual strong coupling weights define the $\mathcal{O}(\beta)$ partition function [39]. Beyond this order, it is not possible to reduce the tensor network to a product of scalar link and site weights depending only on $\{n_p, \bar{n}_p, k_\ell, f_\ell, m_x\}$.

[1] P. de Forcrand, Simulating QCD at finite density, Proc. Sci., LATTICE2009 (**2009**) 010.
[2] C. Gattringer and K. Langfeld, Approaches to the sign problem in lattice field theory, Int. J. Mod. Phys. A **31**, 1643007 (2016).
[3] U. Wolff, Simulating the all-order strong coupling expansion III: O(N) sigma/loop models, Nucl. Phys. **B824**, 254 (2010); Erratum, Nucl. Phys.**B834**, 395 (2010).
[4] U. Wolff, Simulating the all-order strong coupling expansion IV: CP($N-1$) as a loop model, Nucl. Phys. **B832**, 520 (2010).
[5] F. Bruckmann, C. Gattringer, T. Kloiber, and T. Sulejmanpasic, Dual lattice representations for O(N) and CP($N-1$) models with a chemical potential, Phys. Lett. B **749**, 495 (2015); Erratum, Phys. Lett. B **751**, 595 (2015).
[6] C. Gattringer and T. Kloiber, Lattice study of the Silver Blaze phenomenon for a charged scalar π^4 field, Nucl. Phys. **B869**, 56 (2013).
[7] Y. D. Mercado, C. Gattringer, and A. Schmidt, Dual Lattice Simulation of the Abelian Gauge-Higgs Model at Finite Density: An Exploratory Proof of Concept Study, Phys. Rev. Lett. **111**, 141601 (2013).

[8] C. Gattringer, Baryon bags in strong coupling QCD, Phys. Rev. D **97**, 074506 (2018).
[9] C. Gattringer, D. Göschl, and C. Marchis, Kramers–Wannier duality and worldline representation for the SU(2) principal chiral model, Phys. Lett. B **778**, 435 (2018).
[10] F. Bruckmann and J. Wellnhofer, Diagrammatic representation of scalar QCD and sign problem at nonzero chemical potential, Phys. Rev. D **97**, 014501 (2018).
[11] U. Wolff, Simulating the all-order strong coupling expansion I: Ising model demo, Nucl. Phys. **B810**, 491 (2009).
[12] U. Wolff, Simulating the all-order hopping expansion. II. Wilson Fermions, Nucl. Phys. **B814**, 549 (2009).
[13] N. Prokof'ev and B. Svistunov, Worm Algorithms for Classical Statistical Models, Phys. Rev. Lett. **87**, 160601 (2001).
[14] Y. D. Mercado, C. Gattringer, and A. Schmidt, Surface worm algorithm for abelian Gauge-Higgs systems on the lattice, Comput. Phys. Commun. **184**, 1535 (2013).
[15] C. R. Allton, M. Doring, S. Ejiri, S. J. Hands, O. Kaczmarek, F. Karsch, E. Laermann, and K. Redlich, Thermodynamics of two flavor QCD to sixth order in quark chemical potential, Phys. Rev. D **71**, 054508 (2005).
[16] P. de Forcrand and O. Philipsen, The QCD phase diagram for three degenerate flavors and small baryon density, Nucl. Phys. **B673**, 170 (2003).
[17] M. D'Elia and M.-P. Lombardo, Finite density QCD via imaginary chemical potential, Phys. Rev. D **67**, 014505 (2003).
[18] Z. Fodor and S. D. Katz, A new method to study lattice QCD at finite temperature and chemical potential, Phys. Lett. B **534**, 87 (2002).
[19] Z. Fodor and S. D. Katz, Critical point of QCD at finite T and mu, lattice results for physical quark masses, J. High Energy Phys. 04 (2004) 050.
[20] J. Berges and I. O. Stamatescu, Simulating Nonequilibrium Quantum Fields with Stochastic Quantization Techniques, Phys. Rev. Lett. **95**, 202003 (2005).
[21] D. Sexty, Simulating full QCD at nonzero density using the complex Langevin equation, Phys. Lett. B **729**, 108 (2014).
[22] M. Cristoforetti, F. Di Renzo, and L. Scorzato (Aurora Science Collaboration), New approach to the sign problem in quantum field theories: High density QCD on a Lefschetz thimble, Phys. Rev. D **86**, 074506 (2012).
[23] C. Schmidt and F. Ziesché, Simulating low dimensional QCD with Lefschetz thimbles, Proc. Sci., LATTICE2016 (**2017**) 076.
[24] F. Di Renzo and G. Eruzzi, One-dimensional QCD in thimble regularization, Phys. Rev. D **97**, 014503 (2018).
[25] K. Langfeld, B. Lucini, and A. Rago, The Density of States in Gauge Theories, Phys. Rev. Lett. **109**, 111601 (2012).
[26] M. Fromm, J. Langelage, S. Lottini, M. Neuman, and O. Philipsen, Onset Transition to Cold Nuclear Matter from Lattice QCD with Heavy Quarks, Phys. Rev. Lett. **110**, 122001 (2013).
[27] J. Glesaaen, M. Neuman, and O. Philipsen, Equation of state for cold and dense heavy QCD, J. High Energy Phys. 03 (2016) 100.
[28] H. Vairinhos and P. de Forcrand, Integrating out lattice gauge fields, Proc. Sci., CPOD2014 (**2015**) 061.
[29] B. B. Brandt, R. Lohmayer, and T. Wettig, Induced QCD I: Theory, J. High Energy Phys. 11 (2016) 087.
[30] B. B. Brandt, R. Lohmayer, and T. Wettig, Induced QCD II: Numerical results, J. High Energy Phys. 07 (2019) 043.
[31] N. Kawamoto and J. Smit, Effective lagrangian and dynamical symmetry breaking in strongly coupled lattice QCD, Nucl. Phys. **B192**, 100 (1981).
[32] H. Kluberg-Stern, A. Morel, and B. Petersson, Spectrum of lattice gauge theories with Fermions from a $1/D$ expansion at strong coupling, Nucl. Phys. **B215**, 527 (1983).
[33] G. Faldt and B. Petersson, Strong coupling expansion of lattice gauge theories at finite temperature, Nucl. Phys. **B265**, 197 (1986).
[34] K. Miura, N. Kawamoto, T. Z. Nakano, and A. Ohnishi, Polyakov loop effects on the phase diagram in strong-coupling lattice QCD, Phys. Rev. D **95**, 114505 (2017).
[35] P. Rossi and U. Wolff, Lattice QCD with fermions at strong coupling: A dimer system, Nucl. Phys. **B248**, 105 (1984).
[36] F. Karsch and K. H. Mutter, Strong coupling QCD at finit Baryon number density, Nucl. Phys. **B313**, 541 (1989).
[37] D. H. Adams and S. Chandrasekharan, Chiral limit of strongly coupled lattice gauge theories, Nucl. Phys. **B662**, 220 (2003).
[38] P. de Forcrand and M. Fromm, Nuclear Physics from Lattice QCD at Strong Coupling, Phys. Rev. Lett. **104**, 112005 (2010).
[39] P. de Forcrand, J. Langelage, O. Philipsen, and W. Unger, Lattice QCD Phase Diagram In and Away from the Strong Coupling Limit, Phys. Rev. Lett. **113**, 152002 (2014).
[40] G. Gagliardi, J. Kim, and W. Unger, Dual formulation and phase diagram of lattice QCD in the strong coupling regime, EPJ Web Conf. **175**, 07047 (2018).
[41] C. Marchis, C. Gattringer, and O. Orasch, Bag representation for composite degrees of freedom in lattice gauge theories with fermions, Proc. Sci., LATTICE2018 (**2018**) 243 [arXiv:1811.09372].
[42] O. Orasch, S. Chandrasekharan, C. Gattringer, and P. Törek, Baryon bag simulation of QCD in the strong coupling limit, *Proc. Sci.* LATTICE2019 (2019) [arXiv:1910.09249].
[43] W. Unger and P. de Forcrand, Continuous time Monte Carlo for lattice QCD in the strong coupling limit, Proc. Sci., LATTICE2011 (**2011**) 218.
[44] M. Klegrewe and W. Unger, Temporal correlators in the continuous time formulation of strong coupling Lattice QCD, Proc. Sci., LATTICE2018 (**2018**) 182.
[45] J. W. Cherrington, D. Christensen, and I. Khavkine, Dual computations of non-Abelian Yang-Mills on the lattice, Phys. Rev. D **76**, 094503 (2007).
[46] J. W. Cherrington, Dual Non-Abelian Yang-Mills Simulations in Four Dimensions, arXiv:0910.1890.
[47] C. Gattringer and C. Marchis, Abelian color cycles: a new approach to strong coupling expansion and dual representations for non-abelian lattice gauge theory, Nucl. Phys. **B916**, 627 (2017).
[48] M. Creutz, On invariant integration over SU(N), J. Math. Phys. (N.Y.) **19**, 2043 (1978).
[49] J.-M. Drouffe and J.-B. Zuber, Strong coupling and mean field methods in lattice gauge theories, Phys. Rep. **102**, 1 (1983).

[50] G. Gagliardi and W. Unger, Towards a dual representation of lattice QCD, Proc. Sci., LATTICE2018 (**2018**) 224.
[51] O. Borisenko, S. Voloshyn, and V. Chelnokov, SU(N) polynomial integrals and some applications, arXiv:1812.06069.
[52] D. Weingarten, Asymptotic behavior of group integrals in the limit of infinite rank, J. Math. Phys. (N.Y.) **19**, 999 (1978).
[53] I. Bars, Complete integration of U(N) lattice gauge theory in a large N limit, J. Math. Phys. (N.Y.) **21**, 2678 (1980).
[54] I. Bars and F. Green, Complete integration of U(N) lattice gauge theory in a large-N limit, Phys. Rev. D **20**, 3311 (1979).
[55] K. E. Eriksson, N. Svartholm, and B. S. Skagerstam, On invariant group integrals in lattice QCD, J. Math. Phys. (N.Y.) **22**, 2276 (1981).
[56] R. Brower, P. Rossi, and C.-I. Tan, The external field problem for QCD, Nucl. Phys. **B190**, 699 (1981).
[57] J. Carlsson, Integrals over SU(N), arXiv:0802.3409.
[58] B. Collins, Moments and Cumulants of Polynomial random variables on unitary groups, the Itzykson-Zuber integral and free probability, Int. Math. Res. Not. **2003**, 953 (2003).
[59] B. Collins and P. Śniady, Integration with respect to the Haar measure on unitary, orthogonal and symplectic group, Commun. Math. Phys. **264**, 773 (2006).
[60] B. Collins and S. Matsumoto (ALEA), Weingarten calculus via orthogonality relations: new applications, Lat. Am. J. Probab. Math. Stat. **14**, 631 (2017).
[61] J. Novak, Complete homogeneous symmetric polynomials in Jucys-Murphy elements and the Weingarten function, arXiv:0811.3595.
[62] M. Novaes, Elementary derivation of Weingarten functions of classical Lie groups, arXiv:1406.2182.
[63] J.-B. Zuber, Revisiting SU(N) integrals, J. Phys. A **50**, 015203 (2016).
[64] K. M. R. Audenaert, *A Digest on Representation Theory of the Symmetric Group (Notes)* (2006), https://pdfs.semanticscholar.org/78bd/f436a0df9dd59bad52db9572de9c1aae008f.pdf.
[65] A. S. Christensen, J. C. Myers, P. D. Pedersen, and J. Rosseel, Calculating the chiral condensate of QCD at infinite coupling using a generalised lattice diagrammatic approach, J. High Energy Phys. 03 (2015) 068.
[66] P. de Forcrand, W. Unger, and H. Vairinhos, Strong-coupling lattice QCD on anisotropic lattices, Phys. Rev. D **97**, 034512 (2018).
[67] W. Unger, D. Bollweg, and M. Klegrewe, Thermodynamics at strong coupling on anisotropic lattices, Proc. Sci., LATTICE2018 (**2018**) 181.
[68] U. Wenger, Efficient simulation of relativistic fermions via vertex models, Phys. Rev. D **80**, 071503 (2009).
[69] I. Schur, Ueber eine Klasse von Matrizen, die sich einer gegebenen Matrix zuordnen lassen (Dieterich, Berlin, Göttingen, 1901).
[70] H. Weyl, *The Classical Groups: Their Invariants and Representations*, Princeton Mathematical Series Vol. 1 (Princeton University Press, Princeton, NJ, 1939).

Appendix C

Reprint of articles reviewed in Chapter 4

C.1 Continuous Time Monte Carlo for Lattice QCD in the Strong Coupling Limit [C1]

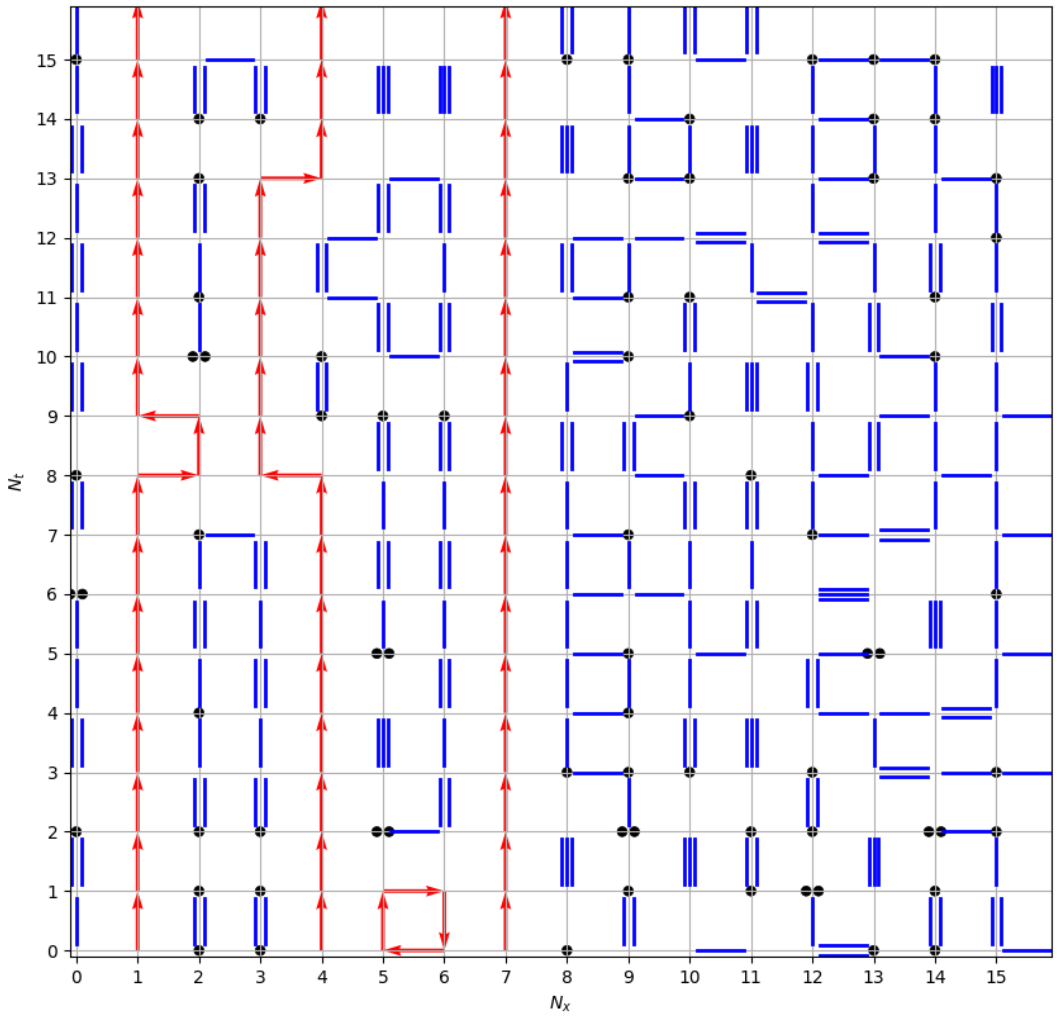

PROCEEDINGS OF SCIENCE

CERN-PH-TH/2011-273

Continuous Time Monte Carlo for Lattice QCD in the Strong Coupling Limit

Wolfgang Unger*
Institut für theoretische Physik, ETH Zürich, CH-8093, Switzerland
E-mail: ungerw@phys.ethz.ch

Philippe de Forcrand
Institut für theoretische Physik, ETH Zürich, CH-8093, Switzerland
CERN, Physics Department, TH Unit, CH-1211 Geneva 23, Switzerland
E-mail: forcrand@phys.ethz.ch

We present results for lattice QCD with staggered fermions in the limit of infinite gauge coupling, obtained from a worm-type Monte Carlo algorithm on a discrete spatial lattice but with continuous Euclidean time. This is achieved by sending both the anisotropy parameter $\gamma^2 \simeq a/a_\tau$ and the number of time-slices N_τ to infinity, keeping the ratio $\gamma^2/N_\tau \simeq aT$ fixed. In this limit, ambiguities arising from the anisotropy parameter γ are eliminated and discretization errors usually introduced by a finite temporal lattice extent N_τ are absent. The obvious gain is that no continuum extrapolation $N_\tau \to \infty$ has to be carried out. Moreover, the algorithm is faster and the sign problem disappears completely.

As a first application, we determine the phase diagram as a function of temperature and real and imaginary baryon chemical potential. We compare our computations with those on lattices with discrete Euclidean time. Discretization errors due to finite N_τ in previous studies turn out to be large at low temperatures.

The XXIX International Symposium on Lattice Field Theory - Lattice 2011
July 10-16, 2011
Squaw Valley, Lake Tahoe, California

*Speaker.

1. Introduction

The determination of the QCD phase diagram, in particular the location of the critical point, is an important, long standing problem, requiring non-perturbative methods. In lattice QCD, several approaches have been developed to investigate the phase transition from the hadronic matter to the quark gluon plasma, but all of them are limited to $\mu_B/T \lesssim 1$, with μ_B the baryon chemical potential [1]. The reason for this is the notorious sign problem, which arises because the fermion determinant for finite μ_B becomes complex, and importance sampling is no longer applicable. In QCD, the sign problem is severe. The relative fluctuations of the complex phase factor grow exponentially with the lattice volume. However, in the strong coupling limit of lattice QCD (SC-QCD) discussed below, the order of integration is reversed: the gauge links are integrated out first, and the partition function is expressed as a gas of hadron world lines. There is no fermion determinant, and the sign problem is much milder. This allows us to obtain the full (μ_B, T) phase diagram.

2. Strong Coupling Lattice QCD in the Continuous Time Formulation

In SC-QCD, the gauge coupling is sent to infinity and hence the coefficient of the plaquette term $\beta = 6/g^2$ is sent to zero. Thus, the Yang Mills part $F_{\mu\nu}F_{\mu\nu}$ of the action is absent. Then, the gauge fields in the covariant derivative can be integrated out analytically. However, as a consequence of the strong coupling limit, the lattice spacing a becomes very large, and no continuum limit can be considered. The degrees of freedom in SC-QCD live on a crystal. We study the SC limit for one flavor of staggered fermions.[1] The action is given by the fermionic part only:

$$S[U,\chi,\bar{\chi}] = am_q \sum_x \bar{\chi}(x)\chi(x) + \frac{\gamma}{2}\sum_x \eta_0(x)\left[\bar{\chi}(x)e^{a_\tau\mu}U_0(x)\chi(x+\hat{0}) - \bar{\chi}(x+\hat{0})e^{-a_\tau\mu}U_0^\dagger(x)\chi(x)\right] + \frac{1}{2}\sum_x\sum_i^d \eta_i(x)\left[\bar{\chi}(x)U_i(x)\chi(x+\hat{i}) - \bar{\chi}(x+\hat{i})U_i^\dagger(x)\chi(x)\right] \tag{2.1}$$

with m_q the quark mass and $\mu = \frac{1}{3}\mu_B$ the quark chemical potential. The anisotropy parameter γ modifies the Dirac coupling of the temporal part. It will be discussed in detail below.

Following the procedure discussed in [2], the gauge link integration for gauge group SU(N_c) can be performed analytically, as the integration factorizes in Eq. (2.1):

$$\mathscr{Z} = \int\prod_x d\bar{\chi}d\chi e^{2am_qM(x)}\prod_\mu\Bigg\{\sum_{k_\mu(x)=0}^{N_c}\frac{(N_c-k_\mu(x))!}{N_c!k_\mu(x)!}\left(\left(\eta_{\hat{\mu}}(x)\gamma^{\delta_{0,\mu}}\right)^2 M(x)M(x+\hat{\mu})\right)^{k_\mu(x)} + \kappa\left(\rho(x,y)^{N_c}\bar{B}(x)B(x+\hat{\mu}) + (-\rho(y,x))^{N_c}\bar{B}(x+\hat{\mu})B(x)\right)\Bigg\} \tag{2.2}$$

$$M(x) \equiv \bar{\chi}(x)\chi(x), \qquad B(x) \equiv \frac{1}{N_c!}\varepsilon_{i_1\ldots i_{N_c}}\chi_{i_1}(x)\ldots\chi_{i_{N_c}}(x) \tag{2.3}$$

The new degrees of freedom are mesons $M(x)$ and baryons $B(x)$: The first part of the expression (2.2) describes the mesonic sector (where $k_\mu(x)$ counts the number of meson hoppings), and the

[1] In the continuum limit of staggered fermions, one flavor represents four degenerate tastes. In the strong coupling limit, one simply has one flavor of spinless fermions on a crystal.

second part describes the baryonic sector, which involves a μ-dependent weight $\rho(x,y)$.[2] After performing the Grassmann integrals analytically, the strong coupling partition function is:

$$\mathscr{Z}(m_q,\mu_q) = \sum_{\{k,n,l\}} \prod_{b=(x,\hat{\mu})} \frac{(N_c-k_b)!}{N_c!k_b!}\gamma^{2k_b\delta_{\hat{0}\hat{\mu}}} \prod_x \frac{N_c!}{n_x!}(2am_q)^{n_x} \prod_l w(l) \tag{2.4}$$

$$\text{with the constraint:} \qquad n_x + \sum_{\hat{\mu}=\pm\hat{0},\ldots\pm\hat{3}} k_{\hat{\mu}}(x) = N_c, \quad \forall x \in V_M \tag{2.5}$$

This system, obtained by an exact rewriting with no approximation other than the strong coupling limit involved, can be described by confined, colorless, discrete degrees of freedom:

- Mesonic degrees of freedom: monomers $n_x \in \{0,\ldots N_c\}$ and dimers $k_{\hat{\mu}}(x) \in \{0,\ldots N_c\}$ which are non-oriented meson hoppings. They obey the Grassmann constraint Eq. (2.5) on mesonic sites $V_M \subset {N_\sigma}^3 \times N_\tau$.
- Baryonic degrees of freedom: they form oriented, self-avoiding loops l with weight $w(l)$ involving the chemical potential, the sign $\sigma(l) = \pm 1$ and winding number $r(l)$ which depend on the geometry of the loops. Baryonic sites are not touched by mesons: $V_B \dot{\cup} V_M = {N_\sigma}^3 \times N_\tau$.

Here, we consider the chiral limit, $m_q = 0$. Then, from Eq. (2.4), monomers are absent: $n_x = 0$.

In Eq. (2.1) we have introduced an anisotropy γ in the Dirac couplings. This complication is necessary because the chiral restoration temperature is given by roughly $aT \simeq 1.5$, and on an isotropic lattice with $aT = 1/N_\tau$ we could not address the physics of interest. Moreover, with the plaquette term being zero, varying γ is the only way to vary the temperature continuously. The temperature, given by the inverse of the lattice extent in the temporal direction, is thus

$$T = \frac{f(\gamma)}{aN_\tau} \qquad \text{with} \qquad f(\gamma) = a/a_\tau. \tag{2.6}$$

However, the functional dependence $f(\gamma)$ of the ratio of the spatial and temporal lattice spacings on γ is not known. Naive inspection of the derivatives in Eq. (2.1) would indicate $f(\gamma) = \gamma$, but this only holds at weak coupling. The mean field approximation of SC-QCD for SU(N_c) gauge group based on $1/d$-expansion with d the spatial dimension [3] yields for the critical anisotropy

$$\gamma_c^2 = N_\tau \frac{d(N_c+1)(N_c+2)}{6(N_c+3)}, \tag{2.7}$$

suggesting that $aT_c = \frac{\gamma_c^2}{N_\tau}$ is the sensible, N_τ-independent identification in leading order in $1/d$. This is also confirmed numerically: In Fig. 1 (top left) we show the variation with N_τ of the chiral susceptibility close to the U(3) chiral transition, and in Fig. 1 (top right) we show the variation with N_τ of the U(3) transition temperature defined as γ_c^2/N_τ. Both quantities approach continuous time (CT) limits, but not monotonically. Corrections to the CT limit, e.g. for the critical temperature T_c, can be parameterized as

$$aT_c(N_\tau) \;=\; aT_c^{CT} + B/N_\tau + C/{N_\tau}^2 + \mathscr{O}({N_\tau}^{-3}) \tag{2.8}$$

[2] Note that baryons transform under gauge transformation $\Omega \in U(3)$ as $B(x) \to B(x)\det\Omega$, hence they are not U(3) gauge invariant. U(3) describes a purely mesonic system ($\kappa = 0$ in Eq. (2.2)), while SU(3) contains baryons ($\kappa = 1$).

where B and C have opposite signs. To circumvent this difficult extrapolation problem, we have developed an algorithm which samples directly the CT partition function in the limit

$$N_\tau \to \infty, \qquad \gamma \to \infty, \qquad \gamma^2/N_\tau \equiv aT \qquad \text{fixed.} \tag{2.9}$$

Hence we are left with only one parameter setting the thermal properties, and all discretization errors introduced by a finite N_τ are removed. Additionally, an algorithm operating in this limit has several advantages: There is no need to perform the continuum extrapolation $N_\tau \to \infty$, which allows to estimate critical temperatures more precisely, with a faster algorithm. And in the baryonic sector of the partition function great simplifications occur: Baryons become static in the CT limit, hence the sign problem is completely absent.

We now explain the partition function we have used for Monte Carlo in the CT limit: after factorizing Eq. (2.4) into spatial and temporal parts, the spatial part simplifies greatly when taking into account which configurations are suppressed with powers of γ^{-1}:

$$\mathscr{Z}(\gamma, N_\tau) \underset{\gamma\to\infty}{=} \gamma^{N_c V} \left(\sum_{\{k\}} \prod_{b_\sigma=(x,\hat{i})} \frac{1}{N_c} \gamma^{-2k_{b_\sigma}} \prod_{b_\tau=(x,\hat{0})} \frac{(N_c-k_{b_\tau})!}{N_c! k_{b_\tau}!} \right) \left(\prod_{x\in V_B} e^{-3\sigma(x)\mu N_\tau/\gamma^2} \right). \tag{2.10}$$

The identity holds only approximately if γ is finite, but becomes exact as $\gamma \to \infty$ because spatial dimers with multiplicity $k_i(x) > 1$ are suppressed by powers of γ and hence disappear when $\gamma \to \infty$. This is illustrated in Fig. 2 (right): as the temporal lattice spacing $a_\tau \simeq a/\gamma^2 \to 0$, multiple spatial dimers become resolved into single dimers. The overall number of spatial dimers remains finite in the CT limit, as the sum over $\mathscr{O}(\gamma^2)$ sites compensates the $1/\gamma^2$ suppression. Temporal dimers can be arranged in chains of alternating k-dimers and (N_c-k)-dimers. In particular, for $N_c = 3$, we denote 3-0-chains as dashed lines, and 2-1-chains as solid lines (see Fig. 2).

The crucial observation is that the weight of these chains in the partition function is independent of their length, because the weight of each k-dimer is the inverse of that of the (N_c-k)-dimer. Hence, the weight of a configuration will only depend on the kind and number of vertices at which spatial hoppings are attached to solid/dashed lines, not on their positions.

For SC-QCD with $N_c = 3$, there are two kinds of vertices, "L"-vertices of weight $v_L = \gamma^{-1}$, where dashed and solid lines join, and "T"-vertices of weight $v_T = 2\gamma^{-1}/\sqrt{3}$, where a solid line emits/absorbs a spatial dimer. The partition function can now be written in terms of these vertices:

$$\mathscr{Z}(\gamma, N_\tau) \underset{\gamma\to\infty}{=} \sum_{\mathscr{G}} e^{3\mu B N_\tau/\gamma^2} \prod_{x\in V_M} \left(\frac{\hat{v}_L}{\gamma}\right)^{n_L(x)} \left(\frac{\hat{v}_T}{\gamma}\right)^{n_T(x)}, \qquad \hat{v}_L = 1, \quad \hat{v}_T = 2/\sqrt{3}. \tag{2.11}$$

The exponents $n_L(x)$ and $n_T(x)$ in Eq. (2.11) denote the number of L-vertices and T-vertices at spatial site $x \in V_M$. In contrast to meson hoppings, spatial baryon hoppings are completely suppressed in the CT limit by a factor $\gamma^2/\gamma^3 = \gamma^{-1}$. Hence, baryons are static in continuous time and the sign problem has completely vanished! In the limit $N_\tau \to \infty$ the CT partition function can be written simply in terms of $\beta = N_\tau/\gamma^2$, up to some normalization constant:

$$\mathscr{Z}_{\mathrm{CT}}(\beta) = \sum_{k\in 2\mathbb{N}} (\beta/2)^k \sum_{\mathscr{G}'\in\Gamma_k} e^{3\mu B\beta} \hat{v}_T^{N_T} \quad \text{with} \quad k = \sum_{b=(x,\hat{i})} k_b, \qquad N_T = \sum_x n_T(x) \tag{2.12}$$

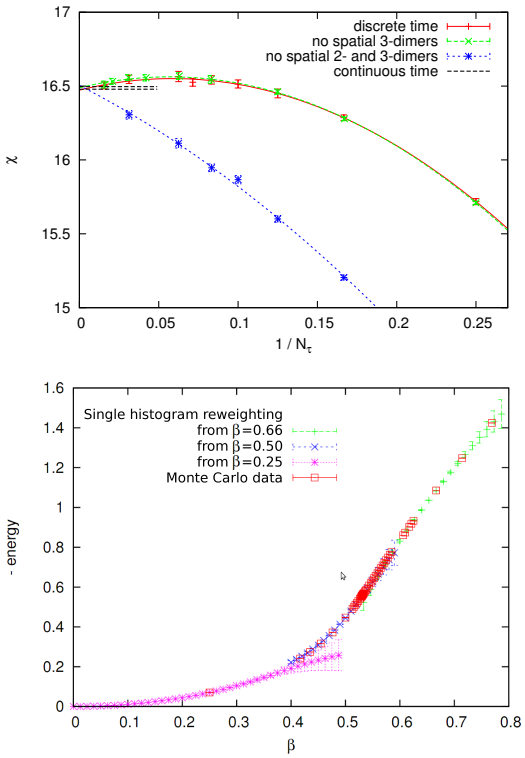

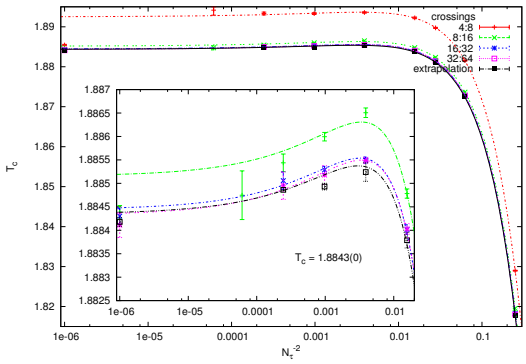

Figure 1: *Top left:* continuous-time limit of the chiral susceptibility χ at $\gamma^2/N_\tau = 1.8$ in the purely mesonic system U(3), exhibiting typical non-monotonic behavior in $1/N_\tau$. Note that the suppression of double and/or triple spatial dimers has no effect on the CT limit. *Top right:* Non-monotonic continuum extrapolation for aT_c and comparison with the continuous time limit. *Bottom:* Reweighting of the energy based on the partition function Eq. (2.12).

where Γ_k is the set of all configurations $\mathscr{G}'$ equivalent up to time shifts of the vertices and with a total number k of spatial hoppings, and B is the baryon number. In Fig. 1 (bottom) we illustrate the single histogram reweighting of the energy in β based on this partition function. An important property of the above partition function Eq. (2.12) is that spatial dimers are distributed uniformly in time. The lengths $\Delta\beta$ of dashed or solid time intervals (which are related to the number of L- and T-vertices) are then, according to a Poisson process, exponentially distributed:

$$P(\Delta\beta) \sim \exp(-\lambda\Delta\beta), \qquad \Delta\beta \in [0, \beta = 1/aT] \tag{2.13}$$

$$\lambda = d_M(x)/4, \qquad d_M(x) = 2d - \sum_\mu n_B(x \pm \hat{\mu}) \tag{2.14}$$

with λ the "decay constant" for spatial dimer emissions. The presence of baryons results in λ being space dependent, with $d_M(x)$ the number of mesonic neighbors at a given coordinate x. Non-trivial meson correlations arise from the entropy of the various configurations. Likewise, baryonic interactions beyond the original hard core repulsion are due to the modification they induce on the meson bath, and thus also arise from entropy.

3. Continuous Time Worm Algorithm

Continuous time (CT) algorithms are now widely used in quantum Monte Carlo (see e.g. [4, 5]), but to our knowledge have not yet been applied to quantum field theories. Special difficulties associated with the local gauge symmetry are absent in our case, since gauge fields have been analytically integrated out. The CT algorithm used here is a Worm-type algorithm, similar to the directed path algorithm introduced for SC-QCD in [6]. In the latter, sites are partitioned into "active" and "passive" depending on their parity with respect to the worm tail position. Here, we similarly have "emission" and "absorption" sites, giving the spatial dimers a consistent orientation.

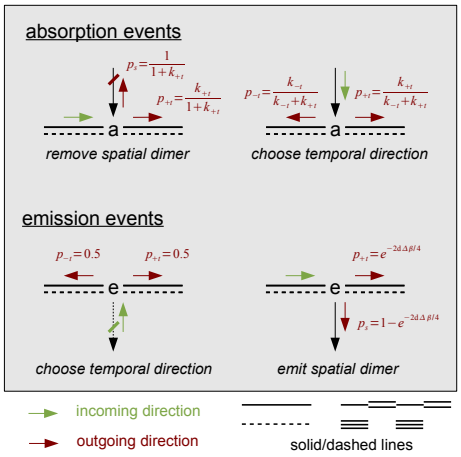

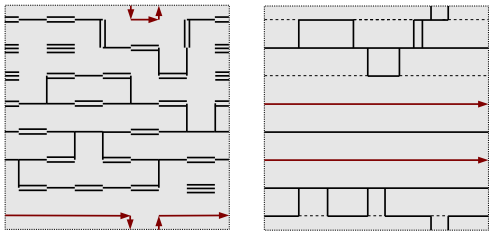

Figure 2: *Left:* updating rules for the continuous time algorithm. *Top:* illustrative 2-dim. configurations (time flows to the right), in discrete time (*left*) and continuous time (*right*). Note how the latter lacks multiple spatial dimers and has only static baryons lines.

In Fig. 2 we outline the updating rules of the continuous time worm, and also show a typical 2-dimensional configuration in continuous time.

In contrast to simulations at finite N_τ, there is no need for a baryonic worm update. A simple heatbath update on static lines with no spatial dimers attached is sufficient: positively (negatively) oriented baryons are (dis)favored by a factor $\exp(\pm 3\mu/T)$ over static meson lines, and their weight is always positive. We found it very useful to resum baryonic and static mesonic degrees of freedom into so-called static polymers similarly to the MDP algorithm [7]: first, this allows to extend simulations to arbitrary imaginary chemical potential. Second, this enables us to adapt the Wang-Landau method for determining the nuclear transition at low temperature very accurately. This technique reduces the uncertainty on the first order line $\mu_c(T)$ greatly. The polymer formulation we have used resums static mesons, baryons and anti-baryons. A configuration with P static polymers has weight[3] $w(P) = (4+2\cosh(3\mu/T))^P$. In our simulation, we only keep track of the polymer number $P = D_0 + B^+ + B^-$, which is the sum of the numbers D_0, B^+, and B^- of static mesons, baryons and anti-baryons, respectively. We calculate the baryon number $B = B^+ - B^-$ from P via a trinomial distribution. In the Wang-Landau method, we hence obtain at fixed T the density of states for baryon number B, $g(B,T)$, from the density of states for static polymer number P, $g(P,T)$.

4. Results on the SC-QCD Phase Diagram

In SC-QCD at low temperature, chiral symmetry, i. e. the $U_A(1)$ symmetry of the one-flavor staggered action, is spontaneously broken according to $U_L(1) \times U_R(1) \to U_V(1)$ and becomes restored at some critical temperature $T_c(\mu)$. Our new results for the phase boundary $T_c(\mu)$ in the chiral limit $m_q = 0$ eliminate systematic errors affecting previous findings based on mean field approximations [8] or Monte Carlo for fixed N_τ [9]. As previously found, the phase transition is second order at small μ, and first order at low T. The tricritical point is located close to its earlier $N_\tau = 4$ estimate [9], if one uses $a/a_\tau = \gamma^2$, i.e. $aT = \gamma^2/N_\tau$, $a\mu = \gamma^2(a_\tau\mu)$. However, the re-entrance predicted by mean field analysis [8] (which fixes $\gamma = 1$ and varies $N_\tau \in \mathbb{R}$) and seen in earlier Monte Carlo studies [9, 10] is absent, see Fig. 3 (top left). As illustrated in Fig. 3 (right) the discretization error from $N_\tau = 4$ or 2 becomes very large at low T, and mimics re-entrance. We have also considered an imaginary chemical potential. As shown in Fig. 3 (bottom), the phase

[3]Note that there are 4 kinds of static mesons: dashed lines and solid lines of even and odd parity.

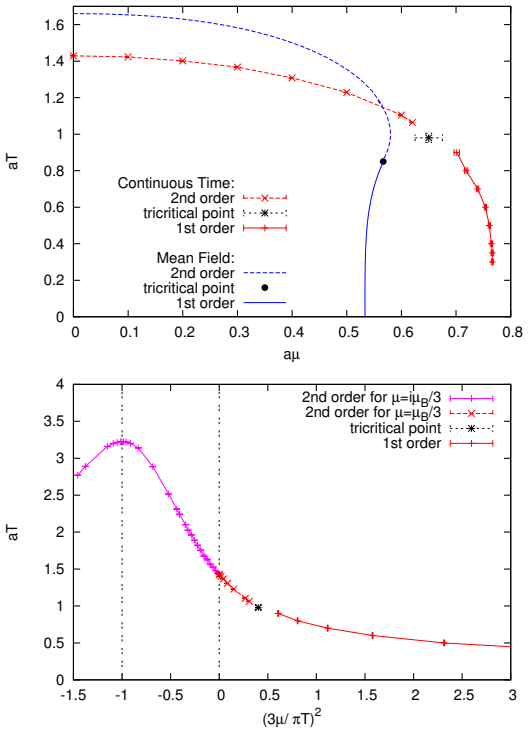

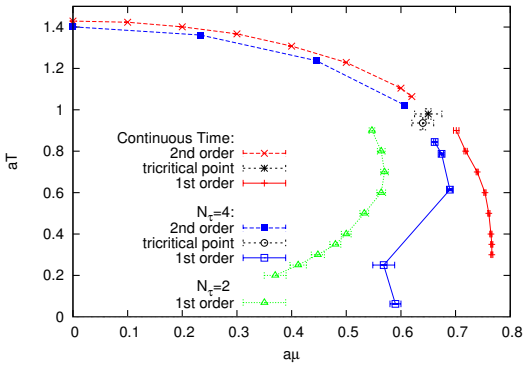

Figure 3: *Top left:* Comparison of SC-QCD phase diagram obtained from mean field [8] and in continuous time. The former predicts a re-entrance which is not present in CT Monte Carlo. *Top right:* The SC-QCD phase diagram obtained with $N_\tau = 2, 4$ using $aT = \gamma^2/N_\tau$, $a\mu = \gamma^2(a_\tau\mu)$ [9] and in continuous time. *Bottom:* Extension of the phase diagram including imaginary chemical potential, with no signal for a Roberge Weiss transition (x=-1) at high T.

diagram displays Z(3) periodicity, but the imaginary μ transition remains second-order and there is no Roberge-Weiss transition at high temperature. This is natural: at high T the partition function Eq. (2.12) is dominated by the $k = 0$ term which is analytic in μ.

In summary, the continuous time formalism allows for a final, unambiguous determination of the strong coupling phase diagram, and is suitable for further extensions like a second quark flavor.

5. Acknowledgments

The computations have been carried out on the Brutus cluster at the ETH Zürich. We thank S. Chandrasekharan, M. Fromm and O. Philipsen for useful discussions. This work is supported by the Swiss National Science Foundation under grant 200020-122117.

References

[1] P. de Forcrand, *PoS (LAT2009) 010* (2009), *arXiv:1005.0539*.

[2] P. Rossi, U. Wolff, *Nucl. Phys. B* **248** (1984) 105.

[3] N. Bilic, F. Karsch, K. Redlich, *Phys. Rev. D* **45** (1992) 3228.

[4] B. B. Beard, U. J. Wiese, *Phys. Rev. Lett.* **77** (1996) 5130.

[5] E. Gull *et al., Rev. Mod. Phys.* **83** (2011) 349.

[6] D. H. Adams and S. Chandrasekharan, *Nucl. Phys. B* **662** (2003) 220.

[7] F. Karsch, K. H. Mütter, *Nucl. Phys. B* **313** (1989) 541.

[8] Y. Nishida, *Phys. Rev. D* **69** (2004) 094501.

[9] P. de Forcrand, M. Fromm, *Phys. Rev. Lett.* **104** (2010) 112005.

[10] W. Unger, P. de Forcrand, *arXiv:1107.1553v1*.

C.2 Strong coupling lattice QCD in the continuous time limit [C2]

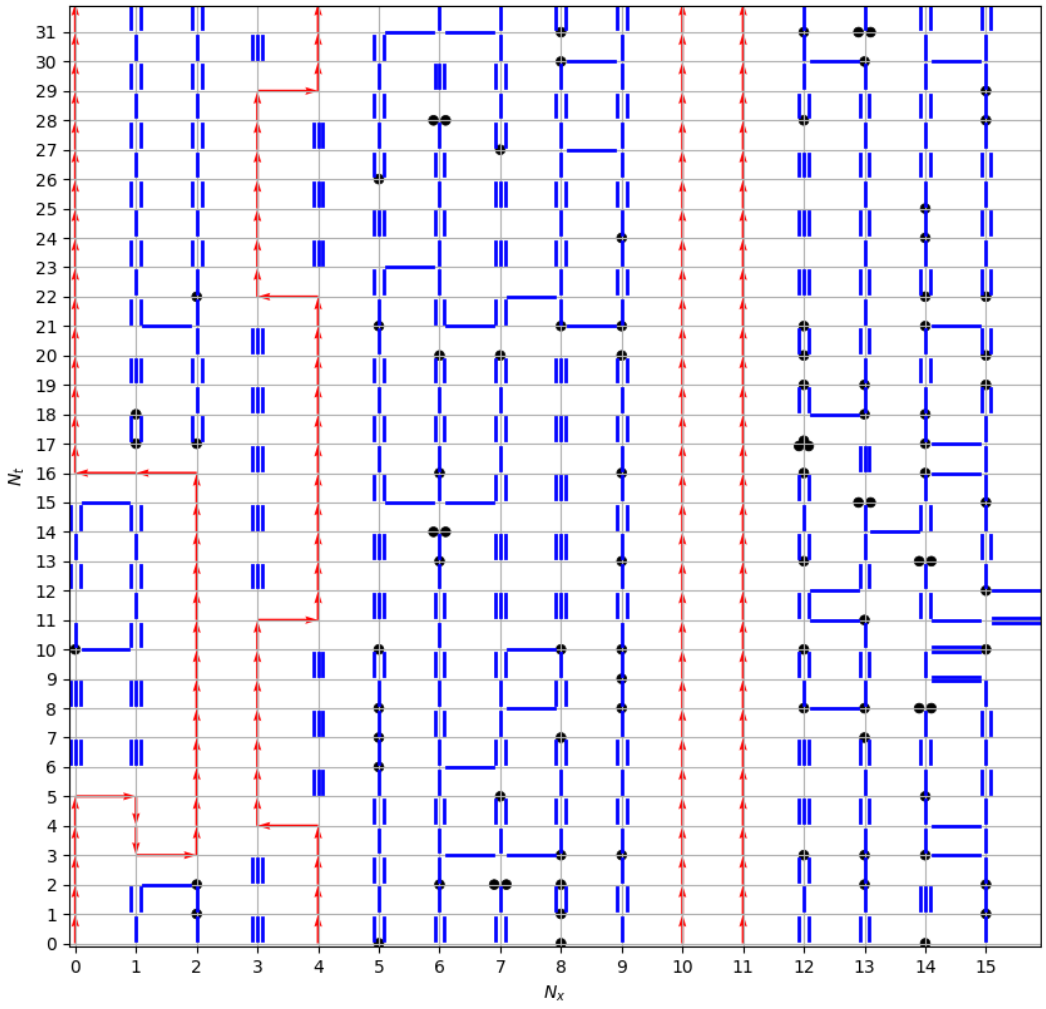

Strong coupling lattice QCD in the continuous time limit

M. Klegrewe[*] and W. Unger[†]

Fakultät für Physik, Bielefeld University, D-33615 Bielefeld, Germany

(Received 26 May 2020; accepted 14 July 2020; published 13 August 2020)

We present results for lattice QCD with staggered fermions in the limit of infinite gauge coupling, obtained from a worm-type Monte Carlo algorithm on a discrete spatial lattice but with continuous Euclidean time. This is obtained by sending both the anisotropy parameter $\xi = a_\sigma/a_\tau$ and the number of time slices N_τ to infinity, keeping the ratio $aT = \xi/N_\tau$ fixed. The obvious gain is that no continuum extrapolation $N_\tau \to \infty$ has to be carried out. Moreover, the algorithm is faster, and the sign problem disappears. We derive the continuous time partition function and the corresponding Hamiltonian formulation. We compare our computations with those on discrete lattices and study both zero and finite temperature properties of lattice QCD in this regime.

DOI: 10.1103/PhysRevD.102.034505

I. INTRODUCTION

The determination of the QCD phase diagram, in particular, the location of the critical end point (CEP), is an important, long-standing problem, requiring nonperturbative methods. In lattice QCD, several approaches have been developed to investigate the phase transition from hadronic matter to the quark gluon plasma, but either they are limited to rather small μ_B/T, with μ_B the baryon chemical potential [1–3], or they cannot yet address full QCD [4–6] or study only low dimensional QCD-like toy models [7–9].

The reason for this is the notorious sign problem [10], which arises because the fermion determinant for finite μ_B becomes complex, and importance sampling is no longer applicable. In lattice QCD, the finite density sign problem is severe. There is however a limit where the sign problem can be made mild: this is the strong coupling limit, where a so-called dual representation in terms of color singlets is possible. In the strong coupling limit of lattice QCD (SC-LQCD) the sign problem is mild enough such that the full (μ_B, T) phase diagram can be measured via Monte Carlo methods based on the dual variables. The method of dual variables has been successfully used in models with Abelian gauge symmetry [11,12]; there have been attempts to dualize non-Abelian gauge theories [13,14], but it has not yet been possible to overcome the finite density sign problem. Our own approach discussed in [15–17] is based on the strong coupling expansion, i.e., an expansion in the inverse gauge coupling $\beta = \frac{2N_c}{g^2}$. It is in principle possible to sample partition functions that include all orders via Monte Carlo, in the spirit of [18,19]. In practice, the sign problem is reintroduced for large β.

In this paper, we will restrict ourselves to the strong coupling limit, since the focus is on deriving the Euclidean continuous time (CT) limit, and apply the new formulation to Monte Carlo studies of QCD thermodynamics. Despite the fact that the strong coupling limit is the converse of the continuum limit, i.e., the lattice is maximally coarse and it is not possible to set the scale, it nevertheless shares important features with lattice QCD on finer lattices: chiral symmetry breaking and its restoration at finite temperature as well as the nuclear liquid gas transition are also present in this model. We will extend the existing studies on SC-LQCD that are either based on mean field theory in the $1/d$ expansion [20–26] or on Monte Carlo [27–29]. In the past either the spectrum or the phase diagram and the nuclear properties [29] have been studied. We investigate these phenomena in the continuous time limit, where the continuum limit of the temporal lattice spacing $a_\tau \to 0$ is taken while leaving the spatial lattice spacing a_σ finite. First simulations of SC-LQCD in continuous time have been performed by one of us in [30]. Here, we improve upon the continuous time formulation and give many more results at zero and nonzero temperature. The main advantage of the CT limit is that ambiguities arising from the anisotropy parameter γ are circumvented. Also, the sign problem is absent, quantum Monte Carlo (QMC) can be applied, and temporal correlation functions can be obtained with high resolution.

[*] mklegrewe@physik.uni-bielefeld.de
[†] wunger@physik.uni-bielefeld.de

This paper is structured as follows: in Sec. II we will derive the quantum Hamiltonian formulation of strong coupling QCD and its generalization to an arbitrary number of colors. In Sec. III we will describe the worm algorithm operating in continuous time in detail and show that it indeed reproduces results consistent with the continuum extrapolation of simulations at finite N_τ. In Sec. IV we apply SC-LQCD in the CT limit to determine zero temperature observables. In Sec. V we investigate finite temperature properties, such as the grand-canonical phase diagram in the μ_B-T plane as well as the canonical phase diagram in the n_B-T plane, with n_B the baryon number density. In Sec. VI A we show that the pressure at finite baryon density can also be reconstructed from Taylor coefficients, and we estimate the radius of convergence. In Sec. VII A we discuss temporal correlation functions and explain how to extract pole masses. We provide both results at finite temperature and density. In the Appendix, supplementary material for the various cross-checks of continuous time Monte Carlo and possible extensions such as for finite quark mass, more flavors, and isospin chemical potential are discussed.

II. STRONG COUPLING LATTICE QCD IN THE CONTINUOUS TIME FORMULATION

A. Staggered action of strong coupling QCD and its dual representation

In SC-LQCD, based on the Euclidean lattice action, the gauge coupling is sent to infinity, and thus the coefficient of the plaquette term $\beta = 2N_c/g^2$ is sent to zero. Hence, the Yang Mills part $F_{\mu\nu}F_{\mu\nu}$ is absent. Then, the gauge fields in the covariant derivative can be integrated out analytically. In fact, the order of integration is reversed compared to the standard representation of lattice QCD in terms of the fermion determinant: the gauge links $U_\mu(x)$ are integrated out before the Grassmann fields $\chi, \bar{\chi}$. Thus, the final degrees of freedom of the partition function are color singlets composed of fermions: mesons and baryons. However, as a consequence of the strong coupling limit, the lattice becomes maximally coarse, and there is no way to set the scale: the lattice spacing a cannot be specified in physical units. We will see however that specific dimensionless ratios can still be compared to continuum physics.

We shortly outline the procedure to obtain the dual representation for staggered fermions in the strong coupling limit where the action is only given by the fermionic part:

$$S[U,\chi,\bar{\chi}] = \sum_x \Big[\gamma\eta_0(x)(\bar{\chi}(x)e^{a_\tau\mu_q}U_0(x)\chi(x+\hat{0}) - \bar{\chi}(x+\hat{0})e^{-a_\tau\mu_q}U_0^\dagger(x)\chi(x)) + \sum_{i=1}^{d}\eta_i(x)(\bar{\chi}(x)U_i(x)\chi(x+\hat{i}) - \bar{\chi}(x+\hat{i})U_i^\dagger(x)\chi(x)) + 2am_q\bar{\chi}(x)\chi(x)\Big]. \tag{1}$$

Here, am_q is the quark mass and $\mu_q = \frac{1}{3}\mu_B$ the quark chemical potential. The bare anisotropy parameter γ in the temporal Dirac coupling is introduced to vary the temperature continuously.

Following the procedure discussed in detail in [28], the gauge link integration over the Haar measure of $\mathrm{SU}(N_c)$ can be performed analytically, as the integration factorizes in Eq. (1); i.e., the partition function can be written as a product of one-link integrals $z_\mu(x)$:

$$Z = \int \prod_x \left(d\bar{\chi}(x)d\chi(x)e^{2am_q\bar{\chi}(x)\chi(x)} \prod_\mu z_\mu(x) \right), \tag{2}$$

$$\begin{aligned} z_\mu(x) \equiv z(x,y)|_{y=x+\hat{\mu}} &= \int_{\mathrm{SU}(N_c)} dU_\mu(x)\exp(\eta_\mu(x)(\bar{\chi}(x)U_\mu(x)\chi(y) - \bar{\chi}(y)U_\mu^\dagger(x)\chi(x))) \\ &= \sum_{k=0}^{N_c}\left\{ \frac{(N_c-k)!}{N_c!k!}((\eta_\mu(x)\gamma^{\delta_{\mu 0}})^2 M(x)M(y))^k \right\} + (\rho(x,y)^{N_c}\bar{B}(x)B(y) + (-\rho(y,x))^{N_c}\bar{B}(y)B(x)), \end{aligned} \tag{3}$$

$$M(x) = \bar{\chi}(x)\chi(x), \qquad B(x) = \frac{1}{N_c}\epsilon_{i_1\ldots i_{N_c}}\chi_{i_1}(x)\ldots\chi_{i_{N_c}}(x), \qquad \rho(x,y) = \eta_\mu(x)(\gamma\exp(\pm a_\tau\mu_q)\delta_{\mu 0} + (1-\delta_{\mu 0})). \tag{4}$$

The new degrees of freedom after link integration are the mesons $M(x)$ and the baryons $B(x)$. The weight of the one-link integral is a sum over the so-called dimer number $k_\mu(x) = 0, \ldots, N_c$ which corresponds to the number of (unoriented) meson hoppings on that link, and on $\rho(x,y)$ which is the weight for a baryon hopping $\bar{B}(x)B(y)$. The final partition function for the discrete system on an ${N_\sigma}^3 \times N_\tau$ lattice, after performing the Grassmann integrals analytically, is an exact rewriting from Eq. (1) and is given by

$$\mathcal{Z}(m_q,\mu_q) = \sum_{\{k,n,\ell\}}^{\mathrm{GC}} \prod_{b=(x,\hat{\mu})} \frac{(N_c-k_b)!}{N_c!k_b!}\gamma^{2k_b\delta_{\hat{0}\hat{\mu}}} \prod_x \frac{N_c!}{n_x!}(2am_q)^{n_x} \prod_\ell w(\ell)$$

$$w(\ell) = \prod_{x\in\ell}\frac{1}{N_c!}\sigma(\ell)\gamma^{N_cN_{\hat{0}}}\exp(N_cN_\tau\omega(\ell)a_\tau\mu_q), \qquad \sigma(\ell) = (-1)^{\omega(\ell)+N_-(\ell)+1}\prod_{b=(x,\hat{\mu})\in\ell}\eta_{\hat{\mu}}(x). \tag{5}$$

The sum over all configurations $\{k,n,\ell\}$ is restricted to those that fulfill, on each site x, the so-called Grassmann constraint (GC):

$$n_x + \sum_{\hat{\mu}=\pm\hat{0},\ldots\pm\hat{d}}\left(k_{\hat{\mu}}(x) + \frac{N_c}{2}|b_{\hat{\mu}}(x)|\right) = N_c \tag{6}$$

which expresses the fact that every Grassmann variable $\bar{\chi}_i(x), \chi_i(x)$ $(i = 1\ldots N_c)$ appears exactly once in the path integral. After this exact rewriting of the strong coupling partition function the system can be described by confined, colorless, discrete degrees of freedom:

(i) Mesonic degrees of freedom: $k_{\hat{\mu}}(x) \in \{0,\ldots N_c\}$ (nonoriented meson hoppings called dimers) and $n(x) \in \{0,\ldots N_c\}$ (mesonic sites called monomers).

(ii) Baryonic degrees of freedom: they form oriented baryon loops ℓ and may wind $\omega(\ell)$ times in the temporal direction, which results in its dependence on the chemical potential μ_q. The sign $\sigma(\ell) = \pm 1$ of the loop ℓ depends on the loop geometry.

(iii) The baryonic loops are self-avoiding and do not touch the mesonic degrees of freedom, which follows from the Grassmann constraint Eq. (6): for a given configuration, this gives rise to a decomposition of the lattice volume into mesonic sites and baryonic sites:

$$\Lambda = {N_\sigma}^3 \times N_\tau = \Lambda_M \dot{\cup} \Lambda_B. \tag{7}$$

It should be mentioned that this representation corresponds to unrooted staggered fermions. Due to the fermion doubling, one flavor of a staggered fermion comes in the multiplicity of four so-called tastes. However, in the strong coupling limit, the fermions are spinless and the taste breaking is maximal. Hence, it is indeed a one-flavor theory with only one pseudoscalar meson as the Goldstone boson. To be more precise, in the chiral limit the action is invariant under the symmetry group $U_B(1) \times U_{55}(1)$:

$$\chi(x) \mapsto e^{i\theta_B + i\epsilon(x)\theta_{55}}\chi(x), \qquad \epsilon(x) = (-1)^{\sum_\mu x_\mu} \tag{8}$$

which is due to the even-odd decomposition of the bipartite lattice for staggered fermions; i.e., even and odd sites can be transformed independently. The symmetry $e^{i\theta_B} \in U_B(1)$ corresponds to baryon conservation, and $e^{i\theta_{55}} \in U(1)_{55}$ is a subgroup of the full $SU_L(4)_L \times SU_R(4)$ chiral symmetry for unrooted staggered fermions. In the spin-taste basis this corresponds to the channel $\gamma_5 \otimes \xi_5$. At finite quark mass $U(1)_{55}$ is explicitly broken, and in the dual representation this is due to the presence of monomers: the number of monomers on even sites equals its number on odd sites. In the chiral limit we expect O(2) critical exponents for the chiral phase transition. This is also the case away from the strong coupling limit, as long as the lattice spacing is finite. In this work we will restrict ourselves to the chiral limit, $m_q = 0$, where monomers are absent: $n_x = 0$. We discuss the prospects of the continuous time formulation at finite quark mass in the Appendix E.

B. SC-LQCD at finite temperature and the continuous time limit

In the staggered action Eq. (1) we have introduced a bare anisotropy γ in order to vary the temperature continuously. Hence, also in the dual representation the weights for temporal meson or baryon hoppings in Eq. (5) contain the anisotropy parameter γ. We will now explain why this is necessary and why it is also a key step to derive the continuous time limit.

The main objective of SC-LQCD is to study thermodynamic properties. Since $\beta = 0$, we cannot vary the temperature $T = 1/(N_\tau a(\beta))$ continuously via the lattice spacing, but only with the lattice extent N_τ. The chiral transition is however at temperatures much higher than $1/2$, such that for temperatures $1/N_\tau$ we are always in the chirally broken phase. The solution is to introduce an anisotropy in the Dirac operator to favor fermion propagation in the temporal direction. In contrast to the chemical potential, the bare anisotropy does not distinguish between the forward and backward temporal direction. The temperature on an anisotropic lattice is given by the inverse of the lattice extent in the temporal direction,

$$T = \frac{1}{a_\tau N_\tau} = \frac{\xi(\gamma)}{a_\sigma N_\tau} \quad \text{with} \quad \xi(\gamma) \equiv \frac{a_\sigma}{a_\tau} \tag{9}$$

but the functional dependence $\xi(\gamma)$ of the ratio of the spatial and temporal lattice spacings on the bare anisotropy is not known *a priori*. Hence, also the dependence of T on γ is unknown. The main motivation for this study is to overcome this difficulty.

The weak coupling analysis of Eq. (1) suggests that $\xi(\gamma) = \gamma$, but this does not carry over to strong coupling, where quarks are confined on links to color singlets. In the mean-field approximation of SC-LQCD [24] based on

$1/d$-expansion (with d the spatial dimension), the critical temperature is given by

$$\gamma_c^2 = N_\tau \frac{d(N_c+1)(N_c+2)}{6(N_c+3)} \tag{10}$$

suggesting that $a_\sigma T_c \propto \frac{\gamma_c^2}{N_\tau}$ is the sensible N_τ-independent identification in leading and next to leading order in d.

It is however possible to determine the function $\xi(\gamma)$ nonperturbatively on anisotropic lattices with

$$N_\sigma a_\sigma = N_\tau a_\tau, \qquad \xi = \frac{N_\tau}{N_\sigma} \tag{11}$$

by a bare anisotropy calibration $\gamma_0(\xi)$ via conserved currents in both the spatial and temporal direction [31]. For large N_τ (implying large ξ and γ), it turns out numerically that ξ diverges as

$$\lim_{N_\tau\to\infty} \xi(\gamma) = \kappa\gamma^2. \tag{12}$$

The precise value of κ can only be determined nonperturbatively and *a posteriori*, based on the values $\gamma_0(\xi)$ measured via the anisotropy calibration (see also Sec. IV A), and has been extrapolated for SU(3) from the set $\xi = \{0.5, 1, 1.5, 2, 3, 4, 5, 6, 8\}$ to $\xi \to \infty$. The function ξ/γ^2, which we call the anisotropy correction factor, can be either parametrized by ξ or γ and is well described by the ansätze

$$\frac{\xi}{\gamma^2}(\xi) \simeq \kappa + \frac{a}{\xi^2} + \frac{b}{\xi^4}, \tag{13}$$

$$\frac{\xi}{\gamma^2}(\gamma) \simeq \kappa + \frac{1-\kappa}{1+\kappa(\gamma^4-1)}, \tag{14}$$

$$\frac{\xi}{\gamma^2}(\xi) \simeq \frac{\xi}{\left(\frac{\xi}{\kappa+A\xi^{Q_1}} + \frac{\xi^{1/2}}{\kappa^{1/2}+B\xi^{Q_2}}\right)^2}. \tag{15}$$

Clearly, the extrapolated value for κ based on $\xi \to \infty$ will depend on the ansatz, as shown in Fig. 1. The Taylor expansion in $1/\xi^2 \sim a_\tau{}^2$ in Eq. (13) is limited to the fit range $\xi \geq 2$ and results in the value $\kappa = 0.7824(1)$, which is consistent with the already determined value in [31]. The second ansatz, Eq. (14), has only κ as a free parameter, and interpolates the data for all ξ surprisingly well, although there are deviations. By construction, $\xi/\gamma^2 = 1$ for $\gamma = 1$. In order to improve on this one-parameter fit, the third ansatz, Eq. (15), introduces three additional independent fit parameters to connect the regime $\xi > 1$ with the opposite regime $\xi < 1$; with $Q_1 > 0$ and $Q_2 < 0$:

$$\lim_{\xi\to\infty} \frac{\xi}{\gamma^2} = \kappa, \qquad \lim_{\xi\to 0} \frac{\xi}{\gamma^2} = \frac{\kappa^2}{\xi}, \qquad \left.\frac{\xi}{\gamma^2}\right|_{\xi=1} = 1. \tag{16}$$

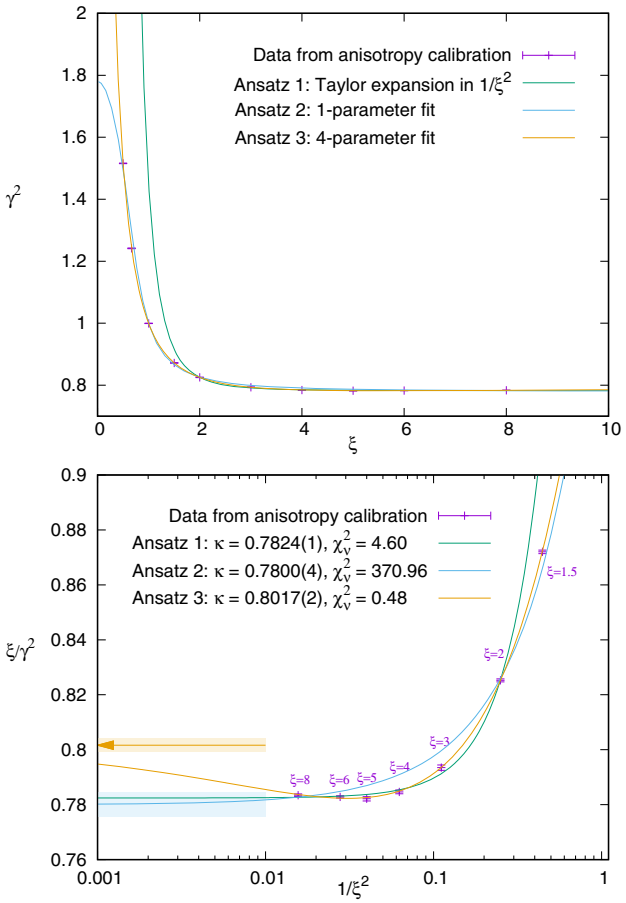

FIG. 1. Top: Interpolation of γ^2 as a function of ξ with ansatz 1, Eq. (13) for $\xi \geq 2$; ansatz 2, Eq. (14); and ansatz 3, Eq. (15), both for all ξ. Bottom: Extrapolation of the anisotropy correction factor $\frac{\xi}{\gamma^2}$ towards $1/\xi^2 \sim a_\tau^2 \to 0$, extracting κ. It is evident that the extrapolated results depend on the ansatz. Clearly, ansatz 3 has the smallest reduced chi-squared.

The fit parameters A and B are thus not independent. This fit results in a nonmonotonic behavior, which reflects the fact that $\frac{\xi}{\gamma^2}|_{\xi=8} = 0.7834(2)$ is larger than $\frac{\xi}{\gamma^2}|_{\xi=6} = 0.7828(2)$. Also, it has the smallest reduced chi-squared. Thus, we think that the extrapolated result $\kappa = 0.8017(2)$ is more trustworthy. The error is purely statistical, and the systematic error due to the choice of the fit ansatz is unknown. In Sec. IV A we will overcome the ambiguities of the extrapolation $a_\tau \to 0$ by measuring κ directly in the continuous time limit.

We will see in Sec. III E that many observables and the phase diagram have a strong N_τ-dependence, which can even be nonmonotonic. This requires large N_τ to have control over the extrapolation. Hence, we want to eliminate γ and N_τ altogether from the partition function Eq. (5) and replace them by the temperature aT. The continuous time definition of the temperature in lattice units is

$$aT_{\mathrm{CT}} = \kappa \lim_{\substack{N_\tau\to\infty \\ \gamma\to\infty}} \mathcal{T}(\gamma, N_\tau), \qquad \mathcal{T} = \frac{\gamma^2}{N_\tau} = \text{const}, \tag{17}$$

where we have dropped the subscript, $a \equiv a_\sigma$. The limit $N_\tau \to \infty$, $\gamma \to \infty$ is a joint limit, and the second condition implies that γ diverges as $\gamma = \sqrt{\mathcal{T} N_\tau}$ for $N_\tau \to \infty$. Likewise, we can define unambiguously the continuous time chemical potential to replace the chemical potential $a_\tau \mu_q$ in Eq. (5):

$$a\mu_{B,\mathrm{CT}} = \kappa \lim_{\substack{N_\tau\to\infty \\ \gamma\to\infty}} \mu_B(\gamma, N_\tau), \qquad \mu_B = N_c \gamma^2 a_\tau \mu_q = \text{const}. \tag{18}$$

which is also consistent with the γ-dependence of the mean-field critical chemical potential $\mu_c(T=0)$ obtained via $1/d$-expansion [23], similar to Eq. (10):

$$a_\tau \mu_{q,c} = \frac{d}{4\gamma^2} + \mathcal{O}(\gamma^6). \tag{19}$$

Now all discretization errors from finite a_τ are removed. The new partition function in continuous Euclidean time will be derived in the next section. We then have to check numerically that the above limits are well defined for the typical observables. We will present a worm-type Monte Carlo algorithm which samples the partition function efficiently. We denote $\mathcal{T}$, μ_B as the bare temperature and bare chemical potential which are then renormalized by κ. We see that we can determine κ nonperturbatively directly by Monte Carlo simulations in the continuous time limit.

C. Continuous time partition function

We will now explain in detail how to derive the continuous time partition function from the discrete time partition function Eq. (5) by tracing the γ-dependence and neglecting subleading terms that vanish in the limit $N_\tau \to \infty$. The first step to obtain these results is to factorize Eq. (5) into the temporal and spatial parts:

$$\mathcal{Z}(\gamma, a_\tau\mu_q, N_\tau) = \gamma^{N_c\Lambda} \sum_{\{k,\ell\}} \left\{ \left(\prod_{x\in\Lambda_M} \delta_{\sum_\mu k_\mu(x), N_c} \frac{(N_c - k_0(x))!}{k_0(x)!} \prod_{i=1}^{d} \frac{(N_c - k_i(x))!}{N_c! k_i(x)!} \gamma^{-2k_i(x)} \right) \right.$$
$$\left. \times \left(\prod_{\ell\subset\Lambda_B} \sigma(\ell) \prod_{(x,\mu)\in\ell} \exp((\delta_{\hat{\mu},+\hat{0}} - \delta_{\hat{\mu},-\hat{0}}) N_c a_\tau \mu) \right) \prod_{i=1}^{d} (\gamma^{-N_c\delta_{\mu i}}) \right\} \tag{20}$$

where the factor $N_c!$ from the site weights for zero monomer number cancels the $1/N_c!$ in the temporal gauge link, and a prefactor $\gamma^{N_c\Lambda}$ was pulled out such that spatial links are now suppressed by $1/\gamma^2$ for mesons and $1/\gamma^{N_c}$ for baryons. Also, we have put the Grassmann constraint Eq. (6) into the above equation via a Kronecker delta and the decomposition Eq. (7). We will now neglect the subleading terms; i.e., we will only keep terms that survive in the limit Eq. (17). For any temperature, the average contribution per time location is $1/\gamma^2$. This will have drastic consequences, as spatial baryons for $N_c \geq 3$ and spatial dimer occupation numbers $k_i > 1$ will vanish. We will later see how to interpret this outcome and also show numerically that this is well justified. For now we note that the average dimer density will depend on the temperature, and (anti)baryons are static for $N_c \geq 3$ for all temperatures and chemical potential. For large γ, N_τ the partition function becomes

$$\tilde{\mathcal{Z}}(\gamma, a_\tau\mu_q, N_\tau) = \sum_{\substack{\{k\}|_{\Lambda^M} \\ \{\omega\}|_{\Lambda^B_\sigma}}} \left\{ \left(\prod_{x\in\Lambda^M} \delta_{\sum_\mu k_\mu(x), N_c} \frac{(N_c - k_0(x))!}{k_0(x)!} \left(\delta_{k_i(x),0} + \delta_{k_i(x),1} \frac{1}{N_c} \gamma^{-2} \right) \right) \left(\prod_{\vec{x}\in\Lambda^B_\sigma} e^{\omega(\vec{x}) N_c a_\tau \mu_q N_\tau} \right) \right\}$$
$$= \sum_{\{\Lambda^M_\sigma, \Lambda^B_\sigma\}} \sum_{\left\{ \substack{k_0\in\{0,\ldots,N_c\} \\ k_i\in\{0,1\}} \right\}\Big|_{\Lambda^M}}^{\mathrm{GC}} \left\{ \left(\prod_{(\vec{x},\tau)\in\{x|k_i(x)=1\}} \frac{v(k_0^-|k_0^+)_{(\vec{x},\tau)} v(k_0^-|k_0^+)_{(\vec{x}+\hat{i},\tau)}}{\gamma^2} \right) (2\cosh(\mu_B/T))^{|\Lambda^B_\sigma|} \right\} \tag{21}$$

where we have dropped the overall prefactor $\gamma^{N_c\Lambda}$ and we have used

$$\mu_B/T = \mu_B/\mathcal{T} = N_c a_\tau \mu_q N_\tau. \tag{22}$$

We have resummed static baryons and antibaryons $\omega = \pm 1$ in the second line, with $|\Lambda^B_\sigma|$ the number of spatial sites occupied by (anti)baryons with $\Lambda^B = \Lambda^B_\sigma \times N_\tau$, $\Lambda^M = \Lambda^M_\sigma \times N_\tau$. The sum over configurations contains all possible partitions of the spatial lattice $\{\Lambda^M_\sigma, \Lambda^B_\sigma\}$ with

$$\Lambda_\sigma^B \dot{\cup} \Lambda_\sigma^M = \Lambda_\sigma \equiv {N_\sigma}^3. \tag{23}$$

The vertex weights introduced in the second line $v_{(\vec{x},\tau)}$ depend on the dimers $k_0^- = k_0(\vec{x},\tau-1)$ and $k_0^+ = k_0(\vec{x},\tau)$, $k_0^- = k_0(\vec{x},\tau-1)$ and simplify due to the Grassmann constraint, $k_0^- + k_0^+ + 1 = N_c$:

$$\begin{aligned} v(k_0^-|k_0^+) &= \sqrt{\frac{1}{N_c}\frac{(N_c-k_0^-)!}{k_0^-!}\frac{(N_c-k_0^+)!}{k_0^+!}} \\ &= \sqrt{\frac{(N_c-k_0^-)(1+k_0^-)}{N_c}}. \end{aligned} \tag{24}$$

They come in pairs of adjacent spatial sites $(\vec{x},\tau)$, $(\vec{x}+\hat{i},\tau)$ at both ends of a spatial dimer on a bond $b = (\vec{x},\tau;i)$. There are N_c types of vertices since k_0^- can take the values from 0 to $N_c - 1$. For $N_c = 3$, there are only three types of vertices,

$$v(0|2) = v(2|0) = 1, \qquad v(1|1) = \frac{2}{\sqrt{3}}. \tag{25}$$

The important observation is that the mesonic part of the partition function only depends on the number of vertices and not on the precise temporal position. The temporal intervals between vertices attached to spatial dimers have a trivial weight: due to the Grassmann constraint on every site where no spatial dimer is attached, $k_0^- + k_0^+ = N_c$ implies that the dimer numbers form alternating chains as shown in Fig. 2 and cancel in weight:

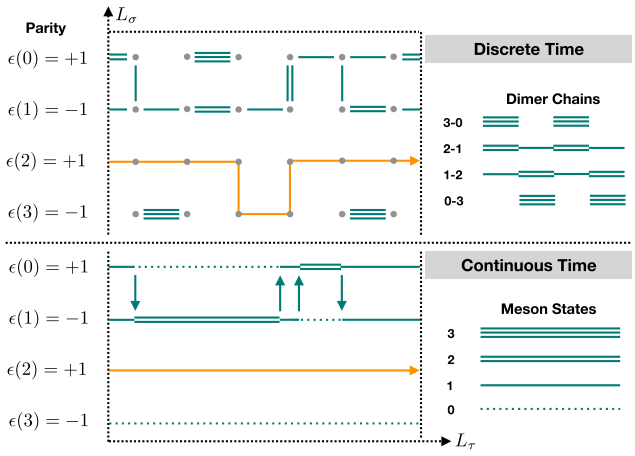

FIG. 2. Correspondence between discrete time configurations in terms of dimer coverings and baryon world lines (top) and in terms of hadron occupation numbers in continuous time (bottom). Multiple spatial dimers become resolved in single spatial dimers (which can be oriented consistently from emission sites $\mathcal{E}$ to absorption sites $\mathcal{A}$, indicated by the arrow), baryons become static, and only vertices of ⌞-shape or T-shape survive as $a_\tau \to 0$.

$$\sqrt{\frac{(N_c-k_0^-)!}{k_0^-!}\frac{(N_c-k_0^+)!}{k_0^+!}} = 1. \tag{26}$$

Only the relative order of the vertices v is important but not the length of the intervals between them. The partition function of SC-LQCD with $N_c = 3$ can be written in terms of these vertices as follows:

$$\tilde{\mathcal{Z}}(\gamma,\mu_B/T,N_\tau) = \sum_{\{\Lambda_\sigma^M,\Lambda_\sigma^B\}}\sum_n \sum_{\left\{\substack{k_0(\vec{x},0),\\ n_\llcorner,n_\intercal}\right\}\Big|_{\Lambda^M}}^{\mathrm{GC}} \left\{\left(\prod_{(\langle\vec{x},\vec{y}\rangle_j,\tau_j,),j=1}^{n}\left(\frac{v_\llcorner}{\gamma}\right)^{n_\llcorner(\vec{x},\tau_j)}\left(\frac{v_\intercal}{\gamma}\right)^{n_\intercal(\vec{y},\tau_j)}\right)(2\cosh(\mu_B/T))^{|\Lambda_\sigma^B|}\right\}. \tag{27}$$

The temporal dimers in the first time slice $k_0(\vec{x},\tau=0)$ are now dynamic variables in the partition sum. The ⌞-vertices and T-vertices at sites $x \in \Lambda^M$ are defined in terms of the previous vertices, $v_\llcorner = v(0|2) = v(2|0)$, $v_\intercal = v(1|1) = \frac{2}{\sqrt{3}}$, and the order in the high temperature expansion is given by the number of spatial dimers:

$$n = \frac{1}{2}\sum_{\vec{x}\in\Lambda_\sigma^M}\int_0^{1/\mathcal{T}} d\tau(n_\llcorner(\vec{x},\tau) + n_\intercal(\vec{x},\tau)) \equiv N_{Ds}. \tag{28}$$

In the partition sum Eq. (27), within the sum denoted by GC, not all temporal positions of the vertices are admisssible due to the Grassmann constraint. We still need to replace γ by the temperature aT, which requires bookkeeping of possible locations for spatial dimers. We will provide the details in the Appendix A. A simplified argument that allows us to understand the temperature dependence is that for the first spatial dimer there are up to N_τ possible locations between two adjacent spatial sites $\langle\vec{x},\vec{y}\rangle$, but due to the even-odd decomposition there are only $N_\tau/2$ possible locations for the second spatial dimer, and likewise for all other dimers, as long as N_τ is large. Hence, every spatial dimer, after summing over possible locations, has weight $\frac{N_\tau}{2\gamma^2} = 1/(2\mathcal{T})$. The final result is

$$\begin{aligned} \mathcal{Z}_{\mathrm{CT}}(\mathcal{T},\mu_B) &= \sum_{\{\Lambda_\sigma^M,\Lambda_\sigma^B\}}\sum_{\{\omega\}|_{\Lambda_\sigma^B}} e^{\omega_{\vec{x}}\mu_B/T}\sum_{n\in2\mathbb{N}}\frac{1}{n!}\frac{1}{(2\mathcal{T})^n} \\ &\quad\times\sum_{\mathcal{G}\in\Gamma_n^{\Lambda_\sigma^M}} v_\intercal^{N_\intercal(\mathcal{G})}, \\ N_\intercal &= \sum_{\vec{x}\in\Lambda_\sigma^M}\int_0^{1/\mathcal{T}} d\tau n_\intercal(\vec{x},\tau), \end{aligned} \tag{29}$$

where $\Gamma_n = \{n_\llcorner(\vec{x},\tau), n_\intercal(\vec{x},\tau)\}$ is the set of all valid configurations on the mesonic sublattice Λ_σ^M with $n \equiv N_{Ds}$ spatial dimers, and $N_\intercal \le 2n$ is the total number of T-vertices,

integrated over the compact temporal direction. Since $v_{\llcorner} = 1$, we do not need to include them in the weight. The prefactor $1/n!$ is due to time-ordering. In the next section we will simplify this result further by a Hamiltonian formulation, where we obtain a meaningful expression for Γ_n.

We now want to discuss the interpretation of the final partition function: as illustrated in Fig. 5, as the temporal lattice spacing $a_\tau \simeq a/\xi(\gamma) \to 0$, multiple spatial dimers become resolved into single dimers. The overall number of spatial dimers remains finite in the CT limit, as the sum over $\mathcal{O}(\gamma^2)$ sites compensates the $1/\gamma^2$ from spatial dimers. Its number is a function of the temperature and will signal spontaneous chiral symmetry breaking, see Sec. V A. As shown in Fig. 4 it takes large N_τ such that double dimers vanish, but it does not require large N_τ to make baryons static. The sign problem has completely vanished as $\sigma(\ell) = 1$ for static baryon loops ℓ. The set of all baryonic sites coincides then with the fermion bags that have been discussed in [32]. The expansion in n is an all-order high temperature expansion. It will also hold at very low temperatures, and we will be able to address zero temperature phenomena.

D. Hamiltonian formulation

In order to rewrite the partition function further, we make use of a diagrammatic expansion. These methods, giving rise to quantum Monte Carlo, are nowadays widely used in condensed matter [33,34]. The general idea is to decompose the Hamiltonian $\mathcal{H} = \mathcal{H}_0 + \mathcal{H}_i$ and express the partition function in terms of an expansion parameter n which keeps track of the number of interactions described by $\mathcal{H}_i$. After summing over all configurations of a given order in n, one integrates over all possible times at which interaction events may take place.

We will take a step back and reformulate Eq. (21) in new degrees of freedom: the temporal dimers $k_0(x)$ are replaced by an occupation number $m(x)$ by the following assignment:

$$k_0(x) \mapsto m(x) = \epsilon(x)\left(k_0(x) - \frac{N_c}{2}\right) + \frac{N_c}{2}$$
$$m(x) \in \{0, 1, \ldots N_c\} \tag{30}$$

with $\epsilon(x) = \pm 1$ the parity of a site introduced in Eq. (8). As a consequence, the alternating dimer chains will be replaced by meson occupation numbers $m(x)$ which are constant on the interval between attached spatial dimers (see Fig. 2), and the dimer-based vertices $v(0|2)$, $v(1|1)$, $v(0|2)$ in Eq. (25) are replaced by occupation number-based vertices $\tilde{v}(m|m')$, which change the meson state by one unit: $m(x) \mapsto m'(x) = m(x) \pm 1$:

$$\tilde{\mathcal{Z}}(\gamma, \mu_B/T, N_\tau) = \sum_{n=0}^{\infty} \sum_{\{m,(\tau,l))\}|_{\Lambda^M}} \left\{ \left(\prod_{(\vec{x},i)\in l_j} \frac{\hat{v}(m^-|m^+)_{(\vec{x},\tau)}}{\gamma} \frac{\hat{v}(m^-|m^+)_{(\vec{x}+\hat{i},\tau)}}{\gamma} \right) (2\cosh(\mu_B/T))^{|\Lambda^B_\sigma|} \right\}. \tag{31}$$

In fact there is a conservation law: if a quantum number $m(x)$ is raised or lowered by a spatial dimer, then at the site connected by the spatial dimer, the quantum number is lowered or raised. This is a direct consequence of its definition Eq. (30): the parity of the two sites connected by a spatial dimer is the opposite. We therefore can replace the vertices by raising and lowering operators:

$$\mathcal{Z}_{\mathrm{CT}}(\mathcal{T}, \mu_B) = \sum_{\{\Lambda^M_\sigma, \Lambda^B_\sigma\}} \left\{ \mathrm{Tr}_{m|\Lambda^M_\sigma} \left[\exp\left(\frac{1}{2\mathcal{T}} \sum_{\langle \vec{x},\vec{y}\rangle} (\hat{v}(\vec{x})_{m,m+1}\hat{v}(\vec{y})_{m,m-1} + \hat{v}(\vec{x})_{m,m-1}\hat{v}(\vec{y})_{m,m+1}) \right) \right] \mathrm{Tr}_{r|_{\Lambda^B_\sigma}} [e^{\hat{\omega}\mu_B/T}] \right\}$$
$$= \mathrm{Tr}_{\hbar}[e^{(\hat{\mathcal{H}}+\hat{\mathcal{N}}\mu_B)/\mathcal{T}}], \quad \hat{\mathcal{H}} = \hat{\mathcal{H}}_0 + \hat{\mathcal{H}}_i, \quad \hat{\mathcal{H}}_0 = 0, \quad \hat{\mathcal{H}}_i = \frac{1}{2}\sum_{\langle \vec{x},\vec{y}\rangle} (\hat{J}^+_{\vec{x}}\hat{J}^-_{\vec{y}} + \hat{J}^-_{\vec{x}}\hat{J}^+_{\vec{y}}), \quad \hat{\mathcal{N}} = \sum_{\vec{x}} \hat{\omega}_x,$$

$$\hat{J}^+ = \left(\begin{array}{cccc|c} 0 & 0 & 0 & 0 & \\ \hat{v}_{\llcorner} & 0 & 0 & 0 & \\ 0 & \hat{v}_{\mathsf{T}} & 0 & 0 & \\ 0 & 0 & \hat{v}_{\llcorner} & 0 & \\ \hline & & & & \begin{matrix} 0 & 0 \\ 0 & 0 \end{matrix} \end{array}\right), \quad \hat{J}^- = (\hat{J}^+)^T, \quad \hat{\omega} = \left(\begin{array}{cccc|c} 0 & 0 & 0 & 0 & \\ 0 & 0 & 0 & 0 & \\ 0 & 0 & 0 & 0 & \\ 0 & 0 & 0 & 0 & \\ \hline & & & & \begin{matrix} 1 & 0 \\ 0 & -1 \end{matrix} \end{array}\right), \quad |\hbar\rangle = |m, \mathscr{b}\rangle = \left(\begin{array}{c} 0 \\ \pi \\ 2\pi \\ 3\pi \\ \hline B^+ \\ B^- \end{array}\right). \tag{32}$$

This result is valid for $N_c = 3, N_f = 1$. A corresponding result for $N_f = 2$ is given in the Appendix C. In the second line we have included the baryonic sites into the trace and introduced the mesonic raising and lowering operators $\hat{J}^+$, $\hat{J}^-$ (which contain the vertices), and the baryon number operator $\hat{\mathcal{N}}$. The block-diagonal structure expresses the fact that the Hilbert space of hadrons is a direct sum of mesonic states and baryonic states, $|\hbar\rangle = |m\rangle \oplus |\mathscr{b}\rangle$, which results in the vanishing commutator

$$[\hat{\mathcal{H}}, \hat{\mathcal{N}}] = 0. \tag{33}$$

The fact that mesons and baryons are mutually exclusive (leading to the factorization into mesonic and baryonic subvolumes) results in one of the two blocks being zero in both operators $\hat{\mathcal{H}}$ and $\hat{\mathcal{N}}$. The meson states $|m\rangle$ count pseudoscalars, and we will denote them as pions π (despite the fact that they are flavorless for $N_f = 1$ and they cannot be distinguished from the η or η' mesons). The pion current is conserved but only in the chiral limit. Monomers would generate a mass to the pion. Since Pauli saturation holds on the level of the quarks and pions have a fermionic substructure, we cannot have more than N_c pions per spatial site. Due to the conservation of the pion current, if we start on each site with N_c pions, or with no pions at all, there cannot be any spatial dimer that transfers a meson to an adjacent site: either all sites are already saturated with mesons, or there is no meson to be transferred. If we omit the additive constant $N_c/2$ from Eq. (30), particle-hole symmetry becomes evident. To see this, consider the anticommutator of the mesonic operators (restricted on mesonic states):

$$[\hat{J}^+, \hat{J}^-] = \begin{pmatrix} -\hat{v}_\downarrow^2 & 0 & 0 & 0 \\ 0 & \hat{v}_\downarrow^2 - \hat{v}_\uparrow^2 & 0 & 0 \\ 0 & 0 & \hat{v}_\uparrow^2 - \hat{v}_\downarrow^2 & 0 \\ 0 & 0 & 0 & \hat{v}_\downarrow^2 \end{pmatrix} = \begin{pmatrix} -1 & 0 & 0 & 0 \\ 0 & -1/3 & 0 & 0 \\ 0 & 0 & 1/3 & 0 \\ 0 & 0 & 0 & 1 \end{pmatrix}. \tag{34}$$

The corresponding algebra has the structure of a spin, and it generalizes via Eq. (24) to arbitrary N_c:

$$\begin{aligned} \hat{J}_1 &= \frac{\sqrt{N_c}}{2}(\hat{J}^+ + \hat{J}^-), \qquad \hat{J}_2 = \frac{\sqrt{N_c}}{2i}(\hat{J}^+ - \hat{J}^-), \\ \hat{J}_3 &= i[\hat{J}_1, \hat{J}_2] = \mathrm{diag}\left(-\frac{N_c}{2}, -\frac{N_c}{2}+1, \ldots \frac{N_c}{2}\right) \\ &= \frac{N_c}{2}[\hat{J}^+, \hat{J}^-] \\ \hat{J}^2 &= \frac{N_c}{2}\mathrm{diag}(\hat{v}_0^2, \hat{v}_1^2 + \hat{v}_0^2, \ldots \hat{v}_{N_c-1}^2 + \hat{v}_{N_c-2}^2, \hat{v}_{N_c-1}^2) \\ &\quad + \frac{1}{4}\mathrm{diag}({N_c}^2, (N_c-2)^2, \ldots {N_c}^2) \\ &= \frac{N_c(N_c+2)}{4}\mathbb{1} \end{aligned} \tag{35}$$

with $\hat{v}_k^2 = (N_c - k)(1+k)/N_c$. The "spin" representation is $d = N_c + 1$ dimensional, with $S = N_c/2$. For $N_c = 1$, $\hat{J}_\pm = \frac{1}{2}(\sigma_x \pm i\sigma_y)$ is expressed in terms of the Pauli matrices, and the continuous time partition function becomes that of the quantum XY model. Although the algebra resembles that of a particle with spin, it has nothing to do with the spin of mesons or quarks. The alternating chains are simply expressing the fact that for staggered fermions, the lattice spacing is $2a_\tau$ rather than a_τ. By shifting the pion occupation numbers by their average value, we can identify the quantum state corresponding to this algebra:

$$\begin{aligned} m \mapsto \jmath &= m - \frac{N_c}{2}: \qquad \hat{J}_3\left|\frac{N_c}{2}, \jmath\right\rangle = \jmath\left|\frac{N_c}{2}, \jmath\right\rangle, \\ \hat{J}^2\left|\frac{N_c}{2}, \jmath\right\rangle &= \frac{N_c(N_c+2)}{4}\left|\frac{N_c}{2}, \jmath\right\rangle, \qquad [\hat{J}^2, \hat{J}_3] = 0. \end{aligned} \tag{36}$$

This remarkable result is due to the fact that pion occupation numbers on the lattice are not just bounded from below but also from above. We conclude this section by providing a physical interpretation of the dynamics on the hadronic states: the pion dynamics encoded in the Hamiltonian is that of relativistic pion gas [35]. In contrast, the fact that the baryon becomes static is due to its nonrelativistic nature. Its rest mass is large but finite (see Sec. IV C).

III. CONTINUOUS TIME WORM ALGORITHM

A. Poisson process

Before we address the algorithm that samples the partition function, Eqs. (29) and (32), we want to emphasize an important property: spatial dimers are distributed uniformly in time. The interval lengths (interpreted as the inter-arrival time between spatial dimers) are then exponentially distributed, and the number of spatial dimers in a fixed time interval is Poisson distributed. Hence, they can be generated via a Poisson process:

$$P(\Delta t) = \exp(-\lambda \Delta t), \qquad \Delta t \in [0, 1] \tag{37}$$

with λ the "decay constant" for spatial dimer emissions. Due to the presence of baryons, λ is space dependent:

$$\lambda = d_M(\vec{x})/(4\mathcal{T}), \qquad d_M(\vec{x}) = 2d - \sum_{\langle \vec{x}, \vec{y} \rangle} |B(\vec{y})| \tag{38}$$

where $d_M(\vec{x})$ is the number of mesonic sites adjacent to $\vec{x}$ where the Poisson process operates. Note that in Eq. (37) we have rescaled the compact time interval $[0, 1/\mathcal{T}] \mapsto [0, 1]$ and thus have put the temperature into the decay constant λ.

The Poisson process of emitting pions from $(\vec{x}, t)$ to an adjacent site $(\vec{y}, t)$ with probability λ gives rise to a decomposition of vertices into emission sites $(\vec{x}, t) \in \mathcal{E}$ and absorption sites $(\vec{y}, t) \in \mathcal{A}$. Spatial dimers can be oriented consistently due to the underlying even/odd decomposition of lattice sites, but is also evident in the

Hamiltonian representation, where J^- is an emission and J^+ is an absorption event. The emission sites $\mathcal{E}$ are simply those that reduce the pion occupation number m in Euclidean time by one unit; the absorption sites $\mathcal{A}$ are those that increase m. Every spatial dimer corresponds to a pion hopping to an adjacent site and connects an $\mathcal{E}$ site with an $\mathcal{A}$ site. The number of $\mathcal{E}$ sites equals the number of $\mathcal{A}$ sites, and due to the periodic boundary conditions in time, this even holds for every spatial site $\vec{x}$:

$$|\{t_i|(\vec{x},t_i)\in\mathcal{E}\}| = |\{t_i|(\vec{x},t_i)\in\mathcal{A}\}|. \tag{39}$$

The continuous time worm algorithm (CT-WA) needs to fulfill detailed balance, such that the emission process is counterbalanced by an absorption process to obtain the equilibrium distribution of spatial dimers according to temperature and chemical potential.

B. Details of the continuous time worm algorithm

Worm algorithms at discrete time (DT-WA) are well established also for strong coupling lattice QCD [29,36,37]. Designing an algorithm that operates directly in the Euclidean continuous time limit has several advantages: (1) the ambiguities arising from the functional dependence of observables on the anisotropy $\xi(\gamma)$—in particular, nonmonotonic behavior—will be circumvented, and (2) we do not need to perform the continuum extrapolation $N_\tau\to\infty$. This will allow us (3) to measure the phase boundaries unambiguously, as the baryonic part of the partition function simplifies such that the sign problem is completely absent, and (4) at all temperatures of interest, the CT algorithm is considerably faster than its discrete version, in particular since the baryon update does not require a worm algorithm but can be replaced by a heat bath update.

In Fig. 3 we clearly see that the CT-worm algorithm outperforms the DT-worm algorithm at temperatures in the vicinity of the transition temperature and above. The lower the temperature, the more spatial dimers are sampled, which makes the average worm update longer. At first glance it seems that the CT-worm becomes more expensive, but one needs to keep in mind that lower temperatures require larger N_τ to get valid estimates for observables. On a lattice with time extent N_τ, temperatures below $1/N_\tau$ (which have $\gamma<1$) will have more spatial dimers than temporal dimers and suffer from saturation effects: the density of spatial dimers is limited to $N_cN_\tau/2$, whereas it is unlimited at continuous time. In Fig. 4 we show the N_τ-dependence of various observables: they have a well-defined CT limit. Also, this figure illustrates that the approximations which led to $\mathcal{Z}_{\rm CT}$ in Eq. (32) are well justified. The extrapolation from discrete time to continuous time is difficult: large N_τ require more statistics, and due to the sign problem, most observables get noisy due to sign reweighting. The first approximation is to make baryons static, which eliminates the sign problem. This step makes the extrapolation much more controlled, and even for $N_\tau=4$, the static baryon approximation is not bad. Next we prohibit sites which have more than 3 spatial dimers, which has only a mild effect at the temperatures considered here. If we also prohibit sites with more than 2 spatial dimers, the deviation at finite N_τ is drastic, but this approximation also extrapolates to the same CT limit for the observable. The point at $1/N_\tau=0$ in Fig. 4 is the outcome of the CT-WA, which has much smaller error bars and better performance with the same number of worm updates.

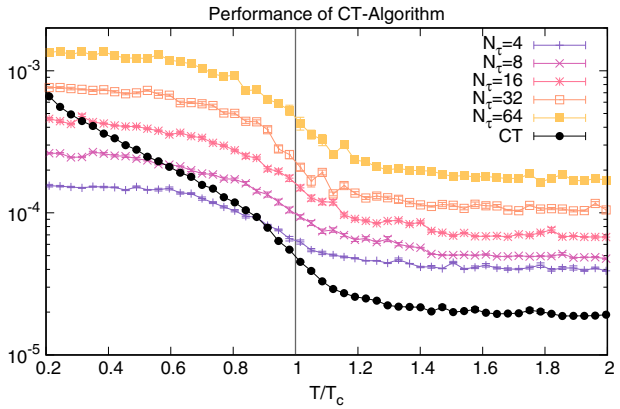

FIG. 3. The performance of the continuous time algorithm compared to the discrete time algorithm for various N_τ. For a large range of temperatures, and in particular at the chiral transition, the CT-WA performs even better than DT-WA for $N_\tau=4$. The lower the temperature, the larger N_τ is required to obtain correct results for the various observables (see also Fig. 4).

CT algorithms for quantum Monte Carlo are now widely used in condensed matter (see e.g., [33,38]), whereas using CT methods in quantum field theories is rather new [30,39–41]. The basic idea of a worm algorithm introduced in [42] is to sample an enlarged configuration space with defects on the lattice known as a worm tail x_T and a worm head x_H. Every worm algorithm consists of two kinds of updates: (1) move updates, which move the head x_H and tail x_T to a new site x_0, and (2) shift updates, which move the head x_H through the lattice until the worm recombines with the tail. Worm algorithms are highly efficient: after recombination, the configuration is globally updated, similar to cluster algorithms. Moreover, during the shift update, two-point correlation functions can be measured. In order to apply a worm algorithm, the partition function needs to be written in terms of bond variables. Those representations are typically available in spin models from the high temperature expansion. In the case of lattice QCD, a dual representation based on the strong coupling expansion also admits the applicability of worm algorithms.

Our CT-WA can be derived from the DT-WA that has been developed for the $\mathrm{U}(N_c)$ gauge group in the strong coupling limit [36], which does not include baryons. This worm algorithm is based on an even-odd decomposition of

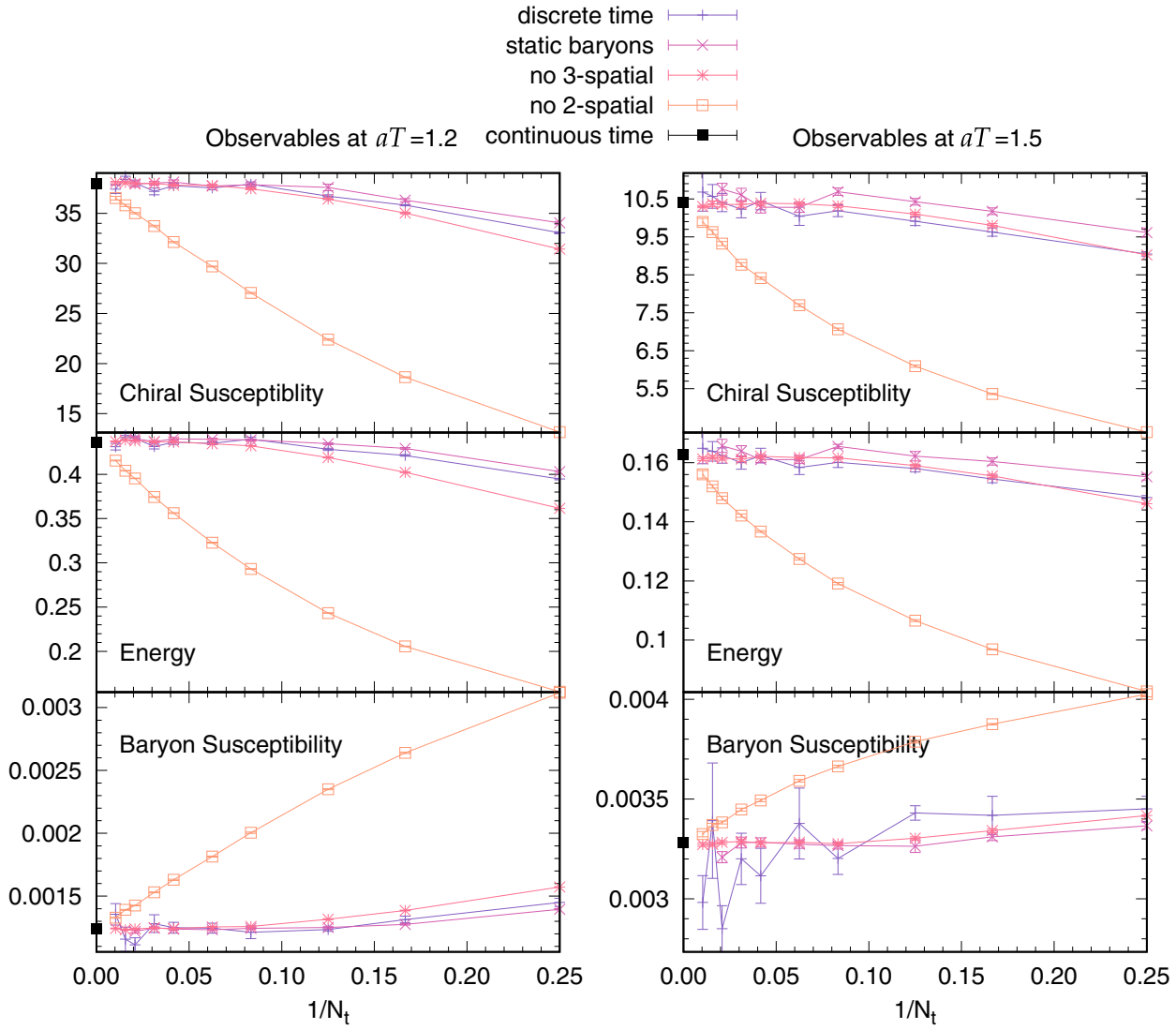

FIG. 4. N_τ-dependence of the chiral susceptibility (top) and the energy (center) and the baryon susceptibility (bottom). We compare the full discrete simulations and various approximations according to the steps in deriving the continuous time limit (static baryon approximation, exclusion of spatial triple dimers, exclusion of spatial double dimers). We have fixed the bare temperature to $\mathcal{T} = 1.2 < \mathcal{T}_c$ and $\mathcal{T} = 1.5 > \mathcal{T}_c$. All observables extrapolate well into the continuum limit, with its Monte Carlo result at $1/N_\tau = 0$ having a much smaller error.

weights: if the parity of the head $\epsilon(x_H)$ is the same as that of the tail $\epsilon(x_T)$, then the head has an active site location; if the parities differ, the head is a passive site. The active sites correspond to the absorption sites $\mathcal{A}$, and the passive sites correspond to the emission sites $\mathcal{E}$ as discussed above.

For the SU(N_c) gauge group, two separate worms are required, one in the mesonic sector and one in the baryonic sector [37]. The mesonic worm for the SU(N_c) group differs from the directed path worm for U(N_c) in one important aspect: in the directed path version, backtracking is prohibited to evolve faster through configuration space (if the update shifts the worm head from x to the adjacent site y, then in the next shift update the worm is not allowed to go back). With the simple baryon loop geometries in the CT limit, we can supplement the continuous time version of the directed path worm algorithm by an additional heat bath update: after the mesonic worm has recombined, we propose, for all sites $\vec{x}$ where no spatial dimers are attached (the so-called static sites), a new hadronic state with the probabilities

$$p(m) = \frac{1}{N_c + 1 + 2\cosh(\mu_B/T)}, \qquad m = 0, \ldots, N_c,$$
$$p(B^\pm) = \frac{e^{\pm\mu_B/T}}{N_c + 1 + 2\cosh(\mu_B/T)}. \tag{40}$$

The consequence is that if the worm head propagates in a positive or negative temporal direction, it will continue to do

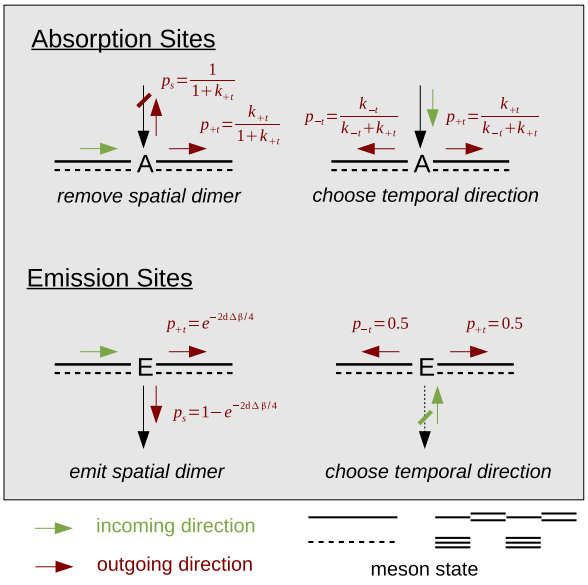

FIG. 5. Updating rules for the continuous time algorithm. Top: An absorption site can be approached either from the temporal direction (left: a spatial dimer may be removed) or from the spatial direction (right: a dimer was emitted in the previous step). Bottom: An emission site can be approached either from the temporal direction (left: a spatial dimer may be emitted) or from the spatial direction (right: a dimer was removed in the previous step).

so until it either emits or absorbs a pion; i.e., it will either add or delete a spatial dimer. It will not change the direction and diffuse: the CT-WA can be regarded as a Poisson process. The updating rules are outlined in Fig. 5. The probabilities for the various cases (approaching or leaving an absorption site $\mathcal{A}$ or emission site $\mathcal{E}$) depend on the involved states m: (1) if an $\mathcal{A}$ site is approached from the temporal direction, the spatial dimer is removed with a heat bath probability determined by J^-, (2) if an $\mathcal{A}$ site is approached from a spatial direction, the new temporal direction is also determined by J^-, (3) if an $\mathcal{E}$ site is approached from a temporal direction, the emission probability to insert a spatial dimer is $1-e^{-\lambda\Delta\tau}$ and the probability to continue in a temporal direction is $e^{-\lambda\Delta\tau}$, (4) if an $\mathcal{E}$ site is approached from a spatial direction, forward and backward temporal direction are chosen with the same probablity. At high temperatures, $\lambda = \lambda(\mathcal{T}) \ll 1$ according to Eq. (38), and the worm head will very likely continue in the temporal direction by some time Δt with probability $p_\tau \simeq 1-\lambda\Delta t$ and emit a spatial dimer with probability $p_\sigma \simeq \lambda\Delta\tau$. The higher the temperature, the longer the worm propagates in the temporal direction, possibly looping through the periodic boundary back to where it started.

In the discrete time algorithm, during worm evolution, whenever the worm head is on a site with opposite parity compared to the worm tail, $\epsilon(x_H) = -\epsilon(x_T)$, both the worm head and tail can be interpreted as monomers [if $\epsilon(x_H) = \epsilon(x_T)$, the head is a sink rather than a source for monomers]. Even in the chiral limit, the monomer two-point function can be accumulated in a histogram (due to translation invariance, only the relative lattice vector $z = x_1 - x_2$ is needed):

$$H_2(z) \mapsto H_2(z) + \frac{\Lambda}{d_M(x_x) + 2\gamma^2}\delta_{z,x_T-x_H} \tag{41}$$

with $d(x)$ defined in Eq. (38). An equivalent definition holds in the CT limit:

$$H_2(\vec{z},\tau) \mapsto H_2(\vec{z},\tau) + \frac{\Lambda_\sigma}{2\mathcal{T}}\delta_{\vec{z},\vec{x}_T-\vec{x}_H}\delta(\tau-(\tau_T-\tau_H))$$
$$G(\vec{z},\tau) = \langle\bar{\chi}\chi_0\bar{\chi}\chi_{\vec{z},\tau}\rangle \simeq \frac{N_c}{Z}H_2(\vec{z},\tau) \tag{42}$$

with Z the number of worm updates and $G(\vec{z},\tau)$ the connected chiral two-point function approximated by an accumulated and normalized histogram. Details on how this and other mesonic two-point correlation functions are determined in practice are given in Sec. VII A.

C. Observables

Almost all observables that can be measured via the DT-WA version can also be measured via CT-WA. This is obviously the case for all observables that can be obtained as derivatives of $\log \mathcal{Z}_{\mathrm{CT}}$. The discrete time observables in terms of the dual variables

$$N_M = \sum_x n_x, \qquad N_{Dt} = \sum_x k_{x,0}, \qquad N_{Bt} = \sum_x |b_{x,0}|,$$
$$N_q = 2N_{Dt} + N_c N_{Bt}, \qquad N_B = \sum_x \omega_x \tag{43}$$

are discussed in [43]. The corresponding dimensionless thermodynamic observables in the CT limit simplify because

$$\lim_{\gamma\to\infty}\frac{\xi(\gamma)}{\gamma}\frac{d\gamma}{d\xi} = \frac{\kappa\gamma^2}{\gamma}\frac{1}{2\kappa\gamma} = \frac{1}{2}, \tag{44}$$

which should be compared to the isotropic case based on Eq. (14):

$$\left.\frac{\xi(\gamma)}{\gamma}\frac{d\gamma}{d\xi}\right|_{\gamma=1} = \frac{1}{2+4\kappa(\kappa-1)} \simeq 0.760(1). \tag{45}$$

Also, in the CT limit we no longer have temporal dimers but only spatial dimers, and we have to consider the chiral limit:

$$N_q = N_c N_\tau {N_\sigma}^3 - 2N_{Ds}, \qquad N_M = 0. \tag{46}$$

We are now able to define the continuous time observables in terms of dual variables, which are always in dimensionless units with $a = a_\sigma$ and $V = {N_\sigma}^3 a^3$. Important observables are (1) the baryon density,

$$a^3 n_B = a^3 \frac{T}{V} \frac{\partial \log \mathcal{Z}}{\partial \mu_B}\bigg|_{V,T} = \frac{\langle N_B \rangle}{{N_\sigma}^3} = \langle \omega \rangle \tag{47}$$

which is given by the average winding number; (2) the energy density,

$$a^4 \epsilon = \mu_B a^3 n_B - \frac{a^4}{V} \frac{\partial \log \mathcal{Z}}{\partial T^{-1}}\bigg|_{V,\mu_B} = C - \kappa \mathcal{T} \langle n_{Ds} \rangle, \tag{48}$$

where the irrelevant additive constant $C = \frac{1}{2} N_c \Lambda$ can be neglected compared to discrete time as we dropped the prefactor $\gamma^{N_c \Lambda}$ in Eq. (21) which contained both the contribution from static mesons and static baryons; (3) the pressure,

$$a^4 p = a^3 \kappa \mathcal{T} \frac{\partial \log \mathcal{Z}}{\partial V}\bigg|_{T,\mu_B} = \frac{a^4 \epsilon}{3} = \frac{1}{3}(C - \kappa \mathcal{T} \langle n_{Ds} \rangle), \tag{49}$$

which in the strong coupling limit and chiral limit is just proportional to the energy density such that the interaction measure $\epsilon - 3p$ vanishes. At finite quark mass, the interaction measure is proportional to the chiral condensate, which is zero here in a finite volume as $\langle \bar{\chi} \chi \rangle \propto \langle n_M \rangle$ (but see Sec. IV); (4) the chiral susceptibility,

$$\begin{aligned} a^6 \chi_q \equiv \chi_\sigma &= \frac{\partial^2 \log \mathcal{Z}}{\partial (2 \hat{m}_q)^2} = \langle n_M^2 \rangle \\ &= a^4 \mathcal{T} \sum_{\vec{z}} \int_0^{1/\mathcal{T}} d\tau G_2(\vec{z}, \tau), \end{aligned} \tag{50}$$

which in the chiral limit only receives contributions from the connected part and $G_2(\vec{x}_1, t_1; \vec{x}_2, t_2) \equiv G_2(\vec{x}_1 - \vec{x}_2, t_1 - t_2)$ is the translation invariant monomer two-point function that is measured during worm evolution, see Eq. (42); (5) the entropy density,

$$a^3 s = \frac{a^3}{VT} \left(\frac{4\epsilon}{3} - \mu_B n_B \right). \tag{51}$$

The chiral condensate vanishes in the chiral limit in a finite volume. This is also evident from the absence of monomers in the dual representation. It is possible to obtain the chiral condensate from a 1/V expansion via chiral perturbation theory in a finite box, as explained in Sec. IV. Note that the pressure defined in Eq. (49) is not equal to

$$a^4 p' = a^3 \frac{\kappa \mathcal{T}}{V} \log \mathcal{Z} \tag{52}$$

because on the lattice the system is not homogeneous. The identity $p = p'$ only strictly holds in the continuum.

D. Polymer formulation and Wang-Landau method

So far we have treated the mesonic and baryonic sectors separately, and there is no need for the resummation known as the Karsch-Mütter trick [28] for real chemical potential as there is no sign problem in the CT limit. However, a resummation of static mesons and baryons proves to be advantageous in the following respects: (1) it allows us to extend simulations to imaginary chemical potential beyond the value of $a_\tau \mu_q = i\pi T/6$, where the baryon density becomes zero (discussed in Sec. V D), and (2) we are able to adapt the Wang-Landau method [44] for determining the first order transition at low temperatures very accurately and also obtain the canonical phase diagram from the density of states at high precision, see Sec. V.

Apart from the usual (anti)baryons denoted by $\mathcal{B}$, we will discuss here two kinds of resummations of quantum states: the superposition of baryons and antibaryons ($\mathcal{P}$-polymers), and including static mesons ($\mathcal{Q}$-polymers):

$$\begin{aligned} |\mathcal{B}\rangle_{\vec{x}} &= |B^+\rangle_{\vec{x}} - |B^-\rangle_{\vec{x}}, & B(C) &= \sum_{\vec{x}} b_{\vec{x}}(C), \\ |\mathcal{P}\rangle_{\vec{x}} &= |B^+\rangle_{\vec{x}} + |B^-\rangle_{\vec{x}}, & P(C) &= \sum_{\vec{x}} p_{\vec{x}}(C), \\ |\mathcal{Q}\rangle_{\vec{x}} &= |P\rangle_{\vec{x}} + \sum_{m=0}^{N_c} |m\rangle_{\vec{x}}, & Q(C) &= \sum_{\vec{x}} q_{\vec{x}}(C), \end{aligned} \tag{53}$$

where for a given configuration C, on each spatial site, the baryon and polymer numbers $B \le P \le Q$ are related via (in the following $V = {N_\sigma}^3$)

$$\begin{aligned} b_{\vec{x}} &\in \{0, \pm 1\}, & B &\in \{-V, \ldots V\}, \\ p_{\vec{x}} &= |b_{\vec{x}}| \in \{0, 1\}, & P &\in \{0, \ldots V\}, \\ q_{\vec{x}} &= p_{\vec{x}} + m_{\vec{x}} \in \{0, 1\}, & Q &\in \{0, \ldots V\}, \end{aligned} \tag{54}$$

with $m_{\vec{x}} = 1$ iff the site is mesonic and static. The corresponding single site weights are

$$\begin{aligned} w_{\mathcal{B}}(\mu_B/T) &= \exp\left(\pm \frac{\mu_B}{T} \right), \\ w_{\mathcal{P}}(\mu_B/T) &= 2 \cosh\left(\frac{\mu_B}{T} \right), \\ w_{\mathcal{Q}}(\mu_B/T) &= N_c + 1 + 2 \cosh\left(\frac{\mu_B}{T} \right). \end{aligned} \tag{55}$$

These weights will be used for the following binomial/trinomial distributions:

$$D^{\mathcal{QP}}_{\mu_B/T}(Q,P) = \binom{Q}{P} \frac{(N_c+1)^{Q-P} w_p(\mu_B/T)^P}{w_q(\mu_B/T)^Q}, \qquad D^{\mathcal{PB}}_{\mu_B/T}(P,B) = \binom{P}{(B+P)/2} \frac{e^{B\mu_B/T}}{w_p(\mu_B/T)^P},$$
$$D^{\mathcal{QB}}_{\mu_B/T}(Q,B) = \sum_{P=|B|}^{Q} \binom{Q}{\frac{P+B}{2}, \frac{P-B}{2}, Q-P} \frac{e^{B\mu_B/T}(N_c+1)^{Q-P}}{w_q(\mu_B/T)^Q}, \tag{56}$$

with $B^{\pm} = \frac{P\pm B}{2}$ the number of (anti)baryon sites and $Q-P$ the number of static mesons. For some observables we need higher moments of the baryon number. We then only keep track of the histogram for $\mathcal{Q}$-polymers, $H^{\mathcal{Q}}_{V,\mathcal{T},\mu_B}(Q)$ (normalized accordingly to be a probability distribution), and get the histogram in the baryon number $H^{\mathcal{B}}_{V,\mathcal{T},\mu_B}(B)$ from the above distributions:

$$H^{\mathcal{P}}_{V,\mathcal{T},\mu_B}(P) = \sum_{Q=P}^{V} D^{\mathcal{QP}}_{\mu_B/T}(Q,P) H^{\mathcal{Q}}_{V,\mathcal{T},\mu_B}(Q),$$
$$H^{\mathcal{B}}_{V,\mathcal{T},\mu_B}(B) = \sum_{P=B}^{V} D^{\mathcal{PB}}_{\mu_B/T}(P,B) H^{\mathcal{P}}_{V,\mathcal{T},\mu_B}(P)$$
$$= \sum_{Q=P}^{V} D^{\mathcal{QB}}_{\mu_B/T}(Q,B) H^{\mathcal{Q}}_{V,\mathcal{T},\mu_B}(Q). \tag{57}$$

For large spatial volumes V, the distributions in Eq. (56) involve large numbers. In practice we use the logarithmic versions of both histograms and binomial/trinomial distributions. The polymer resummation will turn out to be crucial for the measurement of baryon fluctuations for the Taylor coefficients, see Sec. VI A.

The expectation value of very high moments of baryonic observables such as higher moments of B^+, B^- or of the baryon number B given by some function f can be computed from the above histogram,

$$\langle f(B^+,B^-)\rangle = H^{\mathcal{P}}_{V,\mathcal{T},\mu_B}(B^+ + B^-) f(B^+,B^-),$$
$$\langle f(B)\rangle = H^{\mathcal{B}}_{V,\mathcal{T},\mu_B}(B) f(B), \tag{58}$$

which improves drastically over the usual measurement of higher moments. In Fig. 6 we show histograms $H^{\mathcal{Q}}_{V,\mathcal{T},\mu_B}$ for various temperatures and $\mu_B = 0$. The temperature dependence gives insight into the number of static vs dynamic sites: at high temperatures, almost all sites are static, and at low temperatures almost all sites are dynamic; e.g., they interact via pion exchange with adjacent sites. The critical temperature is characterized by a broad distribution.

Another important application of histogram techniques is the Wang-Landau method, which computes the density of states $g(\mathcal{T},B)$. It will allow us to obtain the canonical phase diagram, see Sec. V. We use that the grand-canonical partition sum is related to the canonical partition sum via the Laplace transformation

$$\mathcal{Z}_{GC}(\mathcal{T},\mu_B) = \sum_{B=-V}^{V} \mathcal{Z}_C(\mathcal{T},B) e^{B\mu_B/T}. \tag{59}$$

One method to determine the canonical partition sum $\mathcal{Z}_C(\mathcal{T},B)$ in the context of QCD is to obtain the $\mathcal{Z}_{GC}$ for imaginary chemical potential and reweighting for the resulting Fourier coefficient [45]. In the dual representation, $\mathcal{Z}_C(\mathcal{T},B)$ can be determined directly by the Wang-Landau method since it is in fact the density of states with respect to the canonical conjugate to μ_B and it is approximated by $g(\mathcal{T},B)$ up to the target precision. Then, observables in the GC ensemble are immediately obtained:

$$\langle \mathcal{O}\rangle_{GC} = \frac{\sum_B \mathcal{O}\mathcal{Z}_C(\mathcal{T},B) e^{B\mu_B/T}}{\sum_B \mathcal{Z}_C(\mathcal{T},B) e^{B\mu_B/T}}. \tag{60}$$

The accuracy even improves when the density of states using the polymer resummation $g(\mathcal{T},P)$ is determined via Wang-Landau, and the canonical partition sum is recovered by the binomial transformation Eq. (56):

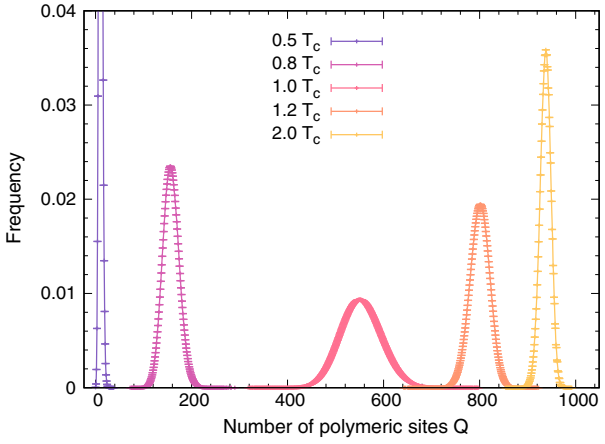

FIG. 6. The $\mathcal{Q}$-polymer histograms are shown for various temperatures, evaluated on a 10^3-CT volume. At low temperature, almost all sites have spatial dimers attached; most configurations have low polymer number. At high temperature, almost all sites are static; most configurations have high polymer number $Q \leq N_\sigma{}^3$. In the vicinity of T_c, the distribution is broad.

$$\mathcal{Z}_C(\mathcal{T},B)=\sum_{P=0}^{V}\sum_{\substack{B^+=0\\B=2B^+-P}}^{V}\binom{P}{B}g(\mathcal{T},P). \tag{61}$$

The Wang-Landau method applied to $g(\mathcal{T},P)$ consists of the following steps:

(1) A CT-worm update is run [which makes $g(\mathcal{T},P)$ temperature dependent].
(2) We loop through all spatial sites $\vec{x}$ and check whether the site is static (has no spatial dimers attached).
(2a) If so, we propose a new configuration with a uniform probability distribution to generate one of the N_c+2 states (N_c+1 mesonic states and one P-state) having equal weight, possibly resulting in a change $P\mapsto P+\Delta P$ with

$$\begin{aligned}&|m\rangle\mapsto|P\rangle\colon\ \Delta P=1, \qquad |P\rangle\mapsto|m\rangle\colon\ \Delta P=-1,\\ &|P\rangle\mapsto|P\rangle\colon\ \Delta P=0, \qquad |m\rangle\mapsto|m\rangle\colon\ \Delta P=0.\end{aligned} \tag{62}$$

(2b) If not, the configuration is unchanged and $\Delta P=0$.
(3) The new configuration is accepted with a metropolis acceptance step:

$$p_{acc}=\min(1,(2\cosh(\mu_B/T))^{\Delta P}). \tag{63}$$

(3a) If accepted, $P'=P+\Delta P$ is the new polymer number,
(3b) If rejected, $P'=P$.
(4) In any case, even if the site is nonstatic and $P'=P$ [option (2b)], the histogram and density of states are updated:

$$\begin{aligned}H(P')&\mapsto H(P')+1,\\ \log(g(P'))&\mapsto\log(g(P'))+\log(f)\end{aligned} \tag{64}$$

with f the modification factor.

We loop through (1)–(4) until the histogram $H(P)$ is flat enough:

$$\sum_{P=0}^{V}|H(P)-\bar{H}|<\delta\Rightarrow f\mapsto\sqrt{f}, \qquad H(P)=0 \tag{65}$$

with $\bar{H}$ the histogram average and δ defining the flatness condition. This step, which refines $g(P)$, is repeated until the final precision is reached, $\log(f)\le\log(f_{\text{final}})$. Then $g(P)$ approximates the true density of states with that precision. In Sec. V we will show the density of states and the canonical phase diagram for various temperatures.

We perform simulations at a set of fixed temperatures and weight the obtained density of states to the critical $a\mu_c$, which is characterized by equal probability of the low and high density phase. In practice, we determine $a\mu_c$ at which both peaks in the first order region have the same height (see Fig. 20).

E. Cross-checks

To check the correctness of our CT-WA implementation, we have made extensive cross-checks. A comparison of the CT algorithm on volumes with an analytic result extrapolated from the $2\times N_\tau$ lattice for gauge group U(1) is discussed in the Appendix B. Since there does not seem to be a simple analytic expression for $N_c>1$, we are left with comparing continuous time simulations with the extrapolation of discrete time simulations. We already discussed the suppression mechanism that led to the continuous time results for various observables in Fig. 4. In Fig. 7 we show a comparison of the discrete time extrapolation and the continuous time simulations for the chiral susceptibility as a function of the temperature, which agree within errors for all temperatures.

Another aspect is to verify that the distribution of spatial dimers is indeed Poissonian, due to the fact that the weight of a configuration does not depend on the interval lengths between subsequent spatial dimers. This is illustrated in Fig. 8. The Poisson distribution

$$P(N(\Delta\tau)=n)=\frac{(\lambda\tau)^n}{n!}e^{-\lambda\Delta\tau} \tag{66}$$

has been fitted to histograms from Monte Carlo via CT-WA. The comparison with the expected values of λ (with $\lambda=\frac{3}{4T}$ for the distribution of spatial dimers per bond and $\lambda=\frac{6d}{4T}$ for the distribution of vertices per site, with $d=3$) is very good for small intervals $\Delta\tau<1$. The deviations to the expected λ for large intervals $\Delta\tau\simeq1$ is due to the periodic boundary conditions, where the Poisson distributions start to overlap.

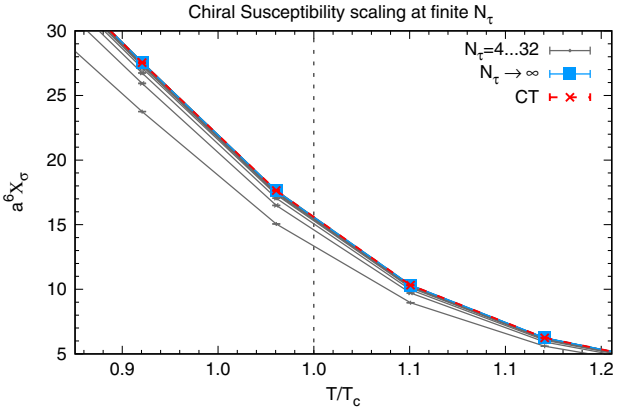

FIG. 7. Extrapolation of the chiral susceptibility from the finite lattices $N_\tau=4,\ldots,32$ towards $N_\tau\to\infty$ and comparison with the continuous time result, showing excellent agreement.

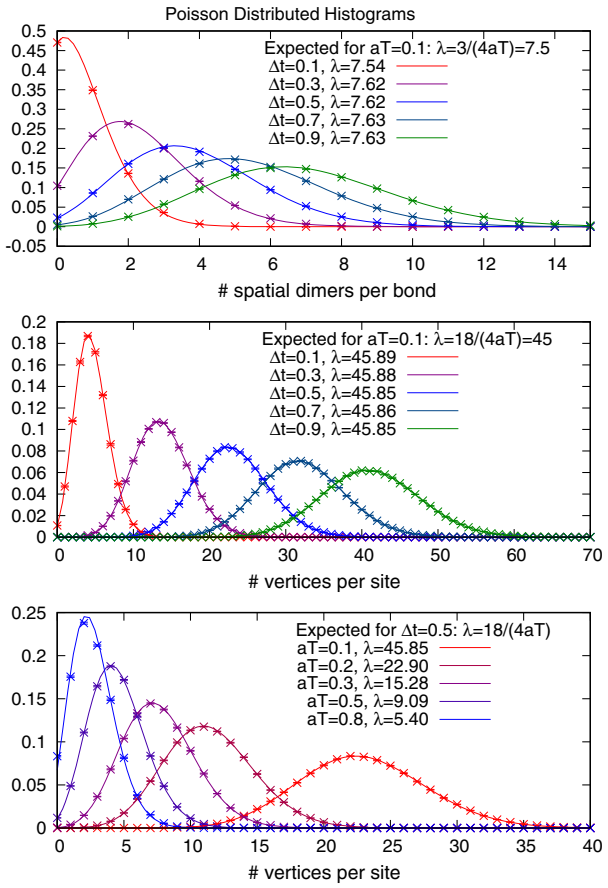

FIG. 8. Distributions of the number of spatial dimers per bond (top) and number of vertices per site (center) for various interval lengths $\Delta\tau$, and for various temperatures (bottom). The quantities are Poisson distributed, with λ fitted according to Eq. (66) to the data, reproducing the expected value. Small deviations for $\Delta\tau \leq 1$ occur as the Poisson process is on a circle rather than an infinite line, and due to the presence of static baryons (which are highly suppressed at low temperatures).

IV. ZERO TEMPERATURE

A. Determination of κ and pion decay constant

The first task that is also relevant to define the temperature and chemical potential nonperturbatively [Eqs. (17) and (18)] is to determine the anisotropy correction factor κ, see Eq. (12). The procedure of anisotropy calibration is discussed in detail for anisotropic lattices at strong coupling in discrete time in [31,46,47]. The coefficient κ is the strong coupling analogue of the Karsch coefficients at weak coupling that have been analyzed in [28,48] and numerically studied at a fixed physical scale in [49]. Anisotropic lattices are also relevant when determining mesonic correlators, e.g., in the FASTSUM Collaboration [50].

Our strategy to obtain κ is based on the variance of the pion current. In the chiral limit, the pion current for discrete time

$$j_\mu(x) = \epsilon(x)\left(k_\mu(x) - \frac{N_c}{2}|b_\mu(x)| - \frac{N_c}{2d}\right) \tag{67}$$

is a conserved current:

$$\sum_{\hat{\mu}}(j_\mu(x) - j_\mu(x-\hat{\mu})) = 0. \tag{68}$$

Likewise, the corresponding pion currents in the CT limit (see Eq. (30) are

$$m_0(\vec{x},\tau) \equiv j_0(\vec{x},\tau) = m(\vec{x},\tau) - \frac{N_c}{2}, \tag{69}$$

$$m_i(\vec{x},\tau) \equiv j_i(\vec{x},\tau) = \epsilon(\vec{x},\tau)k_i(\vec{x},\tau). \tag{70}$$

We have dropped the baryonic contributions and the constant, as they do not contribute at continuous time. The conservation of the currents is now directly linked to the meson occupation numbers:

$$m(\vec{x},\tau_1) + \int_{\tau_1}^{\tau_2} d\tau \sum_{i=1}^{3}(m_i(\vec{x},\tau) - m_i(\vec{x}-\hat{i},\tau)) = m(\vec{x},\tau_2) \tag{71}$$

for all $\tau_2 > \tau_1$, and the temporal/spatial charges are

$$Q_0 = \sum_{\vec{x}} m_0(\vec{x},\tau) \equiv \mathscr{M}_0,$$
$$Q_i = \sum_{\vec{x}\perp\vec{e}_i}\int_0^{1/\mathcal{T}} d\tau m_i(\vec{x},\tau) \equiv \mathscr{M}_i, \tag{72}$$

which have the expectation values

$$\langle\mathscr{M}_0\rangle = \langle\mathscr{M}\rangle - \frac{\Lambda_\sigma N_c}{2} = 0, \qquad \langle\mathscr{M}_i\rangle = 0. \tag{73}$$

The variances are however temperature dependent. If the spatial and temporal variances are equal,

$$\langle(\Delta Q_0)^2\rangle = \langle\mathscr{M}_0^2\rangle \stackrel{!}{=} \langle\mathscr{M}_i^2\rangle = \langle(\Delta Q_i)^2\rangle, \tag{74}$$

that corresponds to equal physical extent in space and time:

$$L = \frac{1}{T} \quad \Rightarrow \quad N_\sigma = \frac{1}{aT} = \frac{1}{\kappa\mathcal{T}}. \tag{75}$$

This allows us to measure κ: given the lattice extent N_σ, we scan the bare temperature $\mathcal{T}$ to determine its value $\mathcal{T}_0$ which corresponds to a physically isotropic lattice:

$$\kappa_{N_\sigma} = \frac{1}{N_\sigma\mathcal{T}_0}, \qquad \kappa = \lim_{N_\sigma\to\infty}\kappa_{N_\sigma}. \tag{76}$$

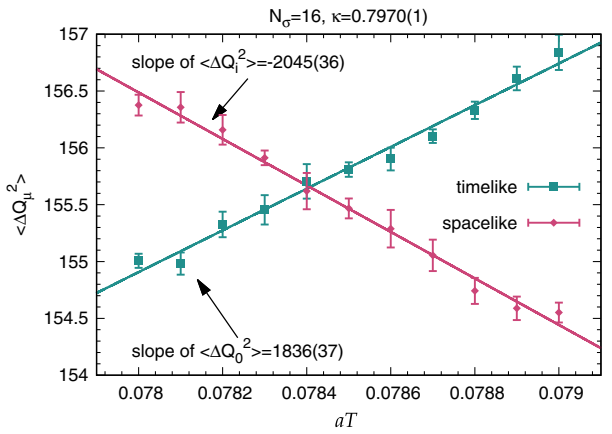

FIG. 9. Anisotropy calibration in the CT limit, measured on a lattice $16^3 \times \mathrm{CT}$, with $\mathcal{T}_0 = 0.07841(1) = \frac{1}{16\kappa}$, resulting in $\kappa = 0.7970(1)$.

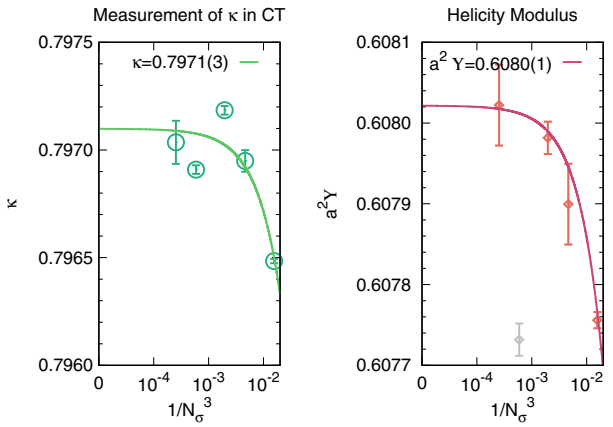

FIG. 10. Left: Thermodynamic extrapolation of anisotropy correction factor κ needed to rescale the temperature and chemical potential. The result is compared to the former result from the extrapolation of discrete time lattices (ansatz 3). Right: Thermodynamic extrapolation of the helicity modulus $a^2\Upsilon$, from which we extract the pion decay constant at zero temperature.

This calibration is shown in Fig. 9; the results for κ for various volumes are shown in Table I and its extrapolation in Fig. 10 (left). The finite size effects are very small. Note that in contrast to the previous study [31], there is no reason to distinguish κ for gauge groups U(3) and SU(3): the thermodynamic extrapolation $N_\sigma \to \infty$ coincides with the zero temperature extrapolation, and since the calibration is performed at $\mu_B = 0$, static baryons are virtually absent (see also Fig. 6). This is not the case at finite ξ (finite a_τ). As discussed in Sec. II B, the determination of κ in [31] suffers from systematic uncertainties as the extrapolation in ξ is based on rather small $\xi \leq 8$. Our final continuous time result $\kappa = 0.797(1)$ is consistent with the extrapolations, favoring ansatz 3.

In Fig. 10 (right) we show the thermodynamic extrapolation of the helicity modulus, which yields the square of the pion decay constant:

$$a^2 F_\pi^2 = \lim_{N_\sigma \to \infty} a^2 \Upsilon, \qquad a^2\Upsilon = \frac{1}{{N_\sigma}^2} \langle \mathscr{M}_0^2 \rangle|_{\mathcal{T}_0}, \tag{77}$$

resulting in $aF_\pi = 0.7797(1)$. This compares well with the extrapolation of discrete time [31] which yields $aF_\pi = 0.78171(4)$, taking into account that the extrapolation of $a^2F_\pi^2$ has similar uncertainties as κ, which are overcome by the continuous time simulations.

The method of anisotropy calibration has also been extended by us to finite quark mass [43] and recently also to finite β. These results are a clear indication that it is possible to define the continuous time limit unambiguously for finite m_q and finite β in the strong coupling regime, with $\kappa = \kappa(m_q, \beta)$.

TABLE I. The values of κ and the helicity modulus for various N_σ and the extrapolation to the thermodynamic limit, as shown in Fig. 10.

V	κ	$a^2\Upsilon$
4	0.7965(1)	0.6078(1)
6	0.7970(1)	0.6079(1)
8	0.7972(1)	0.6080(1)
12	0.7969(1)	0.6077(1)
16	0.7970(1)	0.6080(1)
∞	0.7971(3)	0.6080(1)

B. Chiral condensate and chiral susceptibility

Despite the fact that in the chiral limit, the chiral condensate is zero in a finite volume—in the dual representation this is due to the absence of monomers—it is nevertheless possible to extract the chiral condensate from the chiral susceptibility χ_σ (which is nonzero in a finite volume). The corresponding chiral perturbation theory in a finite box—the so-called ϵ-regime—is an expansion in the inverse volume [51], and for the O(2) model in $d = 4$,

$$a^6\chi_\sigma \simeq \frac{1}{2} a^6 \Sigma^2 {N_\sigma}^4 \left(1 + \frac{\beta_1}{a^2 F_\pi^2 {N_\sigma}^2} + \frac{\alpha}{2a^2 F_\pi^4 {N_\sigma}^4}\right), \tag{78}$$

$$\alpha = \beta_1^2 + \beta_2 + \frac{1}{8\pi^2} \log \frac{a\Lambda_\Sigma^2 N_\sigma}{\Lambda_M}, \tag{79}$$

where $\beta_1 = 0.140461$ and $\beta_2 = -0.020305$ are shape coefficients of a finite 4-dim box. Note that the value Σ that can be extracted from this equation corresponds to the chiral condensate in the thermodynamic limit. In Fig. 11 we show the fit according to ansatz Eq. (78) to obtain the chiral condensate from the Monte Carlo data of the chiral susceptibility for various volumes, all in the CT limit. Apart from Σ, we also treat α as a fit parameter as we do not

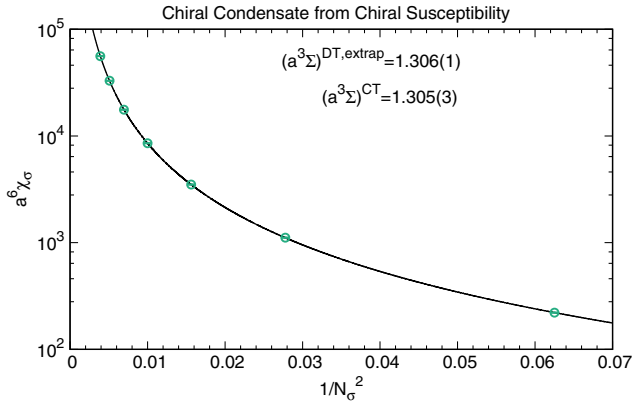

FIG. 11. The infinite volume chiral condensate obtained in the chiral limit via chiral perturbation theory in a finite box, corresponding to the ϵ-regime. In the range $1/N_\sigma{}^2$ considered here, the fit of $a^3\Sigma$ is dominated by the leading order and next to leading order term $\mathcal{O}((LF_\pi)^{-2})$.

know the values of the renormalization group invariant scales Λ_Σ and Λ_M, but it turns out that α is consistent with zero. The value of aF_π determined in the previous section is used. The thermodynamic extrapolation $N_\sigma \to \infty$ coincides with the zero temperature extrapolation as the bare temperature is set to $\mathcal{T} = (\kappa N_\sigma)^{-1}$ to always obtain a physically isotropic lattice. Our result from continuous time simulations yields $a^3\Sigma = 1.305(3)$ and agrees well with the extrapolation of the Monte Carlo data at discrete time as discussed in [31].

C. Energy and baryon mass

The baryon mass m_B is an important quantity to understand the nature of the nuclear interaction, and its value in lattice units am_B is also a good choice to scale other quantities to dimensionless ratios, such as T/m_B, μ_B/m_B. At zero temperature, where the free energy $F = E - TS$ coincides with the internal energy E, the static baryon mass in the strong coupling limit is given by the probability of a baryon to propagate in a temporal direction. This can be immediately expressed by the probability of having a static baryon in the ensemble:

$$p_B = e^{-\Delta F/T}, \qquad \Delta F = -T\log\frac{Z_B}{Z}, \qquad m_B = \lim_{T\to 0}\Delta F. \tag{80}$$

The extrapolation of the static baryon mass towards continuous time has been discussed in [31] with the result $am_B = \xi a_\tau m_B = 3.556(6) = \kappa a m_B^{\mathrm{MF}}$, $am_B^{\mathrm{MF}} = 4.553(7)$, which is about 20% larger than the isotropic value $am_B = 2.877(2)$. Since $p_B \ll 1$, the mass is evaluated via the so-called snake algorithm at discrete time:

$$\frac{Z_B}{Z} = \frac{Z_{N_\tau}}{Z_{N_\tau-2}}\frac{Z_{N_\tau-2}}{Z_{N_\tau-4}}\cdots\frac{Z_2}{Z_0}, \qquad Z_0 \equiv Z, \qquad Z_{N_\tau} \equiv Z_B$$

$$a\Delta F = \frac{\xi}{N_\tau}\log\frac{Z_B}{Z} = \frac{\xi}{N_\tau}\sum_{k=0}^{N_\tau-2}\log\frac{Z_{k+2}}{Z_k}. \tag{81}$$

The ratio $\frac{Z_{k+2}}{Z_k}$ is the probability to extend a static baryon segment of length k by two segments, and the sum results in a static baryon of length N_τ. The method unfortunately does not extend straightforwardly to continuous time: the ratios $\frac{Z_{k+2}}{Z_k}$ cannot be measured since at the end of a static baryon segment there is a finite probability that two spatial dimers are attached at the same location, in contrast to other observables discussed above (Fig. 4). However, we are able to determine the baryon mass from the energy difference based on Eq. (48):

$$\begin{aligned} a\Delta E &= aE_B - aE_0 = \Lambda_\sigma a^4(\epsilon_B - \epsilon_0) \\ &= \Lambda_\sigma\kappa\mathcal{T}(\langle n_{Ds}\rangle_0 - \langle n_{Ds}\rangle_B). \end{aligned} \tag{82}$$

The energy density at zero temperature in the CT limit, if one does not take the irrelevant constant C in Eq. (48) into account (rendering it negative), can be measured at very high accuracy:

$$a^4\epsilon_0^{\mathrm{U}(3)} = -1.82471(2), \qquad a^4\epsilon_0^{\mathrm{SU}(3)} = -1.82475(8), \tag{83}$$

where the value for gauge group U(3) (which does not have baryons) coincides with the value for gauge group SU(3) (where baryons become suppressed with decreasing temperature). The fact that $a^4\epsilon_0 = -\lim_{T\to 0} aT\langle n_{Ds}\rangle$ is finite implies that the number of spatial dimers diverges as $\propto 1/T$. Note that a previous determination of ϵ_0 at discrete time [35] includes the diverging constant: $a^4\epsilon_0 = 0.66(2)\xi$. We measured the energy density without (ϵ_0) and with a

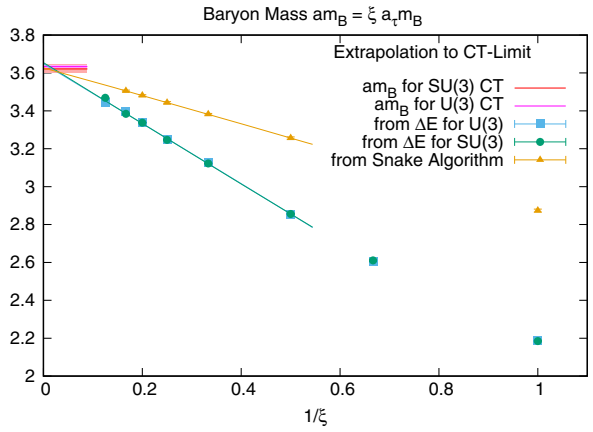

FIG. 12. The baryon mass as obtained from the valence baryon mass, and from the free energy in the zero temperature limit.

TABLE II. The baryon mass from extrapolation or direct measurement, as shown in Fig. 12. Note that ΔE has been evaluated at various temperatures and extrapolated to zero temperature. The result for the snake algorithm valid for SU(3) differs slightly from the value $am_B = 3.556(6)$ given in [31] due to the improved extrapolation used here.

Method	am_B^{extrap}	am_B^{CT}
ΔE for U(3)	3.644(20)	3.640(7)
ΔE for SU(3)	3.649(20)	3.628(22)
ΔF with snake alg.	3.627(6)	…

static baryon (ϵ_B), both on discrete and continuous time lattices. The discrete time measurements of $a\Delta E$ are extrapolated via a polynomial ansatz in $1/\xi$, as shown in Fig. 12. The fit results are summarized in Table II and are compared with the continuous time results. Indeed, we find very good agreement of all extrapolated estimates of the baryon mass with its continuous time result within errors. It should be pointed out that at $\gamma = 1$, where $\langle k_0 \rangle = \frac{N_c}{2d} = \frac{3}{8}$, the static baryon mass from ΔF (via the snake algorithm) differs substantially from the baryon mass obtained from ΔE. But towards the CT limit, both definitions agree. The extrapolation of the discrete time data (obtained from ΔE or ΔF) is in $1/\xi$ rather than $1/\xi^2$: it is more suitable as the extrapolation appears to be almost linear in $1/\xi$, but clearly there are additional uncertainties related to the derivative $d\xi/d\gamma$ that are bypassed by simulations directly in the CT limit.

We distinguish between U(3) and SU(3) results for the baryon mass: in U(3) gauge theory, there is only the valence baryon and no μ_B-dependence of the partition function, whereas SU(3) gauge theory has intrinsic baryon fluctuations. At zero temperature, those baryon fluctuations are largely suppressed. Even though U(3) gauge theory has no baryons, there is no obstacle in measuring the baryon mass in U(3) via the response of a valence baryon to the pion bath, resulting in less statistical noise. Our best estimate of the baryon mass is thus the U(3) result in the CT limit, as it does not suffer from any ambiguities due to extrapolation:

$$am_B = 3.640(7). \tag{84}$$

This baryon mass receives contributions from a pion cloud surrounding the static pointlike baryon.

V. THE SC-LQCD PHASE DIAGRAM

A. Chiral transition

In Sec. IV B we have determined the chiral condensate in the chiral limit at zero temperature. In principle this can be extended to finite temperature, and the chiral transition could be determined by the vanishing of the chiral condensate. It suffices in practice to determine the chiral transition from the chiral susceptibility, which is obtained from the worm algorithm to high precision. Also, this method readily extends to finite density: the chiral transition can be easily obtained from finite size scaling of the chiral susceptibility up to the chiral tricritical point $(a\mu_B^{\mathrm{TCP}}, aT^{\mathrm{TCP}})$. The finite size scaling of the susceptibility in the ϵ-regime is illustrated in Fig. 13 for volumes up to $64^3 \times \mathrm{CT}$ at $\mu_B = 0$. We expect critical behavior in the O(2) universality class in three dimensions, resulting the scaling law [52]

$$\lim_{L\to\infty} \chi(L, T_c) \propto L^{\gamma/\nu}, \qquad \gamma = 1.3177(5), \qquad \nu = 0.67155(27). \tag{85}$$

The result for the transition temperature is

$$\mathcal{T}_c = 1.4276(2), \qquad aT_c = \kappa \mathcal{T}_c = 1.1379(4). \tag{86}$$

We find that the specific heat is also sensitive to the chiral transition: Fig. 14 shows that a weak cusp develops in the vicinity of T_c. Although the strong coupling limit is far away from the continuum for realistic quarks, we can nevertheless compare dimensionless ratios T/m_B with continuum extrapolated ratios. With $m_B \simeq 938$ GeV and the pseudocritical crossover temperature $T_{pc} \simeq 154$ MeV [53], we find that the ratio at strong coupling and in the chiral limit is more than twice as large:

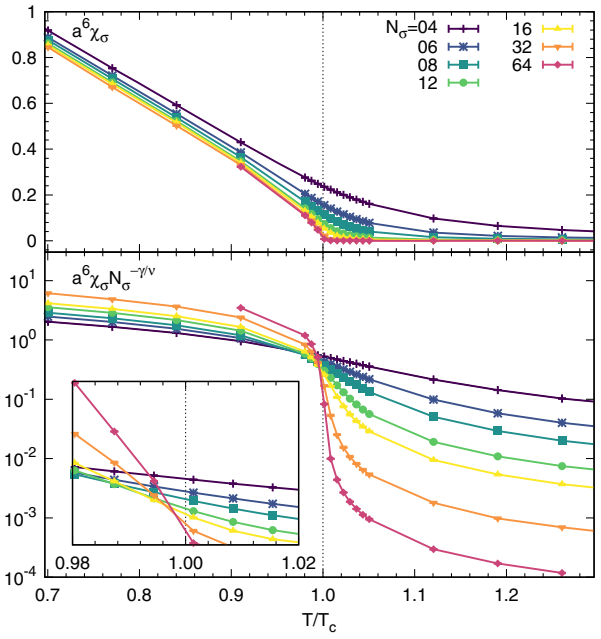

FIG. 13. Finite size scaling for the chiral susceptibility to determine the chiral transition temperature in the chiral limit. Intersections signal the chiral transition temperature $\mathcal{T}_c$. Note the chiral susceptibility is rescaled using O(2) critical exponents, and it does not develop a peak in the chiral limit.

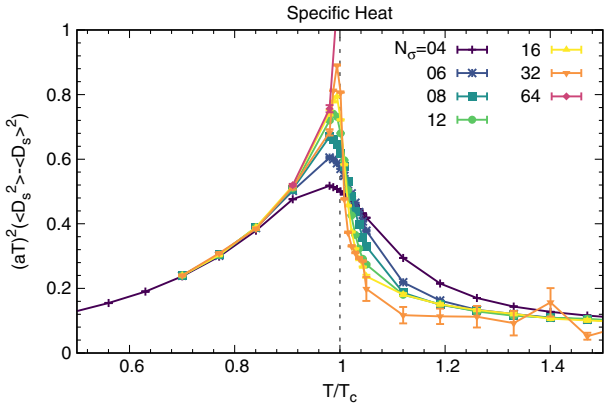

FIG. 14. Specific heat, which is proportional to the susceptibility of spatial dimers [see Eq. (48)]. The typical λ-shape is apparent in the transition region.

$$\left.\frac{T_c}{m_B}\right|_{\mathrm{CT-SC}} = 0.379(1), \qquad \left.\frac{T_{pc}}{m_B}\right|_{\mathrm{cont.}} = 0.164(9). \quad (87)$$

The comparison improves when a finite quark mass is considered at strong coupling, as the pseudocritical transition temperature drops rapidly with the mass while the baryon mass is quite insensitive [54]. We note that the continuous time transition temperature for the U(3) gauge group and its comparison with the $N_\tau \to \infty$ extrapolation have been discussed in [39], with $\mathcal{T}_c^{\mathrm{U}(3)} = 1.8843(1)$.

The determination of aT_c at finite chemical potential is straightforward up to the tricritical point. Figure 15 illustrates the chiral susceptibility χ_σ in the full μ_B-T plane. The second order chiral phase transition turns into a first order

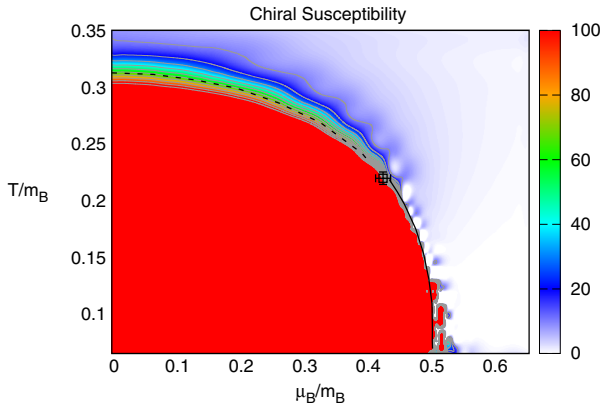

FIG. 15. The chiral susceptibility in the full μ_B-T plane on an $8^3 \times \mathrm{CT}$ lattice, also indicating the first order (solid) and second order (dashed) lines and the location of the tricritical point, obtained from finite size scaling according to Eq. (85). The chiral susceptibility diverges in the chirally broken phase but is much smaller in the chirally restored phase. Along the first order transition which is strong already for $aT < 0.7$ and hinders reliable results below $\mathcal{T} < 0.3$, artificial wiggles appear due to hysteresis of the overlapping low and high density branches.

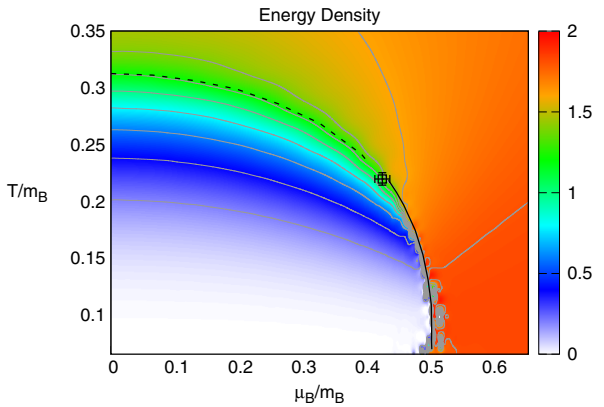

FIG. 16. The energy density in the full μ_B-T plane on an $8^3 \times \mathrm{CT}$ lattice. It is sensitive to the chiral transition. It also shows a strong first order behavior and at low temperatures becomes insensitive to the chemical potential below μ_B^{1st}.

one for $\mu_B > \mu_B^{\mathrm{tric}}$, and the chiral susceptibility—which is $\propto \langle(\bar{\psi}\psi)^2\rangle$ in the chiral limit—behaves as an order parameter and develops a gap. There is no backbending of the first order transition, in contrast to discrete time (due to saturation of spatial dimers, $N_{Ds} \leq N_c\Omega/2$), which has been discussed in [31]. Similarly, the energy density $\epsilon(T) - \epsilon_0$ can be measured in the full μ_B-T plane, as shown in Fig. 16. For small chemical potential and for temperatures below T_c, it behaves according to the Stefan-Boltzmann law [55]:

$$\epsilon(T) - \epsilon_0 = \sigma T^4, \qquad \sigma = \frac{\pi^2}{30}, \quad (88)$$

which corresponds to an ideal pion gas and has already been discussed at zero chemical potential for discrete time [35]. At zero temperature, the energy density jumps at the first order transition to the finite value $-\epsilon_0$ given in Eq. (83), which is the maximal value corresponding to the absence of spatial dimers.

B. Nuclear transition

Strong coupling lattice QCD exhibits not only spontaneous chiral symmetry breaking and its restoration along a second and first order boundary, but also a nuclear liquid gas transition signaled by the baryon density. In order to determine the first order transition line in the phase diagram, we measure the baryon density and its susceptibility, both by direct simulations at finite chemical potential and by the Wang-Landau method explained in Sec. III D. The baryon density in the μ_B-T plane is shown in Fig. 17. The volumes considered are $4^3 \times \mathrm{CT}$, $6^3 \times \mathrm{CT}$ and $8^3 \times \mathrm{CT}$ at low temperatures and additionally $12^3 \times \mathrm{CT}$, $16^3 \times \mathrm{CT}$ in the vicinity of the chiral tricritical point. Simulations at low temperatures across the first order transition are challenging: for $\mu_B < \mu_B^{\mathrm{1st}}$, the phase is

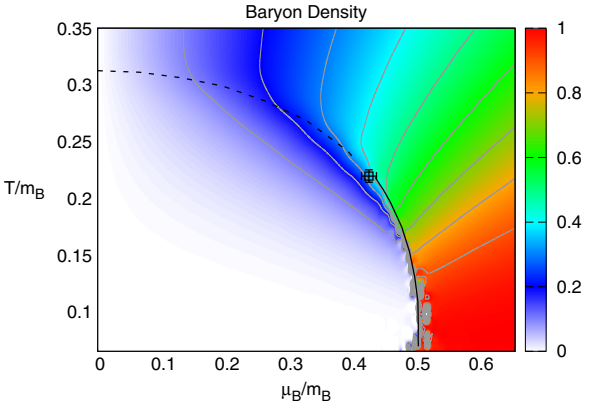

FIG. 17. The baryon density in the full μ_B-T plane on a $8^3 \times \mathrm{CT}$ lattice. It also shows a strong first order behavior and at low temperatures becomes insensitive to the chemical potential below $\mu_B^{1\mathrm{st}}$, which is known as the Silver Blaze property. The first order line terminates in a critical end point which coincides with the chiral tricritical point. The baryon density is not sensitive to the second order chiral transition.

described as an ideal pion gas; for $\mu_B > \mu_B^{1\mathrm{st}}$, the phase is that of a baryon crystal (liquid), resulting in a large latent heat. In a Monte Carlo simulation, tunneling between the phases is exponentially suppressed by the volume, and hysteresis between the low and high density phases shows up. This difficulty is overcome by the Wang-Landau method: in Fig. 18 we show the logarithmic density of states for $\mathcal{P}$-polymer and baryon number, and in Fig. 19 the density of states is applied to recover the baryon density via Eq. (58). We find that the full first order nuclear transition coincides with the chiral first order transition. The determination of $\mu_B^{1\mathrm{st}}$ and the boundaries of the mixed phase is illustrated in Fig. 20 for various volumes. The result of the thermodynamic extrapolation according to

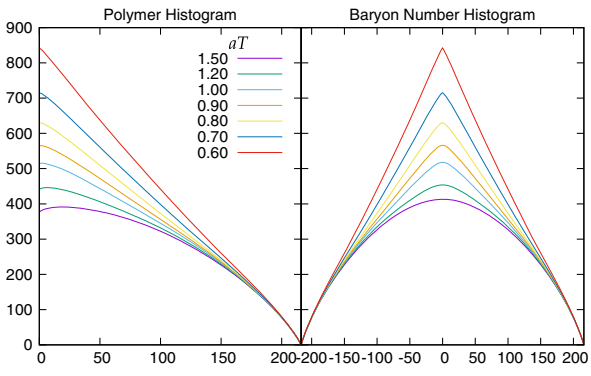

FIG. 18. The logarithmic density of states for $\mathcal{P}$-polymers $\ln g(P)$ (left) and baryon number $\ln g(B)$ (right) on a $6^3 \times \mathrm{CT}$ lattice, obtained via the Wang-Landau method for various temperatures $\mathcal{T}$. For all temperatures, the accuracy was set to $f_{\mathrm{final}} = 10^{-8}$ and the flatness condition is $\delta = 0.1$, see Eq. (65).

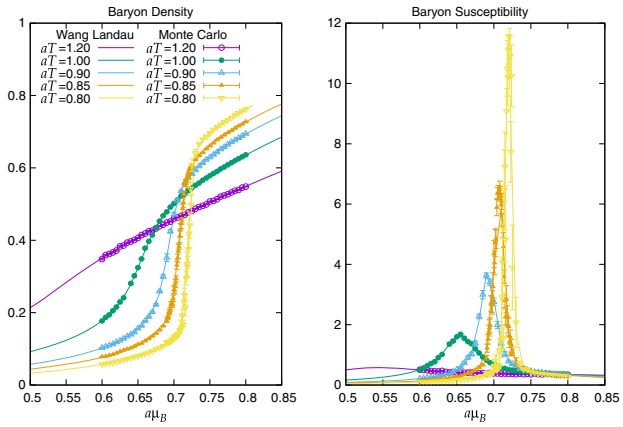

FIG. 19. Comparison of the Wang-Landau method with Monte Carlo data from CT-WA for baryonic observables. Left: The baryon density $a^3\langle n_B\rangle$. Right: The baryon susceptibility $a^6\Lambda_\sigma(\langle n_B^2\rangle - \langle n_B\rangle^2)$. All data are shown as a function of μ_B for various temperatures $\mathcal{T}$ and on a $6^3 \times \mathrm{CT}$ lattice. The Monte Carlo data are in perfect agreement with the more precise data from the density of states. The error bands are obtained by 10 independent Wang-Landau simulations and are too small to be visible.

$$\mu_B{}^{1\mathrm{st}}(N_\sigma) = \mu_B{}^{1\mathrm{st}} + cN_\sigma{}^{-3},$$
$$a^3 n_B^{(i)}(N_\sigma) = a^3 n_{B,c}^{(i)} + \tilde{c}N_\sigma{}^{-1} \quad (i = 1, 2), \tag{89}$$

based on the volumina with $N_\sigma = 4,\ 6,\ 8$ (which is sufficient due to the strong first order behavior) is given in Table III. Even though we cannot get lower than

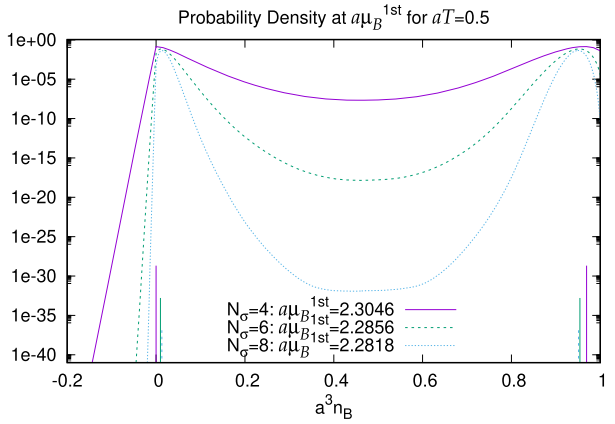

FIG. 20. The probability density, obtained from reweighting the density of states to $a\mu_B^{1\mathrm{st}}(N_\sigma)$ such that the two maxima are of the same height, for various volumes and at a fixed temperature $\mathcal{T} = 0.5$. The first maximum denotes the baryon density $a^3 n_B^{(1)}$ where the mixed phase in the canonical phase diagram begins. The second maximum denotes the baryon density $a^3 n_B^{(2)}$ where the mixed phase ends. These peak densities are indicated as vertical lines. They have been extrapolated to the thermodynamic limit and the results are given in Table III.

TABLE III. Result of the thermodynamic extrapolation of ${\mu_B}^{1st}$, $a^3 n_B^{(1)}$ and $a^3 n_B^{(2)}$ according to Eq. (89) for various bare temperatures $\mathcal{T}$.

$\mathcal{T}$	${\mu_B}^{1st}$	$a^3 n_B^{(1)}$	$a^3 n_B^{(2)}$
0.4	2.301(7)	0.0037(9)	0.967(2)
0.5	2.2784(4)	0.0275(3)	0.931(1)
0.6	2.2538(1)	0.0059(1)	0.8632(6)
0.7	2.2102(1)	0.0979(1)	0.741(3)
0.75	2.1800(3)	0.149(1)	0.675(1)
0.8	2.1444(2)	0.192(1)	0.6062(7)
0.85	2.1037(4)	0.2685(9)	0.535(1)
0.9	2.0587(3)	0.3535(1)	0.4796(3)
0.92	2.0395(2)	0.399(1)	0.455(1)
0.95	2.009(2)	0.415(1)	0.454(4)

$\mathcal{T} = 0.3$ ($T/m_B = 0.066$), we can attempt a zero temperature extrapolation which yields

$$a\mu_B^{1st} = \kappa {\mu_B}^{1st} = 1.86(2), \qquad {\mu_B}^{1st} = 2.34(3), \tag{90}$$

which is not very different from the discrete time determination $a\mu_B^{1st} = 1.78(1)$ valid for isotropic lattices, $\gamma = 1$ [29]. Nuclear matter at strong coupling is in fact a quark saturated phase: the baryon density at zero temperature jumps from $\langle n_B \rangle = 0$ to the maximal value $\langle n_B \rangle = 1$, where every lattice site is occupied by a static baryon. It is no coincidence that chiral symmetry is restored in the nuclear phase: mesons cannot occupy baryonic sites, leaving no room for spontaneous chiral symmetry breaking. Away from the strong coupling limit, where baryons are no longer pointlike and become spread over several lattice spacings, the nuclear phase may have a nonvanishing chiral condensate.

We want to conclude this section by quantifying the interaction strength between baryons. In the CT limit we find

$$\frac{m_B - \mu_B^{1st}}{m_B} \simeq 0.489(6), \tag{91}$$

which should be compared to the discrete time ($\gamma = 1$) ratio [29]

$$\frac{m_B - \mu_B^{1st}}{m_B} \simeq 0.381(3). \tag{92}$$

Hence, the nuclear interactions are enhanced in the CT limit.

C. SC-LQCD phase diagram

We now want to summarize the previous results on the chiral and nuclear transitions and establish the phase boundaries of both the grand-canonical and canonical phase diagrams, shown in Fig. 21. In the grand-canonical phase diagram, one can clearly see that the chiral first order phase boundary and the nuclear transition (obtained from the Wang-Landau method, see Table III) are on top. In the canonical phase diagram, a mixed phase of both nuclear gas and liquid gas persists. The low density boundary $a^3 n_B^{(1)}$ tends to zero, whereas the high density boundary $a^3 n_B^{(2)}$ tends to 1. A meaningful density of nuclear matter cannot be assigned at strong coupling.

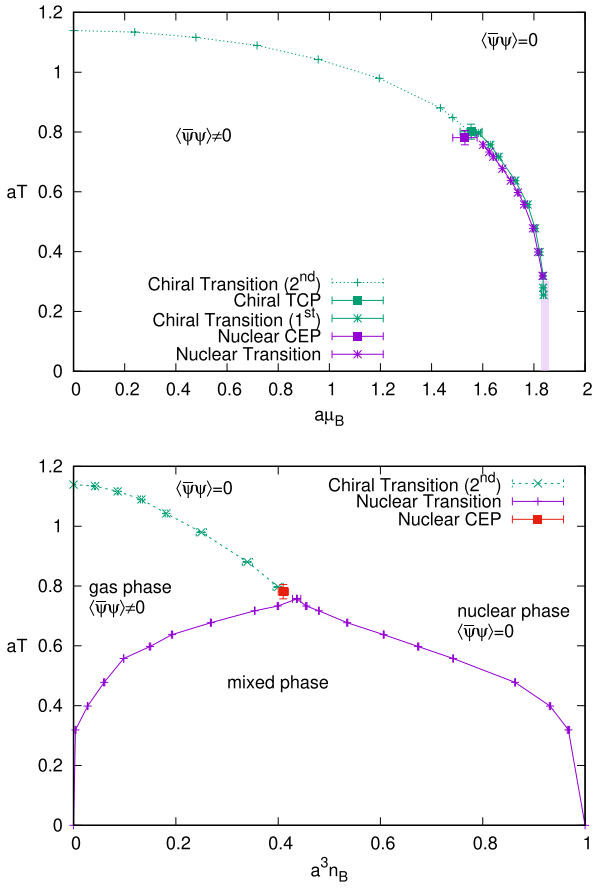

FIG. 21. The SC-QCD phase diagrams in the continuous time and the chiral limit. Results on the chiral transition are obtained via the worm algorithm CT-WA, and the first order nuclear transition is obtained via the Wang-Landau method. Top: The grand-canonical phase diagram in the $a\mu_B$-aT plane. The chiral and nuclear first order transitions are on top within errors. Bottom: The grand-canonical phase diagram in the $a^3 n_B$-aT plane. Note that at zero temperature the mixed phase extends to the maximal value $a^3 n_B = 1$ where Pauli saturation takes place.

There are various strategies to locate the chiral tricritical point, which is characterized as the end point of a triple first order line where the three phases cease to coexist (the nuclear phase and two chirally broken phases for positive and negative quark mass). According to the Gibbs' phase rule, the upper critical dimension is 3, such that the tricritical exponents are analytic:

$$\gamma = 1, \qquad \nu = \frac{1}{2}. \tag{93}$$

To distinguish tricritical second order behavior from O(2) critical behavior, Eq. (85), large volumes are required. There is a better strategy, based on the fact that the tricritical point coincides with the nuclear critical end point (which can be made plausible via a percolation analysis, see Sec. IX C). This is clearly only expected in the strong coupling limit, but it also holds for small values of β at finite N_τ [56]. The nuclear end point is characterized by the vanishing of the mixed phase, resulting in $n_B^{(1)} = n_B^{(2)}$. The corresponding density of states becomes flat as the double peak structure vanishes. Our best estimate for the tricritial point in the CT limit is

$$aT^{\mathrm{TCP}} = 0.78(2), \qquad a\mu_B^{\mathrm{TCP}} = 1.53(5),$$
$$a^3 n_B^{\mathrm{TCP}} = 0.43(2). \tag{94}$$

If one does not take into account the rescaling with κ, then $\mathcal{T}^{\mathrm{TCP}} = 0.98(3)$ and ${\mu_B}^{\mathrm{TCP}} = 1.92(6)$ compare quite well with their determination on a disrete lattice: $\mathcal{T}_{N_\tau=4}^{\mathrm{TCP}} = 0.94(7)$, $\mu_{B N_\tau=4}^{\mathrm{TCP}} = 1.92(9)$ [37], indicating that the N_τ corrections are small up to the critical point and only become large at lower temperatures [31]. We also note that the mean field tricritial point deviates substantially: $\mathcal{T}_{\mathrm{MF}}^{\mathrm{TCP}} = 0.866$, $\mu_{B\,\mathrm{MF}}^{\mathrm{TCP}} = 1.731$ [57]. As soon as a small finite mass is introduced, the chiral tricritical point turns into a chiral critical end point of a Z(2) universality class. Close to the chiral limit, we estimate

$$\mu_B^{\mathrm{CEP}}/T^{\mathrm{CEP}} \simeq \mu_B^{\mathrm{TCP}}/T^{\mathrm{TCP}} = 1.96(7), \tag{95}$$

which may in principle be within reach with conventional hybrid Monte Carlo, based on a fermion determinant such as Taylor expansion [58]. But with increasing quark mass the ratio $\mu_B^{\mathrm{CEP}}/T^{\mathrm{CEP}}$ also increases rapidly ($a\mu_B^{\mathrm{CEP}}$ increases whereas aT^{CEP} decreases), as has been studied for discrete time in [54]. The critical end point is quickly out of reach for methods of circumventing the sign problem via HMC methods. In the Appendix E we elaborate further on the prospects of finite quark masses in the continuous time limit.

Our new results eliminate systematic uncertainties in previous findings in Monte Carlo for fixed N_τ [29].

D. Extension to imaginary chemical potential

Lattice QCD at imaginary chemical potential is usually considered because in contrast to nonzero real chemical potential, the fermion determinant is sign-problem free and it allows us to analytically continue to real chemical potential [2]. It is also interesting in its own right due to the Roberge-Weiss periodicity [59] and the Roberge-Weiss transition [60].

In the dual representation of SC-LQCD at discrete time, it is not straightforward to simulate at imaginary chemical potential. However, at continuous time where baryons are static, we can use $\cosh(i\mu_B^{\mathrm{im}}/T) = \cos(\mu_B^{\mathrm{im}}/T)$, and with the $\mathcal{P}$- and $\mathcal{Q}$-polymer resummation (see Sec. III D):

$$\cos(\mu_B^{\mathrm{im}}/T) \geq 0 \quad \text{for} \quad \mu_B^{\mathrm{im}}/T \leq \frac{\pi}{2}$$
$$N_c + 1 + 2\cos(\mu_B^{\mathrm{im}}/T) \geq 0 \quad \text{for all} \quad \mu_B^{\mathrm{im}}/T. \tag{96}$$

The second equation enables us to measure the chiral transition for arbitrary imaginary chemical potential. Our result is shown in Fig. 22. At the Roberge-Weiss point $\mu_B^{\mathrm{im}}/T = \pi$ we do not find a cusp, in contrast with what would be expected at weak coupling. We also cannot observe a first order transition in the chiral observables, which is expected as the partition function becomes analytic in the high temperature limit. By integrating out the gauge links, the center sectors are no longer distinct. Gauge observables such as the Polyakov loop should be able to signal a first order transition between the center sectors at high temperatures, which requires that one includes a gauge correction. We also want to note that the point at $\mu_B^{\mathrm{im}}/T = \pi/2$ is special as it corresponds to the U(3) transition temperature $\mathcal{T} = 1.8843(1)$ (as discussed in [39]) as $\mathcal{P}$-polymers have weight $w_p = 0$ according to Eq. (53).

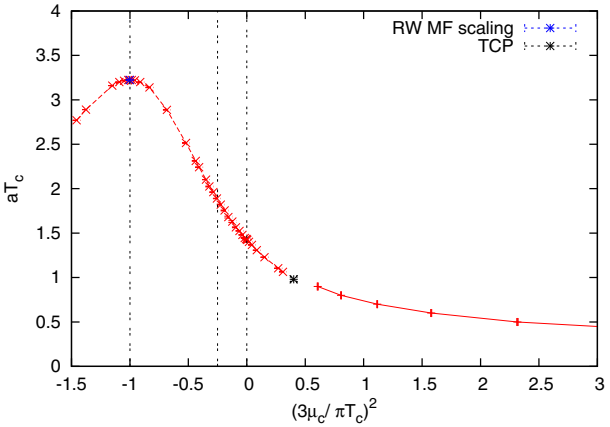

FIG. 22. Extension of the phase diagram to imaginary chemical potential. The chiral transition has the Roberge-Weiss periodicity. The transition at the Roberge-Weiss point $(\mu_B/(\pi T)) = -1$ has a mean-field scaling behavior at strong coupling, but no signature of a first order transition. The second vertical line at $(\mu_B/(\pi T)) = -1/4$ is characterized by the absence of a baryon, resulting in a U(3) gauge theory.

VI. TAYLOR EXPANSION AND RADIUS OF CONVERGENCE

A. Taylor expansion

The dual representation of SC-LQCD is a great laboratory to benchmark other methods to circumvent the sign problem. One of the prominent methods in the context of lattice QCD is the Taylor expansion [3], which might allow

us to estimate the location of a possible chiral critical end point based on estimates for the radius of convergence of the Taylor series. The standard thermodynamic observable that is Taylor expanded for that purpose is the pressure. This requires high orders of the Taylor series to be included in the expansion, but the current state of the art is limited to 6th order (improved action) [58] and 8th order (unimproved action) [61]. It turns out that due to the continuous time limit and by taking into account both the polymer resummations and histogram method presented in Sec. III D, we are able to determine higher orders of Taylor coefficients, both for the pressure and the baryon susceptibility. The Taylor expansion of the pressure Eq. (52) at fixed temperature and about $\mu_B = 0$, where only even orders contribute, is given by

$$p = \frac{T}{V}\log\mathcal{Z} = p(T,\mu_B=0) + \sum_{n=1}^{\infty} c_{2n}\left(\frac{\mu_B}{T}\right)^{2n}$$
$$c_{2n} = \frac{T}{V}\frac{1}{(2n)!}\frac{\partial^{2n}\log\mathcal{Z}}{\partial(\mu_B/T)^{2n}} = \frac{T}{V}\frac{1}{(2n)!}\kappa_{2n}(\omega)\Lambda_\sigma{}^{2n} \qquad (97)$$

where the cumulants κ_n are defined in terms of the moments of the winding number ω via a cumulant-generating function $K(t)$:

$$M(t=\mu_B/T) = \langle e^{t\omega}\rangle = \sum_{r=0}^{\infty}\mu_r\frac{t^r}{r!},$$
$$\mu_m = \left.\frac{d^m M}{dt^m}\right|_{t=0} = \langle\omega^m\rangle,$$
$$K(t) = \log(M(t)) = \sum_{r=0}^{\infty}\kappa_r\frac{t^r}{r!}. \qquad (98)$$

We can measure all Taylor coefficients from the baryon density fluctuations, as $a^3 n_B = \langle\omega\rangle$ according to Eq. (47). We also obtain immediately from the Taylor coefficients of the pressure c_{2n} those of the baryon susceptibility:

$$\chi_B = \frac{\partial^2}{\partial(\mu_B/T)^2}p = \sum_{n=2}^{\infty} n(n-1)c_{2n}\left(\frac{\mu_B}{T}\right)^{2n-2}. \qquad (99)$$

A comparison of discrete and continuous time evaluations of the first cumulants as shown in Fig. 23 demonstrates the cumulants are less noisy in the CT limit. But it further requires the polymer resummations and histogram method to determine the higher order cumulants up to κ_{12}, shown in Fig. 24. From a thermodynamic extrapolation of the inflection points, we obtain an estimate for T_c consistent with its determination in Sec. V A.

A comment on the definition of the pressure used in this section is in order: we have previously discussed that Eq. (52) is only valid in homogeneous systems, as is expected for the continuum limit of lattice QCD. In the strong coupling limit this is not the case. We can however only measure the pressure defined by a volume derivative

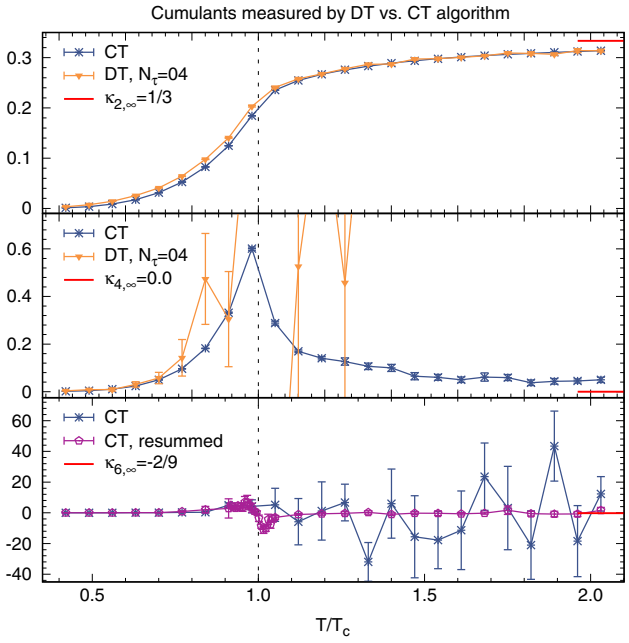

FIG. 23. Measurement of the cumulants κ_2 (top), κ_4 (center) and κ_6 (bottom) as a function of the temperature, comparing DT and CT results. Clearly, the continuous time cumulants are less noisy. Also indicated is the analytic value in the high temperature limit.

according to Eq. (49) in terms of dual variables, and it is of course possible to Taylor expand the spatial dimer density $\langle n_{Ds}\rangle$ as well. But this definition is proportional to the energy density and shows a gap along the first order

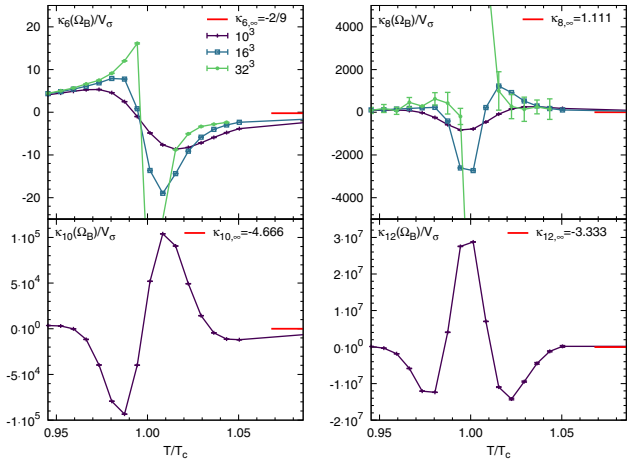

FIG. 24. Measurement of the cumulants κ_6 (top left), κ_8 (top right), κ_{10} (bottom left) and κ_{12} (bottom right) as a function of the temperature in the vicinity of T_c for volume 10^3 or greater. Due to resummations and histogram methods explained in Sec. III D, we are able to get the corresponding Taylor coefficients c_{2n} completely under control. The number of extrema and inflection points increases with the order. Also indicated is the high temperature limit.

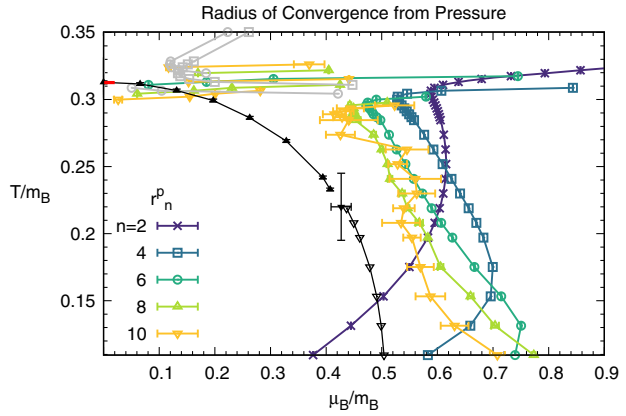

FIG. 25. Radius of convergence, estimated from the pressure, Eq. (100). The data in gray above T_c correspond to imaginary chemical potential $i\mu_B$.

transition. In contrast, Eq. (97) is well behaved as it is proportional to the thermodynamic potential $F = -T \log \mathcal{Z}$, which is continuous along any transition.

B. Estimates for the radius of convergence

We are now in a position to estimate the radius of convergence [62] from these Taylor coefficients:

$$\rho = \lim_{n\to\infty} r_n^p = \lim_{n\to\infty} r_{2n}^{\chi_B}$$
$$r_n^p = \sqrt{\left|(n+2)(n+1))\frac{\kappa_n}{\kappa_{n+2}}\right|},$$
$$r_n^{\chi_B} = \sqrt{\left|n(n-1)\frac{\kappa_n}{\kappa_{n+2}}\right|}. \tag{100}$$

The corresponding results for the various n are given in Figs. 25 and 26, where the radii are plotted within the phase diagram. Above aT_c, the radius becomes imaginary (indicated in gray). Note that we are still in the chiral limit where the whole phase boundary is either second or first order.

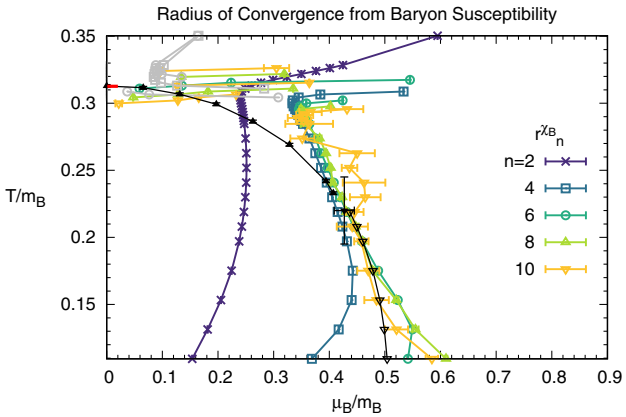

FIG. 26. Radius of convergence, estimated from the baryon susceptibility, Eq. (100). It converges faster to the first order phase boundary compared to that of the pressure.

Hence, we expect that the radius of convergence drops to zero at aT_c. Below aT_c, the first singularity is given by the phase boundary, and we indeed find that the higher orders converge to the phase boundary. This is in particular observed for $r_n^{\chi_B}$, where the first order line is well approximated for $n = 10$.

VII. TEMPORAL CORRELATORS AND MESON POLE MASSES

A. Staggered Euclidean time correlators

We have explained in Sec. III that the monomer two-point correlation function is sampled during worm evolution. We are mainly interested in temporal correlation functions, from which we can extract the ground state energy corresponding to the meson pole mass. In this section we will explain how to extract them and discuss their dependence on temperature and baryon chemical potential.

The basic definition of the temporal correlators at zero momentum $\vec{p} = 0$ for staggered fermions $\bar{\chi}, \chi$, based on the local single-time-slice operators [63], is

$$C_S(\tau) = \sum_{\vec{x}} C_S(\vec{x}, \tau),$$
$$C_S(\vec{x}, \tau) = \langle \bar{\chi}_{\vec{0},0} \chi_{\vec{0},0} \bar{\chi}_{\vec{x},\tau} \chi_{\vec{x},\tau} \rangle g^S_{\vec{x},\tau}, \tag{101}$$

where the spin S of the meson is given by the kernel operators Γ^S in terms of phase factors $g^S_{\vec{x},\tau} \in \{\pm 1\}$. We will only consider operators that are diagonal in spin-taste space: $\Gamma^S \otimes \Gamma^T$ with $\Gamma^T = \Gamma^{S*}$. We will not consider any flavor structure as $N_f = 1$ (but see Appendix D for $N_f = 2$). In every mesonic correlator specified by Γ^S, there is a nonoscillating part and an oscillating part with additional phase factor $(-1)^\tau$, which is due to the even-odd decomposition for staggered fermions. This parity partner has opposite spin, parity and taste content. Thus the nonoscillating and oscillating parts correspond to different physical states; see Table IV. Of particular interest is the pion π_{PS} which is the Goldstone boson for the residual chiral symmetry, Eq. (8). Throughout the worm evolution, monomer two-point correlation functions are accumulated whenever the head and tail are at opposite parities:

TABLE IV. Table of mesonic operators for staggered fermions that are diagonal in the spin-taste basis $\Gamma^S \otimes \Gamma^T$ and the corresponding physical states. The oscillating and nonoscillating states within the same g^S_x are distinguished.

	$\Gamma^S \otimes \Gamma^T$		J^{PC}		Physical states	
$g^S_{\vec{x},\tau}$	NO: 1^τ	O: $(-1)^\tau$	NO	O	NO	O
1	$1 \otimes 1$	$\gamma_0\gamma_5 \otimes (\gamma_0\gamma_5)^*$	0^{++}	0^{-+}	σ_S	π_A
$(-1)^{x_i}$	$\gamma_i\gamma_5 \otimes (\gamma_i\gamma_5)^*$	$\gamma_i\gamma_0 \otimes (\gamma_i\gamma_0)^*$	1^{++}	1^{--}	a_A	ρ_T
$(-1)^{x_j+x_k}$	$\gamma_j\gamma_k \otimes (\gamma_j\gamma_k)^*$	$\gamma_i \otimes \gamma_i^*$	1^{+-}	1^{--}	b_T	ρ_V
$(-1)^{x_i+x_j+x_k}$	$\gamma_0 \otimes \gamma_0^*$	$\gamma_5 \otimes (\gamma_5)^*$	0^{+-}	0^{-+}	$-_V$	π_{PS}

$$C_S(\vec{x}_H - \vec{x}_T, \tau_H - \tau_T) = C_S(\vec{x}, \tau) = N_c \frac{O(C_S(\vec{x}, \tau))}{Z}, \tag{102}$$

with Z the number of worm updates. Such worm estimators are incremented as

$$O(C_S(\vec{x}, \tau)) \to O(C_S(\vec{x}, \tau)) + f g^S_{\vec{x},\tau} \delta_{x_T, x_1} \delta_{x_H, x_2},$$

$$\begin{aligned} f &\equiv f(\gamma), \qquad \tau \in [0, 1, \ldots N_\tau] \quad \text{(discrete time)}, \\ f &\equiv f(T), \qquad \tau \in [0, \mathcal{T}^{-1}] \quad \text{(continuous time)}, \end{aligned} \tag{103}$$

with $f(\gamma)$ given in Eq. (41) and $f(T)$ given in Eq. (42). Summing over the correlators immediately yields the corresponding discrete or continuous time susceptibilities:

$$a^6 \chi_S^{\mathrm{DT}} = \frac{1}{N_\sigma{}^3 N_\tau} \sum_{\vec{x},\tau} C_S(\vec{x}, \tau), \tag{104}$$

$$a^6 \chi_S^{\mathrm{CT}} = \frac{\mathcal{T}}{N_\sigma{}^3} \sum_{\vec{x}} \int_0^{1/\mathcal{T}} d\tau C_S(\vec{x}, \tau). \tag{105}$$

The nonoscillating and oscillating parts of the correlators for discrete time,

$$\begin{aligned} C(\tau) &= C_{\mathrm{NO}}(\tau) + (-1)^\tau C_{\mathrm{O}}(\tau), \\ C_{\mathrm{NO}}(\tau) &= A_{\mathrm{NO}} \cosh(a_\tau M_{\mathrm{NO}}(\tau - N_\tau/2)), \\ C_{\mathrm{O}}(\tau) &= A_{\mathrm{O}} \cosh(a_\tau M_{\mathrm{O}}(\tau - N_\tau/2), \end{aligned} \tag{106}$$

are shown in Fig. 27. It is advantageous to consider the linear combinations

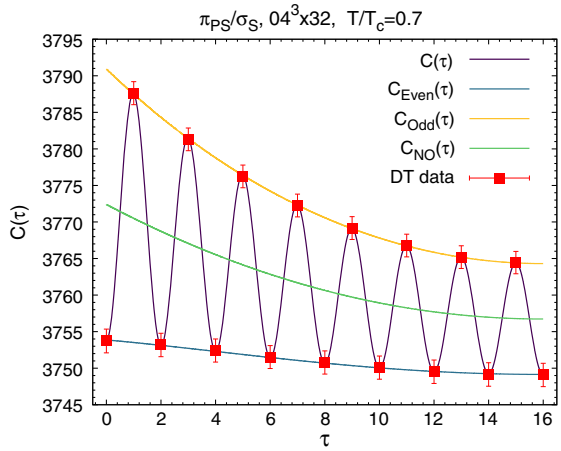

FIG. 27. Discrete time pion correlator for $N_\tau = 32$ at $T/T_c = 0.7$, showing the oscillating behavior, and the decomposition into even and odd contributions, according to Eq. (107). The fit $C(\tau)$ is reconstructed from the fits $C_{\mathrm{Even}}(\tau)$ and $C_{\mathrm{Odd}}(\tau)$.

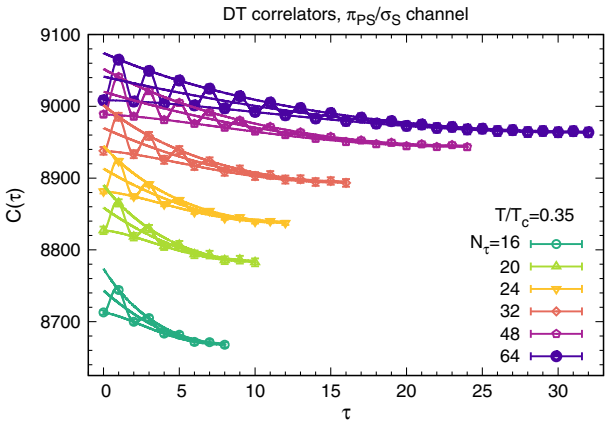

FIG. 28. Discrete time pion correlators for various N_τ, showing that the oscillatory behavior persists for larger N_τ, with a well-behaved continuous time limit.

$$\begin{aligned} C_{\mathrm{Odd}}(\tau) &= C_{\mathrm{NO}} + C_{\mathrm{O}}, \\ C_{\mathrm{Even}}(\tau) &= C_{\mathrm{NO}} - C_{\mathrm{O}}, \end{aligned} \tag{107}$$

and fit the even or odd correlators instead: (1) the fit is more stable, and (2) it generalizes to the continuous time limit, where we can distinguish even and odd τ via emission and absorption events; see Sec. II C. We can reconstruct the physical states by inverting Eq. (107). The discrete time correlators for the pion are shown in Fig. 28. We observe that the correlators for increasing N_τ become more continuous, and their range extends to $N_\tau/2$. In Fig. 29, the continuous time correlators for the pion π_{PS} are reconstructed from

$$\begin{aligned} C_\pi(\tau) &= \frac{1}{2}(C_{\mathrm{Odd}}(\tau) - C_{\mathrm{Even}}(\tau)) \\ &= A_\pi \cosh(M_\pi/T(\tau - 1/2)) \end{aligned} \tag{108}$$

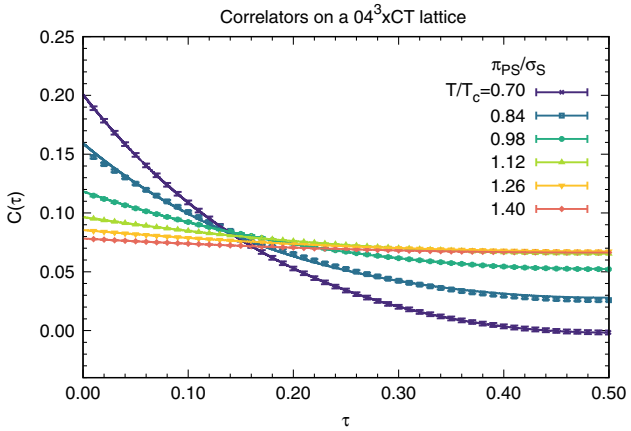

FIG. 29. Continuous time pion correlator fitted according to Eq. (108), for various temperatures, on the full range in Euclidean time τ, for $N = 100$ bins. This is sufficient to extract the pole masses $M_\pi(T)$ to high precision.

with $\tau \in [0, 1/2]$ and spatial kernel $g_{\vec{x}}^{\pi} = (-1)^{x+y+z}$, and likewise for other mesons. This requires bookkeeping of which events contribute to C_{Odd} or C_{Even}, which depends on whether the worm head is located at an absorption event $x_H \in \mathcal{A}$ or an emission event $x_H \in \mathcal{E}$.

Even in the CT limit, it is necessary to discretize the temporal correlators, due to memory limitations and finite statistics. The histograms will depend on the bin size

$$\Delta\tau = \frac{1}{\mathcal{T}N}, \tag{109}$$

with N the number of bins. The finer $\Delta\tau$, the less events are placed in each bin, which makes the determination of the correlator more difficult. On the other hand, the coarser $\Delta\tau$, the less data are available to reconstruct the correlator. In principle, one could measure the continuous time correlators without introducing a binning [64], but in practice, this seems unnecessary as our measurements for $N = 100, 200, 400$ lead to almost identical results.

B. Temperature and density dependence of meson pole masses

Since temporal correlators are measured at zero spatial momentum, the extracted meson masses are pole masses: $E_0(\vec{p} = 0) = M$. We extract the ground state mass M as the dimensionless quantity M/T by multistate fits (including excited states) and by varying the fit range $[\tau_{\mathrm{min}}/\mathcal{T}, 1/(2\mathcal{T})]$. To obtain good balance between the required number of states and the error estimation, we apply the Aikaike information criterion [65]. We adjust τ_{min} to be most sensitive to the mass plateau. To compare discrete time (where we extract $a_\tau M$) to continuous time, we convert via

$$M/T = N_\tau a_\tau M, \qquad aM = \kappa\mathcal{T}M/T, \tag{110}$$

as shown in Fig. 30. Making use of the same fitting scheme, the error bars for the extracted pole masses from CT correlators are much smaller than the corresponding DT correlators. Moreover, the uncertainties when extrapolating DT correlators of about 3% are circumvented.

We have measured the temperature dependence of the pole masses and found that, in particular, the pion becomes heavy at the chiral transition; see Fig. 32. For $N_f = 1$ we find a mass degeneracy for the pairs of states:

$$\begin{aligned} &\sigma_S \leftrightarrow \pi_{PS}, \qquad \pi_A \leftrightarrow -_V, \\ &b_T \leftrightarrow \rho_T, \qquad a_A \leftrightarrow \rho_V, \end{aligned} \tag{111}$$

which corresponds to a multiplication by the parity $\epsilon(x)$, compare Table IV. This is due to the strong coupling and the chiral limit (i.e., we are in the ϵ-regime): e.g., the pion π_{PS} is mass degenerated with the sigma meson σ_S. This degeneracy is lifted as soon as $am_q > 0$; see Appendix E.

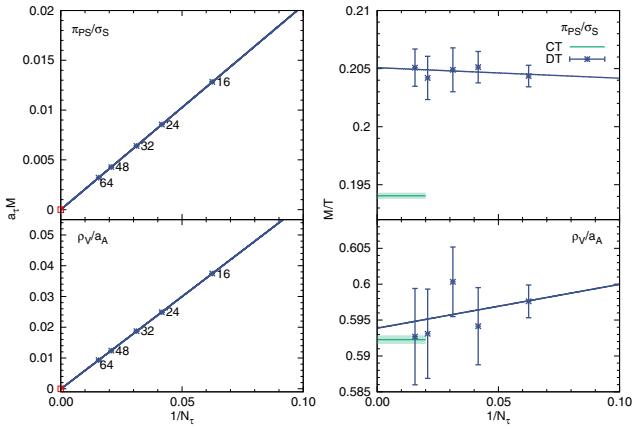

FIG. 30. Pole masses for $\mathcal{T} = 1.8$. Left: Extrapolation of the pion pole masses extracted from discrete time correlators to the continuous time limit. Right: Comparison of the discrete time pole masses to the continuous time pole mass (green band) in units M/T, rescaled via Eq. (110). The discrepancy for the pion mass (top) of about 3% may stem from uncertainties of distinguishing the ground states from the excited states at rather small N_τ. The continuous time pole masses have much smaller statistical errors compared to discrete time.

The pion indeed becomes massless below T_c in the thermodynamic limit, as seen in Fig. 31. But the pion and all other mesons do not acquire a thermal mass, as shown in Fig. 32. Rather, they all tend to the same high temperature value $aM = 0.527(2)$. We suspect that this is an artifact of the strong coupling limit: even at high temperatures, in the chirally restored phase, the quarks are still confined to mesons. Hence, they do not experience the antiperiodic boundary conditions [66] and will not receive contributions from the lowest Matsubara frequencies πT above T_c.

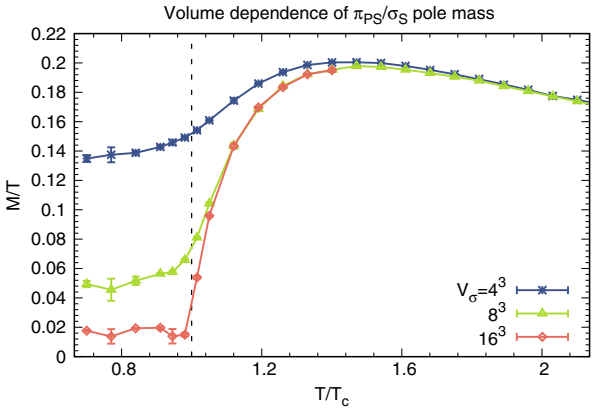

FIG. 31. Pole masses M/T as a function of temperature, for different volumes but the same channel π_{PS}/σ_S, measured in continuous time. Due to finite volume effects, the pion mass is not strictly zero in the chiral limit (ϵ-regime).

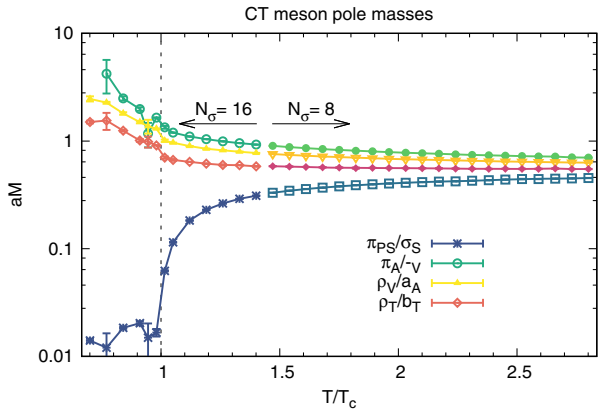

FIG. 32. Pole masses aM for various quantum numbers J^{PC} as a function of the temperature, measured in the CT limit. The mass degeneracies are given in (111). We observe an imprint of the chiral transition on the pole masses (based on $N_\sigma = 16$), and the convergence to the same value $aM = 0.411(1)$ in the large temperature limit (based on $N_\sigma = 8$).

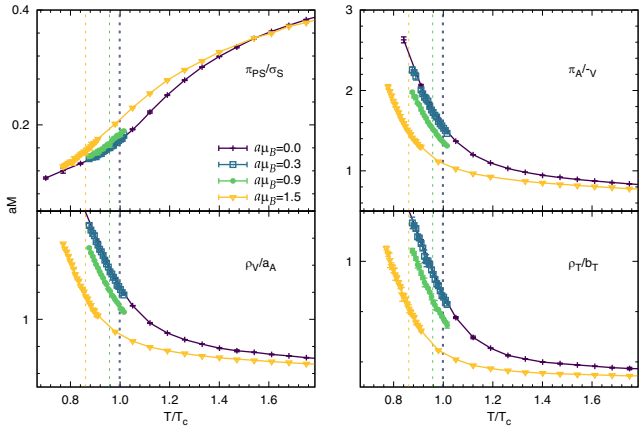

FIG. 33. Pole masses aM for various chemical potentials μ_B, as a function of the temperature. The vertical dashed lines indicate the transition temperatures for the chemical potentials considered. At high temperatures, the dependence on the chemical potential becomes weaker.

The extension to finite chemical potential μ_B is straightforward; the results on the temperature dependence of the pole masses for various chemical potentials below ${\mu_B}^{\mathrm{TCP}}$ are shown in Fig. 33. The pole masses change most at the transition temperature for the respective chemical potential. Their high temperature limits become independent of the chemical potential.

VIII. CONCLUSION

We have demonstrated the power of continuous time simulations of lattice QCD in the strong coupling limit, which makes extrapolations for $N_\tau \to \infty$ obsolete. All ambiguities arising from such an extrapolation are removed. The Hamiltonian formulation gives further insight into the world-line formulation of strong coupling lattice QCD. We discussed in detail the continuous time worm algorithm in terms of a Poisson process, the dual observables, and resummation and histogram techniques to determine the phase diagram both in the μ_B-T plane and n_B-T plane via the Wang-Landau method. The phase boundary can be compared with estimates from the radius of convergence from Taylor coefficients which we can determine via baryon fluctuations at zero density up to c_{12}. We have also investigated temporal correlation functions, which we can measure with high resolution and higher statistics compared to discrete time, and from which we could determine the temperature dependence of the meson pole masses, both at zero and nonzero density. Whether the continuous time correlation functions can also be extended on the Schwinger-Keldysh contour to extract transport coefficients is under investigation. Real time simulations in the dual formulation of SC-LQCD are not completely sign-problem free, but they are much less severe compared to the standard formulation based on the fermion determinant.

Some first steps to extend our Hamiltonian formulation to more flavors and finite quark mass are presented in the Appendix E. We plan to include the gauge corrections from the Wilson gauge action in continuous time in a similar way as we have already successfully implemented in discrete time [15,17,67]. As the continuous time limit is well defined also at finite lattice gauge coupling β, we may improve on the phase diagram by reducing the spatial lattice spacing directly in the continuous time limit via quantum Monte Carlo simulations.

ACKNOWLEDGMENTS

W. U. is grateful to Philippe de Forcrand for providing the initial idea to consider the continuous time limit and is thankful for the many discussions on the continuous time formulation. We would like to thank our colleagues Olaf Kaczmarek and Sören Schlichting for discussions of some aspects related to Euclidean correlators, Christian Schmidt for discussions on Taylor expansion, Owe Philipsen for discussions on the canonical phase diagram, and Jangho Kim for his contributions to our code for discrete time. For the extraction of pole masses from temporal correlators, we are thankful to Hauke Sandmeyer for providing numerical tools. We acknowledge contributions from Aaron von Kamen (on the Wang-Landau method) and Ferdinand Jünnemann (on percolation) to this project. The authors gratefully acknowledge the funding of this project by computing time provided by the Paderborn Center for Parallel Computing (PC). This work is supported by the Deutsche Forschungsgemeinschaft (DFG) through the Emmy Noether Program under Grant No. UN 370/1 and through the CRC-TR 211 "Strong-interaction matter under extreme conditions," Project No. 315477589 TRR 211.

APPENDIX A: DERIVATION OF THE CONTINUOUS EUCLIDEAN TIME LIMIT

In this section we explain how to derive Eq. (29) from Eq. (27). We start from the discrete partition function for gauge group U(N_c), neglecting the baryonic part for a moment. We have to investigate what sequence of vertices is admissible on each site and at the same time conserves the pion current.

We will use the vertices in the meson occupation numbers and introduce the shorthand notation

$$\hat{v}(k|l|m) \equiv \hat{v}(k|l)\hat{v}(l|m). \tag{A1}$$

We classify admissible sequences via the length of the interval: whether it is even or odd. This is determined by the sequence of emission sites $\mathcal{E}$ or absorption sites $\mathcal{A}$. The discussion applies to $N_c = 3$ but generalizes straightforwardly to odd N_c. For even N_c, the meson state $m = N_c/2$ needs a special treatment, which will not be address here. We distinguish via even-odd parity:

(1) *Odd intervals* are those where an $\mathcal{A}$ site is followed by an $\mathcal{E}$ site, or an $\mathcal{E}$ site is followed by an $\mathcal{A}$ site:

$$\begin{aligned} &\hat{v}(0|1|0), \quad \hat{v}(1|2|1), \quad \hat{v}(2|3|2), \\ &\hat{v}(1|0|1), \quad \hat{v}(2|1|2), \quad \hat{v}(3|2|3), \end{aligned} \tag{A2}$$

which is exactly the case when we have two subsequent ⌞-vertices or two subsequent ⊤-vertices.

(2) *Even intervals* are those where an $\mathcal{A}$ site is followed by an $\mathcal{A}$ site, or an $\mathcal{E}$ site is followed by an $\mathcal{E}$ site:

$$\begin{aligned} &\hat{v}(0|1|2), \quad \hat{v}(1|2|3), \\ &\hat{v}(3|2|1), \quad \hat{v}(2|1|0), \end{aligned} \tag{A3}$$

which is exactly the case when a ⌞-vertex is followed by a ⊤-vertex or vice versa.

Since N_τ is even, the number of odd intervals must be an even number. Also, on each site, the number of $\mathcal{E}$ sites equals the number of $\mathcal{A}$ sites. Any CT configuration $\mathcal{G}$ with N_c odd is completely determined by specifying the location and kind of vertices and whether an interval is even or odd: an interval between two vertices of the same type is always of odd length; between two different vertices it is of even length.

If we now consider a spatial bond given by the nearest-neighbor pair $b = \langle \vec{x}, \vec{y} \rangle$ such that there is at least one spatial dimer on b, then the sequence of $\mathcal{E}$ sites and $\mathcal{A}$ sites is exactly opposite if we ignore vertices which do not belong to dimers on b (see Fig. 2). This implies that it is completely determined by the type of vertex whether we have an even or odd interval. The first dimer on b can be put on any of the N_τ temporal locations, but the second dimer can only be put on $N_\tau/2$ locations, and all subsequent spatial dimers $(N_\tau - k)/2$ on temporal locations. Given that the maximal number of spatial dimers is given by the order in $\mathcal{O}(\gamma^{-n_b})$, in the limit $N_\tau \to \infty$ the probability of two spatial dimers on b to be at the same location (effectively forming a double dimer) is zero, and we can disregard the finite N_τ corrections $N_\tau - k$. In this limit, we have $N_\tau (N_\tau/2)^{k_b}$ possible temporal locations. However, we have not yet considered symmetry factors, as in the above argument, the spatial dimers added to the bond are not time ordered. Time ordering is however a global aspect that cannot be considered in isolation of a single bond. If we force the whole set of spatial dimers with $n = \sum_b n_b$ to be time ordered, we have to divide by $n!$ as only one of the permutations is a time-ordered sequence. Another way to see how the symmetry factor arises from time ordering for $N_\tau \to \infty$ with $t \mapsto \tau/N_\tau$, $\tau \in [0, 1[$ is to replace the sums by integrals:

$$\begin{aligned} &\int_0^1 d\tau_1 \int_{\tau_1}^1 d\tau_2 \ldots \int_{\tau_{k-1}}^1 d\tau_k w(\tau_1, \tau_2, \ldots \tau_k) \\ &\quad = \frac{1}{n!} \int_0^1 d\tau_1 \int_0^1 d\tau_2 \ldots \int_0^1 d\tau_k w(\tau_1, \tau_2, \ldots \tau_k) \end{aligned} \tag{A4}$$

where t_i is the temporal location of the ith spatial bond. This holds because the weight $w(t_1, t_2, \ldots t_k)$ does not depend on the locations but just on the number of vertices that appear. We conclude that the total weight of a U(3) configuration is

$$\sum_{n \in 2\mathbb{N}} \frac{1}{n!} \left(\frac{N_\tau/2}{\gamma^2} \right)^n \sum_{\mathcal{G} \in \Gamma_n} v_{⌞}^{N_{⌞}(\mathcal{G})} v_{⊤}^{N_{⊤}(\mathcal{G})} \tag{A5}$$

where Γ_n is the set of topologically inequivalent configurations (which differ in the distribution of ⌞- and ⊤-vertices over sites). In summary, a CT-configuration $\mathcal{G}$ is completely determined by specifying whether the intervals between vertices are even or odd, up to translation by a_τ which corresponds to time reversal,

$$\mathcal{T}: \; m \mapsto N_c - m, \qquad \mathcal{G} \in \Gamma_n \mapsto \mathcal{G}^{\mathcal{T}} \in \Gamma_n \tag{A6}$$

with equal weight: $w(\mathcal{G}) = w(\mathcal{G}^{\mathcal{T}})$. With $N_\tau/\gamma^2 = 1/\mathcal{T}$ we arrive at the mesonic part of the continuous time partition function Eq. (29).

It remains to discuss the baryonic part of the partition function. Since baryons form self-avoiding loops, it suffices to note that spatial baryon hoppings are suppressed by γ^{-N_c}. Hence, for $N_c \geq 3$ spatial hoppings are essentially absent as $\gamma \to \infty$ and baryons become static. This does not happen for $N_c = 1$ (electrons) and $N_c = 2$ (diquarks). In physical terms, only for $N_c \geq 3$ is the baryon heavy and nonrelativistic. Hence, a baryon-antibaryon pair cannot be created from the vacuum.

APPENDIX B: ANALYTIC RESULT FOR U(1)

We have derived an analytic expression for strong coupling U(1) on $2 \times N_\tau$ lattices for arbitrary values of N_τ and γ^2, enabling us to obtain the continuous time result. A generalization to SU(N_c) is not straightforward. The continuous time assumption that spatial dimers with spatial multiplicity $k_i > 1$ are suppressed is (trivially) exact in U(1).

The partition function in the chiral limit for U(1) can be derived from considering all spatial dimers, making use of the fact that the interval length in units of a_τ between subsequent spatial dimers must be odd:

$$\mathcal{Z}_0(\gamma, N_\tau) = \gamma^{2N_\tau}\left(4 + \sum_{n\in 2\mathbb{N}^+}^{N_\tau} 2^n \alpha_n(N_\tau)\gamma^{-2n}\right),$$

$$\alpha_n(N_\tau) = \frac{2}{n!}\prod_{k=0}^{n/2-1}\left(\left(\frac{N_\tau}{2}\right) - k^2\right) = \frac{N_\tau}{n}\binom{(N_\tau+n)/2-1}{n-1}. \tag{B1}$$

Note that n always has to be even as spatial hoppings have to come in pairs to be consistent with the boundary conditions in time. The factor 2^n is due to the fact that each spatial dimer can hop either in the forward or backward direction due to the periodic boundary conditions in space. Note that we have not approximated α_n by $\frac{2}{n!}(\frac{N_\tau}{2})^{n/2}$, as we did in the steps leading to Eq. (A5).

We also want to consider the contribution to the partition sum with a total number of two monomers. For lattices with spatial extent $N_\sigma = 2$, the situation is considerably simple because it is not possible to separate the monomers by spatial dimers. If we decompose configurations into a piece with monomers but no spatial hoppings, and a piece with no monomers, where the first piece has length D and the second piece has length $N_\tau - D$, we can factorize the possible configurations by considering those on the $2 \times D$ lattice and the $2 \times (N_\tau - D)$ lattice where it is required that we not use periodic boundary conditions. This restricts the possible configurations further (no temporal dimers connecting the first and the last site allowed). Note that D may be odd or even, depending on whether the two monomers are on the same spatial site (D even) or on different spatial sites (D odd). The corresponding result in the 2-monomer sector is

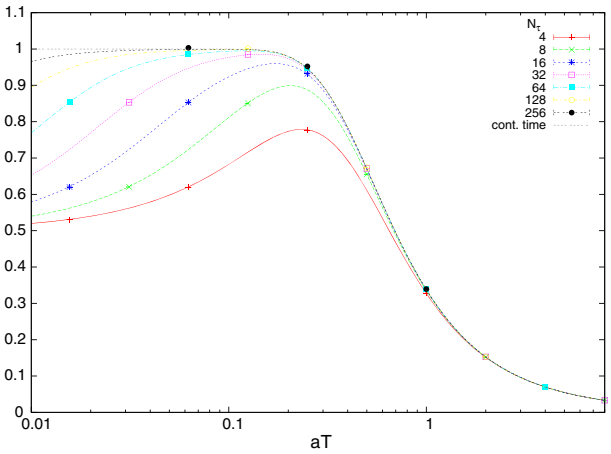

FIG. 34. Chiral susceptibility for the U(1) gauge group at strong coupling as a function of $\mathcal{T}$. Monte Carlo data from the worm algorithm (both discrete and continuous time) are compared to the analytic results, Eqs. (B3) and (B4). Note that the discretization errors are maximal in the low temperature region.

$$\mathcal{Z}_2(\gamma, N_\tau) = \gamma^{2N_\tau-2}\left(\left(\frac{N_\tau}{2}\right)^2(4 + 2N_\tau\gamma^{-2}) + 2N_\tau \sum_{n\in\mathbb{N}^+}^{N_\tau-2} 2^n \sum_{D=1}^{N_\tau-n} \tilde{\alpha}_n(N_\tau - D)\beta(D)\gamma^{-2n-2(D \bmod 2))}\right),$$

$$\tilde{\alpha}_n(C) = \begin{cases} \binom{(C+n-4)/2}{n-2} & \text{for } C \text{ even} \\ \binom{(C+n-3)/2}{n-1} & \text{for } C \text{ odd,} \end{cases} \qquad \beta(D) = \frac{1}{4}\begin{cases} \frac{1}{2}D(D+2) & \text{for } D \text{ even} \\ (D+1)^2 & \text{for } D \text{ odd.} \end{cases} \tag{B2}$$

Both $\mathcal{Z}_0$ and $\mathcal{Z}_2$ are divergent series in γ, but their ratio is not; it gives the chiral susceptibility in the chiral limit:

$$\chi(\mathcal{T}, N_\tau) = \frac{1}{N_\tau}\frac{\mathcal{Z}_2(\sqrt{\mathcal{T}N_\tau}, N_\tau)}{\mathcal{Z}_0(\sqrt{\mathcal{T}N_\tau}, N_\tau)} = \frac{1}{2}\tanh\left(\frac{N_\tau}{2}\operatorname{arcsch}(N_\tau\mathcal{T})\right)\left(\frac{1}{\sqrt{1+(N_\tau\mathcal{T})^{-2}}} + \tanh\left(\frac{N_\tau}{2}\operatorname{arcsch}(N_\tau\mathcal{T})\right)\right) \tag{B3}$$

where we have used the definition of $\mathcal{T}$, Eq. (17). This result is explicitly temperature dependent, with N_τ quantifying the cutoff dependence. In the limit $N_\tau \to \infty$, $\operatorname{arcsch}(x) \simeq 1/x$, and the chiral susceptibility has a well-defined continuous time limit:

$$\chi(\mathcal{T}) = \frac{1}{2}\tanh\left(\frac{1}{2\mathcal{T}}\right)\left(1 + \tanh\left(\frac{1}{2\mathcal{T}}\right)\right). \tag{B4}$$

In Fig. 34 the agreement of Monte Carlo data with the exact result is shown, both at finite N_τ and continuous time.

APPENDIX C: MEAN FIELD AND PERCOLATION ANALYSIS

The mean-field analysis for SC-LQCD based on a $1/d$ expansion has been studied for many decades [20–26,57]. Also, the continuous time partition function derived here can be used as a starting point for a mean-field analysis. Our mean-field analysis assumes that a single site only couples to a mean-field bath of spatial dimers, where the location of $\mathcal{E}$ sites and $\mathcal{A}$ sites on its $2d$ nearest neighbors does not matter. This is well justified at high temperatures, where bonds with spatial dimers are isolated but may also hold approximately at lower temperatures. Our partition sum has only one dynamical site, and all other sites have a fixed number of vertices determined by a self-consistency relation. Neglecting the baryon sector, the resulting partition function in the d spatial dimension is

$$\mathcal{Z}_{\mathrm{MF}}(\mathcal{T}) = \exp\frac{\Lambda_\sigma d(1+v_{\mathsf{T}})}{2\mathcal{T}}. \tag{C1}$$

This implies, for the energy density,

$$a^4\epsilon_{\mathrm{MF}} = \frac{\mathcal{T}}{\Lambda_\sigma}\frac{\partial}{\partial\mathcal{T}^{-1}}\log\mathcal{Z}_{\mathrm{MF}}(\beta) = \frac{d(1+v_{\mathsf{T}})}{2}, \tag{C2}$$

resulting in $a^4\epsilon_{\mathrm{MF}} = \frac{3}{2}+\sqrt{3}$ which should be compared to the discrete time value $a^4\epsilon = \frac{3}{4}$ at $\gamma = 1$.

A qualitative understanding of the phase diagram can also be obtained via a percolation analysis on the spatial volume. We consider mixed percolation, both on bonds and sites [68]:

(1) In the chirally broken phase, the pion correlation length diverges; thus, the phase is characterized by bond percolation, where a bond is activated whenever there is at least one spatial dimer at that bond (for some time location). It can be related to the average bond occupation probability $\theta \simeq p_{\mathrm{bond}}$ with

$$\theta = \frac{1}{\Lambda_\sigma^M}\sum_{b\in\Lambda_\sigma^M}\langle\theta(n_b)\rangle, \qquad \theta(n_b) = \begin{cases} 0 & n_b = 0 \\ 1 & n_b > 0. \end{cases} \tag{C3}$$

(2) In the nuclear phase, where every site is activated if it is occupied by a baryon or an antibaryon ($\mathcal{P}$-polymer), it can be related to the average site occupation probability, $\langle n_{\mathcal{P}}\rangle \simeq p_{\mathrm{site}}$.

Our criterion for percolation is that in the statistical average, the probability that a cluster spans around the periodic lattice in at least one spatial direction is close to 1. The percolation threshold is characterized by a step function in the thermodynamic limit. Clearly, at low temperatures, the vacuum phase is characterized by bond percolation, and the nuclear phase is characterized by site percolation. At higher temperatures, we may have a phase where bond and site percolation coexist. It turns out that this mixed phase exists along the first order transition. The percolation threshold for each bond and site percolation is reached close to the tricritical point; see Fig. 35. It is not surprising that the identification of the bond occupation probability with θ works extremely well, as the pions form a free relativistic gas [35]. In contrast, the identification of p_{site} with the baryon density is not as good, as they do not form a free gas but are subject to strong nuclear interactions.

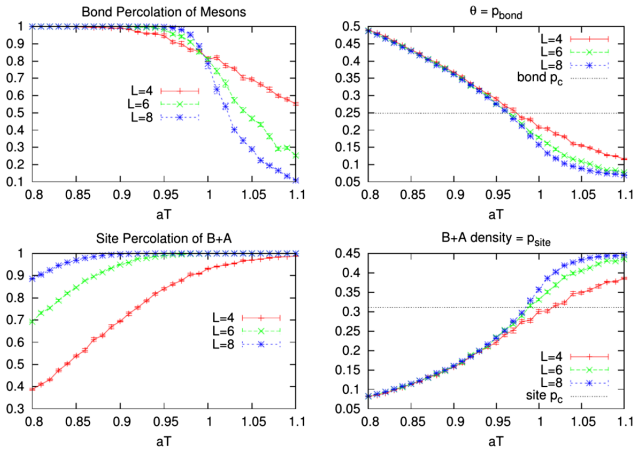

FIG. 35. Percolation analysis at $\mu_B = 0.65$ (close to the tricritical value). Left: Volume dependence of percolation for mesons (top) and $\mathcal{Q}$-polymers (bottom). Right: Comparison with percolation theory, where the critical percolation thresholds are known (for $d = 3$, on bonds: $p_c = 0.2488$; on sites: $p_c = 0.3116$), indicated as dashed lines. If the observable θ is taken to be p_{bond} and the density of $\mathcal{Q}$-polymers as p_{site}, the critical percolation value is obtained close to $\mathcal{T}^{\mathrm{TCP}} = 1.005(25)$.

APPENDIX D: CONTINUOUS TIME LIMIT FOR $N_f = 2$

The two-flavor formulation admits more than one baryon per site, and the Grassmann constraint allows for pion exchange between them, modifying nuclear interactions substantially. It also compares better to the strong coupling limit with Wilson fermions in a world-line formulation, as discussed in the context of Polyakov effective theory [69] which integrates out the spatial but not the temporal gauge links. SC-LQCD with $N_f = 2$ in the dual formulation has been discussed on discrete lattices for the U(1) gauge group in [70]. For the U(3) gauge group, the link integrals have been addressed in [37]. Here, we report on first steps towards a Hamiltonian formulation. The suppression of spatial bonds γ^{-k}, $k > 2$ also applies here. Let us first consider the static lines. We want to establish the basis of quantum states that generalize the $N_f = 1$ states $|m\rangle$ and $|\ell\rangle$. To arrive at this basis, we consider the SU(3) one-link integrals [71]:

$$\mathcal{J}(\mathcal{M},\mathcal{M}^\dagger)=\int_{\mathrm{SU}(3)} dU e^{\mathrm{tr}[U\mathcal{M}^\dagger+U^\dagger\mathcal{M}]}=2\sum_{n_0,n_1,n_2,n_3=0}^{\infty}\frac{1}{(n_0+n_1+2n_2+3n_3+2)!(n_0+n_2+2n_3+1)!}\prod_{k=0}^{3}\frac{x_i^{n_k}}{n_k!}$$
$$x_0=\det[\mathcal{M}]+\det[\mathcal{M}^\dagger],\qquad x_1=\mathrm{tr}[\mathcal{M}\mathcal{M}^\dagger],\qquad x_2=\frac{1}{2}(\mathrm{tr}[\mathcal{M}\mathcal{M}^\dagger]-\mathrm{tr}[(\mathcal{M}\mathcal{M}^\dagger)^2]),$$
$$x_3=\frac{1}{6}(\mathrm{tr}[\mathcal{M}\mathcal{M}^\dagger]^3-3\mathrm{tr}[\mathcal{M}\mathcal{M}^\dagger]\mathrm{tr}[(\mathcal{M}\mathcal{M}^\dagger)^2]+2\mathrm{tr}[(\mathcal{M}\mathcal{M}^\dagger)^3])=\det[\mathcal{M}\mathcal{M}^\dagger] \tag{D1}$$

with $\mathcal{M}$ the quark matrix. The color trace tr can be converted to a sum over colors and a flavor trace Tr:

$$\mathrm{tr}[(\mathcal{M}\mathcal{M}^\dagger)^k]=(-1)^{k+1}\mathrm{Tr}[(M_xM_y)^k],\qquad M_z=\begin{pmatrix}\bar{u}u_z & \bar{u}d_z\\ \bar{d}u_z & \bar{d}d_z\end{pmatrix}. \tag{D2}$$

The sum over n_i $(i=0,\ldots 3)$ terminates due to the Grassmann integration. The corresponding invariants x_i can be evaluated for $N_f=2$:

$$\begin{aligned}
x_0&=B_{uuu}+B_{uud}+B_{udd}+B_{ddd}+\bar{B}_{uuu}+\bar{B}_{uud}+\bar{B}_{udd}+\bar{B}_{ddd}\\
x_1&=\mathrm{Tr}[M_xM_y]=k_U+k_D+k_{\pi^+}+k_{\pi^-}\\
x_2&=\frac{1}{2}(\mathrm{Tr}[M_xM_y]^2+\mathrm{Tr}[(M_xM_y)^2])=x_1^2+x_S\\
x_3&=\frac{1}{6}(\mathrm{Tr}[M_xM_y]^3+3\mathrm{Tr}[M_xM_y]\mathrm{Tr}[(M_xM_y)^2]+2\mathrm{Tr}[(M_xM_y)^3])=x_1^3+\frac{3}{2}x_1x_S\\
x_S&=k^{(2)}_{\pi^+\pi^-,UD}+k^{(2)}_{UD,\pi^+\pi^-}-k_Uk_D-k_{\pi^+}k_{\pi^-},
\end{aligned} \tag{D3}$$

with the fluxes and dimers defined as

$$\begin{aligned}
B_{uud}&=\bar{u}\,\bar{u}\,\bar{d}_xuud_y, & B_{udd}&=\bar{u}\,\bar{d}\,\bar{d}_xudd_y, & B_{uuu}&=\bar{u}\,\bar{u}\,\bar{u}_xuuu_y, & B_{ddd}&=\bar{d}\,\bar{d}\,\bar{d}_xddd_y,\\
\bar{B}_{uud}&=uud_x\bar{u}\,\bar{u}\,\bar{d}_y, & \bar{B}_{udd}&=udd_x\bar{u}\,\bar{d}\,\bar{d}_y, & \bar{B}_{uuu}&=uuu_x\bar{u}\,\bar{u}\,\bar{u}_y, & \bar{B}_{ddd}&=ddd_x\bar{d}\,\bar{d}\,\bar{d}_y,\\
k_U&=\bar{u}u(x)\bar{u}u(y), & k_D&=\bar{d}d(x)\bar{d}d(y), & k_{\pi^+}&=\bar{d}u(x)\bar{u}d(y), & k_{\pi^-}&=\bar{u}d(x)\bar{d}u(y),\\
k^{(2)}_{\pi^+\pi^-,UD}&=\bar{u}d(x)\bar{d}u(x)\bar{u}u(y)\bar{d}d(y), & k^{(2)}_{UD,\pi^+\pi^-}&=\bar{u}u(x)\bar{d}d(x)\bar{u}d(y)\bar{d}u(y).
\end{aligned} \tag{D4}$$

Note that the baryonic fluxes are spinless, and spin arises only when measuring baryonic correlators with the corresponding staggered kernels. We still have to integrate out the Grassmann variables to obtain the quantum states in the occupation number basis, and the corresponding Hamiltonian, where we consider the chiral limit only. The Grassmann constraint then dictates that all quarks u,d and antiquarks $\bar{u},\bar{d}$ are within mesons or baryons. The Grassmann integral in the chiral limit is

$$I_G=\int\prod_\alpha[\mathrm{d}u_\alpha\mathrm{d}\bar{u}_\alpha\mathrm{d}d_\alpha\mathrm{d}\bar{d}_\alpha](\bar{u}u)^{k_U}(\bar{d}d)^{k_D}(\bar{u}d)^{k_{\pi^-}}(\bar{d}u)^{k_{\pi^+}}=(-1)^{\frac{k_{\pi^+}+k_{\pi^-}}{2}}(N_c!)^2\begin{cases}1 & (k_{\pi^+}+k_{\pi^-})/2 \bmod N_c=0\\ \frac{1}{N_c} & \text{otherwise}\end{cases} \tag{D5}$$

which simplifies due to flux conservation:

$$k_{\pi^+}=k_{\pi^-},\qquad k_U+k_D+k_{\pi^+}+k_{\pi^-}=N_c. \tag{D6}$$

Just as for $N_f=1$, we can define vertices in the same way as in Eq. (24). This allows us to compose them into line segments between spatial dimer emission in terms of alternating dimers of k_U, k_D, oriented fluxes k_{π^+}, k_{π^-}, B_{uuu}, $\bar{B}_{uuu}$, etc., or combinations thereof. We note that there are various ways to combine the link states in Eq. (D4): in particular, the flavor singlet dimer combinations k_Uk_D, $k_{\pi^+}k_{\pi^-}$, $k^{(2)}_{\pi^+\pi^-,UD}$ and $k^{(2)}_{UD,\pi^+\pi^-}$ mix and have to be resummed. We do so by defining the matrix in the basis of this order to determine what meson states survive:

$$\Pi_0=\begin{pmatrix}\frac{4}{3} & -\frac{2}{3} & -\frac{\sqrt{2}}{3} & \frac{2\sqrt{2}}{3}\\ -\frac{2}{3} & \frac{4}{3} & \frac{2\sqrt{2}}{3} & -\frac{\sqrt{2}}{3}\\ \frac{2\sqrt{2}}{3} & -\frac{\sqrt{2}}{3} & -\frac{1}{3} & \frac{2}{3}\\ -\frac{\sqrt{2}}{3} & \frac{2\sqrt{2}}{3} & \frac{2}{3} & -\frac{1}{3}\end{pmatrix}. \tag{D7}$$

TABLE V. All 92 possible quantum states for the $N_f = 2$ Hamiltonian formulation with the SU(3) gauge group. The states and their multiplicities are given for the sector specified baryon number B and isospin number I, and meson occupation number m. Note the mesonic particle-hole symmetry $m \leftrightarrow (N_f - |B|)N_c - m$, which corresponds to the shift symmetry by a_τ.

B	I	$m=0$	$m=1$	$m=2$	$m=3$	$m=4$	$m=5$	$m=6$	Σ
-2	0	$\bar{p}\,\bar{n}$							1
-2	Σ	1	0	0	0	0	0	0	1
-1	$\frac{3}{2}$	$\bar{B}_{uuu}$	$\bar{B}_{uuu}\pi_D$	$\bar{B}_{uuu}\pi_D^2$	$\bar{B}_{uuu}\pi_D^3$				4
-1	$+\frac{1}{2}$	$\bar{B}_{uud}$	$\bar{B}_{uud}(\pi_U,\pi_D)$	$\bar{B}_{uud}m_0^2, \bar{B}_{uud}\pi_D^2$	$\bar{B}_{uud}m_0^2\pi_D$				6
-1	$-\frac{1}{2}$	$\bar{B}_{udd}$	$\bar{B}_{udd}\pi_U, \bar{B}_{udd}\pi_D$	$\bar{B}_{udd}m_0^2, \bar{B}_{udd}\pi_U^2$	$\bar{B}_{udd}m_0^2\pi_U$				6
-1	$-\frac{3}{2}$	$\bar{B}_{ddd}$	$\bar{B}_{ddd}\pi_U$	$\bar{B}_{ddd}\pi_U^2$	$\bar{B}_{ddd}\pi_U^3$				4
-1	Σ	4	6	6	4	0	0	1	20
0	-3				π_-^3				1
0	-2			π_-^2	$\pi_-^2\pi_U, \pi_-^2\pi_D$	$\pi_-^2 m_0^2$			4
0	-1		π_-	$\pi_-\pi_U, \pi_-\pi_D$	$2\pi_- m_0^2, \pi_-\pi_U^2, \pi_-\pi_D^2$	$\pi_- m_0^2\pi_U, \pi_- m_0^2\pi_D$	$\pi_- m_0^4$		10
0	0	1	π_U, π_D	$\pi_0^2, \bar{\pi}_0^2, \pi_U^2, \pi_D^2$	$\pi_0^2\pi_U, \bar{\pi}_0^2\pi_U, \pi_0^2\pi_D, \bar{\pi}_0^2\pi_D, \pi_U^3, \pi_D^3$	$\pi_0^2 m_0^2, \bar{\pi}_0^2 m_0^2, m_0^2\pi_U^2, m_0^2\pi_D^2$	$m_0^4\pi_U, m_0^4\pi_D$	m_0^6	20
0	-1		π_+	$\pi_+\pi_U, \pi_+\pi_D$	$2\pi_+ m_0^2, \pi_+\pi_U^2, \pi_+\pi_D^2$	$\pi_+ m_0^2\pi_U, \pi_+ m_0^2\pi_D$	$\pi_+ m_0^4$		10
0	-2			π_+^2	$\pi_+^2\pi_U, \pi_+^2\pi_D$	$\pi_+^2 m_0^2$			4
0	-3				π_+^3				1
0	Σ	1	4	10	20	10	4	1	50
1	$\frac{3}{2}$	B_{uuu}	$B_{uuu}\pi_D$	$B_{uuu}\pi_D^2$	$B_{uuu}\pi_D^3$				4
1	$+\frac{1}{2}$	B_{uud}	$B_{uud}\pi_U, p\pi_D$	$B_{uud}m_0^2, p\pi_D^2$	$B_{uud}m_0^2\pi_D$				6
1	$-\frac{1}{2}$	B_{udd}	$B_{udd}\pi_U, n\pi_D$	$B_{udd}m_0^2, n\pi_U^2$	$B_{udd}m_0^2\pi_U$				6
1	$-\frac{3}{2}$	B_{ddd}	$B_{ddd}\pi_U$	$B_{ddd}\pi_U^2$	$B_{ddd}\pi_U^3$				4
1	Σ	4	6	6	4	0	0	0	20
2	0	$p\,n$							1
2	Σ	1	0	0	0	0	0	0	1
Σ		11	16	22	28	10	4	1	92

This matrix is a projector with eigenvalues (1, 1, 0, 0), such that it can be diagonalized to the $\mathbb{1}_{2x2}$ matrix with the basis vectors

$$\pi_0^2 = \frac{1}{3}(\sqrt{2}k_U k_D + k^{(2)}_{\pi^+\pi^-,UD})$$
$$\bar{\pi}_0^2 = \frac{1}{3}(\sqrt{2}k_{\pi^+}k_{\pi^-} + k^{(2)}_{UD,\pi^+\pi^-}). \quad \text{(D8)}$$

Note that in the strong coupling limit there is no distinction between $\pi_0 = \frac{1}{\sqrt{2}}(\bar{u}u - \bar{d}d)$ and $\eta/\eta' = \frac{1}{\sqrt{2}}(\bar{u}u + \bar{d}d)$, due to the lack of topological features. All other states do not mix. We now list the quantum states for the Hamiltonian formulation, classified by the baryonic sectors $n_B \in \{-N_f, \ldots N_f\}$ and the isosopin sectors $n_I \in \{-N_f, \ldots N_f\}$. Recall that the states are only distinguishable on the quark level, and there are several possible assignments in terms of hadrons:

$$m_0^2 \equiv \pi_U\pi_D = \pi_+\pi_-,$$
$$m_0^6 = B_{uud}\bar{B}_{udd} = B_{udd}\bar{B}_{uud} = B_{ddd}\bar{B}_{uuu} = (m_0^2)^3,$$
$$\bar{p}\,\bar{n} \equiv \bar{B}_{uud}\bar{B}_{udd} = \bar{B}_{uuu}\bar{B}_{ddd},$$
$$pn \equiv B_{uud}B_{udd} = B_{uuu}B_{ddd}. \quad \text{(D9)}$$

The final 92 quantum states are given in Table V. The 50 purely mesonic states can be further classified by the set of charges (Q_{π_0}, Q_{π^+}), resulting in the Hamiltonian

$$\hat{\mathcal{H}} = \frac{1}{2}\sum_{\langle\vec{x},\vec{y}\rangle}(\hat{J}^+_{\pi_0,\vec{x}}\hat{J}^-_{\pi_0,\vec{y}} + \hat{J}^+_{\bar{\pi}_0,\vec{x}}\hat{J}^-_{\bar{\pi}_0,\vec{y}} + \hat{J}^+_{\pi^+,\vec{x}}\hat{J}^-_{\pi^+,\vec{y}} + \hat{J}^+_{\pi^-,\vec{x}}\hat{J}^-_{\pi^-,\vec{y}} + \text{H.c.}) \quad \text{(D10)}$$

with the occupation number raising and lowering operators defined for each conserved charge. The full $N_f = 2$ partition function including the baryonic states and flavored observables will be discussed in a forthcoming publication. We also

TABLE VI. Multiplicities of quantum states (static lines) in the mesonic sector, i.e., from U(N_c) integrals.

	N_f				
N_c	0	1	2	3	4
1	1	2	3	4	5
2	1	6	20	50	105
3	1	20	275	1430	7007
4	1	170	5814	94692	980628

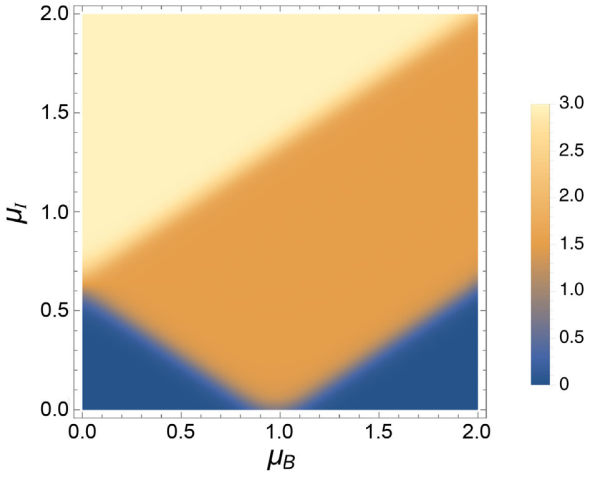

FIG. 36. Isospin density in the μ_B-μ_I plane, based on the limit $T \to 0$ of Eq. (D12), indicating first order phase transition lines where pion condensation takes place.

derived the number of quantum states for arbitrary N_c and N_f, resulting in the 1-dim partition function:

$$Z_{N_f}(\mu_B/T) = \sum_{B=-N_f}^{N_f} \prod_{a=0}^{N_c-1} \frac{a!(2N_f+a)!e^{B\mu_B/T}}{(N_f+a-B)!(N_f+a+B)!}. \tag{D11}$$

For $B = 0$ the multiplicities are given in Table VI. An important application of the $N_f = 2$ partition function is to determine the QCD phase diagram with both finite baryon and isospin chemical potential. Our formulation is still sign-problem free in the continuous time limit. As we have not yet performed dynamical simulations, we can only provide analytic results on the static limit, corresponding to 1-dim QCD. For $N_c = 3$,

$$\begin{aligned} Z\left(\frac{\mu_B}{T},\frac{\mu_I}{T}\right) &= 2\cosh\frac{3\mu_I}{T} + 8\cosh\frac{2\mu_I}{T} + 20\cosh\frac{\mu_I}{T} + 20 \\ &\quad + 2\cosh\frac{\mu_B}{T}\left(8\cosh\frac{\frac{3}{2}\mu_I}{T} + 12\cosh\frac{\frac{1}{2}\mu_I}{T}\right) \\ &\quad + 2\cosh\frac{2\mu_B}{T}. \end{aligned} \tag{D12}$$

Even though interactions will be crucial at low temperatures, we can plot the zero temperature limit of Eq. (D12) to obtain a naive picture of the phases in the μ_B-μ_I plane, shown in Fig. 36.

APPENDIX E: FINITE QUARK MASS

The chiral limit is the most interesting regime when studying the chiral transition, but we need to extend the derivation of the continuous time partition function to finite quark mass to address the quark mass dependence of zero and finite temperature observables. Only then is it possible to study the p-regime where the pion correlation function fits on the lattice. Whereas in the chiral limit, the chiral condensate is strictly zero (in a finite volume), already a small quark mass will result in a nonzero chiral condensate. Likewise, the sigma meson becomes much heavier compared to the pion. This can be best understood in the dual representation: The number of monomers on even sites always equals the number of monomers on odd sites. In the pion correlator, the contributions from monomers at even sites have the *opposite sign* from those at odd sites, resulting in a light pion mass. In the sigma correlator, the contributions from monomers at even sites have the *same sign* as those at odd sites, resulting in a heavy sigma meson.

When attempting to derive the continuous time partition function at finite quark mass in a naive way, i.e., at fixed quark mass am_q, the monomer number will diverge in the limit $N_\tau \to \infty$. We have illustrated in [43] that the continuous time limit is well defined also at finite quark mass, but it turns out that the constant κ is now quark mass dependent. This function $\kappa(m_q)$ has been determined nonperturbatively with a condition for keeping the quark mass constant in the limit $a_\tau \to \infty$. With this knowledge, the continuous time limit can also be derived at finite quark mass, but it is not the bare quark mass am_q but rather the ratio M_π/T which is the input parameter of the continuous time partition function. We are working on an extension of the CT worm algorithm such that the Poisson process incorporates a finite quark mass.

[1] Z. Fodor and S. D. Katz, Phys. Lett. B **534**, 87 (2002).
[2] P. de Forcrand and O. Philipsen, Nucl. Phys. **B673**, 170 (2003).
[3] C. R. Allton, M. Doring, S. Ejiri, S. J. Hands, O. Kaczmarek, F. Karsch, E. Laermann, and K. Redlich, Phys. Rev. D **71**, 054508 (2005).

[4] G. Aarts, L. Bongiovanni, E. Seiler, D. Sexty, and I.-O. Stamatescu, Eur. Phys. J. A **49**, 89 (2013).
[5] D. Sexty, Phys. Lett. B **729**, 108 (2014).
[6] K. Langfeld, B. Lucini, and A. Rago, Phys. Rev. Lett. **109**, 111601 (2012).
[7] A. Alexandru, G. Basar, P. F. Bedaque, G. W. Ridgway, and N. C. Warrington, J. High Energy Phys. 05 (2016) 053.
[8] C. Schmidt and F. Ziesché, Proc. Sci., LATTICE2016 (**2017**) 076 [arXiv:1701.08959].
[9] F. Di Renzo and G. Eruzzi, Phys. Rev. D **97**, 014503 (2018).
[10] C. Gattringer and K. Langfeld, Int. J. Mod. Phys. A **31**, 1643007 (2016).
[11] Y. D. Mercado, C. Gattringer, and A. Schmidt, Comput. Phys. Commun. **184**, 1535 (2013).
[12] C. Gattringer, T. Kloiber, and V. Sazonov, Nucl. Phys. **B897**, 732 (2015).
[13] H. Vairinhos and P. de Forcrand, J. High Energy Phys. 12 (2014) 038.
[14] C. Gattringer and C. Marchis, Nucl. Phys. **B916**, 627 (2017).
[15] G. Gagliardi, J. Kim, and W. Unger, EPJ Web Conf. **175**, 07047 (2018).
[16] G. Gagliardi and W. Unger, Proc. Sci., LATTICE2018 (**2018**) 224 [arXiv:1811.02817].
[17] G. Gagliardi and W. Unger, Phys. Rev. D **101**, 034509 (2020).
[18] U. Wolff, Nucl. Phys. **B810**, 491 (2009).
[19] U. Wolff, Nucl. Phys. **B814**, 549 (2009).
[20] N. Kawamoto and J. Smit, Nucl. Phys. **B192**, 100 (1981).
[21] H. Kluberg-Stern, A. Morel, and B. Petersson, Nucl. Phys. **B215**, 527 (1983).
[22] G. Faldt and B. Petersson, Nucl. Phys. **B265**, 197 (1986).
[23] N. Bilic, K. Demeterfi, and B. Petersson, Nucl. Phys. **B377**, 651 (1992).
[24] N. Bilic, F. Karsch, and K. Redlich, Phys. Rev. D **45**, 3228 (1992).
[25] N. Kawamoto, K. Miura, A. Ohnishi, and T. Ohnuma, Phys. Rev. D **75**, 014502 (2007).
[26] K. Miura, N. Kawamoto, T. Z. Nakano, and A. Ohnishi, Phys. Rev. D **95**, 114505 (2017).
[27] P. Rossi and U. Wolff, Nucl. Phys. **B248**, 105 (1984).
[28] F. Karsch and K. H. Mutter, Nucl. Phys. **B313**, 541 (1989).
[29] P. de Forcrand and M. Fromm, Phys. Rev. Lett. **104**, 112005 (2010).
[30] W. Unger and P. de Forcrand, Proc. Sci.,LATTICE2012 (**2012**) 194 [arXiv:1211.7322].
[31] P. de Forcrand, W. Unger, and H. Vairinhos, Phys. Rev. D **97**, 034512 (2018).
[32] C. Gattringer, Phys. Rev. D **97**, 074506 (2018).
[33] E. Gull, A. J. Millis, A. e. I. Lichtenstein, A. N. Rubtsov, M. Troyer, and P. Werner, Rev. Mod. Phys. **83**, 349 (2011).
[34] L. Pollet, Rep. Prog. Phys. **75**, 094501 (2012).
[35] P. de Forcrand, P. Romatschke, W. Unger, and H. Vairinhos, Proc. Sci., LATTICE2016 (**2017**) 086 [arXiv:1701.08324].
[36] D. H. Adams and S. Chandrasekharan, Nucl. Phys. **B662**, 220 (2003).
[37] M. Fromm, Lattice QCD at strong coupling, Ph.D. thesis, Zurich, ETH, 2010.
[38] B. B. Beard and U. J. Wiese, Phys. Rev. Lett. **77**, 5130 (1996).
[39] W. Unger and P. de Forcrand, Proc. Sci., LATTICE2011 (**2011**) 218 [arXiv:1111.1434].
[40] E. Huffman and S. Chandrasekharan, Phys. Rev. D **96**, 114502 (2017).
[41] E. Huffman and S. Chandrasekharan, Phys. Rev. D **101**, 074501 (2020).
[42] N. Prokof'ev and B. Svistunov, Phys. Rev. Lett. **87**, 160601 (2001).
[43] W. Unger, D. Bollweg, and M. Klegrewe, Proc. Sci., LATTICE2018 (**2018**) 181 [arXiv:1811.03584].
[44] F. Wang and D. P. Landau, Phys. Rev. Lett. **86**, 2050 (2001).
[45] P. de Forcrand and S. Kratochvila, Nucl. Phys. B, Proc. Suppl. **153**, 62 (2006).
[46] S. Chandrasekharan and F.-J. Jiang, Phys. Rev. D **68**, 091501 (2003).
[47] S. Chandrasekharan and C. G. Strouthos, Phys. Rev. D **69**, 091502 (2004).
[48] G. Burgers, F. Karsch, A. Nakamura, and I. O. Stamatescu, Nucl. Phys. **B304**, 587 (1988).
[49] L. Levkova, T. Manke, and R. Mawhinney, Phys. Rev. D **73**, 074504 (2006).
[50] G. Aarts, C. Allton, J. Glesaaen, S. Hands, B. Jäger, and J. Skullerud, Proc. Sci., LATTICE2018 (**2018**) 183 [arXiv:1812.08151].
[51] P. Hasenfratz and H. Leutwyler, Nucl. Phys. **B343**, 241 (1990).
[52] M. Campostrini, M. Hasenbusch, A. Pelissetto, P. Rossi, and E. Vicari, Phys. Rev. B **63**, 214503 (2001).
[53] A. Bazavov *et al.*, Phys. Rev. D **85**, 054503 (2012).
[54] J. Kim and W. Unger, Proc. Sci., LATTICE2016 (**2016**) 035 [arXiv:1611.09120].
[55] H. E. Haber and H. A. Weldon, Phys. Rev. Lett. **46**, 1497 (1981).
[56] P. de Forcrand, J. Langelage, O. Philipsen, and W. Unger, Phys. Rev. Lett. **113**, 152002 (2014).
[57] Y. Nishida, Phys. Rev. D **69**, 094501 (2004).
[58] A. Bazavov, H.-T. Ding, P. Hegde, O. Kaczmarek, F. Karsch, E. Laermann, Y. Maezawa, S. Mukherjee, H. Ohno, P. Petreczky, H. Sandmeyer, P. Steinbrecher, C. Schmidt, S. Sharma, W. Soeldner, and M. Wagner, Phys. Rev. D **95**, 054504 (2017).
[59] A. Roberge and N. Weiss, Nucl. Phys. **B275**, 734 (1986).
[60] C. Czaban, F. Cuteri, O. Philipsen, C. Pinke, and A. Sciarra, Phys. Rev. D **93**, 054507 (2016).
[61] S. Datta, R. V. Gavai, and S. Gupta, Phys. Rev. D **95**, 054512 (2017).
[62] F. Karsch, B.-J. Schaefer, M. Wagner, and J. Wambach, Phys. Lett. B **698**, 256 (2011).
[63] T. DeGrand and C. E. Detar, *Lattice Methods for Quantum Chromodynamics* (World Scientific, New Jersey, 2006), 345 p.
[64] B. A. Berg and R. C. Harris, Comput. Phys. Commun. **179**, 443 (2008).

[65] C. M. Hurvich and C.-L. Tsai, Biometrika **76**, 297 (1989).
[66] G. Boyd, S. Gupta, F. Karsch, and E. Laermann, Z. Phys. C **64**, 331 (1994).
[67] J. Kim, M. Klegrewe, and W. Unger, *Proc. Sci.*, LATTICE2019 (2019) 064 [arXiv:2001.06797]
[68] J. W. Essam, Rep. Prog. Phys. **43**, 833 (1980).
[69] M. Fromm, J. Langelage, S. Lottini, M. Neuman, and O. Philipsen, Phys. Rev. Lett. **110**, 122001 (2013).
[70] D. J. Cecile and S. Chandrasekharan, Phys. Rev. D **77**, 014506 (2008).
[71] K. E. Eriksson, N. Svartholm, and B. S. Skagerstam, J. Math. Phys. (N.Y.) **22**, 2276 (1981).

C.3 New algorithms and new results for strong coupling LQCD [C3]

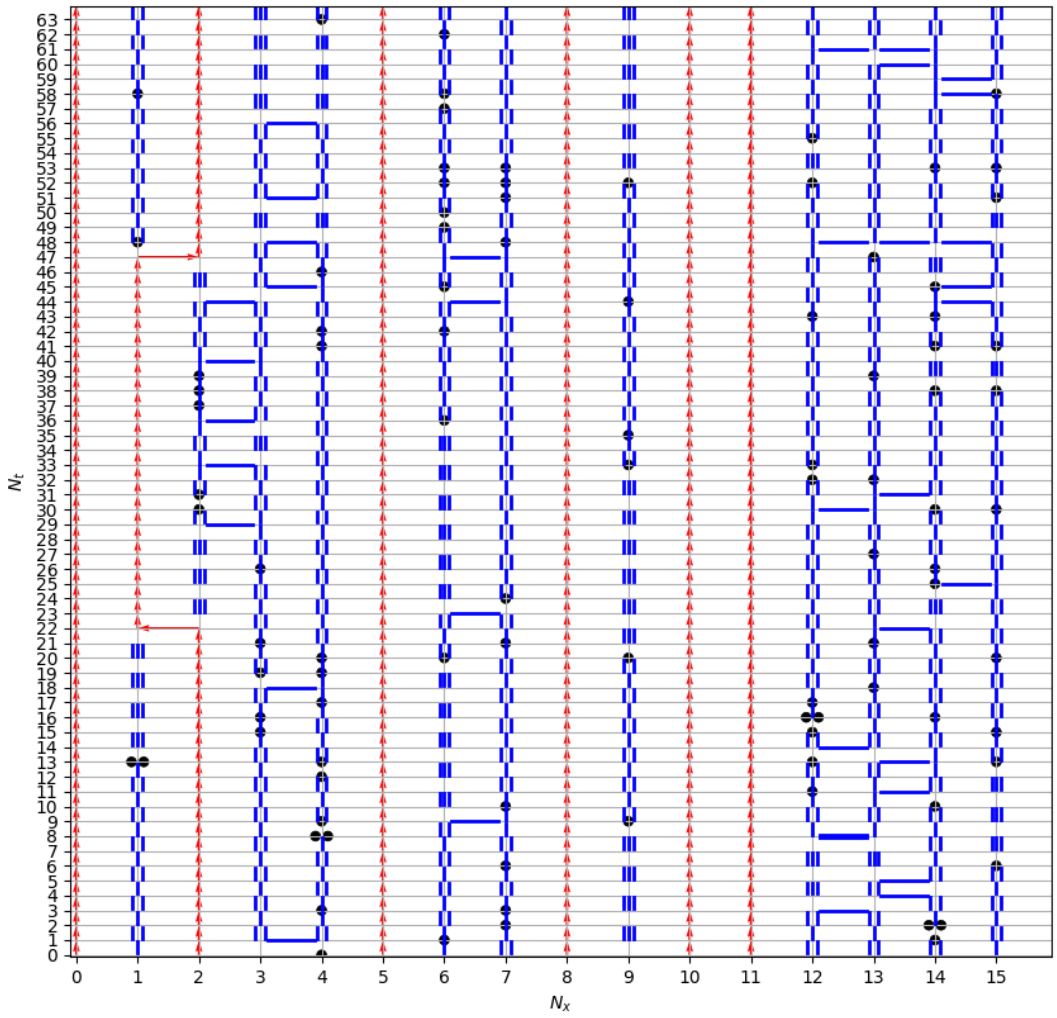

PROCEEDINGS OF SCIENCE

CERN-PH-TH/2012-326

New algorithms and new results for strong coupling LQCD

Wolfgang Unger*
Institut für Theoretische Physik, Goethe-Universität Frankfurt, 60438 Frankfurt am Main, Germany
E-mail: unger@th.physik.uni-frankfurt.de

Philippe de Forcrand
Institut für theoretische Physik, ETH Zürich, CH-8093, Switzerland
CERN, Physics Department, TH Unit, CH-1211 Geneva 23, Switzerland
E-mail: forcrand@phys.ethz.ch

We present and compare new types of algorithms for lattice QCD with staggered fermions in the limit of infinite gauge coupling. These algorithms are formulated on a discrete spatial lattice but with continuous Euclidean time. They make use of the exact Hamiltonian, with the inverse temperature beta as the only input parameter. This formulation turns out to be analogous to that of a quantum spin system. The sign problem is completely absent, at zero and non-zero baryon density. We compare the performance of a continuous-time worm algorithm and of a Stochastic Series Expansion algorithm (SSE), which operates on equivalence classes of time-ordered interactions. Finally, we apply the SSE algorithm to a first exploratory study of two-flavor strong coupling lattice QCD, which is manageable in the Hamiltonian formulation because the sign problem can be controlled.

The 30 International Symposium on Lattice Field Theory - Lattice 2012,
June 24-29, 2012
Cairns, Australia

*Speaker.

1. Introduction

Lattice QCD with staggered fermions in the strong coupling limit (SC-LQCD) is a useful effective model of QCD, as it shares important features of QCD such as confinement and spontaneous chiral symmetry breaking and its restoration at a transition temperature T_c. One can study the nuclear potential as well as the phase diagram at non-zero baryon chemical potential μ_B [1]. These topics can not be properly addressed with conventional, determinant-based lattice QCD using HMC algorithms, due to the notorious sign problem: all methods available today are limited to $\mu_B/T \lesssim 1$ [2]. In contrast, SC-LQCD can be reformulated as a monomer-dimer system [3]. There, the sign problem can be made mild due to a resummation of baryonic and mesonic degrees of freedom [4]. Due to algorithmic developments over the last decade, in particular due to the application of the Worm algorithm to the monomer-dimer partition function [5], SC-LQCD - which has been studied via mean field theory [6] and with Metropolis algorithms [3, 4] since the 1980s - has experienced a revival, as simulations at finite baryon density could be performed with modest computational demands. Moreover, the chiral limit can be studied very economically - simulations are faster than with a finite quark mass. However, limitations remain. In particular, only the 1-flavor (4 tastes) theory has been considered so far in the dimer-formulation. The physically more interesting case of 2 flavors could not be addressed yet due to a severe sign problem in the mesonic sector [7]. Here, we propose a Hamiltonian formulation of strong coupling lattice QCD based on the Euclidean continuous time limit, where further simplifications occur. In particular, we show that this formulation is a generalization of Hamiltonians for spin systems. It can in principle be extended to arbitrary N_f. In this paper, we illustrate the formalism and give first Monte Carlo results obtained via Stochastic Series Expansion for $N_\mathrm{f} = 2$ and U(2) gauge group.

2. The continuous Euclidean time approach

In SC-LQCD, the gauge coupling is sent to infinity and hence the coefficient $\beta = 2N_\mathrm{c}/g^2$ of the plaquette term representing the Yang Mills part $F_{\mu\nu}F_{\mu\nu}$ of the action is zero. The lattice becomes maximally coarse, and no continuum limit can be considered. But the gauge fields in the covariant derivative can be integrated out analytically because the integration factorizes. After the Grassmann integration over the fermions, one obtains the SC-LQCD partition function [3] in the dimer representation, which is an exact rewriting of the 1-flavor staggered fermion action on a $d+1$ dimensional lattice $N_\sigma^d \times N_\tau$:

$$S[U,\chi,\bar\chi] = am_q \sum_x \bar\chi(x)\chi(x) + \frac{\gamma}{2}\sum_x \eta_0(x)\left[\bar\chi(x)e^{a_\tau\mu}U_0(x)\chi(x+\hat 0) - \bar\chi(x+\hat 0)e^{-a_\tau\mu}U_0^\dagger(x)\chi(x)\right] + \frac{1}{2}\sum_x\sum_i^d \eta_i(x)\left[\bar\chi(x)U_i(x)\chi(x+\hat\imath) - \bar\chi(x+\hat\imath)U_i^\dagger(x)\chi(x)\right] \tag{2.1}$$

$$\longrightarrow \qquad Z(m_q,\mu_q) = \sum_{\{k,n,\ell\}}{}' \prod_{b=(x,\hat\mu)} \frac{(N_\mathrm{c}-k_b)!}{N_\mathrm{c}!k_b!}\gamma^{2k_b\delta_{\hat 0\hat\mu}} \prod_x \frac{N_\mathrm{c}!}{n_x!}(2am_q)^{n_x}\prod_\ell w(\ell),$$

$$w(\ell) = \sigma(\ell)\gamma^{N_\mathrm{c}\sum_x|\ell_0(x)|}\exp(N_\mathrm{c}N_\tau r_\ell a_\tau\mu), \tag{2.2}$$

with m_q the quark mass and $\mu = \frac{1}{N_\mathrm{c}}\mu_B$ the quark chemical potential, $\sigma(\ell) = \pm 1$ a geometry dependent sign and $r(\ell)$ the winding number of baryon loop ℓ. The sum $\sum'$ is over admissible configurations, namely those which fulfill the Grassmann constraint

$$n_x + \sum_{\hat\mu=\pm\hat 0,\ldots\pm\hat d}\left(k_{\hat\mu}(x) + \frac{N_\mathrm{c}}{2}|\ell_\mu(x)|\right) = N_\mathrm{c} \quad \forall x \in V. \tag{2.3}$$

Since color degrees of freedom have been integrated out, configurations are defined in terms of mesons - represented by the monomers $n_x \in \{0,\ldots N_\mathrm{c}\}$ and dimers $k_\mu(x) \in \{0,\ldots N_\mathrm{c}\}$ (non-oriented meson hop-

pings) - and baryons - represented by self-avoiding closed loops constituted by $\ell_\mu(x) \in \{-1,0,+1\}$.[1] Here, we consider the chiral limit, $m_q = 0$ where monomers are absent: $n_x = 0$.

In Eq. (2.1) we have introduced an anisotropy γ in the Dirac couplings. This complication is necessary because the chiral restoration temperature is given by roughly $aT \simeq 1.5$, and on an isotropic lattice with $aT = 1/N_\tau$ we could not reach sufficiently high temperatures. Furthermore, varying γ is the only way to vary the temperature continuously. The temperature is thus $aT = f(\gamma)/N_\tau$ with $f(\gamma) = a/a_\tau$. However, the functional dependence $f(\gamma)$ of the ratio of the spatial and temporal lattice spacings on γ is not known. Naive inspection of the derivatives in Eq. (2.1) would indicate $f(\gamma) = \gamma$, but this only holds at weak coupling. In contrast, the mean field approximation of SC-QCD based on a $1/d$-expansion [**?**] suggests that $aT_c = \gamma_c^2 N_\tau$ is the sensible, N_τ-independent identification in leading order in $1/d$. We have emphasized elsewhere [8] by analytic arguments and numerical investigation that this identification is the only suitable one which renders observables like the chiral susceptibility and the specific heat finite in the limit $N_\tau, \gamma \to \infty$. However, this limit (keeping $\gamma_c^2 N_\tau$ fixed) is approached with significant, sometimes non-monotonic $1/N_\tau$ corrections. To circumvent such extrapolation problems, we consider the *continuous Euclidean time (*CT*) limit:* $N_\tau \to \infty$, $\gamma \to \infty$, with $\gamma^2/N_\tau \equiv aT$ fixed. Hence we are left with only one parameter $\beta \equiv N_\tau/\gamma^2$ to set the thermal properties, and all discretization errors introduced by a finite N_τ are removed. Moreover, in the baryonic sector the partition function simplifies greatly: baryons become static in the CT limit, hence the sign problem is completely absent. Additionally, multiple spatial dimers $k_i(x) > 1$ become completely suppressed (see [8]) and one can derive the CT partition function:

$$Z_{\rm CT}(\beta,\mu) = \sum_{k\in 2\mathbb{N}} (\beta/2)^k \sum_{\mathscr{G}'\in\Gamma_k} e^{3\mu\beta B} \hat{v}_L^{N_L} \hat{v}_T^{N_T} \quad \text{with} \quad k = \sum_{b=(x,\hat{\imath})} k_b = \frac{N_L+N_T}{2}, \quad N_{L/T} = \sum_x n_{L/T}(x) \tag{2.4}$$

where B is the baryon number, and Γ_k is the set of equivalence classes $\mathscr{G}'$ of graphs containing a total number k of spatial hoppings, equivalent up to time shifts of the vertices. The vertex weights $v_L = 1$ and $v_T = 2/\sqrt{3}$ label L- and T-types of vertices as illustrated Fig. 1 (left). An important property of the partition function Eq. (2.4) is that spatial dimers are distributed uniformly in time. The lengths $\Delta\beta$ of "dashed" or "solid" time intervals (see Fig. 1 left) are then, according to a Poisson process, exponentially distributed: $P(\Delta\beta) \propto \exp(-\lambda\Delta\beta)$, $\Delta\beta \in [0,\beta]$ with λ the "decay constant" for spatial dimer emission $\lambda = (2d - \sum_\mu n_B(x \pm \hat{\mu}))/4$. This is the basis for the continuous time Worm algorithm presented in [8].

3. The 1-flavor Hamiltonian

The Hamiltonian formulation can be obtained from Eq. (2.4) by realizing that the degrees of freedom can be mapped on a spin system. We can restrict the discussion to the mesonic sector $U(N_{\rm c})$, since baryons are static for $N_{\rm c} > 2$. Notice that, except for spatial hoppings, meson lines are time-like and form dimer chains alternating between $k_0^{\rm even}(\vec{x}) \in \{0,\dots N_{\rm c}\}$ and $k_0^{\rm odd}(\vec{x})$ with $k_0^{\rm odd}(\vec{x}) = (N_{\rm c} - k_0^{\rm even}(\vec{x}))$ on even and odd time-slices. One can then introduce the observable

$$S^z(\vec{x},t) = \frac{(-1)^{x+y+z+t}}{2}(2k_0(\vec{x},t) - N_{\rm c}) \in \{-N_{\rm c}/2,\dots N_{\rm c}/2\} \tag{3.1}$$

which is constant on static lines. The "spin" S_z simply counts the number of time-like meson hoppings, and is in no way related to the spin of the quarks. Spatial dimers can then be oriented consistently, such that for each spatial dimer between a pair of neighboring sites $\langle\vec{x},\vec{y}\rangle$, one unit of spin $\Delta S^z = \pm 1$ is transferred from site $\vec{x}$ to site $\vec{y}$. Hence the total spin $S^z \equiv S^z(t) = \sum_{\vec{x}\in V} S^z(\vec{x},t)$ is globally conserved.

[1] Note that U(3) describes a purely mesonic system, while SU(3) contains baryons.

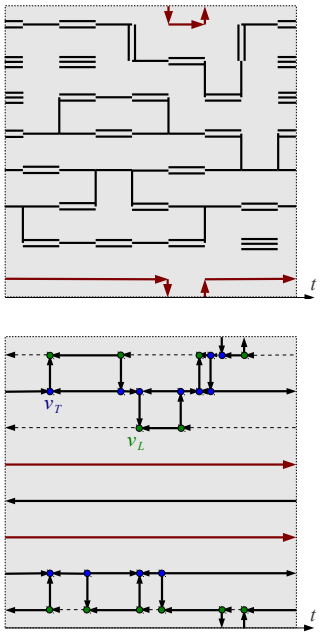

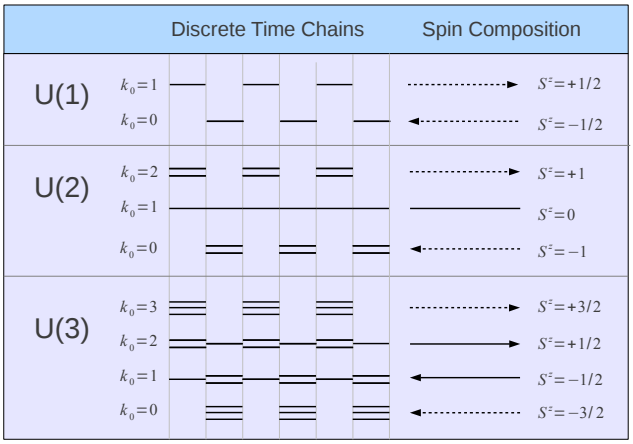

Figure 1: Left: Typical 2-dimensional configurations in discrete (top) and continuous time (bottom) at the same temperature, where multiple dimers are absent and baryons (red) become static. L- and T-vertices have different weights. Meson lines can be oriented in a consistent way. Right: Mapping of static mesons (time-like chains) to a "spin".

In the case of gauge group U(1) (lattice QED in the strong coupling limit), the Hamiltonian is identical to that of the XY Model in zero field: $\hat{H} = \sum_{\langle \vec{x},\vec{y}\rangle} \sigma^+\sigma^-$, with $\sigma^\pm = \sigma_1 \pm i\sigma_2$ the spin raising/lowering operators constructed from the Pauli matrices. The generalization to $U(N_c)$ reads

$$Z(\beta) = \mathrm{Tr}\left[e^{-\beta\hat{H}}\right], \qquad \hat{H} = -\frac{1}{2}\sum_{\langle \vec{x},\vec{y}\rangle}\left(J^+_{\vec{x}}J^-_{\vec{y}} + h.c.\right) \qquad J^+ = \begin{pmatrix} 0 & & & \\ v_1 & 0 & & \\ & \ddots & \ddots & \\ & & v_{N_c} & 0 \end{pmatrix}, \quad v_k = \sqrt{\frac{k(1+N_c-k)}{N_c}} \tag{3.2}$$

with $J^- = (J^+)^T$ which are spin lowering/raising operators. The off-diagonal matrix elements v_k are generalized vertex weights. For $N_c = 3$, we can identify $v_L \equiv v_1 = v_3 = 1$, $v_T \equiv v_2 = 2/\sqrt{3}$. Note that the operators $J^\pm$ reflect the existence of a lowest and highest weight, $J^-|-N_c/2\rangle = 0$, $J^+|N_c/2\rangle = 0$, and fulfill as well the commutation relation $\frac{N_c}{2}[J^+,J^-] \equiv J^z = \mathrm{diag}\,(-N_c/2,\ldots N_c/2)$ with $J^z|S^z\rangle = S^z|S^z\rangle$. This justifies the characterization of static lines in terms of a "spin" quantum number.

4. Stochastic Series Expansion

The partition function Eq. (2.4), which is a sum of weighted diagrams in a perturbative series in β, can be sampled via diagrammatic Monte Carlo techniques such as the continuous time worm algorithm [9] or the *Stochastic Series Expansion* (SSE) [10]. Here, we restrict to SSE: as we will see, it can be easily generalized to $N_f > 1$ once we have constructed the corresponding Hamiltonian. SSE is based on a rewriting of the partition function by inserting identity and diagonal matrix elements:

$$Z(\beta) = \mathrm{Tr}\left[e^{-\beta\hat{H}}\right] = \sum_\chi \sum_{\{S_L\}} \frac{\beta^\kappa (L-\kappa)!}{L!} \left\langle \chi \left| \prod_{i=1}^{L} \hat{H}_{a_i,b_i} \right| \chi \right\rangle, \quad \hat{H}_{1,b} = c\mathbb{1}, \quad \hat{H}_{2,b} = \frac{1}{2}\left(J^+_{\vec{x}}J^-_{\vec{y}} + h.c.\right) \tag{4.1}$$

where χ is a state vector and S_L is a time-ordered sequence of indices: $S_L = \{[a_1,b_1],[a_2,b_2],\ldots[a_L,b_L]\}$ characterizing - together with an initial state χ - a graph in $Z(\beta)$. L is the number of operators and $\kappa < L$ the order in the expansion in β. The indices $a_i = 0$ correspond to the identity, $a_i = 1$ to the diagonal matrix element $c\mathbb{1}$, where c can be adjusted in order to simplify the algorithm, and $a_i = 2$ to non-diagonal matrix elements. The index $b_i = \langle \vec{x},\vec{y}\rangle \in Vd$ denotes a bond on the lattice, and for $a_i = 0$,

$b_i = 0$ denotes a dummy bond. For any finite volume and given temperature, only a finite number of orders in β contribute. L can be set to be larger than this number, making SSE approximation-free. The algorithm consists of two kinds of updates: (1) a Metropolis update changing the order in β:

$$P([0,0] \mapsto [1,b]) = \frac{N_\sigma^3 d\beta \left\langle \chi | \hat{H}_{1,b} | \chi \right\rangle}{L-\kappa}, \quad P([1,b] \mapsto [0,0]) = \frac{L-\kappa+1}{N_\sigma^3 d\beta \left\langle \chi | \hat{H}_{1,b} | \chi \right\rangle}, \tag{4.2}$$

and (2) the operator loop update, visiting a set of bonds in succession, starting from an input leg and determining the output leg with heatbath probability $\propto \left\langle \chi(x)\chi(y) | \hat{H}_{a_i b_i} | \chi'(x)\chi'(y) \right\rangle$. In Fig. 2 we compare different observables obtained from SSE and/or CT-Worm. We want to stress that a new observable, the spin susceptibility $\chi_S = \frac{\beta}{V} \left\langle (\sum_i S_i^z)^2 \right\rangle$, is also sensitive to the chiral transition. It measures the fluctuations in the number of time-like mesons, and is thus analogous (but not equal) to the specific heat.

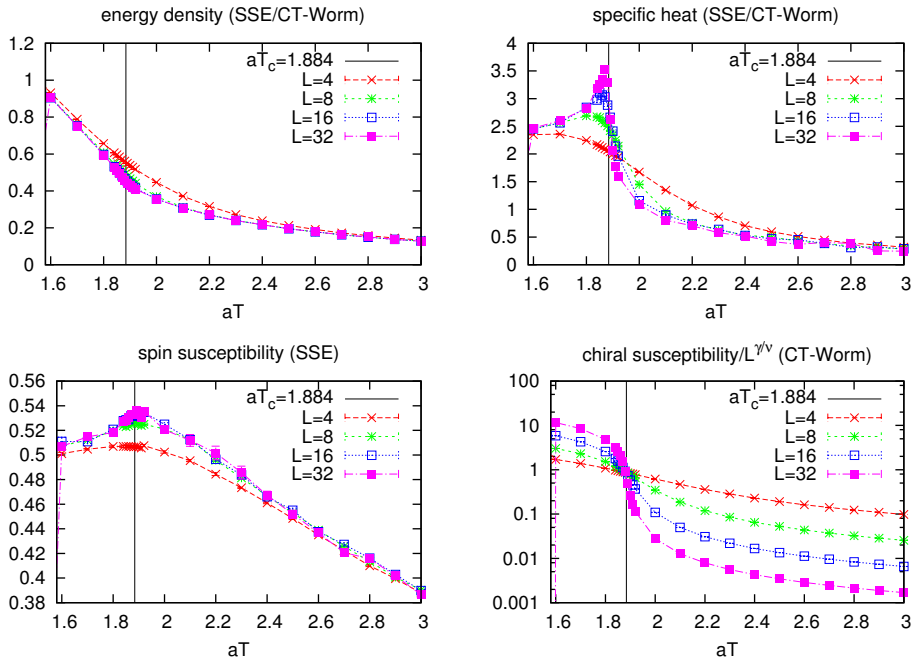

Figure 2: Observables in 1-flavor U(3): (top row) energy density and susceptibility measured with CT-worm and SSE agree; (bottom left) spin susceptibility measured with SSE; (bottom right) chiral susceptibility measured with CT-Worm.

5. The 2-flavor formulation and first results for U(2) gauge group

In the strong coupling limit, only one of the four tastes of staggered fermions remains light, since taste splitting is maximal. It was argued in [1] that the nuclear interaction in 1-flavor SC-LQCD is due to entropic forces: the presence of static baryons modifies the pion bath, with the modulation proportional to the ρ-propagator. However, with 1 flavor pion exchange cannot not occur, because mesons do not couple to baryons. Pion exchange can only be studied by going to $N_\mathrm{f} > 1$. But no 2-flavor formulation of staggered SC-QCD suitable for finite-density Monte Carlo exists, as already the mesonic sector has a severe sign problem [7]. After reviewing the problems with the conventional dimer representation of SC-QCD, we derive a sign-problem-free Hamiltonian formulation in continuous Euclidean time.

The 1-link integrals which appear in the strong coupling limit can be expressed in terms of the gauge-invariant terms [11]. For SU(2) and U(2), the 1-link integals (valid for any N_f) are

$$z_{SU(2)}(x,y) = \sum_{n=0}^{\infty} \frac{(X+\Delta)^n}{n!(n+1)!}, \qquad z_{U(2)}(x,y) = \sum_{i,j=0}^{\infty} \frac{X^i + Z^j}{(i+2j+1)!i!(j!)^2} \tag{5.1}$$

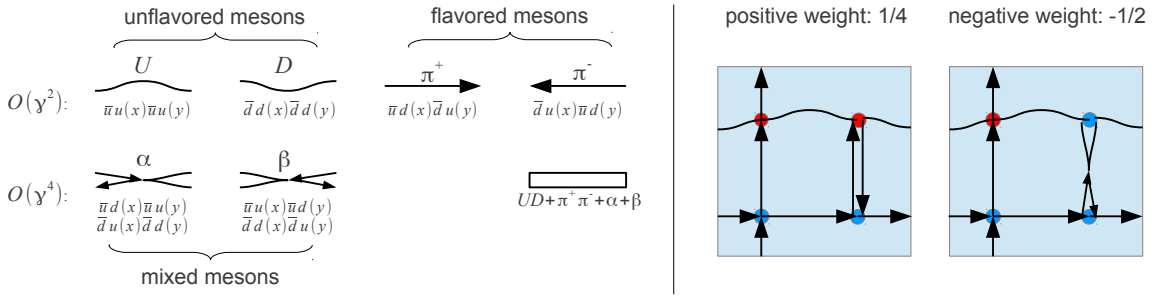

Figure 3: Left: definition of unflavored, flavored, and mixed dimers. Right: 2x2 sample configurations with positive and negative weight.

with $X = tr(mm^\dagger) = U+D+\pi^+ +\pi^-$ the sum of $N_\mathrm{f} = 2$ *unflavored* (U=$\bar{u}u$ and D=$\bar{d}d$) and $N_\mathrm{f}(N_\mathrm{f}-1) = 2$ *flavored* mesons, $\Delta = \det(m) + \det(m^\dagger)$ the diquark+anti-diquark term, and $Z = \det(mm^\dagger) = X^2 - UD - \pi^+\pi^- + \alpha + \beta$ a mesonic term. Here, $\alpha = \bar{u}d_x\bar{d}u_x\bar{u}u_y\bar{d}d_y$ and $\beta = \bar{u}u_x\bar{d}d_x\bar{u}d_y\bar{d}u_y$ are the potentially problematic contributions, which correspond to the mixing of UD and $\pi^+\pi^-$ dimer pairs (obtained via non-trivial Wick-contractions), as illustrated Fig. 3. In particular, if a configuration contains an odd number of α or β links, according to the Grassmann constraint (see [7]) the configuration has a negative sign. The essential feature of the continuous Euclidean time formulation is that multiple spatial dimers, and hence also α and β spatial dimers, are suppressed. They can only enter in static lines, where they can be resummed with other static lines so that the sign problem disappears completely. Combining time-like dimers of alternating orders is analogous to the procedure discussed in the $N_\mathrm{f} = 1$ case [8]: Chains of alternating orders $\mathscr{O}(\gamma^{2k}) \times \mathscr{O}(\gamma^{2N_\mathrm{c}N_\mathrm{f}-2k})$ are resummed in a way consistent with the constraint Eq. (2.3). This gives rise to new conserved quantum numbers: the spin is now composed of N_f separate spins $S^z = \sum_{f=1}^{N_\mathrm{f}} S^z_f \in \{-N_\mathrm{f}N_\mathrm{c}/2, \ldots N_\mathrm{f}N_\mathrm{c}/2\}$, with $S^z_f \in \{-N_\mathrm{c}/2, \ldots N_\mathrm{c}/2\}$ each being conserved, and we also get $N_\mathrm{f}(N_\mathrm{f}-1)/2$ charges $Q_i \in \{-N_\mathrm{c}, \ldots, +N_\mathrm{c}\}$. In the specific case of two flavors ($f = U, D$ and $Q_1 = Q^\pm_\pi$), the spins S_U, S_D can be replaced by S^z and $Q_I = S^z_U - S^z_D \in \{-N_\mathrm{c}, \ldots, +N_\mathrm{c}\}$ which may be viewed as isospin. Here, we find in total 19 types of states, as illustrated in Fig. 4.[2] The state vector and the transition rules at spatial dimers are given by

$$\chi = \bigotimes_{\vec{x}\in V} \left| \{S^z_f(\vec{x})\}_{f=1,\ldots N_\mathrm{f}}, \{Q_i(\vec{x})\}_{i=1,\ldots N_\mathrm{f}(N_\mathrm{f}-1)/2} \right\rangle, \qquad |\Delta S^z| = 1 \quad \text{and} \quad \sum_i |\Delta Q_i| \in \{0,1\}. \tag{5.2}$$

The Hamiltonian for $N_\mathrm{f} = 2$ is now a sum of four contributions, implementing these transition rules:

$$\hat{H} = \frac{1}{2} \sum_{\langle \vec{x},\vec{y} \rangle} \left(J^+_{U(\vec{x})} J^-_{U(\vec{y})} + J^+_{D(\vec{x})} J^-_{D(\vec{y})} + J^+_{\pi^+(\vec{x})} J^-_{\pi^+(\vec{y})} + J^+_{\pi^-(\vec{x})} J^-_{\pi^-(\vec{y})} + h.c. \right) \tag{5.3}$$

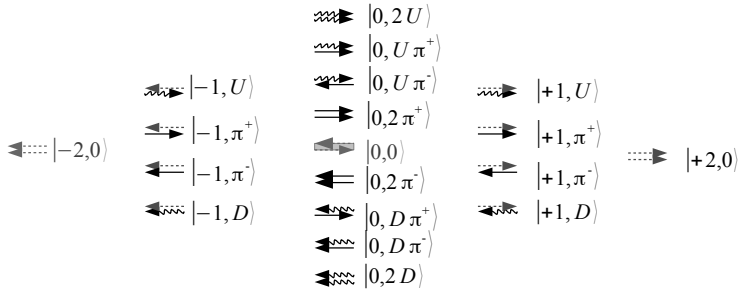

Figure 4: Classification of all static lines for U(2) based on "spin" quantum number and particle content. Each static line consists of two arrows, dashed arrows denoting spin, curly arrows denoting flavor-neutral mesons content, and solid arrows denoting charged mesons.

[2] For SU(2) we also have 3 kinds of diquarks, *uu*, *dd* and *ud*, which are not suppressed in the CT-limit. To avoid this complication, for $N_\mathrm{c} = 2$ we restrict to U(2). For $N_\mathrm{c} = 3$ this restriction is not necessary.

The absorption $J^+_{\pi_i}$, and emission $J^-_{\pi_i}$ operators can be represented as 19×19 lower left/upper right triangular matrices, where the entries are again given by vertex weights: $v_{\hat{\pi}_i} = \frac{1}{\sqrt{2}}$ if states with $S = 0$ and $|Q| = 1$ are connected to the vertex, $v_{\pi_i} = 1$ otherwise. This Hamiltonian can be used in the SSE algorithm to obtain results on the chiral phase transition. Our preliminary $N_\mathrm{f} = 2$ results are compared to mean field predictions in Tab. 1.

N_c	$N_\mathrm{f} = 1$	$N_\mathrm{f} = 2$
1	$3/2$ [1.102(1)]	$5/5$ [0.77(1)]
2	$4/2$ [1.467(1)]	$6/5$ [1.04(1)]
3	$5/2$ [1.884(1)]	$7/5$

Table 1: Comparison of the critical temperature aT_c between mean field results and Monte Carlo results [in brackets] for U(N_c) gauge groups. The new results are in column $N_\mathrm{f} = 2$. The MC value for $N_\mathrm{f} = 2$, U(3) has not been measured yet.

6. Conclusion

We have given a new, Hamiltonian formulation of strong coupling lattice QCD with staggered fermions in the chiral limit. It is based on the insight that strong coupling lattice QCD in the continuous time limit is analogous to a spin system. A new observable, the spin susceptibility, turns out to be sensitive to the chiral transition. Also, the Hamiltonian description allows to apply quantum Monte Carlo methods. In [8] we have studied 1-flavor thermodynamics via the continuous time Worm algorithm. Here, we make the first step towards 2-flavor simulations, by making use of Stochastic Series Expansion, a diagrammatic Monte Carlo technique which we generalize to the Hamiltonian in question. SSE has the advantage that more complicated Hamiltonians can be studied with ease. The drawback of SSE, in contrast to the continuous time Worm, is that we do not know of a way to obtain the two-point function for free. For the computation of the specific heat, the performance of both algorithms is quite similar. We have provided first results on the U(2) transition with two flavors. The extension to SU(3) with finite baryon chemical potential is more involved: the number of static lines increases to 44 in the mesonic sector.

7. Acknowledgments

The computations have been carried out on the Brutus cluster at the ETH Zürich. This work is supported by the Swiss National Science Foundation under grant 200020-122117.

References

[1] P. de Forcrand, M. Fromm, *Phys. Rev. Lett.* **104** (2010) 112005.

[2] P. de Forcrand, *PoS (LAT2009) 010* (2009), *arXiv:1005.0539*.

[3] P. Rossi, U. Wolff, *Nucl. Phys. B* **248** (1984) 105.

[4] F. Karsch, K. H. Mütter, *Nucl. Phys. B* **313** (1989) 541.

[5] D. H. Adams and S. Chandrasekharan, *Nucl. Phys. B* **662** (2003) 220.

[6] P. H. Damgaard, D. Hochberg and N. Kawamoto, Phys. Lett. B **158** (1985) 239.
N. Bilic, F. Karsch, K. Redlich, *Phys. Rev. D* **45** (1992) 3228.
A. Ohnishi, T. Ichihara and T. Z. Nakano, arXiv:1211.2282 [hep-lat].

[7] M. Fromm, *PhD Thesis* (2010) "Lattice QCD at strong coupling: thermodynamics and nuclear physics", ETH Zürich. [http://e-collection.library.ethz.ch/view/eth:2616]

[8] W. Unger, P. de Forcrand, PoS (Lattice 2011) 218 *arXiv:1111.1434*.

[9] B. B. Beard, U. J. Wiese, *Phys. Rev. Lett.* **77** (1996) 5130.

[10] A. W. Sandvik, *Phys. Rev. B* **59** (1999) R14157.

[11] K. E. Eriksson, N. Svartholm and B. S. Skagerstam, *J. Math. Phys. 22* **2276** (1981) 2276

C.4 Temporal Correlators in the Continuous Time Formulation of Strong Coupling Lattice QCD [C4]

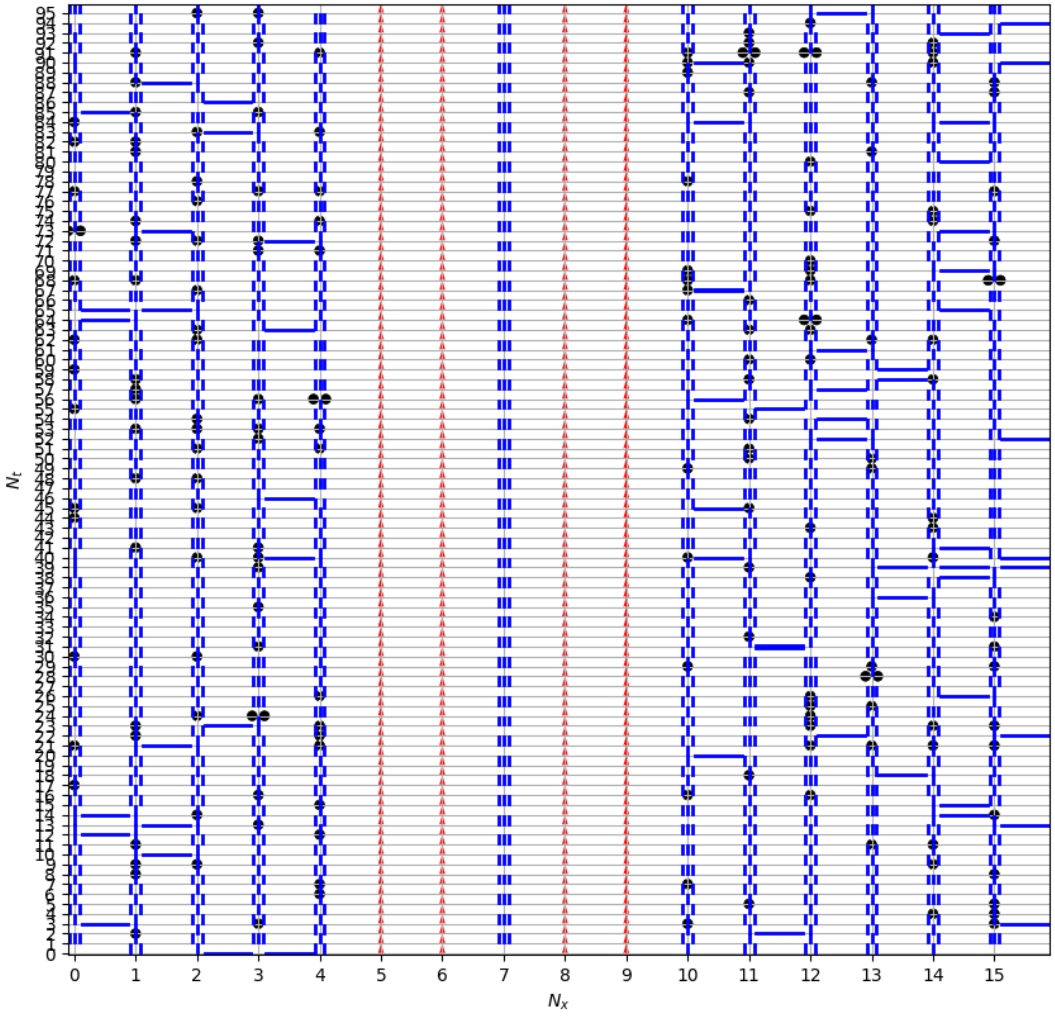

PROCEEDINGS OF SCIENCE

Temporal Correlators in the Continuous Time Formulation of Strong Coupling Lattice QCD

Marc Klegrewe*
Bielefeld University
E-mail: mklegrewe@physik.uni-bielefeld.de

Wolfgang Unger
Bielefeld University
E-mail: wunger@physik.uni-bielefeld.de

We present results for lattice QCD in the limit of infinite gauge coupling on a discrete spatial but continuous Euclidean time lattice. A worm type Monte Carlo algorithm is applied in order to sample two-point functions which gives access to the measurement of mesonic temporal correlators. The continuous time limit, based on sending $N_\tau \to \infty$ and the bare anistotropy to infinity while fixing the temperature in a non-perturbative setup, has various advantages: the algorithm is sign problem free, fast, and accumulates high statistics for correlation functions. Even though the measurement of temporal correlators requires the introduction of a binning in time direction, this discretization can be chosen to be by orders finer compared to discrete computations. For different spatial volumes, temporal correlators are measured at zero spatial momentum for a variety of mesonic operators. They are fitted to extract the pole masses and corresponding particles as a function of the temperature. We conclude discussing the possibility to extract transport coefficients from these correlators.

The 36th Annual International Symposium on Lattice Field Theory - LATTICE2018
22-28 July, 2018
Michigan State University, East Lansing, Michigan, USA.

*Speaker.

1. Introduction

The determination of the full QCD phase diagram, in particular the location of the critical point, is an important, long standing problem, requiring non-perturbative methods. In lattice QCD, several approaches have been developed to investigate the phase transition from the hadronic matter to the quark gluon plasma, but all of them are limited to small $\frac{\mu_B}{T}$ [1]. The reason for this is the notorious sign problem, which arises because the fermion determinant for finite baryon chemical potential μ_B becomes complex, and importance sampling is no longer applicable. In QCD, the sign problem is severe. Dual representations oftentimes solve or milden sign problems as being the case in strong coupling QCD (SC-QCD). Here, first the gauge degrees of freedom are integrated out exactly, which allows replacing the Grassman integration by a sum over fermionic color singlets, resulting in a partition function being expressed as a gas of hadron world lines (c.f. monomer-dimer system [2]). This representation allows us to obtain the full (μ_B, T) phase diagram, and it shares important features of QCD such as confinement and spontaneous chiral symmetry breaking and its restoration at a transition temperature T_c [3]. Moreover, the chiral limit can be studied very economically – simulations are faster than with a finite quark mass. The Continuous Euclidean Time limit with its many assets (c.f. chap. 4) was first proposed to be applied to quantum field theories by Beard and Wiese [4]. Here, we use it to remove the sign problem completely.

2. Strong Coupling QCD

In SC-QCD, the gauge coupling is sent to infinity and hence the coefficient of the plaquette term $\beta = 6/g^2$ is sent to zero. Thus, the Yang Mills part $F_{\mu\nu}F_{\mu\nu}$ is absent. Subsequently, the gauge fields in the covariant derivative can be integrated out analytically. However, as a consequence of the SC-limit, the lattice spacing a becomes very coarse, and no continuum limit can be achieved. We consider the SC-limit for staggered fermions. The final partition function for the discrete system on a ${N_\sigma}^3 \times N_\tau$ lattice, after performing the Grassmann integrals analytically, is given by

$$\mathscr{Z}(\gamma, N_\tau, m_q) = \sum_{\{k,n,\ell\}} \prod_{b=(x,\hat{\mu})} \frac{(N_c - k_b)!}{N_c! k_b!} \gamma^{2k_b \delta_{\hat{0},\hat{\mu}}} \prod_x \frac{N_c!}{n_x!} (2am_q)^{n_x} \prod_l w(\ell, \mu) \tag{2.1}$$

$$\text{Grassmann constraint:} \quad n_x + \sum_{\hat{\mu}=\pm\hat{0},\ldots\pm\hat{d}} \left(k_{\hat{\mu}}(x) + \frac{N_c}{2} |\ell_\mu(x)| \right) = N_c, \quad \forall x \in {N_\sigma}^3 \times N_\tau \tag{2.2}$$

$$w(\ell, \mu) = \sigma(\ell) \gamma^{N_c \Sigma_x |\ell_0(x)|} \exp\left(N_c N_\tau r(\ell) a_\tau \mu\right), \qquad \sigma(\ell) = (-1)^{r(\ell)+N_-(\ell)+1} \prod_{b=(x,\hat{\mu})\in\ell} \eta_{\hat{\mu}}(x) \tag{2.3}$$

where γ is the bare anisotropy coupling. After this exact rewriting of the strong coupling partition function the system is described by confined, colorless, discrete degrees of freedom:

- Mesonic degrees of freedom $k_{\hat{\mu}}(x) \in \{0, \ldots N_c\}$ (non-oriented meson hoppings called dimers) and $n(x) \in \{0, \ldots Nc\}$ (mesonic sites called monomers).
- Baryonic degrees of freedom, which form oriented baryon loops ℓ with sign $\sigma(\ell) = \pm 1$ and winding number $r(\ell)$ that depend on the geometry of the loops Eq. (2.3). These loops are self-avoiding and do not touch the mesonic degrees of freedom.

Both mesonic and baryonic degrees of freedom obey the Grassmann constraint Eq. (2.2). Monomers are absent since we will restrict to the chiral limit $m_q = 0$.

3. Anisotropic lattices

On a bipartite lattice with staggered fermions an even number of lattice points is required in all directions. Thus, the highest temperature that is possible to be addressed on an isotropic lattice is $aT = 1/N_\tau = 0.5$, with N_τ the temporal extent. This is significantly too low to reach the critical temperature of chiral restoration. So, in practice, anisotropic lattices are chosen to study thermodynamical properties of staggered lattice QCD, in particular across the chiral phase transition. The anisotropy parameter $\xi = \frac{a}{a_\tau}$ is introduced into the definition of the lattice temperature

$$T = \frac{1}{a_\tau N_\tau} = \frac{\xi(\gamma)}{aN_\tau}. \tag{3.1}$$

which allows to assign different extents in spatial and temporal direction and thus, to modify the temperature continuously even above the chiral transition. ξ becomes unity when the lattice is isotropic and diverges in the CT limit $a_\tau \to 0$. As highlighted in Eq. (3.1) the anisotropy parameter depends on the bare anisotropy coupling γ. However, the exact functional correspondence is unknown. Recent non-perturbative studies [5] suggest that

$$\xi(\gamma) \simeq \kappa\gamma^2 + \frac{\gamma^2}{1+\lambda\gamma^4}, \quad \kappa = 0.781(1) \text{ for SU(3)}. \tag{3.2}$$

Further simplification is achieved by eliminating γ and N_τ, and to replace them by the temperature aT completely. This is summarized in the continuum limit in Euclidean time:

$$N_\tau \to \infty, \qquad \gamma \to \infty, \qquad \kappa\gamma^2/N_\tau \equiv aT \text{ fixed}. \tag{3.3}$$

Here, $\kappa\gamma^2/N_\tau$ represents the temperature aT in a well defined setup. Only one parameter is left that sets the thermal properties, and all discretization errors introduced by a finite N_τ are removed.

4. Continuous Time Limit and worm algorithm

Designing an algorithm that operates in the continuous time (CT) limit will have several advantages: Since there is no need to perform the continuum extrapolation $N_\tau \to \infty$, critical temperatures can be estimated more precisely, with a faster algorithm which only depends on one parameter, the temperature T. Moreover, ambiguities arising from the functional dependence of observables on the anisotropy parameter will be circumvented. Also in the baryonic part of the partition function great simplifications occur: Baryons become static in the CT limit for $N_c \geq 3$, hence, the sign problem is completely absent. The CT partition function is obtained by the joined limit γ and $N_\tau \to \infty$ and includes:

- dimer contributions of Eq. (2.1) are factorized into a spatial and temporal part and $\mathscr{Z}(\gamma, N_\tau)$ is rewritten such that spatial dimers obtain a weight γ^{-2} [6].
- the limit $\gamma \to \infty$ implies that configurations with only zero or single spatial dimers contribute while configurations with multiple spatial dimers are considered to be suppressed.
- configurations are characterized fully by dimers in the zero time slice $k_0(0) \in \{0, \ldots N_c\}$ and bonds occupied by single spatial dimers which form vertices. Intervals between vertices have a weight of one and are omitted.

- the limit $N_\tau \to \infty$ removes lattice artifacts in a_τ completely. Due to the even-odd decomposition there are $\frac{N_\tau}{2}$ positions available to distribute an oriented spatial dimer which gives rise to the factor $\frac{1}{2aT}$ in Eq. (4.1).

Finally, a merely T dependent partition function is obtained

$$\begin{aligned}(N_c = 3): \qquad \mathscr{Z}(T) &= \sum_{k\in 2\mathbb{N}} \left(\frac{1}{2aT}\right)^k \sum_{\mathscr{G}'\in\Gamma_k} e^{\mu_B B/T}\, \hat{v}_\perp^{N_\perp} \quad \text{with } \hat{v}_\perp^{N_\perp} = 2/\sqrt{3} \\ \text{and } k &= \sum_{b=(x,\hat{\imath})} k_b = \frac{N_\llcorner + N_\perp}{2}, \quad N_{\llcorner/\perp} = \sum_x n_{\llcorner/\perp}(x)\end{aligned} \tag{4.1}$$

with the baryon number B, a non-trivial vertex weight $\hat{v}_\perp^{N_\perp}$, the number of $L/T-$shaped vertices $N_\llcorner/N_\perp$ and Γ_k being the set of equivalence classes $\mathscr{G}'$ of graphs containing a total number k of spatial hoppings, equivalent up to time shifts of the vertices.

Now, to sample this CT partition function a worm type algorithm is used, similar to the directed path algorithm introduced for SC-QCD in [7]. In analogy to the decomposition of the lattice into active and passive sites, we decompose the lattice into emission and absorption sites. By definition the worm tail is located at an absorption site and violates Eq. (2.2). As a consequence, the worm head propagates through the lattice and restores (violates) the constraint in turns while visiting emission (absorption) sites respectively. During propagation the worm head either stops at an absorption site connected to a spatial dimer or emits a spatial dimer after some distance $\Delta\beta$ established by a Poisson process. The Poisson process assures that the oriented vertices, which always connect an emission and an absorption site, are exponentially distributed

$$P(\Delta\beta) = \exp(-\lambda\Delta\beta), \quad \Delta\beta \in [0, \beta = 1/aT], \quad \lambda = d_M(x,t)/4, \quad d_M(x,t) = 2d - \sum_{\hat{\mu}} n_B(x+\hat{\mu})$$

with λ the "decay constant" for spatial dimer emissions. Due to the presence of baryons, λ is space-time dependent, with $d_M(x,t)$ being the number of mesonic neighbors at a given coordinate. Throughout the worm evolution monomer-monomer two-point correlation functions are accumulated whenever the Grassmann constraint is restored by taking into account the respective positions of worm tail and head:

$$C(t_H - t_T, \vec{x}_H - \vec{x}_T) = C(\tau,\vec{x}) = N_c \frac{O(C(\tau,\vec{x}))}{\#\text{worm updates}}. \tag{4.2}$$

Such worm estimators are incremented as $O(C(\tau,\vec{x})) \to O(C(\tau,\vec{x})) + f(\dots)\cdot\delta_{x_T,x_1}\delta_{x_H,x_2}$ with

$$\begin{aligned}\text{discrete time: } f(\gamma), \quad \tau \in [0,\dots N_\tau] \\ \text{continuous time: } f(T), \quad \tau \in [0,\dots 1/T].\end{aligned} \tag{4.3}$$

By summing over them yields immediately the chiral susceptibility:

$$\chi_{\sigma,DT} = \frac{1}{V}\sum_{\vec{x},\tau} C(\tau,\vec{x}) \quad \text{and} \quad \chi_{\sigma,CT} = \frac{1}{V}\sum_{\vec{x}} \int_0^{1/T} d\tau\, C(\tau,\vec{x}). \tag{4.4}$$

5. Temporal Correlators

As for temporal correlators in CT, the increment $f(T)$ of Eq. (4.3) is spread out to bins across the path covered by the worm head in temporal direction. Thus, even for the CT algorithm a discretization is

Table 1: The sign g_x^D defined in Eq. (5.1) yields different correlators for the kernel ($\Gamma^D \otimes \Gamma^F, \Gamma^D = \Gamma^{F*}$). Corresponding continuum and particle states for N_f=1 are named.

g_x^D	$\Gamma^D \otimes \Gamma^F$		J^{PC}		Physical states	
	NO	O	NO	O	NO	O
1	$1 \otimes 1$	$\gamma_0\gamma_5 \otimes (\gamma_0\gamma_5)^*$	0^{++}	0^{-+}	σ_S	π_A
$(-1)^{x_i}$	$\gamma_i\gamma_5 \otimes (\gamma_i\gamma_5)^*$	$\gamma_i\gamma_0 \otimes (\gamma_i\gamma_0)^*$	1^{++}	1^{--}	a_A	ρ_T
$(-1)^{x_j+x_k}$	$\gamma_j\gamma_k \otimes (\gamma_j\gamma_k)^*$	$\gamma_i \otimes \gamma_i^*$	1^{+-}	1^{--}	b_T	ρ_V
$(-1)^{x_i+x_j+x_k}$	$\gamma_0 \otimes \gamma_0^*$	$\gamma_5 \otimes (\gamma_5)^*$	0^{+-}	0^{-+}	$-V$	π_{PS}

introduced, however, it can be chosen by orders finer in comparison to a discrete time lattice extent. It is distinguished between two different histograms, either with even (absorption-absorption) or odd (absorption-emission) temporal distance contributions. Combinations of these histograms allow to construct correlators for the Non-Oscillating (NO) and Oscillating (O) channel. Additionally, by including the sign g_x^D listed in Table 1 various states are addressed for $N_f = 1$. Since temporal correlators at zero spatial momentum are measured, the extracted meson masses are pole masses ($E_0(\vec{p} = 0) = m_0$). The respective correlators are expressed as a sum over the staggered fermion fields $\bar{\chi}_x\chi_x$ with a diagonal dirac-taste kernel ($\Gamma^D = \Gamma^{F*}$), that is realized by the signs g_x^D:

$$C(t) = \sum_{\vec{x}} \langle \bar{\chi}_0\chi_0\bar{\chi}_{\vec{x},t}\chi_{\vec{x},t}\rangle \cdot g_x^D. \tag{5.1}$$

Hereafter, the workflow for continuous time pole mass extraction as well as discrete time is highlighted and results are compared. In order to obtain discrete time temporal correlators the even and odd histograms are fitted via a four parameter ansatz respectively:

$$\begin{aligned} C_{\mathrm{DT,Even}}(\tau) &= a_{NO}\cosh(m_{NO}(\tau - N_\tau/2)) - a_O\cosh(m_O(\tau - N_\tau/2) \\ C_{\mathrm{DT,Odd}}(\tau) &= \underbrace{a_{NO}\cosh(m_{NO}(\tau - N_\tau/2))}_{\text{Non-oscillating Correlator}} + \underbrace{a_O\cosh(m_O(\tau - N_\tau/2)}_{\text{Oscillating Correlator}}. \end{aligned} \tag{5.2}$$

A combined fit to simultaneously describe both data sets is possible, but more challenging when it comes to fit convergence. Finally, by addition/subtraction the correlators are as follows:

$$C_{\mathrm{DT,NO}}(\tau) = \frac{1}{2}\left(C_{\mathrm{DT,Even}}(\tau) + C_{\mathrm{DT,Odd}}(\tau)\right), \quad C_{\mathrm{DT,O}}(\tau) = \frac{1}{2}\left(C_{\mathrm{DT,Even}}(\tau) - C_{\mathrm{DT,Odd}}(\tau)\right). \tag{5.3}$$

Note that in discrete time only histogram data sets are described by the fits as presented in Fig. (1a), however, the final constructed correlators are not. Now, these fits have to be performed for various N_τ (c.f. Fig. (1b)) such that an appropriate $N_\tau \to \infty$ extrapolation can be carried out (c.f. Fig. (1d)). Finally, this workflow is necessary for the different channels and multiple temperatures. In comparison, the added and subtracted histograms out of continuous time simulations

$$\begin{aligned} C_{\mathrm{CT,O}}(\tau) = a_{NO}\cosh(m_{NO}(\tau - 1/2)) &= \frac{1}{2}(C_{\mathrm{Odd}}(\tau) + C_{\mathrm{Even}}(\tau)) \\ C_{\mathrm{CT,NO}}(\tau) = a_O\cosh(m_O(\tau - 1/2)) &= \frac{1}{2}(C_{\mathrm{Odd}}(\tau) - C_{\mathrm{Even}}(\tau)) \end{aligned} \tag{5.4}$$

give directly rise to the (Non)-Oscillating correlators respectively and are fitted in accordance with Eq. (5.4) as shown in Fig. (1c). The resulting pole masses are measured in M/T. Finally, Fig. (2a) shows a com-

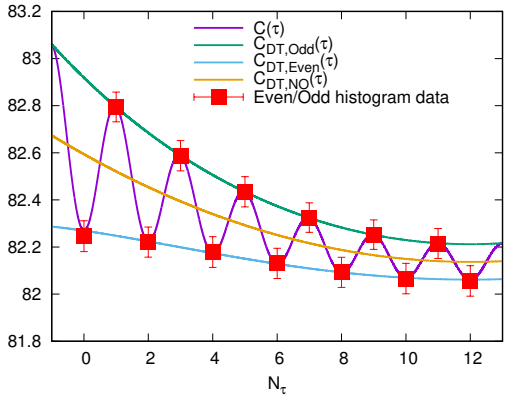

(1a) Histogram data fitted by several approaches, leading to the constructed correlator $C_{DT,NO}(\tau)$.

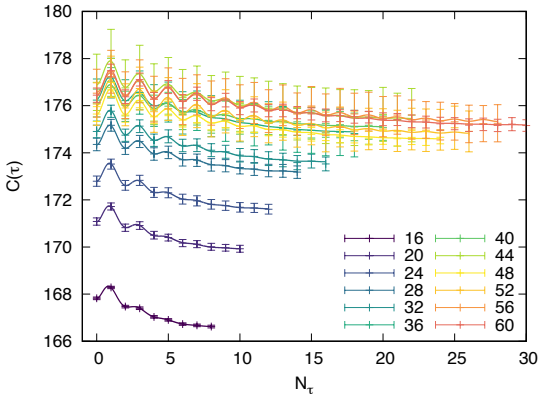

(1b) Histogram data fits for multiple temporal extension ranging from $N_\tau = 16$ to $N_\tau = 60$.

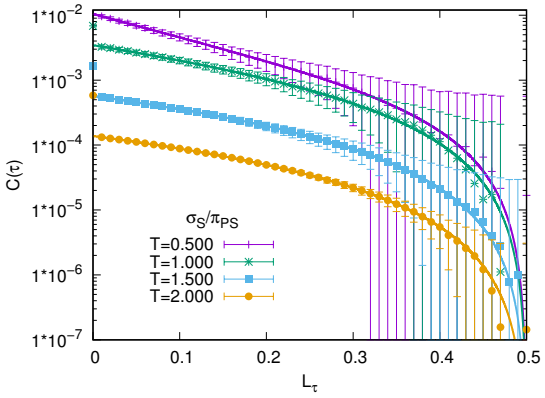

(1c) Continuous time histogram data fitted according to Eq. (5.4) for the mass degenerated channels σ_S/π_{PS}.

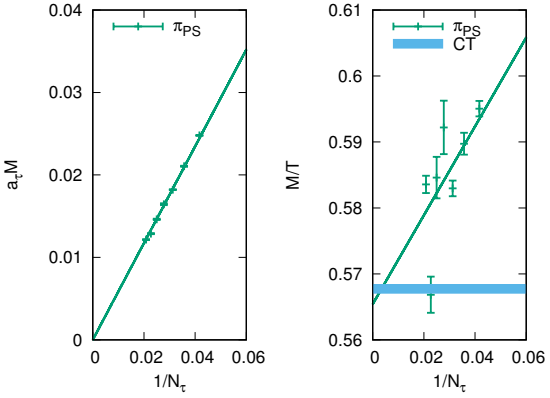

(1d) Extrapolated masses from discrete time simulations. Rescale to units of M/T and compare with continuous time simulation result (blue band).

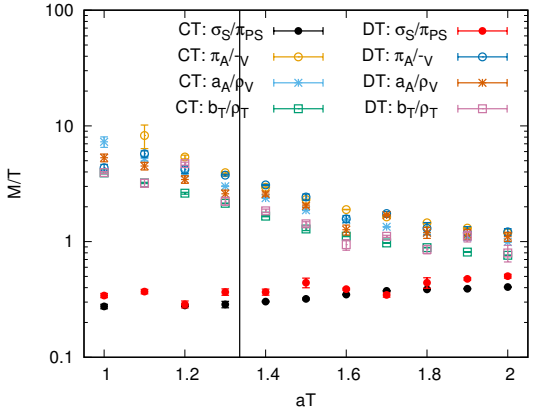

(2a) M/T for different temepratures aT and channels measures either in CT or DT. Certain channels listed in (5.5) are mass degenerated. Agreement between CT and DT is visible.

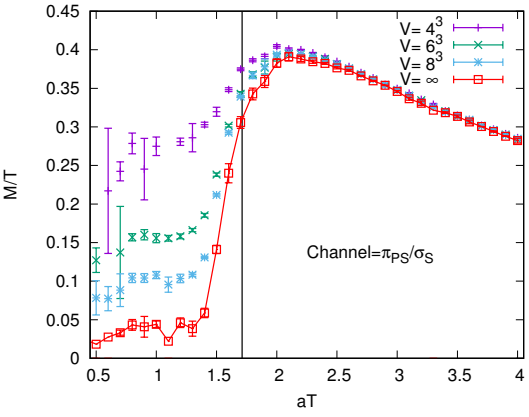

(2b) M/T over aT for different volumes but the same channel π_{PS}/σ_S. The continuum extrapolated red curve supports the expectations to have a zero mass below T_c for simulations in the chiral limit.

parison of the extrapolated masses. For SU(3) the chiral transition is located at $aT \approx 1.403$ where indeed an impact on the masses is obtained. So far, only a small temperature range $aT = \{1.0, \ldots 2.0\}$ is studied since especially small temperatures are expensive and simulations with reliable outcome are presented in the future. Simulations performed in discrete and continuous time give consistent results. Currently, there are still larger fluctuations and errorbars present in the discrete data. On the contrary, continuous time results have a smoother behavior down to the chiral transition but then more statistics and simulation time is needed. For $N_f = 1$ we find a mass degeneracy for the channel pairs:

$$\sigma_S \leftrightarrow \pi_{PS} \qquad \pi_A \leftrightarrow -V \qquad b_T(\gamma_j\gamma_k) \leftrightarrow \rho_T(\gamma_i\gamma_0) \qquad a_A(\gamma_i\gamma_5) \leftrightarrow \rho_V(\gamma_i). \tag{5.5}$$

Since simulations are performed in the chiral limit in a finite volume ($\varepsilon-$-regime) the mass degeneracy of the Non-Oscillating scalar channel with the Oscillating pseudo-scalar channel is expected. Due to finite volume effects non-zero M/T values are obtained also in the regime below T_c, however, a first continuum extrapolation in Fig. (2b) clearly corrects this towards $M/T \to 0$.

6. Conclusion

With the CT worm algorithm we measured monomer-monomer two-point correlation functions and constructed temporal correlators with projected zero spatial momentum. For a temperature range around the chiral transition we obtain consistent pole mass results for discrete and continuous time simulations. Due to simulations being tremendously more expensive for small temperature further analysis is in progress.

The zero momentum meson correlators can be used to calculate the diffusion constant by extracting the spectral function from the correlation data applying standard methods like MEM. In continuous time we profit from being able to choose the temporal discretization by orders finer compared to discrete time computations.

Future calculations will be performed for finite quark masses, multiple flavors by making use of a Hamiltonian formulation [8] which will control and remove the sign problem and finally by including β-corrections to move away from the strong coupling limit.

7. Acknowledgments

Numerical simulations were performed on the OCuLUS cluster at PC2 (Universität Paderborn). We acknowledge support by the Deutsche Forschungsgemeinschaft (DFG) through the Emmy Noether Program under Grant No. UN 370/1 and through the Grant No. CRC-TR 211 “Strong-interaction matter under extreme conditions”.

References

[1] P. de Forcrand, PoS LATTICE **2009** (2009) 010 [arXiv:1005.0539 [hep-lat]].
[2] P. Rossi, U. Wolff, Nucl. Phys. B **248** (1984) 105.
[3] P. de Forcrand, M. Fromm, Phys. Rev. Lett. **104** (2010) 112005.
[4] B. B. Beard and U.-J. Wiese, Phys. Rev. Lett. **77** (1996) 5130.
[5] P. de Forcrand, W. Unger and H. Vairinhos, Phys. Rev. D **97** (2018) no.3, 034512 [arXiv:1710.00611 [hep-lat]].
[6] W. Unger and P. de Forcrand, PoS LATTICE **2011** (2011) 218 [arXiv:1111.1434 [hep-lat]].
[7] D. H. Adams, S. Chandrasekharan, Nucl. Phys. B **662** (2003) 220.
[8] W. Unger and P. de Forcrand, PoS LATTICE **2012** (2012) 194 [arXiv:1211.7322 [hep-lat]].